NORTH ATLANTIC TREATY
ORGANIZATION

SCIENCE AND TECHNOLOGY
ORGANIZATION

AC/323(AVT-282)TP/974

www.sto.nato.int

STO TECHNICAL REPORT **TR-AVT-282**

Unsteady Aerodynamic Response of Rigid Wings in Gust Encounters

(Réponse aérodynamique instationnaire des ailes rigides confrontées à des rafales de vent)

Transverse, streamwise, and vortex gust encounters strong enough to result in large-scale flow separation and large force transients are investigated.

Published October 2020

Distribution and Availability on Back Cover

NORTH ATLANTIC TREATY
ORGANIZATION

SCIENCE AND TECHNOLOGY
ORGANIZATION

AC/323(AVT-282)TP/974

www.sto.nato.int

STO TECHNICAL REPORT **TR-AVT-282**

Unsteady Aerodynamic Response of Rigid Wings in Gust Encounters

(Réponse aérodynamique instationnaire des ailes rigides confrontées à des rafales de vent)

Transverse, streamwise, and vortex gust encounters strong enough to result in large-scale flow separation and large force transients are investigated.

The NATO Science and Technology Organization

Science & Technology (S&T) in the NATO context is defined as the selective and rigorous generation and application of state-of-the-art, validated knowledge for defence and security purposes. S&T activities embrace scientific research, technology development, transition, application and field-testing, experimentation and a range of related scientific activities that include systems engineering, operational research and analysis, synthesis, integration and validation of knowledge derived through the scientific method.

In NATO, S&T is addressed using different business models, namely a collaborative business model where NATO provides a forum where NATO Nations and partner Nations elect to use their national resources to define, conduct and promote cooperative research and information exchange, and secondly an in-house delivery business model where S&T activities are conducted in a NATO dedicated executive body, having its own personnel, capabilities and infrastructure.

The mission of the NATO Science & Technology Organization (STO) is to help position the Nations' and NATO's S&T investments as a strategic enabler of the knowledge and technology advantage for the defence and security posture of NATO Nations and partner Nations, by conducting and promoting S&T activities that augment and leverage the capabilities and programmes of the Alliance, of the NATO Nations and the partner Nations, in support of NATO's objectives, and contributing to NATO's ability to enable and influence security and defence related capability development and threat mitigation in NATO Nations and partner Nations, in accordance with NATO policies.

The total spectrum of this collaborative effort is addressed by six Technical Panels who manage a wide range of scientific research activities, a Group specialising in modelling and simulation, plus a Committee dedicated to supporting the information management needs of the organization.

• AVT	Applied Vehicle Technology Panel
• HFM	Human Factors and Medicine Panel
• IST	Information Systems Technology Panel
• NMSG	NATO Modelling and Simulation Group
• SAS	System Analysis and Studies Panel
• SCI	Systems Concepts and Integration Panel
• SET	Sensors and Electronics Technology Panel

These Panels and Group are the power-house of the collaborative model and are made up of national representatives as well as recognised world-class scientists, engineers and information specialists. In addition to providing critical technical oversight, they also provide a communication link to military users and other NATO bodies.

The scientific and technological work is carried out by Technical Teams, created under one or more of these eight bodies, for specific research activities which have a defined duration. These research activities can take a variety of forms, including Task Groups, Workshops, Symposia, Specialists' Meetings, Lecture Series and Technical Courses.

The content of this publication has been reproduced directly from material supplied by STO or the authors.

Published October 2020

ISBN 978-92-837-2295-3

Table of Contents

Chapter 3 – High-Fidelity Computational Simulation of Transverse Gusts 3-1

Chapter 4 – Force Prediction During Transverse and Vortex Gust Encounters 4-1

Chapter 5 – Non-Circulatory Force on a Finite Thickness Body Encountering a Gust 5-1

List of Figures

List of Tables

AVT-282 Membership List

CO-CHAIRS

Prof. Dr. Oksan CETINER-YILDIRIM*
Istanbul Technical University
TURKEY
Email: cetiner@itu.edu.tr

Dr. Anya JONES*
University of Maryland
UNITED STATES
Email: arjones@umd.edu

MEMBERS

Mr. Ignacio ANDREU-ANGULO*
University of Cambridge
UNITED KINGDOM
Email: ia347@cam.ac.uk

Prof. Holger BABINSKY*
University of Cambridge
GERMANY
Email: hb@eng.cam.ac.uk

Dr. Siva BANDA
US Air Force Research Lab
UNITED STATES
Email: siva.banda@us.af.mil

Mr. Simon CORKERY
University of Cambridge
UNITED KINGDOM
Email: sjc276@cam.ac.uk

Dr. Julian DEPARDAY*
EPFL
FRANCE
Email: julien.deparday@epfl.ch

Dr. Brendan EPPS
Thayer School of Engineering
UNITED STATES
Email: brenden.epps@dartmouth.edu

Mr. Dominique FARCY
ONERA
FRANCE
Email: dominique.farcy@onera.fr

Dr. John FARNSWORTH
University of Colorado Boulder
UNITED STATES
Email: john.farnsworth@colorado.edu

Mr. Manuel GARCIA-VILLALBA*
Universidad Carlos III de Madrid
SPAIN
Email: manuel.garcia-villalba@uc3m.es

Mr. Pascal GEHLERT*
University of Cambridge
GERMANY
Email: pg469@cam.ac.uk

Mr. Sebastian GIERSCH
Universitaet Hannover
GERMANY
Email: giersch@muk.uni-hannover.de

Dr. Arif Cem GOZUKARA*
Aselsan Inc.
TURKEY
Email: cgozukar@aselsan.com.tr

Dr. Justin JAWORSKI*
Lehigh University
UNITED STATES
Email: jaworski@lehigh.edu

Dr. Francis LAGOR
University at Buffalo – The State University of New York
UNITED STATES
Email: flagor@buffalo.edu

---

*Author

**Supporting Author

Dr. Philippe LAVOIE
University of Toronto
CANADA
Email: lavoie@utias.utoronto.ca

Dr. Albert MEDINA*
UNITED STATES
Email: alberto.medina.3@us.af.mil

Dr. Karen MULLENERS*
EPFL
BELGIUM
Email: karen.mulleners@epfl.ch

Dr. Flavio NOCA
University of Applied Sciences of Western Switzerland
SWITZERLAND
Email: flavio.noca@hesge.ch

Dr. Michael OL
Air Force Research Lab, AFRL/VAAA
UNITED STATES
Email: michael.ol@us.af.mil

Prof. Dominique POIREL
Royal Military College of Canada
CANADA
Email: poirel-d@rmc.ca

Dr. Matthew RINGUETTE*
University at Buffalo – The State University of New York
UNITED STATES
Email: ringum@buffalo.edu

Dr. David E. RIVAL*
Queen's University
CANADA
Email: d.e.rival@queensu.ca

Dr. Richard SEMAAN*
Technical University of Braunschweig
GERMANY
Email: r.semaan@tu-bs.de

Dr. Carl SEQUEIRA
Hybrid Air Vehicles Limited
UNITED KINGDOM
Email: carl.sequeira@hybridairvehicles.net

Dr. Marilyn SMITH*
Georgia Institute of Technology
UNITED STATES
Email: marilyn.smith@ae.gatech.edu

Dr. Ignazio_Maria VIOLA
University of Edinburgh
ITALY
Email: i.m.viola@ed.ac.uk

Dr. Bastiaan WILLEM VAN OUDHEUSDEN
Delft University of Technology
NETHERLANDS
Email: b.w.vanoudheusden@tudelft.nl

Dr. Anna YOUNG*
University of Bath
UNITED KINGDOM
Email: amy32@bath.ac.uk

Dr. Weixing YUAN
National Research Council of Canada
CANADA
Email: weixing.yuan@nrc-cnrc.gc.ca

---

*Author

**Supporting Author

ADDITIONAL CONTRIBUTORS

Hülya BILER*
University of Maryland
UNITED STATES

Huansheng CHEN*
Lehigh University
UNITED STATES

Juhi CHOWDHURY*
University at Buffalo – The State University of New York
UNITED STATES

O. FLORES*
Karlsruhe Institute of Technology
GERMANY

Amanda GRUBB**
Georgia Institute of Technology
UNITED STATES

Guosheng HE**
École polytechnique fédérale de Lausanne
SWITZERLAND

Sabrina HENNE**
École polytechnique fédérale de Lausanne
SWITZERLAND

Daniel HEATHCOTE**
Georgia Institute of Technology
UNITED STATES

Matthew MARZANEK*
Queen's University
CANADA

M. MORICHE*
Karlsruhe Institute of Technology
GERMANY

Alex MOUSHEGIAN**
Georgia Institute of Technology
UNITED STATES

Johannes POHL*
Technical University of Braunschweig
GERMANY

Murat SARITAS**
Istanbul Technical University,
TURKEY

Girguis SEDKY*
University of Maryland
UNITED STATES

Cameron SMITH*
University at Buffalo – The State University of New York
UNITED STATES

Amanda SMYTH*
University of Bath
UNITED KINGDOM

David R. Williams*
Illinois Institute of Technology
UNITED STATES

Berk ZALOGLU**
Istanbul Technical University,
TURKEY

---

*Author

**Supporting Author

Unsteady Aerodynamic Response of Rigid Wings in Gust Encounters

(STO-TR-AVT-282)

Executive Summary

Modern air vehicle operations present a new challenge: controlled flight through highly unsteady aerodynamic environments. Many missions of interest, including cargo pickup/drop-off, reconnaissance, and search and rescue, must take place in unsteady aerodynamic environments. Operations such as unmanned reconnaissance, surveillance, and deliveries in urban environments, helicopter operations in complex terrain, and shipboard flight in airwakes are limited by strong transient wind gusts, coherent structures in air wakes, and other flow disturbances. All of these operations are, of course, regularly carried out today, but are currently limited to relatively benign flow disturbances and conservative operational envelopes. The AVT-282 task group was formed with the goal of extending the state of the art in unsteady lift modeling and prediction in support of the development of robust flight vehicle performance where wind gusts are of the same order of magnitude as the vehicle's flight speed, and where disturbance rejection may be achieved via closed-loop flow control. The focus of this group is on the effect of discrete wind gusts and transient flows on wing performance, and the fluid dynamics of a rigid wing's aerodynamic response to a known disturbance. The specific research goals of the group were to:

1) Identify the physical mechanisms by which force and moment transients are produced in large-amplitude gust encounters;
2) Develop analytical models to describe the resulting flows and predict aerodynamic forcing;
3) Identify mechanisms by which highly separated flows might be controlled to attenuate unsteady responses in a large-amplitude gust encounter; and
4) Characterize the magnitude and scales of real-world flow perturbations to define the parameter space over which a transient flow disturbance should be treated as a small perturbation, gust, or quasi-steady flow.

The group first set out to characterize the magnitude and length scales of real-world flow perturbations that would later define the gust encounter parameter space of interest. Using data from previous work in meteorology, flight in airwakes, rotorcraft, wind and tidal turbines, MAVs, UCAVs, vehicles in transition, etc., a parameter space of primary interest was defined as gusts with a length scale of the same order of magnitude as the wing chord, and with speeds of the same order of magnitude as the flight speed of the vehicle. Three canonical gust types were defined: transverse gusts, vortex gusts, and streamwise gusts; and a considerable amount of data were obtained. A typical aerodynamic response for all types of gusts studied consists of a rapid rise in lift to extreme values during the gust encounter with subsequent drop-off as the wing exits the gust. The lift transient experienced by the wing increases with gust strength and wing incidence. Simple predictions of the maximum lift can be derived from the effective angle of attack of the wing at the maximum gust speed, but more accurate and unsteady models of lift require much more nuance. Large transverse or vortex gusts result in massive flow separation, and thus force production is dominated by inviscid effects: circulation shed from the wing and free vorticity in the gust itself. Strong streamwise gusts do not necessarily result in flow separation and thus viscous forces play a larger role. Linear inviscid theories were found to provide reasonable predictions of lift response for gusts much larger than intended but failed in extreme cases. The relationship between the aerodynamic gust response and basic gust parameters, namely the strength and length scale of the gust, has been explored. These results suggest that future analysis should include the effects of the steepness of the gust profile, the distribution of vorticity in the gust, and the effective camber and pitch rate that is induced on the wing by the gust flow during the encounter.

Réponse aérodynamique instationnaire des ailes rigides confrontées à des rafales de vent

(STO-TR-AVT-282)

Synthèse

Les opérations des véhicules aériens modernes présentent un nouveau défi : le vol contrôlé dans des environnements aérodynamiques extrêmement instationnaires. De nombreuses missions d’intérêt, incluant l’enlèvement/le largage de cargaison, la reconnaissance et les opérations de sauvetage, doivent avoir lieu dans des environnements aérodynamiques instationnaires. Des opérations telles que la reconnaissance, la surveillance et les livraisons sans pilote dans les environnements urbains, les opérations d’hélicoptères sur un terrain complexe et le vol depuis un navire dans les sillages aériens sont limitées par les fortes rafales de vent transitoires, les structures cohérentes au sein des sillages aériens et d’autres perturbations d’écoulement. Toutes ces opérations sont, bien entendu, régulièrement menées de nos jours, mais se limitent à des perturbations d’écoulement relativement bénignes et des domaines opérationnels nécessairement prudents. Le groupe de travail AVT-282 a été formé dans le but de faire progresser l’état de la technique de modélisation et prédiction de la portance instationnaire afin d’aider au développement de performances robustes des véhicules aériens, dans lesquelles les rafales de vent sont du même ordre de grandeur que la vitesse de vol du véhicule et dans lesquelles le rejet des perturbations peut être obtenu par un contrôle de l’écoulement en boucle fermée. Ce groupe se concentre sur l’effet des rafales de vent discrètes et des écoulements transitoires sur les performances de la voilure et la dynamique des fluides de la réponse aérodynamique d’une aile rigide à une perturbation connue. Les objectifs de recherche précis du groupe étaient :(1) identifier les mécanismes physiques qui produisent les forces et moments transitoires lors de la rencontre de rafales de grande amplitude ; (2) élaborer des modèles analytiques pour décrire les écoulements qui en résultent et prédire le forçage aérodynamique ; (3) identifier les mécanismes par lesquels des écoulements fortement détachés pourraient être contrôlés pour atténuer les réponses instationnaires lors de la rencontre d’une rafale de grande amplitude ; et (4) caractériser l’ampleur et l’échelle des perturbations en conditions réelles, pour définir le domaine des paramètres dans lequel des modèles de rafales existants peuvent être appliqués.

Le groupe s’est d’abord attaché à caractériser les échelles d’ampleur et de longueur des perturbations d’écoulement en conditions réelles, qui définiraient ensuite le domaine d’intérêt des paramètres de rencontre d’une rafale. À l’aide de données de précédents travaux portant sur la météorologie, le vol dans les sillages aériens, les voilures tournantes, les aérogénérateurs et turbines marémotrices, les MAV, les UCAV, les véhicules en transition, etc., un domaine de paramètres d’intérêt principal a été défini. Il se compose de rafales d’une longueur ayant le même ordre de grandeur que la corde de l’aile et d’une vitesse du même ordre de grandeur que la vitesse de vol du véhicule. Trois types de rafales canoniques ont été définis (les rafales transversales, les rafales tourbillonnaires et les rafales longitudinales) et une quantité considérable de données a été obtenue. Une réponse aérodynamique classique pour tous les types de rafales étudiés consiste en une hausse rapide de la portance jusqu’à des valeurs extrêmes pendant la rencontre de la rafale, suivie d’une chute lorsque l’aile sort de la rafale. La portance transitoire rencontrée augmente en fonction de la force de la rafale et de l’incidence sur l’aile. De simples prédictions de la portance maximale peuvent être déduites de l’angle d’attaque réel de l’aile à la vitesse maximale de la rafale, mais les modèles de portance plus précis et instationnaires nécessitent beaucoup plus de nuances. Les grandes rafales transversales ou tourbillonnaires provoquent un détachement massif d’écoulement ; la production de force est donc dominée par les effets non visqueux : la circulation chassée depuis l’aile et la vorticité libre de

la rafale en soi. Les fortes rafales longitudinales n’entraînent pas obligatoirement de détachement d’écoulement, ce qui signifie que les forces visqueuses jouent un rôle plus important. Le groupe de travail a déterminé que les théories non visqueuses linéaires fournissaient des prédictions raisonnables plus grandes que prévu de la réponse en portance pour les rafales, mais échouaient dans les cas extrêmes. La relation entre la réponse aérodynamique à une rafale et les paramètres de base de la rafale – à savoir l’échelle de force et de longueur de la rafale – a été étudiée. Ces résultats suggèrent que les analyses futures devraient inclure les effets de la profondeur du profil de rafale, la répartition de la vorticité au sein de la rafale et la cambrure et le tangage réels induits sur l’aile par l’écoulement de la rafale pendant la rencontre.

CHAPTER 1 – INTRODUCTION

Anya R. Jones
University of Maryland
UNITED STATES

Oksan Cetiner
Istanbul Technical University
TURKEY

Historically motivated by problems of aerodynamic flutter and/or vehicle maneuvers, the unsteady aerodynamics of moving wings has been a topic of research for nearly a hundred years. Modern air vehicle operations, however, have presented a new challenge: controlled flight through highly unsteady aerodynamic environments. Today we are pushing the bounds of vehicle operational envelopes with new problems in which air vehicles must operate in gusty winds and severe weather where flow disturbances may be of the same order of magnitude as the vehicle flight speed. Operations such as unmanned deliveries in urban environments, helicopter operations in complex terrain, and shipboard flight in airwakes are limited by strong transient wind gusts, coherent structures in air wakes, and other flow disturbances. The engineering challenge is not limited to air vehicles. For example, the efficiency and fatigue life of wind and tidal turbines is affected by unsteady winds, operation in wakes, and blade rotation through shear flows and boundary layers. All of these operations are, of course, regularly carried out today, but are currently limited to relatively benign flow disturbances and conservative operational envelopes. What if wings, blades, and other lifting surfaces could be designed to reject undesirable aerodynamic forcing due to large gusts? With this question in mind, research task group AVT-282 was formed under NATO STO to begin investigating the flow physics and unsteady aerodynamic response of rigid wings in large-amplitude gust encounters. This task group consisted of 31 members from industry, academia, and government, representing ten countries. The results of four years of collaborative planning and research are summarized here, accompanying conference papers (Refs. [1] to [14]) and many other publications including Refs. [15] to [78].

Previous NATO STO task groups such as AVT-101, AVT-149, AVT-182, AVT-184, AVT-202, and AVT-239 have focused on the flight sciences of small and micro unmanned air vehicles, with a special interest in the study of steady and unsteady aerodynamics, technology state-of-the-art identification, and flight characterization. Results of these groups have contributed significantly to our understanding of the relevant aerodynamics and flight dynamics of small air vehicles. Nevertheless, current vehicle designs emphasize cruise and loiter efficiency rather than maneuverability or robust unsteady aerodynamic response. While any solution to improve vehicle maneuverability must not be detrimental to cruise performance, better vehicle handling in a gusty or otherwise unsteady aerodynamic environment would greatly enhance the operational envelope of air vehicles of all sizes. The AVT-282 task group was formed with the stated goal of extending the state-of-the-art in unsteady lift modeling and prediction in support of the development of robust flight vehicle performance where wind gusts are of the same order of magnitude as the vehicle's flight speed, and where disturbance rejection may be achieved via closed-loop flow control. To this end, the group began by defining the flight-relevant parameter space of large-amplitude gust encounters and evaluating the underlying flow physics of unsteady aerodynamic forcing in such an encounter.

An important conceptual question regarding the aerodynamics of vehicle flight performance is the distinction between a vehicle performing maneuvers in a steady environment and a vehicle in steady flight through an unsteady environment, i.e., an accelerating vehicle versus an accelerating fluid. While there has been much previous research on maneuvering wings in hover or in a steady freestream [1], [79], the current goal is to enable vehicles to reject an undesirable gust response and thereby maintain controlled flight in unsteady environments. Previous work in the study of wings in unsteady flows has been largely focused on complex turbulent flows as produced by fan banks, grids, and/or wakes [80], oscillating freestreams as produced in unsteady flow wind tunnels [37], [81] to [85], and/or small disturbances [86], [87]. The effect of discrete wind gusts and transient flows on wing performance has received much less attention, especially for large disturbances. AVT-282 aimed to fill that gap. While the current work is limited in scope to the fluid dynamics of a rigid wing's aerodynamic response to a known disturbance, it should be noted that the underlying engineering problem is not constrained to aerodynamics. Vehicles capable of rejecting gusts and correcting for uncertainties and/or variations in position and orientation will also require new types of sensors, actuators, and control laws. The development of these devices and methods will require a deep understanding of the mechanisms of force production in unsteady separated flows to inform the placement of sensors and actuators, and to ensure the accuracy and robustness of flow/force estimators. It is, therefore, necessary to establish new types of experiments, computational methods, and theoretical models to study the effect of large-amplitude gusts on the unsteady aerodynamic response of a lifting surface.

AVT-282 set out to apply and extend the current understanding of unsteady aerodynamics, specifically transient flows and large-amplitude gust encounters, to better understand the resulting flow structures, the force and moment transients, and the relevant time scales of the flow/force transient response and recovery. The specific research goals of the group were to:

1) Identify the physical mechanisms by which force, and moment transients are produced in large-amplitude gust encounters via numerical simulations and experiments;
2) Develop analytical models to describe the resulting flows and predict aerodynamic forcing;
3) Identify mechanisms by which highly separated flows might be controlled to attenuate unsteady responses in a large-amplitude gust encounter; and
4) Characterize the magnitude and scales of real-world flow perturbations to define the parameter space over which a transient flow disturbance should be treated as a small perturbation, gust, or quasi-steady flow.

1.1 OBJECTIVES AND ORGANIZATION

Building on AVT-149 and AVT-202, AVT-282 set out to experimentally, computationally, and analytically study canonical problems in flow separation with a focus on predicting aerodynamic response and recovery in large-amplitude gust encounters. In this work, large-amplitude gusts are taken to be discrete events where the flow disturbance is of the same order of magnitude as the flight speed, generally resulting in massive flow separation. The research plan was designed to inform future efforts in mitigating disturbance effects at flight-relevant disturbance amplitudes and time scales. To this end, the group studied the fluid mechanics and fluid-structure interaction of canonical and flight-relevant wing shapes executing maneuvers in both quiescent flows and gusty/unsteady environments. Together, the members of AVT-282 developed a work plan consisting of four tasks to be addressed over the three-year duration of the group:

1) Definition of a relevant gust encounter. What parameters define a gust encounter that is representative of unsteadiness typical of the atmospheric boundary layer or other flight-relevant unsteady environment? I.e., what defines a gust that results in a sufficiently large aerodynamic response that it cannot be treated as a small perturbation or a quasi-steady flow, but instead requires a new type of treatment to accurately model and predict the resulting force transient?
2) Identification of non-circulatory effects in a gust encounter. How do highly unsteady flows due to model motion in a steady freestream compare to analogous gust encounters? The emphasis here was on the development of the flow structure and the resulting force/moment transients on a wing undergoing large-amplitude motions over a short-reduced time, and whether this could be taken as an approximation of a gust encounter. The primary focus was on the aerodynamic response and force production due to vorticity transport and non-circulatory forcing. One important consideration in this work was the relaxation time of the flow and how this is affected by motion amplitude or reduced time.
3) Evaluation of classical theories and analytical models applied to highly separated flows. Classical theories including those of Wagner, Küssner, Greenberg, Miles, Theodorsen, and von Kármán and

Sears have been shown to model unsteady flows and gust encounters well for attached flows, small gusts, and small amplitude wing motion. Application to large-amplitude gust encounters, however, requires either extension of these models to high angles of attack, fully separated flows, and/or vortex-dominated flows, or the development of new models. This task aimed to define the parameter space over which existing flow models can be applied to large-amplitude gust encounters and to propose extensions to broaden that space.

4) New diagnostic techniques and numerical methodology development/demonstration for massively separated, unsteady 3D problems. Experimental and computational methods continue to evolve with advances in transducer technology, optics, electronics, and computing power. While the group did not aim to develop new methods per se, the state-of-the-art in experimental and numerical capabilities was expanded to facilitate the research of interest.

The AVT-282 research team consisted of experts in experimental, computational, and theoretical methods. Early in the research effort, experts in meteorology, controls, and flight mechanics were consulted regularly to ensure that the focus of this work, i.e., the baseline gust cases selected, was representative of a severe gust encounter that might occur in the real world.

1.2 ISOLATING A CANONICAL GUST: GUST ENCOUNTERS IN AN URBAN ENVIRONMENT

The problem of gust encounters during air vehicle operation exists for many types of missions (e.g., cargo pickup/drop-off, reconnaissance, and search and rescue) and in many types of complex environments including complex terrain, ship airwakes, severe weather, and urban environments. Understanding the effect of gusts on aircraft is part of the science of aircraft stability and control, and there is a considerable body of knowledge on the effects of atmospheric turbulence on manned aircraft flying well above the ground. These methods commonly reference the stochastic, one-dimensional, continuous gust spectra of Dryden (1939) [88], von Kármán (1948) [89], or Diederich and Drischler (1957) [90] for relatively low amplitude disturbances where flow is assumed to remain attached. However, the flows of primary interest in AVT-282 are characterized by large-amplitude flow disturbances where flow separation is likely to occur, and this type of flow is not well represented by the aforementioned gust spectra. In an effort to characterize and categorize the types of gusts that might be found in real-world flows of interest, the flight of a small vehicle through a representative flow around a cuboid building in an urban environment was studied.

Today, small fixed-wing and multi-rotor craft (generally known as “drones”) are increasingly being used in the urban environment. These vehicles are semi-autonomous, usually considerably smaller, and lighter than their manned counterparts, and fly at relatively low speeds (< 15 m/s). Described as “the most disruptive technology in human history” (Frey, 2019) [91], they are one of the most rapidly developing aspects of aerospace science and technology. However, their small size, low mass, and low flight speed means they are highly susceptible to wind gusts (Watkins et al., 2006 [92] and Mohamed et al., 2014 [93]). Unlike for manned aircraft, or even for large drones, the principal effect of gusts on these vehicles is on the vehicle’s capacity to maintain its trajectory. Aeroelasticity, fatigue, and other effects of gusts on structural integrity are secondary, as least for the smaller vehicles. Furthermore, if there are no passengers, then ride-quality is irrelevant. What is relevant is, firstly, whether the vehicle can even fly through the gust without getting hurled backwards or into the ground. The second consideration is whether the vehicle can perform its mission in gusty conditions, e.g., to place cargo at some specific point or to keep sensors on target. It is possible that a vehicle may manage to fly without outright crashing, but yet be so perturbed by gusts as to be unable to execute its mission acceptably.

Drone flight in the urban environment is desirable for many missions but poses exceptional challenges due to proximity to buildings and their associated wakes. While there have been measurements in flight through the lower part of the atmospheric boundary layer (see, for example, Watkins et al. (2006) [92] and (2010) [94]), very few measurements have been performed in an urban environment, where buildings and other ground obstacles produce wakes and shear layers. Buildings, for example, are bluff bodies with their own wakes and regions of flow separation that depend on the magnitude and direction of winds. Wind may be "steady" over some large spatial extent and range of time, but markedly unsteady in a built environment. As a result, the unsteadiness that low-altitude vehicles encounter may be more severe than what is nominally measured in the atmospheric boundary layer. As such, the most critical parts of a typical flight profile are likely to be very near to buildings; for instance, flying through the shear layer from a building roof or edge as depicted in Figure 1-1. It is here that the most precise maneuvers and flight control are required, e.g., for take-off, landing, or pickup/drop-off.

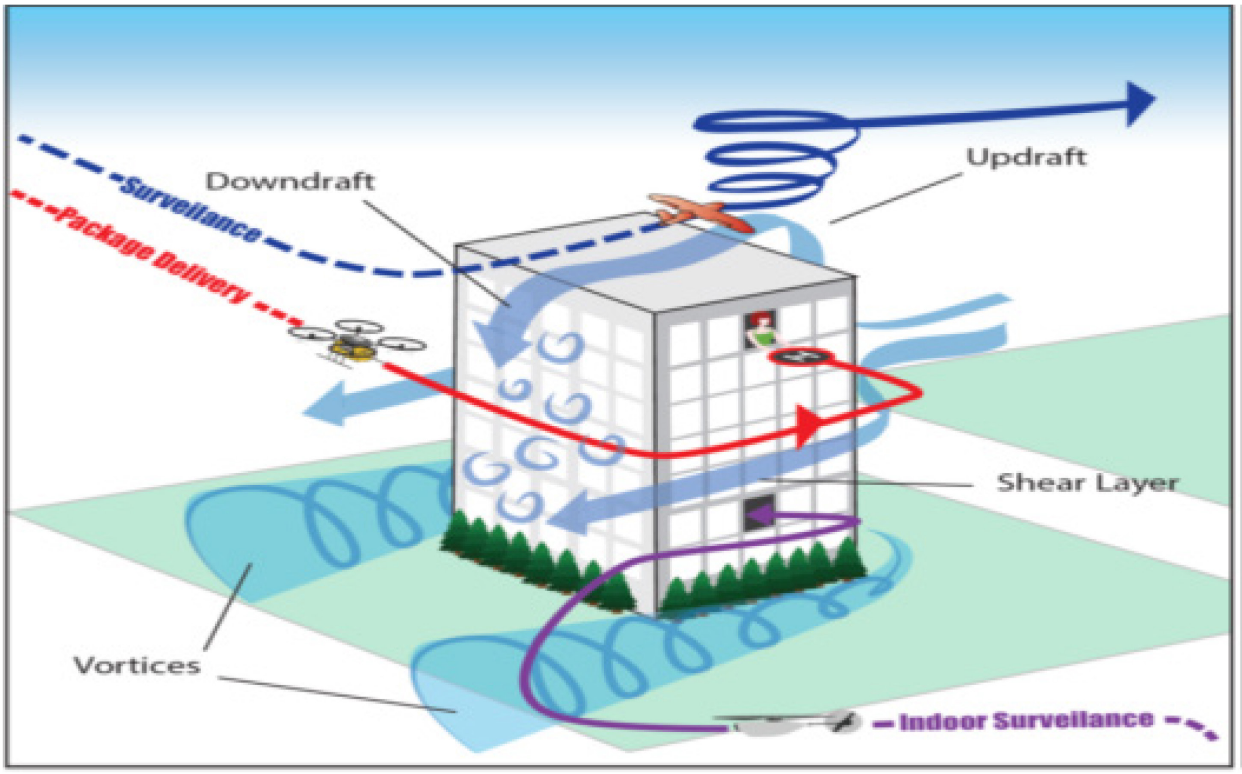

Figure 1-1: Possible Flight Paths Near a Cuboid Building [95].

In Figure 1-1, Watkins et al., [95] provide examples of the flight environment experienced by a small vehicle flying an idealized steady level flight path past a nominally cuboid building. As the aircraft proceeds along its trajectory, the blue "Surveillance" line in Figure 1-1, the event of primary significance is that of encountering the shear layer that is a result of flow separation at the leading edge of the building as shown in Figure 1-2. For nominal flight speeds of 5 m/s (slow, low wing-loading aerobatic vehicle) and 15 m/s (fast, cruise-oriented, higher wing-loading vehicle), histories of the time-varying relative angle of attack and relative flow velocity are shown in Figure 1-2. It can be seen here that flight through this shear layer is a dynamic event. As the vehicle passes through the shear layer, it experiences a large change in angle of attack and relative speed magnitude, as shown in Figure 1-3. This "gust" is a simple, relatively two-dimensional, example of the type of gust encounter that was the focus of AVT-282.

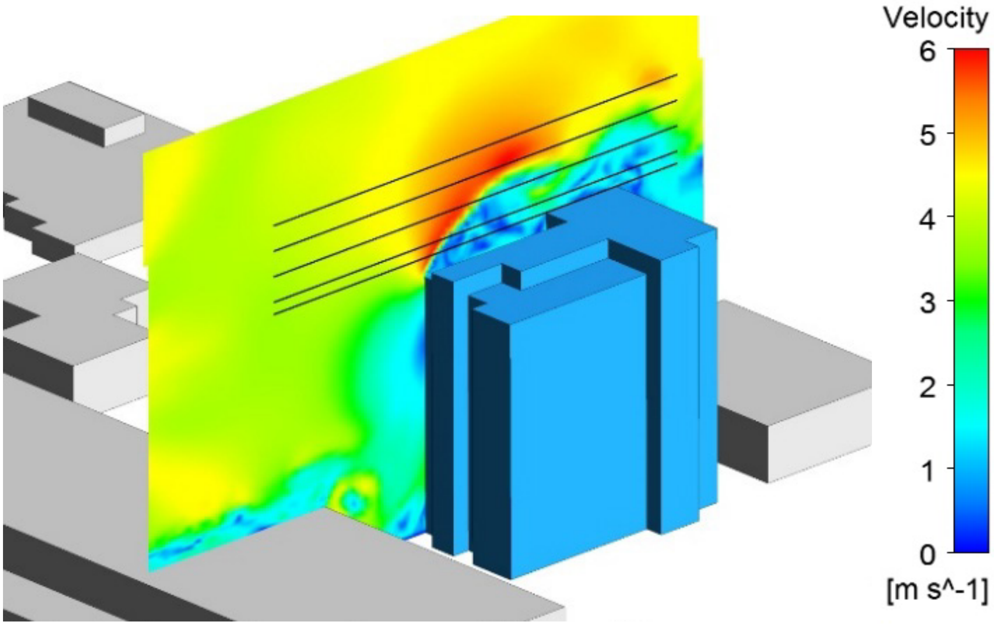

Figure 1-2: CFD Urban-Wind Velocity Contours of Flow Around a Representative Building, with Flight Paths in Vicinity of Building Rooftop Illustrated as Horizontal Lines [95].

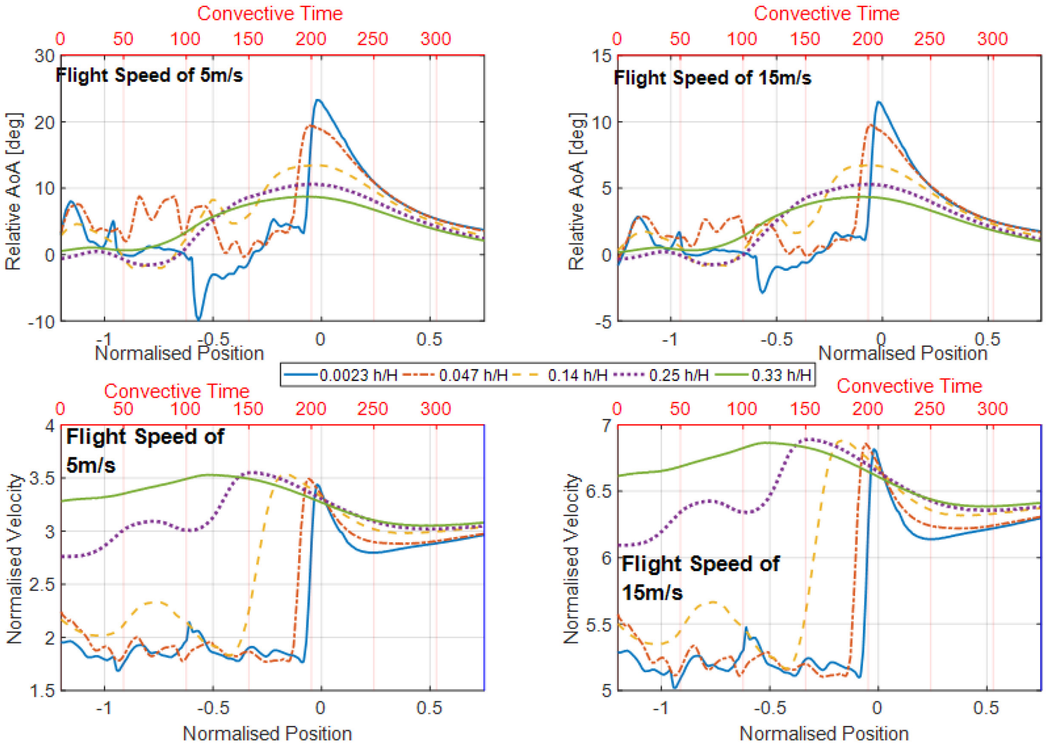

Figure 1-3: Superposition of Imposed Vehicle Flight Speed and CFD-Derived Wind Field [95].

1.3 DEFINITION AND CATEGORIZATION OF GUSTS

1.3.1 Gust Categories

To coordinate the research effort and facilitate the comparison of results across the member research groups, three different types of gusts were defined at the start of AVT-282: a transverse gust encounter, a vortex gust encounter, and a streamwise gust encounter. A schematic of each of these gust types is given in Figure 1-4. Although few real-world gusts would fit cleanly into only one of these categories, defining these canonical cases allowed members of the group to closely coordinate and collaborate to enhance confidence in experimental repeatability, and to explore broader ranges of the parameter space than would have been possible independently.

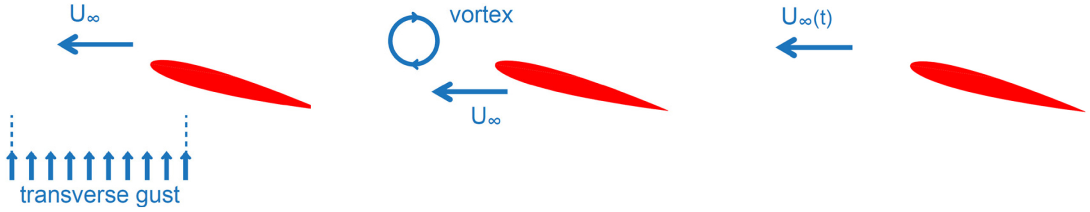

(a) Transverse Gust. **(b) Vortex Gust.** **(c) Streamwise Gust.**

Figure 1-4: Schematic of Three Types of Gust Encounters.

1.3.1.1 Transverse

The transverse gust shown in Figure 1-4(a) represents a wing passing through a well-defined updraft or a strong shear layer. Examples of these types of flows include weather phenomenon and large-scale wakes as in urban environments, naval vessels, mountains, and other complex terrain. In the canonical model of the transverse gust encounter defined by this group, a rigid wing is held at a fixed geometric angle of attack in a steady freestream before passing through a well-characterized updraft. AVT-282 experiments on transverse gusts were most commonly performed in water-filled towing tanks ([20], [44]), this being one of the easier setups for this problem. In this type of experiment, the towing speed of the wing remains constant, as does the geometric incidence of the wing, while the updraft flow remains fixed in space and at a constant velocity. The flow disturbance due to the gust encounter therefore affects only the effective angle of attack of the wing, and only for the finite amount of time that the wing is within the gust flow. This effect, described as a broken-line airfoil in Von Kármán and Sears [87], results in a change in effective angle of attack that varies in time and space along the chord of the wing and is directly related to the spatial variation of the gust (i.e., updraft) flow.

Figure 1-5 gives some examples of transverse gust encounters studied by members of AVT-282. The jet-like sharp-edged and sine-squared gusts produced in the University of Cambridge (CU) and University of Maryland (UMD) towing tanks, Figure 1-5 (a) and Figure 1-5 (c), were fixed in place and test models were towed through the gust to model a transient gust encounter. Figure 1-5 (b) shows a numerical model of the transient sharp-edged transverse gust from Georgia Tech (GT). More information on this approach is given in Ref. [38]. To produce transverse gusts in air, the Young wind tunnel, located at the University of Cambridge Whittle Lab, was equipped with a louver system that generated a flow that was primarily a periodic transverse gust as shown in Figure 1-5 (d), with only small variations in the streamwise flow.

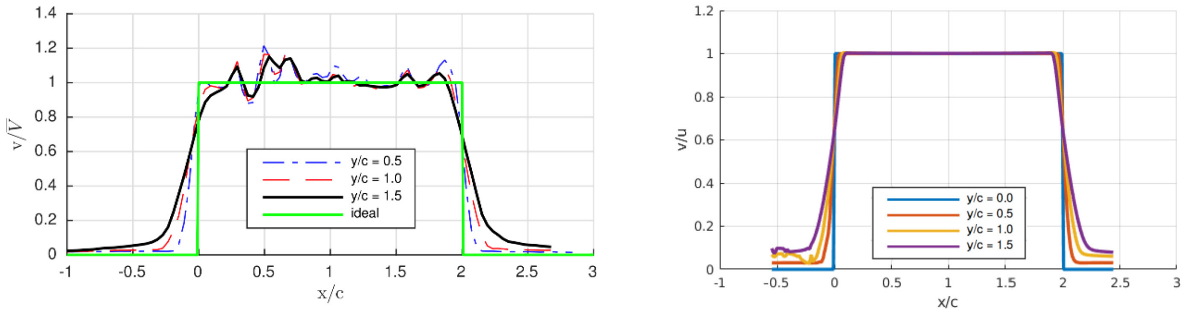

(a) Top-Hat Gust in the CU Towing Tank [44]. **(b) Computational Top-Hat Gust at GT [38].**

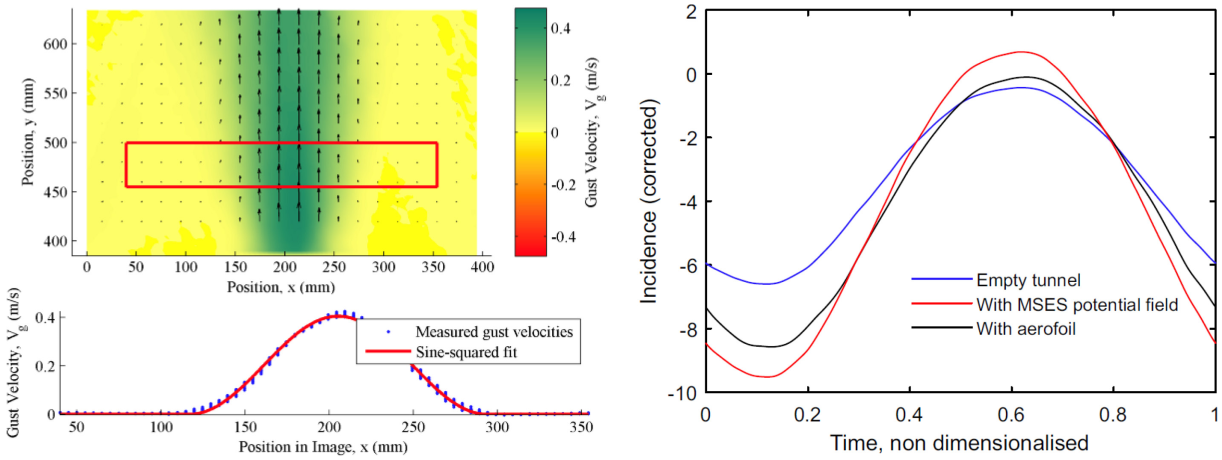

(c) Sine-Squared Gust in the UMD Towing Tank [20]. **(d) Periodic Gust in the Young Wind Tunnel [11].**

Figure 1-5: Examples of Transverse Gusts Produced by Members of AVT-282.

1.3.1.2 Vortex

The canonical vortex gust illustrated in Figure 1-4(b) represents wing-vortex interactions where the diameter of the vortex is of the same order of magnitude as the chord of the wing. These interactions are commonly found in the wakes of other wings/blades (e.g., rotorcraft, wind/tidal turbines, formation flight), other structures (e.g., ship-airwake interactions, urban environments), and in unsteady environments (i.e., atmospheric/seabed turbulence). Blade-Vortex Interactions (BVIs) are a well-studied phenomenon in some fields (e.g., rotorcraft). Within AVT-282, the focus of work in this area was on fundamental flows with nominally two-dimensional (i.e., high aspect ratio) vortices and wings. Most of this work has been on periodic gusts ([31], [69]) such as that produced by a rotating upstream plate in the Istanbul Technical University (ITU) water channel as shown in Figure 1-6(a), or by a rotating cylinder in the U.S. Air Force Research Laboratory (AFRL) water tunnel as shown in Figure 1-6(b). Transient vortex gusts have also been studied experimentally at ITU [47] and TU Braunschweig (TUB) ([9], [33], [72]) (Figure 1-6(c)), and computationally at AFRL [96]. For the purposes of this work, interaction with much larger vortices where the primary net flow disturbance at the wing was in the cross-stream direction was taken to be a periodic transverse gust [11]. In a vortex gust encounter, the wing is once again taken to be at a fixed geometric incidence, but due to the transverse component of velocity induced by the vortex, the effective angle of attack of the wing varies in time and space. In this case, however, there may also be an additional unsteady component of velocity in the streamwise direction. The vortex gust encounter experiments of AVT-282 were largely designed with a particular interest in comparing these results to those from transverse and streamwise gusts.

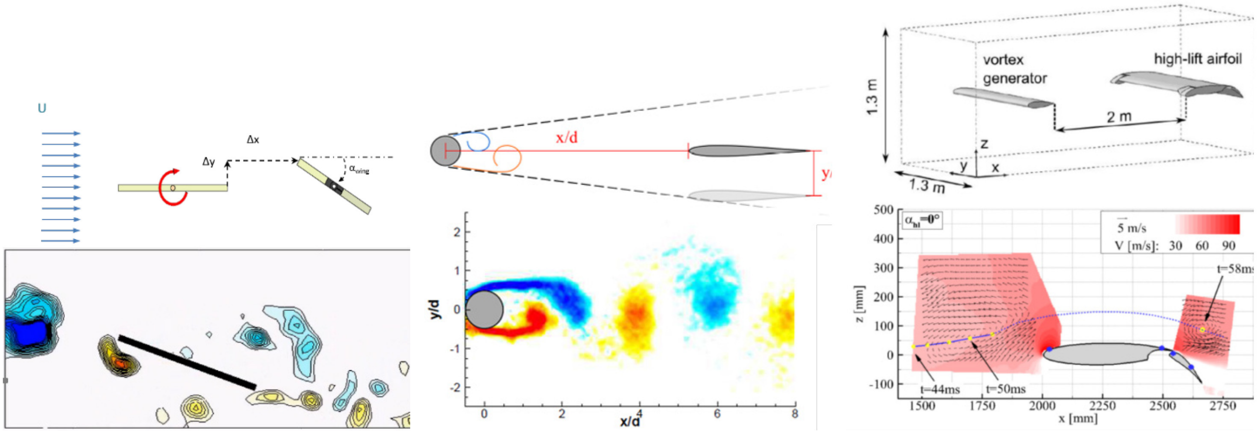

(a) Vortex Gust in the ITU Water Channel, [47].

(b) Rotating Cylinder in the AFRL Water Tunnel [31].

(c) Vortex Gust in the TUB Wind Tunnel [72].

Figure 1-6: Examples of Vortex Gusts Produced by Members of AVT-282.

1.3.1.3 Streamwise

The streamwise gust in Figure 1-4(c) was defined as a wing at fixed incidence experiencing time variations in the streamwise flow. In this case, the effective angle of attack remains constant, though it is thought that unsteady effects could be related to the rate of change of flow speed. Transient streamwise gusts are often (especially in water) most easily produced by moving the model rather than the flow as was done in the University of Buffalo (UB) [13] and UMD [59] towing tanks, shown in Figure 1-7(a). Periodic streamwise gusts in air, however, as shown in Figure 1-7(b) and Figure 1-7(c), can be produced in louver-equipped unsteady wind tunnel facilities such as the Andrew Fejer Unsteady Flow Wind Tunnel at the Illinois Institute of Technology (IIT) [10] and the low speed wind tunnel at the University of Toronto Institute for Aerospace Studies (UTIAS) (Refs. [97] to [99]). The canonical streamwise gust studied by members of AVT-282 was designed to model streamwise fluctuations experienced by lifting surfaces in tides, surging wings, and rotor blades, and for comparison to the transverse and vortex gusts described above.

1.3.1.4 Moving Models

While the focus of this work was primarily on fluid gust encounters in which the model was in steady motion and fluid was accelerated, to better understand the sources of aerodynamic forcing, analogous flows in which the model was driven to produce a similar relative flow were also studied. The aforementioned surging wing experiments at UB [13] and UMD [59] are examples of this type of experiment for the streamwise gust. Similar experiments [43] and computations ([12], [49], [73]) were also performed on pitching, plunging and/or surging wings in an attempt to capture some of the physics of a transverse gust encounter. The moving model version of the vortex gust encounter was taken to be a pitching wing in which the geometric angle of attack was varied in a steady freestream [16]. In both the pitching and plunging wing cases, however, it should be noted that the relative flow is not entirely analogous to the gust encounter. Notably, the spatially varying effective angle of attack that exists in the gust encounter is not modeled by plunging or pitching wings. Nevertheless, comparisons between driven-fluid and driven-model results have provided much insight into the underlying physics of force production.

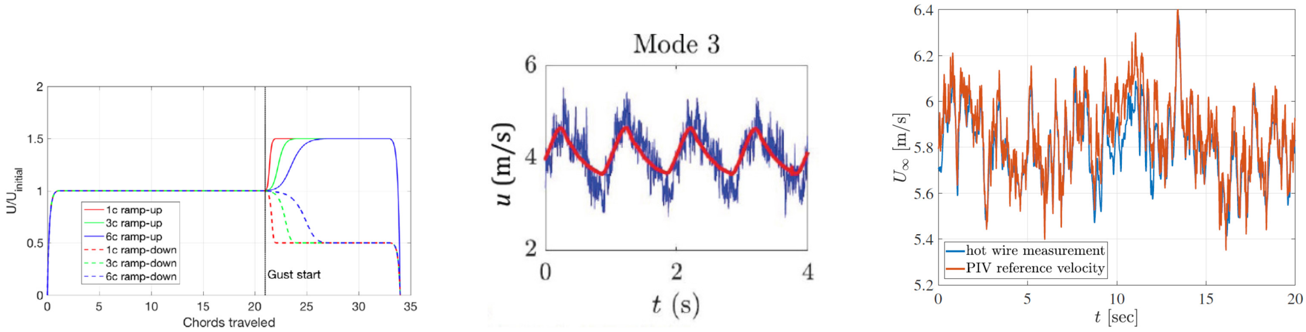

(a) Surging Wing Kinematics in the UB Water Tank [13]. **(b) Streamwise Gust in the UTIAS Wind Tunnel [97], [99].** **(c) Broad-spectrum “Turbulent” Flow in the IIT Wind Tunnel [10].**

Figure 1-7: Examples of Streamwise Gusts Produced by Members of AVT-282.

1.3.2 Parameter Space and Definitions

For each of the types of gust described above, the gust encounter was characterized first by two parameters: the gust ratio and the encounter width. The gust ratio, GR, was defined as the magnitude of the flow disturbance, V, normalized by the freestream, U_∞,

$$GR = \frac{V}{U_\infty} \tag{1-1}$$

The encounter width was defined as the gust width, w, normalized by the wing chord, c, i.e.,

$$W_e = \frac{w}{c} \tag{1-2}$$

Finally, the gust parameter is the gust ratio divided by the gust width, i.e.,

$$G = \frac{GR}{W_e} \tag{1-3}$$

Given these defining parameters, an early version of the parameter space explored by members and other interested parties in communication with the AVT-282 group is represented by Figure 1-8. (Note that at the time of making this figure in April 2018, several of the facilities represented here were still in the design and/or construction phase. The end results will likely differ from this figure; in many cases work is still in progress.) Figure 1-8 also shows the spaces occupied by typical real-world gusts due to building wakes, complex terrain (e.g., mountains), and seabed induced turbulence as experienced by both pigeon-sized and Predator-sized aircraft. Most of the AVT-282 efforts were concentrated in the region where it was expected that the most severe aerodynamic response would occur – where the gust width is of the same order of magnitude as the wing chord, i.e., $w/c \sim O(1)$, and the magnitude of the flow disturbance is of the same order of magnitude as the freestream, i.e., $GR \sim O(1)$.

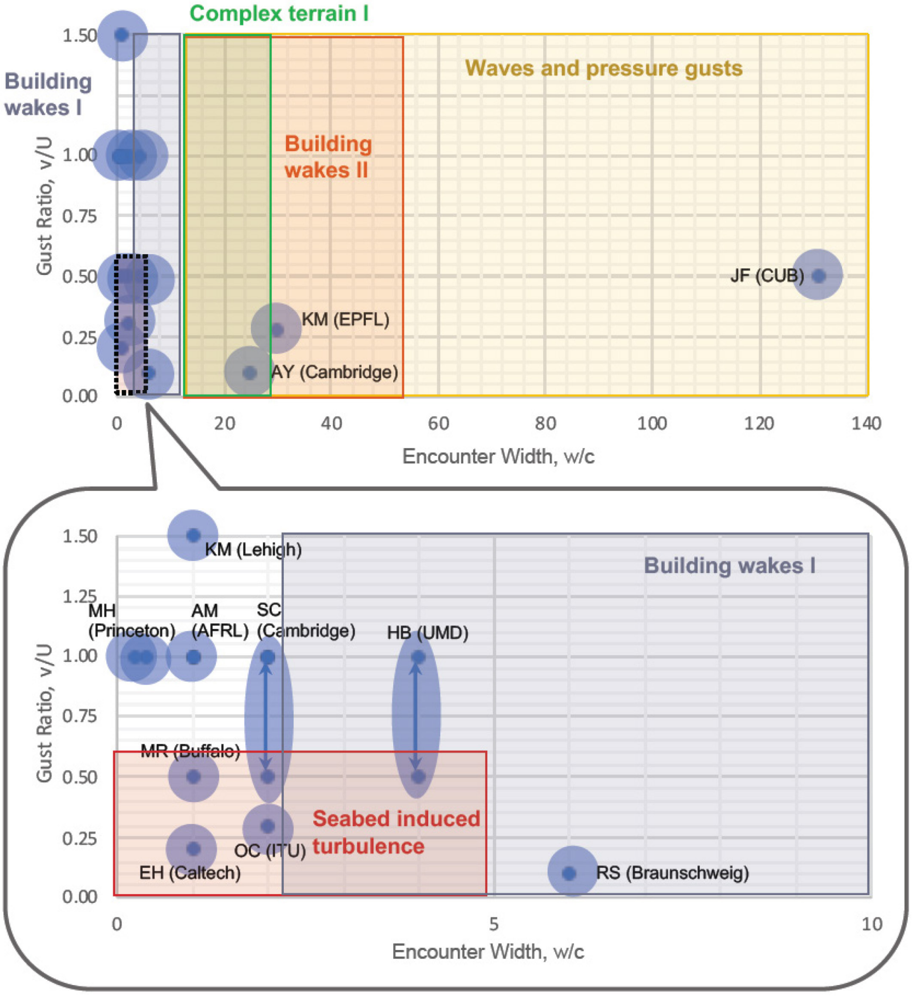

Figure 1-8: Early Version of the Gust Parameter Space Covered by Members of AVT-282.

To facilitate the comparison of results from gust encounters of various types and at various points in the parameter space, several parameters were defined to describe the aerodynamic lift response to a gust encounter. Figure 1-9(a) shows a typical lift response to a large-amplitude gust encounter – an immediate increase in lift to some local maximum, followed by a decrease in lift, and an eventual recovery to steady state. The current work aims to characterize only the initial response, i.e., the build-up of lift as outlined by the yellow dashed line. Let t_r^*, the *response time*, be the convective time that elapses from the start of the initial response, i.e., the point at which lift begins to increase in response to the gust, to the time at which the maximum force is achieved. (See Figure 1-9(b).) In the current work where the focus remains on the lift response, ΔC_F is taken to be ΔC_L, the difference between the maximum lift coefficient produced during the gust encounter and the steady state lift coefficient produced by the wing before the encounter and after full recovery. In the analysis below,

$$\max \Delta C_L = \max\left(C_L - C_{L_{steady}}\right) \tag{1-4}$$

is called the *response magnitude* and represents the maximum lift excursion experienced by the wing during the gust encounter. The *response slope* is the slope of the force response as approximated by a linear ramp, i.e., the response magnitude divided by the response time, maxΔCL/t_r^*. Finally, Figure 1-9(b) illustrates a proposed categorization of gust responses based on these definitions. Here, the aerodynamic force response of a wing to a gust encounter is categorized by both the magnitude of the response, maxΔC_F, and the time over which that response occurs, t_r*. The mildest gust response, where "mild" refers to the high likelihood of successful prediction and control, would be one that has a low response magnitude that builds over a long time, e.g., a Category IA gust as shown in the bottom left of Figure 1-9(b). A severe gust would have a large response magnitude that builds up quickly, e.g., a Category IIB gust as shown in the top right of the figure.

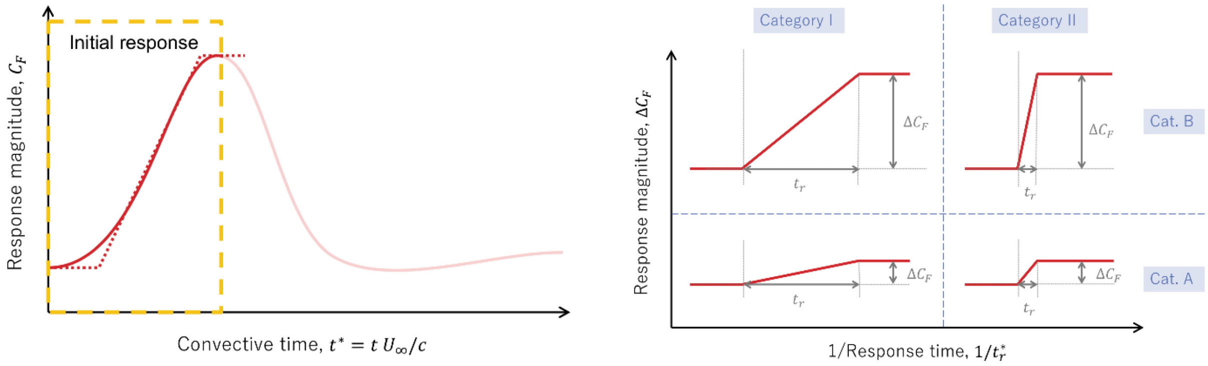

(a) Sketch of a Typical Lift Response. **(b) Categorization Based on Force Response.**

Figure 1-9: Parameters Characterizing and Categorizing a Typical Aerodynamic Force Response to a Transient Large-Amplitude Gust Encounter.

1.4 METHODOLOGIES AND APPROACHES

1.4.1 Experiments

The large-amplitude gusts of interest in AVT-282 required the design and construction of new experiments and new facilities. The parameter space studied (Figure 1-8) was largely driven by the feasibility of conducting the relevant experiments. In general, larger gust ratios and shorter gust widths are achievable in water, while air facilities perform better at lower gust ratios and larger gust widths. One consideration in embarking on gust encounter experiments is that, as a general rule, a given setup or facility, once built, had relatively few degrees of freedom. That is, once a gust generator has been built, the size and shape of the gust are likely fixed, with limited control over the gust magnitude and/or velocity ratio.

Well-characterized transverse gust encounters are most easily generated in a water tank where the background flow is quiescent, and the test model can be towed through a gust. This type of facility has been constructed at the University of Maryland (UMD) ([20], [58]) and the University of Cambridge (CU) [44]. The UMD gust has a sine-squared velocity profile, while the CU gust has a top-hat profile, which has allowed for interesting comparisons of results for similar gust encounters where only the velocity profile differs [2]. Towing tank experiments have been limited to transient gust encounters, but careful design of a louvered wind tunnel can produce periodic transverse gusts [11].

Vortex gusts are more easily generated in a fan- or pump-driven freestream and are relatively easily produced in both wind and water tunnels, though the resulting vortex tends to be more coherent in water where it is easier to drive the gust generator in fast motions relative to the flow speed. Vortex gusts in a freestream are more conducive to periodic generation ([31], [47]) than are transverse gusts. Coherent vortex gusts in wind tunnels [72] tend to be of a larger diameter and either transient or of a lower reduced frequency than those generated in air.

Streamwise gusts have been produced in louvered unsteady flow wind tunnels for many years ([26], [83], [85]), but can also be modeled in towing tanks or water tunnels using surging wings ([13], [59]).

1.4.2 Computations

Computations are theoretically capable of modeling any conceivable gust, making them far more flexible than experiments and thus an invaluable tool. Given the difficulties in generating a physical well-characterized gust, it was originally thought that computations would be the more straightforward way to explore large-amplitude gust encounters. In practice, however, development and validation of computational methods proved a challenge due to the complex flow physics involved. As AVT-282 comes to an end, there now exist computational methods for large-amplitude gust encounters on wings at both low and high incidence, and these been extensively validated against experiments [38]. Preliminary results using computations to explore gusts that are physically difficult to produce are promising [30], and future work will likely expand on these ideas.

1.4.3 Theory and Modeling

One of the goals of the AVT-282 research effort was to understand the physics of a highly separated gust encounter flow. The approach taken by the group was to systematically compare experimental and computational work to well-understood classical theory [21], [44]. This approach led to many of the conclusions detailed below and provided a much deeper understanding of the results than would have otherwise been possible. Theoretical models were also used to begin investigating more complex problems, including aeroelasticity [39], [48]. Since many of the experimental setups in the group relied on water as the working fluid, it is difficult to account for aeroelastic effects as they do not easily scale to air. Theoretical models allow for this extension and thus lay the groundwork for future efforts in this area.

1.5 OUTLINE OF THE REPORT

The current chapter presented the underlying motivation for the large-amplitude wing-gust encounter research conducted by AVT-282. The group's approach and organization were outlined, and methods introduced. In Chapters 2 – 14, the results of individual research groups within AVT-282 are highlighted. While groups maintained separate labs, facilities, and approaches, they worked closely together to both verify each other's results and to broaden the explored parameter space beyond what is capable in any one lab. Chapters 2 – 4 present experimental and computational results on the transverse gust encounter problem, including a detailed analysis of this flow for two separate gust profiles in two separate facilities. Chapter 5 presents an explanation and account of the non-circulatory force generated in a gust encounter. In Chapter 6, a dynamically pitching wing is used to model a gust encounter, and a model for leading edge suction and shear layer development is developed for an airfoil experiencing large-scale flow separation. The effect of a vortex gust encounter is considered in Chapters 7 – 8, first via a comparison of results from a variety of research groups, and then with the addition of aeroelasticity. Chapters 9 and 10 explore the effects of actuated devices installed on wings: a trailing-edge flap on an airfoil experiencing hysteresis, and a rotating wing tip panel in a streamwise gust. The study of streamwise gusts continues in Chapter 11, which presents the effects of a randomly surging flow, and in Chapter 12, with a discussion of the effect of adding a streamwise component to a transverse gust. Finally, three-dimensional effects are explored on a plunging rectangular wing in Chapter 13, and on a surging delta wing in Chapter 14. The report concludes with Chapter 15, in which the results of the entire group are summarized, including answers to the research questions that were laid out in Section 1.1 of the current chapter, and maps of the group's results in the context of the parameters defined in Section 1.3.

1.6 ACKNOWLEDGEMENTS

The authors would like to thank all of the members and participants of AVT-282 for their efforts and contributions to the results presented here. They would also like to specifically thank Simon Watkins and Michael Ol for their work on Section 1.2 of the current chapter. The research presented here was funded by many organizations. Jones's work at UMD was supported by the Air Force Office of Scientific Research under grant FA9550-16-1-0508 and the National Science Foundation under Grant No. 1553970. Cetiner's work at ITU was supported by TUBITAK Grant 115M358 For the Application on UAVs and MAVs, Gust Effect on the Performance of Wings in Motion (Maneuver or Flapping) and Flow Control Attempts.

1.7 REFERENCES

[1] Jones, A.R., and Cetiner, O., Overview of NATO AVT-282: Unsteady aerodynamic response of rigid wings in gust encounters (Invited), AIAA SciTech, American Institute of Aeronautics and Astronautics, Orlando, FL, 2020.

[2] Andreu-Angulo, I., Babinsky, H., Biler, H., Sedky, G., and Jones, A., Wing-gust interactions: The effect of transverse velocity profile (Invited), AIAA SciTech, American Institute of Aeronautics and Astronautics, Orlando, FL, 2020.

[3] Grubb, A., Moushegian, A., Heathcote, D., and Smith, M., Physics and computational modeling of nonlinear transverse gust encounters (Invited), AIAA SciTech, American Institute of Aeronautics and Astronautics, Orlando, FL, 2020.

[4] Biler, H., and Jones, A.R., Force prediction during transverse and vortex gust encounters (Invited), AIAA SciTech, American Institute of Aeronautics and Astronautics, Orlando, FL, 2020.

[5] Gehlert, P., and Babinsky, H., Non-circulatory force on a finite thickness body encountering a gust (Invited), AIAA SciTech, American Institute of Aeronautics and Astronautics, Orlando, FL, 2020.

[6] Mulleners, K., Deparday, J., He, G., and Henne, S., Predicting unsteady flow separation in response to a flow disturbance (Invited), AIAA SciTech, American Institute of Aeronautics and Astronautics, Orlando, FL, 2020.

[7] Medina, A., Cetiner, O., Rockwood, M., Zaloglu, B., Saritas, M., and Gozukara, A., On the effects of discrete and continuous vortex-gust encounters (Invited), AIAA SciTech, American Institute of Aeronautics and Astronautics, Orlando, FL, 2020.

[8] Chen, H., and Jaworski, J., Aeroelastic encounters of spanwise vortex gusts and the self-rotation of trailing vortices (Invited), AIAA SciTech, American Institute of Aeronautics and Astronautics, Orlando, FL, 2020.

[9] Pohl, J., and Semaan, R., Quantification and modeling of dynamic lift on a DLR-F15 research airfoil with active trailing-edge flap (Invited), AIAA SciTech, American Institute of Aeronautics and Astronautics, Orlando, FL, 2020.

[10] He, X., and Williams, D.R., Unsteady aerodynamic loads on an airfoil at high angle of attack in a randomly surging flow (Invited), AIAA SciTech, American Institute of Aeronautics and Astronautics, Orlando, FL, 2020.

[11] Young, A., and Smyth, A., The interaction of a Sears-type sinusoidal gust with a cambered aerofoil in the presence of non-uniform streamwise flow (Invited), AIAA SciTech, American Institute of Aeronautics and Astronautics, Orlando, FL, 2020.

[12] Moriche, M., Flores, O., Sedky, G., Jones, A.R., and García-Villalba, M., Comparison between experiments and simulations of fast plunge maneuvers (Invited), AIAA SciTech, American Institute of Aeronautics and Astronautics, Orlando, FL, 2020.

[13] Chowdhury, J., Smith, C., and Ringuette, M., The lift force produced by an unsteady translating plate with a rotating tip, AIAA SciTech, American Institute of Aeronautics and Astronautics, Orlando, FL, 2020.

[14] Sedky, G., Lagor, F., and Jones, A.R., The unsteady aerodynamics of a transverse wing-gust encounter with closed-loop pitch control, AIAA SciTech, American Institute of Aeronautics and Astronautics, Orlando, FL, 2020.

[15] Jaworski, J.W., Sound from aeroelastic vortex–fibre interactions, Philosophical Transactions of the Royal Society A: Mathematical, Physical and Engineering Sciences, Vol. 377, No. 2159, 2019, p. 20190071.

[16] Deparday, J., and Mulleners, K., Modeling the interplay between the shear layer and leading edge suction during dynamic stall, Physics of Fluids, Vol. 31, No. 10, 2019, p. 107104.

[17] Marzanek, M.F., and Rival, D.E., Separation mechanics of non-slender delta wings during streamwise gusts, Journal of Fluids and Structures, Vol. 90, 2019, pp. 286-296.

[18] Gomez, D.F., Lagor, F.D., Kirk, P.B., Lind, A.H., Jones, A.R., and Paley, D.A., Data-driven estimation of the unsteady flowfield near an actuated airfoil, Journal of Guidance, Control, and Dynamics, Vol. 42, No. 10, 2019, pp. 2279-2287.

[19] Chen, H., and Jaworski, J.W., Acoustic emission of aeroelastic vortex-gust interactions, 23rd International Congress on Acoustics, Aachen, Germany, 2019.

[20] Biler, H., Badrya, C., and Jones, A.R., Experimental and computational investigation of transverse gust encounters, AIAA Journal, Vol. 13, No. 12, 2019, pp. 1-15.

[21] Corkery, S.J., Babinsky, H., and Graham, W.R., Quantification of added-mass effects using particle image velocimetry data for a translating and rotating flat plate, Journal of Fluid Mechanics, Vol. 870, 2019, pp. 492-518.

[22] Badrya, C., Baeder, J.D., and Jones, A.R., Application of prescribed velocity methods to a large-amplitude flat-plate gust encounter, AIAA Journal, Vol. 57, No. 8, 2019, pp. 3261-3273.

[23] Baddoo, P.J., Hajian, R., and Jaworski, J., A Jacobi spectral collocation method for the steady aerodynamics of porous aerofoils, AIAA Aviation 2019 Forum, American Institute of Aeronautics and Astronautics, Dallas, TX, 2019.

[24] Chen, H., Baddoo, P.J., and Jaworski, J., Modeling of Brown-Michael vortices in ground effect, AIAA Aviation 2019 Forum, American Institute of Aeronautics and Astronautics, Dallas, TX, 2019.

[25] Lefebvre, J.N., and Jones, A.R., Experimental investigation of airfoil performance in the wake of a circular cylinder, AIAA Journal, Vol. 57, No. 7, 2019, pp. 2808-2818.

[26] Rennie, R., Catron, B., Feroz, M., Williams, D., and He, X., Dynamic behavior and gust simulation in an unsteady flow wind tunnel, AIAA Journal, Vol. 57, No. 4, 2019, pp. 1423-1433.

[27] Manar, F.H., and Jones, A.R., Evaluation of potential flow models for unsteady separated flow with respect to experimental data, Physical Review Fluids, Vol. 4, No. 3, 2019, p. 034702.

[28] Gomez, D.F., Kirk, P.B., Lind, A., Lind, A.H., Jones, A.R., Paley, D., and Lagor, F., Unsteady DMD-based flow field estimation from embedded pressure sensors in an actuated airfoil, AIAA SciTech 2019 Forum, American Institute of Aeronautics and Astronautics, San Diego, CA, 2019.

[29] Gehlert, P., and Babinsky, H., Linking the unsteady force generation to vorticity for a translating and rotating cylinder, AIAA SciTech 2019 Forum, American Institute of Aeronautics and Astronautics, San Diego, CA, 2019.

[30] Badrya, C., and Baeder, J.D., Numerical study of a flat plate wing response to large transverse gusts at low Reynolds number, AIAA SciTech 2019 Forum, American Institute of Aeronautics and Astronautics, San Diego, CA, 2019.

[31] Medina, A., Suresh Babu, A.V., Rockwood, M.P., Gopalarathnam, A., Gopalarathnam, A., and Ahmed, A., Theoretical and experimental study of wake encounters on unsteady airfoils, AIAA SciTech 2019 Forum, American Institute of Aeronautics and Astronautics, San Diego, CA, 2019.

[32] Corkery, S.J., and Babinsky, H., An investigation into gust shear layer vorticity and the added mass force for a transverse wing-gust encounter, AIAA SciTech 2019 Forum, American Institute of Aeronautics and Astronautics, San Diego, CA, 2019.

[33] Pohl, J., Semaan, R., and Jones, A.R., Dynamic lift measurements on an airfoil with periodic flap motion at high Reynolds number, AIAA SciTech 2019 Forum, American Institute of Aeronautics and Astronautics, San Diego, CA, 2019.

[34] Smyth, A.S., Young, A.M., and Di Mare, L., The effect of 3D geometry on unsteady gust response, using a vortex lattice model, AIAA SciTech 2019 Forum, American Institute of Aeronautics and Astronautics, San Diego, CA, 2019.

[35] Biler, H., Jones, A.R., Saritas, M., Fenercioglu, I., Cetiner, O., and Bronz, M., Investigation of force transients during transverse and vortex gust encounters, AIAA SciTech 2019 Forum, American Institute of Aeronautics and Astronautics, San Diego, CA, 2019.

[36] Jarman, L., Lefebvre, J., Jones, A.R., and Smith, M.J., Dynamics of an airfoil moving through the wake of a circular cylinder, AIAA SciTech 2019 Forum, American Institute of Aeronautics and Astronautics, San Diego. CA, 2019.

[37] Williams, D.R., Stasse, Q., and Rennie, M.R., Lift, drag, and moment response of a UCAS model experiencing longitudinal von Karman gust spectra, AIAA SciTech 2019 Forum, American Institute of Aeronautics and Astronautics, San Diego, CA, 2019.

[38] Moushegian, A., and Smith, M.J., Analysis of a wing moving through a nonlinear gust, AIAA SciTech 2019 Forum, American Institute of Aeronautics and Astronautics, San Diego, CA, 2019.

[39] Chen, H., and Jaworski, J., Aeroelastic trajectory selection of vortex gusts impinging upon Joukowski airfoils, AIAA SciTech 2019 Forum, American Institute of Aeronautics and Astronautics, San Diego, CA, 2019.

[40] Smyth, A., and Young, A., Three-dimensional unsteady hydrodynamic modelling of tidal turbines, Proceedings of the European Wave and Tidal Energy Conference, 2019.

[41] Kirk, P.B., and Jones, A.R., Vortex formation on surging aerofoils with application to reverse flow modelling, Journal of Fluid Mechanics, Vol. 859, 2019, pp. 59-88.

[42] Sedky, G., Lagor, F.D., and Jones, A.R., Lift modeling and regulation for a finite wing during transverse gust encounters, AIAA SciTech, American Institute of Aeronautics and Astronautics, San Diego, CA, 2019.

[43] Perrotta, G., and Jones, A.R., Quasi-steady approximation of forces on flat plate due to large-amplitude plunging maneuvers, AIAA Journal, Vol. 56, No. 11, 2018, pp. 4232-4242.

[44] Corkery, S.J., Babinsky, H., and Harvey, J.K., On the development and early observations from a towing tank-based transverse wing-gust encounter test rig, Experiments in Fluids, Vol. 59, No. 9, 2018.

[45] Henne, S., Parikh, A., Deparday, J., and Mulleners, K., Dynamic stall vortex shedding and associated load fluctuations, 19th International Symposium on the Applications of Laser and Imaging Techniques to Fluid Mechanics, Lisbon, Portugal, 2018.

[46] Jaworski, J., Hydroelastic motions of flexible fibers, 2018 AIAA/CEAS Aeroacoustics Conference, American Institute of Aeronautics and Astronautics, Atlanta, GA, 2018.

[47] Engin, K., Aydin, E., Zaloglu, B., Fenercioglu, I., and Cetiner, O., Large scale spanwise periodic vortex gusts or single spanwise vortex impinging on a rectangular wing, 2018 Fluid Dynamics Conference, American Institute of Aeronautics and Astronautics, Atlanta, GA, 2018.

[48] Chen, H., and Jaworski, J., Vortex interactions with Joukowski airfoil on elastic supports, 2018 Fluid Dynamics Conference, American Institute of Aeronautics and Astronautics, Atlanta, GA, 2018.

[49] Leung, J.M., Wong, J.G., Weymouth, G.D., and Rival, D.E., Modeling transverse gusts using pitching, plunging, and surging airfoil motions, AIAA Journal, Vol. 13, No. 12, 2018, pp. 1-8.

[50] Kal, I., Son, O., Zaloglu, B., and Cetiner, O., Gust effect on a plunging flexible wing, 5th International Conference on Experimental Fluid Mechanics, Munich, Germany, 2018.

[51] Corkery, S.J., and Babinsky, H., Force production mechanisms for a flat plate wing at low Reynolds numbers, 2018 AIAA Aerospace Sciences Meeting, American Institute of Aeronautics and Astronautics, Kissimmee, FL, 2018.

[52] Corkery, S.J., Babinsky, H., and Harvey, J., Response of a flat plate wing to a transverse gust at low Reynolds numbers, 2018 AIAA Aerospace Sciences Meeting, American Institute of Aeronautics and Astronautics, Kissimmee, FL, 2018.

[53] Smith, Z.F., Jones, A.R., and Hrynuk, J.T., Micro air vehicle scale gust-wing interaction in a wind tunnel, 2018 AIAA Aerospace Sciences Meeting, American Institute of Aeronautics and Astronautics, Kissimmee, FL, 2018.

[54] Biler, H., Badrya, C., and Jones, A.R., Experimental and computational investigation of transverse gust encounters, 2018 AIAA Aerospace Sciences Meeting, American Institute of Aeronautics and Astronautics, Kissimmee, FL, 2018.

[55] Eroglu, B., Zaloglu, B., Cetiner, O., and Gozukara, A.C., A computational study for a wing at or pitching up to high angle of attack in presence of a spanwise gust, 9th Ankara International Aerospace Conference, Ankara, Turkey, 2017.

[56] Kal, I., Zaloglu, B., Fenercioglu, I., and Cetiner, O., An experimental investigation of a plunging wing under gust environment, 9th Ankara International Aerospace Conference, Ankara, Turkey, 2017.

[57] Manar, F.H., and Jones, A.R., Transient response of a single degree-of-freedom wing at high angle-of-attack, AIAA Journal, Vol. 55, No. 11, 2017, pp. 3681-3692.

[58] Perrotta, G., and Jones, A.R., Unsteady forcing on a flat-plate wing in large transverse gusts, Experiments in Fluids, Vol. 58, No. 8, 2017, p. 101.

[59] Mulleners, K., Mancini, P., and Jones, A.R., Flow development on a flat-plate wing subjected to a streamwise acceleration, AIAA Journal, Vol. 55, No. 6, 2017, pp. 2118-2122.

[60] Graham, W.R., Pitt Ford, C., and Babinsky, H., An impulse-based approach to estimating forces in unsteady flow, Journal of Fluid Mechanics, Vol. 815, 2017, pp. 60-76.

[61] Eldredge, J.D., and Jones, A.R., Leading-edge vortices: Mechanics and modeling, Annual Review of Fluid Mechanics, Vol. 51, No. 1, 2017, pp. annurev-fluid-010518-040334.

[62] Manar, F.H., and Jones, A.R., Vorticity production at the leading edge of flat plates at high incidence, 55th AIAA Aerospace Sciences Meeting, American Institute of Aeronautics and Astronautics, Grapevine, TX, 2017.

[63] Corkery, S.J., Stevens, R.J., and Babinsky, H., Low Reynolds number surge response of a flat plate wing at 90 degrees incidence, 55th AIAA Aerospace Sciences Meeting, American Institute of Aeronautics and Astronautics, Grapevine, TX, 2017.

[64] Son, O., Zaloglu, B., Percin, M., and Cetiner, O., Force measurement and load estimation studies at ITU for flexible flapping wings and maneuvering wings under gust, NIOPLEX International Workshop on Non-Intrusive Optical Flow Diagnostics, Delft, Netherlands, 2016.

[65] Mulleners, K., Mancini, P., and Jones, A.R., Experimental investigation of a large aspect ratio flat plate encountering a steam-wise gust, 46th AIAA Fluid Dynamics Conference, American Institute of Aeronautics and Astronautics, Washington, DC, 2016.

[66] Jaworski, J., Vortex sound generation from flexible fibers, 22nd AIAA/CEAS Aeroacoustics Conference, American Institute of Aeronautics and Astronautics, Lyon, France, 2016, p. 837.

[67] Perrotta, G.M., and Jones, A.R., Transient aerodynamics of large transverse gusts and geometrically similar maneuvers, 54th AIAA Aerospace Sciences Meeting, American Institute of Aeronautics and Astronautics, San Diego, CA, 2016.

[68] Mancini, P., Manar, F.H., Granlund, K., Ol, M.V., and Jones, A.R., Unsteady aerodynamic characteristics of a translating rigid wing at low Reynolds number, Physics of Fluids, Vol. 27, No. 12, 2015.

[69] Biler, H., Zaloglu, B., and Cetiner, O., Loading on a maneuvering NACA 0012 airfoil under spanwise gust and estimation of loads using DPIV, Workshop on Non-Intrusive Measurements for Unsteady Flows and Aerodynamics, Poitiers, France, 2015.

[70] Biler, H., Zaloglu, B., and Cetiner, O., Effect of a spanwise gust on a wing, 8th Ankara Interntional Aerospace Conference, Ankara, Turkey, 2015.

[71] Son, O., Zaloglu, B., and Cetiner, O., Experimental investigation of a wing performing a pitch-up motion under gust environment, 9th Ankara International Aerospace Conference, 2017.

[72] Klein, S., Hahn, D., Scholz, P., and Radespiel, R., Vortex interactions with a high-lift airfoil in a low speed wind tunnel, 43rd Fluid Dynamics Conference, San Diego, CA, 2013.

[73] Moriche, M., Gonzalo, A., Flores, O., and García-Villalba, M., Fast transverse maneuvers at low Reynolds numbers, AIAA SciTech 2019 Forum, American Institute of Aeronautics and Astronautics, San Diego, CA, 2019.

[74] Chowdhury, J., Cook, L., and Ringuette, M., The vortex formation of an unsteady translating plate with a rotating tip, AIAA SciTech, American Institute of Aeronautics and Astronautics, San Diego, CA, 2019.

[75] Rockwood, M., and Medina, A., Controlled generation of periodic vortical gusts by the rotational oscillation of a circular cylinder and attached plate, Experiments in Fluids, 2020, p. Ahead of Print.

[76] Dai, W., Pisetta, G., and Viola, I.M., Morphing blades for passive load control of tidal turbines, 13th European Wave and Tidal Energy Conference, 2019.

[77] Bird, H.J.A., Otomo, S., Ramesh, K., and Viola, I.M., A geometrically non-linear time-domain unsteady lifting-line theory, AIAA SciTech, San Diego, CA, 2019.

[78] Dai, W., Balaras, E., and Viola, I.M., Self-sustained limit-cycle oscillations in a flapping-foil energy harvester, European Conference on Computational Mechanics (Solids, Structures and Coupled Problems) (ECCM 6) and the European Conference on Computational Fluid Dynamics (ECFD 7), Glasgow, UK, 2018.

[79] NATO STO AVT-202, Extension of fundamental flow physics to practical MAV aerodynamics, Tech. Rep., NATO STO, May 2016.

[80] NATO STO AVT-102, Investigation of airwake control for safer shipboard aircraft operations, Tech. Report, NATO RTO, June 2007.

[81] Granlund, K., Monnier, B., Ol, M., and Williams, D.R., Airfoil longitudinal gust response in separated vs. attached flows, Physics of Fluids, Vol. 26, No. 2, 2014.

[82] Greenblatt, D., Development and testing of an unsteady low-speed wind tunnel, 31st AIAA Aerodynamic Measurement Technology and Ground Testing Conference, American Institute of Aeronautics and Astronautics, Dallas, TX, 2015.

[83] Rennie, M., Catron, B., Feroz, M.Z., and Williams, D.R., Model predictive control of wind-tunnel wind speed for low-Re unsteady aerodynamic testing, AIAA SciTech, American Institute of Aeronautics and Astronautics, 2018.

[84] Choi, J., Colonius, T., and Williams, D.R., Surging and plunging oscillations of an airfoil at low Reynolds number, Journal of Fluid Mechanics, Vol. 763, 2015, pp. 237-253.

[85] Greenblatt, D., Unsteady low-speed wind tunnels, AIAA Journal, Vol. 54, No. 6, 2016, pp. 1817-1830.

[86] Greenberg, J.M., Airfoil in sinusoidal motion in a pulsating stream, Tech. Rep. 1326, NACA, June 1947.

[87] Von Karman, T., and Sears, W.R., Airfoil theory for non-uniform motion, Journal of the Aeronautical Sciences, Vol. 5, 1938, pp. 379-390.

[88] Dryden, H.L., Turbulence investigations at the National Bureau of Standards. Proceedings of the fifth International Congress of Applied Mechanics, September 1938, Cambridge, MA.

[89] von Karman, T., 1948. Progress in the statistical theory of turbulence. Proceedings of the National Academy of Sciences, 34, 530-539.

[90] Diederich, F.W., and Drischler, J.A., Effect of spanwise variations in gust intensity on the lift due to atmospheric turbulence. NACA TN 3920, 1957.

[91] Frey, T., Expert predicts 1 billion drones in world by 2030. Accessed at https://www.insiderobotics.com.au/technology/articles-technology/Expert-predicts-1-billion-drones-in-world-by-2030/ on 26/02/2019.

[92] Watkins, S., Milbank, J., Loxton, B., and Melbourne, W., Atmospheric winds and their implications for microair vehicles, AIAA Journal, Vol. 44, No. 11, 2006, pp. 2591-2600.

[93] Mohamed, A., Massey, K., Watkins, S., and Clothier, R., The attitude control of fixed-wing MAVS in turbulent environments. Progress in Aerospace Sciences, 66, 2014, pp. 37-48.

[94] Watkins, S., Thompson, M., Loxton, B., and Abdulrahim, M., On low altitude flight through the atmospheric boundary layers, International Journal of Micro Air Vehicles, Vol. 2, No. 2, 2010, pp. 55-68.

[95] Watkins, S., Mohamed, A., and Ol, M.V., 2019. Flight-relevant gusts: Computation-derived guidelines for MAV ground test unsteady aerodynamics. AIAA Scitech 2019 Forum, San Diego, USA, January 2019.

[96] Barnes, C.J., and Visbal, M.R., Effects of vertical position and orientation on a vortical-gust/airfoil interaction at a transitional Reynolds number, 47th AIAA Fluid Dynamics Conference, American Institute of Aeronautics and Astronautics, Denver, CO, 2017.

[97] Bansal, S., Azzam, A., and Lavoie, P., On the generation of unsteady flows using an active grid and the effect of freestream turbulence on longitudinal gust response of an airfoil, NATO STO AVT-282 meeting in Athens, Greece, Dec. 2018.

[98] Bansal, S., and Lavoie, P., UTIAS initial research findings for an airfoil in periodic streamwise gusts, Notes from AVT-282, 2019.

[99] Azzam, A., and Lavoie, P., Production of unsteady flows through the use of an active grid, APS Division of Fluid Dynamics, 2017.

Chapter 2 – THE EFFECT OF TRANSVERSE VELOCITY PROFILE

Ignacio Andreu-Angulo and Holger Babinsky
University of Cambridge
UNITED KINGDOM

Hülya Biler, Girguis Sedky and Anya Jones
University of Maryland
UNITED STATES

In this chapter, the flow field and force produced during a wing-gust encounter have been compared between a top-hat and a sine-squared transverse gusts. Experiments are performed at Reynolds number between 20 000 and 30 000 in a water tow tank. Both gusts are generated by disturbing the flow in a section of the tank at different velocities, resulting in gust ratios, GR, equal to 0.5, 0.75, 1.0, and 1.5. Time-resolved force and flow field measurements are analysed and compared with linear theories. The force results show a smoother increase in lift for the sine-squared gust accompanied by a lower maximum lift. The specific range of GRs was selected to capture the non-linear behaviour of the top-hat gust on lift. However, for the same gust ratios, the sine-squared gusts remained in the linear regime. As a result, Küssner's theory is found to accurately predict the loads resulting from the sine-squared gust for a larger range of gust ratios than the top-hat gust. The non-linear behaviour of the top-hat gust on the lift force is linked to higher levels of circulation shed from the wing edges and the development of non-planar wakes. It is concluded that the gust shape is a critical parameter determining the wing-gust encounter characteristics.

2.1 INTRODUCTION

Air vehicle gust encounters are a common occurrence resulting from the turbulent flows in the atmospheric boundary layer. These flows develop as a consequence of terrain roughness and temperature changes [1], [2]. Conventional aircraft travelling at high speeds experience a limited impact from gusts. However, at small scales, vehicle velocities can decrease by two orders of magnitude [3] to [5], as shown in Figure 2-1(a). Therefore, the ratio between the gust velocity V and the flight velocity U increases above 1 for a larger range of meteorological conditions. This relation between the two velocities is known as the gust ratio, GR = V/U. In micro air vehicles, MAVs, the comparatively stronger gust velocities can result in separated flows and large variations in loads. Under these conditions, the ability to maintain control reduces [6]. In addition, micro air vehicles experience more frequent gust encounters in their flight regimes. At lower altitudes and in city terrains, the terrain morphology results in larger values of turbulence intensity [7], as shown in Figure 2-1(b). A good understanding of gust characteristics is critical for MAV design.

Turbulence in the atmosphere can result in a large variety of gusts that affect aerial vehicles. Vortex gusts are characterised by coherent vortical structures that travels in the vehicle proximity and are currently being studied [9]. Moreover, changes in the incoming freestream flow velocity, or streamwise gusts, are also of interest [10]. A third type of gust that results in highly unsteady and separated flows is the transverse gust. In these cases, there is a flow stream in the direction normal to the vehicle cruise direction. Transverse gusts can have different profiles based on the distribution of incoming flow. These variations on the gust velocities will result in different effects on a vehicle as demonstrated in the study presented.

In this paper, two different transverse gusts shown in Figure 2-2 are analysed. The first gust consists of a Top-Hat (TH) edge gust, which is characterised by a sharp variation in transverse flow velocity on the gust edges. Moreover, the gust velocity is constant inside of the gust and presents two thin shear layers on either edge. In this shear layers, the gust vorticity is concentrated. The idealised step gust has been extensively studied since discrete step gusts with these characteristics can be combined to recreate any other gust shape. The second gust studied consists of a Sine-Squared (SS) distribution. This is a more realistic gust shape, similar to those experienced by aerial vehicles. This gust is characterised by a finite gradient of velocity along the entire gust width.

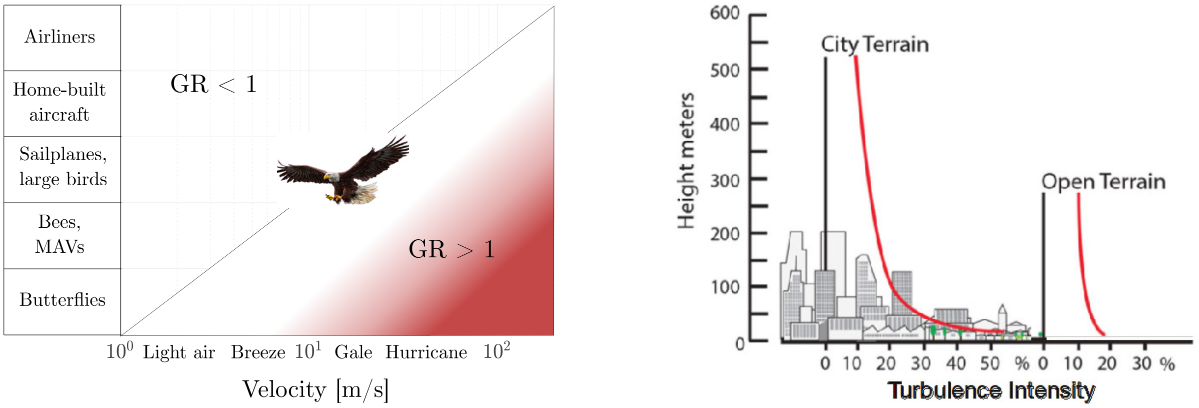

(a) Comparison between Atmospheric Airspeeds and Air Vehicles Cruising Speeds [3].

(b) Turbulence Intensity at Different Heights from the Ground, Adapted from Ref. [8].

Figure 2-1: Characteristics of Micro Air Vehicles Flight Regime.

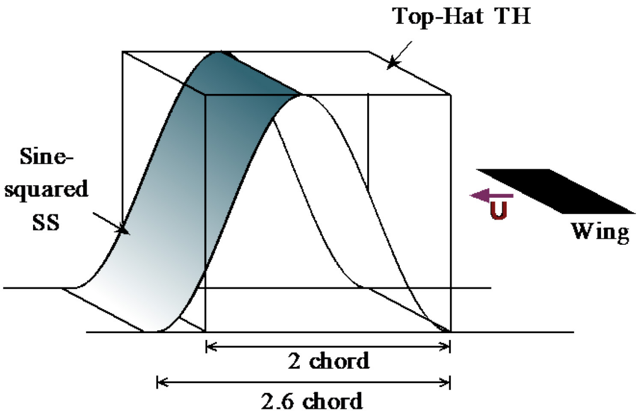

Figure 2-2: Schematic of the Differences Between the Two Gusts Analysed. Coloured surfaces represent the transverse velocity magnitudes for the top-hat (red) and sine-squared (blue).

The aim of this study is to compare the two gusts in order to identify trends that can be extrapolated to a more general variety of gust profiles. Motivated by MAVs applications, the gust ratios under consideration are relatively large, well beyond the regime were linear methods are expected to be valid. Furthermore, one of the goals is to determine the limits of these techniques, specifically Küssner's method, which is considered to be the most useful. It has been widely applied to study low gust ratios. However, there is little known about its accuracy for a variety of gust profiles at large GRs.

2.1.1 Küssner Theory

The Küssner model was developed to predict the forces associated with a transverse gust acting on a wing [11]. It is a simple but powerful linear model that has been validated for a large range of gusts. Nevertheless, its accuracy for high-amplitude gusts is uncertain given the assumptions engraved in the model. Firstly, this model is derived for a potential flow and therefore the flow is assumed to be irrotational and incompressible. In addition, it is assumed that the vorticity elements shed from the wing trailing edge are confined to the horizontal plane and the method does not account for shedding of leading-edge vorticity. Lastly, the gust shear layer is assumed to be rigid and does not deflect during the wing-gust encounter. Experimental results have demonstrated that there is some degree of wing-gust interaction that increases with gust ratio, although it appears to have little influence on the gust force [12]. The lift response predicted by the Küssner model can be expressed as [13],

$$C_l = 2\pi \frac{V}{U} G(s/c) \tag{2-1}$$

This solution approaches the steady result $C_l = 2\pi\alpha$ as $s/c \rightarrow \infty$, where α corresponds to the effective angle of attack V/U. However, this study aims to investigate the unsteady effects that develop at low s/c. Therefore, short gusts profiles are considered. Even though Küssner model is derived for a step change in transverse flow, a Duhamel superposition can be used in order to reproduce the result from an arbitrary gust shape. Using this superposition, the load on the wing is calculated by summing the response of incremental elements in the gust profile. A schematic diagram of the Küssner model applied to an arbitrary shaped gust is shown in Figure 2-3.

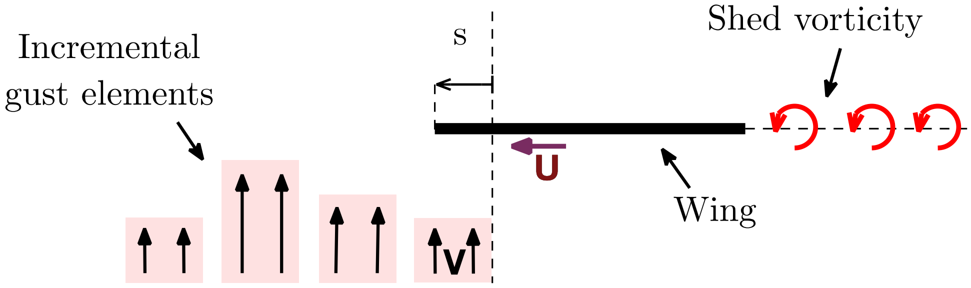

Figure 2-3: Schematic Illustration of the Küssner Model for an Arbitrary Shape Gust. Shed vorticity is confined to the horizontal axis.

Using the Duhamel superposition, the Küssner response for a top-hat gust with a width of 2 chords and a sine-squared gust with a width of 2.6 chords are given in Figure 2-4. Note that this data is valid for all gust ratios due to the linear nature of Küssner's method. These results show that, as the wing enters the gusts, the lift response is expected to rise faster for the top-hat gust case. Furthermore, even though the maximum transverse gust velocity at the gust centre, s/c = 1.8, is identical for the two gusts, the maximum lift experienced by the sine-squared gust is 27% lower than the top-hat edge gust. Both gusts present similar behaviours on the lift response as the wing exits the gust. These results and the assumptions associated with this model are validated against a wide range of experimental results in Section 2.3.

2.1.2 Gust Force Contribution

In order to study the differences in the Küssner responses for both gusts, the result from Figure 2-4 can be decomposed into a force arising exclusively from the gust vorticity and a force resulting from the vorticity shed by the wing. The component that is only dependent on the gust vorticity is referred here as the gust force. The flow field associated with this force is shown in Figure 2-5(a). The gust force result for a sharp-edge gust has been derived by Von Karman and Sears [14] and was experimentally measured by Corkery [12]. However, an analytical solution for an arbitrary gust shape is not found in the literature. Therefore, the sine-squared gust force was calculated numerically. The theoretical results for the gust force contribution of the two gusts are presented in Figure 2-5(b). The remaining force necessary to arrive at the Küssner solution can be attributed to shed vorticity.

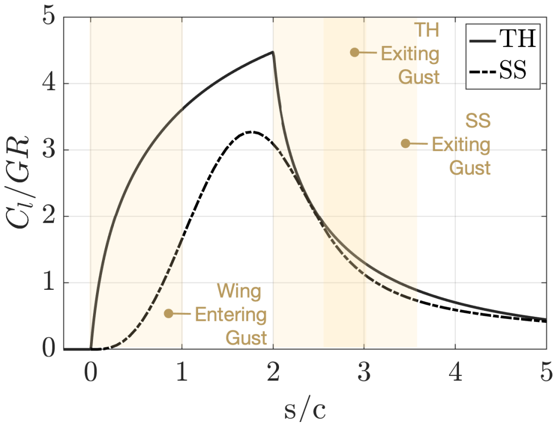

Figure 2-4: Küssner Response Calculated for the Two Gusts.

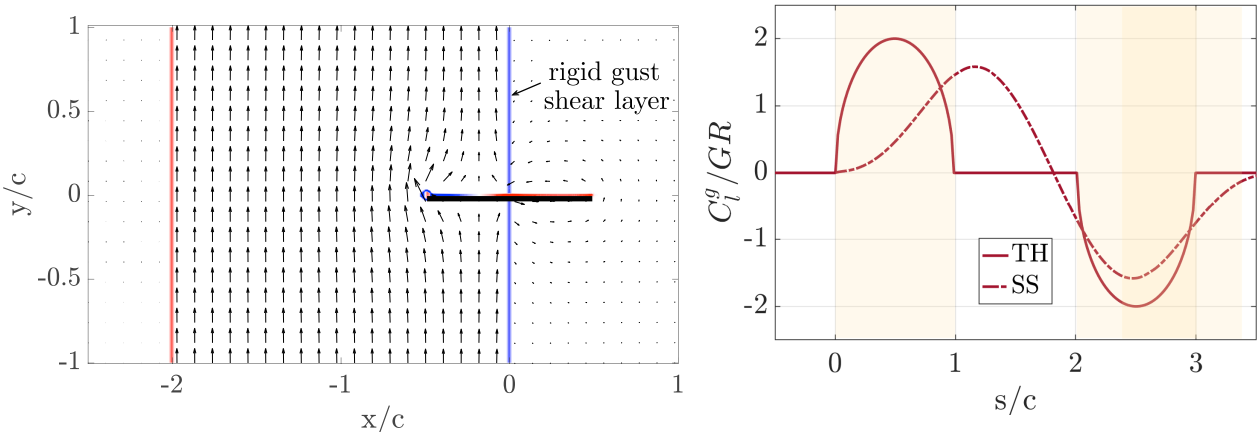

(a) TH Flow Field Associated with the Gust Force. **(b) Gust Force Calculated for the Two Gusts.**

Figure 2-5: Gust Force.

It can be noticed that the gust force is limited to the region where the wing intersects the gust shear layers. For the top-hat gust, these are concentrated into one chord length during gust entry and exit. The vorticity of the SS gust is distributed along its full width and the resulting gust force is therefore present throughout the entire wing-gust encounter. As the wing enters both gusts, the gradient of the TH gust force is much greater than that of the SS gust, demonstrating some of the differences in the Küssner lift responses seen in Figure 2-4. Effectively, a phase shift is observed between the two gusts and the maximum gust force contribution is 2 and 1.5 for the top-hat and sine-squared gusts, respectively.

2.2 EXPERIMENTAL METHODOLOGY

The top-hat gust experiments are performed in the 10 x 1 x 1 meter water tow tank at the University of Cambridge. An overview of the experimental cases is given in Table 2-1. In this facility, models are towed trough stationary water, which facilitates the creation of a transverse gust. The absence of a free stream flow permits the implementation of an undisturbed cross flow. In addition, more accurate force measurements can be achieved in water due to scaling effects, which results in forces approximately 4 times larger than in air for the same flow conditions. The Reynolds number for the experiments is set to 30,000 based on the model chord. The gust ratio is defined as the ratio between the transverse flow velocity and the wing tow velocity, and it is adjusted by varying the first. The tow velocity is determined using an electro-optical sensor with a resolution of 1 mm. The model used in the top-hat gust encounter experiments consists of a glass plate with a chord length of 0.12 m, a span of 0.48 m, and a thickness of 0.004 m. The model is towed vertically with its lower end free and its top end attached to a skim plate as shown in Figure 2-6(a). The top end is directly connected to the force balance.

The sine-squared gust experiments are performed in the University of Maryland (UMD) free surface 7 x 1.5 x 1 meter water towing tank. Streamwise translation of the model is driven by two brushless linear motors (H2W BLDC-08) located on the carriage. The wing model used for the force measurements is a 0.076 m chord, 0.305 m span, and 4.3% thickness ratio aluminium flat plate. In this case, the model is towed horizontally as shown in Figure 2-6(b). In order to avoid laser shadows, a glass flat plate with same dimensions is used for PIV experiments. Both force and PIV experiments were performed at 20,000 Reynolds number which corresponds to freestream speed of 0.26 m/s.

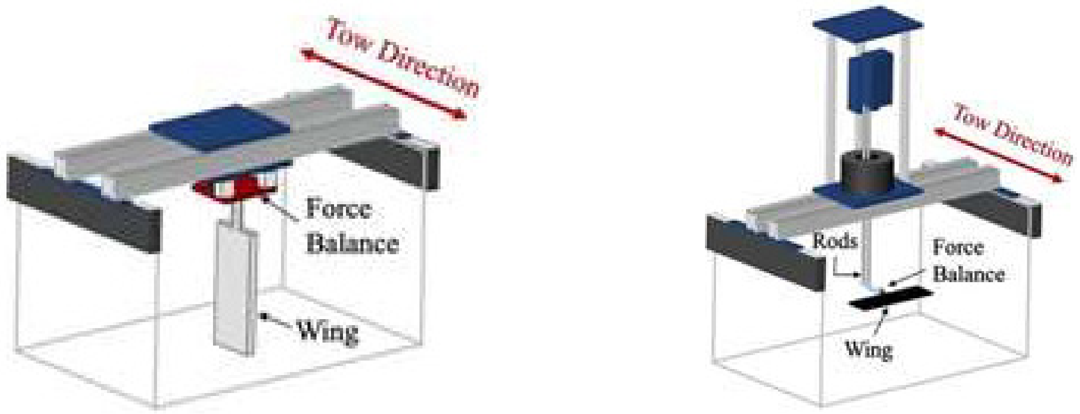

(a) Set-Up for the Top-Hat Edge Gust. **(b) Set-Up for the Sine-Squared Gust.**

Figure 2-6: Experimental Set-Up.

In order to recreate the desired top-hat edge gust, a rig is assembled inside the tow tank test section to produce a cross flow in the direction indicated by the red arrows in Figure 2-9(a). More information regarding the set-up can be found in Ref. [15]. The resulting velocity profile is shown in Figure 2-7 for a distance of 0.10 m from the gust outlet, which corresponds to the travelling location of the wing. The gust has an effective width of 0.24 m equal to two chord lengths. The experimental profile only deviates from the ideal case due to some minor disturbances in the top region and a finite slope on both sides due to the shear layer thickness.

The sine-squared transverse gust in these experiments is created by using a variable speed water jet, shown in Figure 2-9(b). This gust generation system consisted of a swimming pool pump (Hayward TriStar SP3202VSP) allowing for a wide range of pump speeds, PVC pipe plumbing system, plenum and a 36 by 0.5 inch honeycomb with an 1/8 inch individual cell width flow straightener section. The water is drawn from the bottom of the tank to the pump, then directed to the plenum and flow straightener section by the plumbing system. The resulting flow is characterised by using time-resolved PIV for various pump speeds and spanwise locations. The measured gust velocities are extracted from a region where the model tows through, and the best fit to these measurements is found to be a sine-squared profile, $V(x) = V_p$

$\sin^2(\pi x/w)$, where V_p represents the peak gust velocity, x represents streamwise location, and w represents the gust width. The gust characterisation showed that the mean gust width is 0.2 m. A range of peak gust velocities (0.06 to 0.4 m/s) can be obtained with the current set-up. Further details of the characterisation can be found in Ref. [16].

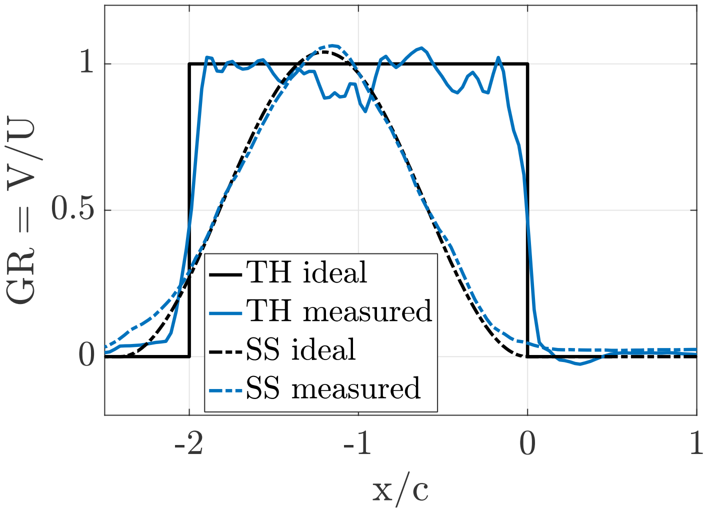

Figure 2-7: Gust Velocity Profile Compared to Ideal.

Table 2-1: Experimental Cases.

	GR = 0.5	GR = 0.75	GR = 1.0	GR = 1.5
Top-hat	α = 0, 20 deg	α = 0 deg	α = 0 deg	α = 0 deg
Sine-squared	α = 0, 20 deg	α = 0 deg	α = 0 deg	α = 0 deg

2.2.1 Force Measurements

Forces were measured and processed with slight differences between the two gusts due to the distinct experimental set-ups. For the TH gust, a two-component force balance is used to acquire the streamwise and stream-normal components of the force experienced by the model. Each of the two components is measured by one load cell with a range of ± 50 N and a resolution of 0.01 N. The force data are normalized by the dynamic pressure and the wing area in order to calculate the coefficients of lift and drag. The raw signal measured exhibits large amplitude noise at 20 Hz. Therefore, a low pass bidirectional filter at a frequency of 18 Hz is applied to the signal. In addition, the natural frequency of the wing model is measured at 4 Hz. The lift coefficient results after the various levels of filtering are shown in Figure 2-8(a). The force uncertainty due to cell crosstalk and bending moment for the force balance used has been determined in Ref. [12]. The results from that study concluded that the total uncertainty is below 2% for data that is ensemble averaged over 5 runs.

In the case of the sine-squared gust set-up, a 6 degree-of-freedom submergible ATI Mini-40 force balance is used to measure forces and moments. The sampling rate for these experiments is 1 kHz. Each case investigated is repeated 5 times, synchronized and ensemble averaged. The measured normal and axial forces are converted to lift and drag components and then non-dimensionalized by dynamic pressure and wing area. Fast Fourier Transform (FFT) is performed and a 5 Hz low pass filter is applied to all cases in order to remove mechanical and electrical vibrations, see Figure 2-8(b).

2.2.2 Particle Image Velocimetry (PIV)

The two experimental facilities also use different PIV set-ups. For the TH gust, planar time-resolved PIV data is acquired at the wing mid-span using the two camera set-up shown in Figure 2-9(a). A high speed Nd:YLF 527 nm laser is used to create a beam pulsing at a frequency of 0.4 kHz. This beam is then transformed into a laser sheet through a set of optics. The laser sheet has a thickness of about 2 mm and illuminates Titanium Dioxide seeding particles placed in the flow. The glass model permits the light to travel through and therefore the entire flow field can be resolved. At the same time, surface reflections are mitigated. The particle data is collected by the two cameras, which have a resolution of 1280 x 800 pixels and are synchronized with the laser using a PTUX unit. The field of view of the first camera resolves the data upstream, and on the wing upper surface. The second camera is positioned to measure the data downstream and on the lower surface. Using the DaVis software, the images from both cameras are later processed and stitched together to obtain the final velocity fields.

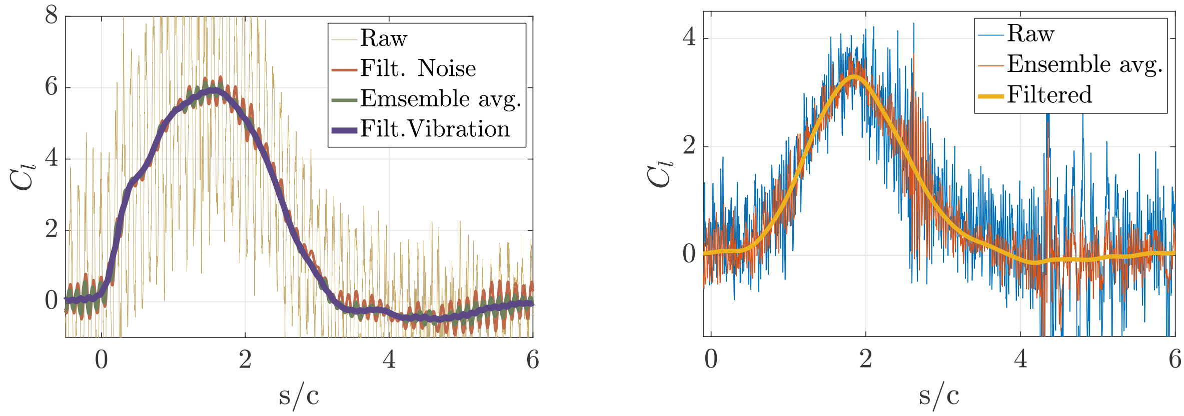

(a) Top-Hat Force Data Processing.

(b) Sine-Squared Force Data Processing.

Figure 2-8: Force Processing Techniques.

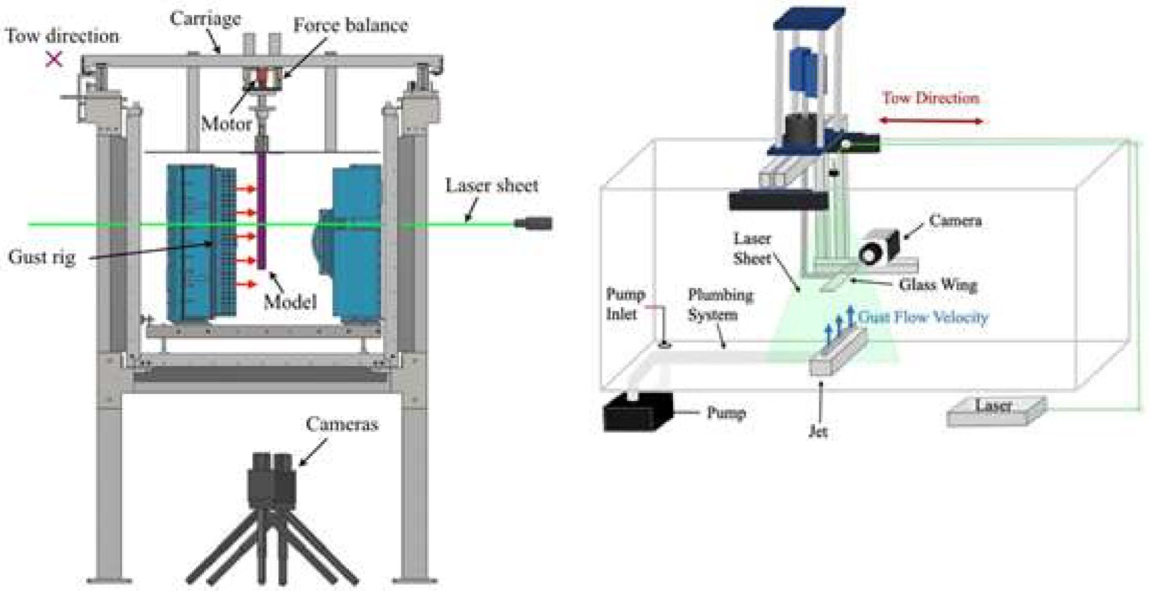

(a) Top-Hat Gust PIV Set-Up.

(b) Sine-Squared Gust PIV Set-Up.

Figure 2-9: PIV Set-Up.

The PIV set-up for the sine-squared gust uses a phantom v641 (4 MP) camera to acquire images at 1 chord length off from mid-span. A Nd:YLF laser (Litron LDY 304, 30 mj pulse, 10 kHz max) are used as the light source and class IV soda lime spheres (diameter of 37 µm) is used as seeding particles. Both the camera and the laser sheet are towed with the carriage to achieve a large investigation range Figure 2-9(b). The PIV experiments are sampled at 0.7 kHz and 4250 images are acquired for each case. All cases are repeated 8 times and ensemble averaged. DaVis v8.1 is used as the processing software. 24 x 24 and 16 x 16 px interrogation windows are used for the first and second passes, respectively.

2.2.3 Measurement of Circulation

In the case of the top-hat gust, the gust vorticity is concentrated in a thin shear layer. This allows for a simple differentiation between the gust vorticity and the shed vorticity. Furthermore, a manual mask was applied to the experimental results in order to isolate the shed vorticity, as shown in Figure 2-10(a). The remaining circulation is then divided into leading edge and trailing edge vorticity and measured directly from the PIV results.

The aforementioned approach cannot be accomplished in the sine-squared gust due to the dispersion of gust vorticity. To compute the LEV circulation in the SS gust, a Control Volume (CV) is defined at the wing leading edge and the circulation flux across the CV is computed. This method is outlined in Ref. [17]. Figure 2-10(b) shows the CV used to calculate the vorticity flux. The CV chosen is a square with a side length equal to 15% of the chord centred offset from the leading edge such that the leading edge is a quarter of the side away from the edge of the square. If all the vorticity produced at the leading edge feeds the strength of the LEV, then the change rate of the LEV's circulation is equal to the vorticity flux leaving the CV,

$$\frac{\mathrm{d}\Gamma}{\mathrm{d}t} = \oint_s \omega \vec{u} \, . \, \hat{n} \, \mathrm{d}s \tag{2-2}$$

Since the vorticity that feeds the LEV is negative, only the negative vorticity is used to calculate the rate of change of LEV circulation.

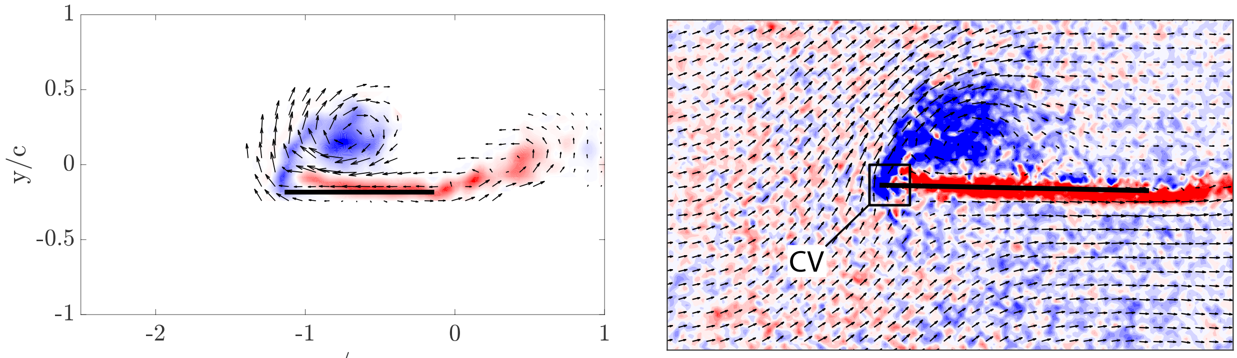

(a) Shed Circulation After Masking the Gust Shear Layers of the Top-Hat Gust.

(b) Procedure to Calculate the Circulation Shed for the Sine-Squared Gust.

Figure 2-10: Methods to Measure the Circulation Shed from the Two Gusts.

2.3 ANALYSIS OF RESULTS

After experiments were performed, the flow velocity fields results were compared between the two gusts. The first case analysed was the lowest Gust Ratio investigated (GR = 0.5), shown in Figure 2-11. The results show the concentrated gust shear layers in the case of the top-hat gust and the smoother vorticity distribution in the sine-squared gust. For this gust ratio, both cases appear to result in similar flow structures. The leading-edge vortex grows as the wing travels along both gusts and stays close to the wing surface. Only a slightly larger LEV in the TH case can be perceived. In Figure 2-11(a), the evolution of the vorticity shed from the trailing edge at s/c = 2.0 deflects above the horizontal axis. This could be a result of stronger shed vorticity or a stronger influence of the gust deformation. These results are also observed from vortex model results presented in Appendix 1. On the other hand, the wake behind the SS wing remains planar.

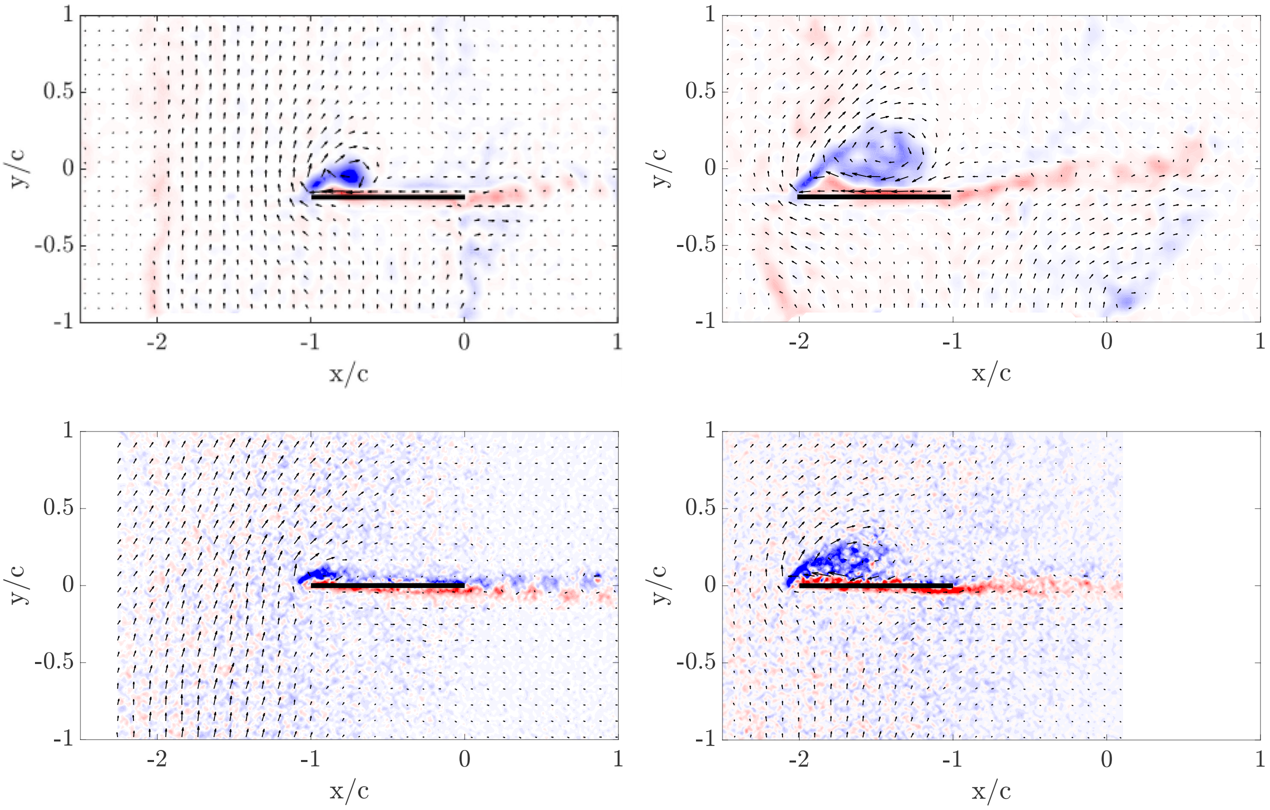

(a) s/c = 1.0. (b) s/c = 2.0.

Figure 2-11: GR = 0.5 Experimental Flow Field Results for TH (Top) and SS (Bottom).

At the higher gust ratio of 1.0, the differences in the flow between the two gusts increase. Once the wing is fully submerged, Figure 2-12(a), the wing in the TH gust presents a much larger leading-edge vortex. In addition, the TEV has already started to roll up. Meanwhile, the LEV development on the SS gust is comparable to the lower GR = 0.5. Similarly, the vorticity shed from the trailing edge still remains planar. The larger differences in the flow between the gust ratios for the TH gust may indicate a larger difference in the loads. These differences continue at s/c = 2, where the LEV in the TH gust of Figure 2-12(b) has advected one chord above the wing. In addition, it has reached the wing trailing edge and starts to interact with the TEV, which results in an increase of the TEV roll up. Furthermore, the differences with the SS case, which presents a more planar wake, increases. The sine-squared gust also presents some degree of LEV separation and TEV roll up at s/c = 2.0. This development is similar to the TH gust at s/c = 1.0. It is also important to note that the TH gust exhibits a larger wing-gust interaction with a very distinct gust shear layer deflection. This interaction is not as clear in the SS gust, which may be a result of the smoother distribution of vorticity in this case. The deformation of the gust shear layer is expected to further differentiate the results from those of the Küssner prediction.

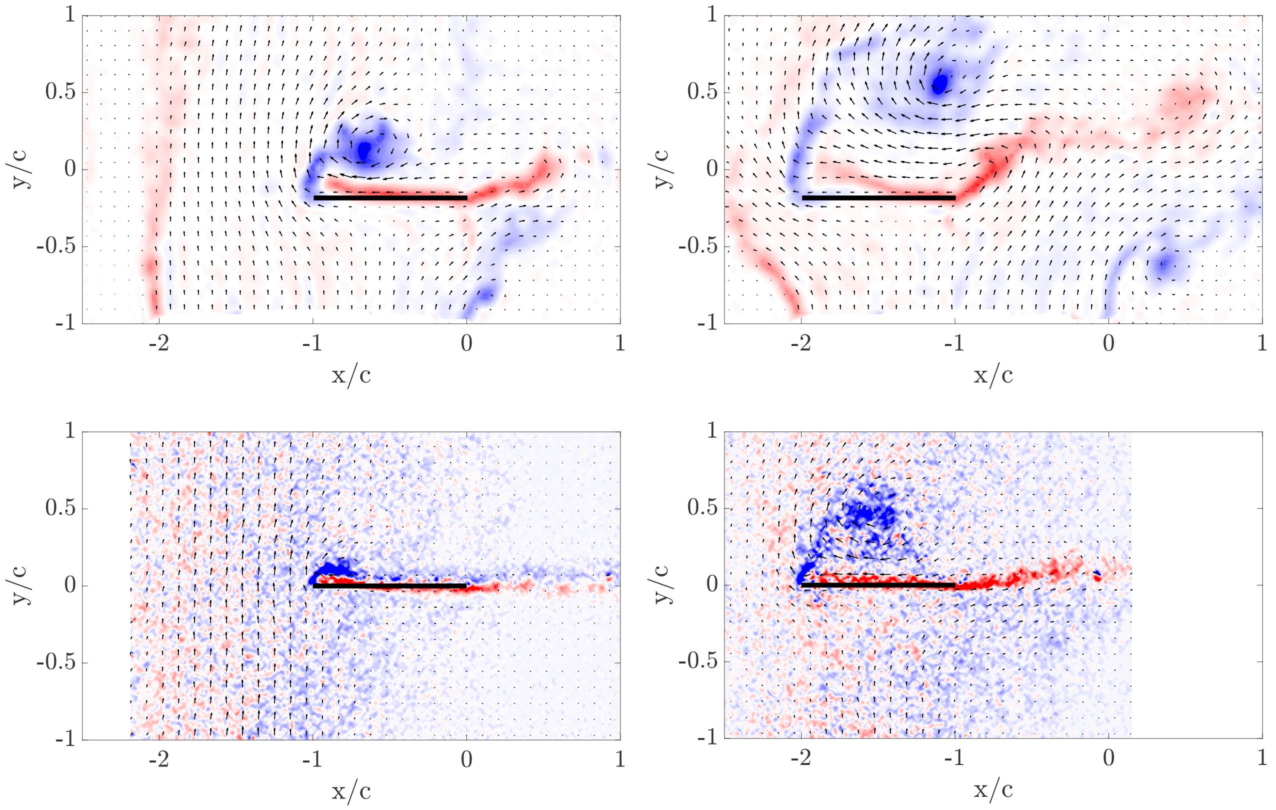

(a) s/c = 1.0. **(b) s/c = 2.0.**

Figure 2-12: GR = 1.0 Experimental Flow Field Results for TH (Top) and SS (Bottom).

The flow fields for the wing at α = 20 deg in Figure 2-13 also present differences between the two gust profiles. These results were acquired at GR = 0.5, nevertheless the flow presents a large LEV for both gust shapes. Both gusts display a more separated flow than the previous case at α = 0 in Figure 2-11. Similar to previous results, the LEV for the top-hat gust develops faster. Furthermore, the interaction between the LEV and the TEV is also stronger for the TH gust.

2.3.1 Circulation Comparison

The circulation shed from the leading edge was measured from PIV data using the method explained in Section 2.2. The LEV circulation measurements for the gust ratio of 0.5 and 1.0 are presented in Figure 2-14. The amount of circulations shed from the two gusts is comparable for GR = 0.5. This case corresponds to the relatively similar flow evolution observed qualitatively in Figure 2-11. The main difference measured occurs at s/c = 1.0, where the LEV in the TH gust is considerably stronger. This indicates that the rate of circulation shedding dΓ/dt is higher for the top-hat when the wing is entering the gust. However, when the wing is completely inside of the gust the sine-squared presents a higher rate of shed circulation.

For GR = 1.0, the difference between the two gust shapes increases. This corresponds to a more developed LEV shown in Figure 2-12(b). The strength of the LEV in the top-hat edge is consistently larger by a value of approximately 2. Once more, the largest difference occurs at s/c = 1.0 and the trends of the shed circulation rate are similar to the GR = 0.5 case. From the flow field measurements and the shed circulation data, we can conclude that gust ratio variations for high-amplitude gusts have a larger impact on the top-hat gust. Remember that this gust has a larger gradient of transverse velocity. This is analysed in more detail with the load results presented in the following section.

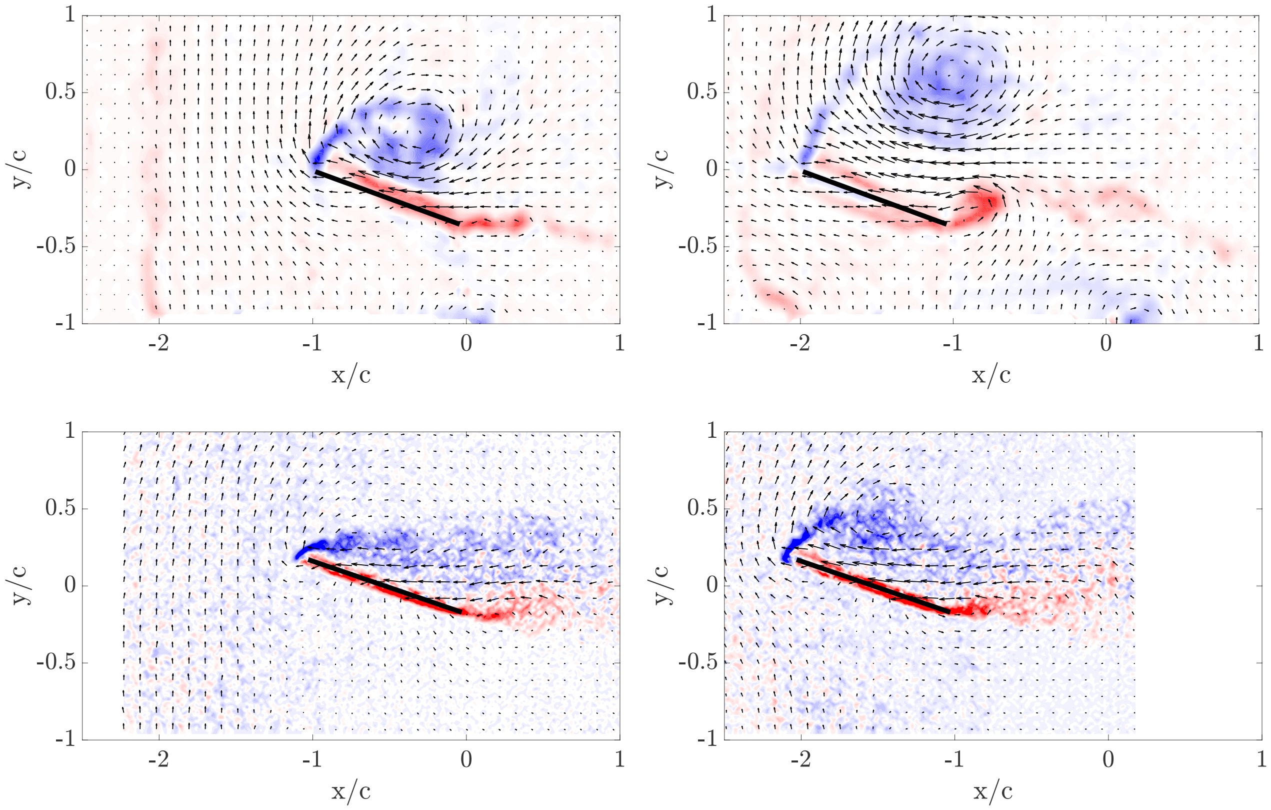

(a) s/c = 1.0.

(b) s/c = 2.0.

Figure 2-13: GR = 0.5, α = 20° Experimental Flow Field Results for TH (Top) and SS (Bottom).

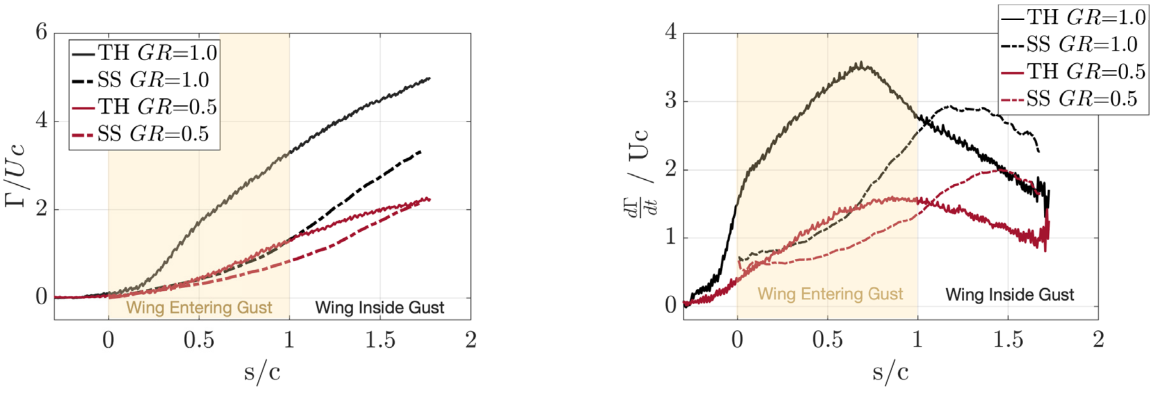

(a) Circulation Shed.

(b) Rate of Circulation Shed.

Figure 2-14: Characteristics of the Shedding of Circulation from the Leading Edge of the Wing for the Two Gusts.

2.3.2 Force Comparison

The lift measurements for the four gust ratios of interest are shown in Figure 2-15 and the peak values are given in Table 2-2. The main difference between the two gust profiles arises from the lift magnitude, which is substantially higher for the TH case. This is true even at GR = 0.5, where the flow morphology and circulation shed from the leading edge is similar between the two gusts. This larger force for the TH gust was partially predicted by Küssner's method, seen in Figure 2-4. However, the experimental results show an even larger discrepancy. For the high gust ratios, the maximum lift experienced by the TH is approximately 1.8 times larger, while Küssner predicted a difference of 1.4.

Table 2-2: Maximum Lift Coefficient.

	GR = 0.5	GR = 0.75	GR = 1.0	GR = 1.5
Top-hat	2.3	4.2	5.8	9.4
Sine-squared	1.6	2.3	3.3	4.9

The two gusts also present distinct shapes of the lift curve. The results from the top-hat gust display a faster lift rise as the wing enters the gust. This was also predicted by Küssner's theory. Some of the differences in the region 0 < s/c < 1 can be attributed to the gust force explained in Section 2.1. The remaining differences are then attributed to the loads resulting from the circulation shed from the wing. It was shown in the previous section that the difference in shed vorticity between the two gusts increases with GR and therefore the load differences are also expected to increase with gust ratio. As the wing approaches s/c = 2.0, the difference in loads decreases. This corresponds to an increase in the gust force and the shedding rate for the sine-squared gust. At the same time, the gust force on the TH gust is zero and the rate of shed vorticity decreases. The difference between the TH and SS lift responses continues to decrease until all values converge at s/c = 3. Furthermore, as the wing leaves the gust s/c > 3, there is a recovery region following the TH gust that is not as noticeable in the SS case. In this region, the lift experienced by the wing becomes negative by an amount proportional to the gust ratio.

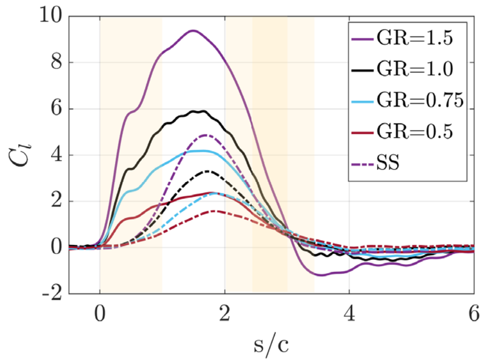

Figure 2-15: Coefficient of Lift Results for the Two Gusts for a Constant α = 0.

A more detailed comparison to the Küssner prediction can be performed after normalizing the results by the gust ratio. The top-hat gust results in Figure 2-16(a) show a linear divergence from Küssner as the gust ratio increases. When the wing enters the gust, the lift values increase above the Küssner prediction. At the same time when the wing is exiting the TH gust the lift is lower. These trends become more evident as the gust ratio increases. This difference can be attributed to the leading-edge separation and the distortion of the trailing edge wake observed in the flow fields. These flow characteristics were less significant for the case of the sine-squared gust. Therefore, the experimental lift measurements for this gust profile agree better with the Küssner prediction. The results in Figure 2-16(b) show a good agreement for all gust ratios up to s/c = 2.0 after which experimental results are lower than the prediction. These results show that the gust ratio effects have a larger influence on the top-hat gust, which at the same time diverges from the Küssner response faster than the sine-squared gust.

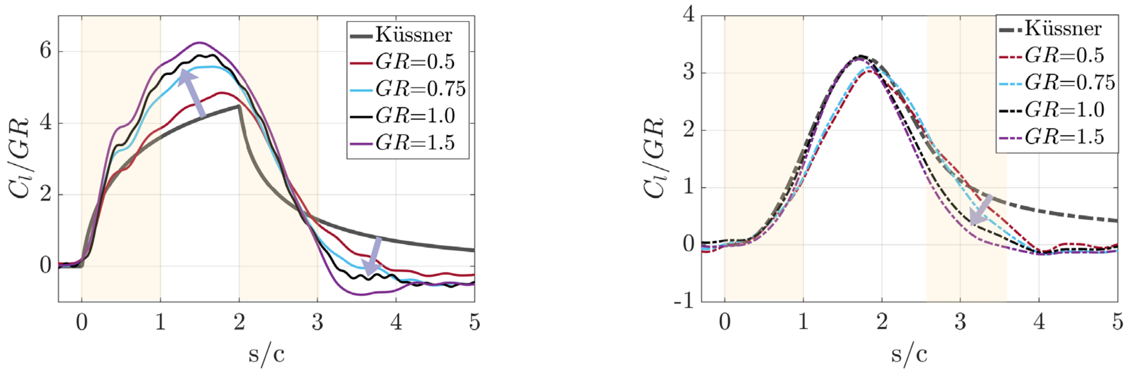

(a) Top-Hat Gust.

(b) Sine-Squared Gust.

Figure 2-16: Comparison of Küssner's Prediction with Experiments at Different Gust Ratios.

2.4 CONCLUSIONS

Two different transverse gust profiles were compared for different gust ratios and angles of attack. Experimental flow field and force measurements for the two gusts were quantified. The main results from this chapter show that:

- Differences in the loads arise directly from the differences in the gust vorticity distribution, even if no vorticity is shed from the wing. This was identified as the gust force and is only present when the wing is intersecting the gust shear layer.
- The trailing vortex sheet was found to remain significantly planar for the sine-squared gust. On the other hand, the TH case presents clear TEV deflection from the horizontal axis. This is attributed to stronger vorticity shed, TEV-LEV interaction and gust shear layer deformation.
- For the same gust ratio, forces were consistently lower for the sine-squared gust even when the maximum transverse flow velocity is the same as in the TH gust. These lower forces were correlated with a lower gust force and a weaker shedding of vorticity from the wing.
- The differences in the flow fields and the forces between the gusts were found to increase with gust ratio. This is a result of the non-linearities arising in the top-hat gust, which starts to diverge from the Küssner response.
- The large differences on the flow field and the loads between the two gusts for the same gust ratio suggests that GR alone is insufficient to characterise different transverse gust profiles. An additional parameter which can characterise the velocity gradient across the gust is necessary.

2.5 ACKNOWLEDGEMENTS

The authors I. Andreu-Angulo and H. Babinsky would like to thank the Cambridge Trust and Sidney Sussex College for financial support. H. Biler and A. R. Jones gratefully acknowledge support by the Air Force Office of Scientific Research under grant FA9550-16-1-0508 and the National Science Foundation under Grant No. 1553970.

2.6 REFERENCES

[1] Fuller, J.R., Evolution of airplane gust loads design requirements, Journal of Aircraft, Vol. 32, No. 2, 2008, pp. 235-246. doi:10.2514/3.46709.

[2] Watkins, S., Mohamed, A., Marino, M., Thompson, M.A., Fisher, A., Thompson, M., Clothier, R., and Ravi, S., The turbulent flight environment close to the ground and its effects on fixed and flapping wings at low reynolds number, Tech. Report, 2013.

[3] Tennekes, H., The Simple Science of Flight, The MIT Press, 2009.

[4] del Estal Herrero, A., Percin, M., Karasek, M., and van Oudheusden, B., Flow visualization around a flapping-wing micro air vehicle in free flight using large-scale PIV, Aerospace, Vol. 5, No. 4, 2018, p. 99. doi:10.3390/aerospace5040099.

[5] De Wagter, C., Karásek, M., and de Croon, G., Quad-thopter: Tailless flapping wing robot with four pairs of wings, International Journal of Micro Air Vehicles, Vol. 10, No. 3, 2018, pp. 244-253. doi:10.1177/1756829318794972.

[6] Watkins, S., Milbank, J., Loxton, B.J., and Melbourne, W.H., Atmospheric winds and their implications for microair vehicles, AIAA Journal, Vol. 44, No. 11, 2006, pp. 2591-2600. doi:10.2514/1.22670.

[7] Watkins, S., Thompson, M., Loxton, B., and Abdulrahim, M., On low altitude flight through the atmospheric boundary layer, International Journal of Micro Air Vehicles, Vol. 2, No. 2, 2010, pp. 55-68. doi:10.1260/1756-8293.2.2.55.

[8] Vance, J. T., Faruque, I., and Humbert, J. S., Kinematic strategies for mitigating gust perturbations in insects, Bioinspiration and Biomimetics, Vol. 8, No. 1, 2013. doi:10.1088/1748-3182/8/1/016004.

[9] Engin, K., Aydin, E., Zaloglu, B., Fenercioglu, I., and Cetiner, O., Large scale spanwise periodic vortex gusts or single spanwise vortex impinging on a rectangular wing, 2018 Fluid Dynamics Conference, 2018. doi:10.2514/6.2018-3086.

[10] Chowdhury, J., Cook, L., and Ringuette, M.J., The vortex formation of an unsteady translating plate with a rotating tip, AIAA Aerospace Sciences Meeting, San Diego, California, 2019. doi:10.2514/6.2019-0348.

[11] Küssner, H.G., Untersuchung der bewegung einer platte beim eintrill in eine strahlgrenze. *Luftfahrtforschung*, 1930, p. 425.

[12] Corkery, S.J., Unsteady Aerodynamics of Wing Gust Encounters, Ph.D. thesis, The University of Cambridge, 2018.

[13] Leishman, J.G., Principles of Helicopter Aerodynamics, 2nd ed., Cambridge University Press, Cambridge, 2000.

[14] Von Karman, T., and Sears, W., Von Karman, Airfoil theory for non-uniform motion, Journal of the Aeronautical Science, Vol. 5, No. 10, 1938, pp. 379-390.

[15] Corkery, S.J., Babinsky, H., and Harvey, J.K., On the development and early observations from a towing tank-based transverse wing–gust encounter test rig, Experiments in Fluids, Vol. 59, No. 9, 2018. doi:10.1007/s00348-018-2586-0.

[16] Biler, H., Badrya, C., and Jones, A.R., Experimental and computational investigation of transverse gust encounters, AIAA Journal, 2019, pp. 1-15. doi:10.2514/1.j057646.

[17] Manar, F., and Jones, A.R., Evaluation of potential flow models for unsteady separated flow with respect to experimental data, Physical Review Fluids, Vol. 4, No. 3, 2019, pp. 1-35. doi:10.1103/PhysRevFluids.4.034702.

[18] Katz, J., A Discrete vortex method for the non-steady separated flow over an airfoil, Journal of Fluid Mechanics, Vol. 102, 1981, pp. 315-328. doi:10.1017/S0022112081002668.

[19] Andreu-Angulo, I., and Babinsky, H., Negating gust effects by actively pitching a wing, AIAA Aerospace Sciences Meeting, 2020, Orlando, Florida, 2020, pp. 1-15

Appendix 1: VORTEX MODEL RESULTS

The Küssner model provides information on the wing performance. However, in order to acquire an understanding of the flow features that can be calculated from potential flow, a vortex model is necessary. Such a model has been developed by adapting the guidelines in Ref. [18]. Additional details of the specific model used can be found in Andreu-Angulo and Babinsky [19]. In order to compare the two gust shapes, especial attention was given to the gust's vorticity distribution. The gusts were modelled with a vorticity field, which allows to implement gust shear layer deformation if necessary. The top-hat edge gust is modelled with two lines of vortices on either side of the gust, which results in constant transverse flow in between. The shear layers were extended 20 chords in the stream-normal direction from the wing and the gust vortices were placed Udt away from each other. In the case of the sine-square gust, a single shear layers are not enough to model the resulting transverse flow. However, this gust can still be well approximated using a series of weaker shear layers. In this work, 40 shear layers were used to recreate the desired velocity field in the gust. The circulation strength of each shear layer is varied in order to recreate the desired profile.

The calculated flow field results for the two gusts at GR = 1 are compared in Figure 2A-1. One of the major differences predicted is the divergence of the trailing edge shed vorticity from the horizontal axis. This indicates that Küssner assumptions of a planar wake hold better in the sine-squared gust. In addition, the LEV also advects faster from the wing surface in the case of the top-hat gust. It can therefore be predicted that the gust with the lower velocity gradient can be better predicted by Küssner's model.

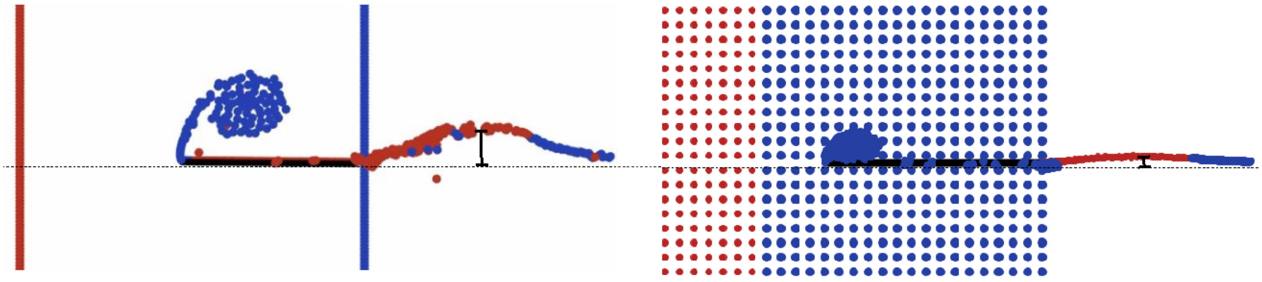

(a) Top-Hat Gust. **(b) Sine-Squared Gust.**

Figure 2A-1: Flow Results from the Vortex Model for the Two Gusts at *s/c* = 1.0 and *GR* = 1.

CHAPTER 3 – HIGH-FIDELITY COMPUTATIONAL SIMULATION OF TRANSVERSE GUSTS

Marilyn Smith, Amanda Grubb, Alex Moushegian, and Daniel Heathcote
Georgia Institute of Technology
UNITED STATES

The next generation of Unmanned Aerial Vehicles (UAV) will have missions that are dominated by strong transient aerodynamics. Understanding the physics of these transient aerodynamics, specifically large amplitude transverse gusts and the resulting vehicle response is crucial to the success of future UAV development. This chapter explores the numerical simulation of transverse gusts using a modified boundary condition in a state-of-the art Computational Fluid Dynamics (CFD) solver. The modified boundary condition generates a transverse top-hat jet with velocity (*W*) through which a flat plate wing is "towed" through the jet at velocity (*U*), mimicking a transverse gust. Mesh independence and sensitivities are examined, as well as several angles of attack. Results from numerical simulations are compared and validated against towed wing-gust encounter experiments at the University of Cambridge. The new approach is shown to be valid and accurate. The maximum lift is shown to correlate linearly with gust ratio. Distributed vorticity analyses confirm that non-circulatory terms over the gust remain constant for all gust scenarios and with the inclusion of viscous effects, supporting the original assumption from Küssner theory.

3.1 INTRODUCTION

The advent of non-traditional rotary-wing vehicles and smaller Urban Air Mobility (UAM) and Unmanned Aerial Vehicles (UAV) with missions that reside primarily in urban environments where transients are much stronger has resulted in new studies of these phenomena and their impact on vehicle response. Understanding and prediction of the unsteady aerodynamics and loads encountered in urban canyons and nap-of-the-earth flight is a fundamental necessity for the design of new and novel aviation applications. In particular, very large amplitude gusts will be encountered whose current state-of-the-art modeling is limited to linear indicial aerodynamic theories (Küssner, Sears and Wagner) applicable to small Gust Ratios (GR). As such, a greater understanding of the flow physics of large canonical wing-gust interactions is required in order to accurately model these physics during vehicle design, especially for manned and autonomous control law development. This understanding requires the development of physical and computational experiments that accurately capture the details of the flowfield so that existing linear models can be expanded, or new theories developed. This chapter, complementary to its experimental counterparts by the University of Cambridge [1], explores the high-fidelity simulation methodologies necessary to capture the gust-vehicle interactions when large gust ratios introduce non-linearities. These simulations and the resulting physical insights are validated and correlated with experiments conducted at the University of Cambridge [1].

Computational evaluations on linear gusts have indicated that the approach of modeling an internal gust without considering the impact of the lifting surface on the gusts is finite but small. Thus, these coupling computational terms which arise from first-principles derivations, have been neglected. However, when gust ratios (the ratio of the transverse gust velocity to the lifting surface forward flight speed) become significant ($GR > 0.5$), the non-linearities in the flowfield, modeled by these coupling terms cannot be neglected. Thus, when adding the gust as an integral part of the solution methodology, additional source terms are required to accurately model the physics [2], [3], [4].

In many instances, the ability to model these gusts relies on commercial solvers where the ability to modify the solver coding is not an option. In these instances, the gust needs to be modeled via traditional boundary conditions. With an overset mesh with dynamic motion, the lifting surface can be "flown" through the gust, modeled in a separate mesh. The gust needs to be modeled by a dual set of jet boundary conditions that provide both an entrance and an exit so that the gust velocity is maintained in the simulation and is not dissipated [5]. If the solver is not capable of overset modeling, gusts can still be modeled through a hybrid mesh motion and an adapted boundary condition. Here, the lifting surface can still "fly" through the gust, though its adaptability to new scenarios, such as maneuvering, may be limited.

Identification of non-circulatory effects in a gust encounter. How do highly unsteady flows due to model motion in a steady freestream compare to analogous gust encounters? The emphasis here was on the development of the flow structure and the resulting force/moment transients on a wing undergoing large-amplitude motions over a short, reduced time, and whether this could be taken as an approximation of a gust encounter. The primary focus was on the aerodynamic response and force production due to vorticity transport and non-circulatory forcing. One important consideration in this work was the relaxation time of the flow and how this is affected by motion amplitude or reduced time.

Evaluation of classical theories and analytical models applied to highly separated flows. Classical theories including those of Wagner, Küssner, Greenberg, Miles, Theodorsen, and von Kármán and Sears have been shown to model unsteady flows and gust encounters well for attached flows, small gusts, and small amplitude wing motion. Application to large-amplitude gust encounters, however, requires either extension of these models to high angles of attack, fully separated flows, and/or vortex-dominated flows, or the development of new models. This task aimed to define the parameter space over which existing flow models can be applied to large-amplitude gust encounters and to propose extensions to broaden that space.

3.2 METHODOLOGY

3.2.1 Experimental Data

The computations were compared and validated against the towed wing-gust encounter experiments performed at the University of Cambridge [6]. A specially designed gust rig was developed for the Cambridge University 9 m × 1 m × 1 m ($x \times y \times z$) towing tank. A ducting system on the sides of the tank, coupled with a pump-based actuation system, provided a crossflow jet that mimics a transverse gust equal to two wing chord lengths, as illustrated in Figure 3-1. The water tunnel provides higher Reynolds numbers at lower speeds so that the gust-wing interactional physics can be explored with Particle Image Velocimetry (PIV). In addition, this setup replicates a gust-wing interaction that mimics the flight behavior (i.e., the vehicle is moving through a stationary gust). In this effort, a sharp-edged top-hat gust profile is evaluated. Additional details on the gust actuation system may be found in Corkery et al. [6]

The wing model is a flat plate (120 mm chord × 480 mm semi-span × 4 mm thickness) oriented parallel to the tunnel walls and orthogonal to the jet (zero degrees angle of attack). Lift and drag forces were obtained via a two-component force balance with a resolution of 0.1N. The PIV system captured the flowfield at 200 Hz (with every other frame processed) over a series of 12 × 12 pixel windows with 50% overlap, resulting in an estimated 3.15% error. Force and PIV measurements were averaged over five runs to provide a 1.5% error. The velocity and position of the wing was measured by two three-component accelerometers (wing and towing tank carriage) to provide an accuracy of 0.01mm.

The wing was towed at a velocity of $U = 0.167$ m/s. The jet strength was varied to provide a range of gust ratios, GR, which is defined as the ratio between the gust velocity, W, and the wing velocity, U.

3.2.2 Numerical Methodology

While there are multiple approaches to model gusts [2], [5] for this effort numerical simulations utilize an in-house developed CFD solver, GTSim, with a modified boundary condition. This state-of-the-art code [7] was specifically designed for modeling statically and dynamically separated flows [8], [9], [10]. GTsim employs a finite volume (cell-centered) formulation with fourth-order spatial and second order (Backward Differentiation Formula) temporal discretization schemes in a block structured approach to ensure high accuracy. A variety of turbulence closures are available; for this effort the Unsteady Reynolds-Averaged Navier-Stokes (URANS) simulations utilized the k-ω SST turbulence model [11] with and without Delayed Detached Eddy Simulation (DDES) [12], as well as a Hybrid RANS-Large Eddy Simulation (HRLES) [8], [13] with a subgrid-scale model. The solver includes both incompressible and compressible paths.

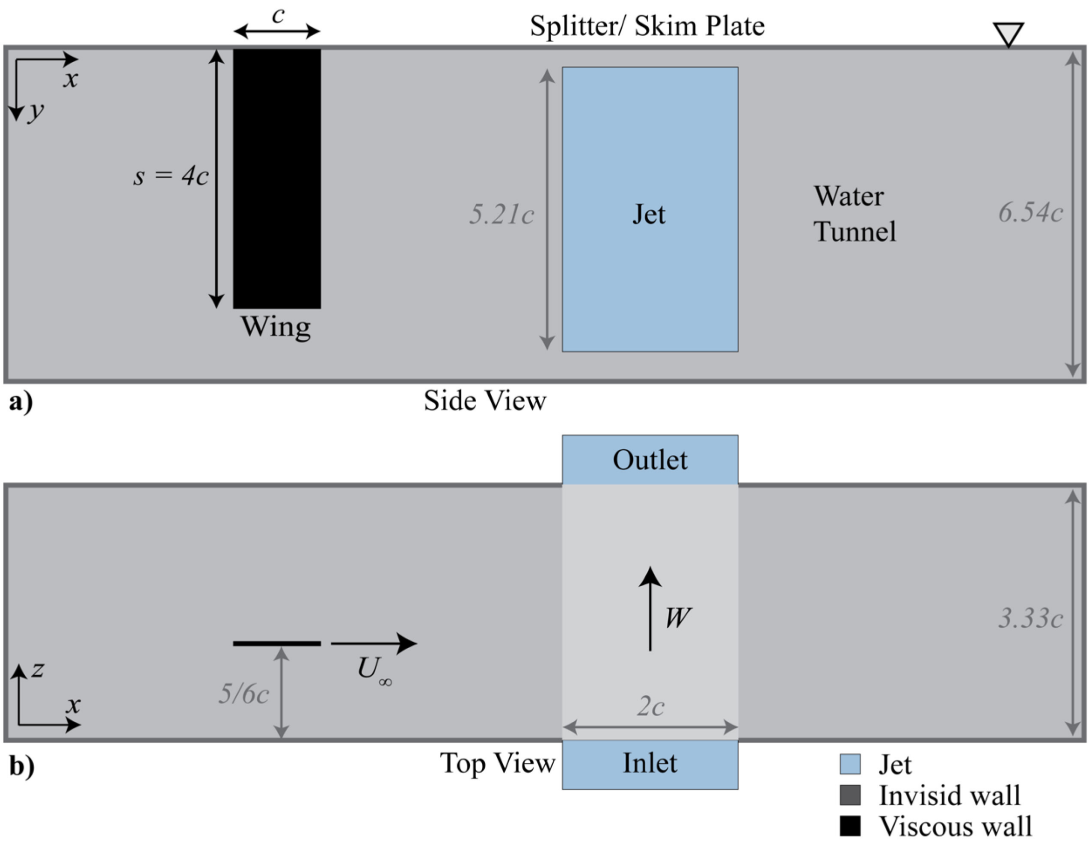

Figure 3-1: Schematic of the Gust-Wing Interaction Showing (a) Planform View, (b) Transverse View. Boundary conditions applied in the CFD analysis are color-coded.

GTSim has been validated with experimental data and correlated with extant CFD solvers for a full suite of canonical flows [7], and its ability to accurately predict the fluid mechanics of models in experimental tunnels has been previously demonstrated [14]. For steady simulations, the computations were allowed to converge to residual error of ($\varepsilon < 10^{-13}$). For unsteady simulations, the residual error reduced typically three orders of magnitude (to local convergence) before continuing to the next timestep.

A new gust boundary condition was combined with grid motion to mimic the moving gust in the water tunnel experiments. Using a frame transformation, the wing mesh moves at a non-dimensionalized velocity, $\overline{U} = 1.0$, over stationary jet boundary conditions located on the sides of the water tunnel. This is analogous to the experimental setup described earlier and by Corkery et al. [6] To capture the gust over the same time frame as the experiments, the mesh moved an equivalent distance of three chords to capture the gust-airfoil interaction from $s/c = 0.0$ to 3.0, which includes an equivalent time equal to a chord length before and after the interaction. The gust ratio was established by setting the strength of the jet with respect to the wing velocity $\overline{U}$, which mimics the experimental approach.

A total of three meshes (Table 3-1) was employed to evaluate the mesh and time step independence of the simulations, and to ensure that their influence in the integrated lift, flow physics, and circulatory analyses were minimalized with respect to the solver. The coarse mesh in Figure 3-2 illustrates the grid orientation of the two, abutting point-matched blocks that comprise the upper and lower wing surfaces. The spacing along the chordwise or *x*-axis is constant for stability reasons with the gust boundary condition. The wing is modeled as a viscous wall on the block boundary, while a patched boundary condition exchanges flow information between blocks. The walls of the water tunnel were considered to be inviscid when the jet was not present with Riemann invariant boundary conditions applied at the upstream and downstream extents of the tunnel.

Table 3-1: Summary of Meshes Used in GTsim Simulations.

	Coarse	**Mid**	**Fine**
Upper Block Size, *i, j, k*	1000 x 103 x 25	1320 x 160 x 40	2000 x 174 x 46
Lower Block Size, *i, j, k*	1000 x 103 x 35	1320 x 160 50	2000 x 175 x 61
Total Cell Count	5, 916, 000	23, 040, 000	36, 540, 000
Total Mesh Size	20c x 6.54c x 3.33c	20c x 6.54c x 3.33c	20c x 6.54c x 3.33c
BL Spacing, y^+	0.02 ($y^+ = 10$)	0.002 ($y^+ = 1$)	0.002 ($y^+ = 1$)
Wing Chord Points	50	60	100
Timestep, Δt	0.02	0.01667	0.01

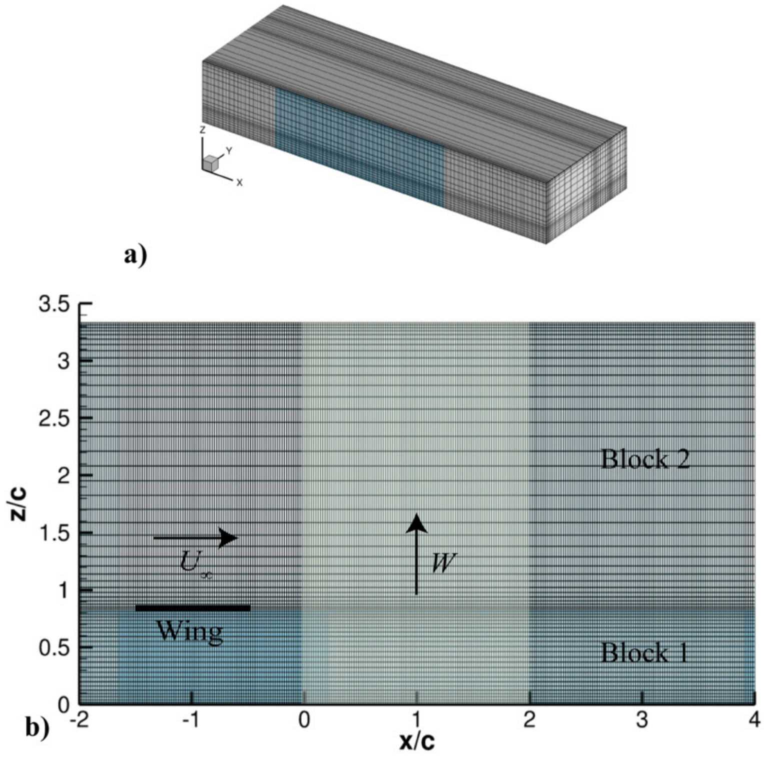

Figure 3-2: Illustrative Views of Two-Block Layout and Transverse-Plane Computational Topology. (a) Isometric view, (b) Transverse view.

3.3 ANALYSIS TECHNIQUES

To provide correlation with the experimental data and to evaluate the physics of the gust-wing interactions, the integrated lift coefficient and PIV flowfield features were examined. A circulation analysis to understand how the gusts compare with traditional indicial theory was also undertaken.

3.3.1 Integrated Lift Analysis

The available experimental integrated aerodynamic data consisted of the wing lift, as measured by the load balance. An analysis was undertaken to quantify the difference between numerical simulation and the experiment. The mean and maximum lift values were quantified between $-0.5 < s/c < 5$. As a first estimate, percentage differences were quantified using the Symmetric Mean Absolute Percentage Error (SMAPE) method. This method substitutes the experimental reference denominator value, which can be zero, for an average of the absolute values of the experimental and simulated lift responses:

$$\Delta\, C_L(s/c)\ (\%) \ = \frac{C_L(s/c)_{CFD} - \ C_L(s/c)_{Exp}}{|C_L(s/c)_{Exp}| + |C_L(s/c)_{CFD}|} \text{ x } 100 \tag{3-1}$$

This approach is not optimal as it does add a small bias but provides an estimate of the percent errors for comparison to examine the sensitivities of the numerical variations for variables that are near zero.

3.3.2 Flowfield Feature Analysis

The computational flowfield measurements were spatially averaged to provide an accurate correlation basis with the experimental PIV data, creating a "numerical PIV." The computational meshes have a different spatial resolution than the PIV measurements, requiring interpolation and/or averaging to obtain a comparable value. Near the viscous wall of the wing, where the computational meshes are the most refined, a smearing of the vorticity can be observed when the data points are averaged as the PIV misses the stronger vorticity near the wing. This implies that interpolation only may be a more appropriate approach for correlation with experimental data, but the CFD resolution provides a more accurate insight into the physics near the wing which the PIV is not able to capture.

The center of the Leading-Edge Vortex (LEV) was extracted from the flowfield measurements and has been compared to the experimental PIV measurements for both the original and numerical PIV. The leading-edge vortex center location and value were extracted from the minimum spanwise vorticity ω_y shed from the leading edge. Using this same approach, the experimental LEV characteristics were extracted from the PIV data.

3.3.3 Distributed Vorticity Analysis

Using the PIV measurements, the Cambridge researchers quantified the bound, wake (circulatory), and non-circulatory (apparent or added mass) vorticity contributions. A comparable process was applied here, using the exact approach as the experimental group for correlation. The bound distributed vorticity, γ^b, is assumed to be contained within the PIV windows closest to the wing surface, within a normal distance of $z/c \pm 0.075$. Computationally, the wing was discretized into 50 elements ($\Delta x/c = 0.02$) within $z/c \pm 0.075$, comparable to the PIV windows. The velocity along these bounds, shown in red in Figure 3-3 was integrated to provide the bound vorticity for each element and then summed to provide the airfoil bound vorticity. The circulatory or wake vorticity, γ^c, is calculated from the vorticity outside the bound contribution. The vorticity generated by the gust shear layer is excluded. The non-circulatory vorticity, γ^{nc}, is computed from the equation $\gamma^{nc} = \gamma^b - \gamma^c$.

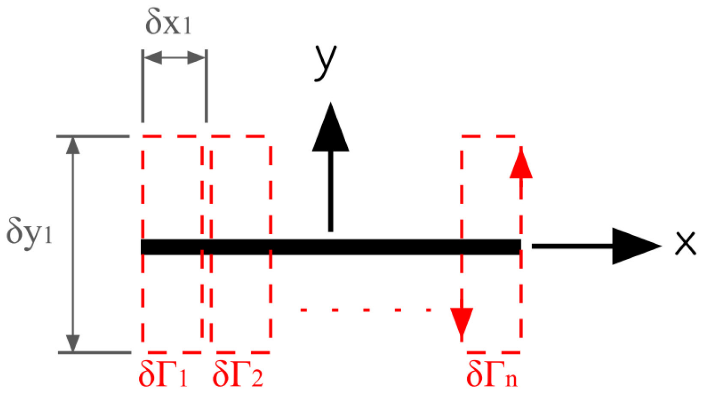

Figure 3-3: Schematic Illustrating the Elements for the Bound Vorticity Calculation.

Comparison with experimental values, and between different simulations were evaluated through plots and percentage differences. The SMAPE approach was again applied. Because the vorticity also asymptotes to infinity for some regions, the error can be artificially inflated. To remove this inflation, an iteration where averaged and Root Mean Square (RMS) values beyond the standard deviation were removed until the errors did not change within 1% of the previous values was performed. This approach was observed to require typically two iterations and the averaged and RMS values converged without introducing a bias as outlying values were removed.

3.4 RESULTS

The unsteady simulations presented in this section will be represented by a transformation of the time to the plate's location in the water tunnel, *s/c*. The *s/c* length provides the distance between the leading edge of the plate and the nominal entrance of the jet as a fraction of the plate chord. At *s/c* = 0, the plate leading edge has entered the jet. At *s/c* = 1, the plate trailing edge enters the rectangular jet. At *s/c* = 2, the plate leading edge exits the rectangular jet. At *s/c* = 3, the plate has completely exited the rectangular jet. Plots versus *s/c* include a shaded gray area to indicate full immersion in the gust.

Results are compared to Küssner theory, a linear approach to model sharp-edged gusts at zero velocity, which is the configuration in this study. The Küssner function, ψ(s), can be defined as:

$$\psi(s) = \frac{1}{2\pi i}\int_{-\infty}^{\infty} \frac{F_{SG}(k) + iG_{SG}(k)}{k} e^{ik(s-1)} dk \tag{3-2}$$

Where:

$$F_{SG}(k) + iG_{SG}(k) = C(k)\,[J_o(k) - i\,J_1(k)] + i\,J_1(k) \tag{3-3}$$

where *C(k)* is the Theodorsen function and $J_n(k)$ are Bessel functions. These are a function of the reduced frequency, *k,* and provide results in terms of nondimensional time, *s*. The lift is then computed from the equation:

$$L = 2\pi\rho U b \omega_g \psi(s) \tag{3-4}$$

where ρ is the fluid density and ω_g is the gust amplitude. The rectangular function of the jet is modeled through the Duhamel superposition integral [15].

3.4.1 Independence and Sensitivity Studies

Before conclusions can be drawn about the physics of the gust-wing interactions, the optimum approach for the numerical simulations must be defined. To this end, in addition to the traditional mesh and timestep independence analysis, additional sensitivity studies to two-dimensional to three-dimensional analysis, plate thickness, turbulence modeling, Reynolds number, and wingspan evaluation location were examined.

3.4.1.1 Mesh and Timestep Independence

The gust boundary condition couples the time step to the grid spacing, so that mesh refinement in the streamwise (*x*) direction also refines the time step. For consistency, the analysis was performed on the infinitely thin plate at a gust ratio of one for a 40,000 Reynolds number with the $k\omega$-SST-DDES turbulence closure. The variation in the lift coefficient maximum and Root Mean Square (RMS) values was evaluated to determine independence. The values for the medium and fine meshes were within 1%, indicating that, within the bounds of the methodology, the mesh and time steps were sufficient. For many of the evaluations, the fine mesh was utilized to capture as many of the flowfield features as possible.

3.4.1.2 Sensitivity Studies

3.4.1.2.1 Two- versus Three-Dimensions

The first evaluation consisted of determining the accuracy of a two-dimensional analysis in CFD with the full wing computation. Two-dimensional analyses are popular in some engineering groups due to their cost-savings. For this examination, the fine mesh (in two dimensions, the chordwise mesh) was applied for the gust ratio of 1.0 at the 40,000 Reynolds number. The turbulence closure was the $k\omega$-SST-DDES model. Figure 3-4 illustrates that the two-dimensional simulation predicts a stronger response to the gust, with a higher lift peak when the airfoil is immersed in the gust and lower lift deficit when the airfoil emerges from the gust.

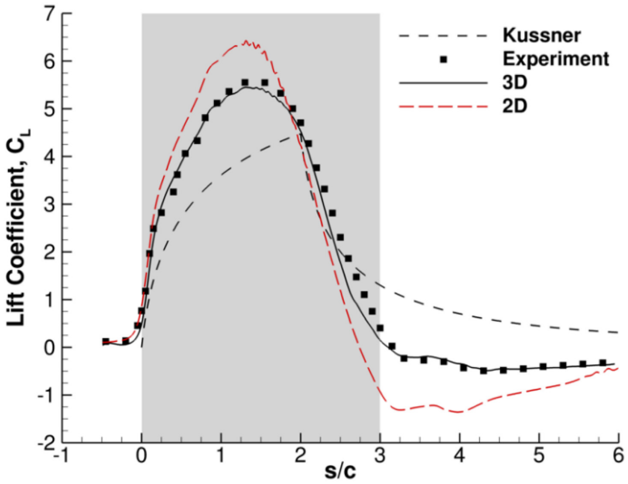

Figure 3-4: Lift Response as a Function of Distance into Gust, *s/c*, for a Gust Ratio, *GR* = 1.0, Comparing Two- and Three-Dimensional Simulations.

Further analysis of the flowfield indicates that the LEV position and strength is responsible for this discrepancy. The LEV location moves farther aft in the two-dimensional simulation than the three-dimensional simulation by more than 10% of the chord length. The two-dimensional LEV is stronger as the airfoil enters the gust. The three-dimensional LEV begins to break down as the wing exits the gust, recovering the lift behavior observed in experiment and in indicial theory, while the two-dimensional results overcompensate.

The behavior observed here is very similar to the two- versus three-dimensional behavior observed for dynamic stall and other highly separated flows [16]. Constraining the mesh to two dimensions distorts the unsteady flow features, resulting in larger magnitudes for integrated lift. The influence of the detached eddy simulation is masked for the two-dimensional simulations, as the underlying RANS is the only turbulence closure that is active [17]. Therefore, all simulations henceforth in this article will be three-dimensional.

3.4.1.2.2 Wing Thickness

The experimental wing was 4mm thick, while indicial theory and the computational analyses assume an infinitely thin wing. The influence of the wing thickness was examined by adding meshes of the plate thickness before, aft and outboard of the wing that interfaced with the upper and lower meshes. These new meshes added about 5.5% or 2.27 million additional cells to the original mesh. The fine mesh was evaluated at *GR* = 0.5 and 1.0 for the 40,000 Reynolds number. The addition of the thickness influenced the maximum, averaged, and RMS lift coefficient by 4% or less compared to the infinitely thin flat plate wing, usually, but not always closer to the experimental values. Location of the vortex structures is not changed, but the magnitudes are slightly increased with thickness. Interestingly, the vorticity analysis indicates that the infinitely thin wing is closer to experiment than the wing with finite thickness. The experimental analysis is also aligned with the theoretical non-circulatory vorticity, which is also based on an infinitely thin flat plate. Since the ultimate goal is to evaluate the vorticity behavior with indicial theory and experiment, the infinitely thin flat plate was used for the remainder of the evaluations. This has the additional advantage of fewer mesh points and shorter simulation times.

3.4.1.2.3 Reynolds Number

The Cambridge experiments obtained force measurements at a Reynolds number of 40,000 and PIV measurements at a Reynolds number of 20,000. The ensure that these two Reynolds numbers did not bias the results between the lift data and PIV, simulations at each Reynolds number on the coarse grid, using the $k\omega$-SST-DDES turbulence model, for a gust ratio of 1.0, were performed. The difference between the numerical and experimental peak lift coefficients increased by about 1% when the Reynolds number was increased from 20,000 to 40,000 in the numerical simulations. Lift predictions for $s/c \geq 2.0$ showed slight variations in lift prediction as well, as shown in Figure 3-5. However, the overall agreement between the numerical simulations at Reynolds numbers of 20,000 and 40,000 illustrates that the results are largely independent of Reynolds number for the range considered.

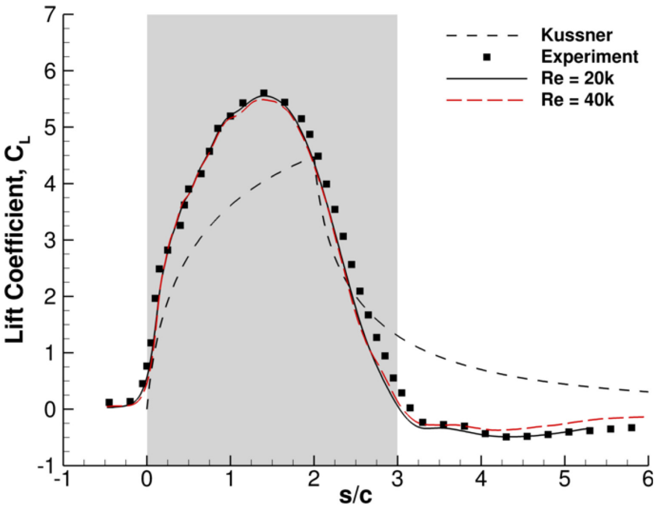

Figure 3-5: Variation in Lift Due to Reynolds Number for a Gust Ratio of One.

3.4.1.2.4 Ideal versus Real Gust

The experimental top-hat gust is not the idealized velocity profile due to the boundary layers in the turning vanes which introduce small but finite oscillations in the velocity (Figure 3-6(a)). While the numerical experiments can mimic the ideal sharp-edged top-hat gust profile (Figure 3-6(b)), it is important to quantify the sensitivity to determine if the idealized top-hat profile can provide adequate representation of the gust-wing interaction. The experimental gust profile is more indicative of the gust profiles that will be encountered in urban canyons [18].

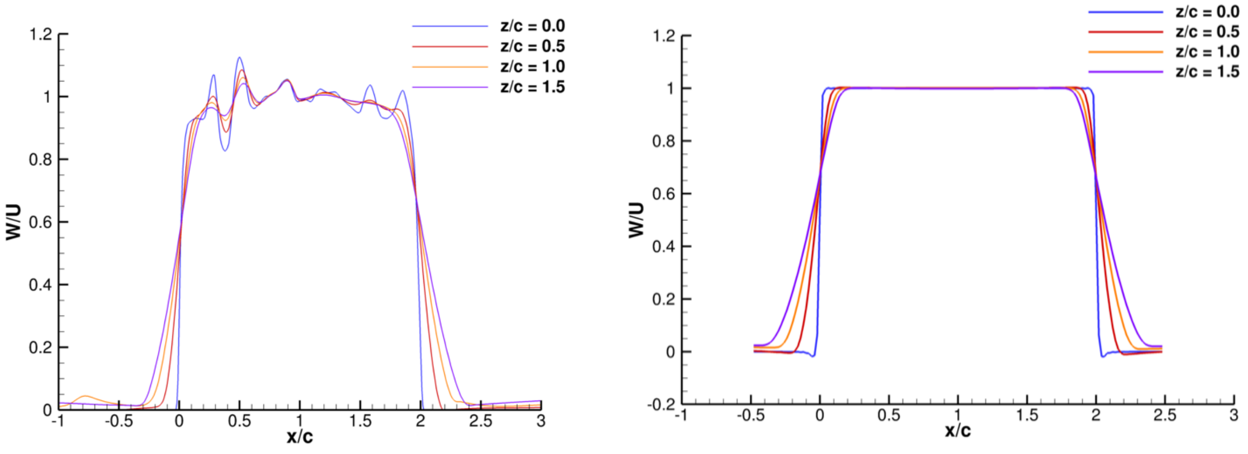

(a) (b)

Figure 3-6: Experimental Versus Idealized Top-Hat Gust Profile.

The velocity profile at the gust inlet was extracted from the experimental data and used to modify the CFD boundary condition. Results indicate that the unsteady character of the shear layers observed in the experiments is highly dependent on the gust input profile. Figure 3-7 shows that the leading-edge vortex begins to break down at *s/c* = 2.0 when the flat plate is subjected to the ideal top-hat gust. Much like the experimental results, when the flat plate is subjected to the experimental gust profile, the leading-edge vortex does not begin to break down at *s/c* = 2.0. While the gust shear layers demonstrate two different behaviors when exposed to the experimental versus ideal gust profile, the integrated lift quantities remain largely the same, so that the ideal top-hat gust profile was used for the gust ratio analyses.

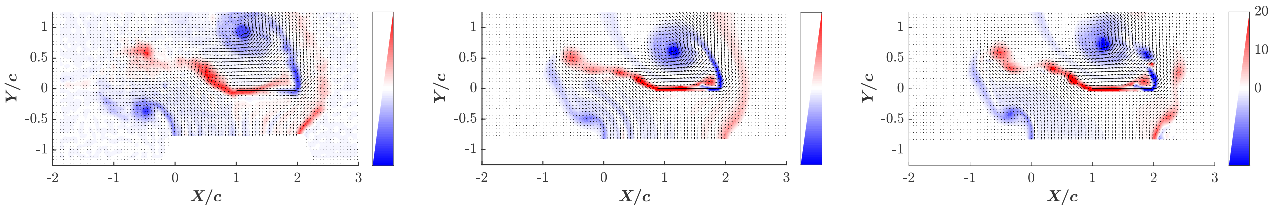

(a) Experiment. **(b) CFD, Experimental Gust Profile.** **(c) CFD, Idealized Gust Profile.**

Figure 3-7: Comparison of Flowfield Measurements Comparing the Ideal Gust Profile to the Experimentally Derived Gust Profile, *GR* = 1.0.

3.4.1.2.5 Span Location for the Airfoil Response

The experimental analysis in this study is based on an equivalent airfoil, using a single span location for data extraction. Using CFD, it is possible to evaluate various spanwise locations to determine sensitivity of this equivalent airfoil to span location, as the experiments (numerical and physical) are based on a finite wing. CFD flowfield results were extracted at various locations along the span to determine how flowfield features changed with spanwise location. As the flat plate enters the gust, the formation of the leading-edge vortex is consistent across the span of the wing. As the plate moves through the gust, the leading-edge vortex remains strong near the root (Y/b = 0.25) but breaks down near the tip (Y/b = 0.75). The data location for the experimental data captured the more two-dimensional aspects of the wing-gust ratio. This analysis suggests future computational analyses can complement the experiments by the extraction on of pressure coefficient and force data at various spanwise locations to further understand the effects that the spanwise flowfield has on the finite wing response. As this is difficult to achieve with the experiments, this is an excellent example of how computational-experimental collaborations can advance research.

3.4.1.2.6 Wing Immersion

The experiments at Cambridge were accomplished in two different test campaigns. In the first series, the gust edge closest to the splitter plate and wing root (Figure 3-1) was offset by 24 mm (Y/b = 0.05), while in the second series, the gust was offset by 33.6 mm (Y/b = 0.07). In examining this impact, it is evident that the lift coefficient magnitude is reduced as the offset increases (Figure 3-8). The flowfield features are almost identical, with only small changes associated with the location and strength of the leading and trailing-edge vortices. Therefore, all analyses should be done at the same offset location to guarantee that the wing area that is immersed in the gust is consistent when drawing conclusions about a series of gust ratios.

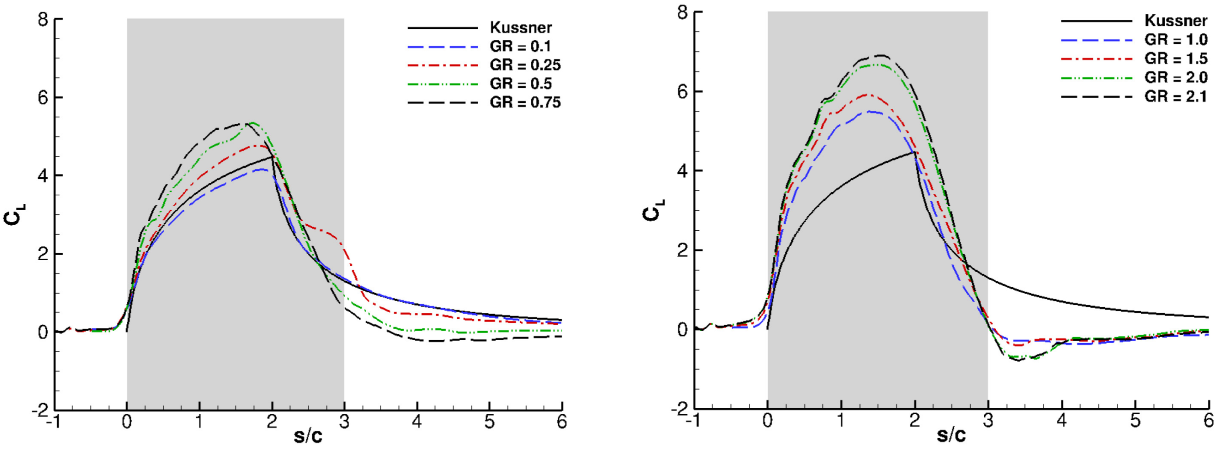

(a) $GR \leq 1.0$. (b) GR $\geq$ 1.0.

Figure 3-8: Lift Response of the Wing to Increasing Gust Ratio.

3.4.2 Wing-Gust Interactions at Varying Gust Ratios

After the sensitivity studies provided guidance in the appropriate simulations to examine the physics, a sweep of gust ratios was studied. Gust ratios of 0.25, 0.75, 1.5, and 2.1, chosen at the same experimental gust ratios, were evaluated to provide a spectrum of the gust-wing interactional physics. The lift response for the varying gust ratios are illustrated in Figure 3-8. Prior to a gust ratio of 0.5, the lift behavior follows the trend of the Küssner indicial function (computed for a GR = 0.2), which characterizes a linear gust. The lift increases steadily until an s/c = 2.0 when the wing trailing edge exits the gust. At this point, the influence of the gust on the wing is mitigated, and the lift coefficient decreases. This sharp discontinuity at s/c = 2.0 at the point where the airfoil begins to exit the gust, is pronounced since the flow is attached, as illustrated by the flowfield (Figure 3-9). The gusts are marked by the presence of a vortex that rolls up at the leading edge. The primary difference as the gust ratio increases is that the secondary flow separation just behind the leading edge appears at gust ratios at or greater than 0.5. This secondary feature interacts strongly with the LEV, resulting in the LEV departing from the wing as early as the wing trailing edge enters the gust (*s/c* = 1.0). The secondary separation increases over the chord of the representative airfoil and moves aft. Therefore, the presence of a distinct LEV (rather than a vortex rollup that is still attached to the airfoil, as shown for *GR* = 0.25) appears to signal the start of separated flow over the upper surface of the wing.

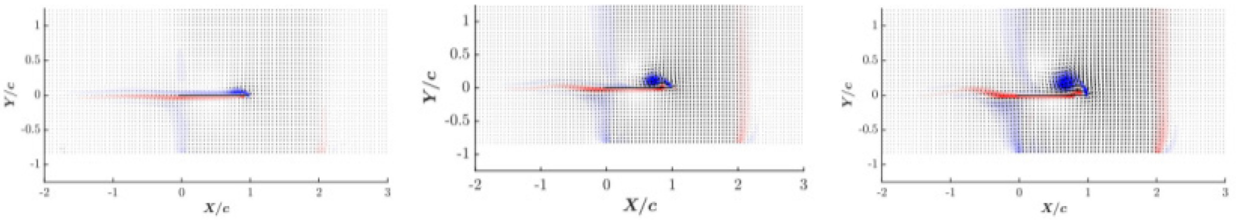

(a) *s/c* = 1.

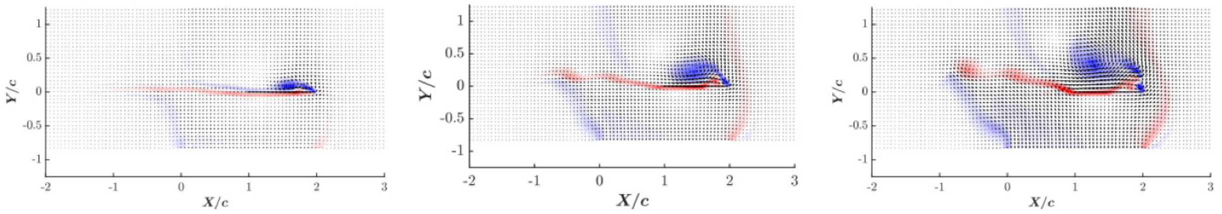

(b) *s/c*=2.

Figure 3-9: Flowfield Visualizations for Gust Ratios of 0.25 (Left Column), 0.5 (Middle Column) and 0.75 (Right Column).

This behavior strengthens and becomes more apparent as the gust ratio increases above 1.0 (Figure 3-10). The LEV is stronger and is translated higher above the wing as gust ratio increases. By a gust ratio of 1.5, the separated region encompasses almost the entire upper surface when the wing is fully immersed in the gust (between *s/c* = 1.0 and 2.0), and the flow is completed separated by a gust ratio of 2.1. Another interesting observation from these flowfield visualizations is that the influence of the wing on the gust is markedly increased by observing how the forward and aft gust shear layers are increasingly distorted by the wing as the gust ratio increases.

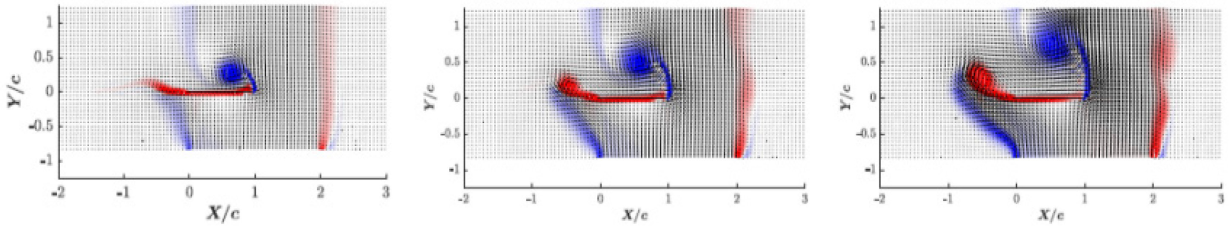

(a) *s/c* = 1.

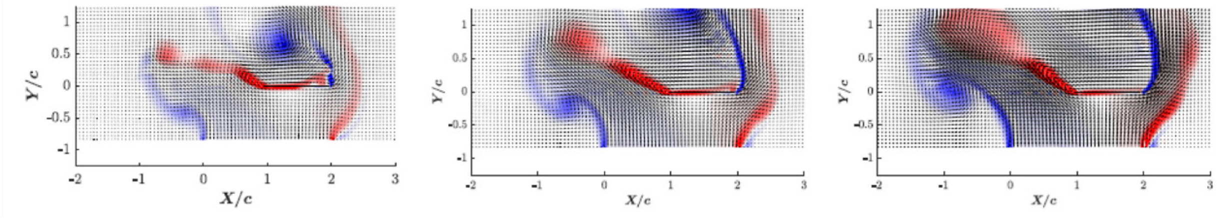

(b) *s/c* = 2.

Figure 3-10: Flowfield Visualizations for Gust Ratios of 1.0 (Left Column), 1.5 (Middle Column) and 2.1 (Right Column).

The location of the maximum lift becomes relatively constant at gust ratios at and above one, which is indicative of the amount of separation on the wing. The maximum lift coefficient continues to increase with increasing gust ratio based on the definition of the lift coefficient, which is relative to the constant wing speed rather than the resultant wing and gust speeds. The lift coefficient-gust ratio relationship for the gust ratios appears to be linear, as illustrated in Figure 3-11. The influence of the area of the wing that is immersed in the gust is clearly visible as well; the experimental results with different wing immersions hint at a similar linear relation that may have a different slope. This will be further explored computationally in future efforts.

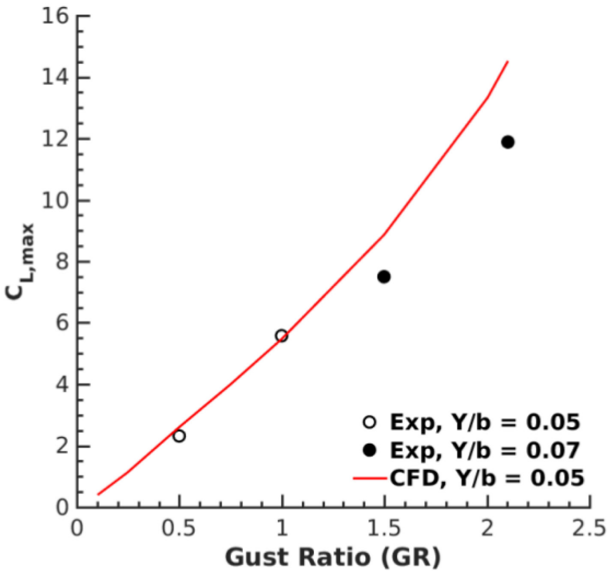

Figure 3-11: Maximum Lift Coefficient Variation with Gust Ratio.

The distributed vorticity for these cases provides further insight into the physics, as illustrated by Figure 3-12. The extent of the separated flow over the gust-immersed wing can be observed by the behavior of the bound vorticity, γ^b (red lines). For a gust ratio of 0.1, the vorticity increases from leading edge (-0.5) to trailing edge (0.5), indicative of attached flow. By a gust ratio (GR = 0.5), the negative vorticity indicates separation over most of the airfoil, with interactions with the LEV and Trailing-Edge Vortex (TEV) aft of the quarter chord. For a gust ratio of GR = 1.0, the vorticity is relatively constant and negative due to the strong flow separation with minimal interaction with the LEV, which has moved away from the wing. What is most interesting is the relative consistency in the non-circulatory vorticity. There is a small change in the vorticity just aft of the three-quarter chord, which needs to be further studied. This analysis was accomplished using the same bounds as the experimental analysis so that validation and correlation could be made to ensure that the CFD approach is valid. These results can be further explored using smaller bound vorticity boxes (Figure 3-3) that are optimized to the ability of the CFD refinement in the boundary layer, rather than the PIV from experiments. Initial computations indicate that the normal spacing of the boxes can be decreased to about 0.05 with improved correlations. Further analysis is on-going, and full results will be published in a future publication.

To further understand the predictions at different gust ratios, the effect of uncertainty in the gust ratio magnitude was analyzed. At gust ratios of 0.5 and 1.0, the gust ratio was varied by ±5% and compared with the original simulations. The lift response indicated that at a gust ratio of 1.0 (Figure 3-13(a)), there is a one-to-one correspondence (linear) in the change in lift coefficient magnitude with only slight changes in the location of the lift peak, as illustrated by the translational shift in *s/c* of the slope as the wing leaves the gust. At a gust ratio of 0.5, the change in lift coefficient magnitude is not as consistent

(Figure 3-13(b)). The magnitude change between the gust ratio of 0.475 to 0.5 and between 0.5 to 0.525 increases from 4 % to 8 %, respectively, resulting in a non-linear response that is larger than the higher gust ratio. Though not shown, the flowfield variability was also more significant at the 0.5 gust ratio than at the 1.0 gust ratio. In addition, since this is the transitional range between the traditional Küssner result to the non-linear behavior, the character of the lift response is changing. The gust-wing flowfield is comparable as the wing enters the gust (Figure 3-14(a)), but the difference once the airfoil is immersed in the gust (Figure 3-14(b)) is evident, even for a gust ratio of 1.0. Interestingly, the vorticity distribution analysis indicates that the change in the bound vorticity on the airfoil is offset by the wake vorticity so that the non-circulatory component remains essentially constant (Figure 3-15).

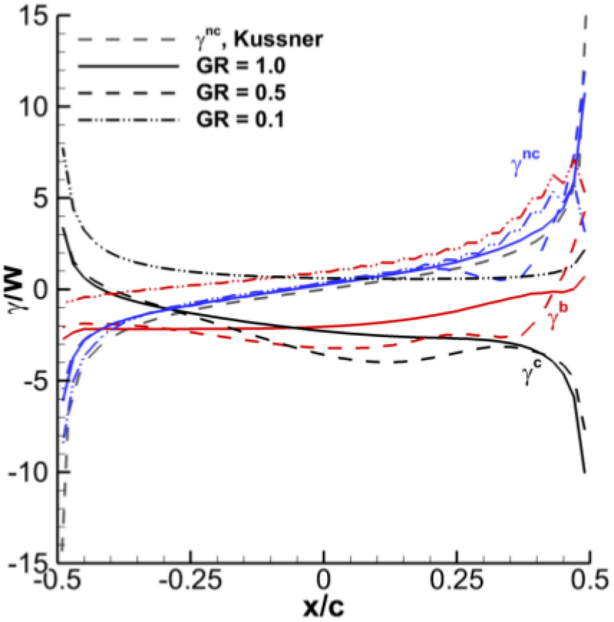

Figure 3-12: Vorticity Distribution Over the Wing Representative Airfoil at Three Different Gust Ratios.

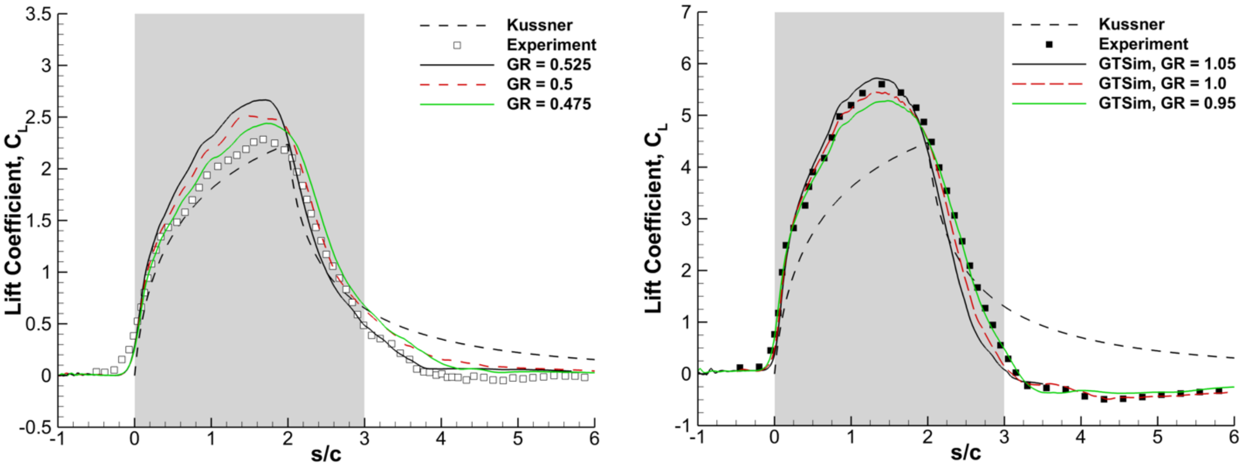

(a) GR = 1.0

(b) GR = 0.5

Figure 3-13: Lift Response Through a Gust (*s/c)* Considering ±5% of the Nominal Gust Ratio.

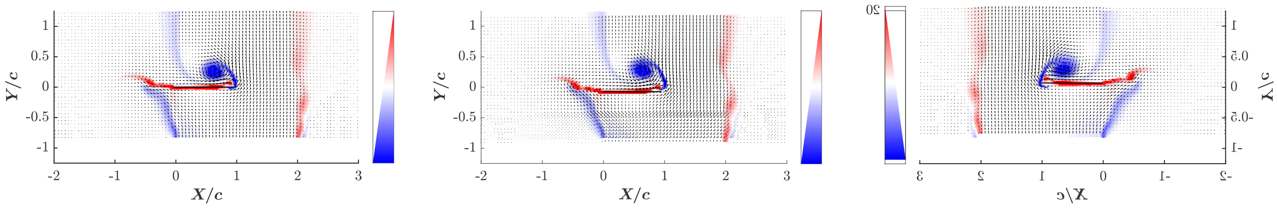

(a) ***GR*** **= 0.95,** ***s/c*** **= 1.0.** **(b)** ***GR*** **= 1.0,** ***s/c*** **= 1.0.** **(c)** ***GR*** **= 1.05,** ***s/c*** **= 1.0.**

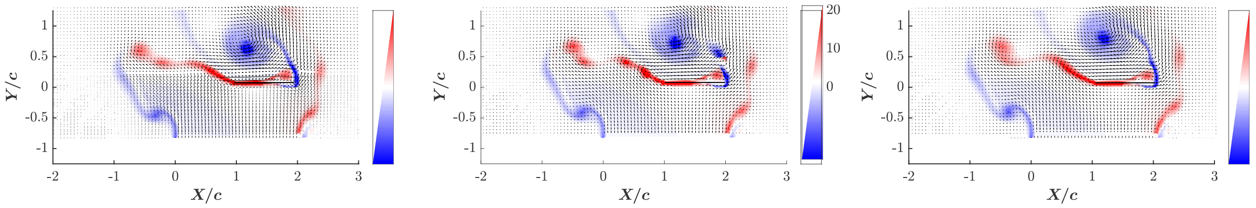

(d) ***GR*** **= 0.95,** ***s/c*** **= 2.0.** **(e)** ***GR*** **= 1.0,** ***s/c*** **= 2.0.** **(f)** ***GR*** **= 1.05,** ***s/c*** **= 2.0.**

Figure 3-14: Comparison of Flowfield Measurements Considering ±5% of the Nominal Gust Ratio *GR* = 1.0 as the Airfoil Enters the Gust (*s/c* = 1.0) and When it is Fully Immersed (*s/c* = 2.0).

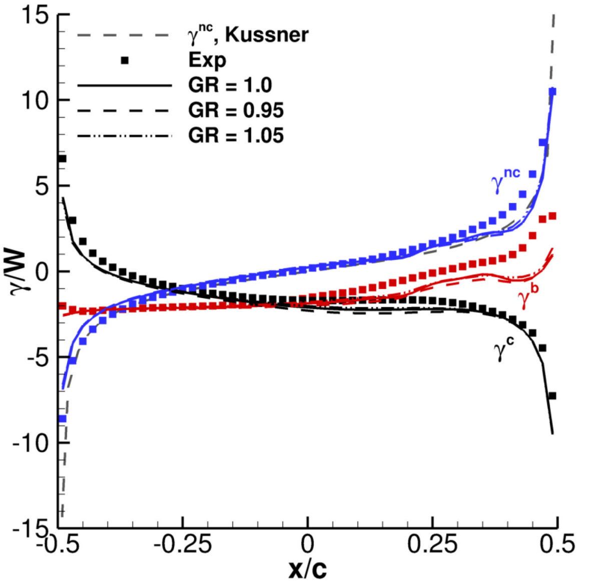

Figure 3-15: Distributed Vorticity, Averaged Between *s/c* = 1.0 and 2.0 for *GR* = 1.0 Considering ±5% of the Nominal Gust Ratio, Compared to Küssner Theory and Cambridge Experiments.

3.4.3 Wing-Gust Interactions at Large Angles of Attack

To model actual vehicles in flight, the gust-wing interactions for different orientations of the flight vehicle needs to be evaluated. The influence of two angles of attack, 10° and 20 °, for two gust ratios *GR* = 0.5 and 1.0 was examined. The impact of the angle of attack is apparent in both the integrated aerodynamic lift and the flowfield phenomena. The lift coefficient is comparable to the steady-state lift at the nominal angle of attack as it enters the gust, as observed in Figure 3-16. After the wing enters the gust, the overall lift response is almost identical for both the angles of attack throughout the gust interaction. The response after the gust-wing interaction is different due to the unsteady interactions with the flat plate at high angles of attack, and these differences are not unexpected. At a *GR*=0.5, there appears to be a difference in the lift responses between the angles of attack, which is due to the amount of separation found on the wing during the gust interaction. The lift responses at *GR*=1.0 have very similar responses because the maximum amount of separation has already been reached. The change in the lift coefficient decreases with angle of attack, similar to the lift response at and beyond the stall angle of attack.

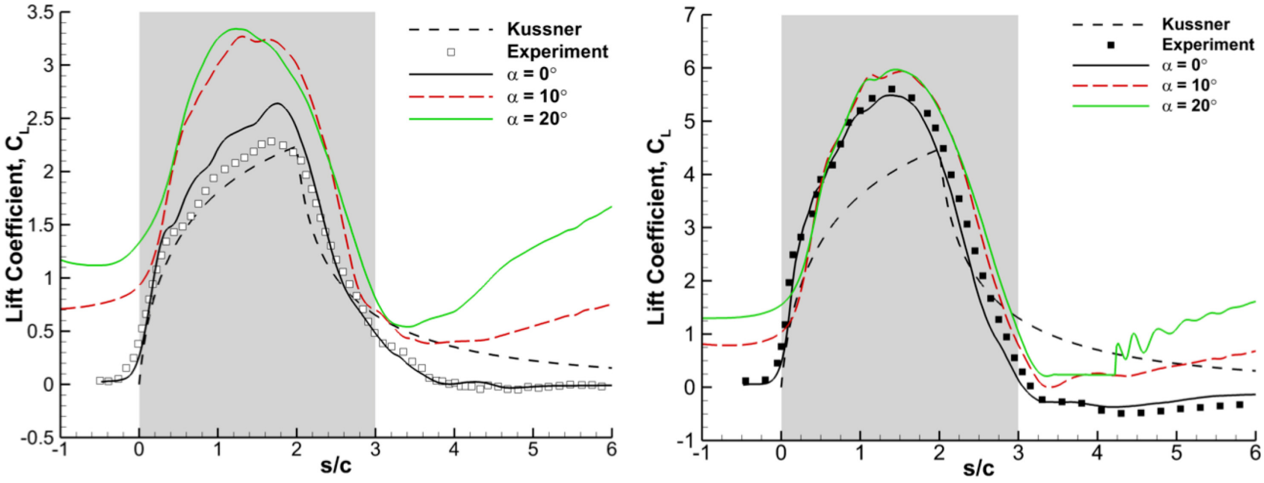

(a) GR = 0.5. **(b) GR = 1.0**

Figure 3-16: Lift Coefficient Response Due to Angle of Attack on Gust-Wing Interactions.

Additional insights can be observed from the flowfield responses in Figure 3-17. Prior to entry in the gust, the leading-edge shear layer and trailing-edge vortices are similar to their steady-state counterparts. Upon entrance into the gust, the flowfield is dominated by the presence of the leading-edge vortex and secondary phenomena observed at zero angle of attack for the large gust ratios. The influence of the angle of attack increases the strength and the offset distance of the LEV.

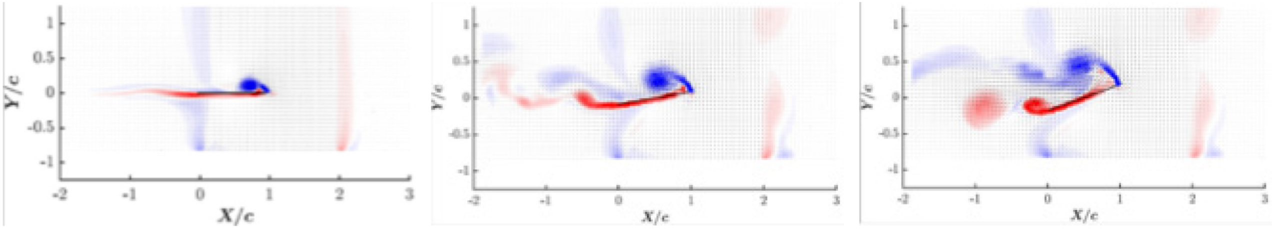

(a) *GR* = 0.5, α = 0°. **(b) *GR* = 0.5, α = 10°.** **(c) *GR* = 0.5, α = 20°.**

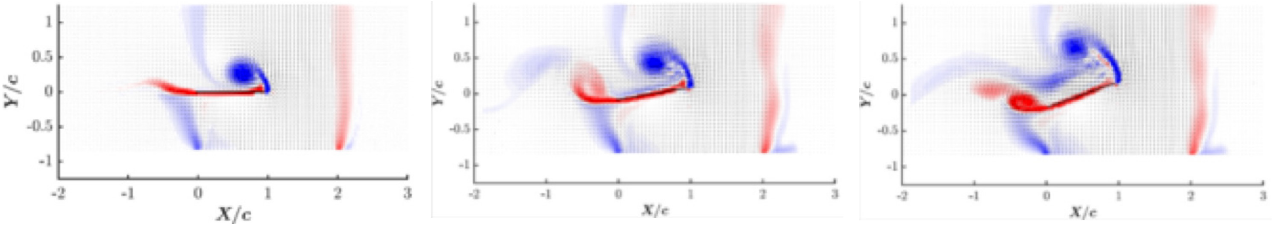

(d) *GR* =1.0, α = 0°. **(e) GR = 1.0, α = 10°.** **(f) GR = 1.0, α = 20°.**

Figure 3-17: Comparison of Flowfield Measurements at the Gust Entrance *s/c* = 1.0 for Gust Ratios of 0.5 and 1.0.

3.5 CONCLUSIONS AND FURTHER WORK

Evaluation of a flat plate wing encountering a two-chord width gust was successfully demonstrated computationally and correlated with experimental data. Several conclusions from this initial study can be drawn about the computational methodology and the physics of these wing-gust interactions:

- The approach of the stationary jet boundary conditions with the relative mesh motion is demonstrated, via correlations with experiments, to be a valid and accurate computational methodology to model wing-gust interactions.
- Computational modeling must include at minimum a three-dimensional mesh with a hybrid Reynolds-Averaged Navier-Stokes / Large Eddy Simulation (RANS/LES) turbulence closure to capture the unsteady separated flows.
- The onset of the characteristic of the non-linear gust appears to be when a leading-edge vortex distinct from the boundary layer first appears, rather than the onset of separation, which occurs at a gust ratio of about 0.5.
- Using the definition of lift coefficient referenced to the wing speed, the maximum lift coefficient forms a linear relation with gust ratio. The location of the maximum lift during the gust event remains relatively constant once a significant amount of flow separation is encountered at gust ratios of one and above.
- The influence of the wing on the gust itself increases with increasing gust ratio. This is observed by the distortion of the forward and aft edges of the gusts as gust ratio increases.
- The non-circulatory terms over the gust remain constant over all evaluated gust scenarios. This assumption was made in original Küssner theory for linear, potential flows, but the vorticity analysis based on the computational simulations thus far indicates that this assumption remains valid even in the presence of large gusts with separated flows and viscous assumptions. This finding infers that lower-fidelity approaches can be developed by focusing on the bound and near-wake vorticity, where similar approaches for unsteady bluff body analyses have already been validated and demonstrated to be accurate.
- The addition of an angle of attack, in the preliminary studies introduced herein, demonstrates a direct relationship to the equivalent gust ratios at zero angles of attack. This too will be important for the development of models for comprehensive codes.

Future research will include the optimization of the vorticity analysis for the computational approaches. The influence of the extent of the wing immersed in the gust on the wing response, as well as the further explorations of the influence of angle of attack, are planned.

3.6 ACKNOWLEDGMENTS

The authors would like to thank the University of Cambridge experimental research group directed by Holger Babinsky for their data, post-processing, and collaboration in this effort. In addition, the authors appreciate the insights and suggestions from the entire NATO AVT 282 technical panel.

The authors would like to thank Nicholson Koukpaizan and Carlota Bonnet for their contributions to this effort.

This research is funded through the U.S. Army/Navy/NASA Vertical Lift Research Center of Excellence at Georgia Tech via Task 16 under the direction of Mahendra Bhagwat of ADD-A, Agreement No. W911W6-17-2-0002. The U.S. Government is authorized to reproduce and distribute reprints notwithstanding any copyright notation thereon. The views and conclusions contained in this document are

those of the authors and should not be interpreted as representing the official policies, either expressed or implied, of the U.S. Government.

3.7 REFERENCES

[1] Corkery, S.J., Babinsky, H., and Graham, W.R., Quantification of added-mass effects using article image velocimetry data for a translating and rotating flat plate, Journal of Fluid Mechanics, Vol. 870, 2019, pp. 492-518. doi:10.1017/jfm.2019.231.

[2] Wales, C., Jones, D., and Gaitonde, A., Prescribed velocity method for simulation of aerofoil gust responses, Journal of Aircraft, Vol. 52, No. 1, 2015, pp. 64-76.

[3] Golubev, V., Hollenshade, T., Nguyen, L., and Visbal, M., High-accuracy low-re simulations of airfoil-gust and airfoil-vortex interactions, AIAA-2010-4868, 40th Fluid Dynamics Conference and Exhibit, Chicago, Illinois, USA, 2010. doi:10.2514/6.2010-4868, Accessed at https://arc.aiaa.org/doi/abs/10.2514/6.2010-4868.

[4] Smith, M.J., Jacobson, K., and Bern, A., Initial computational assessment for nonlinear gust analysis (Invited), September 29 – 30 2016. Presentation at the NATO AVT 282 Panel Meeting, Avila, Spain.

[5] Moushegian, A., Weston, C., and Smith, M.J., Analysis of a wing moving through a nonlinear gust (Special Session), AIAA-2019-0637, AIAA Fluid Dynamics Conference, San Diego, CA, 2019.

[6] Corkery, S.J., Babinsky, H., and Harvey, J.K., On the development and early observations from a towing tank-based transverse wing-gust encounter test rig, Experiments in Fluids, Vol. 59, No. 9, 2018, p. 135.

[7] Hodara, J., Hybrid RANS-LES Closure for Separated Flows in the Transitional Regime, Ph.D. thesis, Georgia Institute of Technology, Atlanta, Georgia, 2016. https://smartech.gatech.edu/handle/1853/54995.

[8] Hodara, J., Lind, A., Jones, A., and Smith, M.J., Collaborative investigation of the aerodynamic behavior of airfoils in reverse flow, Journal of the American Helicopter Society, Vol. 61, No. 2, 2016, p. 032001. doi:110.4050/JAHS.61.032001.

[9] Hodara, J., and Smith, M.J., Hybrid Reynolds-averaged Navier-Stokes/Large-eddy simulation closure for separated transitional flows, AIAA Journal, Vol. 55, No. 6, 2017, pp. 1948-1958. doi:10.2514/1.J055475.

[10] Koukpaizan, N.K., Peterson, C.J., Glezer, A., and Smith, M.J., A Coupled numerical/experimental study of flow separation suppression over a curved surface using fluidic oscillators, Proceedings of the 45th European Rotorcraft Forum, Warsaw, Poland, 2019.

[11] Menter, F.R., Kuntz, M., and Langtry, R., Ten years of industrial experience with the SST turbulence model, turbulence, Heat and Mass Transfer, Vol. 4, No. 1, 2003, pp. 625-632.

[12] Spalart, P.R., Deck, S., Shur, M.L., Squires, K.D., Strelets, M.K., and Travin, A., A new version of detached-eddy simulation, resistant to ambiguous grid densities, Theoretical and Computational Fluid Dynamics, Vol. 20, No. 3, 2006, p. 181. doi:10.1007/s00162-006-0015-0, Accessed at https://doi.org/10.1007/s00162-006-0015-0.

[13] Sanchez-Rocha, M., and Menon, S., The compressible hybrid RANS/LES formulation using an additive operator, Journal of Computational Physics, Vol. 228, No. 6, 2009, pp. 2037-2062.

[14] Jarman, L., Lefebvre, J., Jones, A.R., and Smith, M.J., Dynamics of an airfoil moving through the wake of a circular cylinder, AIAA-2019-0075, AIAA Fluid Dynamics Conference, San Diego, CA, 2019.

[15] Bisplinghoff, R., Holt, A., and Halfman, R., Aeroelasticity, Dover Publications, 1996.

[16] Smith, M.J., Liggett, N., and Koukol, B.C.G., The aerodynamics of airfoils at high and reverse angles of attack, Journal of Aircraft, Vol. 48, No. 6, 2011, pp. 2012-2023. doi:10.2514/1.55358.

[17] Jones, A., Hodara, J., Smith, M.J., Granlund, K., Mulleners, K., and Ol, M., Blade sections in streamwise oscillations into reverse flow, Proceedings of the American Helicopter Society 71st Annual Forum, Virginia Beach, VA, 2015.

[18] Berry, A.J., Gu, D., Howitt, J., and I., P., A Continuous local motion planning framework for unmanned vehicles in complex environment, J Intell Robot Syst, 2012. Vol. 66, pp. 477-494. doi:10.1007/s10846-011-9633-x.

Chapter 4 – FORCE PREDICTION DURING TRANSVERSE AND VORTEX GUST ENCOUNTERS

Hülya Biler and Anya R. Jones
University of Maryland
UNITED STATES

This chapter proposes a flowfield-based force prediction method for both transverse and vortex gust encounters and examines the behavior of the maximum lift coefficient experienced during the transverse gust encounters. A sine-squared transverse gust was created in a water towing tank by using a water jet, whilst a vortex gust was created in a water channel by rotation of an upstream gust generator plate. Forces and flowfields were acquired for both gust types and examined. Average velocity variations in time were obtained along an upstream line, and variations in the effective angle of attack and lift coefficient were then computed based on these average velocities. A sensitivity study was performed and coupling between the wing and the transverse gust was found to be important. For both gust types, lift coefficients from the measurements and the predictions were found to agree well with each other if the prediction results were multiplied with the span of the wing. The transients in the lift force were observed to match the variations in the effective angle of attack. Furthermore, the peak lift coefficient experienced by a wing encountering sine-squared transverse gust was found to depend on the maximum effective angle of attack rather than individual values of the geometric angle of attack or the gust ratio.

4.1 INTRODUCTION

Inflow conditions significantly affect the aerodynamic performance of wings and blades. Unsteady environments can cause stability and control difficulties; therefore, it can affect the quality of the flight. In such cases, aerodynamic force prediction becomes paramount, especially for Unmanned Air Vehicles (UAVs) since their small size and low speed makes them vulnerable to wind gusts [1]. A better understanding of the flow physics will provide valuable information for the development of a physics-based low-order aerodynamic model. Such a model can be incorporated into an onboard flight controller, enhancing the safety, and expanding the operational envelope of these air vehicles in unsteady environments.

Linearized aerodynamics models, such as Küssner's model for sharped edge gusts [2], assume attached flow and small perturbations. For the cases when the flow is separated and these assumptions are not applicable, experiments become the main source of information. There are three different types of gust established in the literature: longitudinal, transverse, and vortex gusts. Longitudinal gusts can be easily created by oscillating the freestream or the test model, causing streamwise fluctuations in the flow. This type of gust has been extensively investigated in the past [3], [4], [5]. Transverse gusts can be defined as the fluctuations in the stream-normal direction and was first generated in 1939 by Kuethe [6]. He achieved a gust ratio (i.e., the ratio of the gust velocity to the freestream) of 0.24 by using an open section wind tunnel. Later, Holmes used a closed jet system and achieved a range of gust ratios between 0.05 and 0.095 [7]. However, there has been no research performed for large amplitude gust encounters until recently. The increasing interest in the development of the UAVs increased the number of projects performed for large amplitude transverse gust encounters. Perrotta and Jones used a water jet and created a sine-squared transverse gust in a water towing tank and achieved gust ratios as high as 1 [8]. Building on this study, Biler and Jones used a similar setup to achieve various gust velocities in the water tank by using a variable speed water pump, and achieved gust velocities up to 0.4 m/s (which can correspond to gust ratios up to 3) [14]. Corkery designed a unique crossflow test rig to obtain a Küssner-type gust which was then characterized to have a top-hat velocity profile. By using this setup, he was able to achieve gust ratios up to 2 [9]. Recent studies on these large amplitude transverse gust encounters showed that the forces are significantly increased from their steady-state values. Lastly, vortex gusts cause fluctuations in both streamwise and stream-normal directions. It can be created by placing a pitching wing upstream of a test model and was found to cause a dramatic decrease in the lift force [10], [11], [12].

Previous studies [13], [14] showed that forces experienced during both transverse and vortex gust encounters are caused by the change in the effective angle of attack. In order to investigate this further, this study focuses on the lift response of both gust types. The objectives of this work are:

1) To investigate the relation between the effective angle of attack and the lift force,
2) To introduce a novel flowfield-based force prediction method, and
3) To examine the wing gust coupling.

4.2 METHODOLOGY

4.2.1 UMD Methodology

The facility used for transverse gust encounter experiments was the 7 m x1.5 m x 1 m water towing tank at the University of Maryland (UMD). The tank has glass walls that allow optical access for Particle Image Velocimetry (PIV) experiments. A 4 degree-of-freedom model motion system was used to obtain streamwise, stream-normal, and pitching motions of the test model. The experimental setup can be seen in Figure 4-1(a).

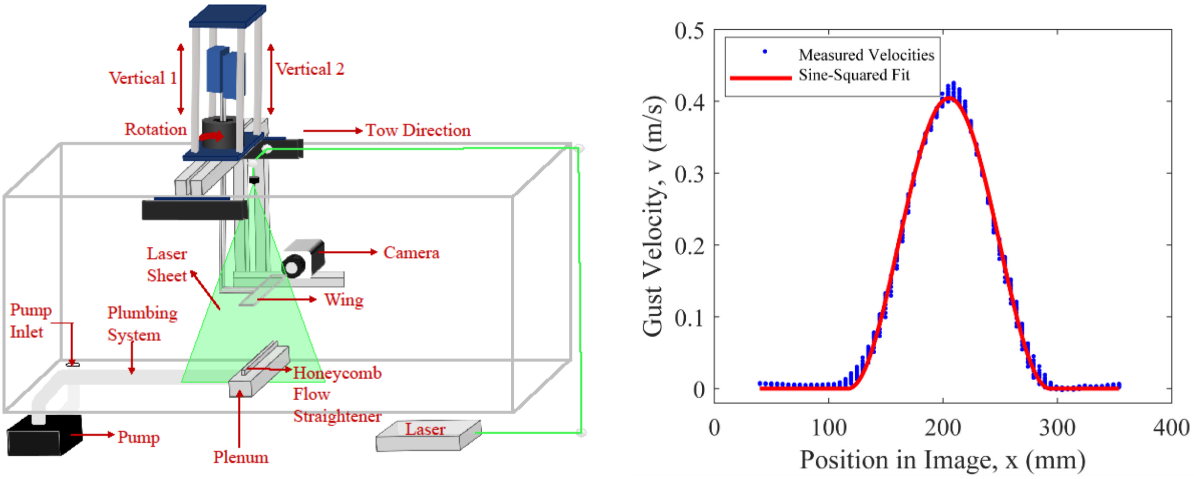

(a) UMD Experimental Setup. **(b) Sine-Squared Gust Velocity Profile.**

Figure 4-1: UMD Experimental Setup and Transverse Gust Velocity Profile.

A variable speed water jet was used to create the transverse gust. The gust generation system, (shown in Figure 4-1(a)), consisted of a swimming pool pump (Hayward TriStar SP3202VSP), plumbing system, plenum, and a honeycomb flow straightener (36 in x 0.5 in) with a 1/8 inch individual cell width. The water is drawn from the inlet at the bottom of the tank to the pump, which re-directs the water to the flow straightener through the plumbing system. The resulting flow was characterized for various pump speeds and spanwise locations by using time-resolved PIV without the test model installed in the setup. The streamwise mean measured velocities were extracted from a region where wing passes and the best-fit found to be a sine-squared profile (Figure 4-1(b)) and defined as: $V(x) = V_p \sin^2(\frac{\pi x}{w})$, where V_p represents the peak gust velocity, x represents the streamwise position, and w represents the gust width calculated based on the points where fluid velocity is zero. Peak velocity of the gust was found to be linearly dependent on pump speed which allows for a wide range of peak gust velocities between 0.06 m/s and 0.4 m/s in the tank. The mean gust width was found to be 198 mm with a coefficient of variation of 11%. Further analysis of the characterization can be found in Ref. [14].

Three different test models were used for the force measurement experiments presented in this chapter. The first test model (wing 1) was of aspect ratio 4 (5 cm chord, 20 cm span) and 3% thickness ratio brass flat plate while the second test model (wing 2) and the third test model were of aspect ratio 6 (3 in chord, 18 in span) and aspect ratio of 4 (3 in chord, 12 in span) and 4.3% thickness ratio aluminium flat plates. Therefore, the gust width corresponds to 4 chords for wing 1 and 2.62 chords for wings 2 and 3. The experiments were performed at 40,000 (wing 1 and wing 2), and 20,000 (wing 3) Reynolds number. Different gust ratios $GR = \frac{V_p}{U_\infty}$ were achieved by changing the peak gust velocity. For all cases, the model was accelerated to a constant freestream speed before it encountered the transverse gust and decelerated to a stop approximately 30 chord lengths past the gust encounter.

A 6 degree-of-freedom force balance (submergible ATI Mini-40) was used to measure forces and moments on the wing. All of the force measurements were sampled at 1 kHz, repeated 5 times, synchronized, and ensemble averaged. The mean normal and axial forces were then converted to lift and drag components and non-dimensionalized by the dynamic pressure and the wing area. Fast Fourier Transforms (FFT) were performed for all cases. In order to remove mechanical and electrical vibrations, 10, 4, and 5 Hz low pass filters were applied to the measurements for wing 1, 2, and 3, respectively.

To provide insight about the flow physics, PIV was performed using a glass flat plate with same dimensions as wing 3 was used to avoid a laser shadow in the field of view. A Phantom v641 (4 MP) was used with an 85 mm Nikon lens to acquire the images 1 chord length off mid-span. Class IV soda lime glass spheres (diameter of 37 µm) was used as seeding particles and Nd:YLF laser (Litron LDY 304, 30 mJ/pulse,10 kHz max) was used as the light source. The laser sheet and the camera were towed with the carriage to achieve a wide investigation range (Figure 4-1:(a)). The PIV experiments were sampled at 0.7 kHz and 4250 images were acquired for each case, which was repeated 8 times and ensemble averaged. DaVis v8.1 was used as the processing software. 24 x 24 and 16 x 16 px interrogation windows were used for the first and second passes. 50% and 75% region overlaps were used, respectively.

4.2.2 ITU Methodology

The facility used for the vortex gust encounter experiments (shown in Figure 4-2(a)) was the free surface water channel located at the Istanbul Technical University (ITU). The vortex gust was generated by a half counterclockwise rotation of a gust generator plate which was an aspect ratio 4 (10 cm chord, 40 cm span) Plexiglas flat plate. The motion of the gust generator lasted for 4 convective times. Figure 4-2(b) shows the vortex gust 3 convective times after the motion of the gust generator started; the characterization was performed based on this instant. The vortex gust was found to have a width-to-chord ratio 0.4 (width is defined as the half-length of the vortex) and a gust ratio of approximately $\frac{\tilde{u}}{U_\infty} \approx \frac{\tilde{v}}{U_\infty} \approx 1$. One thing to note about this gust type is that the characterized parameters change as it convects downstream due to the deformations it undergoes. The variations in the streamwise and transverse velocities were found to be $\tilde{u} = \pm 0.1$ m/s and $\tilde{v} = \pm 0.125$ m/s, respectively. The details of this characterization can be found in Ref. [12].

An aspect ratio 2 (10 cm chord, 20 cm) test model (the free surface acts as a symmetry plane) was placed approximately 60 mm downstream (distance between the leading edge of the wing and the trailing edge of the gust generator) and 15 mm below the gust generator plate, as shown in Figure 4-2(a), for the force and flowfield measurements. All experiments were performed at 10,000 Reynolds number which corresponds to 0.1 m/s of freestream speed.

Force and moments acting on the test model were measured using a 6 degree-of-freedom ATI Nano-17 IP68 force/torque sensor. The sensor was attached to the vertical cantilevered mounting beam of the test model. The pitch motion of the gust generator plate was accomplished with a Kollmorgen/Danaher Motion servo motor which was connected to a computer via a ServoSTAR digital servo amplifier. The motor motion profile was generated by a signal generator in Labview Virtual Instrument (VI) for a given rotation and duration. Synchronization was achieved using a National Instruments PCI-6601 timer.

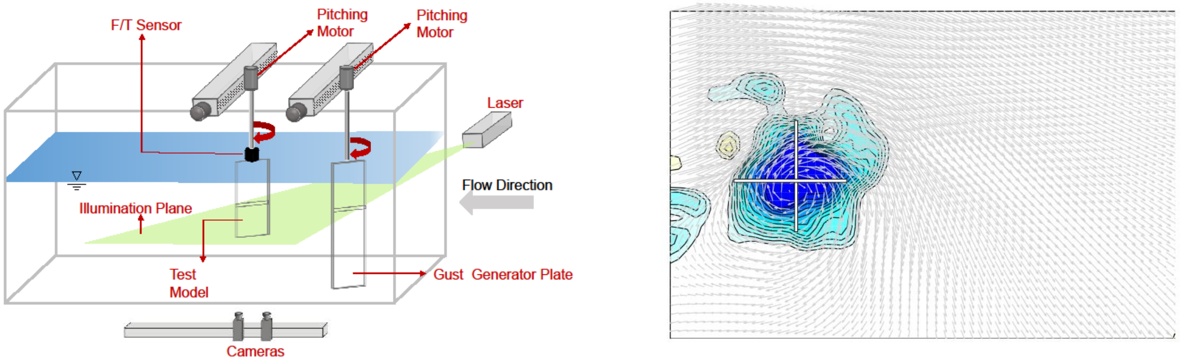

(a) ITU Experimental Setup. **(b) Vortex Gust.**

Figure 4-2: ITU Experimental Setup and Vortex Gust.

PIV was used to record flow fields around and in the near wake of the model and therefore to analyze the vortical structures during the vortex gust encounters. The flow was illuminated by a dual cavity Nd:Yag laser (max 120 mJ/pulse) and the water was seeded with Polyamide Seeding Particles (PSP) with a mean diameter of 50 µm. Two 10-bit cameras with 1600 x 1200 pixel resolution were positioned underneath the water channel to obtain the velocity fields. Recorded images were stitched together using an in-house code, and then interrogated using a double frame cross-correlation technique with a window size of 32 x 32 pixels and 50% overlap in each direction.

4.3 RESULTS

4.3.1 Trends on Forces and Flowfields

This section includes the lift response and the flowfields from both transverse and vortex gust encounters to provide further inside to the analysis performed in Sections 4.3.2 and 4.3.3

4.3.1.1 Sine-Squared Transverse Gust

Figure 4-3 shows the lift response and flowfields during the transverse gust encounter for various angles of attack at a gust ratio of 0.5. The x-axis in Figure 4-3(a) shows the convective time, i.e., chord lengths travelled by the wing. The leading edge of the wing enters the gust at $t^*=0$ and trailing edge of the wing exits at $t^*=3.62$ for a flat plate at 0° angle of attack. This wing/gust overlap is highlighted with a grey box in this plot. As can be seen from this figure, the lift force experiences a peak value when the mid-chord of the wing is in the center of the gust. This peak value increases as the angle of attack increases for the cases investigated here. An earlier study [14] showed that the further increase in angle of attack ($\alpha > 20°$) causes the lift peak to decrease. The lift force relaxes back to its steady-state value as it exits the gust for the flat plate at 0° angle of attack. However, for the $\alpha > 0°$ cases, the lift force experiences a local minimum as it exits the gust, and recovery from the gust takes a longer time. Furthermore, a secondary peak occurs around $t^*=7$ for angle of attack of 20°.

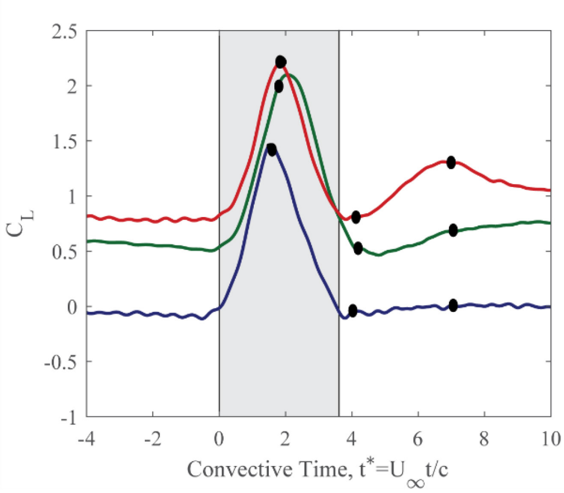

(a) Lift Coefficient for Various Angles of Attack at Gust Ratio of 0.5, Circles on this plot correspond to flowfield images given in (b), (c), and (d) below.

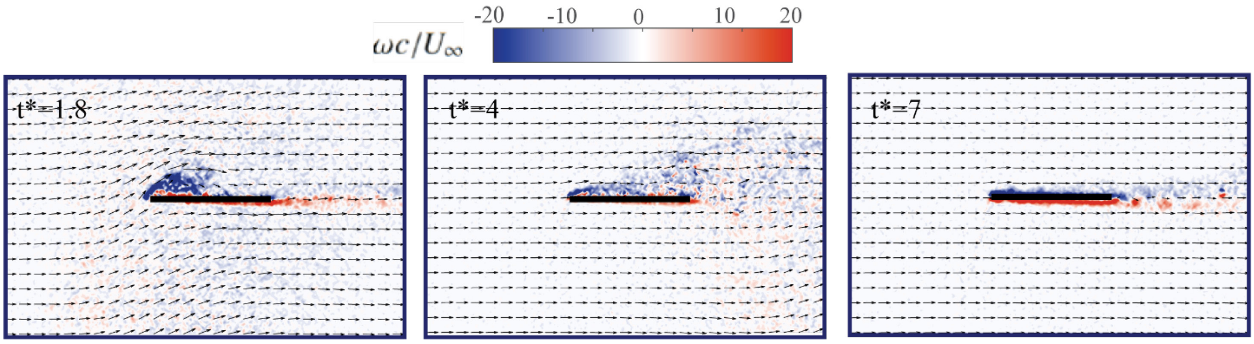

(b) GR = 0.5; $\alpha = 0°$.

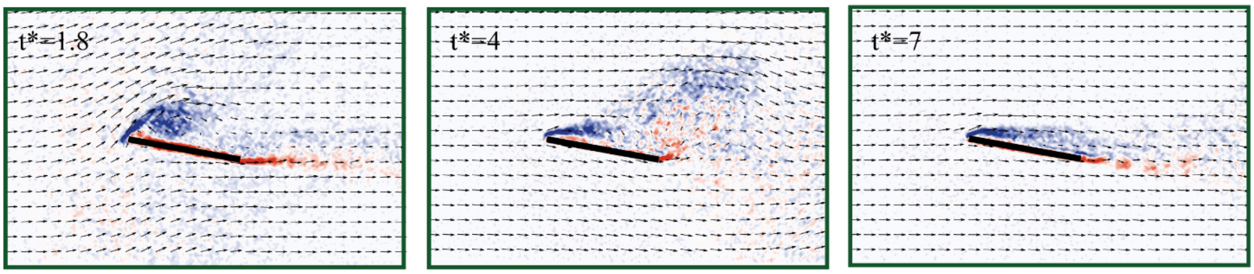

(c) GR = 0.5; $\alpha = 10°$.

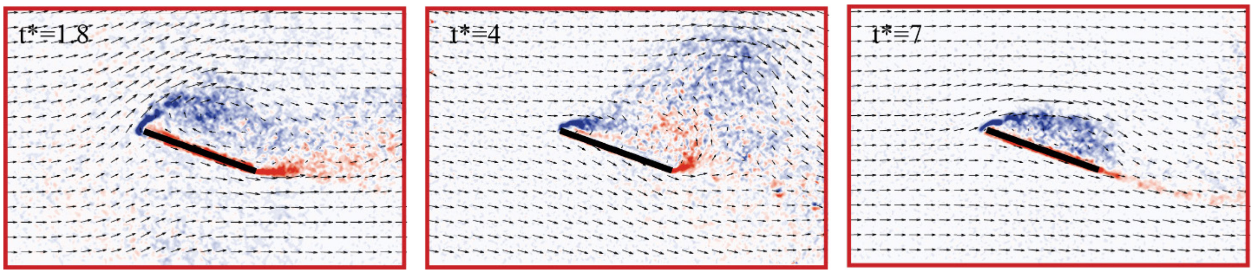

(d) GR = 0.5; $\alpha = 20°$.

Figure 4-3: Lift Coefficient and Flowfields for Various Angles of Attack at Gust Ratio of 0.5 During Sine-Squared Gust Encounter.

Figure 4-3(b) shows flowfields for several convective times ($t^* = 1.8, 4, 7$) that correspond to the circles marked in Figure 4-3(a). At t^*=1.8, when the wing is approximately centered in the gust, a leading-edge vortex forms which presumably is the reason why the lift forces experience a peak value. At $t^* = 4$, right after the wing exits the gust, a trailing edge vortex forms and causes the lift coefficient to drop to a minimum value for the $\alpha = 10°, 20°$ cases. The trailing edge vortex later induces a leading-edge vortex for the high angle of attack, $\alpha = 20°$, case and causes the lift coefficient to experience a secondary peak around $t^* = 7$.

4.3.1.2 Vortex Gust

Figure 4-4 shows the lift force and the flowfields for a flat plate at 0° encountering a vortex gust of gust ratio 1. The *x*-axis in Figure 4-4(a) represents the convective time. The region representing the motion of the gust generator is marked with a grey box. The *y*-axis in the same figure shows the lift coefficient which experiences a negative peak around $t^* = 2.5$. Lift force reverts back to its steady-state value after the motion of the gust generator ends.

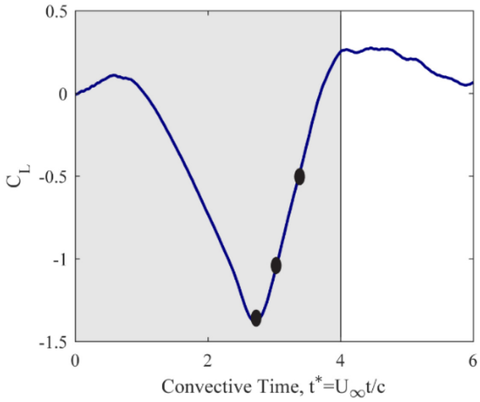

(a) Lift Coefficient for 0° Angle of Attack and Gust Ratio of 1 Case. Circles on this plot corresponds to flowfield images given below.

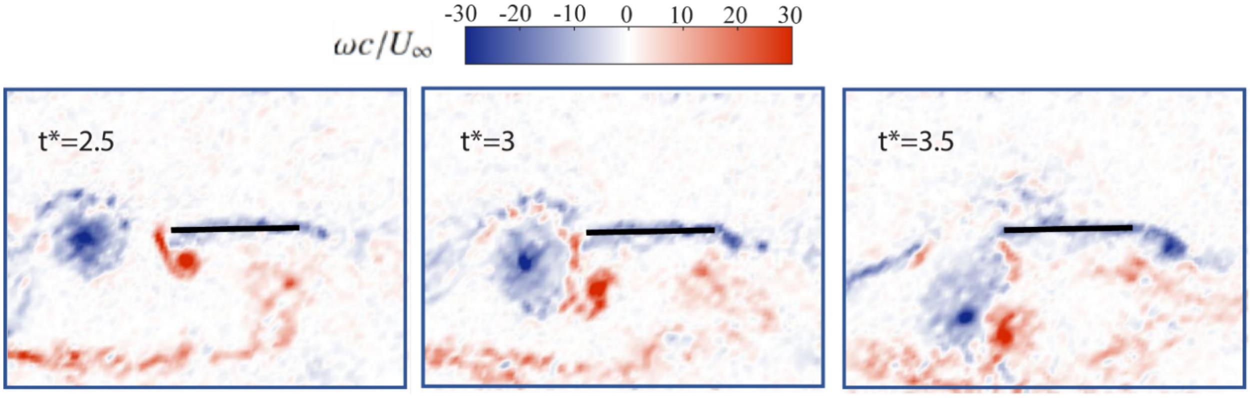

(b) GR=1; $\alpha = 0°$.

Figure 4-4: Lift Coefficient and Flowfields for 0° Angle of Attack and Gust Ratio of 1 Case During Vortex Gust Encounter.

Figure 4-4(b) shows the PIV measurements corresponding to the circles in Figure 4-4(a). Flowfields at $t^* = 2.5$ show that as the negative vortex gust moves towards the wing, a positive leading-edge vortex forms and causes the aforementioned negative peak in the lift coefficient. At t^*=3, the vortex gust reaches the plate and disrupts the positive leading-edge vortex. At t^*=3.5, both the vortex gust and the positive leading-edge vortex convect downwards and the lift force begins to revert back to its steady-state value.

4.3.2 Flowfield-Based Force Prediction

This section includes a description of the flowfield-based force prediction method and a comparison of these predictions to the force measurements for transverse and vortex gust encounters. Figure 4-5(a) and (b) show sample vorticity contours for the sine-squared transverse gust and vortex gust encounters, respectively. The x and y axes represent the normalized streamwise and stream-normal positions. In both of these plots, a vertical line is depicted upstream of and symmetric to the leading edge. The distance from the leading edge to the line is defined as d and the length of the line is defined as l. Average vertical and horizontal velocities in time are obtained from flowfield measurements along this line. From these velocities, the time-varying effective angle of attack is calculated and defined as $\alpha_{eff} = \alpha + \tan^{-1}(\frac{V(t^*)}{U(t^*)})$, where t^* is the convective time, i.e chord lengths travelled, $V(t^*)$ and $U(t^*)$ are the computed time-varying vertical and horizontal velocities, α is the geometric angle of attack, and $\alpha_{eff}(t^*)$ is the time-varying effective angle of attack. In order to calculate the lift response, classical thin airfoil theory is used by replacing geometric angle of attack with computed effective angle of attack: $C_l(t^*) = 2\pi\alpha_{eff}(t^*)$. The obtained quantities are shifted in time considering the convection with the freestream ($t_{shift} = \frac{d}{U_\infty}$) to obtain the variations at the leading edge.

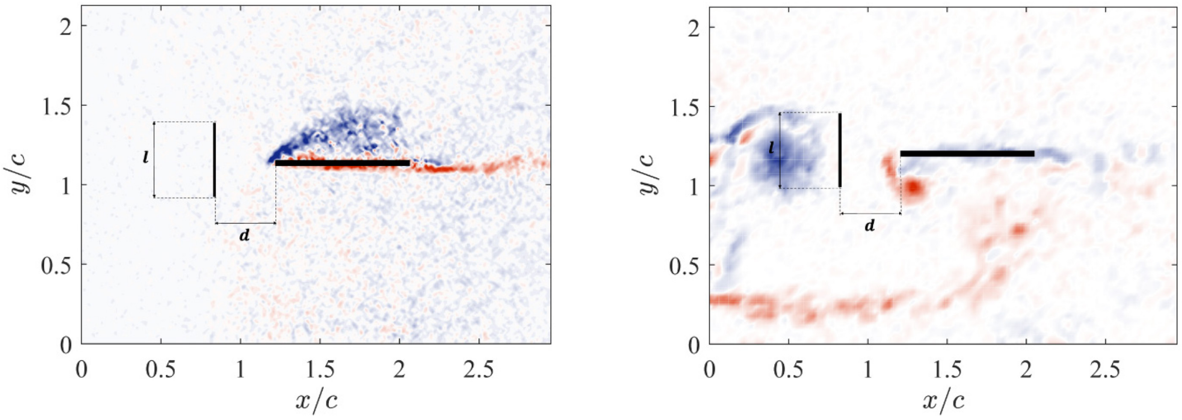

(a) Vorticity Contours at t^*= 1.81 for a Wing at 0° Angle of Attack Encountering Transverse Gust (GR = 0.5).

(b) Vorticity Contours at t^*= 2.25 for a Wing at 0° Angle of Attack Encountering Vortex Gust (GR = 1).

Figure 4-5: Vorticity Contours for Transverse and Vortex Gusts. The lines upstream of the leading edges are used to compute the average velocities for both gust types.

4.3.2.1 Sine-Squared Transverse Gust

Even though the sine-squared gust is well characterized (see Section 4.2.1 for details), characterization was necessarily performed without the wing installed, the presence of the wing does affect the gust profile encountered. A sensitivity study was performed not only to understand this coupling effect in detail, but also to examine the effects of parameters l and d. Figure 4-6 to Figure 4-8 show the deformations in vertical and horizontal velocities computed on the aforementioned line for a flat plate at 0° incidence encountering a sine-squared transverse gust. In these plots, the x-axis represents the chord lengths travelled, and the wing/gust overlap is highlighted with a grey region.

Figure 4-6(a) and Figure 4-6(b) show horizontal and vertical velocity variations, respectively, on a chord length long line at various distances from the leading edge of the flat plate wing. In both of these plots, black lines show the theoretical values. For horizontal velocity, this theoretical value corresponds to the freestream velocity, whereas it is the characterized gust profile for the vertical velocity. When the selected line is sufficiently far from the leading edge (*d* = *c/2*), both the horizontal and vertical measured velocities exhibit similar values to the theoretical ones, which suggests that the flow is not coupled with the wing. However, as the line gets closer to the leading edge, deflections in both horizontal and vertical velocities increase. Whilst the horizontal velocities slow down due to the presence of the wing, vertical velocities increase, likely because of the leading-edge vortex formation shown in Section 3.1.1. Therefore, the distance *d* is selected as c/16 for further analysis to account for the full coupling between the gust and the wing.

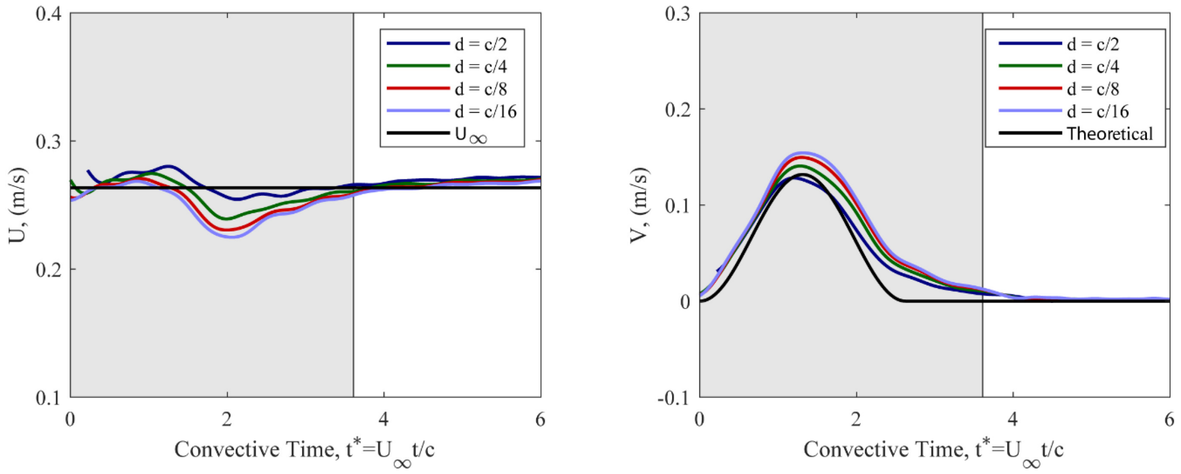

(a) Horizontal Velocities for a Chord Length Long Line. **(b) Vertical Velocities for a Chord Length Long Line.**

Figure 4-6: Horizontal and Vertical Velocities Calculated for a Chord Length Long Line at Various Distances from the Leading Edge for Gust Ratio of 0.5 and 0° Angle of Attack Case.

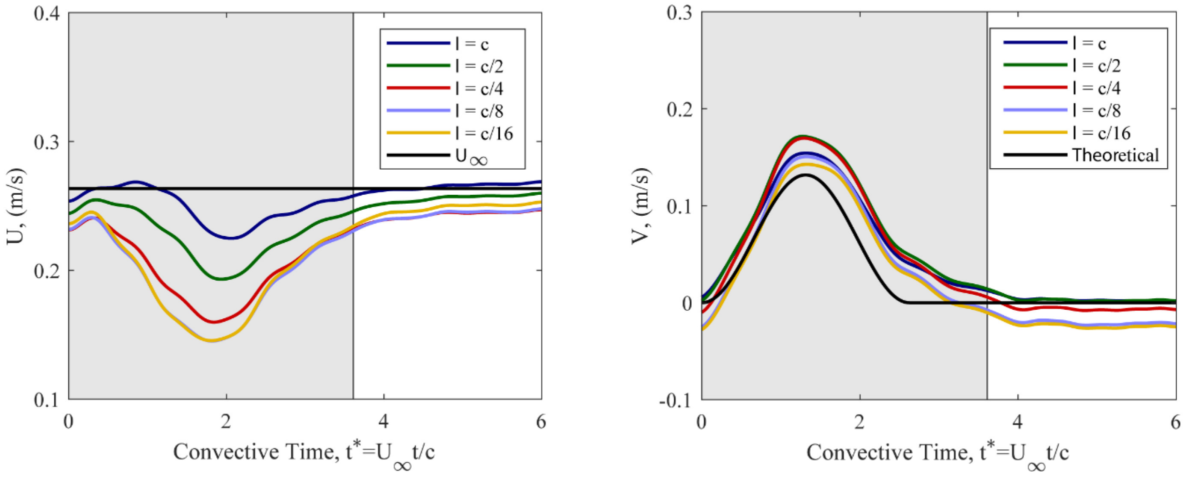

(a) Horizontal Velocities for a Line c/16 Upstream of the Leading Edge. **(b) Vertical Velocities for a Line c/16 Upstream of the Leading Edge.**

Figure 4-7: Horizontal and Vertical Velocities Calculated for a Line c/16 Upstream of the Leading Edge with Various Line Lengths for Gust Ratio of 0.5 and 0° Angle of Attack Case.

Figure 4-7(a) and (b) show horizontal and vertical velocity variations computed for various line lengths located c/16 upstream of the leading edge. As can be seen from Figure 4-7(a), as the line gets shorter, the deflections in the horizontal velocities increase. Since flow further away from the leading edge is not greatly disturbed, it experiences velocities closer to the freestream. Therefore, longer line lengths inevitably produce smaller average horizontal velocity deflections. For the vertical velocity deflections (Figure 4-7(a)), decreasing length increases these deflections up to d = c/2, but a further decrease in the length decreases these deflections. This is thought to be caused by the leading-edge vortex formation on the upper surface (see Section 4.3.1.1). Therefore, it can be said that the length of the line should be long enough to account for the region where the flow is disturbed, but short enough to avoid adding non-disturbed velocities in the averaging process. Moreover, a further decrease in length after l = c/8, does not change the results significantly in either horizontal or vertical velocity. Therefore, c/8 was chosen to be the length of the line for calculating the effective angle of attack and lift coefficient in the following analysis.

Figure 4-8 shows the horizontal and vertical velocity deflections calculated on the d = c/16, l = c/8 line for various gust ratios at 0° angle of attack. It should be kept in mind that these different gust ratios are achieved using different pump/gust speeds. As can be seen from the figure, the deflections in both of the averaged velocities increase with increasing gust ratio/speed. One thing to note here is that for the highest gust ratio investigated here (GR = 1.5), the averaged horizontal velocities become negative, suggesting that flow is redirected in the direction opposite the freestream, presumably due to the very large aforementioned leading-edge vortex formation.

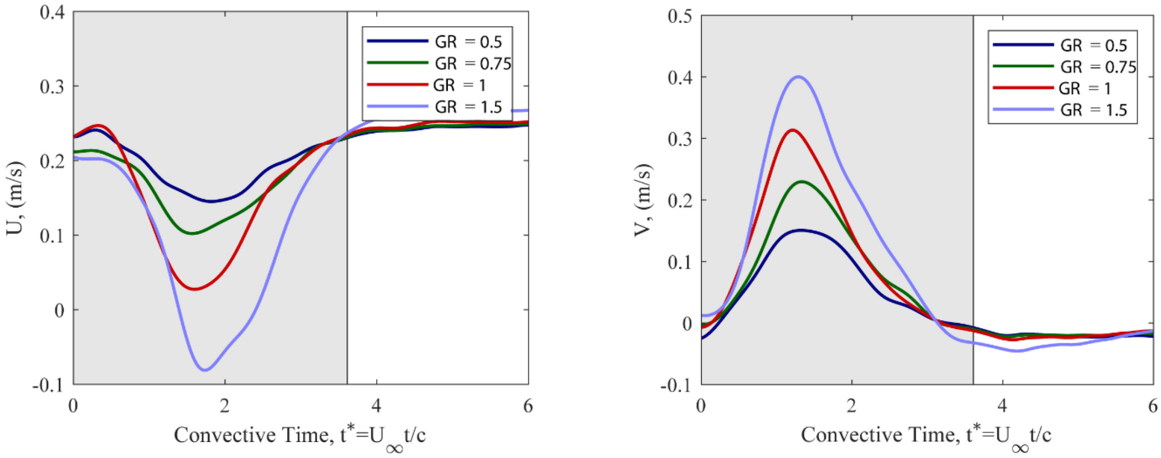

(a) Horizontal Velocities for a Line c/16 Upstream of the leading Edge.

(b) Vertical Velocities for a Line c/16 Upstream of the leading Edge.

Figure 4-8: Horizontal and Vertical Velocities Calculated for a c/8 Length Long Line at c/16 Upstream of the Leading Edge for Various Gust Ratios at 0° Angle of Attack.

After computing the velocities, effective angle of attack and lift coefficient on the selected line were found as previously described. The lift coefficient multiplied by the span of the wing is shown in Figure 4-9 compared to the lift coefficients obtained from the force measurements. The *y*-axis on the left shows the lift coefficient from the measurements; the *y*-axis on the right shows the lift coefficient multiplied by the wingspan from the flowfield measurements. One thing to point out here is that these axes do not have the same units. Whilst the lift coefficient from measurements is dimensionless, the unit of the coefficient calculated from the predictions is 1/m, though the limits are the same for both *y* axes. Figure 4-9(a) shows these coefficients (solid lines represent the force measurements and dashed lines represent the flowfield-based predictions) for various gust ratios for a flat plate at 0° incidence. For this analysis, the line is selected to be d = c/16, l = c/8 as concluded from the sensitivity study described above. As can be seen from this figure, even though the units of the coefficients do not match, the lift coefficient is successfully predicted in terms of both trends and the peak value with this method up to a gust ratio of 1.5, at which point the horizontal velocity is redirected for this very high gust ratio. Figure 4-9(b) shows these coefficients for 10° (on a line d = c/16, l = c/4) and 20° (on a line d = c/16, l = c/2) angles of attack at a 0.5 gust ratio. The lengths of the lines chosen are increased compared to the 0° angle of attack case since the flow is deflected more in the stream-normal direction for higher angles of attack. The lift coefficients calculated from the force measurements (solid line) are in good agreement with the computations during the encounter. However, this method fails to predict the second peak for 20° of incidence since this peak results from a secondary leading edge vortex formation after wing exits the gust, induced by the previously shed trailing edge vortex, not the change of the inflow conditions. Although in the results shown here, a constant factor of wingspan appears to be required for predictions to agree, it is of interest that this method is able to predict the general trends in the lift coefficient.

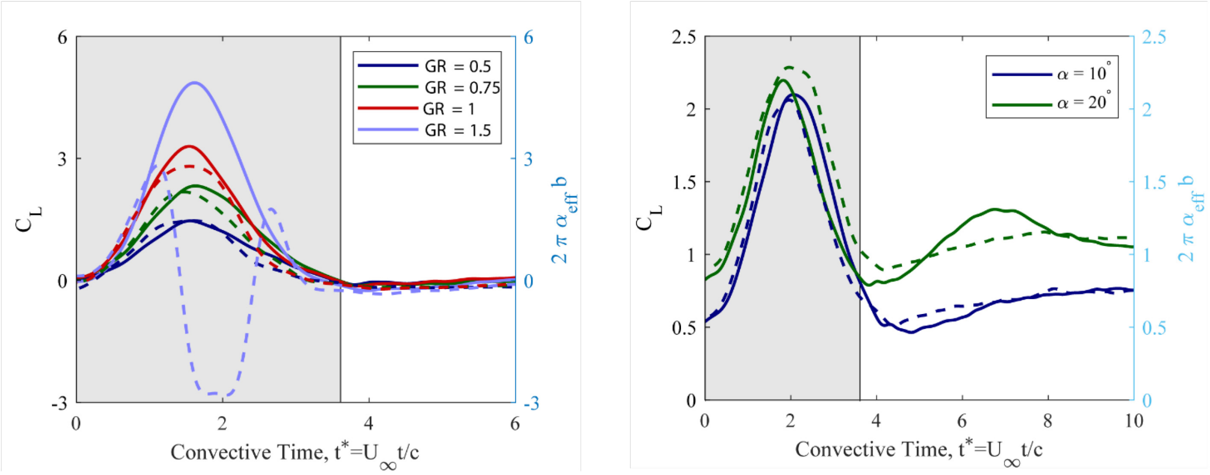

(a) Lift Coefficient from Force Measurements (Solid Line) and Lift Coefficient Multiplied with Span (Dashed Line) from Predictions for Various Gust Ratios at 0° Angle of Attack.

(b) Lift Coefficient from Force Measurements (Solid Line) and Lift Coefficient Multiplied with Span (Dashed Line) from Predictions for Various Angles of Attack at 0.5 Gust Ratios.

Figure 4-9: Lift Coefficient from Force Measurements (Solid Line) and Lift Coefficient Multiplied with Span (Dashed Line) from Predictions.

4.3.2.2 Vortex Gust

As mentioned in Section 4.2.1, the vortex gust was generated by a half counterclockwise rotation of the upstream flat plate wing and was characterized to have *w/c* of 0.4. The width here represents the half-length of the vortex generated, so the full length of the vortex is indeed 0.8 chords. The gust generator motion starts at t^*=0 and lasts for 4 convective times; this region is marked with a grey box in Figure 4-10. Since the vortex gust is not continuous in the stream-normal direction (unlike transverse gust), and it deforms as it convects with the freestream speed through the downstream flat plate, it is not possible to reliably perform a sensitivity study for this gust type. However, it is crucial for the flowfield-based force prediction method to select the line parameters carefully. Since the distance between the fully developed vortex gust and the leading edge is about half a chord length, the line was selected to be located c/4 upstream of the leading edge to capture the variations in time correctly. The length of the line was selected to be equal to the chord length to account for the full length of the vortex gust (0.8 chords). The computations are performed as described in the previous section along this d=c/4, l=c line. Figure 4-10 shows the lift coefficient from force measurements with a solid line (*y*-axis on the left) and the lift coefficient from the predictions for a wing at 0° angle of attack. Similar to the transverse gust results, lift transients are captured by the flowfield-based measurements in terms of both trend and minimum lift coefficient.

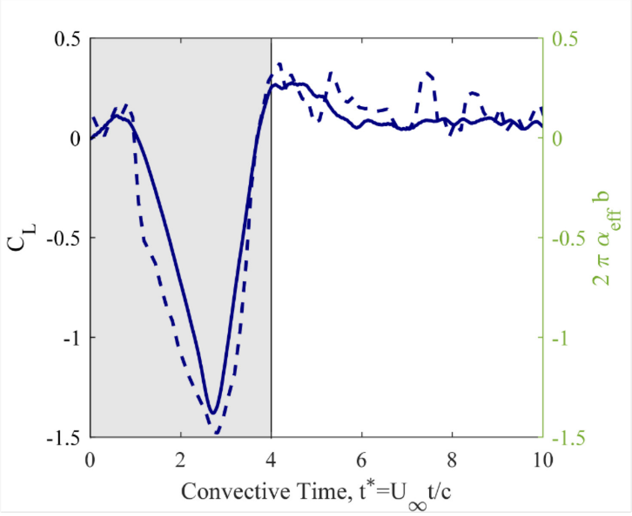

Figure 4-10: Lift Coefficient from Force Measurements (Solid Line) and Lift Coefficient Multiplied with Span (Dashed Line) from Predictions for a Flat Plate at 0° Angle of Attack.

4.3.3 Maximum Effective Angle of Attack and Lift

As discussed earlier in Section 4.3.1.1, the lift coefficient experiences a peak during the transverse gust encounter. It was discussed in an earlier study [14] that the peak lift coefficient was found to be dependent on the maximum effective angle of attack at the leading edge ($\alpha_{eff} = \alpha + \tan^{-1}(\frac{V(t^*)}{U(t^*)})$) rather than the individual values of the gust ratio and angle of attack. However, this hypothesis depended only on one case for one wing. In order to investigate this relation further, data sets from 4 different wings for various gust ratios and angles of attack are used and presented here. In the top of Figure 4-11, the y-axis represents the peak lift coefficient and the x-axis shows the maximum effective angle of attack achieved during the gust encounter. Different marks are used to represent different sets from the 3 different wings and 4 different cases are shown here. In the bottom of the same figure, the lift coefficient time histories of these cases are shown. As can be seen from this plot, the peak lift coefficients are similar for similar maximum effective angles of attack if the geometric angle of attack of the wing is less than or equal to 10°. Interestingly, this relation works well for effective angles of attack as high as 40°. It is therefore concluded that by just having the prior information on the gust (i.e., the geometric incidence of the wing and the maximum transverse velocity in the gust flow), it is possible to predict the maximum lift coefficient with reasonable accuracy.

4.4 CONCLUSIONS

An experimental investigation of force transients during sine-squared transverse and vortex gust encounters has been performed. A novel flowfield-based force production method was introduced and adopted for both gust types. The resulting lift histories were found to agree with the experimental measurements. Furthermore, the behavior of maximum lift coefficient and maximum effective angle of attack was examined.

A line upstream of and symmetric to the leading edge was used to compute the horizontal and vertical average velocity variations in time from experimental flowfields. The effective angle of attack and lift coefficient were then calculated based on these velocities. In order to obtain the variations at the leading edge, these quantities were shifted in time considering the convection with the freestream. A sensitivity study was performed for transverse gust encounters to investigate the wing gust coupling and the effects of the length and the distance of the line selected. The results from this study showed that the coupling between the wing and the gust is important. It was concluded that the line should be close to the leading edge so that the deflections that arise from the coupling are captured. Also, it should be short enough to avoid adding the non-disturbed far away velocities in the averaging process. A similar study was found to be not applicable to the vortex gusts since it is not continuous in the stream-normal direction and deforms as it convects with the freestream speed through the wing. For this gust type, the width and the travelling distance of the vortex were used to select this line. For both gust types, the computed lift coefficients were multiplied with the span of the wing while comparing them to the lift coefficients obtained from the measurements. This comparison yielded good agreements for gust ratios up to 1 during sine-squared gust encounters. However, it failed to do so for a gust ratio of 1.5 since in this case the leading-edge vortex is sufficiently strong to re-direct the horizontal velocity opposite to the freestream. Furthermore, the method accurately predicted the maximum lift coefficient for angle of attack higher than 0°, but failed to predict the second lift peak occurred since this peak is induced by the previously shed trailing edge vortex rather than the change in inflow conditions. The comparison also worked well for a flat plate at 0° encountering a vortex gust. Variations in the lift for both gust types depend on the effective angle of attack.

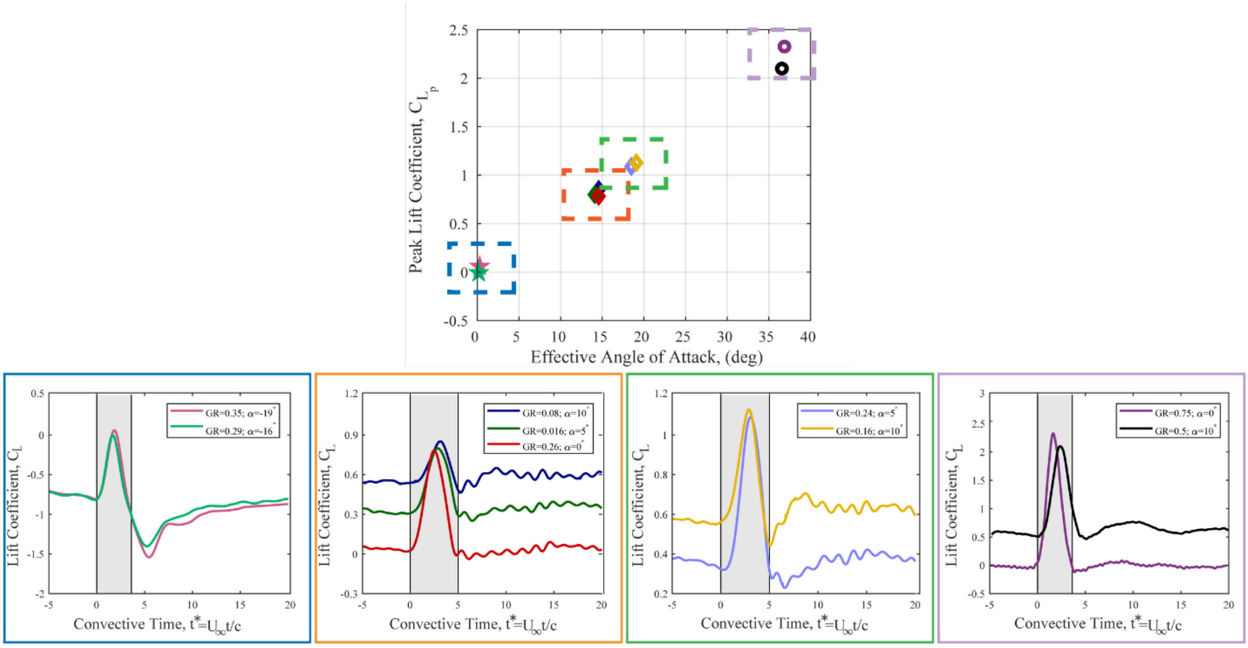

Figure 4-11: Peak Lift Coefficients with Similar Peak Leading Edge Effective Angle of Attack for Different Wings.

The dependence of the peak lift coefficient value on the maximum effective angle of attack has also been examined for the sine-squared transverse gust encounters. It was concluded that the cases in which gust ratio and geometric angle of attack were selected to produce a given value of effective angle of attack were found to produce similar lift peak coefficients if the geometric angle of attack is less than 10°. In addition, the results showed that this is applicable even for wings with different aspect ratios.

4.5 ACKNOWLEDGEMENTS

This work is supported in part by the Air Force Office of Scientific Research under grant FA9550-16-1-0508 and the National Science Foundation under Grant No. 1553970. The authors would like to thank Murat Saritas for proving experimental data.

4.6 REFERENCES

[1] Viswanath, K., and Tafti, D.K., Effect of frontal gusts on forward flapping flight, AIAA Journal, Vol. 48, No. 9, 2010, pp.2049-2062. doi:10.2514/1.J050263.

[2] Küssner, H. G., Zusammenfassender bericht über den instationären auftrieb von flügeln, Luftfahrtforschung, Vol. 13, No. 12, 1936, pp. 410-424.

[3] Granlund, K., Monnier, B., Ol, M., and Williams, D.R., Airfoil longitudinal gust response in separated vs. attached flows, Physics of Fluids, Vol. 26, No. 2, 2014. doi:10.1063/1.4864338.

[4] Williams, D.R., and Grimaud, L., Scaling vehicle dynamics and fluid dynamics in gusting flows, 52nd Aerospace Sciences Meeting, AIAA Paper 2014-1456, National Harbor, MD, 2014.

[5] Greenblatt, D., Unsteady low-speed wind tunnels, AIAA Journal, Vol. 54, No. 6, 2016, pp. 1817-1830. doi:10.2514/1.J054590.

[6] Kuethe, A., Circulation measurements about the tip of an airfoil during flight through a gust, NACA Technical Report 685, Feb. 1939.

[7] Holmes, D., Lift and measurements in an aerofoil in unsteady flow, ASME International Gas Turbine Conference and Products Show, Paper No. 73-GT-41, Washington, DC, 1973.

[8] Perrotta, G., and Jones, A.R., Unsteady forcing on a flat-plate wing in large transverse gusts, Experiments in Fluids, Vol. 58, No. 8, 2017. doi:10.1007/s00348-017-2385-z.

[9] Corkery, S., Babinsky, H., and Harvey, J., On the development and early observations from a towing tank-based transverse wing-gust encounter test rig, Experiments in Fluids, Vol. 59, No. 9, 2018, p. 135. doi:10.1007/s00348-018-2586-0.

[10] Roadman, J., and Mohseni, K., Gust characterization and generation for wind tunnel testing of micro aerial vehicles, 47th AIAA Aerospace Sciences Meeting including The New Horizons Forum and Aerospace Exposition, 2009, p. 1290.

[11] Shao, K., Wu, Z., Yang, C., Chen, L., and Lv, B., Design of an adaptive gust response alleviation control system: Simulations and experiments, Journal of Aircraft, Vol. 47, No. 3, 2010, pp. 1022-1029.

[12] Engin, K., Aydın, E., Zaloglu, B., Fenercioglu, I., and Cetiner, O., Large scale spanwise periodic vortex gusts or single spanwise vortex impinging on a rectangular wing, AIAA Aviation Forum, 2018.

[13] Biler, H., Jones, A. R., Saritas, M., Fenercioglu, I., Cetiner Yildirim, N. L., and Bronz, M., Investigation of force transients during transverse and vortex gust encounters, AIAA Scitech 2019 Forum, 2019, p. 0636.

[14] Biler, H., Badrya, C., and Jones, A. R., Experimental and computational investigation of transverse gust encounters, AIAA Journal, Vol. 57, No. 1, 2019, pp. 4608-4622. doi:10.2514/1.J057646.

Chapter 5 – NON-CIRCULATORY FORCE ON A FINITE THICKNESS BODY ENCOUNTERING A GUST

P. Gehlert and H. Babinsky
University of Cambridge
UNITED KINGDOM

Many low-order models for unsteady flows divide the force into circulatory and non-circulatory components. The former is associated with vorticity in the flow field, whilst the latter is often synonymous with the added mass force. Investigating a cylinder sharp-edged gust encounter, at a Reynolds number of 6000, probes the origin of these respective forces. Vorticity residing in the flow field does not only originate from the cylinder but it is also located in the gust shear layers, which delimit the vertical gust velocity from the surrounding quiescent fluid. It is possible to represent the body surface by a vortex sheet where individual components, satisfying the non-through flow condition, originate from different sources. All vorticity external to the body generates a complementary contribution to this surface vortex sheet. A further vortex sheet component is uniquely attributed to linear acceleration of a body and linked to the added mass effect. Finally, a non-circulatory vortex sheet forms due to the induced velocity by the gust vorticity. In Küssner's potential flow gust model this latter vortex sheet contribution is attributed to added mass. However, because the gust encounter is not associated with any body acceleration, the force must rather be linked to the growth and redistribution of this vortex sheet, due to the relative advection of the gust shear layer vorticity. Particle image velocimetry validates this result using a surging and rotating cylinder at gust ratios of 0.5 and 1. Force balance measurements show that the force originating from the rate of change of the non- circulatory gust vortex sheet, unlike in the case for an infinitely thin plate, vastly over-predicts the initial rise in force as the cylinder enters the gust. This is because, when considering the rate of change of the vortex sheet, it is implicitly assumed that all of the vertical momentum of the gust flow inside the region occupied by the cylinder, is lost. The overestimation is a result of the rigid shear layer assumption inherent to the Küssner model. In reality, the gust shear layers deflect, causing a spread of vertical momentum. The deflection of the shear layers can be analytically approximated by removing the contribution due to the rate of change of momentum inside the cylinder. This improves the force prediction but does not fully recover the experimental force measurements during the initial entry into the gust. On a practical level this suggests that for bodies of finite thickness the non-circulatory force cannot be easily calculated, as it is difficult to quantify the effect of the body volume.

5.1 INTRODUCTION

Gusts are a ubiquitous feature in the flight envelope of Micro Aerial Vehicles (MAV) [1], [2], [3]. Furthermore, the low flights speeds of MAV's result in strong relative gust ratios. Large scale separations, resulting from wing gust interactions, lead to highly unsteady forces imposing limitations on their versatility. The surrounding flow field as well as reduced low-order models have subsequently been studied extensively to mitigate the forces experienced by such gust encounters [4], [5], [6], [7]. Pre-emptively predicting what the force will be, rather than counteracting it from a purely reactionary perspective, as is the case in simple closed-loop control systems, could provide an avenue for enhanced gust rejection abilities.

Von Karman and Sears [8] divide the force experienced by a flat plate entering a sharp-edged gust into a component associated with shed circulation and one with a non-circulatory vortex sheet residing on the body surface. By evaluating the rate of change of this non-circulatory vortex sheet, a force component can be calculated. Von Karman and Sears attribute this to *apparent* or *added mass* forces. This effect is central to Küssner's model when the plate is entering the gust, as it is then, that the non-circulatory vortex sheet distribution changes.

Corkery and Babinsky [9] experimentally confirmed the physical existence of an added mass vortex sheet and the related force for an accelerating flat plate. Experimental evidence regarding the added mass vortex sheet has been further extended to objects of finite thickness [10]. By experimentally investigating a flat plate sharp-edged gust encounter, Corkery and Babinsky [11] have further shown that the non-circulatory vortex sheet, attributed to added mass by von Karman and Sears, is the result of vorticity residing in the gust shear layers; rather than due to any spurious and non-existent body acceleration. To avoid any future confusion that could arise when studying more complex flow fields, the authors therefore suggested that the term *added mass* should only be related to forces that arise due to the acceleration of a body.

Splitting up forces into individual components can make it possible to calculate each contribution separately using simple relations. Subsequently, these can be linearly superimposed. This is an attractive quality for low-order models, as it makes real time simulations possible. The correct determination of the non-circulatory force observed in flat plate gust encounters is therefore, a substantial step in the right direction.

MAV’s often feature wings that can be approximated as infinitely thin flat plates, making the flat plat results directly applicable. However, many realistic geometries such as helicopter blades or water turbines cannot be assumed to have negligible volume. The forces they need to withstand are nonetheless also governed by their interaction with these respective gusts.

The aim of this chapter is therefore to evaluate the applicability of the non-circulatory force, equivalent to that observed in thin flat plate gust encounters, for objects of finite volume. The investigation seeks to explore whether a non-circulatory vortex sheet, matching the theoretical prediction, can be determined experimentally as a consequence of gust shear layers. If this is possible, the respective force is to be evaluated and compared to experimental force measurements. The outcome of this will shed light on the applicability of the respective non-circulatory Küssner like force experienced by a body when entering the gust and how the finite volume affects the force. As subject of this investigation, an object with a thickness to cord ratio of 1 will be used, namely a circular cylinder. To generate lift, the cylinder is subjected to rotational motion. Varying the spin rate allows the investigation of a range of lift coefficients without needing to change the geometry.

5.2 NON-CIRCULATORY VORTEX SHEET

In potential flow a body may be represented by a vortex sheet located on the body surface. It enforces the no-penetration condition at the surface around which the inviscid irrotational solution is valid [12]. This vortex sheet encompasses the entire vorticity of the boundary layer, where the origin of the vorticity can be traced back to various sources and is split up into circulatory and non-circulatory components [9], [10], [11], [13], [14],

$$\gamma^b = \underbrace{\gamma^{nc}_{am} + \gamma^{nc}_{ext.}}_{non-circulatory} + \underbrace{\gamma^r + \gamma^c_{cyl}}_{circulatory} \tag{5-1}$$

The component γ^{nc}_{am} is derived from enforcing the no-penetration condition due to body translation. When an object undergoes a linear acceleration γ^{nc}_{am} changes strength and this is then associated with the added mass force. γ^c_{cyl} is the vortex sheet component arising from any vorticity shed by the cylinder. This induces a velocity on the cylinder surface necessitating a vortex sheet to guarantee no through flow. If the body is rotating, a slip velocity between the wall velocity and quiescent fluid surrounding it results in a further vortex sheet, γ^r. Finally, if there is any vorticity in the flow field that was not originally shed by the cylinder but created through external means, for example a gust shear layer, it will also induce additional velocities on the body surface. This requires $\gamma^{nc}_{ext.}$ to maintain the no-through-flow condition. The vortex sheet due to external vorticity will have zero net circulation, as it will be equal and opposite in magnitude to the external vorticity, which itself must have zero total circulation [15].

The general flow field around a body immersed in a sharp-edged gust is shown in Figure 5-1. Externally created vorticity, associated with the gust, resides in the two gust shear layers. Together with vorticity shed by the wing and the kinematic motion, this gives rise to boundary layer vorticity, which can be represented by the vortex sheet, γ_b. The vortex sheet associated with the gust shear layer vorticity will be referred to as the non-circulatory vortex sheet, $\gamma_{ext.}^{nc}$ throughout this chapter. Its contribution can be theoretically calculated by considering the gust shear layers and determining the vortex sheet required to enforce the no-penetration condition. Alternatively, von Karman and Sears' 'added mass' result may be used [8], however, this only exists for flat plates. For a thin flat plate gust encounter, the existence of $\gamma_{ext.}^{nc}$ was experimentally confirmed by Corkery and Babinsky [11]. When the plate is fully immersed in the gust, $\gamma_{ext.}^{nc}$ although similar in shape to that on a plate travelling normal to its chord, is created because it is the mirror image of the vorticity residing in the gust shear layers.

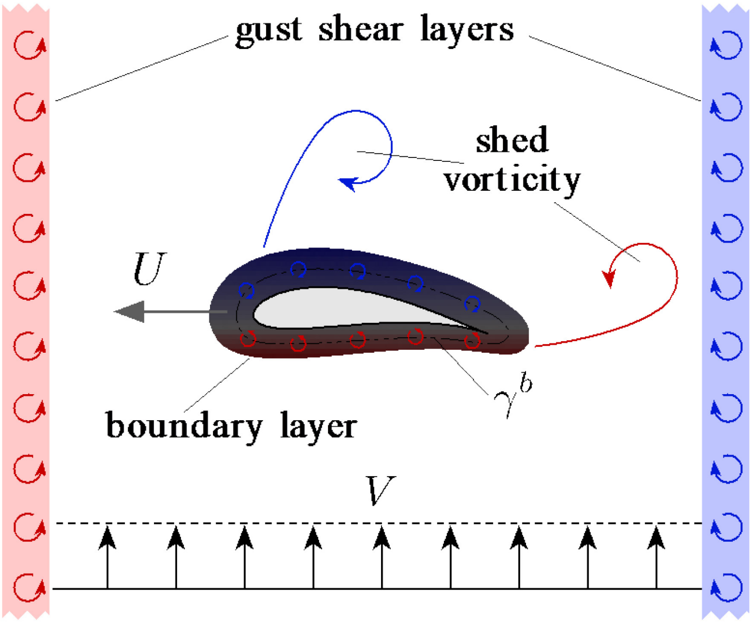

Figure 5-1: Schematic Illustration a Wing Inside an Idealised Rigid Top-Hat Shaped Gust.

The force acting on an object in unsteady flow can be found by investigating the time variation of the vorticity distribution in the flow field [16]. Applied to the boundary layer vortex sheet or a component of it can hence provide information regarding its contribution to the total force. Evaluating the time rate of change of the vortex sheet attributed to the gust shear layer vorticity gives a related non-circulatory force,

$$\gamma^b = \underbrace{\gamma_{am}^{nc} + \gamma_{ext.}^{nc}}_{non-circulatory} + \underbrace{\gamma^r + \gamma_{cyl}^c}_{circulatory} \tag{5-2}$$

ρ is the fluid density. Here $I_{ext.}^{nc}$ is the impulse and for a vertical force is defined as

$$I_{ext.}^{nc} = \int \gamma_{ext.}^{nc} x \, dl \tag{5-3}$$

where x is the coordinate aligned with the horizontal axis. The variation of $\gamma_{ext.}^{nc}$ as the plate enters the gust is schematically illustrated in Figure 5-2.

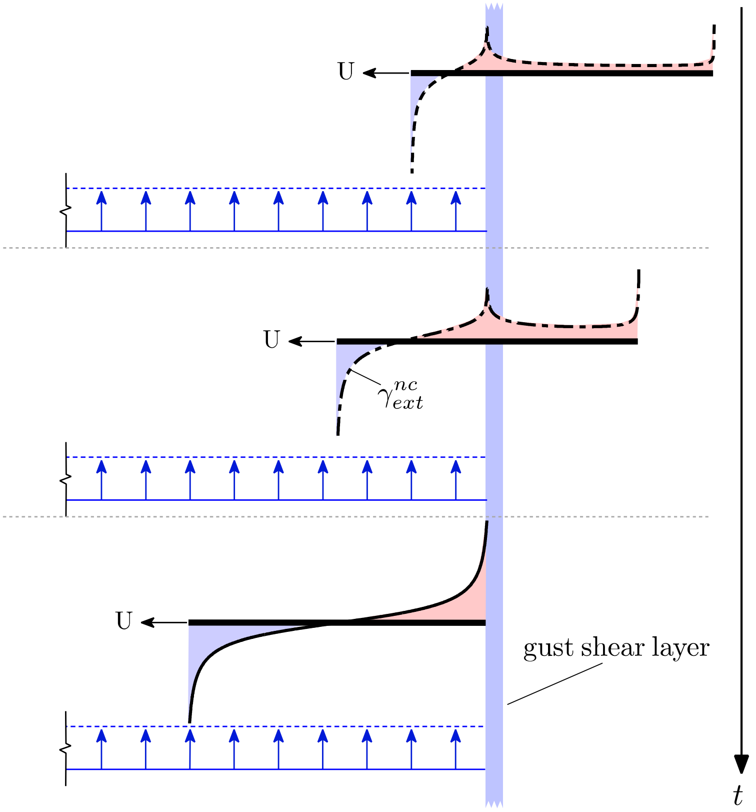

Figure 5-2: Schematic Illustration of a Thin Flat Plate Entering a Gust and its $\gamma^{nc}_{ext.}$ Distribution.

Von Karman and Sears showed for a potential flow that the rate of change of this vortex sheet, as a flat plate enters a top-hat shaped gust, leads to a force that can be approximated by:

$$F_y^{nc} = 2\,\rho UV\,\sqrt{s(c-s)} \tag{5-4}$$

c is the chord and s is the distance travelled into the gust. U and V are the plate translation and the vertical gust velocity.

Although later research [11] has shown that this vortex sheet is the consequence of the presence of the gust shear layers, in this particular example it makes no difference in practice. The vortex sheet distribution and force are identical to that calculated by von Karman and Sears on the basis of added mass.

When the plate is fully outside or inside the gust $\gamma^{nc}_{ext.}$ seizes to change and thus does not result in a force. A comparison between the theoretical force according to Equation 5-4 and the force balance measurements for a flat plate gust encounter are shown in Figure 5-3. When the wing has just entered the gust, the force experienced by the flat plate increases sharply. Likewise, the force due to the gust shear layers $\gamma^{nc}_{ext.}$ increases and initially matches the force balance measurement. This indicates that the non-circulatory gust force dictates the force response during the early stages of a flat plate gust encounter. As vorticity sheds from the leading and trailing edge, the forces begin to be governed by the respective growth and advection of these vortices. This explains the departure of C_l from $C^{nc}_{l_{ext:\,plate}}$. The theoretically calculated force assumes infinitely thin shear layers, whereas the shear layers in the experiment have some associated thickness. This leads to the small discrepancy between the measured and analytical force just before the plate enters the gust.

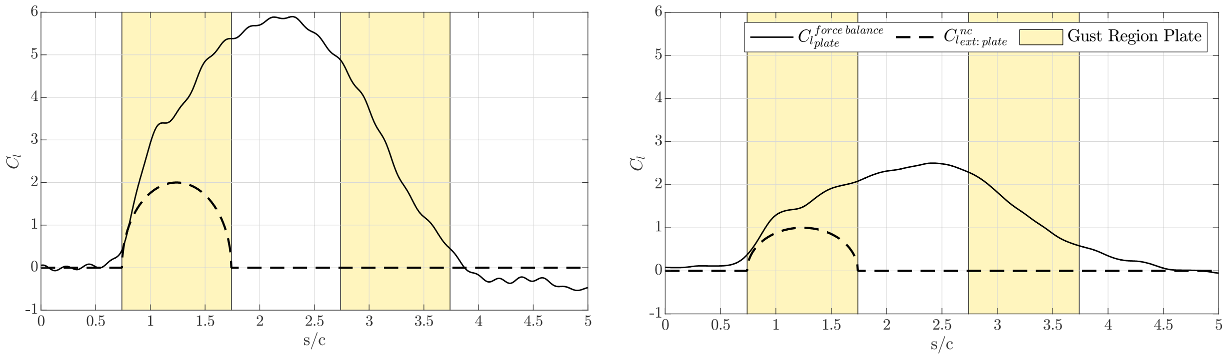

(a) $GR = 0.5$. **(b) $GR = 1$.**

Figure 5-3: C_l History for a Flat Plate Gust Encounter. The theoretical non-circulatory force due to a rigid gust is also shown. The shaded fields indicate the regions when the plate is entering and exciting the gust. Data adapted from Ref. [17].

To investigate a circular cylinder gust encounter, two rigid, non-deforming gust shear layers are assumed. The same simplification is made in the Küssner model for a flat plate gust interaction. When the cylinder enters the gust, this assumption implies that the gust remains unperturbed and does not deflect. Unlike for the infinitely thin flat plate this will, however, result in an additional unphysical force, as will be explained in the following. The theoretical non-circulatory vortex sheet during such a gust encounter can be obtained with a panel method approach. The gust encounter is illustrated in Figure 5-4, which also shows the resulting vortex sheet distribution at various times during the gust entry. It is observed, that similar to when a flat plate enters the gust, the vortex sheet distribution varies and hence gives rise to a force. Furthermore, once fully immersed the vortex sheet distribution is, as expected, equivalent to that of a circular cylinder in cross-flow.

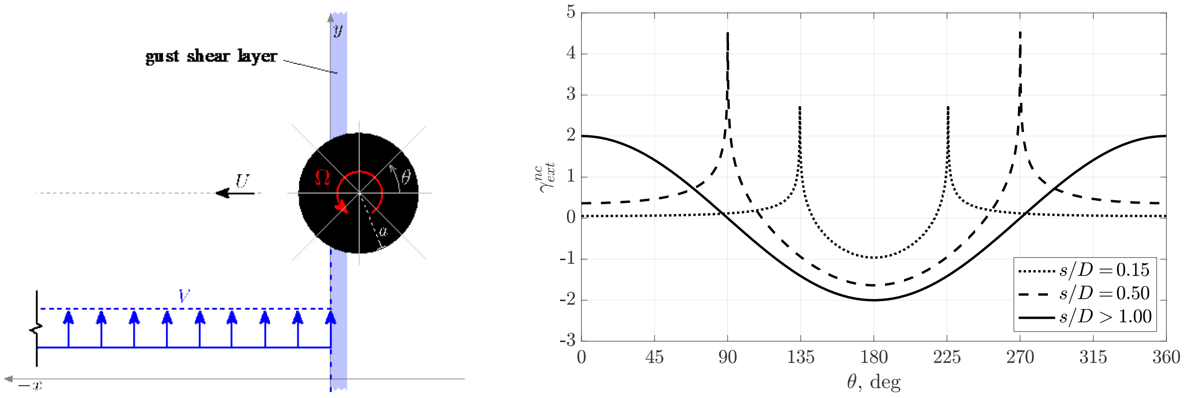

(a) Geometry. **(b) Non-Circulatory Vortex Sheet.**

Figure 5-4: Cylinder Entering a Rigid, Non-Deforming Gust.

The rate of change of the non-circulatory gust vortex sheet is linked to the rate of change of momentum of the flow field. The resulting force is the Küssner force equivalent for a circular cylinder. Initially, prior to the cylinder entering the gust, there is vertical fluid momentum inside the gust, as schematically indicated in Figure 5-5. As the cylinder encroaches on the gust, some of the volume inside the gust is occupied by the cylinder. The vortex sheet will develop accordingly, causing a change in flow velocity around the cylinder and flow inside the cylinder to mirror the solid body motion. Since the cylinder is traversing horizontally, fluid that is assumed to be inside the cylinder no longer has vertical momentum. Hence, any vertical momentum that existed in the gust, prior to being encroached upon by the cylinder, is lost. This is a consequence of the unphysical rigid shear layer assumption.

The force due to the change in momentum inside the cylinder is:

$$F_{\delta V_{cyl}} = \rho U \; GR \; \frac{d\,V_{cyl}}{dt}, \tag{5-5}$$

where $\frac{d\,V_{cyl}}{dt}$ is the rate at which the volume of the cylinder inside the gust has changed and GR is the gust ratio. In reality, the shear layers will not be rigid but deform. Hence, the vertical momentum is not lost but deflected around the cylinder.

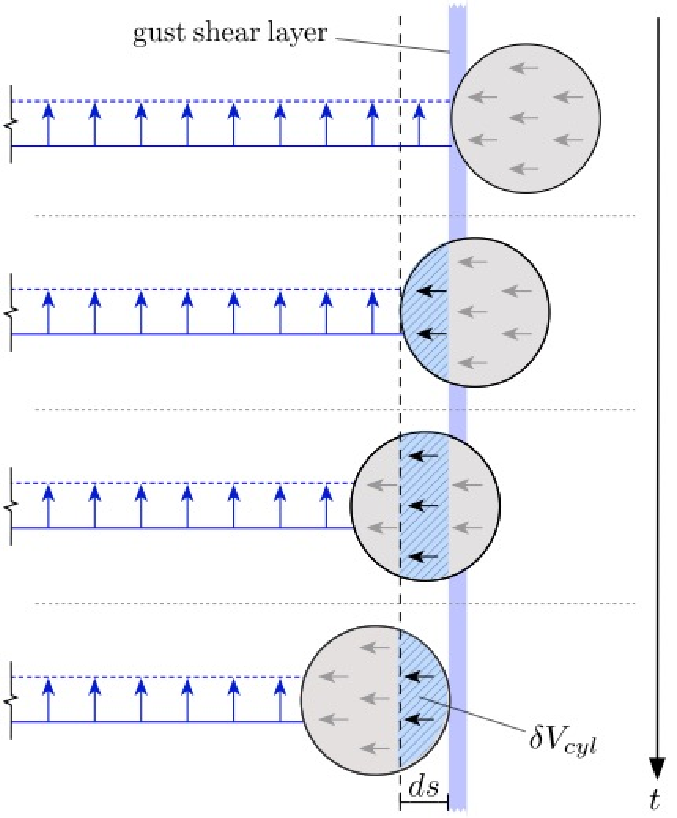

Figure 5-5: Schematic Illustration Indicating the Change in vertical Momentum as the Cylinder Enters the Gust.

Assuming a rigid gust edge, the force due to rate of change of $\gamma^{nc}_{ext.}$ is evaluated for a surging cylinder, $C^{nc}_{l_{ext:\,cyl}}$. The contribution due to the 'lost' vertical momentum inside the cylinder, Equation 5-5 is half of this force. Removing its contribution

$$C^{\;nc}_{l_{cyl}} = \frac{F^{nc}_{ext} - F_{\delta\,V_{cyl}}}{\frac{1}{2}\rho U^2_\infty a}, \tag{5-6}$$

results in the same inviscid gust force as is calculated for a thin flat plate, as shown in Figure 5-6.

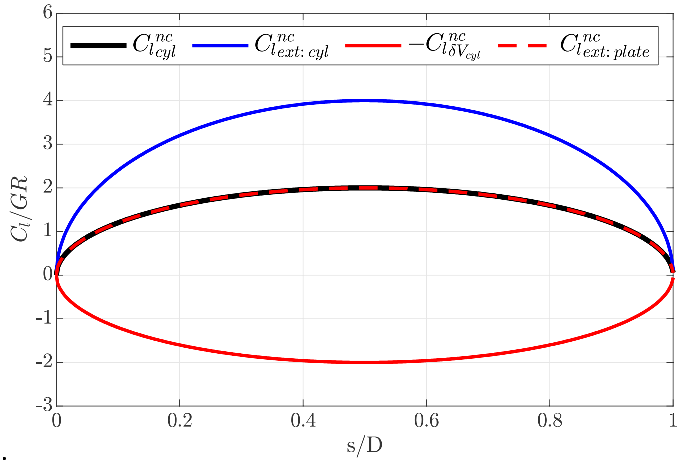

Figure 5-6: Inviscid Forces Calculated by Evaluating the Time Rate of Change of $\gamma^{nc}_{ext.}$ for a Cylinder and Flat Plate Entering a Rigid Sharp-Edged Gust.

5.3 EXPERIMENTAL CYLINDER GUST ENCOUNTER

Having explored the origin of the boundary layer vorticity components as well as the relevant forces from a theoretical and potential flow perspective, an experimental cylinder gust encounter is investigated to test the validity of the proposed ideas.

5.3.1 Experimental Set-Up

The towing tank facility at the University of Cambridge is used to experimentally recreate the cylinder gust interaction. The 9 m long and 1 m wide tank is filled up to 0.8 m and the cylinder is vertically mounted to a force balance. An EC synchronous motor, fitted with a digital encoder to measure the rotational speed, is connected to a carbon fibre drive shaft. This shaft is housed inside a load bearing aluminium tube and connects to the outer circular cylinder at the bottom end. The outer cylinder is 0.06 m in diameter and 0.48 m long and sits on two bearings at either end that allow it to spin freely around the aluminium tube. Further details of the cylinder design are provided in Ref. [10].

The servo motor driven carriage is moved along the length of the tank. The gust rig, specifically designed for the facility, is located such that the cylinder intersects the transverse flow as to create a sharp edge gust encounter. A schematic illustration of the set-up is shown in Figure 5-7.

The gust rig consists of an outlet and a collector, both of which are connected to each other via a pump generating the flow. They create a flow perpendicular to the motion of the carriage. A gap in the collector allows for the laser sheet to pass through it and to illuminate the flow at midspan of the cylinder. This results in a shadow region on the other side of the cylinder, where no flow data can be collected, as shown in Figure 5-7(b). Furthermore, reflections of the laser sheet of the cylinder surface lead to missing data directly around it. As outlined in Ref. [10], the missing vorticity data is recovered by interpolating between the measured cylinder surface velocity and the flow field. This preserves the magnitude of vorticity located directly around the cylinder but leads to an error in the surface normal distribution of the vorticity. The problems due to reflections only extends approximately 1 – 2 mm into the flow field. Therefore, the error in the distribution of wall normal vorticity is only minor and does not adversely affect the results.

Planar particle image velocimetry is conducted to assess the flow. Titanium dioxide particles are illuminated by a Nd:YLF 527 nm laser and two high-speed Phantom M310 cameras are positioned in a dual camera arrangement to ensure optical access to all regions of the flow field. The sampling rate is adjusted to 250 Hz and 400 Hz for the individual test cases and 8 runs are conducted per kinematic case from which an ensemble average is obtained. The cross-correlation process, using the commercial LaVision Flowmaster 2D system, features an adaptive interrogation window with a size of 16 × 16 pixels during its final pass with an overlap of 50%.

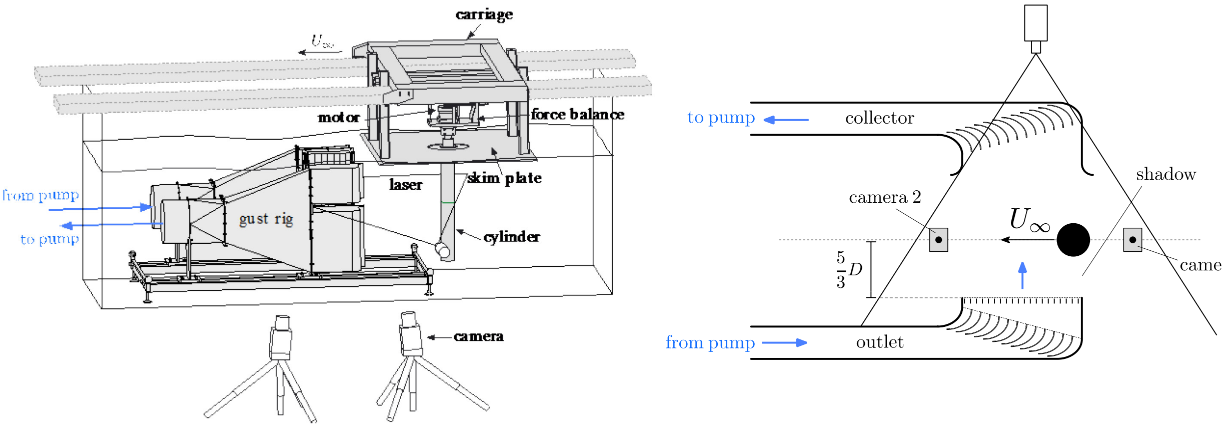

(a) Gust Rig and Cylinder Arrangement.

(b) Top View of PIV Set-Up.

Figure 5-7: Experimental Set-Up.

To ensure that peak locking effects do not dominate the Root Mean Square (RMS) velocity error estimation [18], the illumination of the particles is smeared over approximately two pixels. This reduces the associated RMS position error to 0.02 pixels [19]. An average displacement of 3 – 4 pixels between frames leads to a conservative velocity error estimation of 0.6%. The shift in the correlation peak, when an interrogation window is mapped back to its original position according to the calculated displacement vector, can be further assessed to estimate the measurement uncertainty [20]. The associated uncertainty is calculated by DaVis, and after being reduced according to $\frac{1}{\sqrt{N}}$ where N is the number of samples [21], is 3%. The total uncertainty of the velocity measurements is therefore, below 4%.

The vorticity contours of the gust are shown in Figure 5-8(a). The path taken by the cylinder centre as it traverses the gust is also indicated. The cylinder centre is offset by 0.1 m from the gust outlet; equivalent to $\frac{3}{5}D$. The vertical velocity profile normalised by the average velocity, $\bar{V}$, at various locations inside the gust is shown in Figure 5-8(b). It is observed that the gust shear layers diffuse further away from the gust outlet, leading to a less sharp gust profile. Furthermore, a small yet non-zero velocity is recorded outside the gust. This is due to flow being entrained by the gust; however, its magnitude is negligible compared to the gust velocity itself. A more detailed description of the gust rig and its respective flow field can be found in Ref. [22].

Five different test cases are investigated, each compromising of a different cylinder kinematic and gust ratio combination. The Reynolds number, Re, based on final cylinder surge velocity, is 6000 for all cases. The cylinder is stationary $1.24D$ upstream of the first gust shear layer. It proceeds to accelerate within $0.5D$ to its final velocity of 0.129 ms^{-1}. When the cylinder rotates, it does so at 41 revolutions per minute, RPM, which is equivalent to a rotation ratio, $\alpha = \frac{\Omega_\infty a}{U_\infty}$ of 1, either in the clockwise or counter-clockwise direction. It reaches its final angular velocity within 2.4 mm or s/D $= \frac{D}{24}$. The test cases are summarised in Table 5-1.

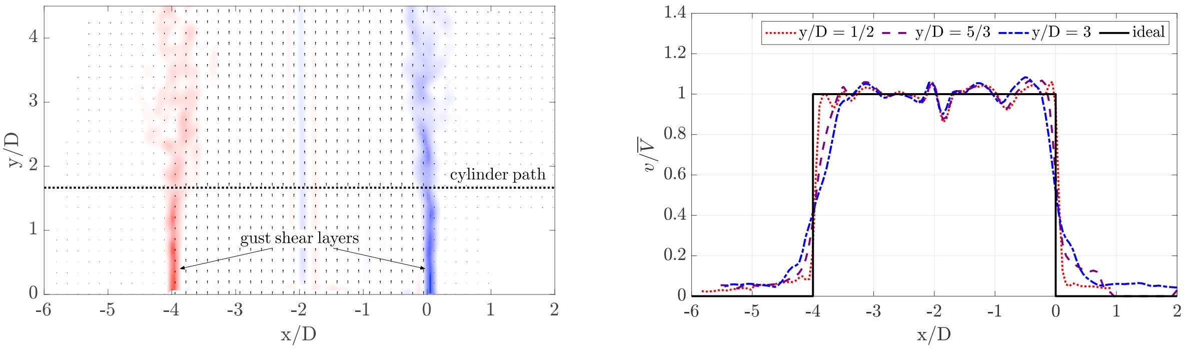

(a) Vorticity Contours of the Gust Flow Field.

(b) Velocity Profile of Gust at Various Vertical Locations.

Figure 5-8: Gust Flow Field.

Table 5-1: Summary of the Test Cases. Positive rotation is in the counter-clockwise direction.

Case	α	RPM	GR	U_∞	Re
1	-	0	0.5	0.129	6000
2			1		
3	-1	-41	0.5		
4			1		
5	1	41	0.5		

5.3.2 Extracting $\gamma^{nc}_{ext.}$

The approach outlined by Corkery and Babinsky in Ref. [11] to isolate $\gamma^{nc}_{ext.}$ is adapted to the current problem geometry. This will test the generally validity of the existence of $\gamma^{nc}_{ext.}$ and whether its rate of change can predict the initial force experienced by an object of finite volume as it enters a sharp-edged gust.

The boundary layer vortex sheet is made up of two non-circulatory and two circulatory components, as stated in Equation 5-1. These can be re-arranged such that all non-circulatory terms and those related to the kinematic motion of the cylinder are grouped together,

$$\gamma^{nc+r} = \gamma^{nc}_{am} + \gamma^{nc}_{ext} + \gamma^{r} = \gamma^{b} - \gamma^{c}_{cyl}. \tag{5-7}$$

When the cylinder is fully immersed in the gust, the flow field relative to the cylinder is a superposition of a horizontal freestream velocity and a vertical gust velocity. γ^{nc}_{am}, due to the surging motion of the cylinder, is found from horizontal potential flow to be $-2U\ sin\ \theta$ and recovered experimentally for a surging and rotating circular cylinder [10]. The vortex sheet due to the vertical gust is simply due to a rotation of the uniform freestream flow field from the horizontal to the vertical, leading to $\gamma^{nc}_{ext.} = 2V\cos\theta$. γ^{r} is related to the tangential surface velocity and constant along the cylinder surface. Therefore, γ^{nc+r} can be calculated solely considering the kinematics and problem geometry.

To experimentally isolate $\gamma^{nc}_{ext.}$, therefore, requires a measurement of the boundary layer to obtain γ_b as well as identifying any vorticity that has been shed by the cylinder, which gives rise to γ^{c}_{cyl}. The former is measured using the boundary layer measurement method outlined in Ref. [10]. The cylinder circumference and surrounding flow field are split up into a number of wedges, as shown in Figure 5-9. By integrating the velocity aligned with the contour of each wedge, the circulation of each segment, $\delta\Gamma_n = \oint u\ dl$, is found. The velocity along the surface of the cylinder is set to the true physical surface velocity obtained by tracking the translation velocity and rotation rate. Dividing $\delta\Gamma_n$ by the segment length, δs_n, yields the vortex sheet strength for each element[1],

$$\gamma_n = \frac{\delta\Gamma_n}{\delta s_n} \tag{5-8}$$

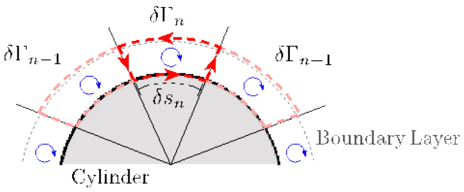

Figure 5-9: Discretization of the Cylinder and Surrounding Flow Field to Obtain γ^b from Experimental Data.

γ_{cyl}^c is identified by manually masking the flow field to only include vorticity shed by the cylinder, in a manner similar to Corkery and Babinsky [11]. An example of this at two instances in time is shown in Figure 5-10.

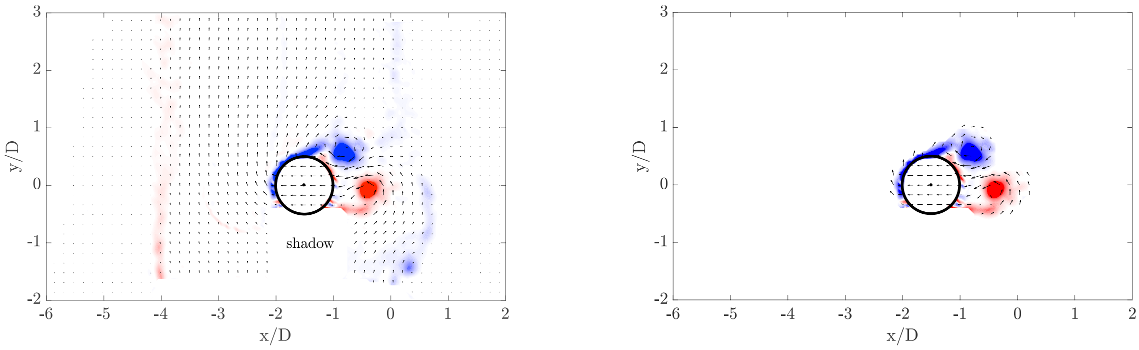

(a) Vorticity of Complete Flow Field, 1.5D Inside Gust.

(b) Gust Vorticity is Masked, 1.5D Inside Gust.

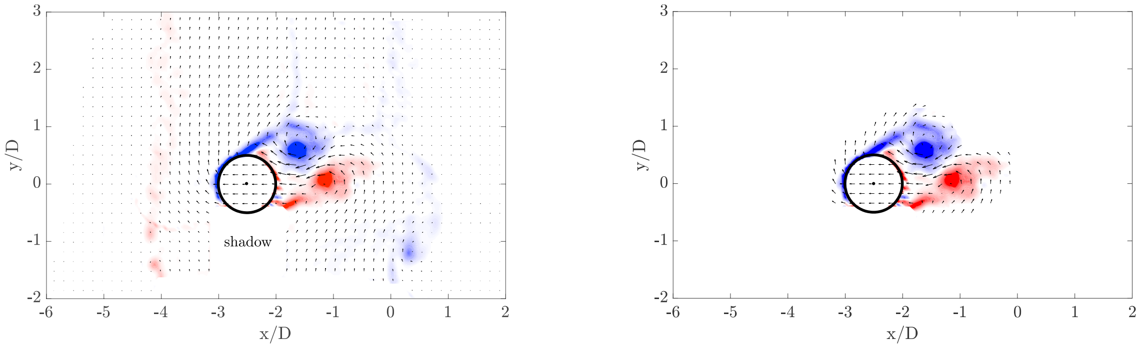

(c) Vorticity of Complete Flow Field, 2.5D Inside Gust.

(d) Gust Vorticity is Masked, 2.5D Inside Gust.

Figure 5-10: Normalised Vorticity Field by Maximum Vorticity Used to Calculated γ_{cyl}^c for Case 1, Surge Only, $GR = 0.5$.

---

[1] Note that it is not necessary to fully resolve the boundary layer velocity profile in order to recover γ^b. Velocity vectors close to the surface will be almost tangential to the surface. Their contribution will therefore cancel. Effectively it suffices to measure the velocity difference between a point just outside the boundary layer and the body surface velocity.

The cylinder is translating and rotating at a constant velocity whilst immersed in the gust. This causes γ^{nc}_{am} and γ^{r} to remain unchanged. Likewise, $\gamma^{nc}_{ext.}$ does not vary when the cylinder is completely inside the gust. As a result, the experimental measurement of $\gamma^{b} - \gamma^{c}_{cyl}$ can be averaged over all time instances whilst the cylinder is fully inside the gust, thus reducing the noise in the measurements. Figure 5-11 shows the results for the individual test cases. It is observed that γ^{nc+r} matches extremely well to the theoretical distribution in all cases. Some small discrepancies are seen between $340° < \theta < 360°$. This corresponds to the bottom right hand side of the cylinder. Some of the shed vorticity just upstream of this location is missing, due to the described shadow region. The adverse effect on γ^{c}_{cyl} is strongest in close proximity to this region whilst it is only minute everywhere else. Hence, γ^{c}_{cyl} is not entirely correct between $340° < \theta < 360°$ which explains the observed discrepancies.

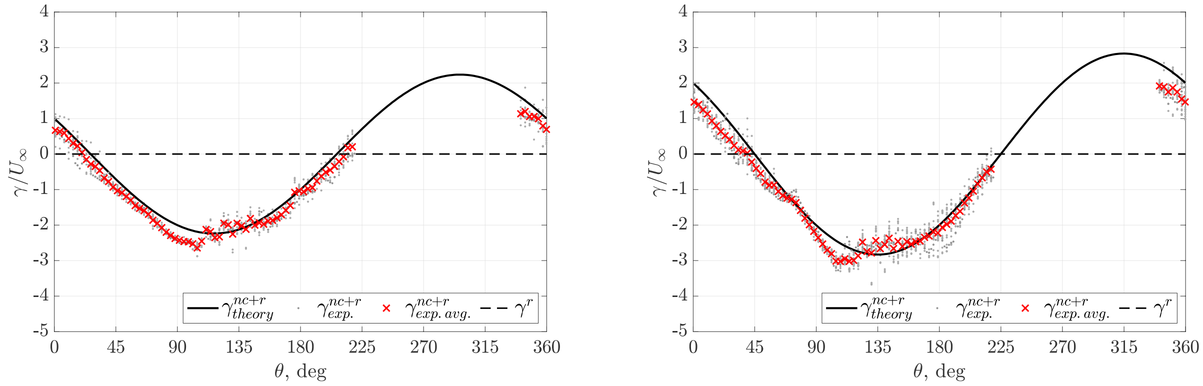

(a) Surge Only, $GR = 0.5$, Case 1.

(b) Surge Only, $GR = 1$, Case 2.

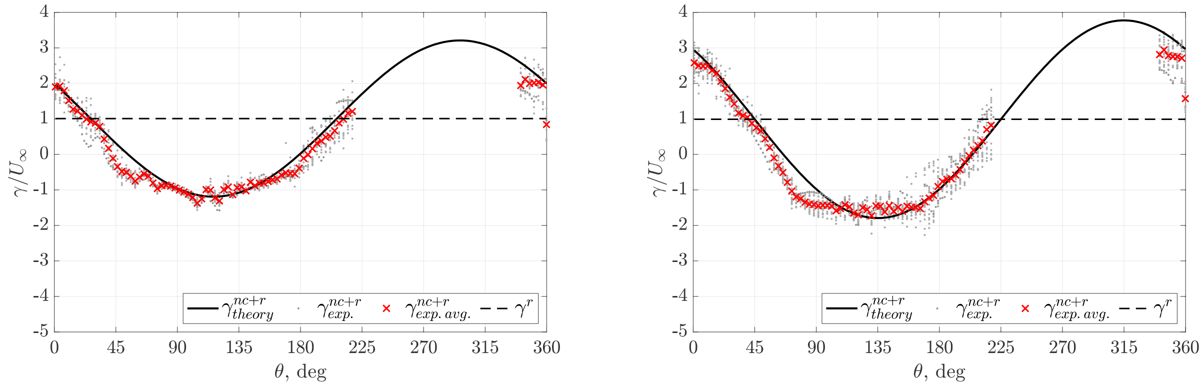

(c) Rotating CW, $\alpha = -1$, $GR = 0.5$, Case 3.

(d) Rotating CW, $\alpha = -1$, $GR = 1$, Case 3.

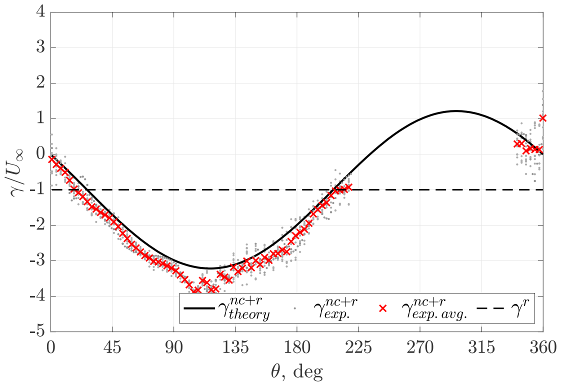

(e) Rotating CCW, $\alpha = 1$, $GR = 0.5$, Case 5.

Figure 5-11: $\gamma^{nc+r} = \gamma^{nc}_{am} + \gamma^{nc}_{ext.} + \gamma^{r}$.

As a ‘sanity check’, the vortex sheet due to the gust shear layers can also be calculated by directly using the respective vorticity distribution obtained from PIV measurements. Applying the same methodology that is used to compute γ_{cyl}^{c} to the gust shear layers should yield a distribution equivalent to $2V\cos\theta$. The field of view measured by PIV, however, does not extend to infinity. Consequently, the gust shear layers are terminated prematurely. The flow field is therefore, augmented by point vortices at the same x-location above and below the gust shear layers, effectively extending them to infinity. This is shown in Figure 5-12 for an arbitrary instance when the cylinder is inside the gust. Figure 5-12(b) shows the vorticity field after a mask is applied that removes any vorticity associated with the cylinder.

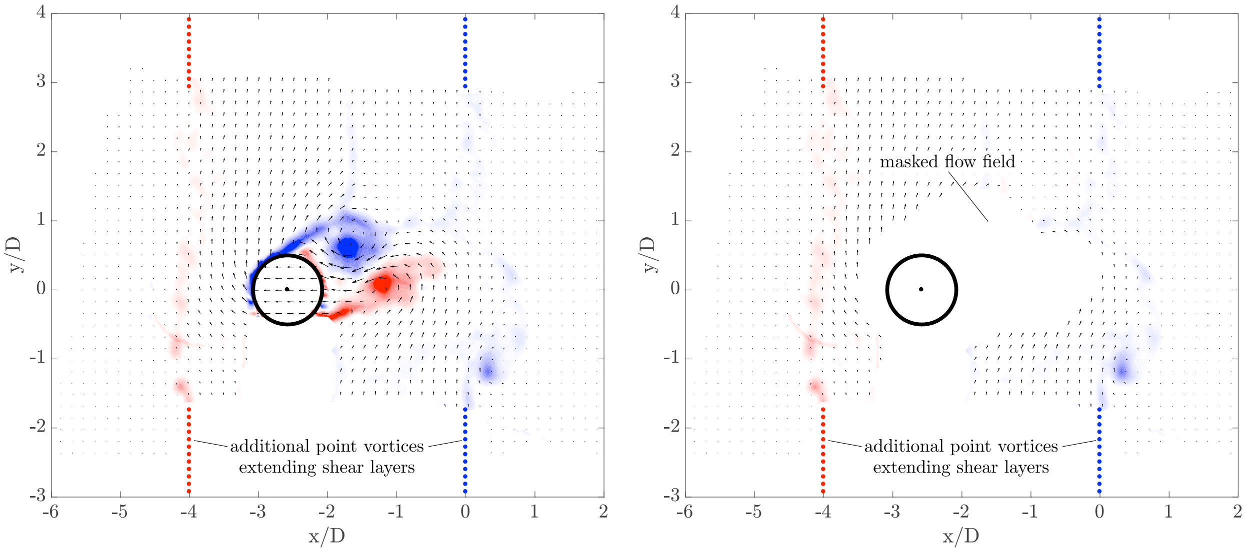

(a) Flow Field with Additional Shear Layers. **(b) Masked Vorticity Field Used to Calculate $\gamma_{ext.}^{nc}$.**

Figure 5-12: Extension of the Gust Shear Layers with Point Vortices. PIV vorticity contours are normalised by maximum vorticity.

A direct calculation of γ_(ext.)^nc, using only the PIV vorticity data, is shown in Figure 5-13. This excludes the additional point vortices and yields a distribution that is correct in shape but of the wrong magnitude. Incorporating the point vortices in the computation recovers the theoretical vortex sheet.

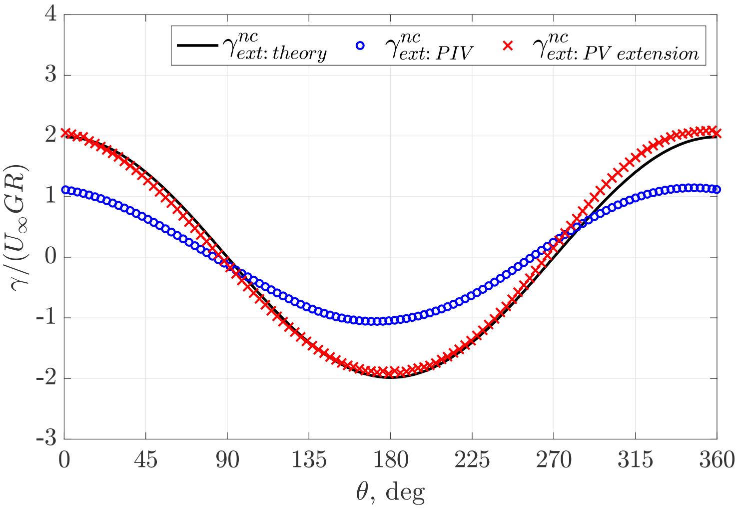

Figure 5-13: $\gamma_{ext.}^{nc}$ from Vorticity Field, Case 1.

Furthermore, if γ^{r} and γ^{nc}_{am} are removed from γ^{nc+r} for all kinematic cases, then only the non-circulatory contribution due to the gust, $\gamma^{nc}_{ext.}$ remains. As the gust is the same for all cases, albeit with a different gust ratio, $\gamma^{nc}_{ext.}$ should be identical when scaled with gust ratio. The result of this is shown in Figure 5-14. $\gamma^{nc}_{ext.}$ for all cases collapse on to the theoretical prediction. This shows that the theoretical vortex sheet due to gust vorticity not only persists in potential flow but has a tangible contribution to the real boundary layer vorticity and can be measured for any object. Thus, the validity of the presence of $\gamma^{nc}_{ext.}$ has been extended from a volumeless flat plate to bodies of finite thickness, which may also be undergoing rotary motion, in real viscous flows.

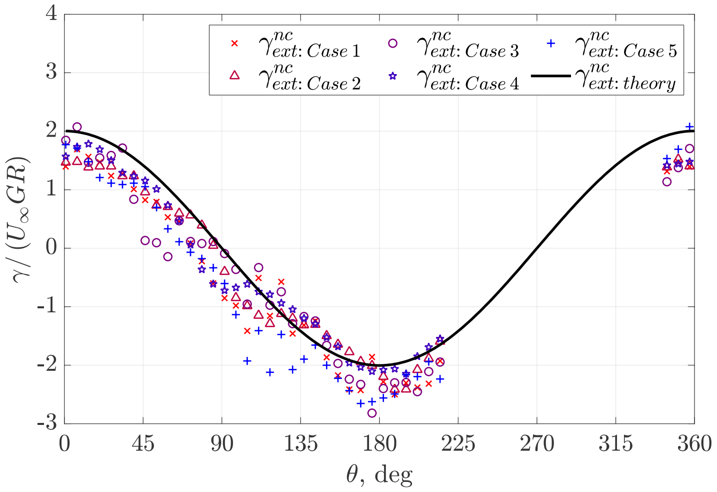

Figure 5-14: $\gamma^{nc}_{ext.}$ for All Cases.

5.4 FORCE RESULTS

The existence of $\gamma^{nc}_{ext.}$ suggests that there must necessarily be a force associated with any changes in vortex sheet distribution. Importantly, it was shown that this change does not only arise in an idealised potential flow setting. The absence of acceleration implies that the force is not related to an 'added mass effect'. Rather, $\gamma^{nc}_{ext.}$ evolves because of the relative motion between the body and the gust shear layers, leading to an observed force. This force can therefore be calculated from potential flow when rigid non-deforming shear layers are assumed. Figure 5-15 shows the force balance measurements for a surging, non-spinning cylinder entering a sharp edge gust, when $GR = 0.5$ and 1. The force due to the rate of change of $\gamma^{nc}_{ext.}$, accounting for the effect of cylinder volume is also indicated. Additionally, the force experienced by a thin flat plate at zero angle of attack entering the gust is added for completeness [17]. Upon entering the gust, C_l rises quickly for both the cylinder and the flat plate, where the maximum C_l of the plate exceeds that of the cylinder.

Two key aspects of the cylinder gust encounter are:

- A small positive force exists even before the cylinder enters the gust, 0 < s/D < 0.74. Prior to a von Karman shedding pattern developing, an 'attached' symmetric separation bubble, containing two opposing vortices, forms behind the cylinder. The symmetry of this results in a zero net lift force. Therefore, the growth and advection of cylinder shed vorticity cannot be the reason for the measured force whilst the cylinder is still outside the gust.
- Removing the force associated with the change in momentum of fluid internal to the cylinder from that obtained by evaluating the rate of change of $\gamma^{nc}_{ext.}$, improves the match between the theoretical and measured force response, when the cylinder has just entered the gust. For $GR = 0.5$, $C^{nc}_{l_{ext:\,cyl}}$

and the force balance measurements are observed to roughly match, however for $GR = 1$, $C_{l_{ext:\,cyl}}^{nc}$ still overestimates the experienced force.

The implication of the difference between $C_{l_{ext:\,cyl}}^{nc}$ and the measured force is that for bodies of finite thickness, computing the non-circulatory force term is difficult. Omitting the effect of the body volume can lead to vast over-predictions of the force. Whilst the force due to the rate of change of the gust vortex sheet can be found, the implicit assumption, that all the vertical momentum of fluid inside the cylinder is lost, is wrong. Neglecting momentum changes internal to the body, therefore analytically correcting for the 'lost momentum', improves but does not entirely rectify the result.

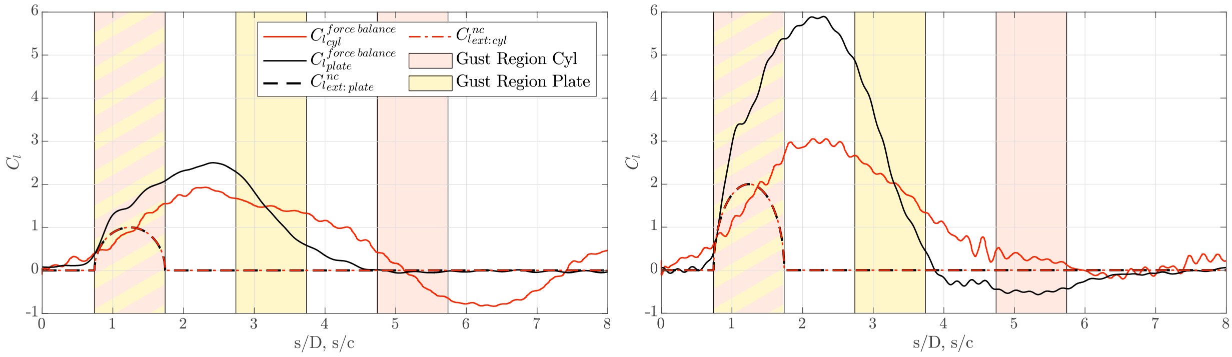

(a) $GR = 0.5$. **(b) $GR = 1$.**

Figure 5-15: C_l History for a Flat Plate and Cylinder Gust Encounter. The theoretical non-circulatory force when entering a rigid gust is also shown. The translation distance is normalised by the cylinder diameter or plate chord, respectively. The shaded fields indicate the regions when the plate and cylinder are entering and exiting the gust. The chord length of the plate is twice that of the cylinder diameter. The normalised distance for which the plate is inside the gust is therefore half that of the cylinder and the region where the plate and cylinder exit the gust appears offset in the figure. Flat plate data from Ref. [17].

Relaxing the assumption of a rigid shear layer and letting it deflect, has two effects. Firstly, the evolution of $\gamma_{ext.}^{nc}$ is changed, leading to a different force contribution. Secondly, because the shear layer deflects before the cylinder enters the gust, a non-zero force acts on the cylinder. This can explain the departure from $C_l = 0$ prior to gust entry.

A further consideration is that the gust shear layers in the experiment are of finite thickness. They diffuse and spread the further they move away from the gust rig outlet. The cylinder, therefore, enters the gust more gradually and begins to feel the effect earlier. This more benign entry into the gust can further explain the difference between $C_{l_{ext:\,cyl}}^{nc}$ and the force measured during experiments. However, the exact nature of the discrepancy remains somewhat obscure.

5.5 CONCLUSION

For a flat plate entering a sharp-edged gust an added mass term exists within the Küssner model. Von Karman and Sears [8] attribute this force to the rate of change of a non-circulatory vortex sheet. Corkery and Babinsky [11] showed that this vortex sheet forms because of the vorticity located in the gust shear layers. The evolution of it results in the added mass term in the Küssner model. However, because there is no acceleration, this force cannot be attributed to added mass in the conventional sense. Rather, the force originates from the evolution of the non-circulatory vortex sheet, which is linked to the vorticity in the gust shear layers.

This chapter investigates an extension of the non-circulatory force and the origin of the boundary layer vorticity for a body that, unlike an infinitely thin flat plate, has some attributed volume.

From a theoretical potential flow perspective, an equivalent theoretical non-circulatory vortex sheet on the cylinder surface can be calculated, assuming two rigid gust shear layers. The rate of change of the respective sheet, similar to the flat plate gust encounter, results in a force. However, unlike for the flat plate, the non-circulatory force for the cylinder does not match well to the initial rise in force experienced by the cylinder as it enters the gust. In fact, it vastly overestimates the force. This is because the change in momentum calculated assumes that all the vertical momentum inside the gust is lost once the cylinder occupies the space within the gust. This is a result of the rigid shear layer assumption. In the equivalent physical situation, the gust shear layers would deflect, causing a spread of vertical momentum. Excluding the change in momentum inside the cylinder leads to a closer match between the theoretical non-circulatory force and the measured rise in force but still fails to capture it to the same extent as was possible for the flat plate.

Recovering the non-circulatory vortex sheet due to the gust shear layer vorticity was successful for varying gust ratios and kinematic surge and cylinder rotation combinations. Thus, the physical existence and the ability to experimentally recover the respective non-circulatory vortex sheet is extended from a simple infinitely thin flat plate to any object of finite thickness.

Even though, the theoretical non-circulatory vortex sheet distribution exists, the fact that the non-circulatory force did not match that observed in experiments suggests that, for bodies of finite volume, the non-circulatory force cannot be easily found. Whilst the Küssner equivalent, the force due to the rate of change of the non-circulatory vortex sheet, is easily obtainable, quantifying the effect due to the volume of the body is not. An additional calculation, for example using a panel method code where the gust shear layers are allowed to deflect naturally, would be required. However, since low-order models used to help gust rejection, need to be solved in real time, this reduces some of the attractiveness of the non-circulatory force that previously existed for the infinitely thin flat plate, as additional time dependent calculations are required.

5.6 ACKNOWLEDGMENTS

The author would like to acknowledge the Engineering and Physical Science Research Council (EPSRC) for providing financial support.

5.7 REFERENCES

[1] Watkins, S., Milbank, J., Loxton, B.J., and Melbourne, W.H., Atmospheric winds and their implications for microair vehicles, AIAA Journal, Vol. 44, No. 11, 2006, pp. 2591-2600.

[2] Watkins, S., Thompson, M., Loxton, B., and Abdulrahim, M., On low altitude flight through the atmospheric boundary layer, International Journal of Micro Air Vehicles, Vol. 2, No. 2, 2010, pp. 55-68.

[3] White, C., Lim, E.W., Watkins, S., Mohamed, A., and Thompson, M., A feasibility study of micro air vehicles soaring tall buildings, Journal of Wind Engineering and Industrial Aerodynamics, Vol. 103, 2012, pp. 41-49.

[4] Stevens, P.R.R.J., and Babinsky, H., Experiments to investigate lift production mechanisms on pitching flat plates, Experiments in Fluids, Vol. 58, No. 1, 2017, pp. 1-17.

[5] Babinsky, H., and Stevens, P.R.R.J., Low order modelling of lift forces for unsteady pitching and surging wings. AIAA, 2016, pp. 1-12.

[6] Eldredge, J.D., and Jones, A.R., Leading-edge vortices: mechanics and modeling, Annual Review of Fluid Mechanics, Vol. 51, No. 1, 2019, pp. 75-104.

[7] Andreu-Angulo, I., and Babinsky, H., Negating gust effects by actively pitching a wing, 2020 AIAA Aerospace Sciences Meeting, 2020, pp. 1-15.

[8] Karman, T., and R., S.W., Airfoil theory for non – uniform motion, Journal of the Aeronautical Sciences,Vol.5,1938.

[9] Corkery, S.J., and Babinsky, H., Quantification of added mass using piv measurements for a translating and rotating flat plate, Journal of Fluid Mechanics, 2019.

[10] Gehlert, P., and Babinsky, H., Linking the unsteady force generation to vorticity for a translating and rotating cylinder, AIAA Scitech Proceedings, 2019, pp. 1-18.

[11] Corkery, S.J., and Babinsky, H., An investigation into the added mass force for a transverse wing-gust encounter, AIAA Scitech 2019 Forum, 2019, pp. 1-18.

[12] Saffman, P.G., Vortex Dynamics, Cambridge University Press,1992.

[13] Eldredge, J.D., A Reconciliation of viscous and inviscid approaches to computing locomotion of deforming bodies, Experimental Mechanics, Vol. 50, No. 9, 2010, pp. 1349-1353.

[14] Graham, W.R., Pitt Ford, C.W., and Babinsky, H., An impulse-based approach to estimating forces in unsteady flow, Journal of Fluid Mechanics, Vol. 815, 2017, pp. 60-76.

[15] Kelvin, L., On Vortex Motion, Trans .Roy. Soc .Edinb.,Vol.25,1869,pp. 217-260.

[16] Wu, J.C., Theory for aerodynamic force and moment in viscous flows, AIAA Journal, Vol. 19, No. 4, 1981, pp.432-441.

[17] Andreu-Angulo, I., Babinsky, H., Biler, H., Jones, A.R., and Girguis, S., Wing-gust interactions: The effect of transverse velocity profile, 2020 AIAA Aerospace Sciences Meeting, 2020, pp. 1-13.

[18] Westerweel, J., Fundamentals of digital particle image velocimetry, Meas. Sci. Technol, Vol. 8, 1997, pp. 1379-1392.

[19] Raffel, M., Willert, C.E., and Kompenhans, J., Particle Image Velocimetry, 3rd ed., Springer, 2018.

[20] Wieneke, B., PIV Uncertainty quantification from correlation statistics, Measurement Science and Technology, Vol. 26, No. 7, 2015.

[21] Adrian, R.J., and Westerweel, J., Particle Image Velocimetry, Cambridge University Press, 2011.

[22] Corkery, S.J., Babinsky, H., and Harvey, J.K., On the development and early observations from a towing tank-based transverse wing-gust encounter test rig, Experiments in Fluids, Vol. 59, No. 9, 2018, pp. 1-16.

CHAPTER 6 – PREDICTING UNSTEADY FLOW SEPARATION IN RESPONSE TO A FLOW DISTURBANCE

Karen Mulleners, Julien Deparday, Guosheng He, and Sabrina Henne
École polytechnique fédérale de Lausanne
SWITZERLAND

We present here a summary of the activities and results of dynamically stalling airfoils from the UNFoLD lab at EPFL that have been presented at the meetings of the NATO AVT-282 discussion group on *Unsteady aerodynamic response of rigid wings in gust encounters* during the past three years. The results are based on experimental data for a sinusoidally pitching OA209 airfoil in a wind tunnel at $Re = 9.2 \times 10^5$, a sinusoidally pitching NACA0015 airfoil profile with a trailing-edge flap in a wind tunnel at $Re = 5.5 \times 10^5$, and a sharp-edged flat plate undergoing a ramp-up motion in a recirculating water channel at $Re = 77\,500$. The first two data sets are used to study the onset of dynamic stall and the third one is used to analyse post-stall load fluctuations. Based on the experimental data, we derived a new model of the leading-edge suction parameter that accurately predicts the value and the timing of the maximum leading-edge suction and dynamic stall onset on a pitching airfoil. The model is based on thin airfoil theory and links the evolution of the leading-edge suction and the shear layer during stall development. By including an oscillating trailing-edge flap, the lift polars can be significantly altered but the dynamic stall time delay is only marginally affected by the kinematics of the flap. The maximum lift coefficient is strongly affected by both the main wing and the trailing-edge flap kinematics. For a flat plate without flap, the maximum lift coefficient and the subsequent post stall peak values increase with increasing pitch rate up to a critical pitch rate beyond which the entire lift response become independent of the pitch rate. The convective time delay to reach the primary lift peak decreases with increasing pitch rate up to the critical pitch rate and the time delay between subsequent peaks slightly decreases until the limit cycle oscillation period is reached.

6.1 INTRODUCTION

Unsteady flow separation or dynamic stall occurs on lifting profiles subjected to an unsteady increase in angle of attack beyond the static stall angle. The increase in angle of attack can be the result of a prescribed motion of the blades or due to the encounter of a flow disturbance or gust [1], [2], [3]. Among the characteristic features associated with dynamic stall are the delay of flow separation beyond the static stall angle and a lift overshoot. Although stall delay and lift overshoot sound beneficial, dynamic stall is generally a phenomenon that is to be avoided. Large excursions of the highly unsteady aerodynamic loads following stall onset decrease the aerodynamic efficiency and yield strong vibrations and increasing structural forces and bending moments that cause fatigue and potential damage to the airfoil and the structure supporting it [4], [5], [6]. To protect the integrity of the airfoil and the supporting structure and avoid loss of aerodynamic performance, it is essential to accurately predict the dynamic stall development, onset, and post stall behaviour.

In this contribution, we present results from our lab that are deemed of interest for the NATO AVT-282 discussion group on *Unsteady aerodynamic response of rigid wings in gust encounters*. Our contributions include results of water channel and wind tunnel experiments with airfoil profiles that are subjected to pitch angle variations leading to flow separation. All experiments combine velocity field measurements with airfoil surface pressure or force measurements. The water channel experiments are conducted with a sharp edges flat plate subjected to a linear ramp-up motion. The wind tunnel experiments are conducted with a two dimensional OA209 airfoil and a NACA0015 airfoil profile that is equipped with a trailing-edge flap. The trailing-edge flap is dynamically pitched to mimic the effect of a flow disturbance. In all cases, we analyse the time-resolved flow development in response to the disturbance and focus on the reaction time scales as a function of the characteristic parameters describing the disturbance.

6.2 EXPERIMENTAL SET-UPS AND METHODS

6.2.1 Sinusoidally Pitching OA209 Airfoil at Re = 9.2 x 10^5

This experimental data has been used for various in-depth analyses on the onset and development of dynamic stall [7], [8], [9], [10]. The experiments were conducted in a closed-circuit, low-speed wind tunnel of the German Aerospace Centre (DLR) in Göttingen. The wind tunnel had an open test section with a rectangular nozzle measuring 0.75 m × 1.05 m. The experiments included synchronized unsteady surface pressure and Time-Resolved Particle Image Velocimetry (TR-PIV) in the vertical plan and mid-span for a sinusoidally pitching OA209 airfoil. The model had a chord length of c = 0.3 m and was placed in a uniform flow of $U_\infty = 50$ m/s which correspond to a Reynolds number of Re = 9.2 × 10^5. The unsteady pressure distribution was determined using a series of 41 surface-mounted pressure transducers, which were sampled at a rate of 6 kHz and integrated to obtain the lift history. The TR-PIV data were evaluated using a multi-grid algorithm with a final interrogation window size of 32 px x 32 px and an overlap of approximately 80%. The velocity field was measured with a spatial resolution of 1.2 mm, or 0.004 c, at an acquisition rate of 1500 Hz. The airfoil was sinusoidally oscillated around its quarter-chord location. The mean incidence angle α_0, amplitude α_1, and oscillation frequency f_{osc} have been varied to obtain a wide range of dynamic stall cycles with reduced frequencies $k = \pi f_{osc} c/U_\infty$ varying between 0.05 to 0.1. To better describe the influence of the unsteadiness of a sinusoidal pitching motion on dynamic stall development, we have previously introduced the instantaneous effective unsteadiness $d\alpha_{ss}/dt\ c/U_\infty$, which is defined as the rate of change of the angle of attack at the moment when the static stall angle is exceeded, non-dimensionalised by the convective time.

6.2.2 Sinusoidally Pitching NACA0015 Airfoil with an Oscillating Trailing-Edge Flap at Re = 5.5 x 10^5

More recently, we obtained experimental data on a pitching NACA0015 airfoil with an oscillating trailing-edge flap. The trailing-edge flap is dynamically pitched to mimic the effect of a flow disturbance. The airfoil was mounted into the same closed-circuit, low-speed wind tunnel of the German Aerospace Centre that was used for the first data set. This time, the incoming free-stream velocity was at $U_\infty = 30$ m/s. The chord length was c = 0.3 m, leading to a Reynolds number based on the chord of Re = 5.5 x 10^5.

The airfoil was pitched around the quarter-chord axis and had a movable trailing-edge flap with the rotation axis at 0.72. The movement of the main airfoil and of the flap were actuated by servomotors and could be independently controlled. The main airfoil was pitched around the static stall angle of attack $\alpha_0 = 20°$ with an amplitude of $\alpha_1 = 8°$ and frequency of f_{osc}. The reduced frequency for the main airfoil ranges from 0.025 to 0.15. The flap was either defected at a fixed angle $\beta_0 \in \{-20°, -10°, 0°, 10°, 20°\}$ or oscillated around the symmetrical plane at $\beta_0 = 0°$ with an amplitude of $\beta_1 = 20°$. A phase shift φ between the sinusoidal oscillation of the main airfoil and the flap was varied. The variation of the phase shift was deemed to influence the leading-edge stagnation point while keeping the geometric leading-edge motion constant. The objective of these measurements was to characterize the role and the interplay between the leading-edge suction and the leading-edge stagnation point during dynamic stall.

The airfoil surface pressure distribution was measured using 36 pressure transducers integrated in the model mid-span cross section. Lift and pitching moment histories were obtained by integration of the pressure distribution around the airfoil. The sampling rate for the pressure measurement was 20 kHz.

Two dimensional TR-PIV was used to measure the flow field in the vertical plane at the model mid-span. The flow field was illuminated by a dual-pulsed laser and the particle images were recorded by two PCO DIMAX HS cameras with 1800 px × 1600 px sensors. The first camera was zoomed in near the leading edge and the second camera had a larger field of view covering the rest of the airfoil. The sampling rate for the PIV was 1.5 kHz. A multi-grid algorithm used to obtain the velocity vectors with a final window size of 48 px × 48 px and 50% overlap.

6.2.3 Sharp-Edged Flat Plate Undergoing a Ramp-Up Motion at Re = 77 500

To focus on the load fluctuation and following dynamic stall onset, we conducted these experiments in the SHARX recirculating water channel at EPFL. The facility has a 0.6 m × 0.6 m × 3.0 m test section and can reach a free-stream velocity $U_\infty = 1$ m/s. A sharp-edged flat plate of chord length c = 0.15 m and span s = 0.6 m (aspect ratio AR = s/c = 4) was placed at the centre of the test section. The plate was made from plexiglass and was suspended vertically in the channel, with a minimal gap between the tip and the lower wall of the channel in order to minimise tip effects. The upper tip extended above the free surface to serve as the mounting point for the flat plate airfoil.

The airfoil was actuated to undergo a ramp motion, moving from an angle of attack a = 0° to a = 30° at a constant pitch rate. The dimensionless pitch rate was varied from 0.75 to 7.5. The chord Reynolds number was 77 500. Time-resolved PIV was used to measure the velocity field around and behind the airfoil. Two high-speed cameras with 1024 px × 1024 px sensors (Photron, ILA 5150 GmbH), were placed side by side to cover a region of interest including the airfoil and the wake. A double cavity diode pumped Nd:YLF laser (527 nm) with a maximum pulse energy of 30 mJ was used to create the laser sheet. The light sheet was oriented horizontally at a distance of 0.2 m from the bottom of the water channel to reduce the influence of the free surface. For every ramp-up motion, we recorder 10 000 images an acquisition rate of 500 Hz yielding a total measurement time of 20 s. The measurement series covers the initial ramp-up motion and the transient decay of the flow to a quasi-steady state. The images were processed for both cameras separately according to standard procedures, with the multi-grid algorithm with image deformation, a final window size of 64 px × 64 px, and an overlap of 50%.

A NEMA17 stepper motor geared at a ratio of 1:25 rotated the plate about its quarter-chord position. The shaft was connected directly to a 6-component ATI load cell, which served as the interface between the motor and the airfoil to enable direct measurement of hydrodynamic forces. The load data was recorded with a sampling frequency of 1 kHz, a sensing range of 125 N, and a resolution of 0.02 N.

6.3 RESULTS AND DISCUSSION

6.3.1 Sinusoidally Pitching OA209 Airfoil at Re = 9.2 x 10^5

The typical response of the flow to a sinusoidal pitching measured by simultaneous unsteady surface pressure and time-resolved velocity field measurements is presented in Figure 6-1. The flow initially remains attached during the pitch-up motion even when the angle of attack is larger than the static stall angle. The resulting lift coefficient is larger than for a steady case. Figure 6-1 presents the time evolution of the lift coefficient during one oscillating period T, as well as according to the associated angle of attack a and the convective time t^*. The static stall angle is reached at t_{ss}. When the static stall is exceeded, the lift keeps increasing but at a lower rate than before t_{ss}. During this period, the flow is attached at the leading edge and starts to detach near the trailing edge (Figure 6-1(a) and (b)). This is the first stage of the dynamic stall development (light shading in Figure 6-1) as defined in Refs. [8] and [10]. Later during the pitch-up motion, counter clockwise vorticity appears between the shear layer and the suction side of the wing. The shear layer starts to roll up into a large scale dynamic stall vortex (Figure 6-1(c)). The lift coefficient is decreasing even though the angle of attack continues to be increased. The stage that is dominated by the formation of the dynamic stall vortex (dark shading in Figure 6-1) ends when the dynamic stall vortex detaches from the airfoil (Figure 6-1(d)) and is shed downstream. After these two stages describing the dynamic stall development, the flow is completely detached and the wing experiences a significant decrease of the lift coefficient with large variations of loads during the end of the pitch-up motion and during the pitch-down motion until the flow reattaches (Figure 6-1(f)).

The lift overshoot before the unsteady detached phase is a typical response of a pitching motion, which is described by the two-stage dynamic stall development. The duration of the first stage decreases linearly with the unsteadiness of the pitching motion, which can be quantified by the normalised effective unsteadiness.

The duration of the second stage, about four times shorter than the first stage, is independent of the normalised effective unsteadiness. The two-stage dynamic stall development was independently confirmed by global velocity field and local surface pressure measurements around the leading edge.

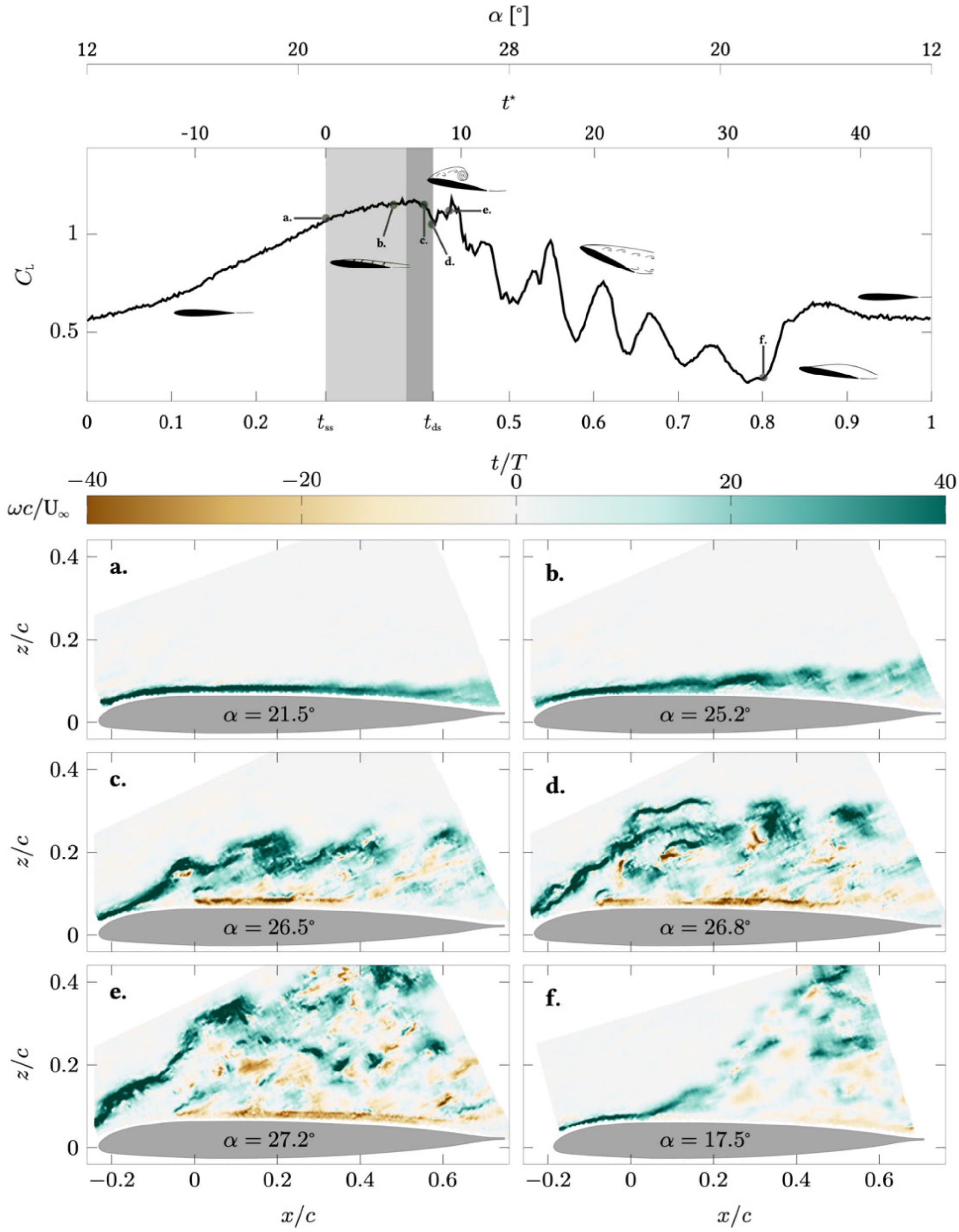

Figure 6-1: Temporal Evolution of the Lift Coefficient During a Single Pitching Cycle Described by α0 = 20°, α1 = 8°, k = 0.05. The labels a. to f. in the lift history indicate the timing of the velocity and vorticity field snapshots. The shaded regions refer to the stall development stages between the time when the static stall angle of attack is exceeded t_{ss} and the dynamic stall onset is reached.

The leading-edge pressure signals for the sinusoidally pitching airfoil at Re = 9.2×10^5 were combined into a single leading-edge suction parameter and we recently developed an improved model of the leading-edge suction parameter based on thin airfoil theory. Thin airfoil theory determines the aerodynamic force on an airfoil as the result of the potential pressure field induced by a vortex sheet [11]. The circulation distribution for a generalized camber line can be described as a Fourier series. The first Fourier coefficient A_0 represents the leading-edge suction peak resulting from the acceleration of the flow around the airfoil's leading edge and is called the leading-edge suction parameter [12], [13]. The leading-edge suction parameter can also be determined experimentally from the pressure at the leading edge. We have recently proposed an improved model of this leading-edge suction parameter based on thin airfoil theory and linking the evolution of the leading-edge suction and the shear layer growth during stall development [10]. The influence of the growth of the shear layer during dynamic stall development on the flow around the airfoil is described in terms of an increase of the effective camber and a decrease of the effective angle of attack of the airfoil. The effective angle of attack is defined as:

$$\alpha_{eff} = \alpha - \tan \Delta z^{*} \tag{6-1}$$

with Δz^* the experimentally determined dimensionless chord-wise average of the shear layer height. The effective camber of the virtually altered airfoil profile due to the presence of the shear layer is expressed as:

$$K_{\eta,eff} = K_{\eta} + \Delta z^{*} \tag{6-2}$$

with K_η the original geometric camber line. By considering this twofold influence of the shear layer development, our new model of the leading-edge suction parameter reads:

$$A_{0,theor'} = \sin \alpha_{eff} + \dot{\alpha}\frac{c}{4U_{\infty}} - K_{\eta} \cos \alpha_{eff} - \Delta z^{*} \cos \alpha_{eff} \tag{6-3}$$

This modified model accurately predicts the value and the timing of the maximum leading-edge suction on the pitching airfoil (Figure 6-2).

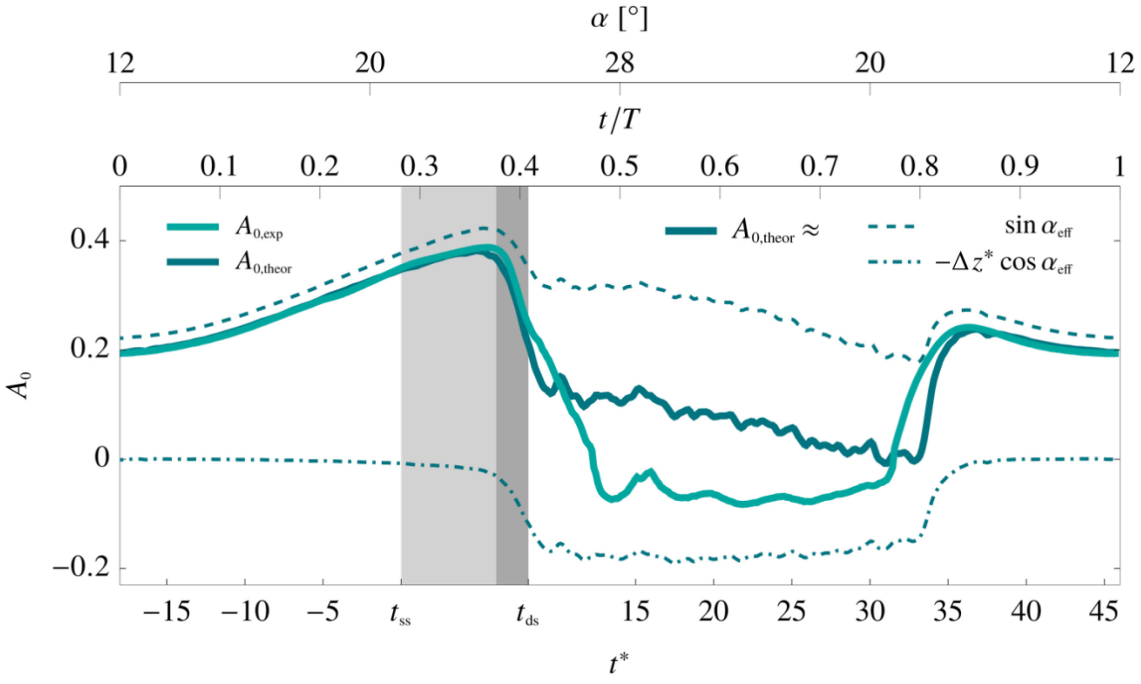

Figure 6-2: Examples of Transverse Gusts Produced by Members of AVT-282.

6.3.2 Sinusoidally Pitching NACA0015 Airfoil with an Oscillating Trailing-Edge Flap at Re = 5.5 x 10^5

The typical response of the flow to the sinusoidal pitching of the NACA0015 with the trailing-edge flap fixed at $\beta_0 = \beta_1 = 0°$ is similar to the response described in the previous section. The lift polar for the fixed, non-deviated flap presented in the left panel of Figure 6-3 has the same characteristic features as the lift polar for the thinner, non-symmetric OA209 presented in the previous section. The lift coefficient increases linearly during most of the pitch-up part of the cycle beyond the static stall angle of $\alpha_{ss} = 20°$. Stall is delayed to a higher angle of attack and there is a significant lift overshoot with respect to the maximum statically attainable lift coefficient. The maximum lift coefficient is reached around $\alpha = 24°$. After reaching the global lift maximum, the shear layer starts to roll up and the lift coefficient drops until the first stall vortex is shed and the lift increases again before reaching the maximum angle of attack. During the pitch-down part of the cycle, the lift drops rapidly and strong fluctuations are observed that can be directly linked to the formation and shedding of subsequent large scale vortices.

The corresponding evolution of the stream-wise position of the leading-edge stagnation point during the selected pitching cycle is presented in the right panel of Figure 6-3. The stagnation point is located on the pressure surface of the airfoil during the entire pitching cycle and its stream-wise position was directly extracted from the velocity field measurements in the leading-edge region. More specifically, it was identified as the extrapolated intersection of the ridge in the positive time FTLE that indicates the leading-edge stagnation line with the airfoil surface. This is indicated in Figure 6-4 where we show an instantaneous snapshot of the velocity field obtained from the camera with the leading-edge field of view. In addition to the velocity vectors, the scalar positive time FTLE is colour coded.

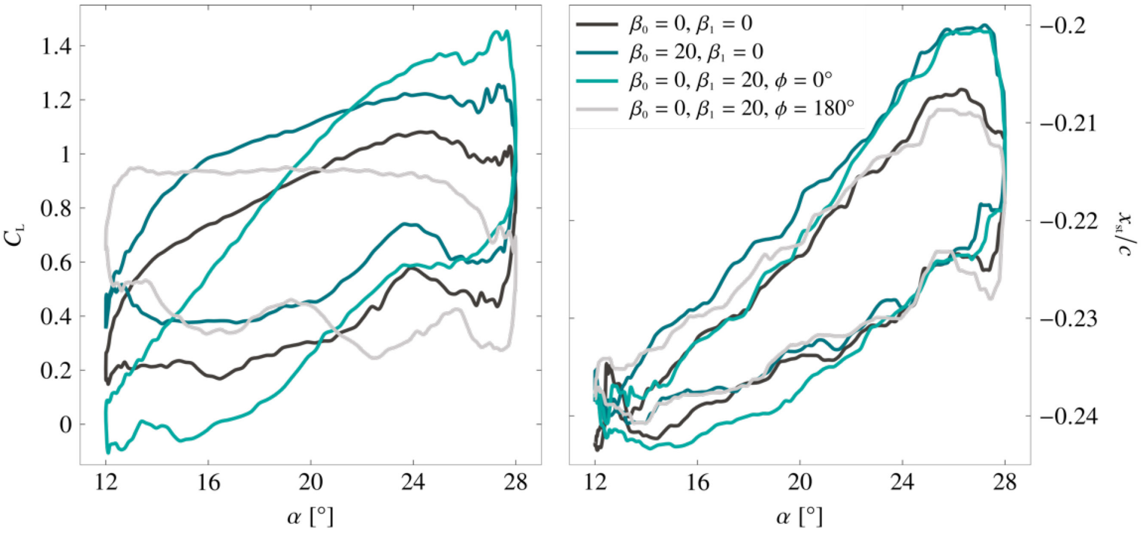

Figure 6-3: Lift Coefficient and Stagnation Point as a Function of Angle of Attack of the Main Airfoil During a Single Pitching Cycle for the Various Configurations of the Trailing-Edge Flap where β_0 Refers to the Mean flap Angle with Respect to the Chord Length,β_1 Refers to the Flap Amplitude, and φ Refers to the Phase Difference Between the Sinusoidal Pitching of the Main Airfoil and the Flap.

With increasing angle of attack, the stagnation point moves downstream, i.e., towards the trailing edge, until it reaches a maximum values for $\alpha \approx 24°$, when the lift reaches its maximum value as well. Thereafter, the stagnation point gradually moves back to its initial most upstream location at which it was at the start of the pitch-up (Figure 6-3, right). By deviating the trailing flap to a fixed angle $\beta_0 = 20°$, the entire lift polar is shifted up by a constant amount of $\Delta C_L \approx 0.15$ (Figure 6-3, left). When the flow is attached, this is exactly what we would expect as the fixed flap deviation increases the effective camber of the airfoil. During this attached flow portion of the cycle, the leading-edge stagnation point is also shifted downstream on the pressure surface by a nearly constant amount with respect to the stagnation point location for the oscillation with a fixed, non-deviated flap (Figure 6-3, right). After dynamic stall onset, the stagnation point moves back upstream and follows the same position evolution as it does for the non-deviated flap configuration. Once the flow fully stalls the stagnation point location is no longer influenced by the deviation of the flap, but the lift coefficient remains larger than the for the non-deviated flap configuration by approximately the same amount as during the attached flow stage (Figure 6-3, left).

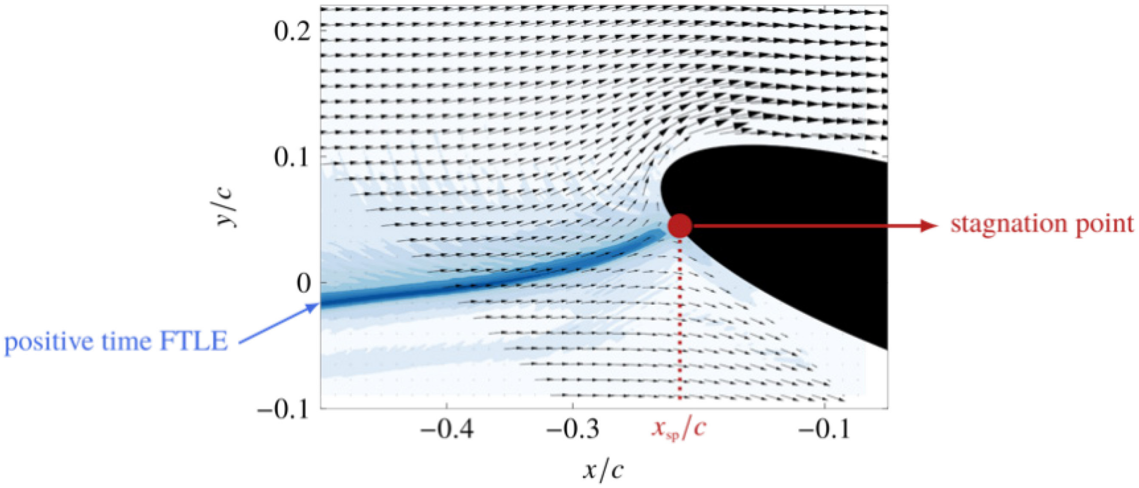

Figure 6-4: Instantaneous Snapshot of the Velocity Field in the Leading-Edge Region of the Airfoil. In addition to the velocity vectors, the positive time FTLE is colour coded to indicate the leading-edge stagnation line.

When the flap is oscillated in phase with the main airfoil ($\varphi = 0°$), the dynamic stall lift polar curve seems to be rotated (Figure 6-3, left). It reaches an even larger maximum lift than for the configuration with the flap fixed at $\beta_0 = 20°$ even though their instantaneous geometry at maximum angle of attack is the same. This indicates that the instantaneous effective geometrical angle of attack is not sufficient to predict the lift coefficient and the time history of the flap kinematics need to be considered. The stagnation point location on the other hand seems to be mainly influenced by the effective geometric angle of attack during the attached flow stage (Figure 6-3, right).

When the flap is oscillated out of phase with the main airfoil ($\varphi = 180°$), the dynamic stall lift polar curve seems to be further rotated (Figure 6-3, left) such that the lift coefficient during most of the pitch-up motion is approximately constant. The timing at which the lift drops due to massive flow separation does not seem to be affected when compared with the other configurations.

The variations in stall delay for various pitching kinematics of the trailing-edge flap and various reduced frequencies of the main airfoil oscillations are summarised in Figure 6-5. The stall delay was calculated here as the convective time delay between the point at which the static stall angle of attack was exceeded and the occurrence of the first local minimum after the maximum lift coefficient. We have shown in the previous section, that the fist local minimum corresponds to the shedding of the primary dynamic stall vortex and stall onset. The stall delay is plotted as a function of the instantaneous effective unsteadiness which describes well the influence of the unsteadiness of a sinusoidal pitching motion on dynamic stall development. In accordance with previous results [7] the dynamic stall delay decreases with increasing unsteadiness and the trailing-edge flap kinematics seem to have very little effect on the stall delay.

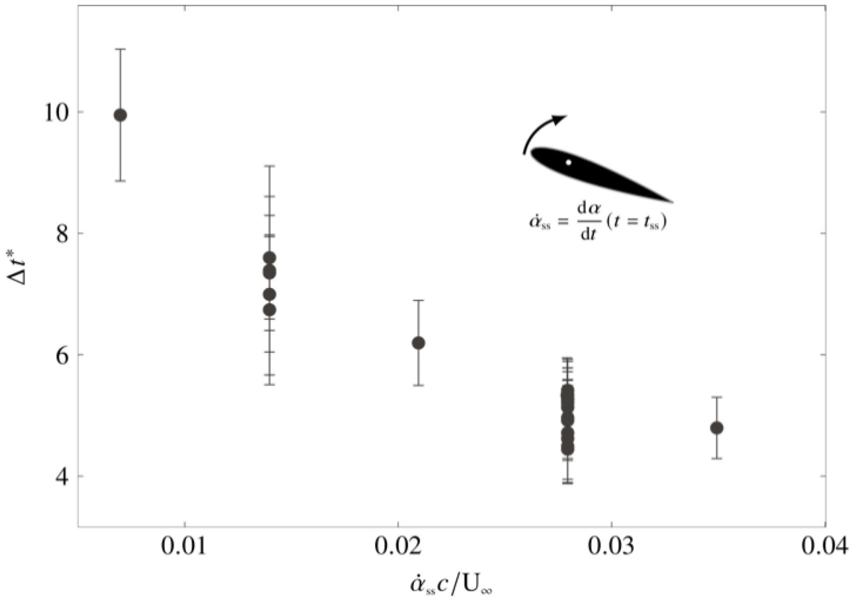

Figure 6-5: Dynamic Stall Delay for Various Combinations of Trailing-Edge Flap Pitching Kinematics for Sinusoidal Oscillations of the Main Wing Around α0 = 20° with an Amplitude α1=8° for Various Reduced Frequencies. The stall delay is plotted as a function of the instantaneous effective unsteadiness.

6.3.3 Sharp-Edged Flat Plate Undergoing a Ramp-Up Motion at Re = 77 500

A flat plate subjected to quick ramp-up motion from $\alpha = 0°$ up to $a = 30°$ at a Reynolds number Re = 77500 with varying pitch rates was investigated to analyse in more detail the post stall load fluctuations. The lift responses for various motions with different dimensionless pitch rates are presented in Figure 6-6. In general, the lift increases more or less linearly over time until it reaches a maximum value which is higher than the lift coefficient associated with a static flat plate at $\alpha = 30°$. After reaching the maximum value, the lift coefficients oscillate around a slowly decreasing value that converges towards the steady state value. For the range of experiments conducted, we observe up to three clearly distinguishable lift peaks that are directly linked to the growth and separation of three successive leading-edge vortices. For $\dot{\alpha}c/U_\infty > 4$ the lift curves exhibit an additional peak before the actual global maximum is reached, which is due to the added mass effect.

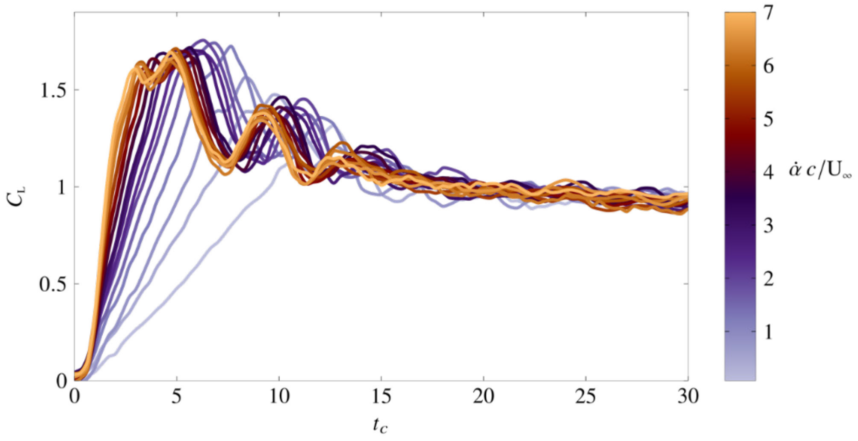

Figure 6-6: Temporal Evolution of the Lift Coefficient Over Convective Time for Dimensionless Pitch Rates Ranging from 0.75 to 7.5.

The initially increasing slope of the lift coefficients becomes steeper with increasing pitch rate and the various load oscillations become more pronounced. The higher the pitch rate $\dot{\alpha}c/U_\infty$, the closer the lift curves become and they completely overlap for the highest investigated dimensionless pitch rates. The magnitude of the three local lift maxima initially increases with dimensionless pitch rate and they all reach constant critical values for $\dot{\alpha}c/U_\infty > 3$ (Figure 6-7). The convective time between the start of the motion and the time at which the first maximum is reached decreases initially with dimensionless pitch rate until it reaches an approximately constant value of 5 for $\dot{\alpha}c/U_\infty > 3$ (Figure 6-8). For higher pitch rates, higher levels of vorticity are generated. This leads to stronger vortices that separate earlier than at low pitch rates.

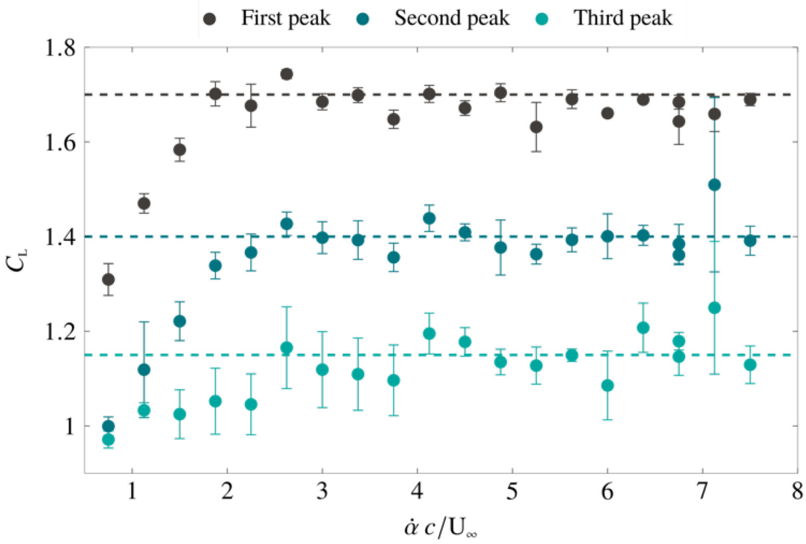

Figure 6-7: Magnitude of Local Lift Coefficient Maxima Versus the Dimensionless Pitch Rate.

The timing between the first and the second and the second and the third maxima are constant and independent of the pitch rate for all dimensionless pitch rates. The convective time delay between the start of the motion and the first peak is ≈ 5 for high pitch rates, the convective time delay between the first and the second peak is ≈ 4.5 and it decreases further to ≈ 4 between the second and the third peak. This means that the vortex shedding frequency or Strouhal number slight increases for the subsequent shedding cycles until reaching the limit cycle oscillation value.

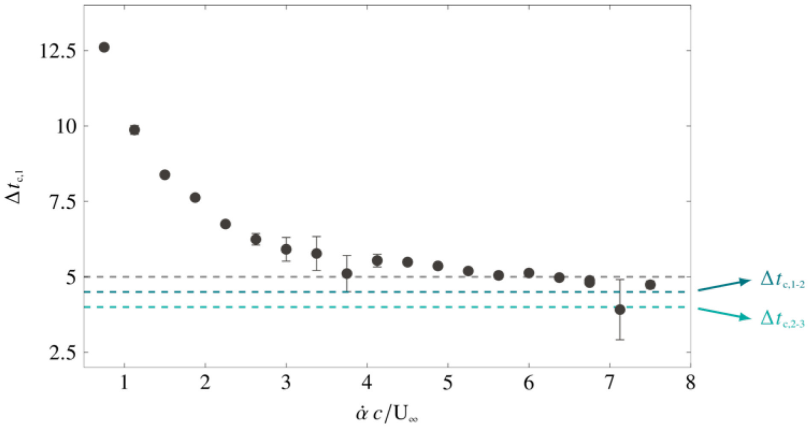

Figure 6-8: Convective Time Between the Start of the Motion and the First Lift Maximum versus the Dimensionless Pitch Rate.

6.4 CONCLUSION

In this chapter, we presented recent activities and results of dynamically stalling airfoils that have been presented at the meetings of the NATO AVT-282 discussion group on *Unsteady aerodynamic response of rigid wings in gust encounters* during the past three years. The three experimental data sets presented include time-resolved PIV and airfoil surface pressure measurements for a sinusoidally pitching OA209 airfoil at $Re = 9.2 \times 10^5$ and for a sinusoidally pitching NACA0015 airfoil profile with an oscillating trailing-edge flap at $Re = 5.5 \times 10^5$ and time-resolved PIV and global load measurements for a sharp-edged flat plate undergoing a ramp-up motion in a recirculating water channel at Re = 77 500. Based on the first experimental data, we proposed an improved model of the leading-edge suction parameter has been described in more detail in a recent paper by Deparday and Mulleners [10]. The model is based on thin airfoil theory and links the evolution of the leading-edge suction and the shear layer during stall development. By taking into account the influence of the shear layer development in terms of a change in the effective angle of attack and effective camber, the new model of the leading-edge suction parameter accurately predicts the value and the timing of the maximum leading-edge suction on the pitching airfoil.

To further explore the potential of the leading-edge suction parameter for identifying and predicting stall onset, we conducted new dynamic stall experiments with a NACA0015 equipped with an oscillating trailing-edge flap. By varying the phase delay between the oscillation of the main airfoil and the oscillation of the flap, we were able to influence the stagnation point independent of the velocity of the airfoil's leading edge. By doing so, we can study the role and interaction of the leading-edge suction and the leading-edge stagnation point. Preliminary results from this data set indicate that the stall delay is only marginally influenced by the flap deflection and motion but the lift polars and the evolution of the leading-edge stagnation point are highly influence by the flap kinematics. The stagnation point location is mainly influenced by the instantaneous deflection of the flap. The lift response is not only affected by the instantaneous flap deflection but also by the time history of the flap motion.

With the third experiment, we focus our attention to the load fluctuations that follow dynamic stall onset. For a flat plate that is subjected to a linear ramp-up motion, the lift increases linearly until it reached its maximum value which is well above the static stall limit of the flat plate. Additional lift peaks are observed following full stall. These lift peaks subsequently decrease in magnitude and the timing between them is independent of the pitch rate of the initial motion. The magnitude of the lift maximum and the subsequent post stall peak values increase with increasing pitch rate up to a critical pitch rate beyond which the entire lift response become independent of the pitch rate. The convective time delay to reach the primary lift peak decreases with increasing pitch rate up to the critical pitch rate and the time delay between subsequent peaks slightly decreases until the limit cycle oscillation period is reached.

6.5 REFERENCES

[1] McCroskey, W.J., and Fisher, R.K., Dynamic stall of airfoils and helicopter rotors, Tech. Rep. AGARD, 1972.

[2] Laneville, A., and Vittecoq, P., Dynamic stall: The case of the vertical axis wind turbine, Journal of Solar Energy Engineering, Vol. 108, No. 2, 1986, pp. 140-145.

[3] Perrotta, G., and Jones, A.R., Unsteady forcing on a flat-plate wing in large transverse gusts, Experiments in Fluids, Vol. 58, No. 8, 2017, p. 101.

[4] Shih, C., Lourenco, L., Van Dommelen, L., and Krothapalli, A., Unsteady flow past an airfoil pitching at a constant rate, AIAA Journal, Vol. 30, No. 5, 1992, pp. 1153-1161.

[5] Spentzos, A., Barakos, G.N., Badcock, K., Richards, B., Wernert, P., Schreck, S.J., and Raffel, M., Investigation of three-dimensional dynamic stall using computational fluid dynamics, AIAA Journal, Vol. 43, No. 5, 2005, pp. 1023-1033.

[6] Morris, W.J., and Rusak, Z., Stall onset on aerofoils at low to moderately high Reynolds number flows, Journal of Fluid Mechanics, Vol. 733, 2013, pp. 439-472.

[7] Mulleners, K., and Raffel, M., The onset of dynamic stall revisited, Experiments in Fluids, Vol. 52, No. 3, 2012, pp. 779-793. doi:10.1007/s00348-011-1118-y.

[8] Mulleners, K., and Raffel, M., Dynamic stall development, Experiments in Fluids, Vol. 54, No. 2, 2013, pp. 1469-1477.

[9] Ansell, P., and Mulleners, K., Multi-scale vortex characteristics of dynamic stall from empirical mode decomposition, AIAA Journal, 2019, pp. 1-18.

[10] Deparday, J., and Mulleners, K., Modeling the interplay between the shear layer and leading edge suction during dynamic stall, Physics of Fluids, Vol. 31, No. 10, 2019, p. 107104. doi:10.1063/1.5121312.

[11] Katz, J., and Plotkin, A., Low-Speed Aerodynamics, 2nd ed., Cambridge Aerospace Series, Cambridge University Press, 2004.

[12] Ramesh, K., Gopalarathnam, A., Granlund, K., Ol, M.V., and Edwards, J.R., Discrete-vortex method with novel shedding criterion for unsteady aerofoil flows with intermittent leading-edge vortex shedding, Journal of Fluid Mechanics, Vol. 751, 2014, pp. 500-538. doi:10.1017/jfm.2014.297.

[13] Ramesh, K., Granlund, K., Ol, M.V., Gopalarathnam, A., and Edwards, J.R., Leading-edge flow criticality as a governing factor in leading-edge vortex initiation in unsteady airfoil flows, Theoretical and Computational Fluid Dynamics, Vol. 32, No. 2, 2018, pp. 109-136.

CHAPTER 7 – DISCRETE AND CONTINUOUS VORTEX-GUST ENCOUNTERS

Albert Medina
Air Force Research Laboratory
UNITED STATES

Berk Zaloglu, Murat Saritas, and Oksan Cetiner
Istanbul Technical University
TURKEY

Arif Cem Gozukara
Aselsan Inc.
TURKEY

The field of unsteady aerodynamics is concerned with the quantification of rapid changes in bound circulation, apparent-mass effects, separation, instabilities, and shedding characteristics of lifting bodies and the identification of simplified models encompassing the linear and nonlinear responses of such processes. Resulting flow fields are recognized by the ubiquity of their vortex-laden domain. In a stark departure from quasi-steady aerodynamics, which omits consideration for the effects of the wake on the airfoil, the load transients central to unsteady investigations arise through complex interactions between the lifting body and the vortical dynamics of on-board and near-wake formations. Recent work in this field has disseminated the respective contributions to transient loading in kinematic-driven canonical problems where the lifting body is engaged in high-rate maneuvers often achieving effective angles of attack in excess of the stall angle. A corollary to these efforts is the study of load transients induced by unsteadiness of the environment in otherwise benign operations of the lifting body.

The unsteady environment is cause for disturbance to flight conditions, disturbances termed gusts. Here the term ‘gust’ is reserved for brief excursions in velocity from a fully developed flow typically endured over a finite number of convective times.

Gust exposures can lead to structural failure when unexpected loading exceeds design metrics. This has ushered in a number of works seeking to mitigate, negate, or exploit gust effects. Among the mitigation strategies, and perhaps the most explicit, is the application of kinematic-based analogs to those gusts to render the disturbance minimal. Often this approach requires advanced knowledge of the gust’s composition to enact the appropriate maneuvers. However, for a subset of flapping kinematics there appears to be an inherent ability to reduce random gust effects. Such was the case investigated by Fisher et al. [1] where high frequency flapping across a range of replicated atmospheric turbulence intensity saw significant reductions in the random fluctuating component of lift. Medina et al. [2] explored the use of mechanical flap actuation as a mitigation strategy for kinematic-driven vertical gust. Results demonstrated an 87% cancellation in gust-induced lift via flap actuation, verifying the limited, but substantially applicability of Theodorsen’s model. The exploitation of a disturbance or gust is perhaps best demonstrated in wake-capture configurations such as that investigated by Dabiri et al. [3] in which vertical axis wind turbines achieved greater power output per unit land area when distributed in counterrotating arrays.

Underlying these gust alleviation efforts is the need to develop a fundamental understanding of the mechanics governing unsteady interactions. To this end, encounters with vortical gusts, be they an isolated vortex or periodic formation, offer superb candidacy as sources of spatiotemporal disturbance. Computational work by Barnes and Visbal [4] examined the effects of periodic impingement of a wing-parallel vortex. The resulting complexities included the formation of a leading-edge vortex stemming from vortex interactions with the laminar separation bubble, highlighting the potential for gusts to promote significant load transients. The theme of the current study continues with vortical gusts. In this study the aerodynamic response of a NACA 0012 subjected to vortex impingement is investigated. The vortices are oriented wing-parallel and are issued upstream of the wing as singular and periodic disturbances.

7.1 EXPERIMENTAL SETUP

7.1.1 Experiments at the US Air Force Research Laboratory

Experiments at the US Air Force Research Laboratory were performed in the Horizontal Free-surface Water Tunnel. The tunnel has a 4:1 contraction and a 46cm wide by 61cm high test section with a free-surface, a speed range of 3 – 105 cm/s, and a u-component turbulence intensity of 0.4% at 5 – 40 cm/s. The tunnel is fitted with a tree degree of freedom motion rig, consisting of a triplet of H2W linear motors, driven by AMC DigiFlex servo-drives controlled by a Galil DMC 4040 4-channel card, with user-selected Proportional/Integral/Derivative (PID) constants for each channel. This allows for the pitching, plunging, and surging of test articles.

In this study a wing is positioned downstream of a cylindrical bluff body such that the vortical wake of the body acts to perturb the aerodynamics of the wing, as illustrated in Figure 7-1. Results are presented for two airfoils representing both nominal two-dimensional flows and three-dimensional flow fields. Firstly, a symmetric SD7003 airfoil measuring c = 10.16 cm in chord length is considered, made symmetric by shift of the airfoil profile to a zero-camber configuration. The wing spans the width of the test section to provide a nominally two-dimensional flow. Secondly, a NACA0012 wing of c = 10.16 cm and 35.56 cm span is cantilevered off a tunnel wall (Figure 7-1). This configuration preserves one chord length distance from the wing tip to the proximal tunnel wall resulting in a three-dimensional flow field. The wing was comprised of 3D printed plastic (VeroWhite) with spanwise carbon-fiber rod reinforcement. The upstream cylinder measures d = 2.54 cm in diameter and spans the width of the tunnel test section to satisfy an aspect ratio of L/d = 18. The longitudinal axis of the cylinder is oriented normal to the tunnel walls, parallel to the wing ledge edge. In this manner the cylinder generates a harmonic disturbance for the downstream airfoil in the form of a von Kármán street with a gust ratio of $GR = 0.4$ and a gust width of $W_e = 0.5$. Note these gust metrics are quantified exclusively on fluctuations of the vertical component of velocity induced by the vortex street, as measured at the centerline of the cylinder at the downstream position of $x/d = [8, 10]$. The resulting street vortices are comparable in size to leading-edge vortices formed about the wing in dynamic stall. The cylinder was supported at the tunnel walls via low-profile vertical plate inserts. Further, a timing belt was integrated flush into a vertical plate to provide rotary motion about the longitudinal axis of the cylinder via stepper motor. To reduce spurious cycle-to-cycle variation of the cylinder shedding pattern, the cylinder was driven about its longitudinal axis in a sinusoidal angular profile of rotational amplitude 45° and at natural shedding frequency corresponding to a Strouhal number of St = 0.2. The driven cylinder preserves the spatial layout of the naturally shedding static cylinder, as demonstrated in Figure 7-1. Experiments were performed at a diameter-based Reynolds number of $Re_d = 7500$ and a chord-based Reynolds number of $Re_d = 3 \times 10^4$.

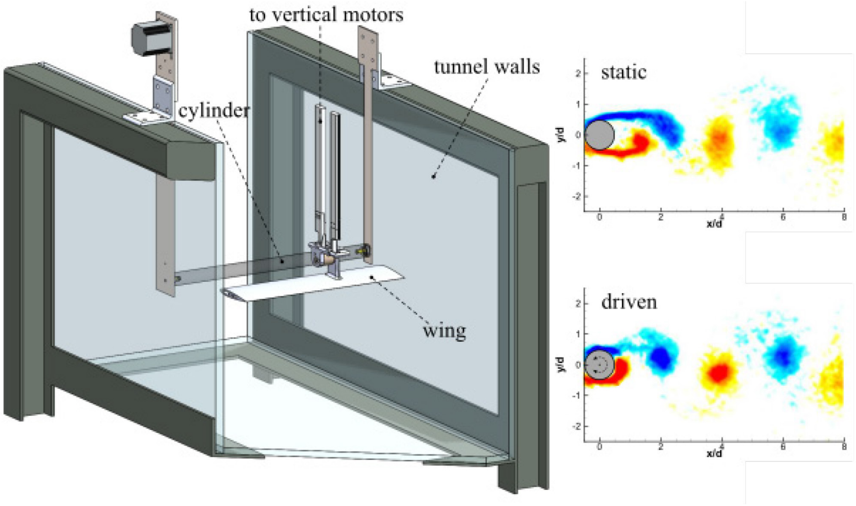

Figure 7-1: (Left) Experimental Setup of NACA0012, (Right) Wakes of Static and Driven Cylinder.

The motivation to drive the cylinder stems from the desire to command the relative position of proximal wake vorticies as the airfoil initiates its respective kinematic schedule. The phasing convention, illustrated in Figure 7-2, corresponds to the relative position of the wake vortices with respect to the wing leading edge. At these select instances the airfoil also initiates a pitch motion about the leading edge. Phases explored in the current work include $\varphi = [0, 90, 180, 270°]$. The airfoil is located sufficiently downstream so as to not bear influence on the cylinder shedding cycle. Vertical placement of the wing, y/d, spans a centerline position (zero-lift line coincident with the center of the cylinder) and an offset position wherein the vortical street traverses only suction surface of the airfoil. In this study the effect of the wake on the aerodynamic loading and vortical shedding of the airfoil is examined in both static and dynamic cases. When dynamic, the airfoil executes a pitch-hold-return maneuver following the C^{∞} – smoothing ramp function suggested by Eldredge et al. [5] and corresponding to Test Case 1 of Ramesh et al.'s [6] work on LESP modeling. The resulting airfoil motion is given by:

$$G(t) = \ln\left[\frac{\cosh\left(\frac{aU}{c}\cdot(t-t_1)\right)\cosh\left(\frac{aU}{c}\cdot(t-t_4)\right)}{\cosh\left(\frac{aU}{c}\cdot(t-t_2)\right)\cosh\left(\frac{aU}{c}\cdot(t-t_3)\right)}\right] \tag{7-1}$$

$$\alpha(t) = \alpha_0 G(t)/G_{\max} \tag{7-2}$$

where α_0 is the maximum angle of attack (=25°), a is the smoothing parameter (=11), U the freestream velocity, c the chord length, and $G_{\max}$ is taken over the interval of interest such that $\alpha = \alpha_0$ is achieved when G reaches its maximum. The airfoil motion achieves a non-dimensional pitch rate of $K = 0.11$ for the non-smoothed kinematic profile. Constants t_1 and t_2 correspond to the start and stop of the non-smoothed pitch-up phase, respectively. Similarly, t_3 and t_4 apply to the return phase.

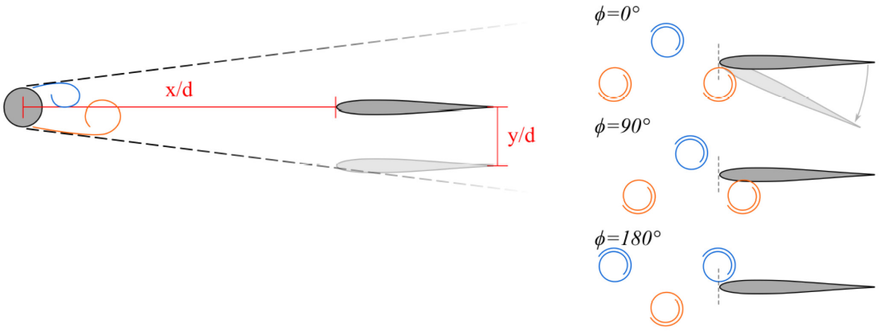

Figure 7-2: (Left) Cylinder-Wing Configuration, (Right) Phasing States of Pitch Initiation.

Direct force measurement was conducted via an ATI NANO-25 IP68 six-component force balance. Measurements were sampled at a rate of 1 kHz and treated with a Chebyshev 2 low-pass filter with a cut-off frequency of 16 Hz. Force measurements were ensemble-averaged over 10 runs. Time-resolved Particle Image Velocimetry (PIV) measurements were planar, confined to the in-plane velocity field. The water tunnel was seeded with polyamide particles of 60 μm-diameter (LaVision, SG = 1.03) and illumination was provided by an Nd:YLF laser sheet (Photonics Industries DM50-527, 50mJ/pulse, 10kHz max) oriented in the streamwise direction and positioned at the three-quarter span of the wing. Images were recorded by high-speed camera (PCO Dimax S4, 4MP, 1279 fps at max resolution). The velocity vectors were calculated using Fluere version 1.3. Two passes of interrogation areas, with initial and final sizes of 64 px^2 and 32 px^2, respectively, were used to determine the particle displacements from single frame images samples at 350 Hz. An interrogation area overlap of 50% was used. The resultant vector fields contained 123 × 123 vectors with a resolution of (Δx/d, Δy/d) = (0.074, 0.074).

7.1.2 Experiments at Istanbul Technical University

The experiments are conducted in the large scale, free-surface water channel located in the Trisonic Laboratory of Istanbul Technical University, Faculty of Aeronautics and Astronautics. A flat plate as the gust generator and either a NACA0012 profile airfoil (for periodic vortex-gust cases) or a rectangular flat plate (for a transient vortex-gust case) wing are mounted in a cantilevered arrangement inside the water channel. The gust generator flat plate is mounted from its mid-chord position and the pitching airfoil from its quarter chord position. The Plexiglas flat plate has a chord (c) of 10cm and span (s) of 40cm, the airfoil has a chord (c) of 10cm and span (s) of 30cm, the flat plate model with a thickness of less than 5% and sharp edges has a chord (c) of 10cm and span (s) of 20cm. Due to symmetry with respect to the free-surface (for a transient vortex-gust case) or an end plate used on top of the free-surface (for periodic vortex-gust cases), the NACA0012 wing has an aspect ratio of 6 and the rectangular flat plate wing has an aspect ratio 4. For all cases investigated, the flow speed is 0.1 m/s which corresponds to Reynolds number of 10000. Both mounting beams are connected to pitch motors which are connected to linear tables which allow the plunging motion. The experimental arrangement can be seen in Figure 7-3.

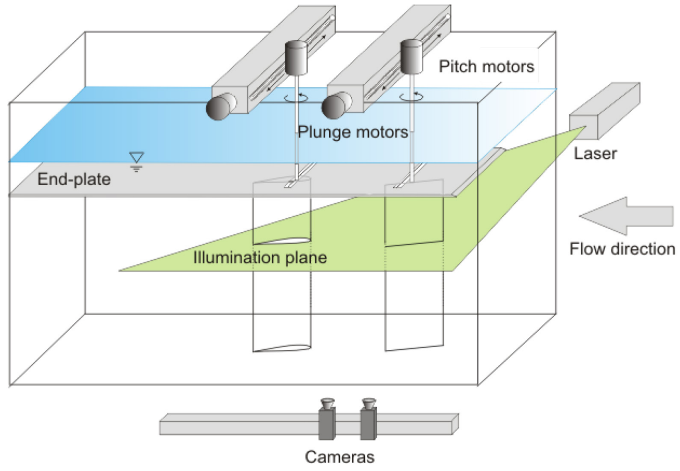

Figure 7-3: Experimental Setup of ITU.

Digital Particle Image Velocimetry (DPIV) technique is used to record flow fields around and in the near wake of the plunging airfoil and therefore to analyze the vortical structures and the velocity fields. The flow is illuminated by a dual cavity Nd:Yag laser (max. 120 mJ/pulse). The velocity fields are obtained using two 10-bit cameras with 1600 × 1200 pixels resolution, positioned underneath the water channel. Recorded images are stitched using an in-house code and then interrogated using a double frame, cross-correlation technique with a window size of 32 × 32 pixels and 50% overlapping in each direction.

Force and moments acting on the plunging airfoil are measured using a six-component ATI NANO-17 IP68 Force/Torque (F/T) sensor. The sensor is attached to the vertical cantilevered mounting beam of the test model, oriented with its cylindrical z-axis normal to the pitch-plunge plane. The motion of the gust generator plate and the models are accomplished with Kollmorgen/Danaher Motion servo motors which are connected to a computer via ServoSTAR digital servo amplifiers. Motor motion profiles are generated by a signal generator Labview Virtual Instrument (VI) for the given amplitude and frequency. The same VI triggered the PIV system and synchronization is achieved using a National Instruments PCI-6601 timer device.

The gust generator plate undergoes pitching and plunging motion, and the amplitude of the plunge motion is calculated in accordance with the frequency and pitch amplitude, so that the feathering conditions are met. The spectral analysis of the velocity field in the wake of the oscillating plate were used to characterize the gust [7], [8]. Three different gust types with varying frequencies and amplitudes have been obtained and identified such that all can be considered as spanwise gusts where the streamwise fluctuations are minimized. Figure 7-4 illustrates time variation of fluctuating velocity components, 0.25c upstream of the model, for all three gust cases. The gust ratios (v'_{ampl}/U_{∞}) and widths are given in Table 7-1. The gust width is calculated based on the frequency of the gust and is determined multiplying the half period and the convective time of the flow.

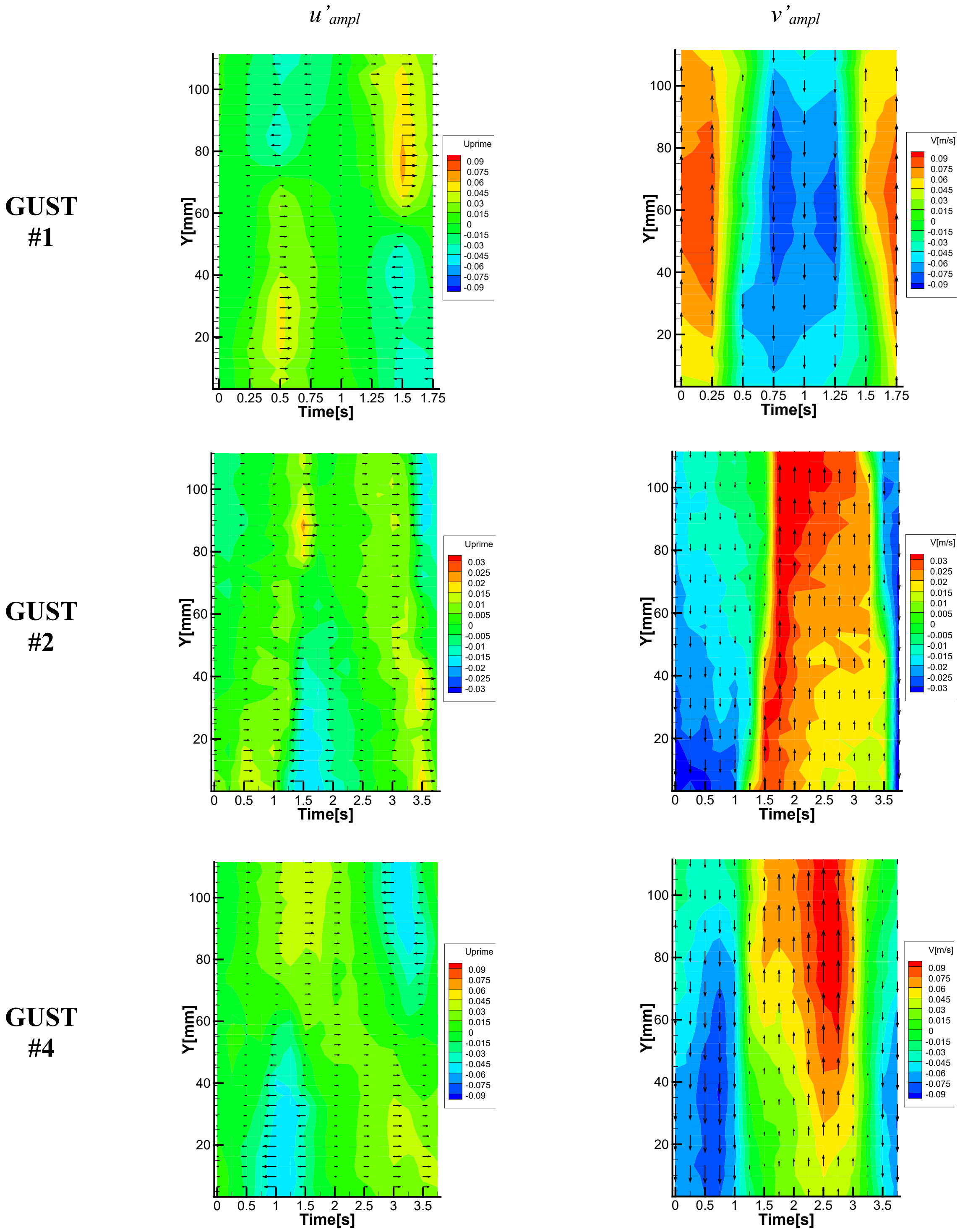

Figure 7-4: Time Variation of Fluctuating Velocity Components, 0.25c Upstream of the Model.

Table 7-1: Periodic Gust Cases of ITU.

	Gust Freq (Hz)	Gust Ratio (v_{amp}/U_{∞})	Gust Width (In Chords)
Gust #1	0.5	1	1
Gust #2	0.25	0.3	2
Gust #4	0.25	1	2

7.2 COMPUTATIONAL MODEL (PERIODIC VORTEX GUST)

The URANS simulations are performed by using the commercial software package ANSYS Fluent 19.1. The computational model of the wing has a NACA 0012 section with an aspect ratio of 6. The chord length of the wing in the computational model is 0.1 meters which is same with the experimental model. The fluid density and viscosity are assumed to be constant and SIMPLE method [9] had been used for pressure-velocity coupling in the computations.

Spatial discretization is made by using second order upwind-type schemes and for the temporal discretization an implicit second order scheme is used. The time step size is chosen accordingly, to satisfy the residual drop with at least two order of magnitudes for 20 sub-iterations. For this purpose, one convective time that corresponds to one chord of travel is divided into 500 equal time steps in the computations. The k-ω Shear Stress Transport (SST) [10] model had been utilized for the turbulence closure in the URANS simulations. The flow domain is constructed as a prismatic volume with 35 chords of length, width, and height. A symmetry boundary is used which is positioned at the mid-span of the wing, to reduce the number of mesh elements by reducing the size of the computational domain. Therefore, the actual domain width is 17.5 chords. The wing is positioned at least 14.5 chords away from the wall boundaries, 5.25 and 29 chords away from inlet and outlet boundaries respectively in the computational domain. The position of the wing and the boundaries in the computational model can be seen in Figure 7-5.

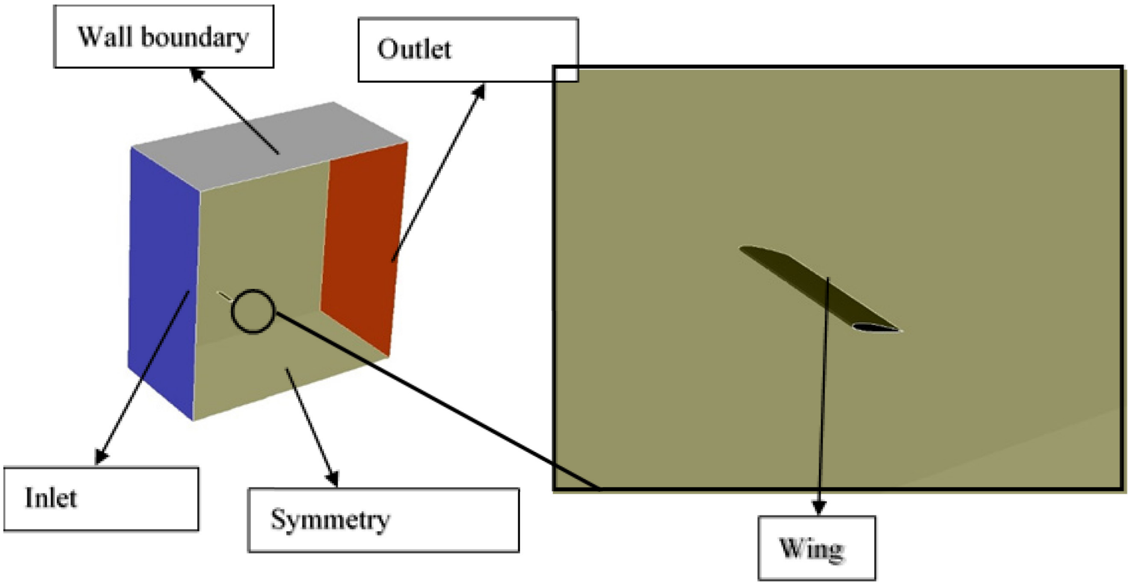

Figure 7-5: The Position of the Wing and the Boundaries in the Computational Model.

Unstructured mesh is used in the computations which is composed of tetrahedral and prismatic elements. Prismatic elements with a predetermined cell height had been generated over the wing boundary to resolve the near wall region by satisfying y^+~1 condition. The mesh density is increased in the separation region for improving the resolution of the flow structures.

Freestream velocity of the flow is imposed to the model by defining the longitudinal velocity component at the inlet boundary as a constant value, which is uniformly distributed over the boundary. The gust effect had been imposed to the computational model by defining transverse component of velocity at the inlet as a sinusoidal function of physical time. The function used for defining the transverse velocity component at the inlet boundary can be written as follows:

$$v = A\sin(\omega t)$$

where A is the amplitude of the gust, ω is the frequency of gust and t is the physical time. The side, top and bottom walls of the domain and the wing are defined as the no-slip wall boundaries. Constant pressure value is specified at the outlet boundary. As an initial condition for the transient computations, the results obtained from RANS simulations with constant freestream velocity and without gust effect had been used. The unsteady simulations cover 10 periods of the defined sinusoidal gust. Grid convergence study is carried out by using three different number of mesh elements. The coarse mesh is composed of approximately 14 million mesh elements, the medium sized mesh is composed of approximately 28 million elements and the fine mesh is composed of 56 million elements. The transient lift and drag coefficient variations for wing exposed to the Gust #4 and at an 45° angle of incidence had been used for comparison of the results obtained from computations by using different mesh resolutions. Since the maximum difference between drag and lift coefficients obtained from medium and fine mesh simulations is less than 1%, the meshing procedure used for generating the medium sized mesh is used for rest of the study.

The lift and drag coefficients obtained from the simulations have a recurring transient variation after the wing being exposed to 7 periods of gust. Therefore, instead of ensemble averaging the simulation results, the lift and drag coefficients obtained from the 10th period of gust had been used. The distance between gust generator and the wing, in the experimental setup is different from the distance between inlet boundary and the wing in the computational model. This results in a phase difference between the results obtained from experiments and the simulations. The phase difference is calculated, and the results of simulations had been shifted in time accordingly.

7.3 RESULTS OF EXPERIMENTS AT THE US AIR FORCE RESEARCH LABORATORY

7.3.1 Two-Dimensional Flow: Pitching Wing

A nominally two-dimensional flow field is provided by cylinder and wing test articles that span the width of the tunnel test section. The wing is positioned downstream of the cylinder a streamwise distance of x/d = 8. The vertical positions explored, with respect to the cylinder center, include a centerline position of y/d = 0 and an offset of y/d = 1.5. At y/d = 0 the von Kármán street is bisected by the downstream wing when at a zero-lift orientation of $\alpha = 0°$. When positioned at y/d = -1.5 the vortex street convects over the suction surface of the wing devoid of direct impingement for the duration of the pitch cycle.

7.3.1.1 Pure Pitch of a NACA0012 Wing

The aerodynamic load history of the symmetric SD-series wing executing the pitch-hold-return maneuver in the absence of an imposing upstream disturbance is presented in Figure 7-6. The wing originates parallel to the direction of the freestream in a zero-lift orientation of α_0. Given the initial orientation, as the airfoil proceeds to pitch upward much of the non-circulatory loading contributes predominantly to lift. This aids in the rise of an inertial spike in lift shortly after t_1. Thereafter, lift continues a steady climb owing to bound circulation in pitch. Shortly before completing the pitch-up motion, the disparity between lift and drag production is nominally reconciled. At the completion of the pitch-up phase, the wing experiences a second inertial spike near t_3 that acts to reduce lift and drag. The concurrent formation of a leading-edge vortex on the airfoil is then cause for the subsequent rise in lift and drag during the hold-phase of motion, where drag surpasses lift production. Prior to the leading-edge vortex shedding from the wing, the pitch-down (return) phase begins and is punctuated by start and stop inertial spikes enclosing a steady decline of lift and drag. Similar inertial trends are observed in the moment coefficient.

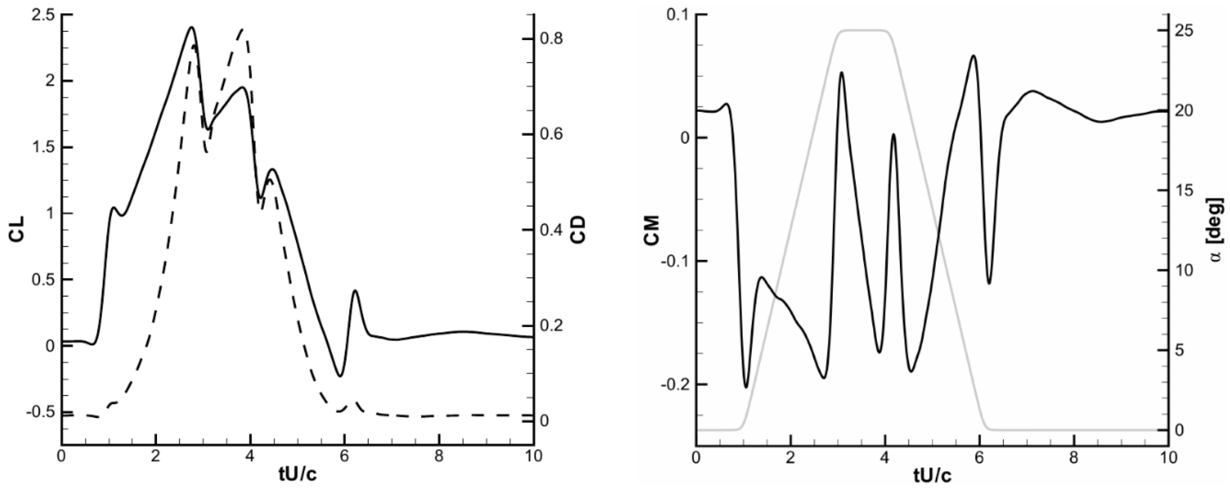

(a) Lift (–) and Drag (– –) Coefficient.

(b) Moment Coefficient (–) and Angle of Attack.

Figure 7-6: Baseline Aerodynamic Load History and Kinematic Profile.

As previously alluded, the pitch amplitude is cause for the formation of a leading-edge vortex which is a significant contributor to the ensuing force and moment transients experienced by the wing. The resulting vortical dynamics are displayed in Figure 7-7, and establish the baseline flow characteristics of an unperturbed state. As motion commences near $t^* = 1.0$ the wing remains at zero attack angle and the flow is fully attached. The wake is largely representative of minor vorticity oscillations within oppositely-signed shear layers emanated from the trailing edge. At $t^* = 2.0$ there appears boundary layer growth over the trailing edge region and nascent roll-up of shear about the leading edge. As the wing progresses further in pitch, $t^* = 3.0$, roll-up has advanced to produce a leading-edge vortex. Further, above the trailing edge is also host to secondary roll-up owing to interactions of flow entrainment toward the wing surface and oppositely-signed trailing-edge shear. In holding at peak pitch at $t^* = 4.0$ the leading-edge vortex has appreciated in size and strength to become the dominate feature governing the flow field. At this phase, the leading-edge vortex is easily discernible from the free shear layer as the shedding process has begun. By $t^* = 5.0$ the leading-edge vortex has severed communication to the leading-edge shear layer and has convected downstream. Through interactions of mutual entrainment with the eruption vorticity layer, the composition of the shed leading-edge vortex is quite mixed. During this phase, the leading-edge shear layer exhibits continued roll-up to produce a secondary leading-edge vortex which ultimately convects along the wing surface as the wing resumes its initial pitch angle at $t^* = 6.0$.

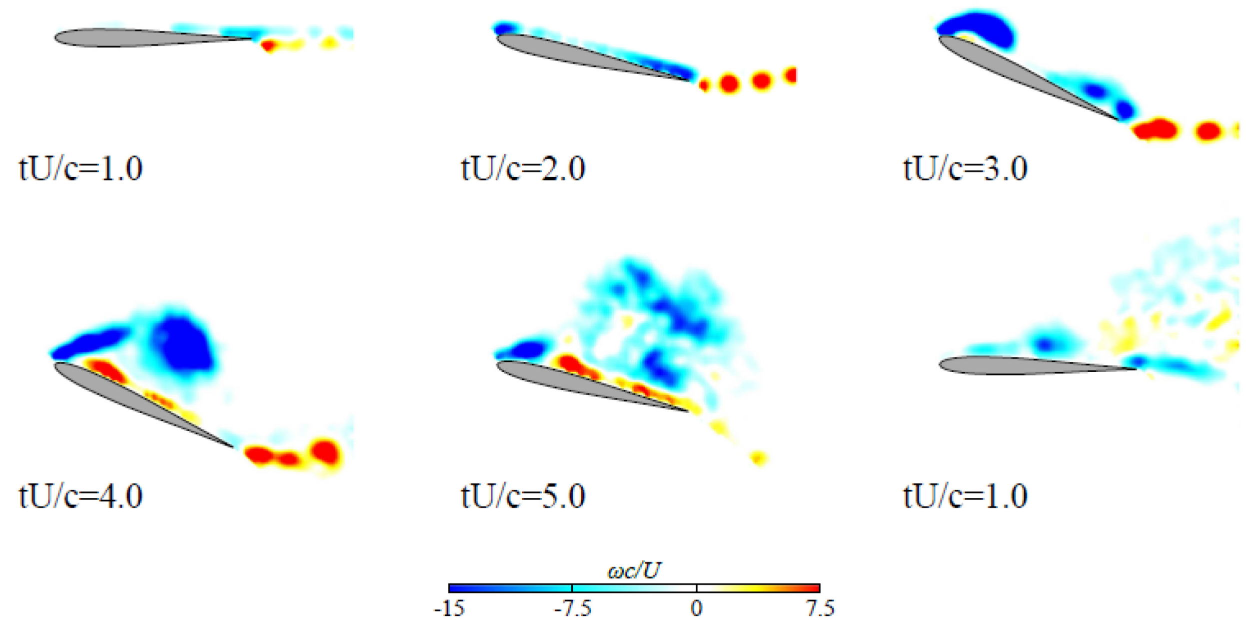

Figure 7-7: Vorticity Field Dynamics of Pure Pitch.

7.3.1.2 Pitching Under Wake Impingement: Lift

The influence of the impinging wake on the dynamic wing is presented in Figure 7-8 through direct force measurement, where the lift coefficient is selected here to gage performance deviations.

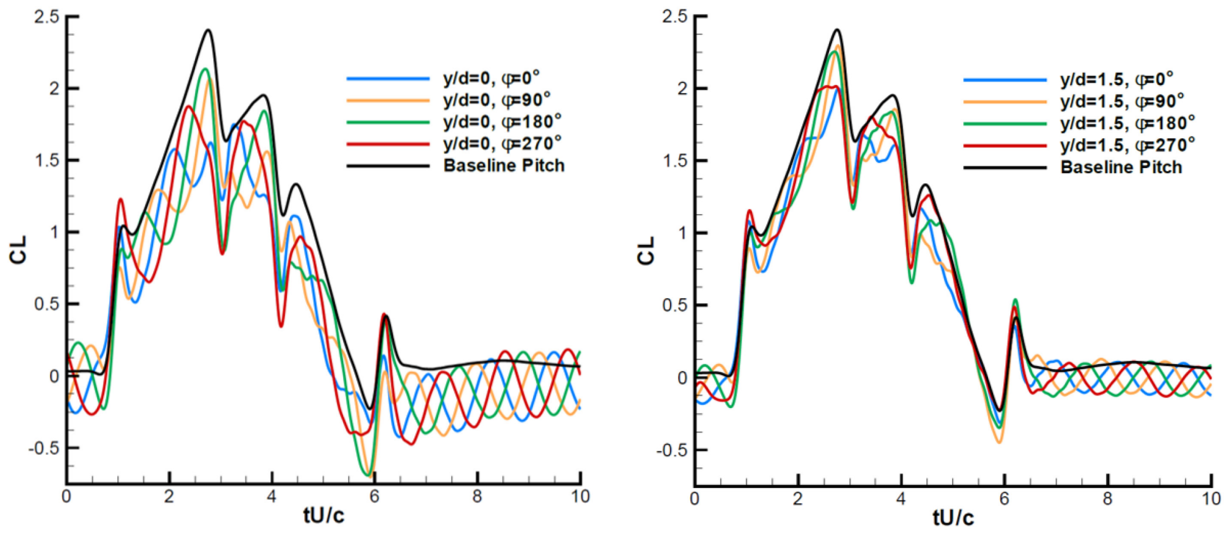

(a) Lift Coefficient: y/d = 0.

(b) Lift Coefficient: y/d = -1.5

Figure 7-8: Lift Response to Vortical Wake Encounter.

The four wake-phases are 90° apart, as visible in their respective lift fluctuations at times prior to and post motion. When no vertical offset is imposed, $y/d = 0$, the overarching observation to be made of the transient lift profile during motion under wake influence is a force history distinguished by oscillation in accordance with the periodic wake. Indeed, for a given phase φ the undulation in lift during wing motion showcases a notional superposition of the wake-generated lift with that of the pitch-generated lift. These oscillations, however, appear comparatively muted during the pitch-down return stage of motion. Among the four phases explored, lift histories are unified in prominent inertial spikes as discussed in the pure pitch case. Lastly, for y/d = 0 the interaction of the periodic wake with the pitching wing provides no avenues for exploitation of lift enhancing mechanisms. That is, the lift performance of a given phase φ case is limited to the performance of a wing in pure pitch devoid of a wake encounter. The various oscillations in lift induced by the wake provide a net decrease in lift. These observations extend to adjustment in vertical offset to y/d = -1.5. In this configuration the vortex street is convected along the suction surface of the wing and precludes the possibility of direct impingement of a wake vorticity parcel onto the wing for all stages of motion. The wake influence on lift amounts to the nominal preservation of profiles observed for y/d = 0 but to an abated effect.

7.3.1.3 Vortical Dynamics of Impingement

The vortical dynamics of impingement are explored here where the centerline (y/d = 0) vertical position is selected to elicit greater interaction between the bluff-body wake and the pitching wing. Further, discussion here highlights phases $\varphi = 0°$ and $180°$ for their polarized vortical states and for their placement of a proximal vortex at the leading edge at the time of pitch initiation. Additionally, phases $\varphi = 0°$ and $180°$ account for the minimum and maximum lift production achieved near completion of the pitch-up motion among the four phases considered.

The wake encounter for a pitching wing with phase $\varphi = 0°$ is catalogued in Figure 7-9. As previously defined, $\varphi = 0°$ is classified by the positively signed (CCW) vortex aligned with the wing leading edge at the start of pitch, $t^* = 1.0$. This vortex is partially obscured by the shadow imposed by the wing during data acquisition. Given the direction of pitch, the CCW-components of the vortex street will largely interact with the bound circulation of the wing while CW-components will interact directly with wing leading-edge formations. As early as $t^* = 2.0$ the disparity in leading-edge phenomena is quite apparent from the pure pitch case of Figure 7-7. Rather than nascent roll-up, the leading edge appears populated by advanced leading-edge vortex formation owing in part to enhanced entrainment fed by the proximal CW vortex just aft of the leading-edge vortex. As the CW vortex of interest passes at $t^* = 2.5$ its influence is diminished, allowing the leading-edge vortex to elongate along the wing surface. However, interactions with the subsequent CW vortex at $t^* = 3.0$ is cause for contraction and concentration once again of the leading-edge vortex resulting in an undulatory formation cycle during pitch-up. The timing of leading-edge vortex shedding appears undisturbed as shown at $t^* = 4.0$. During pitch-down the secondary leading-edge vortex observed in pure pitch is absent, having been suppressed by neutralizing interactions between the leading-edge shear layer and a CCW vortex parcel.

As demonstrated by inspection of $\varphi = 0°$ flow field evolution, the influence of the cylinder wake can be considerable. If instead the phase is shifted to $\varphi = 180°$ such that a CW vortex is initially aligned with the wing leading edge at the start of motion one would anticipate a fundamental shift in dynamics as well. The wake encounter for a pitching wing with phase $\varphi = 180°$ is catalogued in Figure 7-10. It becomes evident that the undulations previously reported during pitch-up for $\varphi = 0°$ are now relegated to minor boundary layer fluctuations in early leading-edge vortex development for $\varphi = 180°$, namely between $t^* = 1.5$ and 2.0. By $t^* = 3.0$ the leading-edge vortex showcases growth in size and strength exceeding both the pure pitch case and the $\varphi = 0°$ counterpart. At $t^* = 3.5$ the CW wake vortex above the wing appears to hasten the separation of the leading-edge vortex from the leading-edge shear layer. Arguably, the induced velocity of the same CW vortex subsequently aids in the leading-edge vortex's stability as it convects the separated region close to the wing surface, as shown at $t^* = 4.0$. At this instant, the CCW vortex is being entrained into the shear layer, resulting in significant neutralization of the shear layer roll-up at $t^* = 4.5$. As pitch-down continues, the resumption of leading-edge roll-up is apparent.

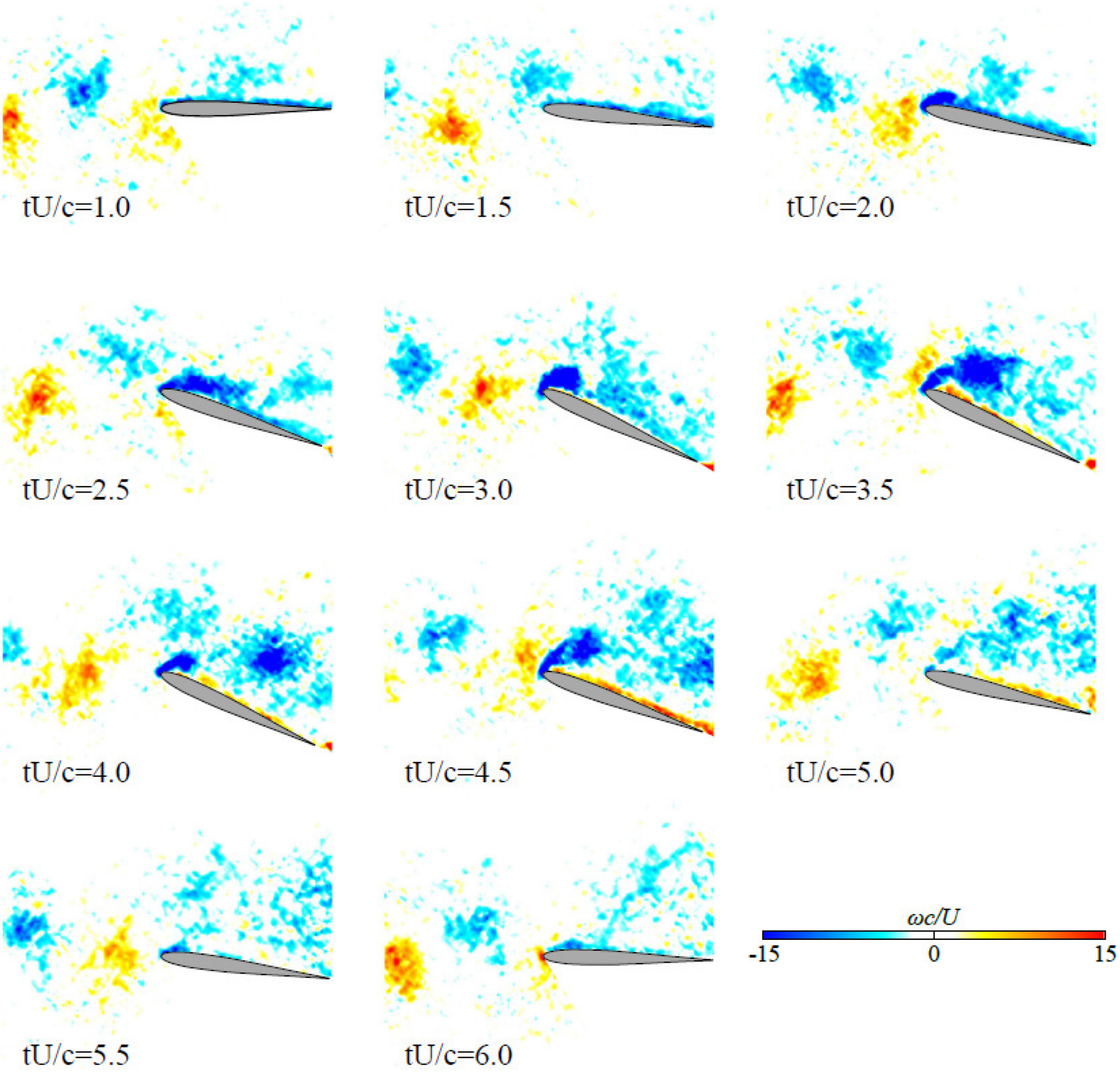

Figure 7-9: Vortical Flow Field Evolution: $\varphi = 0°$.

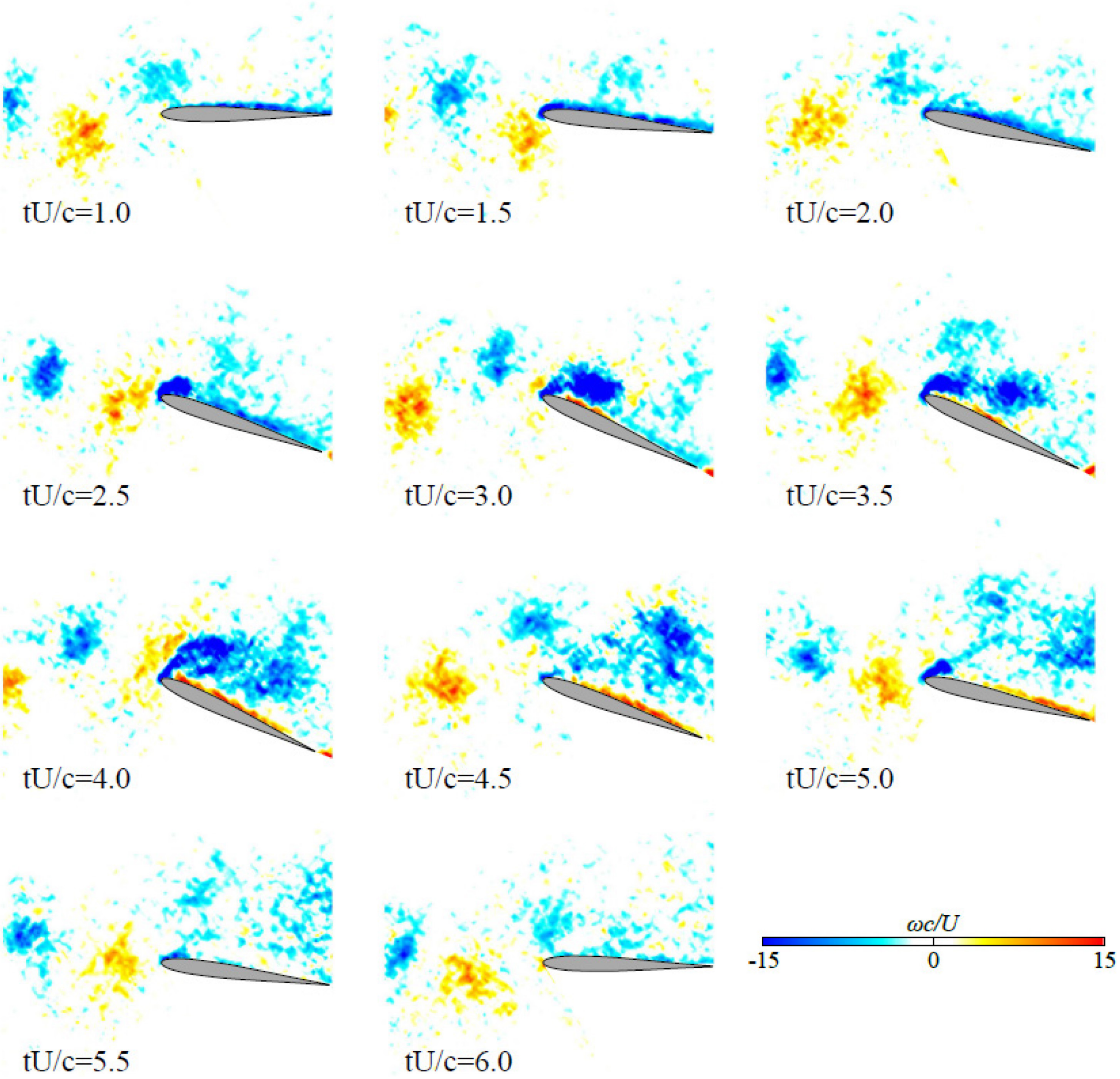

Figure 7-10: Vortical Flow Field Evolution: $\varphi = 180°$.

7.3.2 Three-Dimensional Flow: Static Survey

The effect of a periodic gust on a static wing is further explored within a von Kármán vortex street of a bluff body where a NACA0012 wing is positioned downstream of a circular cylinder undergoing periodic vortex shedding. The wing is of effective finite aspect ratio with a single free end generating a tip vortex. Figure 7-11 documents the time-averaged lift response of the wing positioned downstream of the driven cylinder. The two articles are separated by a streamwise distance of 10 diameters, as measured from the cylinder center to the leading-edge of the wing. The baseline lift curve, identified by the black line, details the transition from attached flow to detached flow in the absence of the gust generator. When the flow is attached, lift coefficient increases with angle of attack. As separation is realized, notionally at 9° angle of attack, slope inflection is followed by a decremented lift state. Note the zero-lift state of 0° registers as a non-zero value owing to the mounting apparatus of the wing.

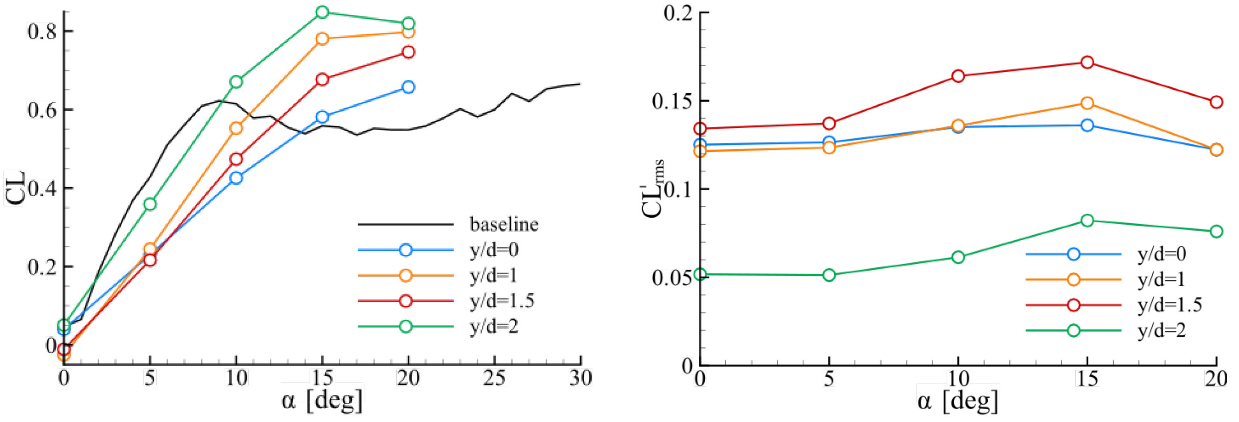

Figure 7-11: Time Average Lift Coefficient (Left) and rms Fluctuating Lift Coefficient (Right) at Fixed Angles of Attack.

In quantifying the effect of gust encounter a sparse survey of static angle of attack is performed with angles selected to capture representative lift phases of crucial metric to the baseline case, $\alpha = [0, 5, 10, 15, 20^\circ]$. Further, the effect of vertical displacement is quantified on the quasi-static lift. A vertical displacement of y/d = 0 corresponds to a wing positioned coincident with the centerline of the cylinder. In this manner the nature of gust interaction is fundamentally altered. At zero incidence the vortex street is bisected about the wing chord for y/d = 0. At a displacement of y/d = 2 direct impingements are notionally avoided. Rather, the vortex street traverses adjacent to the suction surface of the wing. For $\alpha = 5^\circ$ all displacement cases experienced a loss in lift from that of the baseline profile. The case of y/d = 2 presents a departure from the remaining displacement positions, generating greater lift than its offset counterparts. This trend remains true within the purview of angles studied. For an angle of $\alpha = 10^\circ$ the centerline case of zero offset emerges as the least productive case in lift generation. Offsetting the wing to 1 diameter above the centerline is cause for lift gains, however, those gains are diminished when the vertical position is increased to 1.5d. In all three instances of vertical offset the time-averaged lift generated remains below the baseline case. As the wing position is increased further to y/d = 2 there exists a surge in lift to exceed the baseline performance. Established trends in the relative lift performance among the offset cases remain intact henceforth. Contrary to the baseline case at $\alpha = 15^\circ$, which is marked by a decrease in lift, the offset cases appear to boast further increases in lift under the influence of the vortex street. Indeed, the suite of vortex encounters showcase enhancements in lift over that of the baseline within this massively separated regime. The cyclic loading of the wing adopts the shedding frequency of the cylinder.

The rms fluctuation in lift is quantified in Figure 7-11 where fluctuation amplitude minimized as the wing resides external to the vortex street at y/d = 2. The greatest fluctuations are reserved for y/d = 1.5 offset which notionally places the leading edge in the path of a given shed vortex, thus ensues a complex interaction of vortex splitting. The calculated rms profile appears common among the offset cases with greater fluctuation observed with increasing angle of attack until a peak at $\alpha = 15^\circ$. The relation between attack angle and lift fluctuation highlights the enhanced receptivity of the wing to periodic disturbance when instabilities inherent in the wing aerodynamics, namely the leading-edge shear layer, are presented at greater angles of attack.

Drag measurements of Figure 7-12 reveal drag reduction among the offset cases for $\alpha \leq 15^\circ$. At greater angle, a drag penalty is incurred for y/d = 1 and 2. The resulting (sparse) profile generally matches that of the baseline case for all offsets, in contrast to the lift profile. This is due to the deviations in the vertical component of velocity, induced by a proximal vortex, being a greater contributor to changes in effective angle of attack than the streamwise component of induced velocity imposed over the freestream. The cumulative effect on quasi-steady performance in gust is demonstrated in the lift-to-drag ratio of

Figure 7-12. With the exception of the centerline position, offset performance is characterized by gains in lift-to-drag. These gains are most pronounced within the attached flow regime of $\alpha = 5°$. Moreover, the various offset cases appear to largely collapse onto a common profile despite inviting vastly differing physical formations in response to vertical offset displacement.

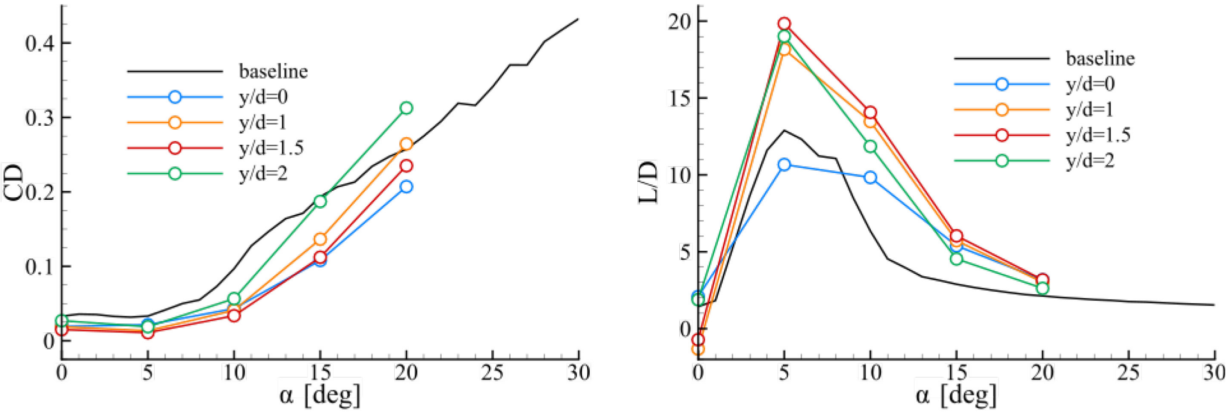

Figure 7-12: Time Average Drag Coefficient (Left) and Lift-to-Drag Ratio (Right) at Fixed Angles of Attack.

7.4 RESULTS OF EXPERIMENTS AT ITU

7.4.1 Periodic Vortex-Gust Encounter – NACA0012 Wing

Figure 7-13 shows the lift coefficient variation in a period of gust for the periodic gust cases investigated. On the left, the time axes are shifted and therefore adjusted according to the cross-spectra plots in order to have comparable gust fronts in time. Lift variations exhibit a nearly sinusoidal variation in accord with the transverse velocity. The average value of the lift coefficients increases with increasing angle of attack. Peak-to-peak values of lift coefficient variation is mostly related to the gust amplitude. For comparison purposes, two angles of attack cases, namely α = 0° and 4°, are extracted and shown in Figure 7-14 repeating for couple of gust cycles. On the other hand, after the gust front is adjusted in time, the same results are scaled using the encounter width (w/c) and the gust ratio (v'/U∞); and shown in Figure 7-15.

In terms of quantitative flow visualization results, Figure 7-16 shows the effect of the periodic gusts on the wing when it is at an angle of attack of 20° together with the no gust case for comparison. Figure 7-14 includes two instants in time separated by the half of the gust period. The gust front and its encounter with the wing is evident; the separation is promoted, and a leading-edge vortex formation and separation are evident.

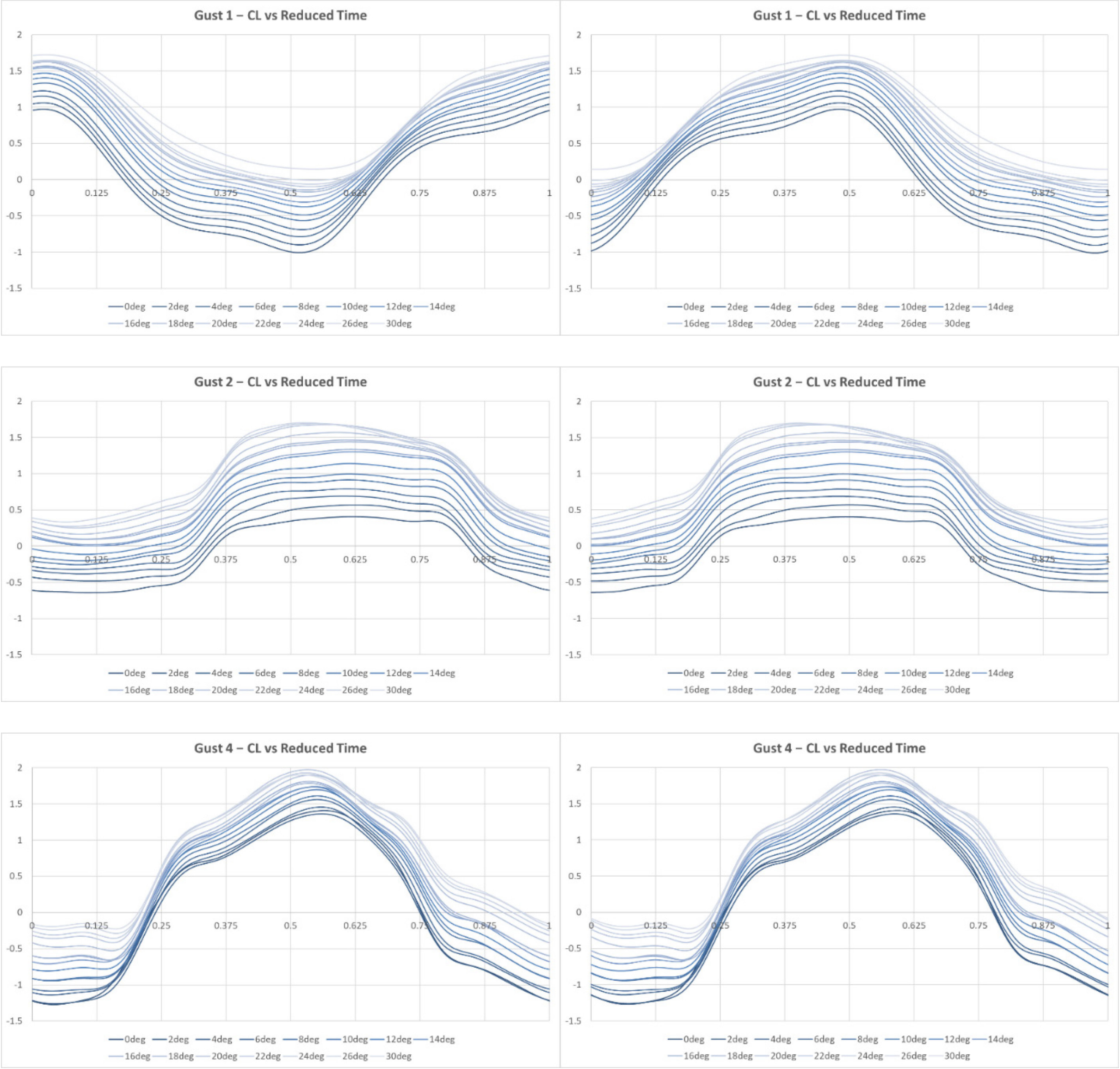

Figure 7-13: Lift History for Periodic Vortex Gusts Encountering a NACA0012 Airfoil at Various Angles of Attack, Acquired Variations are Given on the Left and Phase Shifted Variations Depending on the Gust Front on the Right.

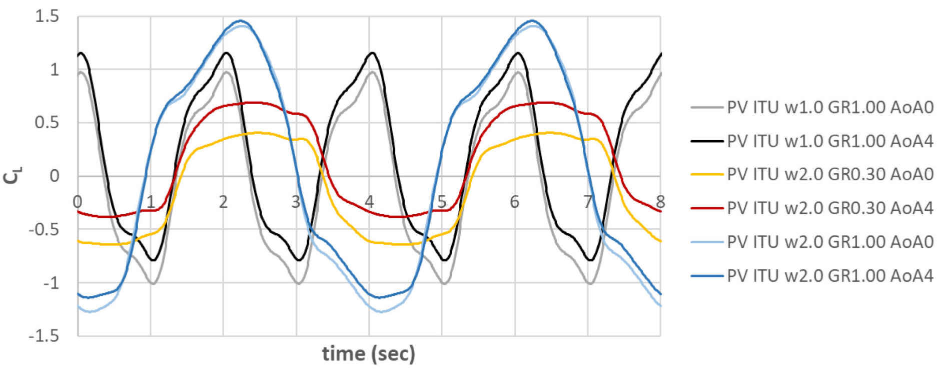

Figure 7-14: Three Gusts and AoA = 0°, 4° Before the Gust Front is Adjusted in Time.

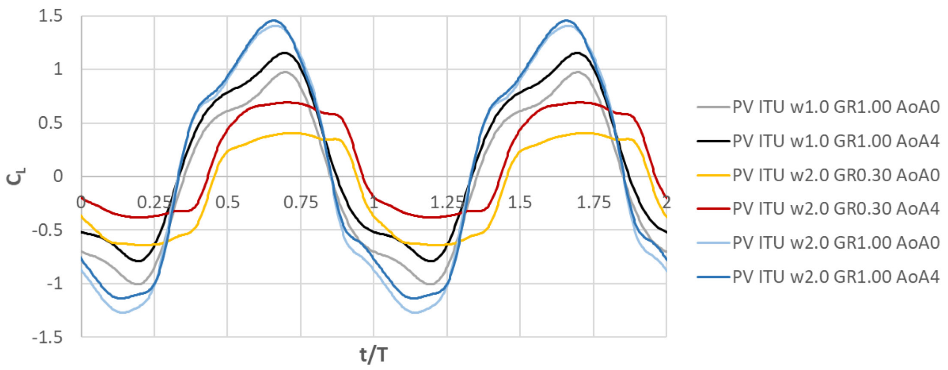

Figure 7-15: Three Gusts and AoA = 0°, 4° After the Gust Front is Adjusted in Time and the Axes are Scaled.

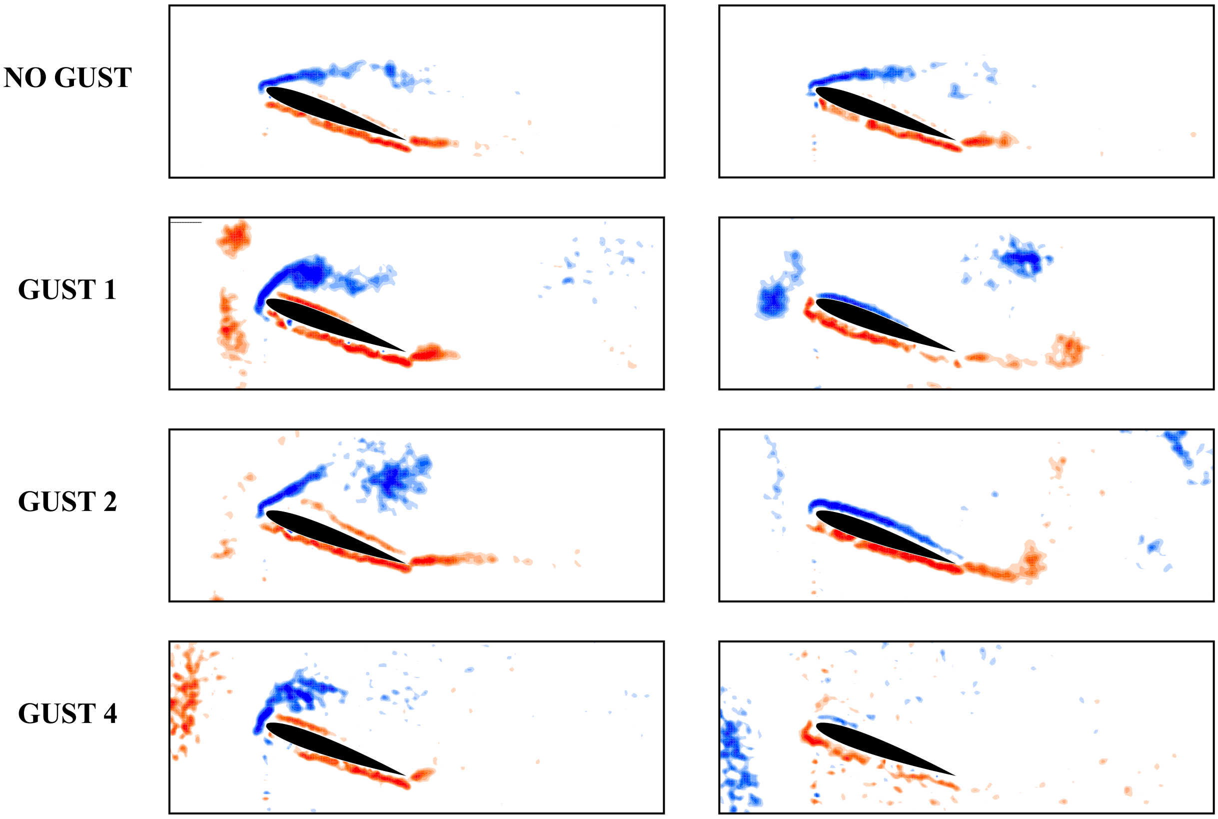

Figure 7-16: Vorticity Distributions for the Wing at Angle of Attack of 20° (The Right Images are Half Period of Gust Later Than the Left Images).

7.4.2 Transient Vortex-Gust Encounter – Flat Plate

Transient vortex is generated using a clockwise half rotation of the gust generator plate. The gust width is $w/c = 0.4$ and the gust ratio is approximately $u'/U_\infty \approx v'/U_\infty \approx 1$.

The typical response for a transient vortex gust is shown in Figure 7-17. Although the encounter of a large negative vortex is studied, its counterpart also affects the flat plate and a local positive peak appears first in the lift transient. Then, the large negative vortex creates a downwash and accordingly, the lift experiences a major negative peak, a positive leading-edge vortex is formed at the lower side of the flat plate. The lift recovers after experiencing a second local positive peak when the negative vortex-gust forces to shed the positive leading-edge vortex and hits the leading edge. The negative vortex gust encountering the wing moves on the suction side and the newly formed positive vortex attaches the leading edge, forms gradually an attached vorticity layer at the pressure side. Finally, the flow field is back to its form before the gust encounter.

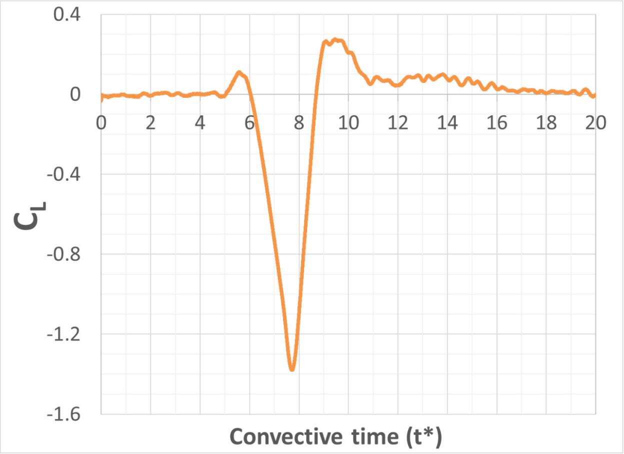

Figure 7-17: Lift and Effective Angle of Attack History for Single Vortex Gust.

Although the Reynolds number is quite different, the computational study of a vortex gust [4] yields very similar results. The angle of attack is 4° in the computations; however, it is shown that the rotation sense of the vortex causes the lift variation to flip approximately around *x*-axis. Taking it into consideration, the experimental data obtained for a clockwise vortex interaction and at an angle of attack of 5° is flipped around *x*-axis. Then, the experimental and numerical results are scaled using the encounter width (w/c) and the gust ratio (v'/U_∞); and Figure 7-18 is obtained showing the effect of the vertical offset on counter clockwise interaction.

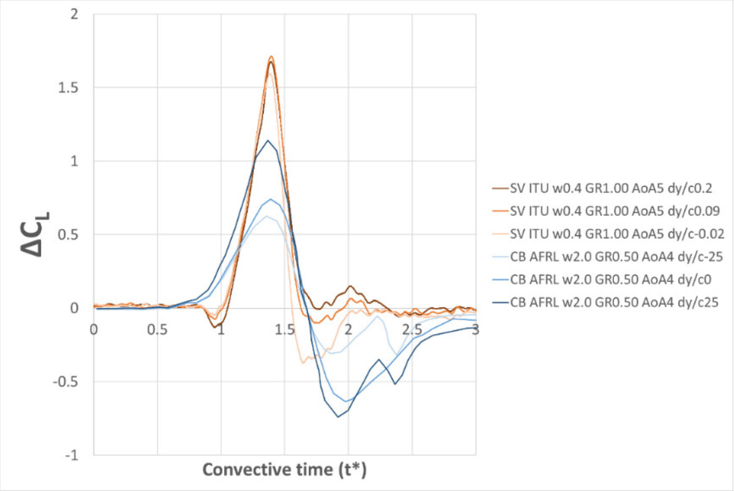

Figure 7-18: Experimental and Numerical Results on the Lift Coefficient Variation in Time Showing the Effect of the Vertical Offset on Counter Clockwise Interaction.

Figure 7-19 shows the numerical results in comparison with the experimental results for the two strong gust cases. Taking into account that the numerical results consider an ideal periodic sinusoidal transverse gust, the match between the lift coefficient variations and vorticity fields are found be very close. The gust fronts are not visible in the numerical results due to their low vorticity levels. In addition, for visual purposes there is a mismatch in the color levels between numerical and experimental data presentations.

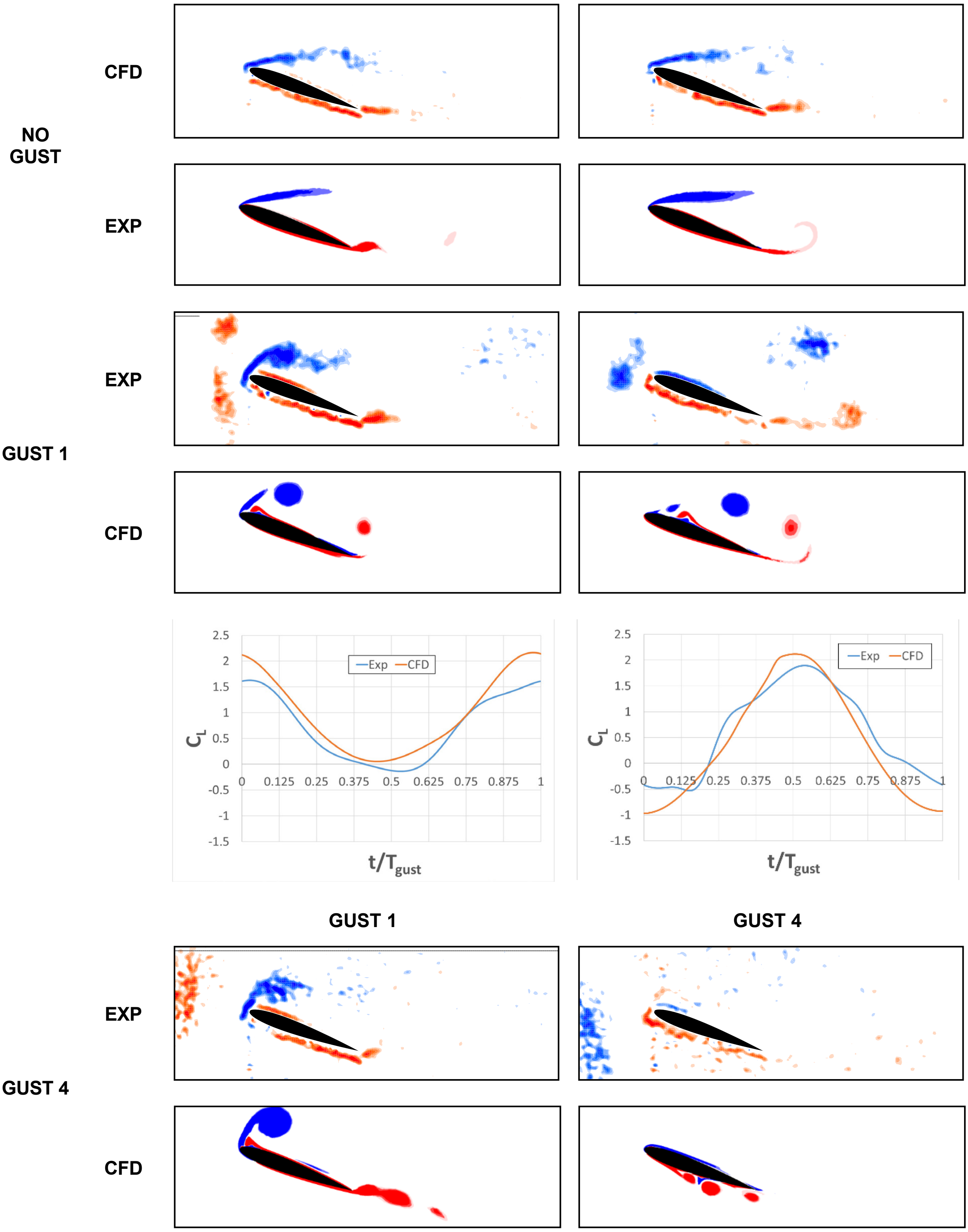

Figure 7-19: Numerical Results in Comparison with the Experimental Results for the Two Strong Gust Cases.

7.5 CONCLUDING REMARKS

7.5.1 Experiments at the US Air Force Research Laboratory

In this study the aerodynamic response of a wing encountering vortex gusts has been investigated in static and dynamic operations, and in two- and three-dimensional flow fields. Vortical gusts were selected for their spatiotemporal variation and were generated using a rotating cylinder upstream of the wing. Although the vortical gusts provide both streamwise and transverse disturbance to the flow field, the vertical component of induced velocity was deemed most influential on the aerodynamics. A two-dimensional survey of gust-phase effects on lift transients of a pitching wing revealed a lift profile that was in effect a superposition of the baseline lift history with the oscillatory signature of the wake. This notional superposition was to the detriment of overall lift production in that the baseline wake-free case provided peak lift production and the introduction of a wake for any given phase was degraded from the wake-free benchmark. In three-dimensional static operations in a vortex street the mean lift was shown to increase with increasing angle of attack. The effect of the wake was shown to enhance lift generation particularly for the post-stall regime and with increasing effect as the wing was removed of the cylinder centerline position. When quantifying lift-to-drag it was shown that the gust profiles exceeded that of the baseline (gust-less) case and exhibit a collapse in profile for centerline-offset conditions.

7.5.2 Experiments at Istanbul Technical University

In this study, vortical gusts were generated using a rotating flat plate upstream of the wing. Although the vortical gusts provide both streamwise and transverse disturbance to the flow field, the vertical component of induced velocity was deemed most influential on the aerodynamics.

The aerodynamic response of a NACA0012 wing encountering vortex gusts has been investigated using experimental and computational approaches for continuous encounters. The lift coefficient peak-to-peak value variation was shown to be mostly related to the gust amplitude. Further, the gust encounter was shown to induce separation on the wing to create a leading-edge vortex. With noted differences between experimental and computational approaches results agreed well.

The aerodynamic response of a flat plate wing encountering a transient vortex gusts has been investigated experimentally and compared with the results of a computational study in the literature. Although the Reynolds numbers used in experimental and computational approaches are quite different, the results agreed well and indicate a typical lift response. In transient vortex-gust encounters the resulting peak in lift is also observed to be directly dependent on the direction of vortex rotation.

7.6 ACKNOWLEDGMENTS

ITU work is supported by TUBITAK Grant 115M358 (For the Application on UAVs and MAVs, Gust Effect on the Performance of Wings in Motion (Maneuver or Flapping) and Flow Control Attempts).

7.7 REFERENCES

[1] Fisher, A., Ravi, S., Watkins, S., Watmuff, J., Wang, C., Lui, H., and Peterson, P. The gust-mitigation potential of flapping wings, Bioinspir. Biomim, Vol. 4, (11): 046010, 2016.

[2] Medina, A., Hemati, M.S., and Rockwood, M. (2018) Lift disturbance cancellation with rapid-flap actuation, 48th AIAA Fluid Dynamics Conference, Atlanta, United States, 2018.

[3] Dabiri, J.O., Potential order-of-magnitude enhancement of wind farm power density via counter-rotating vertical-axis wind turbine arrays, Journal of Renewable and Sustainable Energy, Vol. 3, No. 4, Paper 043104, 2011.

[4] Barnes, C.J., and Visbal, M.R., Effects of vertical position and orientation on a verticall-gust/airfoil interaction at a transitional Reynolds number, 47th AIAA Fluid Dynamics Conference, AIAA, Paper 2017-3320, 2017.

[5] Ol, M.V., Eldredge, J.D., and Wang, C., High-amplitude pitch of a flat plate: An abstraction of perching and flapping, International Journal of MAVs, Vol. 1, No. 3, 2009, pp. 203-216.

[6] Ramesh, K., Gopalarathnam, A., Granlund, K., Ol, M.V., and Edwards, J.R., Discrete-vortex method with novel shedding criterion for unsteady aerofoil flows with intermittent leading-edge vortex shedding, J. Fluid Mech., Vol. 751, 2014, pp. 500-538.

[7] Engin, K., Aydın, E., Zaloglu, B., Fenercioglu, I., Cetiner, O., Large scale spanwise periodic vortex gusts or single spanwise vortex impinging on a rectangular wing, AIAA Aviation Forum – Fluid Dynamics Conference, 2018. doi: 10.2514/6.2018-3086

[8] Biler, H., Zaloglu, B. and Cetiner, O. Effect of spanwise gust on a wing, 8th Ankara International Aerospace Conference, 10-12 September, METU, Ankara, Turkey, 2015.

[9] Patankar, S.V. and Spalding, D.B., A calculation procedure heat, mass and momentum transfer in three-dimensional parabolic flows, Int. J. Heat and Mass Transfer, Vol.15, 1972, pp. 1787-1806.

[10] Menter, F.R., Kuntz, M., and Langtry, R.B., Ten years of industrial experience with the sst turbulence model turbulence, Heat and Mass Transfer, Vol. 4, No. 1, 2003, pp. 625-632.

Chapter 8 – AEROELASTIC ENCOUNTERS OF SPANWISE VORTEX GUSTS AND THE SELF-ROTATION OF TRAILING VORTICES

Huansheng Chen, and Justin W. Jaworski
Lehigh University
UNITED STATES

Vortex structures in the atmosphere and in the wakes of aircraft generate fluid loads that may be beneficial (e.g., a reduction of induced drag) or detrimental (e.g., cause unsteady buffeting or dynamic instability) depending on the aerodynamic scenario at hand. Two distinct models are developed here to:

1) Investigate separately the aeroelastic effects of spanwise-oriented gusts encountering an airfoil; and
2) Predict the self-rotation of a perturbed streamwise-oriented trailing vortex.

In Part I, the dynamically-coupled interactions of vortex gusts encountering a symmetric Joukowski airfoil on linear elastic supports is formulated analytically and evaluated numerically using a time-dependent conformal mapping technique. The Brown and Michael framework models the unsteady shedding of vorticity from the airfoil into the wake.

Special attention is paid to the influence of the strength of the incident vortex and the airfoil natural frequency on the initial upstream placement of a vortex gust that achieves direct impingement on the airfoil. The results indicate a weak sensitivity of initial vortex position in the limits of a small or large structural natural frequency, while the initial vortex position changes monotonically with vortex strength. A comparison of the present numerical inviscid model to available experimental vortex gust measurements over stationary airfoils highlights the appropriate use of the point-vortex model for inviscid vortex-airfoil interaction problems without vortex strength decay, but also its inability of the model to model the dominant viscous interactions that occur for close vortex-airfoil encounters.

Part II employs the asymptotic analysis of a sinusoidally-deformed infinite vortex with a finite core to estimate the self-induced rotation of a trailing vortex produced by a wing tip. A comparison of the model against high-fidelity computational simulations indicates that the theory overpredicts the rotation rate, which depends generally on the amplitude of vortex deformation that is not present in the theoretical analysis.

8.1 INTRODUCTION

The encounter of a vortex gust with an aerodynamic body is a canonical fluid-structure interaction with implications for the prediction of transient loads on fliers and swimmers and their generation of vortex sound. Among the various orientations that the incident vortex can take with respect to the solid body (cf. Rockwell [1]), the alignment of the spanwise vortex with the orientation of the bound vorticity on the body, the wake, and the boundary-layer vorticity allows for their coupled interactions during a vortex-airfoil encounter. For this reason, a number of theoretical, numerical, and experimental studies have been carried out to understand and model two-dimensional vortex-structure interactions.

Dynamic structural motions affect the paths of the incident vortex and the unsteady vorticity shed into the wake, which thereby affect the unsteady fluid loading on the aerodynamic structure. These structural motions may be either prescribed or the result of aeroelastic coupling, where in the latter case the elasticity of the structure or its supports provides the route for two-way energy transfer between the solid and fluid. Early research carried out by Howe [2] involved a line vortex cut by a flat rigid plate under spring supports, which caused energy to be transferred from the turbulence to the restoring spring force. In a later contribution, Manela [3] studied the combined effects of a vortex converting past by a flexible sheet. These model problems focus only on a setup where the structure has unprompted motion under external loads, such as spring forces, but the fluid load and the effects of the structure motion on the turbulence are both ignored. Recently, Manela [4] considered the nonlinear effects of flow unsteadiness on a flat plate with periodic oscillation motions, which include the effects of the plate motion on the turbulence. However, existing studies have not considered the *coupled* effects of incident vorticity and structure under *aeroelastic* motion, which motivates the present work. An investigation by Manela [4] also provides the verification case in the present work for the limit of zero airfoil thickness.

Apart from these studies of vortex-structure interactions listed above, special attention has been paid to the effects of structure configuration and vortex placement on direct vortex impingement. Early experiments performed by Rockwell and Knisely [5] investigated the impinging vortex motions excessively, later Ziada and Rockwell [6] observed a point vortex impinging upon the leading edge of a wedge. Other numerical modelling works of the associated flow physics in the vortex-structure interaction has been developed by Conlisk and Rockwell [7], Conlisk and Veley [8], and Panaras [9]. So far, analytical investigations of direct vortex impingement have not been developed for structures under aeroelastic motions and is a key contribution of the present study.

The present work is organized into two independent parts. The first part models the vortex-wake interactions for non-flat airfoil geometries, and the aeroelastic interactions with linear elastic mount. The model may be used to predict the conditions for direct vortex impingement. The model scenario and dynamic formulation are discussed in this chapter has been studied previously by Chen and Jaworski [10]. This chapter also contains comparison results of previous analytical and experimental study for simple setups of airfoil, and the investigation on the effects of vortical or structural parameters on vortex impingement. The second part starting in Section IV develops a simple model for the self-rotation of an infinite, finite-core vortex that is initially straight and is given a small-amplitude, planar sinusoidal deformation along its axis. The rotation rate from asymptotic analysis is compared against high-fidelity computations by Garmann and Visbal [11] for a Batchelor vortex emerging from an inflow boundary. The predicted and computed rotation rates are compared and contrasted with respect to the flow parameters and the different physical scenarios of the theoretical and computational setups.

PART I

8.2 MATHEMATICAL FORMULATION

Figure 8-1 illustrates the model problem of a Joukowski airfoil on elastic supports in two-dimensional uniform flow with an incident line vortex Γ and the vorticity field Σ shed into the wake. All vortices are defined to have positive circulation in the anticlockwise direction. The strength of the trailing-edge vortex γ_n satisfies the Kutta condition, and its motion obeys the emended Brown and Michael equation [12]. The mathematical formulation of the aeroelastic system is now described.

8.2.1 Mapping

The conformal mapping of t`he Joukowski airfoil between the physical z and the mapped ζ-plane is described by:

$$\zeta(z) = \frac{1}{2}\left(z + \sqrt{z^2 - 4\lambda^2}\right) - f_0. \tag{8-1}$$

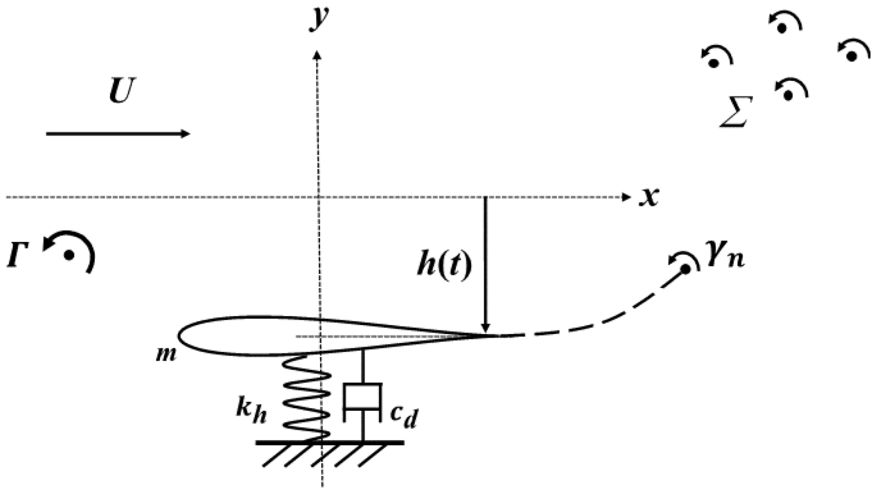

Figure 8-1: Schematic of the Generalized Model Problem of an Incident Vortex Interaction with a Symmetric Joukowski Airfoil on Elastic Translational Support in a Uniform Flow, Where U is the Flow Speed and $\mathrm{h(t)}$ Denotes the Displacement of the Airfoil. The airfoil can be considered as a damped harmonic oscillator with mass m damping coefficient $\mathrm{c_d}$, and spring stiffness $\mathrm{k_h}$, Γ denotes the incident line vortex, and γ_n is the tethered trailing-edge vortex whose motion is determined by the emended Brown and Michael equation. Σ is the set of free vortices generated at the airfoil trailing edge due to unsteady airfoil loads in response to the incident line vortex or the airfoil motion. The airfoil has zero angle of attack.

Using Equation 8-1, the Joukowski airfoil in the physical z-plane ($z = x + iy$) with its trailing edge locating at $(2\lambda, 0)$ is mapped to a circle with radius $r = 1$ in the f-plane ($f = f_1 + if_2$), as shown in Figure 8-2. Note the offset of the circle center at $f_0 = f_{x0} + if_{y0}$ and the corresponding trailing edge at $(2\lambda, 0)$. For the symmetric Joukowski airfoils considered in this work, $f_{y0} = 0$. The unit circle in the f-plane is then shifted by an elementary mapping to the origin in the ζ-plane.

When time-dependent airfoil motions are considered, Equation 8-1 becomes:

$$\zeta(s) = \frac{1}{2}\left[s(z,t) + \sqrt{s^2 - 4\lambda^2}\right] - f_0, \tag{8-2}$$

where $s(z,t) = z - ih(t)$. The airfoil displacement $h(t)$ may be either prescribed or be part of the solution, as in the case of aeroelastic airfoil motions.

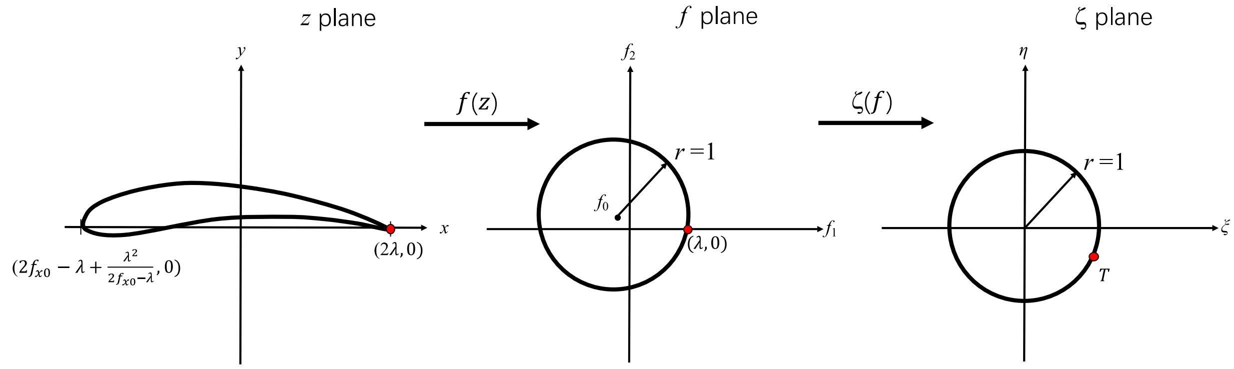

Figure 8-2: Successive Mappings of a Generalized Joukowski Airfoil in the Physical z-Plane to a Unit Circle Centered at the Origin in the ζ-Plane, T is the Trailing Edge Location.

8.2.2 Flow Complex Potential

The complex potential of the flow is:

$$w(\zeta) = w_\gamma + w_\Gamma + w_h + U\left(\zeta + f_0 + \frac{\lambda^2}{\zeta + f_0}\right), \tag{8-3}$$

where $w_\gamma(\zeta)$, $w_\Gamma(\zeta)$, and $w_h(\zeta)$ are the contributions due to the shed and free vorticity field, the incident vortex, and the airfoil motion, respectively. The last term of Equation 8-3 represents the uniform background flow.

The complex potential of the incident vortex $w_\Gamma(\zeta)$ is determined from the model of a vortex moving around a cylinder [13], which yields,

$$w_\Gamma(\zeta) = -\frac{i\Gamma}{2\pi}\log(\zeta - \zeta_\Gamma) + \frac{i\Gamma}{2\pi}\log\left(\zeta - \frac{1}{\zeta_\Gamma^*}\right) - \frac{i\Gamma}{2\pi}\log\zeta, \tag{8-4}$$

where the last two terms guarantee that the total circulation inside the cylinder is initially zero, and the asterisk superscript denotes the complex conjugate. Similarly, the complex potential of the vortices shed into the wake is:

$$w_\gamma(\zeta) = \sum_{k=1}^{n}\left(-\frac{i\gamma_k}{2\pi}\log(\zeta - \zeta_{\gamma_k}) + \frac{i\Gamma}{2\pi}\log\left(\zeta - \frac{1}{\zeta_{\gamma_k}^*}\right)\right). \tag{8-5}$$

By appeal to Kelvin’s theorem, the bound vorticity inside the cylinder at any time has total circulation $-\sum_{k=1}^{n}\gamma_k$, which is used to compute the aerodynamic lift force.

The complex potential of the airfoil motion is [14],

$$w_h(\zeta) = iV\left(\zeta - \frac{1}{\zeta}\right), \tag{8-6}$$

where $V = dh/dt$ is the instantaneous velocity of the airfoil in the downward direction.

8.2.3 Vortex Shedding and the Emended Brown and Michael Equation

The motions of the shed vortices are described by the emended Brown and Michael equation [12],

$$\frac{dx_{\gamma_n}}{dt}\cdot\nabla\Psi_j + \frac{\Psi_j}{\gamma_n}\frac{d\gamma_n}{dt} = v_{\gamma_n}\cdot\nabla\Psi_j, j = 1{,}2, \tag{8-7}$$

where x_{γ_n} represents the location of a shed vortex tethered to the trailing edge with circulation γ_n, and v_{γ_n} is the fluid velocity when the local velocity induced by γ_n is excluded. Here a Cartesian coordinate system is considered, where $x \equiv (x, y)$. $\Psi_j(x,t)$ denotes the stream function of the complex potential of the flow in the j-direction. For a Joukowski airfoil mapped to the ζ-plane, the components of the stream function are [15]:

$$\Psi_1 = Im\left\{\zeta + \frac{1}{\zeta}\right\} \ and\ \Psi_2 = Im\left\{-i\left(\zeta - \frac{1}{\zeta}\right)\right\}. \tag{8-8}$$

The instantaneous circulation of the tethered vortex $\gamma_n(t)$ is obtained by enforcing the Kutta condition at the trailing edge of each instant in time,

$$\gamma_n(t) = \frac{\left|T^*\zeta_{\gamma_n} - 1\right|^2}{\left|\zeta_{\gamma_n}\right|^2 - 1}\left(\frac{2\Gamma(1 - Re\{T^*\zeta_\Gamma\})}{|T^*\zeta_\Gamma - 1|^2} - \sum_{k=1}^{n-1}\gamma_k\frac{\left|\zeta_{\gamma_k}\right|^2 - 1}{\left|T^*\zeta_{\gamma_k} - 1\right|^2} - 2\pi V Re\{T^*\}\right), \tag{8-9}$$

in which T^* is complex conjugate of the trailing edge T location ($T = \lambda - f_0$) in the ζ-plane. The tethered trailing-edge vortex is released and becomes a free vortex when $d\gamma_n/dt$ changes sign, at which time another tethered vortex is placed at the airfoil trailing edge whose motion and instantaneous circulation are determined by Equation 8-7 and Equation 8-9, respectively.

Equation 8-7 can be rearranged into the equivalent scalar form:

$$\frac{dz^*_{\gamma_n}}{dt} + (H_1 - iH_2)\frac{1}{\gamma_n}\frac{d\gamma_n}{dt} = v^*_{\gamma_n}. \tag{8-10}$$

where $z^*_{\gamma_n} = x - iy$ and $v^*_{\gamma_n} = v_x - iv_y$. The functions H_1 and H_2 involve the stream functions Ψ_j and their derivatives. Equation 8-10 is the equivalent scalar form of the emended Brown and Michael equation, which is employed for the theoretical analysis in this work. Specific details related to the derivation of Equation 8-10 and the expressions of H_1 and H_2 from Ref. [16] are presented in the Appendix for reference. Also,

$$v^*_{\gamma_n} = -\frac{i\gamma_n\zeta''\left(z_{\gamma_n}\right)}{4\pi\zeta'\left(z_{\gamma_n}\right)} + F'_{\gamma_n}\left(z_{\gamma_n}\right), \tag{8-11}$$

is the complex velocity of the shed vortex with self-potential velocity excluded [13], and the first term on the right side of Equation 8-11 is the so-called Routh's correction [17], and the second term is the desingularized complex velocity at z_{γ_n},

$$F'_{\gamma_n}\left(z_{\gamma_n}\right) = \zeta'\left[\frac{dw}{d\zeta} + \frac{i\gamma_n}{2\pi}\frac{1}{\zeta - \zeta_{\gamma_n}}\right]. \tag{8-12}$$

8.2.4 Kinematics of the Incident and Free Vortices

Similarly, the complex velocity of the incident line vortex at s_Γ is [13]:

$$\frac{ds^*_\Gamma}{dt} = -\frac{i\Gamma\zeta''(s_\Gamma)}{4\pi\zeta'(s_\Gamma)} + F'_\Gamma(s_\Gamma), \tag{8-13}$$

where:

$$F'_\Gamma(s_\Gamma) = \zeta'\left[\frac{dw}{d\zeta} + \frac{i\gamma_n}{2\pi}\frac{1}{\zeta - \zeta_\Gamma}\right]. \tag{8-14}$$

Also, the equation of motion for each of the $n - 1$ free vortices is:

$$\frac{ds^*_{\gamma_k}}{dt} = -\frac{i\gamma_k\zeta''\left(s_{\gamma_k}\right)}{4\pi\zeta'\left(s_{\gamma_k}\right)} + F'_{\gamma_k}\left(s_{\gamma_k}\right), \tag{8-15}$$

where:

$$F'_{\gamma_k}(s_{\gamma_k}) = \zeta' \left[\frac{dw}{d\zeta} + \frac{i\gamma_k}{2\pi} \frac{1}{\zeta - \zeta_{\gamma_k}} \right]. \tag{8-16}$$

8.2.5 Airfoil Motion and Loads

The airfoil moves aeroelastically under its lift force and the equation of motion of the elastic mount,

$$m \frac{d^2 h}{dt^2} + c_d \frac{dh}{dt} + k_h h = -L', \tag{8-17}$$

where $h(t)$ denotes the vertical displacement of the airfoil (positive downward). The airfoil suspension is modelled as a linear harmonic oscillator with mass m, damping coefficient c_d, and spring stiffness k_h. The unsteady lift force L' is determined by [18]:

$$L' = \rho U \Gamma_a(t) + \rho \int_0^c \frac{\partial}{\partial t} \Gamma_a(x,t) dx. \tag{8-18}$$

8.3 RESULTS

In this section we first compare the results of a simpler case against Manela's work [19] to validate the mathematical framework, then plot new findings for the aeroelastic case. The model equations are nondimensionalized by $\bar{x} = x/(2\lambda)$, $\bar{y} = y/(2\lambda)$, $\bar{t} = Ut/(2\lambda)$, which produce the following parametric groups that define the numerical simulations [20]:

$$\bar{\Gamma} = \frac{\Gamma}{4\pi U \lambda}, \quad \bar{\omega}_n = \frac{2\lambda\omega_n}{U}, \quad \mu = \frac{4\rho_a l_t}{\pi \rho c}, \quad \xi = \frac{c_d}{2m\omega_n}.$$

The last three parameters are related to the airfoil suspension, where ρ_a is the airfoil density, $\omega_n = \sqrt{k_h/m}$ is the natural frequency of the suspension. The airfoil chord length and λ are related by $c = 3\lambda - 2f_{x_0} - \lambda^2/(2f_{x_0} - \lambda)$.

8.3.1 Comparison with Experiments

First, a comparison is made with an experimental study by Peng and Gregory [21] on the interaction of an incident vortex with an NACA0012 airfoil immersed in uniform flows. They investigated the vortex decay during the interaction, and the vortex trajectories with different initial vertical vortex locations. In our current study, we used a symmetric Joukowski airfoil with 12% thickness by setting the circle center f_0 to $(-0.092, 0)$. Different dimensionless initial vertical locations are set to be $\bar{y}_{\mathrm{initial}} = \{0, -0.1, -0.2, -0.3\}$. It is worth noting that the decaying of vortex strength is not considered in current analytic work due to inviscid model setup. We choose the same initial vortex strength $\Gamma/(Uc) = -0.427$ (clockwise), c is the chord length of the airfoil. Figure 8-3 shows the comparison between current inviscid model simulation and experimental measurements. The experimental results are marked in asterisks with different colors for different initial vortex positions, and the associated simulation results are shown in dashed lines with different colors. In the experiment, the viscous mechanism becomes dominant when the vortex is enough far from the airfoil and leads to mild vortex decay due to the shear stress near the surface of the airfoil. Therefore, for the initial vortex locations at -0.2 and -0.3, both blue and black dash lines agree with the experiment results when the vortex is far from the airfoil, and small deviations of the results are observed after the vortex passing by $x/c > -0.3$ which may due to the displacement thickness of the boundary layer.

However, for the initial vortex location at -0.1 and 0, large deviations of the vortex trajectories between the current simulation and the experiments when the vortex is in the proximity of the airfoil. From Figure 16(b) in Peng and Gregory [21] although a significant loss in vortex strength (30% to 40%) is found due to the deceleration effects of the strong adverse pressure gradient near the leading edge of the airfoil, the vortex decay may still not explain the large deviations of the results. Need to note that for the initial location at 0, the experiment result shows that the vortex collides with the airfoil leading edge due to the large radius of vortex core ($0.1c$), and its trajectory is cut into two separate branches either below or above the airfoil, and such results are not reflected by current simulation result due to a point-vortex setup. Thus, our inviscid simulation model may not well predict the experimental measurements when the vortex is near the airfoil due to the complexity of the vortex decay, the vortex boundary-layer interaction, the vortex leading edge interaction, viscous effects, etc. However, our model shows good agreement with the experimental results when there is enough distance between the vortex and the airfoil.

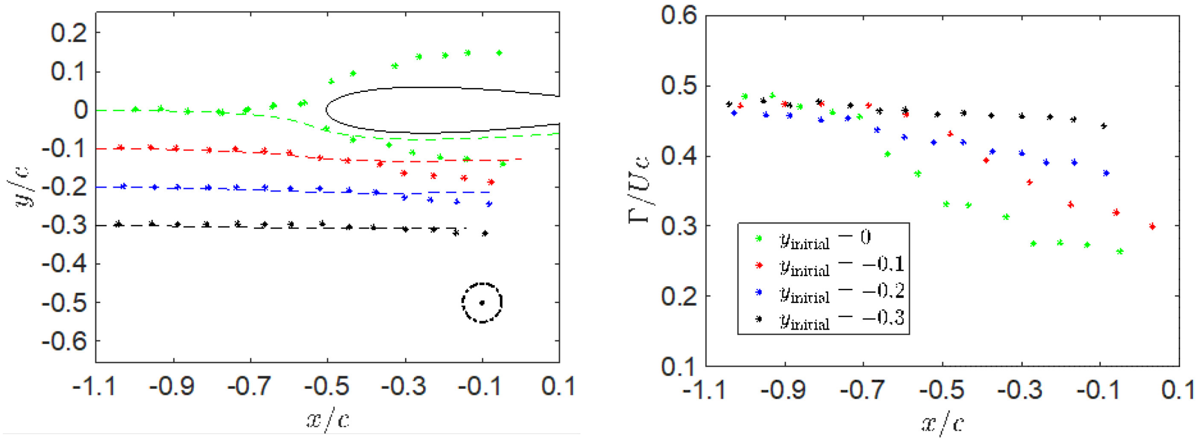

(a) **(b)**

Figure 8-3: Comparisons of Analytic Simulation and Experimental Measurement [21] on Vortex Trajectories and Strength with Different Initial Vertical Locations at $y/c = 0, -0.1, -0.2$, and -0.3. Curves with asterisks are experimental results, dash lines are analytic results. The circle in (a) denotes the size vortex core in the experiment, whose diameter is $0.1c$.

Another comparison is made between current analytic simulation model and another experimental work by Peng and Gregory [22]. The initial vortex strength is set to be $\Gamma/(Uc) = -0.196$ (clockwise), and vortex decay is also not considered in the analytic simulation. Figure 8-4(a) shows the comparisons of vortex trajectories for different initial locations at 0.05 and -0.05, the dash lines denotes the analytic results, and the curve in asterisks are the experimental results. Similar to the results shown in Figure 8-3 large deviations of vortex trajectories are observed in Figure 8-4(a) when the separation distance between the vortex and the airfoil is small. For the initial location at 0.05, however, the vortex passes above the airfoil in the experimental measurements, while it still passes below the airfoil in the current simulation. Attention is paid to the conditions that makes the vortex pass above the airfoil. First, by fixing the vortex strength, we study the effect of different vortex locations in determining the vortex trajectory. Figure 8-4(b) shows that the increasing of vortex initial location $\bar{y}_{\text{initial}}$ significantly affects the corresponding vortex trajectories. As the location increases to 0.111, the vortex finally passes above the airfoil and the vortex trajectory offsets downward due to its clockwise direction and its interaction with the airfoil. It is worth mentioning that the effect of vortex strength is also considered in the current study, by fixing the initial location, our simulation result shows that the decreasing of vortex strength cannot make the vortex pass above the airfoil due to the lower initial vortex location.

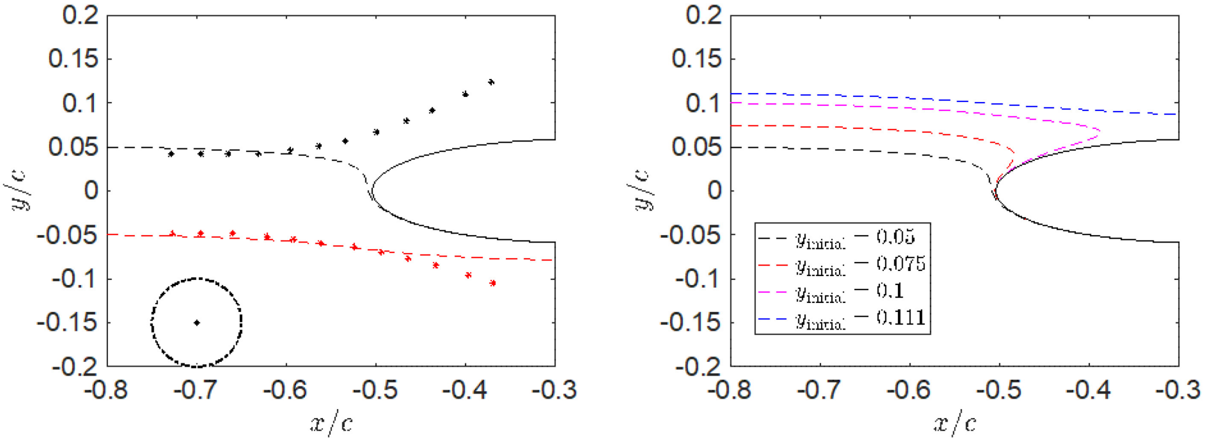

(a) **(b)**

Figure 8-4: (a) Comparisons of Analytic Simulation and Experimental Measurement [22] on Vortex Trajectories with Different Initial Vertical Locations at $y/c = 0.05$ and -0.05, (b) Vortex Paths with Different Initial Vortex Locations at 0.05, 0.075, 0.1 and 0.111. Curves with asterisks are experimental results, dash lines are analytic results. The circle in (a) denotes size of the vortex core in the experiment, whose diameter is $0.1c$.

8.3.2 Aeroelastic Case

Attention is now turned to the aeroelastic interactions between the airfoil, the incident, wake, and bound vorticity. The conditions to achieve direct vortex impingement on the airfoil are explored with respect to different aerodynamic parameters. The numerical simulations are initialized with initial shed vortex location, $\bar{z}_\gamma(0) = z_\gamma(0)/(2\lambda) = (1, 10^{-6})$ and the initial x-coordinate of the incident vortex is $\Delta\bar{x} = x_0(0)/(2\lambda) = -20$. The mass ratio is fixed to $\mu = 10$, which is representative of an aluminum airfoil with 12% thickness in air. The airfoil thickness is controlled by setting the circle center f_0 in Equation 8-2 time-dependent) to $(-0.092,0)$, and the angle of attack is not considered. Structural damping is neglected ($\xi = 0$) in all cases presented in this work.

In terms of the initial conditions, the mathematical model is controlled by two dimensionless parameters: the strength of the incident vortex, $\bar{\Gamma}$, and the reduced natural frequency of the oscillator, $\bar{\omega}_n$. Different initial locations of the incident vortex result in the passage of the incident vortex either above or below the airfoil. Here, the bisection method is used to infer the initial vortex position $\Delta\bar{y}$ to achieve direct airfoil impingement given $\bar{\Gamma}$ and $\bar{\omega}_n$. The accuracy of $\Delta\bar{y}$ is controlled by the tolerance of the bisection method, which is set to be $\bar{\emptyset} = \emptyset/(2\lambda) = 0.01$ in the present work. Figure 8-5 shows the incident vortex trajectories for different initial vortex positions and the corresponding time histories of the airfoil circulation. Figure 8-5(a) compares the trajectories of the incident vortex in the aeroelastic simulations with different initial locations, including the impingement-occurring location $(\Delta\bar{x}, \Delta\bar{y}) = (-20, -0.31)$ determined by the bisection method, respectively, against the steady streamlines of the flow field in the absence of vortices for visual reference. For the initial location (20, -0.4), the incident vortex follows initially the steady streamline from the left inflow locations and moves below the airfoil at large times. As the initial location moves up to the impingement location (20, -0.31), the incident vortex aligns with the steady streamline at early times. However, near the airfoil, the vortex path deviates backward under influence of the shed vorticity and airfoil motion and moves along a path near the stagnation streamline at the airfoil. As the initial location of the incident vortex moves upward, smaller deviation of the path of the incident vortex is observed in Figure 8-5(a).

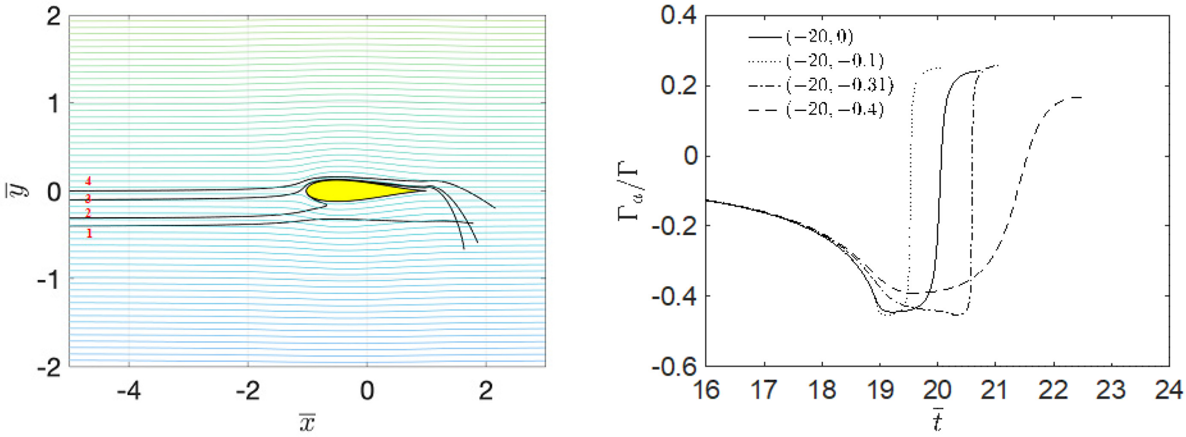

(a) **(b)**

Figure 8-5: Time Histories of Incident Vortex Trajectories and the Bound Circulation for Different Initial Vortex Positions, with Reduced Natural Frequency $\bar{\omega}_n = 0.5$, and the Strength of the Incident Vortex $\bar{\Gamma} = 0.1$. (a) Time-varying trajectories of the incident line vortex Γ (denoted 1, 2, 3, 4) resulting from an incident vortex Γ with different initial positions at $(-20, -0.4)$, $(-20, -0.31)$, $(-20, -0.1)$, and $(-20, 0)$ past along a symmetrical Joukowski airfoil with 12% thickness. The streamlines in the flow field are for the case where all vortices are absent, and the motion of the incident vortex across these lines under the influence of the airfoil is noted; (b) Time variations of corresponding bound circulation on the airfoil during the shedding of the first two trailing-edge vortices.

Figure 8-5(b) presents the time variations of the airfoil circulation for the shedding of the first two trailing-edge vortices. For the cases when the initial vortex location is $(-20, 0)$ and $(-20, -0.1)$, which causes the incident vortex to move above the airfoil, the corresponding magnitudes of the airfoil circulation time histories increase similarly at early times. These time histories have a sharp change when the incident vortex passes closest to the airfoil due to the shedding of the second vortex. However, for the case when the initial vortex will moves below the airfoil, a small limit and an extended flat response in the airfoil circulation with respect to time can be seen in the dashed line of Figure 8-5(b), which may infer a weak interaction between the incident vortex and the airfoil. When the initial vortex location is set to $(-20, -0.31)$, which results in vortex impingement, a similar variation of the airfoil circulation can be observed in the dash-dot line of Figure 8-5(b), compared with the solid line and the dotted line. However, the shedding of the second vortex is delayed when the incident vortex passes near the stagnation streamline at the airfoil.

Furthermore, the effects of different aeroelastic parameters such as $\bar{\Gamma}$ and $\bar{\omega}_n$ on the selection of initial incident vortex locations to achieve vortex impingement are studied. In testing the current numerical scheme, the vortex impingement commonly occurs in the shedding of the first trailing-edge vortex, in which time the downwash effect of the wake may be neglected. The tolerance of the bisection method is set to be $\bar{\emptyset} = \emptyset/(2\lambda) = 0.01$ in the present work. This tolerance produces accurate results, but the solver developed by the authors did not permit smaller tolerance values due to the sensitivity of the numerical scheme to the complexity of aerodynamic model.

Figure 8-6(a) presents results for the vortex initial vertical position to achieve direct airfoil impingement as a function for $\bar{\omega}_n$ for $\bar{\Gamma} = 0.1$. In these simulations, the downwash effect of the airfoil wake has been neglected in the aerodynamic model to achieve a reasonable numerical tolerance. It is clear from Figure 8-6(a) that there are upper and lower asymptotic limits on the values of $\Delta\bar{y}$, where $\Delta\bar{y} \rightarrow -0.17$ for small values of $\bar{\omega}_n$, and $\Delta\bar{y} \rightarrow -0.328$ for large values. Recalling that these simulations are performed at fixed mass ratio, $\mu = 10$, and have no structural damping, ξ, the lower and upper limits correspond to negligible spring restoring force (free airfoil) and dominant spring (rigid support) limits. Importantly, the results demonstrate a monotonic change in initial vortex position $\Delta\bar{y}$ with respect to the reduced natural frequency for a given value, and these values of $\Delta\bar{y}$ are bounded by the low and high frequency limits of $\bar{\omega}_n$.

Next consider the case of a fixed reduced natural frequency, $\bar{\omega}_n = 0.5$, where the initial incident vortex locations $\Delta\bar{y}$ can be determined as a function of the incident vortex strength $\bar{\Gamma}$ as shown in Figure 8-6(b). In Figure 8-6(b), the monotonically decreasing value of $\Delta\bar{y}$ with increasing $\bar{\Gamma}$ indicates the need for lower vortex positioning for direct impingement for stronger incident vortices.

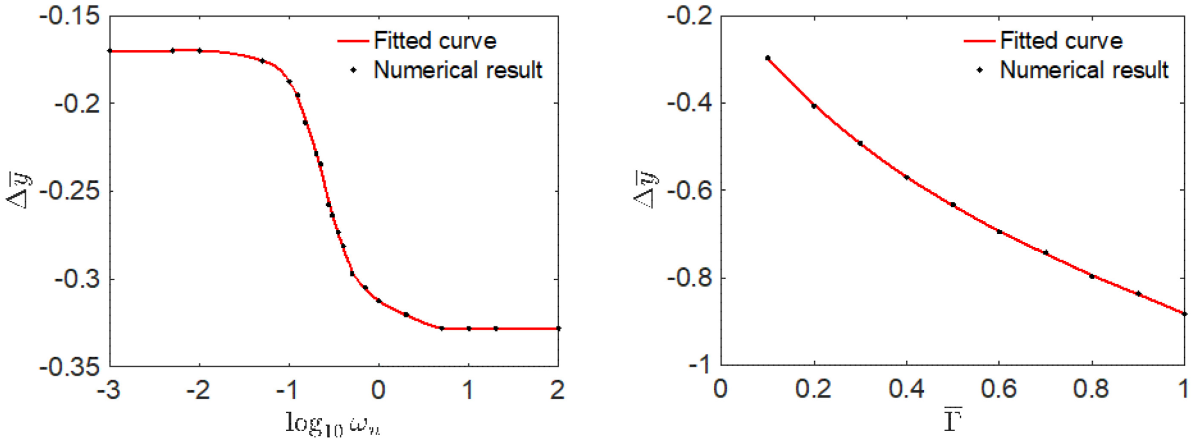

(a) **(b)**

Figure 8-6: (a) Effect of Reduced Natural Frequency $\bar{\omega}_n$ on the Initial Incident Vortex Vertical Position $\Delta\bar{y}$ to Achieve Direct Airfoil Impingement. Incident vortex has a strength of $\bar{\Gamma} = 0.1$ and moves past a symmetric Joukowski airfoil with 12% thickness; (b) Variations of selection of initial incident vortex location $\Delta\bar{y}$ with varying strength of incident vortex $\bar{\Gamma}$ when vortex impingement occurs, with reduced natural frequency $\bar{\omega}_n = 0.5$.

PART II

8.4 SELF-INDUCED ROTATION OF TRAILING VORTICES

Self-induced motion arises when vortices are deformed or curved. A kinematical understanding of these structures is important for the trajectory prediction of trailing vortices that result from either prescribed or aeroelastic motions of an aircraft wing. Seminal computational work by Garmann and Visbal [11] into wing encounters with such vortices led to the observation that a these vortex structures rotated as they advected away from the inflow condition towards the wing. This unexpected result motivated a theoretical investigation to determine whether or not the vortex rotation was indeed a fluid dynamical effect or some other effect, such as a numerical error or long-range vortex-wing interaction.

To this end, the work of Bliss [23] on the kinematics of perturbed trailing vortices was revisited and recast into parameters suitable to for modern characterization of the Batchelor trailing vortex and other vortex types. The theoretical analysis assumes a sinusoidal distortion of an infinitely long vortex, which is different from the computational situation of prescribing a vortex plane on the inflow boundary and allowing it to evolve downstream. Nonetheless, the analysis supports the conclusion that the rotation of the vortex structure is due to the self-induced motion, where the direction of vortex rotation is observed and predicted to be in the opposite direction of the rotation of the flow within the vortex core. Preliminary quantitative predictions from theory furnish rough estimates of the vortex rotation observed in Ref. [11] which motivates a refinement of the theoretical model to include the effect a variation in the swirl and axial velocity profiles along axis of the vortex.

8.4.1 Mathematical Model for Vortex Location

Bliss [23] predicts the dynamics of a sinusoidally-perturbed finite-core vortex that is initially straight with axisymmetric (but otherwise arbitrary) swirl and axial velocity radial profiles. The spatial perturbation of the vortex centerline is assumed to be planar, i.e., $a_y \sin kx$, where k is related to the wavelength λ by $k = 2\pi/\lambda$. Widnal et al. [24] survey the matched asymptotic procedure of Bliss [23], where the flow solutions internal and external to the vortex core are matched using the ratio of the vortex core radius to the radius of curvature, $\epsilon = r_0/R \ll 1$. Choosing the minimum value of the local curvature of the perturbation, the asymptotic matching parameter may be written as:

$$\epsilon = (2\pi)^2 \frac{r_0 a_y}{\lambda^2}. \tag{8-19}$$

The perturbed vortex executes a rigid body rotation about the unperturbed vortex axis with constant angular velocity (cf. Equation (6.39) in Ref. [23]):

$$\Omega_p = \frac{1}{2}\kappa k^2 \left[\ln\frac{1}{kr_0} + A - C + (\ln 2 - \gamma)\right], \tag{8-20}$$

where $\kappa = \Gamma/(2\pi)$, Γ is the vortex circulation, γ is Euler's constant, and A and C are constants related to the initial swirl and axial velocity profiles, respectively. Note that the rotation due to Ω_p is in the direction *opposite* to the rotation of fluid inside the vortex core.

The constant A is defined by (cf. Equation (3.71) in Ref. [23]):

$$A \equiv I_1(s) - \ln s, \tag{8-21}$$

where:

$$I_1(s) = \int_0^{\bar{r}} \bar{r} v_0^2 d\bar{r} \;\; for\; 0 \le \bar{r} < s. \tag{8-22}$$

The swirl velocity profile must satisfy the form:

$$v_0 = \begin{cases} v_0(\bar{r}) & 0 \le \bar{r} \le s, \\ 1/\bar{r} & s \le \bar{r} \le \infty, \end{cases} \tag{8-23}$$

and s is chosen by the asymptotic matching procedure such that $v_0 = 1/\bar{r}$ for $\bar{r} > s$. Similarly, the constant C is defined by (cf. Equation (3.80) in Ref. [23]):

$$C \equiv -I_3(s), \tag{8-24}$$

where:

$$\int_0^{\bar{r}} \bar{r}^2 \frac{d(w_0^2)}{d\bar{r}} d\bar{r} = \begin{cases} I_3(s) & 0 \le \bar{r} \le s, \\ -C & s < \bar{r} < \infty. \end{cases} \tag{8-25}$$

and:

$$w_0 = \begin{cases} w_0(\bar{r}) & 0 \le \bar{r} \le s, \\ 0 & s < \bar{r} < \infty. \end{cases} \tag{8-26}$$

It must be emphasized that, despite the form of Equations 8-21 and 8-24, A and C are constants and do not depend on s.

For a Batchelor vortex [25] with a decaying vortex core, Equations (4.32) and (4.48) in Ref. [23] provide the following nondimensional swirl and axial velocity profiles,

$$v_0 = \frac{1}{\bar{r}}\left[1 - e^{-\bar{r}^2}\right], w_0 = \begin{cases} w_0(\bar{r}) & 0 \leq \bar{r} \leq s, \\ 0 & s < \bar{r} < \infty. \end{cases} \tag{8-27}$$

$$w_0 = \alpha e^{-\bar{r}^2} \tag{8-28}$$

where the velocities have been rescaled by κ/r_0 [24] and α is a specified nondimensional value. Bliss [23] shows that these velocity distributions lead to:

$$A = \frac{\gamma}{2} - \frac{1}{2}\ln 2 \approx -0.058, \tag{8-29}$$

$$C = \frac{\alpha^2}{2} \tag{8-30}$$

Note that C is positive semi-definite, i.e. the effect of the axial velocity profile on the vortex motion does not depend on whether or not there is an axial velocity excess or deficit.

We now recast the results of Bliss [23] in terms of the vortex parameters relevant to the computational study carried out by Garmann and Visbal [11]. In their formulation, the dimensional swirl and axial velocity profiles of the vortex imposed on the inflow boundary condition are:

$$v_0 = \frac{\Gamma}{2\pi r}\left[1 - e^{-(r/r_0)^2}\right], \tag{8-31}$$

$$w_0 = \Delta u \, e^{(r/r_0)^2}, \tag{8-32}$$

again noting that the sign of Δu is irrelevant on the vortex rotation within the context of the theoretical model, (cf. Equation 8-30). The relationship between the swirl and axial velocities is the swirl parameter q defined by:

$$q = \frac{\Gamma}{2\pi r_0 \Delta u} = \frac{\kappa}{r_0 \Delta u}. \tag{8-33}$$

Now nondimensionalizing the velocities in Equations 8-31 and 8-32 by κ/r_0in the same manner as Bliss [23] and letting $\bar{r} = r/r_0$,

$$v_0 = \frac{1}{\bar{r}}\left[1 - e^{-(\bar{r})^2}\right], \tag{8-34}$$

$$w_0 = \frac{1}{q} e^{-(\bar{r})^2}, \tag{8-35}$$

where we recover the same swirl velocity profile as Equation 8-27 and identify $\alpha = 1/q$.

The rotation rate of the vortex Equation 8-20 may now be expressed as:

$$\Omega_p = 2\pi^2 q \frac{\Delta u \, r_0}{\lambda^2} \left[\ln \frac{\lambda}{2kr_0} + \frac{1}{2} q^{-2} + \frac{1}{2} (\ln 2 - \gamma) \right]. \tag{8-36}$$

Note that the rotation rate of the vortex structure does not depend on the amplitude of the sinusoidal perturbation a_y; however, this value remains important in establishing the range of validity for the theoretical model per Equation 8-19.

Let us now presume that the vortex structure advects with a uniform background flow U such that its change in location may be written as $\Delta x = Ut$ and the change in angular displacement of the vortex can be expressed by $\theta_p = \Omega_p t = \Omega_p \Delta x / U$.

$$\theta_p = 2\pi^2 q \frac{\Delta u}{U} \frac{\Delta x \, r_0}{\lambda^2} \left[\ln \frac{\lambda}{2\pi r_0} - \frac{1}{2} q^{-2} + \frac{1}{2} (\ln 2 - \gamma) \right]. \tag{8-37}$$

8.4.2 Comparison with Computational Results

Garmann and Visbal [11] use the following parameters to define their trailing vortex, where the lengths are referenced to an airfoil chord length c.

$$q = 2.0$$

$$\Delta u = 0.4U$$

$$r_0 = 0.1c$$

$$\lambda = 5c$$

$$a_y = 0.25c, 0.5c$$

These values furnish the result:

$$\theta_p = 0.1268 \frac{\Delta x}{c} = 7.26 \frac{\Delta x}{c}, \tag{8-38}$$

where the amount of vortex rotation at locations $\Delta x / c = 5$ and 9.5 are $\theta_p = 36.3°$ and $69.0°$, respectively. We underscore that these results are based upon an assumption that the vortex centerline continues to remain planar as the vortex structure rotates about the axis of the originally undeformed (and axially uniform) vortex; the vortex in Ref. [11] continues to evolve downstream of the inflow condition and is not strictly periodic in the streamwise direction. For the parameters in Ref. [11], the logarithm term in Equation 8-37 dominates the terms in the square brackets. Also, it should be noted that the values of the asymptotic matching parameter are $\epsilon = 0.039$ and 0.079 for $a_y = 0.25c$ and $0.5c$, respectively. The theoretical predictions for θ_p are independent of the amplitude of the vortex deformation, a_y.

In Figure 7 of Ref. [11], the sinusoidal, linear motion of the vortex at the inflow persists downstream as the entire vortex structure rotates, particularly for the small-amplitude case where $a_y = 0.25c$. For this case at $\Delta x / c = 5$ and 9.5, $\theta_p \approx 16°$ and $47°$, which are less than predicted by the Bliss theory. However, θ_p increases faster than a linear function of the streamwise distance, indicating that the differences between the physical scenarios of the theory and computation, as well as perhaps the evolution of the swirl and axial velocity profiles in the computation, impact the rotation of the vortex structure.

8.5 CONCLUSIONS

Part I of this chapter simulates the aeroelastic interactions of an incident line vortex with a symmetric Joukowski airfoil of 12% thickness on an elastic suspension. The mathematical framework is modelled by using dynamic conformal mapping techniques. The dynamical problem for the incident vortex motion and trailing edge wake evolution is studied using the potential flow theory and the Brown and Michael equation, and thin airfoil theory is applied to analyze the aeroelastic motion of the airfoil with the vortical field.

Results from the mathematical framework are compared against recent experimental study by Peng and Gregory [21], where the present simulations match well with the experiments when the vortex is far from the airfoil with mild decay of strength. However, the inviscid model developed in this work may not be used to simulate the vortex motions near the airfoil due to multiple aspects of influence, such as viscous vortex-boundary-layer interaction, vortex decay, or viscous vortex-leading-edge interaction. An additional comparison of the inviscid numerical model with the experimental campaign of Peng and Gregory [22] studies the effects of different vortex strength and initial locations on the vortex trajectories. The present simulation results show similar vortex trajectories to the experiments by increasing the initial vortex locations.

Apart from these comparisons for vortex interactions with fixed airfoils, the present work also extends consideration to the aeroelastic case, in which the conditions to achieve direct impingement of an incident line vortex with the elastically mounted airfoil are explored. The aeroelastic results of a symmetric Joukowski airfoil with 12% thickness demonstrate that the incident vortex follows initially the steady streamline in the uniform flow, but deviates backward and then moves along a path near the stagnation streamline at the airfoil near where the vortex impingement occurs. The numerical results also indicate a weak sensitivity of the vortex initial vertical position to the reduced natural frequency of the airfoil elastic suspension when this frequency is either small or large, but the initial vortex placement for airfoil impingement changes monotonically with the natural frequency in a specific range that depends on the vortex strength.

The work in Part I is an extension and combination of previous efforts in other work by Chen and Jaworski [10], [16], [20], involving similar gust-airfoil interaction problem with different model setups. The present framework can be extended to consider the vortex-airfoil response in air or water. The extension of this work may involve a corresponding acoustic analysis in the future.

Part II develops a simple predictive model for the self-induced rotation of a streamwise-oriented vortex with a planar, sinusoidal deformation along its axis. The small-deformation theory of Bliss [23] yields angular displacements of the vortex that are larger by more than a factor of two when compared against numerical simulations of undulating Batchelor vortices. The source of this analytical and numerical discrepancy is the subject of ongoing research and may be related to differences in configuration as well as the evolution of the vortex core and its influence on vortex kinematics that are not accounted for in Bliss's theory.

8.6 ACKNOWLEDGEMENTS

This work was supported in part by the Air Force Office of Scientific Research under AFOSR grants FA9550-15-1-0148 and FA9550-19-1-0095, monitored by Drs. Douglas Smith and Gregg Abate, and by the National Science Foundation under awards 1805692 and 1846852, monitored by Dr. Ronald Joslin. Preliminary results from this chapter appeared previously as parts of AIAA conference papers [16], [20], [26]. Results presented in Part I are under peer review for journal publication [27].

8.7 REFERENCES

[1] Rockwell, D., Vortex-body interactions, Annual Review of Fluid Mechanics, Vol. 30, 1998, pp. 199-229.

[2] Howe, M.S., Elastic blade-vortex interaction noise, Journal of Sound and Vibration, Vol. 177, No. 3, 1994, pp. 325-336.

[3] Manela, A., Sound generated by a vortex convected past an elastic sheet, Journal of Sound and Vibration, Vol. 330, No. 3, 2011, pp. 416-430.

[4] Manela, A., Nonlinear effects of flow unsteadiness on the acoustic radiation of a heaving airfoil, Journal of Sound and Vibration, Vol. 332, No. 26, 2013, pp. 7076-7088.

[5] Rockwell, D., and Knisely, C., The organized nature of flow impingement upon a corner, Journal of Fluid Mechanics, Vol. 93, No. 3, 1979, pp. 413-432.

[6] Ziada, S., and Rockwell, D., Vortex-leading-edge interaction, Journal of Fluid Mechanics, Vol. 118, 1982, pp. 79-107.

[7] Conlisk, A., and Rockwell, D., Modeling of vortex-corner interaction using point vortices, The Physics of Fluids, Vol. 24, No. 12, 1981, pp. 2133-2142.

[8] Conlisk, A., and Veley, D., The generation of noise in impinging vortex motion past a step, The Physics of Fluids, Vol. 28, No. 10 1985, pp. 3004-3012.

[9] Panaras, A., Numerical modeling of the vortex/airfoil interaction, AIAA Journal, Vol. 25, No.1, 1987, pp. 5-11.

[10] Chen, H., Vortex gust interactions with oscillating Joukowski airfoil, Master's thesis, Lehigh University, May 2018.

[11] Garmann, D., and Visbal, M., Unsteady interactions of a wandering streamwise-oriented vortex with a wing, 32nd AIAA Applied Aerodynamics Conference, Atlanta, GA, Paper AIAA-2014-2105, 2014.

[12] Howe, M.S., Emendation of the Brown & Michael equation, with application to sound generation by vortex motion near a half-plane, Journal of Fluid Mechanics, Vol. 329, 1996, pp. 89-101.

[13] Howe, M.S., Theory of vortex sound. Vol. 33, Cambridge University Press, United Kingdom, 2003.

[14] Batchelor, G.K., An introduction to fluid dynamics, Cambridge University Press, United Kingdom, 1967.

[15] Howe, M.S., Acoustics and aerodynamic sound, Cambridge University Press, United Kingdom, 2014.

[16] Chen, H., and Jaworski, J.W., Vortex interactions with Joukowski airfoil on elastic supports, AIAA Fluid Dynamics Conference, Atlanta, GA, Paper AIAA-2018-2907, 2018.

[17] Clements, R., An inviscid model of two-dimensional vortex shedding, Journal of Fluid Mechanics, Vol. 57, No. 2, 1973, pp. 321-336.

[18] Katz, J., and Plotkin, A., Low-Speed Aerodynamics. 2nd ed., Cambridge University Press, United Kingdom, 2001.

[19] Manela, A., and Huang, L., Point vortex model for prediction of sound generated by a wing with flap interacting with a passing vortex, The Journal of the Acoustical Society of America, Vol. 133, No. 4, 2013, pp. 1934-1944.

[20] Chen, H., and Jaworski, J.W., Aeroelastic trajectory selection of vortex gusts impinging upon Joukowski airfoils, 2019 AIAA Scitech Forum, San Diego, CA, Paper AIAA-2019-0897, 2019.

[21] Peng, D, and Gregory, J.W., Vortex dynamics during blade-vortex interactions, Physics of Fluids, Vol. 27, No. 5, 2015, 053104.

[22] Peng, D, and Gregory, J.W., Asymmetric distributions in pressure/load fluctuation levels during blade-vortex interactions, Journal of Fluids and Structures, Vol. 68, 2017, pp. 58-71.

[23] Bliss, D.B., The dynamics of curved rotational vortex lines, Master's thesis, Massachusetts Institute of Technology, 1970.

[24] Widnall, S.E., Bliss, D., and Zalay, A., Theoretical and experimental study of the stability of a vortex pair, Aircraft Wake Turbulence and its Detection, Springer, Boston, MA, 1971. pp. 305-338.

[25] Batchelor, G.K., Axial flow in trailing line vortices, Journal of Fluid Mechanics, Vol. 20, No. 4, 1964, pp. 645-658.

[26] Chen, H., and Jaworski, J.W., Aeroelastic encounters of spanwise vortex gusts and the self-rotation of trailing vortices, 2020 AIAA Scitech Forum, Orlando, FL, Paper AIAA-2020-0555, 2020.

[27] Chen, H., and Jaworski, J.W., Aeroelastic interactions and trajectory selection of vortex gusts impinging upon Joukowski airfoils, Journal of Fluids and Structures. Vol. 96, p. 103026, July 2020.

Appendix 1: SCALAR FORM OF EMENDED BROWN AND MICHAEL EQUATION

The original emended Brown and Michael equation is [12]:

$$\frac{dx_{\gamma_n}}{dt} \cdot \nabla\Psi_i + \frac{\Psi_i}{\gamma_n}\frac{d\gamma_n}{dt} = v_{\gamma_n} \cdot \nabla\Psi_i, i = 1{,}2. \tag{8-39}$$

Equation 8-39 can be expanded in vector formats as :

$$\left(\frac{dx}{dt}, \frac{dy}{dt}\right) \cdot \left(\frac{\partial\Psi_1}{\partial x}, \frac{\partial\Psi_1}{\partial y}\right) + \frac{\Psi_1}{\gamma_n}\frac{d\gamma_n}{dt} = \left(v_x, v_y\right) \cdot \left(\frac{\partial\Psi_1}{\partial x}, \frac{\partial\Psi_1}{\partial y}\right), \tag{8-40}$$

$$\left(\frac{dx}{dt}, \frac{dy}{dt}\right) \cdot \left(\frac{\partial\Psi_2}{\partial x}, \frac{\partial\Psi_2}{\partial y}\right) + \frac{\Psi_2}{\gamma_n}\frac{d\gamma_n}{dt} = \left(v_x, v_y\right) \cdot \left(\frac{\partial\Psi_2}{\partial x}, \frac{\partial\Psi_2}{\partial y}\right). \tag{8-41}$$

Equations 8-40 and 8-41 can be also expanded respectively as:

$$\frac{dx}{dt}\frac{\partial\Psi_1}{\partial x} + \frac{dy}{dt}\frac{\partial\Psi_1}{\partial y} + \frac{\Psi_1}{\gamma_n}\frac{d\gamma_n}{dt} = v_x\frac{\partial\Psi_1}{\partial x} + v_y\frac{\partial\Psi_1}{\partial y}, \tag{8-42}$$

$$\frac{dx}{dt}\frac{\partial\Psi_2}{\partial x} + \frac{dy}{dt}\frac{\partial\Psi_2}{\partial y} + \frac{\Psi_2}{\gamma_n}\frac{d\gamma_n}{dt} = v_x\frac{\partial\Psi_2}{\partial x} + v_y\frac{\partial\Psi_2}{\partial y}. \tag{8-43}$$

From Equations 8-42 and 8-43, the general scalar form of emended Brown and Michael equation may be written as:

$$\frac{dx}{dt} + \frac{\Psi_1\frac{\partial\Psi_2}{\partial y} - \Psi_2\frac{\partial\Psi_1}{\partial y}}{\frac{\partial\Psi_1}{\partial x}\frac{\partial\Psi_2}{\partial y} - \frac{\partial\Psi_2}{\partial x}\frac{\partial\Psi_1}{\partial y}}\frac{1}{\gamma_n}\frac{d\gamma_n}{dt} = v_x, \tag{8-44}$$

$$\frac{dy}{dt} + \frac{\Psi_1\frac{\partial\Psi_2}{\partial x} - \Psi_2\frac{\partial\Psi_1}{\partial x}}{\frac{\partial\Psi_1}{\partial y}\frac{\partial\Psi_2}{\partial x} - \frac{\partial\Psi_2}{\partial y}\frac{\partial\Psi_1}{\partial x}}\frac{1}{\gamma_n}\frac{d\gamma_n}{dt} = v_y. \tag{8-45}$$

Let:

$$H_1 = \frac{\Psi_1\frac{\partial\Psi_2}{\partial y} - \Psi_2\frac{\partial\Psi_1}{\partial y}}{\frac{\partial\Psi_1}{\partial x}\frac{\partial\Psi_2}{\partial y} - \frac{\partial\Psi_2}{\partial x}\frac{\partial\Psi_1}{\partial y}}, \tag{8-46}$$

$$H_2 = \frac{\Psi_1\frac{\partial\Psi_2}{\partial x} - \Psi_2\frac{\partial\Psi_1}{\partial x}}{\frac{\partial\Psi_1}{\partial y}\frac{\partial\Psi_2}{\partial x} - \frac{\partial\Psi_2}{\partial y}\frac{\partial\Psi_1}{\partial x}}. \tag{8-47}$$

Expressions 8-44 and 8-45 can be rearranged into:

$$\frac{dz_{\gamma_n}^*}{dt} + (H_1 - iH_2)\frac{1}{\gamma_n}\frac{d\gamma_n}{dt} = v_{\gamma_n}^*, \tag{8-48}$$

where $z_{\gamma_n}^* = x - iy$, and $v_{\gamma_n}^* = v_x - iv_y$.

Equation 8-48 can be regarded as a general scalar form of the emended Brown and Michael equation for future theoretical analyses. Once the stream function Ψ_i $(i = 1,2)$ is known, it is possible to get $\nabla\Psi_i = (\partial\Psi_i/\partial x, \partial\Psi_i/\partial y)$, thus H_1 and H_2 are known, and the vortex motion can be analyzed from Equation 8-48.

Chapter 9 – QUANTIFICATION AND MODELING OF DYNAMIC LIFT ON A DLR-F15 RESEARCH AIRFOIL WITH ACTIVE TRAILING-EDGE FLAP

Johannes Pohl and Richard Semaan
Technische Universität Braunschweig
GERMANY

Experimental investigations on a DLR-F15 research airfoil with an active trailing-edge flap are conducted. Two types of dynamic flap motions with different frequencies, amplitudes and starting and ending flap angles are investigated. Dynamic lift hysteresis is quantified and analyzed through a newly-proposed metric, the hysteresis measure H^*, which shows a maximum at relatively low actuation frequencies. A new empirical model for the unsteady lift is presented and assessed. A good agreement between the model predictions and the measured lift is found.

9.1 INTRODUCTION

Dynamic hysteresis is a complex flow phenomenon that is generated from airfoil motion. It is associated with the phase lead of non-circulatory flow effects and the phase lag due to vortex convection into the wake. This phase lag, and correspondingly the hysteresis, has been reported in the literature (e.g., Williams et al. [1]) to continually increase with both increasing oscillation amplitude and frequency. In other words, the airfoil response to the angle of attack change should increasingly get delayed with larger unsteadiness. This could lead to the situation where, while pitching beyond the critical static stall angle of attack, the flow may still remain attached. At high angles of attack near or exceeding the critical angle for static stall, the hysteresis behavior becomes more complicated. Here, the so-called dynamic stall becomes relevant. Dynamic stall was extensively investigated and categorized by McCroskey [2], where three types of dynamic stall was identified, stall onset, light stall, and deep stall. Much research has been conducted on dynamic hysteresis (Leishman [3], Gupta [4], Rival [5]) to better understand the various mechanisms driving this phenomenon. However, and to the authors' knowledge, there exist no metric that automatically and unbiasedly quantifies the various hysteresis types.

Modeling the lift coefficient of an airfoil undergoing dynamic hysteresis is key to understanding the physics involved. First attempts to model such flows were conducted by Wagner [6] and Theodorsen [7]. Whereas Wagner modeled the flow in the time domain, Theodorsen derived his model in the state-space. Both approaches rely on the same, rather restrictive, assumptions of a thin airfoil and small angle variations, which limits their application in many relevant applications. Since the publication of these two seminal works, many variations and improvements on the original formulation have been conducted (e.g., Brunton [8]), where the applicability range was expanded. Besides these mathematically-derived models, there exists several other empirical or semi-empirical modeling approaches, such as the low-order model from Babinsky et al. [9], the ONERA model [10], the Beddoes-Leishman model [3] and the Snel model [11]. Despite their broader applicability range with respect to Theodorsen and Wagner, these models have been shown to suffer from low accuracy (Holierhoek [12]), especially for the deep stall regime. Recent modeling approaches have used the Goman-Khrabrov model [13] to model dynamic hysteresis [1]. Despite their improved performance Goman-Khrabrov (GK) models still suffer from a range of issues, such as initialization problem and lack of accuracy for certain regimes. In addition, the GK models have not been constructed for flows undergoing dynamic stall. Moreover, none of the afore-mentioned studies have investigated dynamic hysteresis on a ramp motion, nor for a significant Reynolds number. Recently, we have attempted to circumvent these shortcomings and construct a data-driven model of the dynamic lift [14] using the current configuration at $\mathrm{Re} = 1.8 \cdot 10^8$. The resultant model, inspired by SINDy [8], was however static. Hence, it was not a dynamical system and therefore suffered from low accuracy over a range of conditions.

In this chapter, we attempt to quantify and model the dynamic lift hysteresis on a DLR-F15 research airfoil with 10% c trailing-edge flap. We introduce a new hysteresis measure to quantify and categorize the various types of hysteresis. The lift models presented in Ref. [14] are improved and dynamical. The results are assessed and validated on experimental data from wind tunnel experiments. The results show previously unknown hysteresis sensitivities. The dynamical low order models have good prediction accuracy at the two angles of attack tested.

9.2 EXPERIMENTAL SETUP

The dynamic lift of the DLR-F15 research airfoil with actively adjustable flap (Figure 9-1 and Figure 9-2) is investigated in the "Modell-Unterschallkanal Braunschweig" (MUB) wind tunnel at the Institute of Fluid Mechanics at TU Braunschweig. The MUB is a closed-circuit wind tunnel with a test section of 1.3 m × 1.3 m × 5.0 m cross section. Experiments are conducted at $Re_c = 1.8 \cdot 10^6$ with $U_\infty \approx 50$ m/s. The airfoil and flap chord length are $c = 600$ mm and $c_F = 0.1c = 60$ mm, respectively, which leads to a convective time of $t^* = c/U_\infty \approx 12$ ms.

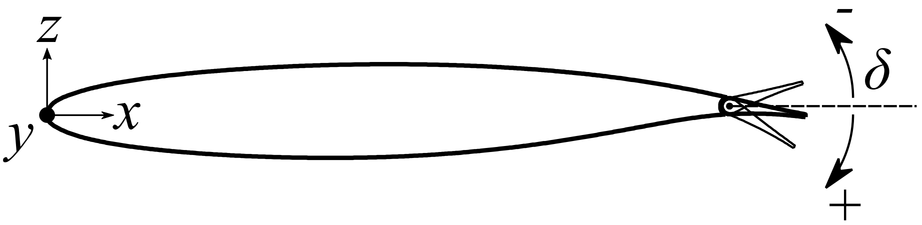

Figure 9-1: Schematic of the DLR-F15 Airfoil with Deflecting Flap.

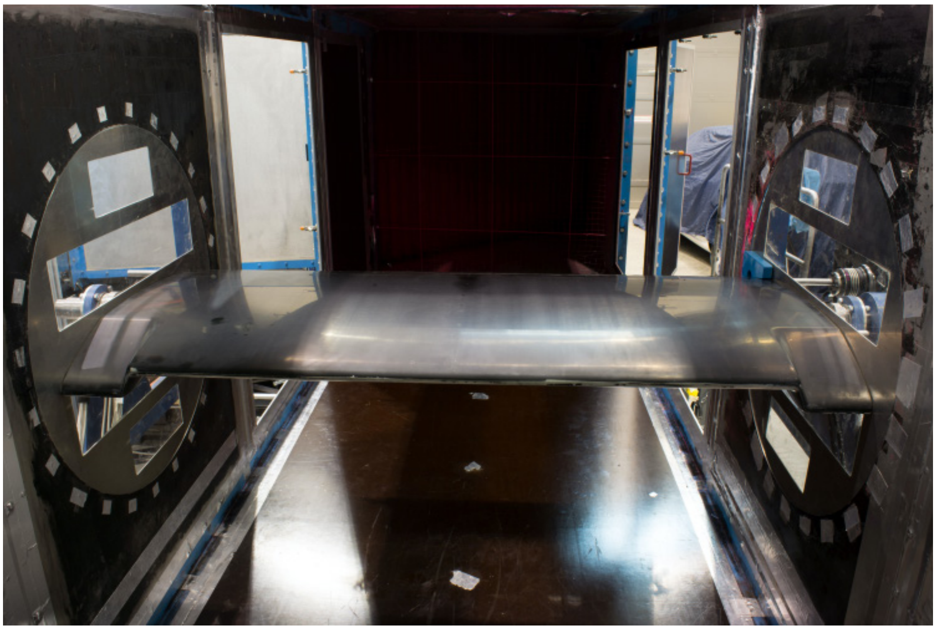

Figure 9-2: Experimental Model Installed Inside the MUB Wind Tunnel.

The active flap is driven by two rotary servo motors outside the wind tunnel (Figure 9-3). Real-time angular position of the flap is read from two rotary encoders mounted on the flap drive shafts. Dynamic lift is inferred from the unsteady pressure distribution recorded along the airfoil mid-span. The spatially sparse unsteady pressure distribution from the 17 time-resolved sensors is interpolated to higher spatial resolution with a mapping technique (described in Ref. [14]), using finely-resolved steady pressure distributions. Steady pressure readings from 83 surface taps are sampled on a DTC Initium system with ESP-HD pressure scanners. Encoder and unsteady pressure data are sampled on a NI cRIO FPGA controller at a rate of 100 kHz.

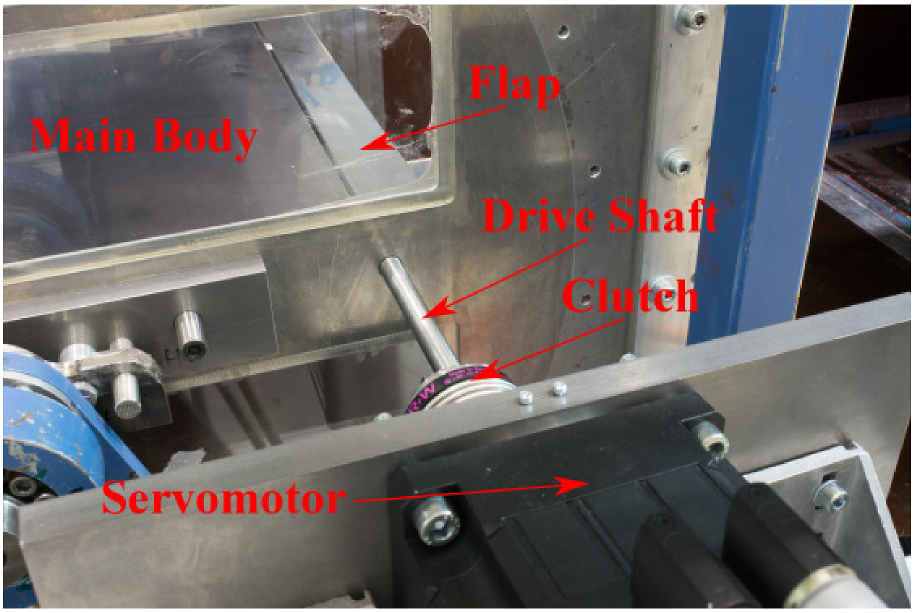

Figure 9-3: Drive Assembly Outside the Wind Tunnel with a View of the Flap.

All data are collected at two angles of attack: $\alpha = 0°$ at attached flow conditions, and $\alpha = 12°$ close to static stall. Two periodic flap actuation modes are investigated: sine wave and ramp actuation, which are mathematically expressed as:

$$\delta(t) = \bar{\delta} + \frac{\Delta\delta}{2}\sin(2\pi f t) \tag{9-1}$$

for the sine actuation, and:

$$\delta(t) = \begin{cases} \delta_{\text{min}} & \text{for } 0 \leq t < t_d \\ \delta_{\text{min}} + \dot{\delta}t & \text{for } t_d \leq t < t_d + t_r \\ \delta_{\text{max}} & \text{for } t_d + t_r \leq t < 2t_d + t_r \\ \delta_{\text{max}} - \dot{\delta}t & \text{for } 2t_d + t_r \leq t < 2t_d + 2t_r \end{cases} \tag{9-2}$$

for the ramp motion. δ denotes the nominal flap angle, $\Delta\delta = \delta_{\text{max}} - \delta_{\text{min}}$ is the amplitude, and δ is the time derivative of the flap motion which infers the rate of angular change. Both actuation patterns with their defining variables are illustrated in Figure 9-4. The second actuation mode is practically a ramp-pause motion with a finite rise time $t_r\Delta\delta = \dot{\delta}$ and hold time t_d (c.f. Figure 9-4). t_d is chosen long enough, so that each ramp can be considered as an independent event at similar incident flow conditions ($t_d = 500$ ms $\approx 42t_c$ for the presented results). Actuation frequencies are traditionally presented in a non-dimensionalized form as $k=\pi f t_c$. Here, we purposely refrain from using the reduced frequency $k = \pi f t_c$ due to the presence of the ramp motion. Instead, we define $f^* = f\ t_c$ and $\delta^* = \delta\ t_c$. After initial transition time of 5 actuation periods to allow the flow to stabilize to the conditions, all periodic motion time traces are phase-averaged over 100 consecutive actuation periods.

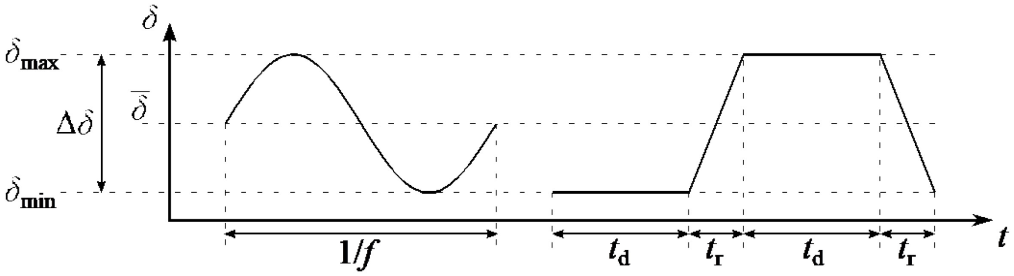

Figure 9-4: The Two Modes of Periodic Flap Actuation.

For both modes, a wide range of actuation settings (frequency, amplitude) is tested. For validation, two additional sets of quasi-random sinusoidal flap motion with varying frequency and amplitude are acquired. An overview of all test cases is given in Table 9-1.

Table 9-1: Summary of Different Test Cases and Actuation Parameters. For the periodic cases, $\delta_{min} \in$ [-25, 20°] and $\delta_{max} \in$ [-20, 25°] are varied in 5° increments. *: Actuation with increased motor power.

Type	α [°]	$f[Hz]$ / $\dot{\delta}[°/s]$	$f^*[-]$ / $\dot{\delta}[°]$	# of Cases
Sine	0	0.5, 1, 2, 5, 10, 20	0.006, 0.012, 0.024, 0.060, 0.120, 0.240	330
Ramp	0	50, 100, 200, 500, 1000	0.6, 1.2, 2.4, 6.0, 12.0	275
Random sequence	0	Continuous	Continuous	10
PSine	12	0.5, 1, 2, 5, 10, 20	0.006, 0.012, 0.024, 0.06, 0.12, 0.24	330
Ramp	12	50, 100, 200, 500, 1000	0.6, 1.2, 2.4, 6, 12	275
Random sequence	12	Continuous	Continuous	10
Sine*	12	10, 15, 20, 25, 30, 35, 40, 45, 50	0.120, 0.180, 0.240, 0.300, 0.360, 0.420, 0.480, 0.540, 0.600	119
Ramp*	12	10000	120	6

9.3 QUANTIFICATION OF DYNAMIC HYSTERESIS

9.3.1 Unsteady Lift

Visualizing the lift coefficient C_L over flap angle δ is the first step to identify hysteresis. Figure 9-5 shows the hysteresis loops for sine actuation with $f^* = 0.024$ at (a) $\alpha = 0°$ and (b) $\alpha = 12°$. The flap pitch amplitude $\Delta\delta$ is varied between 10 and 50° around the nominal flap angle $\delta = 0°$. It is worth noting that the static lift C_L^S, marked by the red squares, is measured only in one flap motion direction, namely for the downstroke towards positive δ, and thus does not account for any possible static lift hysteresis. This gap in the data will be remedied in the upcoming measurement campaign. The superscripts s denotes static parameters. As seen in the figure, C_L^s increases with higher flap angles. For $\alpha = 12°$, C_L^s exhibits a small kink in the distribution at $\delta = 10°$, which is indicative of the static stall onset.

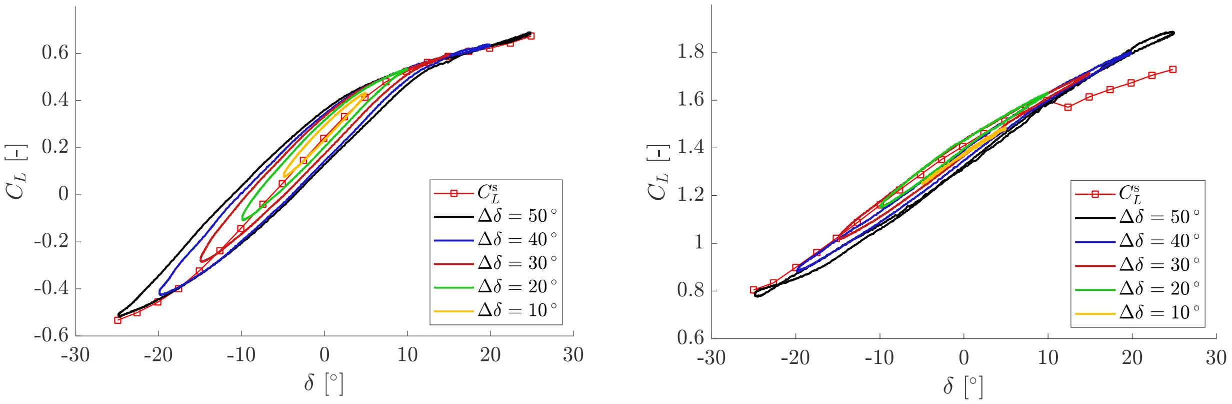

(a) **(b)**

Figure 9-5: Dynamic Lift Coefficient for Periodic Sine Actuation with f^* = 0.024 and Various $\Delta\delta$ at (a) $\alpha = 0°$ and (b) $\alpha = 12°$.

Examining the dynamic lift distributions for both angles of attack in Figure 9-5 shows the typical hysteresis behavior, where larger flap angle motion yield larger hysteresis loop. In contrast to, for example Ol et al. [15], no lift overshoot (undershoot) peak on the upstroke (the downstroke) with respect to the static lift is observed within the examined parameter range, as added mass effects are comparably low. The estimated added mass effects from classical flat plate theory support these observations.

For $\alpha = 0$ ° in Figure 9-5(a), the hysteresis loops exhibits saturation for flap angles $\delta > 10°$ above which all lift coefficient loops collapse onto the static lift distribution. At these large flap angles, the pressure distributions (not shown) reveal that this lift saturation is due to flow separation over the flap suction side, which affects both the static as well as the dynamic lift. The onset of separation is also reflected in the decrease in the static lift gradient $\frac{\mathrm{d}C_L^s}{\mathrm{d}\delta}$ for $\delta > 10°$. Starting at the upstroke from $\delta_{\max}$ somewhere in the range of $10 - 25°$, the flow over the flap suction side is separated and does not influence the pressure distribution around the airfoil much. These small pressure variations over the airfoil suction side contribute, in turn, little to the total lift. In this range, only pressure variations on the airfoil pressure side contribute to the lift decrease. Approaching $\delta \rightarrow 10°$ on the upstroke, the flow reattaches, and an onset of hysteresis is observed. Starting with $\delta \leq -20$ ° on the upstroke, separation over the flap pressure side starts to take shape.

For $\alpha = 12$ ° presented in Figure 9-5(b), the flow response to dynamic actuation is more complicated by the presence of static stall at around $\delta = 10°$. The typical growth of the hysteresis loop with increasing $\Delta\delta$ is still observed for most, but not all cases, such as for $\Delta\delta = 50°$, where the hysteresis loop crosses over itself twice. Moreover, all hysteresis loops exhibit sharp turning points at δmin and $\delta_{\max}$, which is caused by an onset of flap separation. This separation starts at around $\delta = 10°$ over the flap and gradually extends over rear part of the airfoil main element. These observations are corroborated by the time-resolved pressure distributions.

The separation behavior is different for ramp actuation (not shown), where the flow remains attached to the main airfoil for several convective times even for fast ramp motions with $\delta_{\max} \in [15, 25°]$. After a finite time, the flow starts separating from the trailing edge of the main airfoil element, resulting in a strong shift in the pressure distributions and a subsequent decrease in the lift coefficient C_L.

For periodic actuation with $f^*= 0.024$, no large separation fully evolves while the flap is close to $\delta_{\max}$. Instead, especially for the test case with $\Delta\delta = 50°$, a separation bubble grows during the flap upstroke, resulting in a gradual increase in the lift penalty due to separation growth during the downstroke. This explains why a lift undershoot is observed not only on the upstroke, but also on the downstroke for $\Delta\delta = 50°$ at $f^*= 0.024$. On the upstroke, reattachment of the flow can only be considered fully concluded for $\delta \leq -10°$. Thus, for flap motion with $\delta_{\min} > -10°$, the flow remains partially detached and a slight C_L penalty due to separation persists. On the upstroke, as is the case for $\alpha = 0°$, separation over the flap pressure side is observed starting with $\delta < -20°$.

To isolate the effect of flap speed on the unsteady lift, Figure 9-6 presents the C_L distributions over δ for a constant nominal actuation amplitude $\Delta\delta = 40°$ and various flap speeds f^* ranging between $f^* = 0.006$ and $f^* = 0.06$ for $\alpha = 0°$ and between $f^* = 0.006$ and $f^* = 0.018$ for $\alpha = 12°$. As the figure shows, the hysteresis at constant $\Delta\delta$ increases with actuation frequency for both actuation types, but only up to a certain limiting frequency. At higher actuation frequencies, we note two observations. First, the hysteresis loop growth reverses and starts shrinking. A more detailed analysis of this effect is presented in Section 9.3.2. Second, the mean slope of the hysteresis loop decreases with actuation speed. An observation which has already been reported in the literature (e.g., Bak et al. [16]). Both observations are likely caused by the time lag. As actuation speed increases, the flow state closer to the airfoil leading edge lags behind the flap motion. This means that the faster the flap is actuated the smaller the difference between minimum and maximum pressure in one measurement point on the airfoil upstream of the flap becomes. Ultimately, the phase lag of the upstream measurement points causes a decrease in the amplitude of periodic pressure fluctuations upstream the flap, and thus, in lift. This reduces both, the peak maximum and minimum lift seen throughout one actuation period (which, together with the constant $\Delta\delta$, define the mean slope), as well as the size of the loop (i.e., included area).

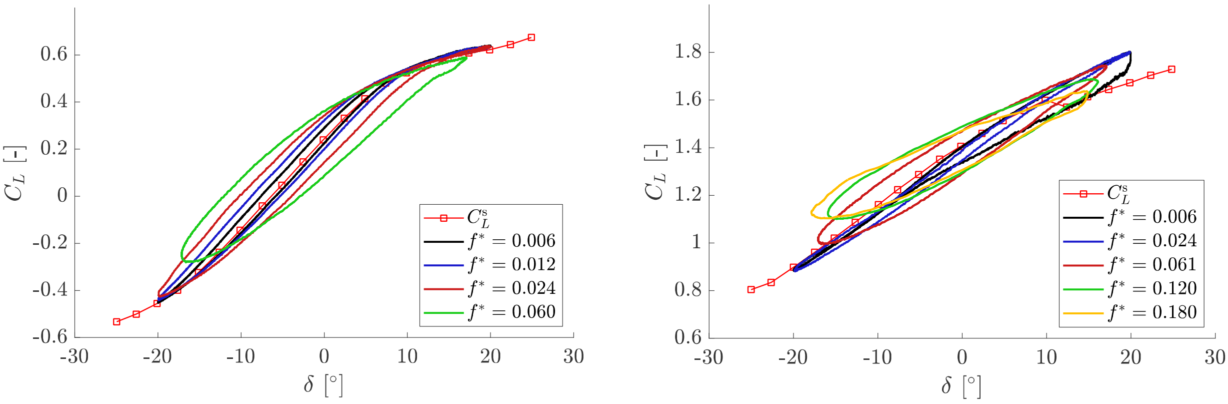

(a) **(b)**

Figure 9-6: Dynamic Lift Coefficient for Sine Motion with $\Delta\delta$ = 40° and Various f^* at (a) α = 0° and (b) α = 12°.

9.3.2 Hysteresis Characterization

A quantification approach is made to describe the amount of lift hysteresis during flap motion and to reveal dependencies on the minimum and maximum flap angles and flap speed. We define the hysteresis measure H as:

$$H = -\oint C_L \cdot \mathrm{d}\delta \tag{9-3}$$

The negative sign accounts for the lift undershoot usually observed on the downstroke for actuation cases without separation, where positive values for H are desired. Figure 9-7 presents H over a range of flap speeds for a limited set of δmin and δmax combinations for the sine actuation.

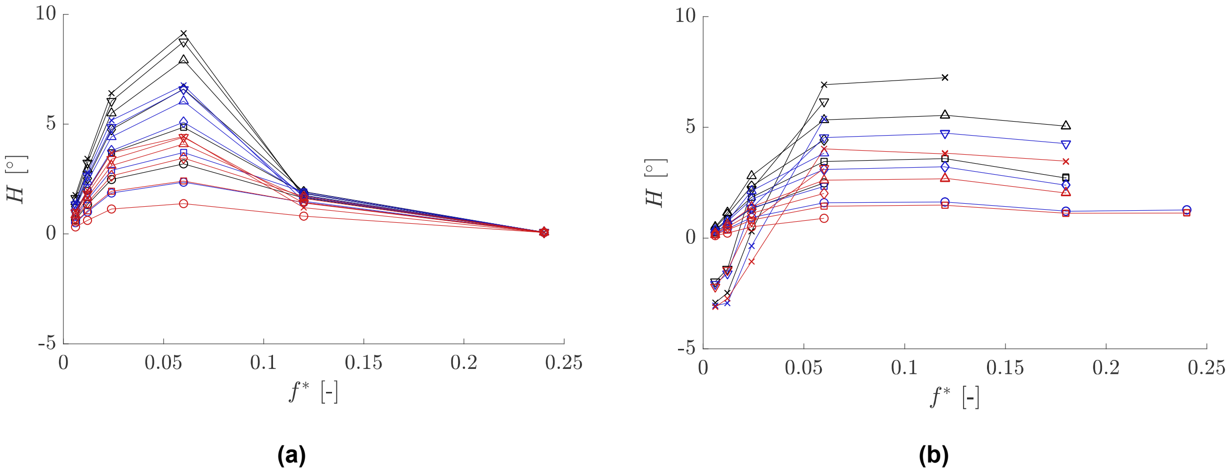

Figure 9-7: Hysteresis Measure H Distributions for Various Sine Actuation Cases with δ_{min} = {−25, −20, −15°}, Denoted {Red, Blue, Black}, and δ_{max} = {0,5,10, 15,20,25°}, Denoted {○,□,♦,△,▽,×}, at (a) α = 0° and (b) α = 12°.

The general trends observed in Section 9.3.1 are also mirrored in the current analysis. H increases with increasing flap speed ($f*$), increasing δmax and decreasing δmin. For α = 0 °, the data are distorted for $f^* \geq 0.12$ when the flap servo motors were run at low power, as the nominal flap angles δ_{min}, δ_{max} could not be sustained. Only flap amplitudes much smaller than the nominal flap amplitudes are achieved for these cases. For α = 12°, the separation effects observed in Section 9.3.1 are clearly visible for lower flap speeds $f^* \leq 0.024$. In some cases, H even shows negative values. This can be the case when the direction of rotation of the hysteresis loop reverses and the lift on the upstroke drops below the lift on the downstroke, as seen for $f^* = 0.006$ in Figure 9-6(b).

To separate the influence of the two main drivers of hysteresis, the flap amplitude $\Delta\delta$ and the flap speed (f^* for sine motion; $\dot{\delta}^*$ for ramp motion), we normalize H as,

$$H^* = \frac{H}{\Delta C_L^s \cdot \Delta\delta} \tag{9-4}$$

where ΔC_L^s is the static lift gain defined as,

$$\Delta C_L^s = C_L^s(\delta_{\mathrm{max}}) - C_L^s(\delta_{\mathrm{min}}) \tag{9-5}$$

for an attached main airfoil element. The normalized results H^* are shown in Figure 9-8.

The H^* distributions collapse very well for most attached cases for α = 0° and α = 12°. Cases with separation, such as those with high δ_{max} at lower speeds show deviations from the main collapsed distribution. This is particularly the case for α = 12°, where negative H^* is observed at slower flap speeds $f^* \leq 0.06$, caused by the increased separation magnitude. With increasing flap speed, the separation effects diminish and the agreement among the cases improves. For both angles of attack, the H^* distributions exhibit a similar shape that increases from low actuation frequencies, reaches a maximum, and slowly decays afterwards. For α = 0°, this maximum of $H^*_{\mathrm{max}} \approx 0.22$ lies around $f^* = 0.06$, whereas for α = 12° it is located at $H^*_{\max} \approx 0.25$ and $f^* = 0.12$. It is not clear at this point whether the shift in $H^*_{\max} \approx$ is physical or whether it lies within the measurement uncertainties. Near-future measurements shall shed light on this point.

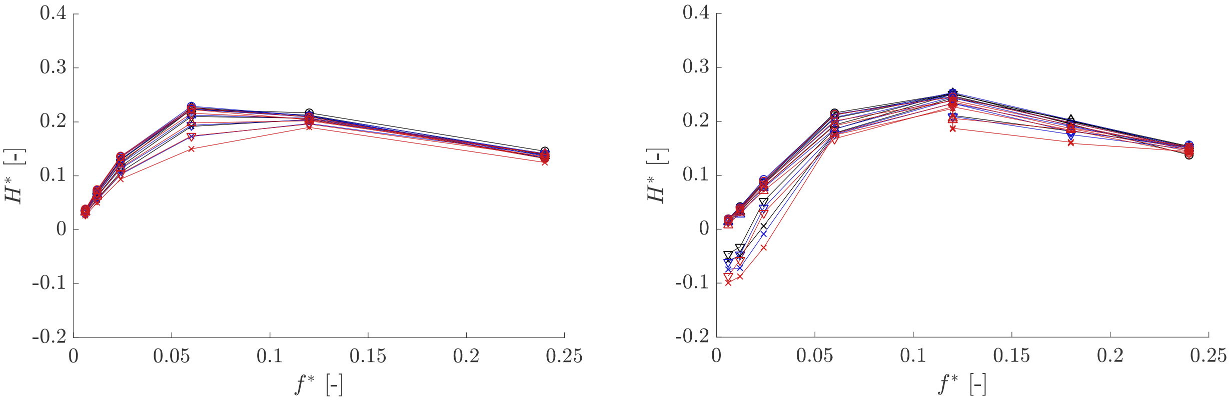

(a) (b)

Figure 9-8: Normalized Hysteresis Measure H^* Distributions for Various Sine Actuation Cases with $\delta_{\min}$ = {-25, -20, -15°}, Denoted {Red, Blue, Black}, and $\delta_{\max}$ = {0,5,10, 15,20,25°}, Denoted {○,□,♦,△,▽,×}, at (a) α = 0° and (b) α = 12°.

Unlike the sine wave motion, the H^* distributions for ramp actuation show larger scatter. Figure 9-9 presents the same test cases as those in Figure 9-8 for ramp actuation. The distributions show comparable trend but with larger scatter. This suggests the existence of additional factors affecting the hysteresis for ramp actuation. At $\alpha = 12°$, the strongly separated test cases are very well distinguishable from the mostly attached cases, which form the upper cluster of lines in Figure 9-9(b). In contrast to sine actuation, separation is omnipresent for ramp actuation and its existence is independent of the flap speed. Only the separation amplitude appears to depend on $\delta_{\max}$.

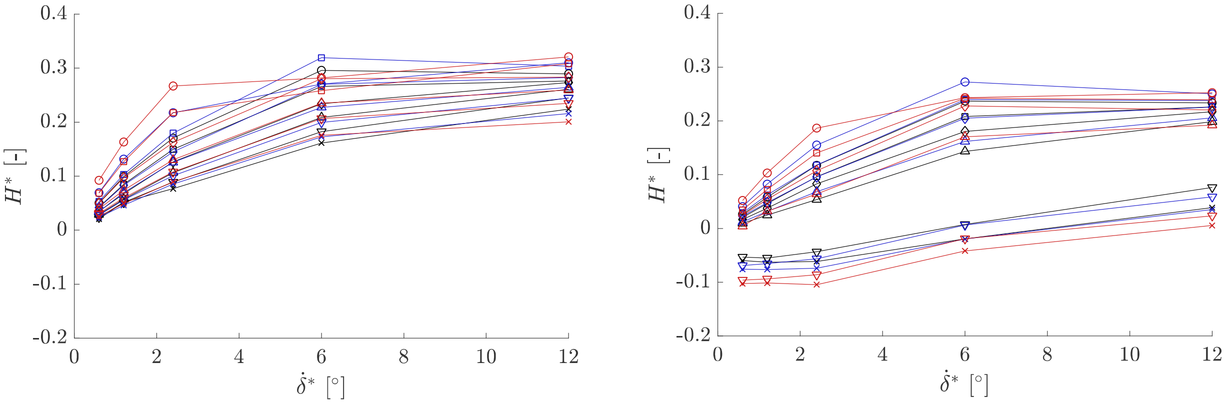

(a) (b)

Figure 9-9: Normalized Hysteresis Measure H^* Distributions for Various Sine Actuation Cases with $\delta_{\min}$ = {−25, −20, −15°}, Denoted {Red, Blue, Black}, and $\delta_{\max}$ = {0,5,10, 15,20,25°}, Denoted {○,□,♦,△,▽,×}, at (a) α = 0° and (b) α = 12°.

9.4 MODELING THE UNSTEADY LIFT

9.4.1 Methodology

Accurate dynamical modeling of the unsteady lift is relevant for closed-loop control and can shed light onto the various flow sensitivities. In a previous work [14], we have compared our data-driven model to that of Theodorsen [7] and to that of Mancini and Jones [17]. All three models were incapable of accurately predicting the dynamic lift hysteresis, especially during dynamic stall. In hindsight, this failure is expected since the tested models were too simple and non-dynamic to represent the complex structures. As detailed in Taha and Rezaei [18], [19], the unsteady aerodynamics problem should be treated as a dynamical system whose input is the angle of attack (or airfoil motion) and output is the lift force. In this chapter, we use the same data-driven approach to infer a dynamical model of the unsteady lift. The general mathematical equation describing the model can be expressed as:

$$\dot{C}_L = f(C_L, \alpha, \delta, \dot{\delta}, \ddot{\delta}) \tag{9-6}$$

where the flap motion is explicitly described by δ, $\dot{\delta}$ and $\ddot{\delta}$ in the model. Due to the lack of test cases with angle of attack variations, α is excluded as a model variable. Instead, separate models are derived for both angles of attack investigated (α = 0° and α = 12°). The current approach is a variant of the Sparse Identification of Nonlinear Dynamical Systems (SINDy) method [8]. Specifically, we are concerned with identifying a sparse nonlinear model for the lift based on the experimentally measured data for a range of actuation parameters δ δ, $\dot{\delta}$ and $\ddot{\delta}$. The collected time traces of the state $\boldsymbol{x} = [C_L, \delta, \dot{\delta}, \ddot{\delta}]$ and the compute time derivative of the lift coefficient C_L are formulated as a regression problem to infer the equation of motion f. Specifically, the data sampled at different times $t_1^*, t_2^*, \cdots, t_n^*$ are arranged into two matrices:

$$\boldsymbol{x} = \begin{bmatrix} x_1(t_1^*) & x_2(t_1^*) & \cdots & x_m(t_1^*) \\ x_1(t_2^*) & x_2(t_2^*) & \cdots & x_m(t_2^*) \\ \vdots & \vdots & \vdots & \vdots \\ x_1(t_n^*) & x_2(t_n^*) & \cdots & x_m(t_n^*) \end{bmatrix} \tag{9-7}$$

And:

$$\dot{\boldsymbol{x}} = \begin{bmatrix} \dot{x}_1(t_1^*) & \dot{x}_2(t_1^*) & \cdots & \dot{x}_m(t_1^*) \\ \dot{x}_1(t_2^*) & \dot{x}_2(t_2^*) & \cdots & \dot{x}_m(t_2^*) \\ \vdots & \vdots & \vdots & \vdots \\ \dot{x}_1(t_n^*) & \dot{x}_2(t_n^*) & \cdots & \dot{x}_m(t_n^*) \end{bmatrix} \tag{9-8}$$

We then construct an augmented library $\boldsymbol{\Theta}$ consisting of candidate nonlinear functions of the columns of $\boldsymbol{x}$. For example, $\boldsymbol{\Theta}$ may consist of constant and polynomial terms:

$$\boldsymbol{\Theta} = \begin{bmatrix} | & | & | & \cdots & | & | & \\ 1 & \boldsymbol{x} & \boldsymbol{x}^{P_2} & \cdots & \sin(\boldsymbol{x}) & \cos(\boldsymbol{x}) & \cdots \\ | & | & | & \cdots & | & | & \end{bmatrix} \tag{9-9}$$

Here, $\boldsymbol{x}^{P_i}$ denote higher polynomials. For the current study, the highest polynomial order is set to five. The library of possible functions is further enriched with time-delays of the flap angle $\delta^* = [\delta(t_1^* - \Delta t^*), \delta(t_2^* - \Delta t^*), \ldots, \delta(t_n^* - \Delta t^*)]^T$, which are particularly required to model the portion of the cycle when δ exceeds the static stall angle [2].

Each column of $\mathbf{\Theta}$ represents a candidate function for the model in Equation 9-6. The solution to this overdetermined system is obtained by solving:

$$\dot{\mathbf{C}}_{\boldsymbol{L}} = \mathbf{\Theta\Xi} \tag{9-10}$$

which yields the sparse vector of coefficients $\mathbf{\Xi} = [\xi_1, \xi_2, \ldots, \xi_p]^T$, with the total number of constant and polynomial terms p. There is a large number of possible entries in this matrix of nonlinearities. Since we are seeking a parsimonious model, only a few of these nonlinearities are active. The solution is obtained using a linear least-squares regression:

$$\boldsymbol{\xi} = \underset{\xi'}{\operatorname{argmin}} \|\mathbf{\Theta}\boldsymbol{\xi}' - \boldsymbol{C_L}\|_2 \tag{9-11}$$

A desired degree of sparsity N_ξ is typically achieved by subsequent elimination of the ξ of least influence until the desired number N_ξ of non-zero components in Ξ is reached.

The described modeling method is very powerful, yet computationally costly. Due to the massive size of the collected data and the high degrees of freedom in $\mathbf{\Theta}$, it was not possible to solve the recursive regression problem with all possible functional combinations (i.e., SINDy) to identify the model coefficients. Instead, a heuristic sequential approach is used to manually solve the least-squares problem Eq. 10 using different combinations of $\mathbf{\Theta}$. The model is then selected based on accuracy and complexity considerations.

The model complexity N_ξ is defined as the number of non-zero coefficients in the model. For example, a dynamic model $\dot{C}_L = \xi_0 + \xi_{C_L} C_L + \xi_\delta \delta$ is considered a model of complexity $N = 3$. Figure 9-10 presents the accuracy of all the tested model combinations against their respective complexity for both angles of attack. The accuracy is quantified through the root mean square error:

$$E_{\mathrm{RMS}} = \sqrt{\left\langle \left(\hat{C}_L(t) - C_L(t)\right)^2 \right\rangle}, \tag{9-12}$$

where $\hat{C}_L$ is the model estimate, and $\langle\ \rangle$ is the time averaging operator. It is worth noting that the models are simultaneously trained on both actuation forms using all acquired test cases, excluding the quasi-random sequences.

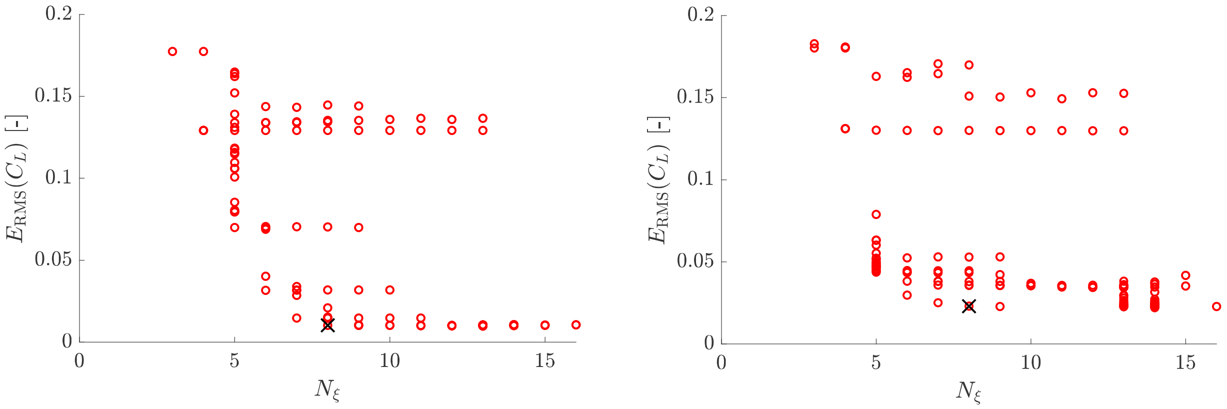

(a) (b)

Figure 9-10: Model Prediction Error versus Complexity N_ξ for (a) α = 0° and (b) α = 12°. The chosen winners for each angle of attack are marked with a black ×.

As can be seen in the figure, a clear Pareto front is observed for both cases indicating a trade-off between complexity and accuracy. For both angles of attack, the error initially drops sharply with increasing N_ξ and asymptotes for $N_\xi > 8$. As such, the winning models are selected with $N_\xi = 8$ yielding a root mean square accuracy of $E_{\mathrm{RMS}} = 0.0102$ and $E_{\mathrm{RMS}} = 0.0230$ for $\alpha = 0°$ and 12°, respectively. The two winning models read:

$$\alpha = 0° \quad \dot{C}_L = \xi_0 + \xi_{C_L} C_L + \xi_\delta \delta + \xi_{\delta^2}\delta^2 + \xi_{\delta^3}\delta^3 + \xi_{\delta^4}\delta^4 + \xi_{\delta^5}\delta^5 + \xi_{\dot{\delta}}\dot{\delta} \tag{9-13}$$

$$\alpha = 12° \quad \dot{C}_L = \xi_0 + \xi_{C_L} C_L + \xi_\delta \delta + \xi_{\delta^2}\delta^2 + \xi_{\delta^3}\delta^3 + \xi_{\delta^4}\delta^4 + \xi_{\dot{\delta}}\dot{\delta} + \xi_{\delta_{6t_c}}\delta_{6t_c} \tag{9-14}$$

where the values ξ_i are listed in Table 9-2. Alternatively, both models can be expressed in a generalized form as:

$$\dot{C}_L = \xi_0 + \xi_{C_L} C_L + \xi_\delta \delta + \xi_{\delta^2}\delta^2 + \xi_{\delta^3}\delta^3 + \xi_{\delta^4}\delta^4 + \xi_{\delta^5}\delta^5 + \xi_{\dot{\delta}}\dot{\delta} + \xi_{\delta_{6t_c}}\delta_{6t_c} \tag{9-15}$$

Table 9-2: Model Coefficients of the Two Dynamic Lift Models for Both Angles of Attack.

ξ_i	$\alpha = 0°$	$\alpha = 12°$
ξ_{C_L}	**-0.4418**	**-0.0885**
ξ_0	**0.1181**	**0.1245**
ξ_δ	**0.9105**	**0.1788**
ξ_{δ^2}	**-1.0004**	**-0.1261**
ξ_{δ^3}	**-2.6689**	**-0.1112**
ξ_{δ^4}	**2.9083**	**0.3585**
ξ_{δ^5}	**5.8247**	**0.0000**
$\xi_{\dot{\delta}}$	**0.9282**	**0.9875**
$\xi_{\delta_{6t_c}}$	**0.0000**	**−0.0635**

With $\xi_{\delta^5} = 0$ for $\alpha = 12°$ and $\xi_{\delta_{6t_c}} = 0$ for $\alpha = 0°$. We note the following observations for both models:

- The models rely on higher order flap angle deflection (fifth order for $\alpha = 0°$, and fourth order for $\alpha = 12°$). These higher order flap angles are not easily physically interpretable and require further investigations.
- The models depend on first order flap angle deflection rate $\dot{\delta}$, but not on any higher order thereof.
- There are no relevant mixed polynomials, such as $\delta\dot{\delta}$, despite their inclusion in the library of functions.
- There are no trigonometric terms, such as $\sin(\delta)$, despite their inclusion in the library of functions and despite the imposed periodic motion.
- The time delayed flap angle δ_{6t_c} appears only in the $\alpha = 12°$ model. The inclusion of a time delayed term is expected for light dynamic stall cases, where air loads depend mainly on the time history of δ [2].
- All these observations require further investigations and interpretations, which the authors are currently pursuing.

- There is no contribution from the flap acceleration $\ddot{\delta}$. This exclusion is expected, as added mass effects were estimated using the classical flat plate theory to be very low.

All these observations require further investigations and interpretations, which the authors are currently pursuing.

9.4.2 Model Assessment and Validation

Our initial data-driven approach [14] to model the unsteady lift of the DLR-F15 research airfoil focused on constructing static lift models of the form:

$$C_L = \xi_0 + \xi_\delta \delta + \cdots \tag{9-16}$$

In this work, we present two dynamic models and compare them against the previous static models and the reference measured lift. We first assess the models prediction on individual test cases for the sinusoidal (c.f. Figure 9-11) and the ramp motion separately (c.f. Figure 9-12) before validating them on test sets.

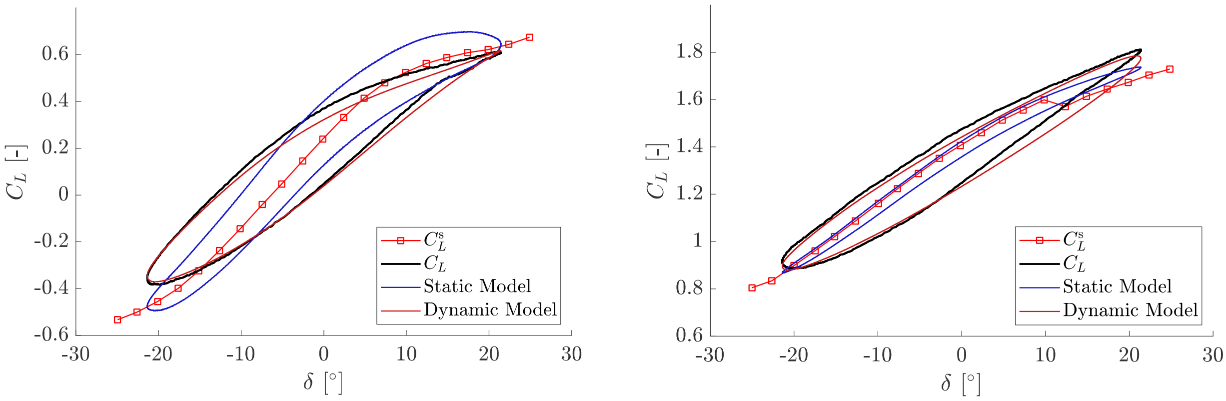

(a) **(b)**

Figure 9-11: Static and Dynamic Model Predictions Compared to the Reference Lift Coefficient for Sine Actuation with $\Delta\delta$ = 50° and f^* = 0.06 at (a) α = 0° and (b) α = 12°.

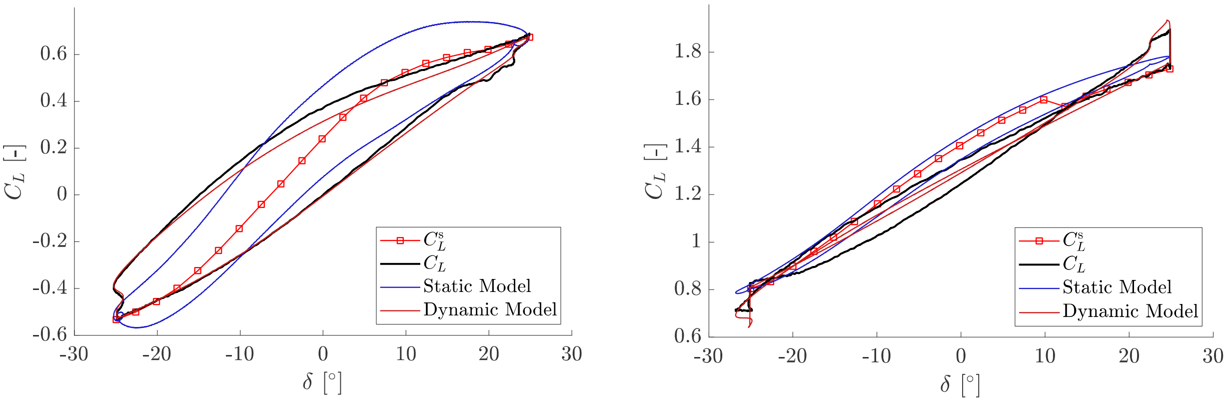

(a) **(b)**

Figure 9-12: Static and Dynamic Model Predictions Compared to the Reference Lift Coefficient for Ramp Actuation with $\Delta\delta$ = 50° and $\dot{\delta}^*$ = 1000 at (a) α = 0° and (b) α = 12°.

Figure 9-11 presents the dynamic model lift predictions and those of the previously-developed static model [14] and compares them to the measured reference lift coefficient. Also shown is the measured static lift distribution. As can be seen, the new dynamic model performs much better than the static one. For α = 0° in Figure 9-11(a), the static model deviates from the reference data on both the upstroke and the downstroke. On the other hand, the dynamic model almost exactly reproduces the measured lift at the lower flap angles and only lacks some accuracy at high positive flap angles, where separation effects become significant. Similarly, for α = 12°, the static model fails to predict the hysteresis loops, whereas the dynamic model accurately reproduces the unsteady lift.

For the ramp motion at α = 0° shown in Figure 9-12(a), the dynamic model again shows good prediction accuracy. Even the little excursion close to δ_{min}, which is caused by the motion control overshoot, is well predicted. The static model exhibits poor performance through the hysteresis loop. For α = 12°, the dynamic stall caused by the main airfoil separation renders the unsteady lift more complicated. Here, the static model completely fails to predict any of the separation effects. It is unable to reproduce the fallback to the detached flow state at δ_{max} nor the flow reattachment around δ_{min}. In contrast, the dynamic model is capable of predicting the lift fairly accurately in both regimes. Only a little prediction overshoot is observed on the fallback at δ_{max}, and a slight undershoot at the fallback at δ_{min}. The lift hysteresis in the mid-range is also well reproduced by the dynamic model, with a slight over-prediction on the downstroke and a small under-prediction on upstroke.

As with any data-driven approach, we validate our model on a separate test dataset that was excluded from the training set. The two test datasets for the two angles of attack are generated from sinusoidal motion with quasi-random variations in amplitude and frequency including transients between actuation settings. This dataset is a very suitable to assess the model performance in untested regimes with fast transients. Figure 9-13 presents the reference lift coefficient time sequence along with the static and dynamic model predictions. Surprisingly, at α = 0° both models perform well. Only for some periods of the test signal, the dynamic model performs slightly better than the static one with less overshoot. In addition, the static model appears to be slightly delayed for the steep flap angle ramps. For α = 12° in Figure 9-13(b), the supremacy of the dynamic model becomes clear. Here, the dynamic model accurately represents the lift variations during all regions and during sharp angular variations. Overall, the dynamic model not only reproduces the unsteady lift with low average error but is capable of predicting C_L during separation phases.

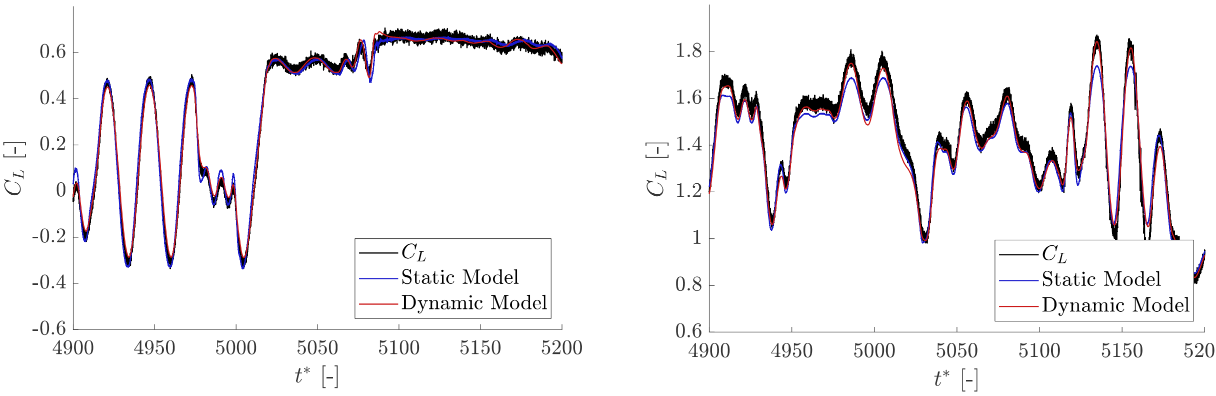

(a) **(b)**

Figure 9-13: Static and Dynamic Model Predictions Compared to the Reference Lift Coefficient for Pseudo-Random Actuation at (a) α = 0° and (b) α = 12°.

9.5 Conclusions

This study attempts to characterize and model lift hysteresis on a DLR-F15 research airfoil with a 10% c active trailing-edge flap using wind tunnel experimental data. The experiments are conducted at two angles of attack $\alpha = 0°$ and $12°$ with sinusoidal and ramp motion. The unsteady lift is measured using an array of static and time-resolved pressure sensors distributed along the model midsection. The lift hysteresis characterization is performed through a newly defined metric. The lift coefficient is modeled using a data-driven technique similar to SINDy [8].

The hysteresis characterization relies a newly defined metric H and its normalized counterpart H^*. The hysteresis measure H exhibits the expected increase with larger flap amplitude $\Delta\delta$, whereas the sensitivity to actuation frequency is inconclusive. Normalization of H is better suited to examine the hysteresis dependency on the actuation frequency. Here, H^* exhibits a clear maximum between $f^* = 0.06$ and $f^* = 0.12$ for the sine motion actuation for both angles of attack. This suggests that hysteresis does not continuously increase with frequency. No clear trends are observed for the ramp actuation, which awaits further investigations. It is the authors intentions to further refine the quantification method and possibly combine it with other metrics to classify all dynamic hysteresis. We aim for an expanded taxonomy of McCroskey [2] to include pre- and post-stall dynamic hysteresis.

A data-driven approach similar to SINDy [8] is used to model the dynamic lift coefficient. The method relies on recursive least-squares regression to fit dynamic lift model onto the reference measurements. Two separate models are constructed for the two tested angles of attack at $\alpha = 0°$ and $12°$. The current approach differs from our previous work [14] in that the models are dynamic. Dynamic models not only deliver higher prediction accuracy over static ones but are also better physically motivated [18]. The trained models are compared against the reference lift and against the former static models on individual actuated cases and on two separate test signals with quasi-random variations in frequency and amplitudes. The results show high prediction accuracy of the dynamic models over a range of actuation settings. Future efforts are geared toward interpreting and generalizing the constructed models.

9.6 REFERENCES

[1] Williams, D.R., Reißner, F., Greenblatt,D., Müller Vahl, H.F., and Strangfeld, C., Modeling lift hysteresis with a modified Goman-Khrabrov model on pitching airfoils, 45th AIAA Fluid Dynamics Conference, 2015, pp. 1-11.

[2] McCroskey, W.J., Unsteady airfoils, Annual Review of Fluid Mechanics, Vol. 14, 1982, pp. 285-311.

[3] Leishman, J.G., and Beddoes, T.S., Asemi-empirical model for dynamic stall, Journal of the American Helicopter Society, Vol. 34, No. 3, 1989, pp. 3-17.

[4] Gupta, R., and Ansell, P.J., Unsteady flow physics of airfoil dynamic stall, AIAA Journal, Vol. 57, No. 1, 2019, pp.165-175.

[5] Rival, D., and Tropea, C., Characteristics of pitching and plunging airfoils under dynamic-stall conditions, Journal of Aircraft, Vol. 47, No. 1, 2010, pp. 80-86.

[6] Wagner, H., Uber die Entstehung des dynamischen auftriebes von traflgugeln, Zeitschrift fur Angewandte Mathematic und Mechanik, Vol. 35, 1925, p. 17.

[7] Theodorsen, T., General theory of aerodynamic instability and the mechanism of flutter, Tech. Rep. 496, 1935.

[8] Brunton, S.L., Proctor, J.L., Kutz, J.N., and Bialek, W., Discovering governing equations from data by sparse identification of nonlinear dynamical systems, Proceedings of the National Academy of Sciences of the United States of America, Vol. 113, No. 15, 2016, pp. 3932-3937.

[9] Babinsky, H., and Stevens, P.R.R.J., Experiments to investigate lift production mechanisms on pitching flat plates, Experiments in Fluids, 2017, pp. 1-17.

[10] McAlister, K.W., Lambert, O., and Petot, D., Application of the ONERA model of dynamic stall, Tech. Rep., 1984.

[11] Snel, H., Heuristic modelling of dynamic stall characteristics, EWEC Conference, 1998, pp. 429-433.

[12] Holierhoek, J.G., De Vaal, J.B., Van Zuijlen, A.H., and Bijl, H., Comparing different dynamic stall models, Wind Energy, Vol. 16, No. 1, 2013, pp. 139-158.

[13] Goman, M., and Khrabrov, A., State-space representation of aerodynamic characteristics of an aircraft at high angles of attack, Journal of Aircraft, Vol. 31, No. 5, 1994, pp. 1109-1115.

[14] Pohl, J., Semaan, R., and Jones, A.R., Dynamic lift measurements on an airfoil with periodic flap motion at high Reynolds number, AIAA Scitech 2019 Forum, 2019, pp. 1-16.

[15] Ol, M.V., Medina, A., Mancini, P., and Jones, A., Revisiting conventional flaps at high deflection-rate: Separation control, AIAA Aviation, Washington, D.C., 2016.

[16] Bak, C., Gaunaa, M., Andersen, P.B., Buhl, T., Hansen, P., and Clemmensen, K., Wind tunnel test on airfoil Riso-B1-18 with an active trailing edge flap, Wind Energy, Vol. 13, No. 2-3, 2010, pp. 207-219.

[17] Mancini, P., Medina, A., and Jones, A.R., Experimental and analytical investigation into lift prediction on large trailing edge flaps, Physics of Fluids, Vol. 31, No. 1, 2019.

[18] Taha, H., and Rezaei, A., On the dynamics of unsteady lift and circulation and the circulatory-non-circulatory classification, AIAA Scitech 2019 Forum, 2019, pp. 1-13.

[19] Taha, H., and Rezaei, A.S., Viscous extension of potential-flow unsteady aerodynamics: The lift frequency response problem, Journal of Fluid Mechanics, Vol. 868, 2019, pp. 141-175.

Chapter 10 – THE LIFT FORCE PRODUCED BY AN UNSTEADY TRANSLATING PLATE WITH A ROTATING TIP

Juhi Chowdhury, Cameron Smith, and Matthew J. Ringuette
University at Buffalo
UNITED STATES

Dynamic effects of wing planform changes are investigated with the goal of gust alleviation. Force measurements are done on a low-aspect ratio, high angle of attack translating wing having a rectangular planform that further incorporates a moving tip with in-plane rotation and sweep. The wing is towed in a water tank with various velocity ramps starting from a constant motion, which are categorized as step-up (increasing velocity) and step-down (decreasing velocity); ramps over distances of 1, 3, and 6 chords traveled are used for both types of gusts. The tip panel is rotated inward for step-up cases with an aim to lower the gust lift peaks, and similarly rotated outward for step-down gusts to reduce the negative force change. The forces from the actuation cases are compared with those of two reference geometries corresponding to pre- and post-gust wing shapes, namely rectangular and static sweep where the tip panel is fully retracted or extended, respectively. Further, the sensitivity of the actuation effects to Aspect Ratio (*AR*) is examined. The lift coefficient, C_L, uses the instantaneous main-wing translation velocity and the varying wing area to compare across all cases. The step-up gust C_L resembles that of the starting flow for the 1-chord ramp, as reported by others. The step-down gusts exhibit a C_L minimum then an increase to a circulatory-force peak. For both gust types, apart from the 6-chord step-up case, when the C_L curves are aligned at 50% of the gust-ramp travel, the post-gust circulatory peaks coincide. For the step-up gusts and tip-panel actuation-out, the $AR = 2$ case yields a more substantial C_L reduction (gust mitigation) but it is not sustained compared to the $AR = 4$ actuation effect. Wingtip actuation at the 50% gust location produces a more sustained, lower C_L but does not affect the gust peak, while actuation before the peak for the longer ramp cases reduces the peak value but the mitigation effect is not prolonged. For the step-down gusts, actuation-out is effective at increasing the C_L. For $AR = 4$ the effect is greatest for the 1-chord ramp and yields a C_L plateau between the gust minimum and recovery peak that is higher than for $AR = 2$. However, for the longer deceleration ramps the $AR = 2$ actuation-out case produces relatively larger actuation peaks and earlier gust recovery.[1]

10.1 INTRODUCTION

The goal of the present work is to test whether a moving wingtip surface that employs in-plane rotation and sweep can aid in mitigating the lift changes from simplified step-up and step-down streamwise gusts. The rotating tip surface, referred to here as a tip panel, dynamically changes the wing planform. The panel is deployed on a low-aspect ratio translating wing at high angle of attack (α). The long-term application of this research is to develop a method of flow control for Unmanned Aerial Vehicles (UAVs) to employ for maneuvers or gust alleviation.

For wings in unsteady translation at high α, dynamic stall will occur for which the flow separates and a Leading-Edge Vortex (LEV) forms that yields large lift then sheds [1], [2]. Tip effects occur for wings of finite Aspect Ratio (AR), and Taira and Colonius [3] performed numerical simulations to examine AR = 1 – 4 translating wings at large α starting from rest and undergoing long travel distances. They showed that Tip Vortex (TV) downwash lowers the wing lift coefficient, CL, an effect which progresses as the AR becomes smaller and the TV influence increases. At AR = 1, the LEV remains attached due to the dominant TVs, but for higher AR this is only true near the wingtips and the inboard LEV lifts off into an arch shape and sheds.

---

[1] The content for this Chapter is primarily taken from Chowdhury, J., Smith, C., and Ringuette, M.J., *AIAA Paper 2020-2045*.

Jardin et al. [4] similarly found that the TV promotes LEV attachment, for simulations of flapping wings in translation. For further recent work on the forces and flow structure for finite-AR wings in unsteady translation, see Stevens et al. [5] which covers results from the NATO AVT-202 group. Here we consider AR = 2 and 4 wings to ensure that inboard LEV shedding will occur and observe how the moving tip panel may alter the flow.

For wings in unsteady, pure rotation, several studies have shown that the LEV is attached for low local Rossby number (Ro), also in the context of TV and AR effects, e.g., Refs. [6], [7], [8], [9], [10], [11]. The low-AR rotating tip panel examined here is superimposed on the main-wing translation, for which the advance ratio J incorporating wing translation and rotation is also important. Section 10.2.3 discusses this and leverages the rotating-wing study of Harbig et al. [12] for varying J.

The moving tip panel studied here incorporates aft sweep as it rotates. For unswept translating rectangular wings the LEV and TV are distinct [13], [14], but although sweep and the spanwise flow it produces do not alone yield LEV attachment, sweep can facilitate an LEV-TV connection [15]. For low-AR translating wings, swept and curved planforms also cause the LEV and TV to connect, which yields outboard vorticity transport, and delays both the LEV shedding and peak CL [3]. However, for a wing in translation with added flapping (lateral rotation about the root), which produces a spanwise vorticity gradient, sweep can enhance spanwise flow and aid in LEV attachment [16], [17]. Numerical simulations by Jardin and David [18] also showed that although a spanwise velocity gradient across the wing span can alone promote LEV attachment, for wing rotation the LEV is closer to the wing and generates larger lift. van Oorschot et al. [19] performed tests on actual bird wings with either fixed, aft sweep outboard or the sweep reduced and area increased by extending the wing, done in a freestream flow or for steady revolving. Sweep produces a larger CL at a higher α in the freestream flow, but for revolving the extended wings generate greater CL.

Recently, Hayostek et al. [20] experimentally investigated unswept and swept AR = 2 and 6 wall-mounted wings in a water channel using dye visualization and S-PIV. They identified tip, wake, and wall regions, which for AR = 2 have overlap and affect one another, but for AR = 6 the end influences are more isolated. Aft sweep introduces outboard spanwise flow, which lowers the TV strength, and the flow separation and vortex shedding are substantially lessened. A follow-on direct-numerical-simulation study by Zhang et al. [21], using instead a root symmetry-plane condition, showed a persistent TV for all configurations with strength most affected by α, and that tip effects lower the performance versus 2-D cases. In addition, periodic shedding of spanwise vortices was found for AR = 4, and for AR = 6 a vortex “dislocation” was discovered in the shedding region closer to the symmetry plane. Between the tip and spanwise shedding is a region of slanted, zigzag “interaction vortices” which have the same shedding frequency as the spanwise structures. Such structures, although more diffuse, are also visible in our longer-time dye visualizations [22]. Also, Medina et al. [23] used experiments and computations to investigate the dynamic stall of a 30°-swept wing with a semi-span AR = 2, but sinusoidal pitching about 1/4-chord. An arch vortex was observed inboard of the TV which unpins, then connects with the TV itself as the TV unpins, leading to full tip stall.

Static tip sweep was also examined by Nicolic [24] and Lee and Pereira [25], who employed half delta-wing, i.e. swept, tip shapes also referred to as strakes. Depending on the main-wing and strake orientations, the results showed increased CL and maximum lift-to-drag ratio, likely due to strake vortex lift. Although this research was done for lower $\alpha < 25°$ and a steady freestream versus the high-α, unsteady conditions of the present work with variable tip geometry, it shows that such tip shapes can improve performance.

The proposed chapter uses a rotating tip geometry, and prior work has also been done on dynamically changing wing shapes. For example, Reynolds et al. [26] showed that a steppe eagle quickly lowers (“tucks”) its wings below its body in response to a headwind gust followed by some disturbance like a downdraft that produces a drop in lift. The tucking is likely the response of muscle tension to a suddenly reduced wing loading, but they speculate that it could also be a mechanism for damping the gust perturbation. Wang et al. [27] used DNS to study slow-flying bats, and showed that a dynamic increase in wingspan during flapping, compared to a fixed-span case, produces greater lift and efficiency by enhancing the LEV strength, in addition to the effect of the larger wing area. Returning to birds, Harvey et al. [28] examined freely-gliding gulls and cadaver wings in wind tunnels, and demonstrated that variations in wing elbow angles, which alter the camber and aerodynamic center, could vary the bird's static pitch stability. For additional discussions on the forelimb adaptations of bat and bird wings and potential inspiration for robotic drones, see Ref. [29].

Considering more simplified engineering approaches, building off the work of Wibawa et al. [30], Steele et al. [31] investigated the fast spanwise retraction of vertically mounted wings towed at constant-α in a water tank. The square-tip wing (emulating a "vanishing body") creates spanwise vortices and a vortex ring that makes the wake unstable, the square but hollow tip ("melting body") requires less energy to retract than the first since it does not produce further momentum in the spanwise direction and is more favorable for flow control, while the rounded tip ("shrinking body") generates weaker spanwise vortices and results in added-mass energy recovery and thrust. Recently Scofield et al. [32] studied LEV vorticity transport control for an AR = 3 flat-plate wing translating from rest, via a tip that bends dynamically in the suction direction by 35°. Experiments using PIV indicated that at 80% span the LEV circulation growth and shedding are delayed, and DNS demonstrated that the bending increases spanwise vorticity convection.

Di Luca et al. [33] designed and fabricated a bird-inspired morphing wing with the left and right outboard portions each consisting of multiple artificial feathers, which when fully extended produce outboard sweep, or by rotation inboard with overlap the feathers can fold the wing to decrease the span and lower the area by 41%. From wind tunnel tests measuring time-averaged forces, they showed that the expanded wing provides greater CL and maneuvering capability, while retraction reduces the drag coefficient for higher speed. Also, installing the wings on a drone, they demonstrated that asymmetric actuation can be used for roll control. This variable wing geometry shares similarities with that of the present study, however we employ a rigid wingtip panel and examine the unsteady forces and flow.

Regarding streamwise gusts, here the focus is on simple non-periodic changes in velocity. Recent experiments have shown that using a moving model with respect to a constant (or zero) freestream velocity to produce a gust-like interaction is equivalent to employing a stationary wing in a wind tunnel having time-varying freestream velocity changes, provided that the buoyancy effects from this accelerating freestream and the wing-model inertial loads for the moving-wing case are accounted for [34], [35], [36]. Mulleners et al. [37] conducted experiments on an $\alpha = 30°$ flat-plate wing, and compared the LEV and TEV development and CL decay for: 1) starts from rest and 2) a streamwise acceleration from a fully-developed state at constant velocity to a final velocity 50% higher than the initial wing velocity. They found that after the initial startup, both cases are similar in terms of time-varying flow and CL variations and decay. Marzanek and Rival [38] studied a non-slender delta-wing at $\alpha = 20°$ and 30° accelerating from rest in a freestream to a new speed that is 50% faster, to emulate a headwind gust, via constant acceleration over 1c – 6c. For $\alpha = 30°$, they found sensitivity to the acceleration rate: e.g., for the 1c case, it exhibits high sustained CL associated with a favorable pressure gradient and flow separation with subsequent reattachment.

Initial work on the present wing configuration was done using qualitative dye flow visualization with an AR = 6.8 wing in a water towing-tank facility [22]. This AR value is twice that of the vertically submerged wing, excluding the tip panel, accounting for the reflected free-surface boundary condition. The wing was a flat plate in unsteady translation with $\alpha = 45°$ and a Reynolds number of Re = 10,000. Tests included a starting flow with outward panel actuation, meant to increase lift, and a 50% 1/2-sine streamwise gust (surge) at 21 chords (21c) traveled with inward panel rotation, intended to shed the panel's leading or Swept-Edge Vortex (SEV) and promote inboard LEV shedding to reduce the gust lift increase. The azimuthal speed of the panel's tip was a factor of 1.49 greater than the main-wing translation speed. For the starting flows, outward panel rotation at 0.1c traveled generates a panel SEV, stretches the TV and Trailing-Edge Vortex (TEV) outboard and upstream, and displaces the adjacent LEV outboard; these behaviors should increase the lift. By comparison, the SEV for a reference case with panel fixed in its extended, swept position is not as closely attached. For both moving and fixed-panel configurations, the outboard LEV entrains the SEV vorticity and weakens it for a time. Starting the panel actuation at 1.3c traveled has a reduced effect, because the LEV is stronger when the actuation begins, as is its entrainment of the SEV flow. The gust tests showed that panel retraction causes shedding of the SEV and local TEV, consistent with the vanishing-body case of Steele et al. [31], and as desired yields LEV shedding similar to the rectangular wing that is more pronounced than in the fixed-sweep case. Moreover, the moving panel produces an inboard shift of the TV flow, which should lower the lift.

The objective of the current chapter is to build on this prior work and quantitatively examine how the moving panel affects the CL. The same water towing-tank is used with a force transducer to measure the wing lift. Two main questions are considered:

1) To what level can the increased lift due to a streamwise, headwind gust be reduced via inward panel rotation?
2) How effective is outboard panel rotation at mitigating the lift lost during a streamwise, tail-wind gust?

To address (1) and (2), simple “step-up” and “step-down” streamwise gusts are tested, starting from a constant velocity and accelerating or decelerating, respectively, to a new constant velocity. The parameters varied include the gust acceleration duration, the panel actuation timing, and the main-wing AR; ARs of 2 and 4 are studied, to ensure inboard LEV shedding but reduce the entrainment effect from the strong LEV found for AR = 6.8. The moving-panel results are compared to two reference cases having fixed planforms at the extremes of the panel actuation: the main wing with no tip panel deployed (“rectangular” wing), and a fixed tip panel fully extended outward with constant sweep (“static sweep” case).

10.2 EXPERIMENTAL SETUP AND METHODS

10.2.1 Facility and Wing Model

The facility is a 4 m × 1.5 m × 1.1 m glass-walled towing tank with water as the working fluid (Figure 10-1(a)). It is open at the top, and the bottom and side walls are supported by a steel frame which elevates it 1 m for imaging from underneath. Above the tank is a further frame of extruded-aluminum beams, and four cross beams support a 3 m long brushless linear stage (H2W Technologies DRS-120-08-006-01-EX) for towing models. A tray is installed adjacent to the stage which supports the cable bundle attached to the stage’s carriage, plus the cabling for the wingtip actuation motor, providing smooth cable travel as the carriage moves. A Galil DMC4040 controller employing encoder feedback provides programmable motion profiles for the linear stage and the tip-panel actuation. The coordinated motions are developed and carried out using Galil Design Kit software. The position accuracy of the linear stage encoder is rated at 1 micron, however maximum deviations of about 100 microns, or ~0.1% c, occur during the gust motions.

The main wing is made from two carbon-fiber composite sheets of thicknesses 3.18 mm and 0.79 mm, with a chord length of c = 81 mm. A cavity is machined out of the thicker plate to allow room for the actuation mechanism and retracting tip panel; the two plates are glued together with marine epoxy to form the complete wing with 3.97 mm thickness. The rotating tip panel is a 1.59 mm thick carbon-fiber composite plate cut into an approximately 1/8-circle shape, the apex of which is pivoted at the leading edge and tip corner of the main wing via a binding barrel. The tip panel is rotated via a small motor above the free surface, called the tip motor (brushed DC servo motor, Micromo model 2642W012CXRIE3-1024L+26A 16:1+MG26, with 65536 encoder counts per revolution), that is mounted on an aluminum plate which also supports the main wing.

The panel motion is accomplished as follows (see Figure 10-1(b)). A stainless-steel control rod connects to an arm collared on the tip-motor shaft; the rod/arm connection is a rotational joint. The rod passes down through the wing cavity and connects at its lower end to the aft/inboard corner of the pivoted tip panel, also with a rotational joint. The control rod connection to the arm is 68.6 mm from the center of the tip-motor axle, which is approximately the same distance between the tip-panel pivot point and its connection to the rod. Therefore, the panel rotates with the tip motor via the rod, with a nearly one-to-one conversion. Some part of the tip panel is always inside the main wing even when fully extended; the exposed panel has an average radius of 73 mm from the exposed panel apex. The sweep angle between a line parallel to the main-wing Leading Edge (LE) and the panel LE is Λ (Figure 10-1(b)), and the angle between the tip edge of the rectangular main wing and the panel LE is $(90° - \Lambda)$. Using the latter angle, 46.72° of motor rotation yields 45° of exposed tip rotation. The tip panel can completely retract into the main wing ($\Lambda = 90°$), or fully extend giving $\Lambda = 45°$. The panel rotational velocity is verified using 240 frame-per-second movies of the panel motion. The angular position of its LE over time is determined from still images using Gimp software. The manual edge-finding incurs some error but shows that the average angular panel velocity from the images is within 0.3% of the motor velocity.

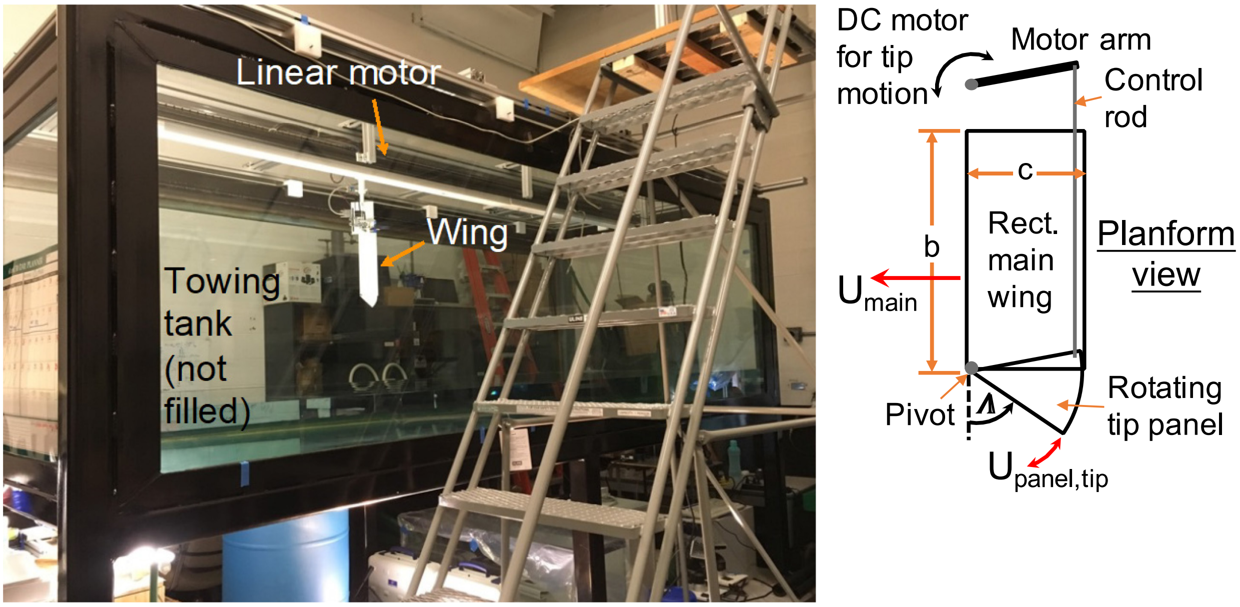

(a) (b)

Figure 10-1: Experimental Setup. (a) Towing-tank facility, indicating the wing and linear motor. (b) Schematic of the wing, giving the tip-panel actuation scheme, wing geometry, and wing velocities.

10.2.2 Force Measurements

The lift force is measured using a 6-axis ATI Gamma force/torque sensor attached between the linear stage carriage plate and the wing's sting support. The transducer's negative y-direction is aligned with the wing's lift direction. The Gamma signals are acquired with a 16-bit National Instruments DAQ card (PCIe-6323) via LabVIEW and sampled at 1 kHz after receiving a trigger signal from the motion controller. For each case, N = 10 runs are taken in water and in air; the latter allow the model inertial forces to be subtracted off, leaving the fluid-dynamic forces of interest. MATLAB is used for data processing, and the mechanical vibrations and noise of the system are analyzed from strike tests as well as air and water runs by estimating the power spectral density. A 3rd-order Butterworth filter with a 4 Hz cutoff frequency is applied to the data which retains the flow-related forces while removing most of the vibration contributions. After filtering, all runs are aligned in time via a correlation, the air and water runs are separately averaged, then the air results are subtracted out.

The Gamma uses the ATI SI-32-2.5 calibration, and its accuracy is checked using static tests with precision weights for forces of ~0.2 – 2 N, covering the range of the experiment; the results are within 1.5% of the calibration. For a given case, the random uncertainty in the average lift coefficient, $\delta C_{\mathrm{L}}(t)$, is computed at each time instance using the precision error of the mean from the run-to-run variations of the water measurements, $\delta C_{\mathrm{L,water}}(t) = t_{\nu,0.95}\sigma_{\mathrm{water}}(t)/\sqrt{N}$, and that of the air measurements, $\delta C_{\mathrm{L,air}}(t) = t_{\nu,0.95}\sigma_{\mathrm{air}}(t)/\sqrt{N}$, where $t_{\nu,0.95}$ is the Student's t-distribution for a 95% confidence level with N – 1 degrees of freedom, and the sample standard deviation is σ. Overall, the mean lift coefficient and its precision error for each case are $\bar{C}_{\mathrm{L}}(t) \pm \delta C_{\mathrm{L}}(t) = \left(\bar{C}_{\mathrm{L,water}}(t) \pm \delta C_{\mathrm{L,water}}(t)\right) - \left(\bar{C}_{\mathrm{L,air}}(t) \pm \delta C_{\mathrm{L,air}}(t)\right)$. Figure 10-2 shows two AR = 4 cases with tip-panel actuation, the step-up and step-down gust with the gust acceleration or deceleration occurring over 1c of travel. For the step-up gust, actuation-in starts at 21.5c traveled, and for the step-down gust actuation-out begins at the same distance. These were chosen since they are representative of the whole measurement set. The gray band in each plot shows the precision-error bounds and note that for the mean CL the overline is omitted and implied from this point forward and in all plots. Also, in computing CL the instantaneous Umain and wing area are employed, which yield more similar values before and after the gust. The precision error is overall lowest in the initial Re = 18,000 portion of the step-down gust, and highest after the step-down to Re = 9,000 where the data have more variation and the signal is smallest. For the cases shown in Figure 10-2, the time-average of the precision error in the mean CL over the full motion duration is ±4% (±0.05) and ±6.7% (±0.08) for the step-up and step-down gusts, respectively.

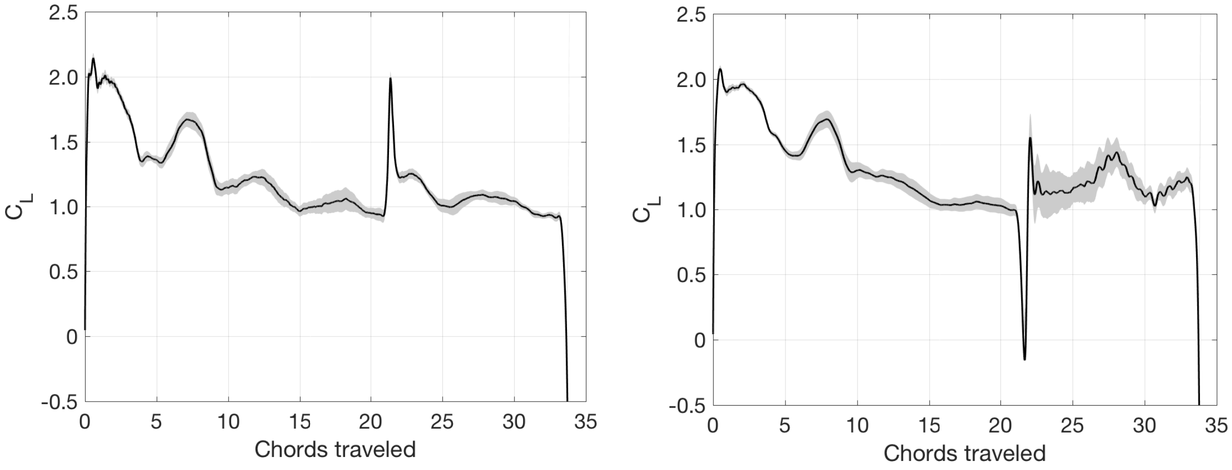

(a) **(b)**

Figure 10-2: Plots Showing the Filtered C_L from the Mean of 10 Runs in Water with the Average of 10 Runs in Air Subtracted Off (Black Line), and the Corresponding Precision Error Calculated as Described in the Text (Gray Band). Note: The instantaneous U_{main} and wing area are used in calculating the C_L, which make the pre- and post-gust values more comparable. The cases are the AR = 4 wing for: (a) the 1*c* step-up gust with tip-panel actuation-in at 21.5*c* traveled and (b) the 1*c* step-down gust with panel actuation-out at the same distance traveled.

10.2.3 Experimental Parameters

The main rectangular wing is oriented vertically through the free surface, which acts as a reflected (symmetry) boundary condition [31], [30]. For the rectangular wing with the tip panel fully retracted, the physically submerged Aspect Ratio is AR = b/c, set by varying the water level, where b is the wingspan. Submerged AR = 1 and 2 are used for the rectangular-wing portion, doubled to 2 and 4 by the reflection; all ARs reported are the reflected values. The CL for the reflected AR = 2 and 4 cases is similar to available starting-flow data from the NATO RTO task group AVT-202 for fully-submerged wings of the same ARs [5], supporting the reflected-boundary assumption. The main-wing Reynolds number ($\mathrm{Re} = U_{\mathrm{main}} c/\nu$), where ν is the kinematic viscosity and Umain is the translational velocity of the main wing, is of order 10,000 or slightly below this for all cases. This is appropriate for small UAVs [30], and yields sufficiently-high signals from the force sensor. The CL at Re = 12,000, which exhibits minimal free-surface deformations, matches that at the maximum Re = 18,000 tested within the error, for which the free-surface disturbances are somewhat larger particularly in the vortex cores, but otherwise small compared to the wing span. This indicates that adverse free-surface effects are not substantial over the Re-range tested. The angle of attack of the main wing is $\alpha = 45°$, chosen to produce flow separation with strong vortices, and due to the substantial prior work at this value. At $\alpha = 45°$, AR = 4 and with the tip panel extended, the blockage ratio (submerged frontal-projected wing area divided by the filled tank cross-sectional area) is only ~1%.

The main-wing motions tested are simplified streamwise gust-like profiles, each having parameters varied; the tip-panel actuation is described below. Similar to Mulleners et al. [37] and Marzanek and Rival [38] we examine "step-up" gusts, but also "step-down" gusts. Using a moving model with respect to a constant (or zero) freestream velocity to produce a gust-like interaction has been shown to be equivalent to employing a stationary test article in a time-varying freestream, provided that the buoyancy effects from this accelerating freestream are accounted for [34], [35], [36]. Marzanek and Rival [38] point out that this has so far only been tested using nominally 2-D bodies (airfoils), however parameter variations using 3-D bodies in either configuration will produce insightful trends. The step-up and step-down cases can be thought of as emulating headwind and tail-wind gusts, respectively. The gust cases all begin with acceleration from rest over 1c to constant Umain, initial, using a hyperbolic-tangent profile to mitigate mechanical vibrations. The hyperbolic-tangent curve is scaled to have the same average acceleration and duration as a constant-acceleration (linear) profile. At 21c traveled, the wing executes an additional acceleration to a higher constant velocity of 1.5Umain, initial for step-up gusts or deceleration to 0.5Umain, initial for step-down. Therefore the gust amplitude is 50% in each case, as for the step-up gusts of Mulleners et al. [37] and Marzanek and Rival [38]. Hyperbolic-tangent velocity profiles are also used during the acceleration and deceleration portions of the gust motions until the desired constant velocity is reached. The gusts are initiated after 20c so startup effects are not prominent, since the CL approximately levels off to a low value and the wing exhibits more periodic LEV and TEV shedding (based on our prior flow visualization [22]). Greater than 30c may be ideal [37], [41], which could depend on AR and Re, however the present tank length cannot accommodate this. Similar to the step-up study of Marzanek and Rival [38], acceleration/deceleration or "ramp" distances of 1c, 3c, and 6c before the wing reaches the final step-up/step-down velocity, respectively, are tested. After 12c of travel beyond the gust start to observe the response, the wing decelerates and stops at a distance of 34c.

Figure 10-3 shows the dimensionless wing velocity profiles versus chords traveled, nondimensionalized by U_{main}, initial. The Re values for the force measurements are a balance between ensuring sufficient sensor signals in the final phase for the step-down gust, and limiting the wing velocity to mitigate free-surface deformations for the initial portion of the step-down gust and last phase of the step-up gust. For the step-up and step-down cases, the constant velocity before/after the gust has Re = 12,000/18,000 and Re =18,000/9,000, respectively. Reynolds number effects on CL in this range have been shown to be minimal [42] and are not the focus of the present study.

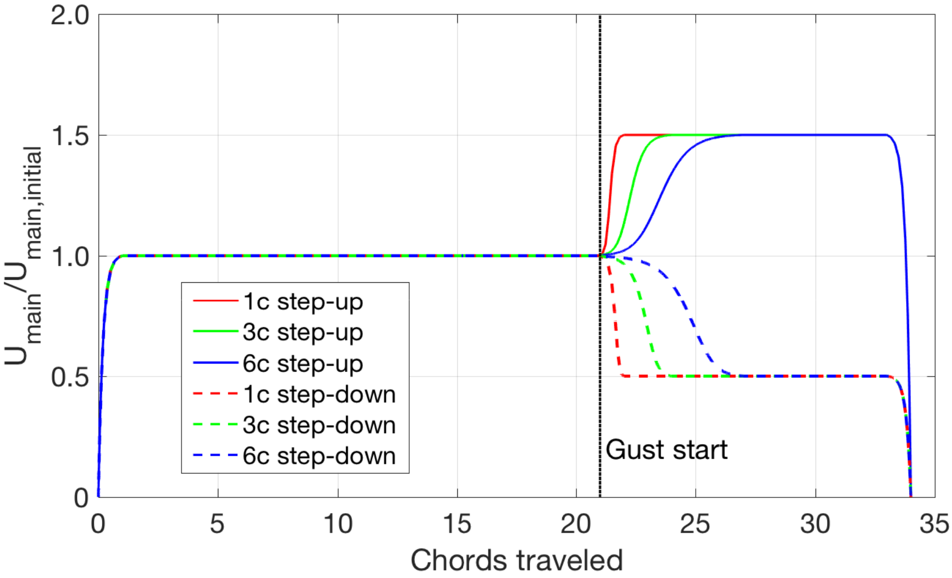

Figure 10-3: Main-Wing Motion Profiles for the Step-Up and Step-Down Gust Cases.

The goal of this chapter is to examine whether the tip-panel actuation can mitigate the lift change produced by the step-up/step-down gusts. However, as indicated in Section 10.1 the aim here is to understand the panel's effect and not to do flow control or lift optimization. Inward rotation ("actuation-in") is employed to reduce the lift after the step-up gust, while outward rotation ("actuation-out") is used to increase the post-gust lift for the step-down case. For the former, the starting and ending values of Λ are 45° and 90°, while these are swapped for the latter. Chowdhury et al. [22] showed that actuation timing can substantially affect the flow structures, and here it is varied to study its influence on the lift. For all 1c – 6c step-up/step-down acceleration/deceleration ramps, two actuation timings are tested:

1) Early actuation at 21.5c of travel, i.e. shortly after the gust initiation at 21c; and
2) Actuation at 50% of the travel distance during the ramp, namely at 21.5c, 22.5c, and 24c traversed for the 1c, 3c, and 6c ramp, respectively; for the 1c ramp the two timings are the same.

The wing area and AR will vary for each case. With the panel retracted (Λ = 90°), the AR cases are simply the rectangular values of 2 and 4. For the fully-extended tip panel with Λ = 45°, the AR increases to 4.1 and 6, respectively, with corresponding increases in wing area of 31.7% and 15.8%. As mentioned earlier, two reference cases with the same Umain profiles but fixed tip geometries are tested for comparison:

1) The "rectangular" case with the tip panel fully retracted (final geometry for actuation-in), and
2) The "static-sweep" case where the tip panel is extended to Λ = 45° (final geometry for actuation-out).

Table 10-1 summarizes the motion cases.

The tip-panel motion is in addition to Umain, and is characterized using the advance ratio, J. For flapping-wing flight [43], typically J is taken as the forward velocity divided by the absolute value of the average azimuthal (rotational) wingtip velocity (excluding the superimposed translational velocity). Harbig et al. [44] studied LEV dynamics for rotating wings with a horizontal stroke plane in constant forward motion. For the downstroke, they created a J vs. AR diagram to show which values yielded a "stable" (mainly attached) or "unstable" (shed) LEV. The present tip panel has a tilted 45° rotational stroke plane, and to better compare with Harbig et al. [44] the component of the forward velocity in the plane of rotation, $U_{\text{main}} \cos \alpha$, is used similar to the definition for helicopters with a tilted rotor plane [45]. Further, since the panel does not rotate outward past 45° its LE never achieves orthogonality with Umain as an insect wing typically does, so a factor of $\cos \Lambda$ is used to obtain the component of $U_{\text{main}} \cos \alpha$ orthogonal to the LE, i.e., parallel to the panel's chord direction. The final expression is $J = U_{\text{main}} \cos \alpha \cos \Lambda / U_{\text{panel,tip}}$. For all cases, the tip-panel motion profile is trapezoidal with constant acceleration and deceleration occurring over the first and last 10% of the duration, respectively, having constant Upanel,tip in between; the rotational amplitude is always 45° giving Λ = 45°. The maximum, constant Upanel,tip is used in the J formula. The constant-velocity magnitude for all cases, whether inward or outward panel rotation, is Upanel,tip = 1.5Umain, initial. The Umain changes during wing acceleration/deceleration for step-up/step-down gusts, with the largest value being for the 50% step-up profiles that yields a maximum advance ratio of J = 0.5; this is the maximum J for all cases tested. For outward panel rotation, from extrapolation of the Harbig et al. [44] diagram for the AR ≈ 1 of the tip panel, J ≤ 0.5 should produce an attached LEV (here SEV). The effective angle of attack for the 3-D tip-panel flow cannot be determined without quantitative velocity data, however our prior [22] flow visualization indicates the formation of an attached SEV for outward rotation, showing consistency with the results of Harbig et al. [44]; for inward panel actuation, our earlier study [22] found that the panel vortex system sheds.

Table 10-1: Cases Tested for the Step-Up / Step-Down Gust Motions for AR = 2 and 4; the Reynolds Numbers are Given in the Text.

Gust Type	Gust Acceleration/Deceleration Distribution	Tip Conditions Tested
50% step-up gust at 21c traveled: $U_{\text{main}}/U_{\text{main, initial}} = 1.5$	1c	Rect., static sweep, actuation-in at 21.5c (50% gust dist.)
	3c	Rect., static sweep, actuation-in at 21.5c and 22.5c (50% dist.)
	6c	Rect., static sweep, actuation-in at 21.5c and 24.0c (50% dist.)
50% step-down gust at 21c traveled: $U_{\text{main}}/U_{\text{main, initial}} = 0.5$	1c	Rect., static sweep, actuation-out at 21.5c (50% dist.)
	3c	Rect., static sweep, actuation-out at 21.5c and 22.5c (50% dist.)
	6c	Rect., static sweep, actuation-out at 21.5c and 24.0c (50% dist.)

Harbig et al. [44] and Lentink and Dickinson [6] also describe the role of Ro for a rotating wing in forward motion, concluding that if Ro is small, i.e. for short radial distances, LEV attachment can occur for low J. For rotating wings in hover, attached LEVs have been reported for approximately Ro ≤ 1.5, using Ro = rg/c, with rg being the radius of gyration [6], [8]. Considering instead the local radial distance from the axis of rotation, attached LEVs have been found for about r/c < 3 – 4 for small root cutouts (offsets) for wing rotation in hover [4], [7], [46]. Several recent papers have shown the importance of having low Ro for LEV attachment and large lift, and how the effects of AR can be isolated from Ro and/or Re, with Refs. [9], [10], [11], [46] being representative. The tip panel's small AR should also have a sufficiently low Ro for SEV attachment, which our earlier flow visualization showed [22], as mentioned above.

10.3 RESULTS

The results from the force measurements are presented here. First the rectangular reference case is used to show the key features of the step-up and step-down gust motions without tip-panel actuation, next the actuation cases are covered.

10.3.1 Rectangular Wing

Figure 10-4(a) gives the dimensional lift force, L, for the AR = 4 rectangular step-up and step-down gust cases, to show their behavior prior to calculating CL. For the starting-flow portion with acceleration from rest over 1c, all curves exhibit an initial peak due to fluid-inertial (added-mass) force and circulatory force from the vortex growth. This is followed by a second peak (after acceleration ceases) due to vortex formation and shedding, and then a third, lower peak corresponding again to a formation and shedding cycle. Mulleners et al. [37] describe the interactions with the prior flow structures which cause this last, prominent circulatory peak to be reduced. This behavior is similar to that of the fully-submerged AR = 4 starting-flow cases from the NATO AVT-202 study, as reported in Stevens et al. [5]. Consistent with the 50% step-up gust study of Mulleners et al. [37], here the qualitative lift trends for the 1c-acceleration starting flow and 1c step-up gust resemble one another.

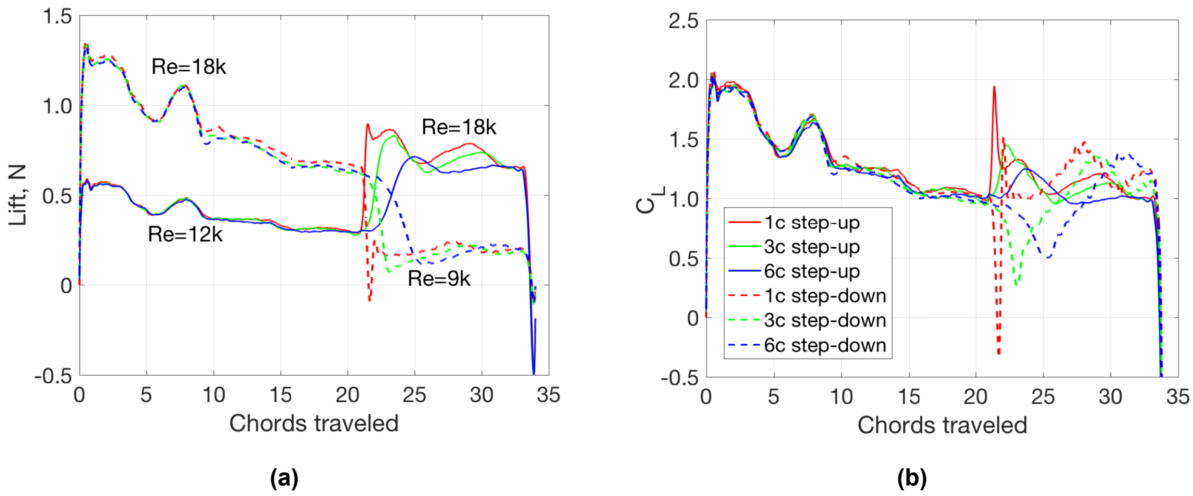

(a) (b)

Figure 10-4: Force Measurements for the *AR* = 4 Rectangular-Wing Cases: (a) Dimensional Forces with Reynolds Numbers Before and After the gust Motion Labeled for the Step-Up and Step-Down Gusts, and (b) C_L Incorporating the Instantaneous Main-Wing Velocity, U_{main}. All Gusts Start at 21*c* of Wing Travel.

Figure 10-4(b) shows the corresponding CL plot. The CL is defined using the instantaneous main-wing velocity, Umain, from Figure 10-3, so that the time-varying Umain is accounted for and any remaining CL features can be attributed to unsteady-flow phenomena. This gives $C_L = 2L/\rho U_{\text{main}}^2 S$, where ρ is the fluid density and S is the wing area. For the initial 1c startup acceleration, the CL is instead nondimensionalized using the constant-velocity value just after acceleration, Umain, initial, since starting-flow scaling is not the focus of this chapter. The CL curves for Re = 12,000 and Re = 18,000 prior to the gust collapse very well, as expected given the Re independence mentioned above. Further, Figure 10-4(b) indicates that using the instantaneous Umain for CL makes the pre- and post-gust values more comparable. Considering the 1c step-down case (red dashed curve), just after the gust there is a negative force peak from the added-mass contribution followed by a brief positive peak; the CL scaling increases their relative magnitudes versus the dimensional lift. The positive peak could be the continuation of the reducing circulatory-force value through the gust after the added-mass force ceases (see Figure 10-4(a)), or just mechanical backlash. Further tests on the relative behavior of this second peak at different speeds are needed to determine the cause.

For the 3c ramp the added-mass and initial circulatory lift produce only a single peak, followed by a second, lower circulatory-force maximum. The 6c step-up gust also generates a single, broad first peak with the same contributions as that for the 3c ramp, but there is only a very weak second circulatory-force maximum that lies within the experimental error.

For the step-down gust, the 1c-ramp case exhibits a CL < 0 peak during maximum deceleration, and the 3c and 6c ramps also each show a clear CL minimum, but with CL > 0, corresponding to their maximum deceleration (Figure 10-5(b)); the magnitudes of these minima are progressively smaller with greater deceleration distance. During deceleration, the prior wake produced by the wing must impinge on it, be deflected by the wing, and likely widen; this is detrimental for lift production. Note that the magnitudes of the CL minima for the step-down gusts, relative to the CL prior to the gust initiation, are larger than those of the related positive peaks for the step-up cases. This may be caused by a greater added-mass force from the step-down wake impingement versus that from acceleration for the step-up case, however there is no way to determine this without quantitative flow data. For the step-down gusts, after the CL minima as the deceleration gives way to the slower constant-velocity motion, all cases show a CL recovery (increase) to a positive circulatory-force maximum.

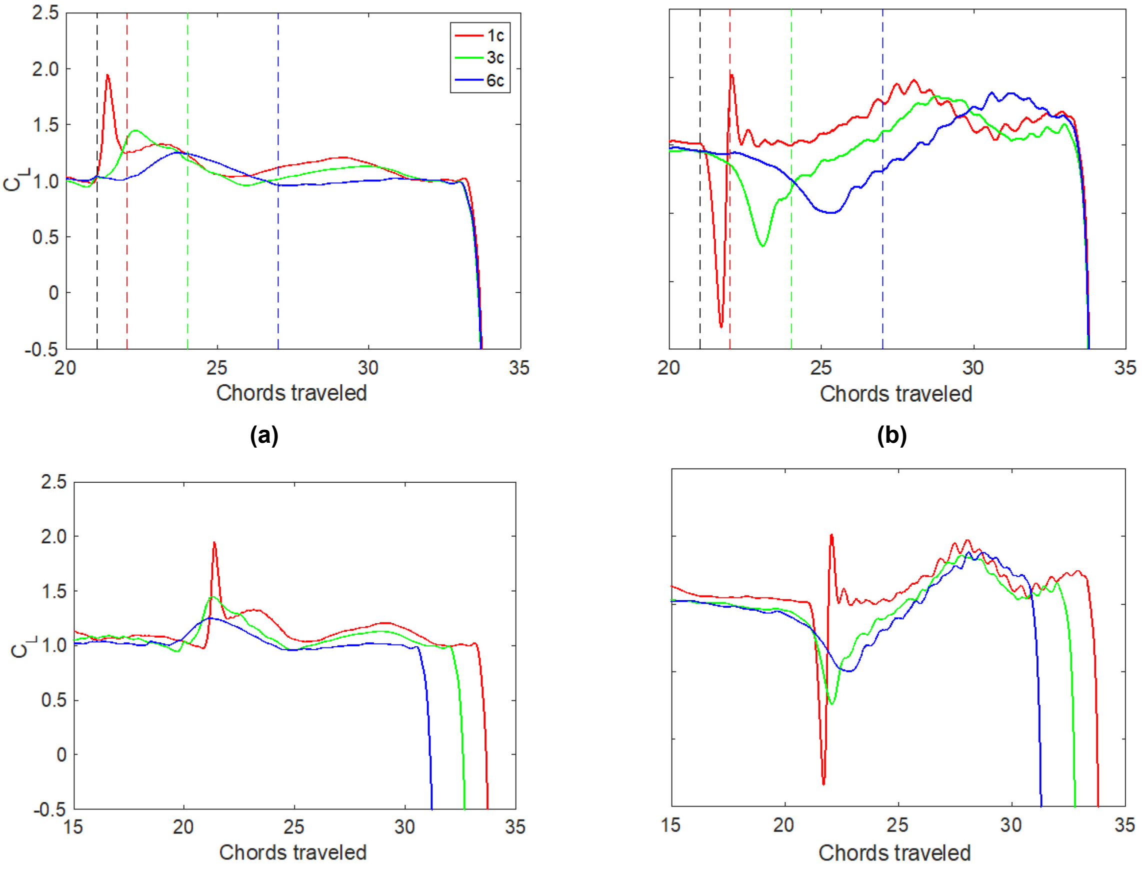

(a) **(b)**

(c) **(d)**

Figure 10-5: Lift Coefficients for the *AR* = 4 Rectangular-Wing Cases, Focusing on the Gust Portion of the Wing Motion. (a) Step-up gusts, (b) step-down gusts, (c) step-up gusts with the 3*c* and 6*c* cases having the chords traveled shifted backward by half the gust acceleration distance, i.e. by 1.5*c* and 3*c*, and (d) step-down gusts with the 3*c* and 6*c* results also shifted backward by the same respective values of chords traveled. The C_L incorporates the instantaneous main-wing velocity, U_{main}. The black dashed vertical line indicates the start of each gust at 21*c* traveled, whereas the colored dashed vertical lines designate the end of the gust acceleration or deceleration, with the colors corresponding to the gust distances in the legend.

Figure 10-5(a) and Figure 10-5(b) focus on the gust forces for the rectangular step-up and step-down cases. For the step-up gust, the 1c acceleration ramp yields a sharp initial peak with contributions from both added-mass and circulatory force, followed by two progressively lower and broader circulatory-lift peaks (Figure 10-5(a)).

For Figure 10-5(c) and Figure 10-5(d) the chords traveled for the 3c and 6c gusts are shifted backward by half the gust width, i.e. 1.5c and 3c for the 3c and 6c gusts, respectively, for both the step-up and step-down types. This shift yields an improved collapse of the step-up gust cases in terms of the timing of the 1c added-mass dominated peak and the first peaks for the 3c and 6c accelerations, and for the second circulatory peaks of the 1c and 3c gusts (Figure 10-5 (c)); however, the overall collapse is not very good. For the step down gusts, the shift brings the low CL peaks closer in terms of chords traveled as expected (Figure 10-5(d)). However, they do not line up perfectly because the greatest deceleration does not occur exactly at 50% in terms of chords traversed, but rather at 50% of the total deceleration duration in time. The CL recovery after the minimum shows a much better collapse via the shift, with the 3c and 6c cases being very close for nearly the full increase and peak afterward. The 1c gust instead shows a CL plateau after the brief positive (backlash) peak, but beyond ~25c traveled it collapses with the other two cases. The broad CL peak after each gust finishes must be due to circulatory lift, and all peaks have similar magnitudes to e.g., the first circulatory peak of the 1c step-up gust case.

10.3.2 Tip-Panel Actuation and Aspect Ratio Effects

Figure 10-6 and Figure 10-7 show the step-up gust cases including tip-panel actuation-in and step-down gust results with actuation-out, respectively. They also compare data for AR = 4 (top row) and 2 (bottom row); recall that the AR refers to the rectangular portion of the wing. Actuation occurring at 21.5c is tested for all acceleration/deceleration gust-ramps, as well as “50% actuation” which is done at the midpoint of the gust in terms of chords traveled. The 50% actuation happens at 22.5c and 24c traveled for the 3c and 6c gusts, respectively, and is the same as the 21.5c-actuation timing for the 1c gust. For the tip-panel actuation cases, the CL versus time incorporates both the instantaneous Umain for the velocity scale and the time-varying wing area. This again ensures that any deviations from the rectangular and static-sweep reference cases can be attributed to unsteady flow phenomena.

For the step-up gusts with actuation-in (Figure 10-6), the wing starts in the static-sweep condition, then after actuation the tip panel is fully retracted to the rectangular-wing case. Considering AR = 4, for the 1c ramp actuation-in at 21.5c (50% actuation) is too late to affect the added-mass dominated initial peak, but appreciably reduces both circulatory peaks compared to the static reference cases. A lower CL from actuation versus the rectangular case indicates a truly unsteady-flow effect that cannot be accounted for by simply using the instantaneous wing area (and translating-wing velocity) in defining CL. The flow visualization results of Chowdhury et al. [22] indicate that a key contributor to this CL reduction is likely the shedding of the panel SEV-TV-TEV loop as the panel quickly retracts into the wing. Note that in between the circulatory peaks (~25.5c traveled), presumably after the main-wing vortex system sheds, the CL for all 1c-ramp cases is nearly the same. The overall CL reduction effect from inward actuation lasts for the remainder of the measurement, at least 12.5c traveled beyond the gust. The 50% actuation-in for the 3c ramp also does not affect the first peak CL magnitude, but just after this the actuation lowers the CL below that of the reference cases for the rest of the motion, except again near the local minimum where shedding occurs. For the 6c gust, the 50% actuation timing also reduces the CL between the first peak and shedding, although the effect is slightly smaller, after which the actuation-in case is similar to the reference geometries except for a slight CL decrease again near the end of the motion. The 21.5c actuation-in for the 3c-ramp reduces the peak CL during the gust, but afterward the CL nearly matches the reference cases. For the 6c-ramp and 21.5c actuation, the CL curve is essentially the same as those of the reference wings. This does not mean that the moving panel has no effect on the dimensional lift, but rather that its effect can be scaled to be similar to the reference cases by also including the instantaneous wing area in the CL. Overall, the 50% actuation timing has the greatest and most sustained CL reduction effect, being most pronounced for the 1c ramp and only slight for the 6c gust, but it is too late to influence the gust peak itself for the 1c ramp and the initial gust-peak value for the 3c and 6c ramps.

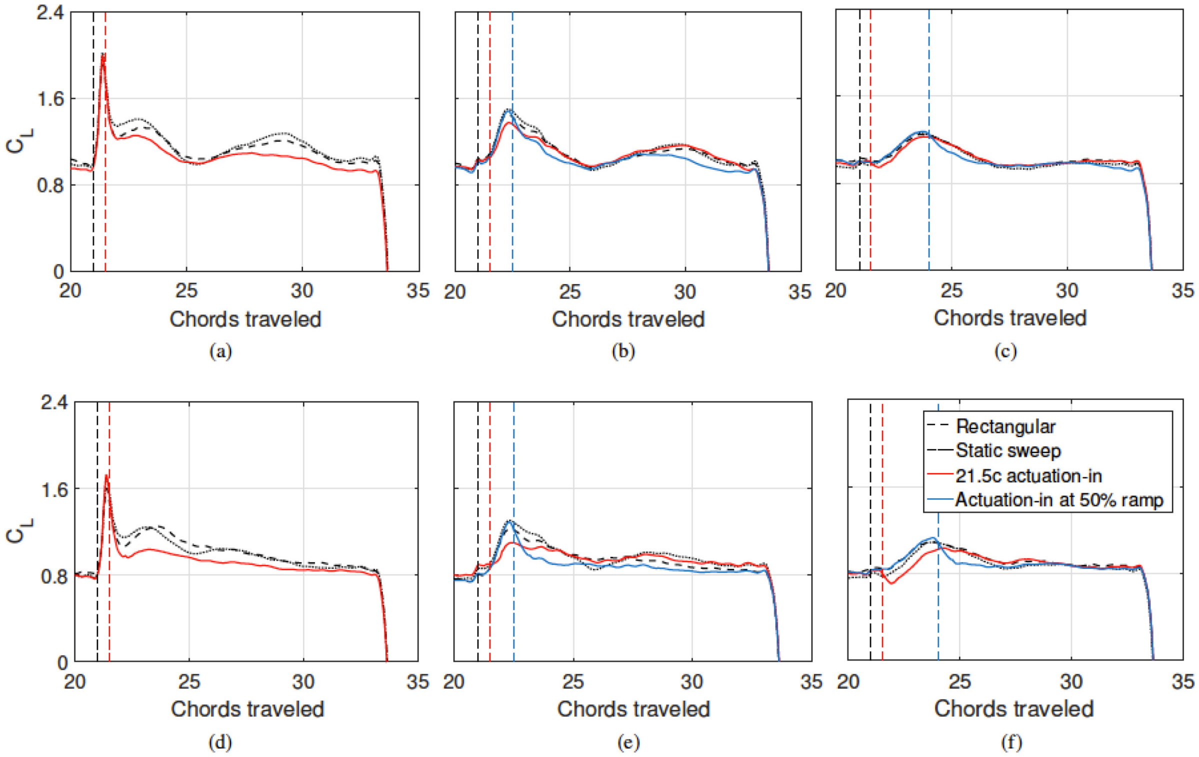

Figure 10-6: Results for the Step-Up Gust Cases with Tip-Panel Actuation-In for *AR* = 4 (Top Row) and *AR* = 2 (Bottom Row). (a,d), (b,e), and (c,f) show the 1*c*, 3*c*, and 6*c* gusts, respectively. The cases for each C_L curve are given by the legend, corresponding to the rectangular, static-sweep, and various actuation-in timings. The black dashed vertical line marks the start of all gusts at 21*c* traveled, and the red and blue dashed vertical lines indicate the initiation of the tip-panel actuation at 21.5*c* traveled and 50% of the ramp, respectively, per the legend colors. The 50%-ramp actuation (same as the red dashed line for the 1*c*-gust, blue dashed line for 3*c* and 6*c*) occurs at a distance traversed that is half-way through the gust acceleration, i.e. at 21.5*c*, 22.5*c*, and 24*c* for the 1*c*-, 3*c*-, and 6*c*-gust, respectively. The C_L is defined using the instantaneous U_{main} as the velocity scale and a wing area equal to that of the main wing plus the instantaneous exposed tip-panel area.

The corresponding AR = 2 step-up gust cases are shown in the second row of Figure 10-6. Compared to AR = 4, the CL curves for AR = 2 have an overall lower magnitude, consistent with the smaller AR. For the 1c and 3c ramps, for AR = 2 a second circulatory-force peak is not present in almost all cases, except where a slight maximum exists for the static-sweep geometry, whereas this feature is prominent for AR = 4. Considering that the step-up gust shows similarities with starting flows, this is consistent with the starting-flow AR trends from Stevens et al. [5] and Taira and Colonius [3]. The latter study showed less-pronounced CL peaks from vortex shedding for AR = 2 versus 4 at $\alpha = 40°$ due to the greater effect of downwash from the wingtip vortices.

Overall, actuation-in for AR = 2 produces a larger change in CL magnitude (with respect to the reference cases) during and shortly after the gust compared to AR = 4, which is expected given that the extended AR = 2 tip panel has a relatively greater percentage of the total wing area. However, this change is related to a dynamic flow effect, since the variable wing area is accounted for in CL. This AR difference occurs for the 1c-ramp actuation-in case during the first circulatory-force peak, and for the 3c-ramp with 21.5c actuation which has a relatively lower gust peak and with 50% actuation where the post-gust CL is smaller compared to the reference geometries. Also, for the 6c ramp the 21.5c and 50% actuation-in cases yield measurably lower CL before and after the peaks for the reference cases, respectively, which is not found for AR = 4. However, for AR = 2 the panel's actuation effect is less sustained for the 1c- and particularly 3c-ramp cases versus AR = 4; for the 3c ramp the actuation influence is negligible after 25c of travel. This may be related to the lack of a prominent, second circulatory-force peak for AR = 2, perhaps indicating that for AR = 4 the moving panel's performance is enhanced by an interaction with the expected stronger inboard LEV formation, and its shedding; further quantitative flow information is needed to explore this.

Figure 10-7 gives the actuation-out cases for the step-down gusts. The wing begins with the rectangular geometry then the tip panel rotates outward to have the static-sweep planform. For AR = 4 (top row), overall, the actuation increases the CL compared to the reference cases both during and after the gust, depending on the ramp length. The most pronounced effect is for the 1c ramp, for which the magnitude of the negative CL peak is reduced substantially, and the post-gust CL plateau is higher than the reference cases. The flow visualization of Chowdhury et al. [22], albeit for a starting flow, shows an SEV forming on the outward rotating panel and an increase in the TEV/TV vortex loop size. If similar flow structures are present for the gust case, which has forces resembling those of the starting flow, these features would contribute to this enhanced CL. For the 3c ramp, the 21.5c actuation-out produces a high CL peak, then the CL lowers but maintains a larger value than the references cases until the first circulatory recovery peak at ~28.5c traveled. The 50% actuation-out at 22.5c traveled for the 3c ramp occurs just prior to the CL minimum from the gust. At first it yields a CL similar to the 21.5c actuation case, but then the CL is reduced and gradually converges to essentially match the reference cases just prior to the recovery peak. As with the step-up gust cases, tip-panel actuation for the 6c-ramp step-down gust has the smallest effect. For 21.5c actuation-out, the CL overshoots that of the reference cases initially, then after 2c of further travel the CL becomes very close to the reference results, within the error. For 50% actuation-out at 24c traversed, there is again an overshoot CL peak and the CL during the gust minimum is somewhat higher than that of the fixed-geometry reference cases (and the 21.5c actuation result). The CL continues to be sustained slightly above all other cases until the recovery peak, but this improvement level remains close to or within the uncertainty. In summary, for the AR = 4 step-down gusts, actuation-out not long before the CL gust minimum can reduce the magnitude of the drop in lift, and for the 1c and 3c ramps the actuation effect is sustained above the uncertainty until approximately the CL recovery peak.

The AR = 2 actuation-out results for the step-down gusts are shown in Figure 10-7, second row. The rectangular and static-sweep reference cases show more deviation from one another compared to AR = 4, with the static-sweep wing exhibiting reduced CL after the gust but before the recovery to maximum lift. This is likely due to the relatively greater change in outboard sweep and AR between the rectangular and static-sweep cases versus AR = 4, but without flow data the exact cause is unknown. Recall that for actuation-out the rectangular and static-sweep geometries represent the states before and after actuation, respectively. For the AR = 2, 1c ramp, the actuation-out at 21.5c reduces the magnitude of the CL < 0 gust peak, similar to AR = 4; just after this, the AR = 2 forces show two positive peaks that again may indicate mechanical backlash. Next, in the CL recovery before the maximum peak, the actuation-out curve follows both the rectangular and static-sweep cases, then the static-sweep case lags behind the others, until all CL curves converge at the maximum recovery peak and remain similar to the end of the motion. This converging behavior also occurs for AR = 4.

For the AR = 2, 3c ramp, the 21.5c and 50% actuation-out CL both exhibit overshoot peaks from the initial actuation that are above the reference cases, similar to the AR = 4 wing in terms of timing but relatively larger; the actuation effects persist and reduce the magnitude of the gust minimum. For AR = 2 the CL increase after the minimum has a higher initial slope for the rectangular and actuation cases (all overlap), compared to AR = 4. Conversely, the AR = 2 static-sweep case shows substantially reduced CL in the recovery portion, consistent with the 1c-ramp gust. Interestingly, the CL recovery-peak magnitude is slightly larger and occurs earlier for the 21.5c actuation-out, versus the other AR = 2 cases. The AR = 2, 6c-ramp case also shows similar but relatively greater initial CL overshoot behavior for the actuation cases just after the gust, compared to AR = 4. The 6c-ramp 50% actuation has a higher slope than all other 6c gust cases and therefore a faster initial recovery, but the CL then reaches a plateau slightly below the maximum value for the reference wings. For

21.5c actuation-out, similar to the 3c-ramp the increasing CL overlaps at first with the rectangular case, then achieves a higher and earlier CL maximum, albeit larger than that of the 3c ramp. These larger and earlier peaks from 21.5c actuation for the 3c and 6c ramps occur at approximately the same chords traveled as the AR = 4 recovery peaks, perhaps related to the higher AR achieved near the beginning of the gust.

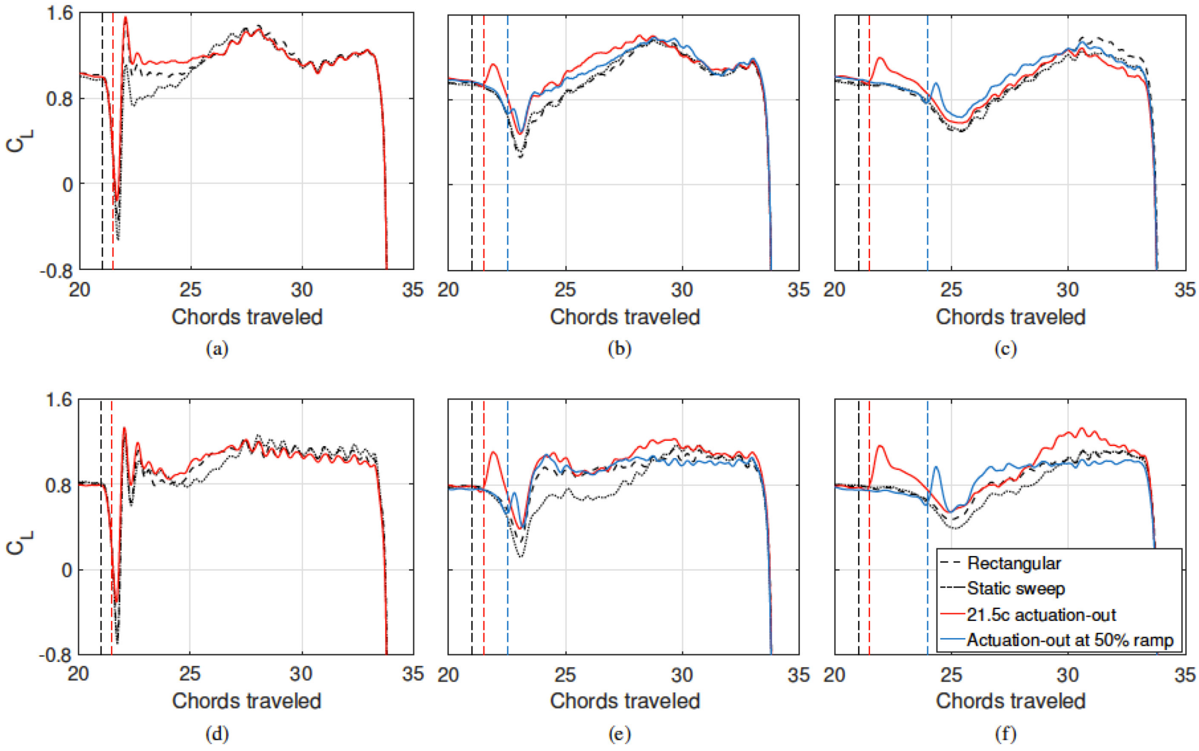

Figure 10-7: Results for the Step-Down Gust Cases with Tip-Panel Actuation-Out for *AR* = 4 (Top Row) and *AR* = 2 (Bottom Row). (a,d), (b,e), and (c,f) show the 1*c*, 3*c*, and 6*c* gusts, respectively. The cases for each C_L curve are given by the legend, corresponding to the rectangular, static-sweep, and various actuation-out timings. The black dashed vertical line marks the start of all gusts at 21*c* traveled, and the red and blue dashed vertical lines indicate the initiation of the tip-panel actuation at 21.5*c* traveled and 50% of the ramp, respectively, per the legend colors. The 50%-ramp actuation (same as the red dashed line for the 1*c*-gust, blue dashed line for 3*c* and 6*c*) occurs at a distance traversed that is half-way through the gust deceleration, i.e. at 21.5*c*, 22.5*c*, and 24*c* for the 1*c*-, 3*c*-, and 6*c*-gust, respectively. The C_L is defined using the instantaneous U_{main} as the velocity scale and a wing area equal to that of the main wing plus the instantaneous exposed tip-panel area.

For the step-down gusts, a summary comparison of the actuation-out effect between AR = 4 and 2 is somewhat confounded by differences in the CL behavior of the rectangular and static-sweep reference cases for each AR. These aside, the tip-panel actuation-out for both ARs yield similar reductions of the peak magnitude during the CL minimum from the gust, which is beneficial for gust mitigation. For the two longer ramps, the AR = 2 actuation cases produce relatively larger peaks just after actuation, versus the reference geometries, compared to AR = 4. Further, for AR = 2 the rectangular and actuation cases allow for a faster post-gust recovery (CL increase) for the 3c ramp, and 50% actuation yields a similarly earlier recovery for the 6c-ramp, not found for AR = 4. Also, for AR = 2 the 21.5c actuation generates higher and earlier CL recovery peaks versus the reference cases, which is not observed for AR = 4. However, for the 1c-ramp the AR = 4 actuation case results in more sustained CL between the gust minimum and the recovery peak. Overall, for longer ramps the AR = 2 actuation-out cases are superior for producing higher relative CL faster, to aid in gust mitigation.

10.4 CONCLUDING REMARKS

A tip panel with aft sweep was rotated inward or outward on a low-AR, α = 45° rectangular main-wing in translation, to study its ability to mitigate lift variations from streamwise gusts of two kinds: step-up and step-down, respectively. Three gust-ramps over distances traveled of 1c, 3c, and 6c with two actuation timings – near the gust start (21.5c traveled) and at 50% of the ramp distance – were tested for AR = 4 and 2, where the AR values correspond to the rectangular-wing portion only. The actuation cases were compared to two fixed-geometry references: the rectangular (panel retracted) and static-sweep (panel extended) wings. The CL definition used both the instantaneous main-wing translation velocity and the variable wing area. The 1c step-up gust exhibits unsteady lift behavior similar to that of the 1c starting motion, as found by others. For the step-down gusts, the deceleration produces a CL minimum, then the force recovers to a circulatory peak. Except for the 6c step-up gust, all gust cases show a circulatory peak in the post-gust constant motion part for the rectangular AR = 4 wing. The position and magnitude of this peak coincide across those gust-ramp cases when their 50% ramp locations are aligned. The step-down gust force magnitudes are higher than the step-up cases, although the step-up acceleration magnitude is larger than the deceleration for the step-down gusts. Only one value of the tip-panel rotation speed was used, which can be varied in future studies. For this tip rotation speed both inward and outward, the most pronounced effect for AR = 4 was observed for the 1c-ramp case. Conversely, for AR = 2 the overall greatest tip-actuation influence was found for the 6c step-down ramp. For the step-up gusts with actuation-in, the AR = 2 wing produces a greater decrease in CL, but the effect diminishes sooner compared to AR = 4. This may be due to interactions with the more pronounced AR = 4 LEV formation. For both ARs, actuation-in at the 50% ramp distance yields the most sustained reduction in CL but does not affect the gust peak, whereas the early actuation at 21.5c for the 3c ramp (and the 6c ramp for AR = 2) lowers this peak magnitude. Considering the step-down gusts, for AR = 4 overall the actuation-out increases the CL compared to the reference cases both during and after the gust, depending on the ramp length. For the longer 3c and 6c ramps, the AR = 2 actuation-out case generates relatively higher actuation peaks in CL and the gust recovery is faster, versus AR = 4. For the 1c ramp, actuation-out lowers the gust-peak magnitude for both ARs, but the AR = 4 case generates a higher CL plateau between the gust minimum and the recovery peak. Lastly, the rectangular and static-sweep reference cases have somewhat similar post-gust CL behavior for the step-up gusts, but this is not true for the AR = 4, 1c step-down case and all the AR = 2 step-down gusts.

10.5 ACKNOWLEDGMENTS

We would like to thank Karan Shah for his assistance with the experimental setup and with acquiring some of the results. This work is supported by the National Science Foundation, award no. CBET-1706453, supervised by Dr. Ronald Joslin.

10.6 REFERENCES

[1] McCroskey, W.J., Unsteady airfoils, Annu. Rev. Fluid Mech., Vol. 14, No. 1, 1982, pp. 285-311.

[2] Dickinson, M.H., and Gotz, K.G., Unsteady aerodynamic performance of model wings at low Reynolds numbers, J. Exp. Biol., Vol. 174, No. 1, 1993, pp. 45-64.

[3] Taira, K., and Colonius, T., Three-dimensional flows around low-aspect-ratio flat-plate wings at low Reynolds numbers, J. Fluid Mech., Vol. 623, 2009, pp. 187-207.

[4] Jardin, T., Farcy, A., and David, L., Three-dimensional effects in hovering flapping flight, J. Fluid Mech., Vol. 702, 2012, pp. 102-125.

[5] Stevens, P.R.R.J., Babinsky, H., Manar, F., Mancini, P., Jones, A.R., Nakata, T., Phillips, N., Bomphrey, R.J., Gozukara, A.C., Granlund, K.O., and Ol, M.V., Experiments and computations on the lift of accelerating flat plates at incidence, AIAA J., Vol. 55, No. 10, 2017, pp. 3255-3265.

[6] Lentink, D., and Dickinson, M.H., Rotational accelerations stabilize leading edge vortices on revolving fly wings, J. Exp. Biol., Vol. 212, 2009, pp. 2705-2719.

[7] Kruyt, J.W., van Heijst, G.F., Altshuler, D.L., and Lentink, D., Power reduction and the radial limit of stall delay in revolving wings of different aspect ratio, J. R. Soc. Interface, Vol. 12, 2015, pp. 20150051.

[8] Wolfinger, M., and Rockwell, D., Flow structure on a rotating wing: effect of radius of gyration, J. Fluid Mech., Vol. 755, 2014, pp. 83-110.

[9] Lee, Y.J., Lua, K.B., and Lim, T.T., Aspect ratio effects on revolving wings with Rossby number consideration, Bioinspir. Biomim., Vol. 11, No. 5, 2016, pp. 056013.

[10] Jardin, T., and Colonius, T., On the lift-optimal aspect ratio of a revolving wing at low Reynolds number, J. R. Soc. Interface, Vol. 15, No. 143, 2018.

[11] Bhat, S.S., Zhao, J., Sheridan, J., Hourigan, K., and Thompson, M.C., Uncoupling the effects of aspect ratio, Reynolds number and Rossby number on a rotating insect-wing planform, J. Fluid Mech., Vol. 859, 2019, pp. 921-948.

[12] Harbig, R.R., Sheridan, J., and Thompson, M.C., Reynolds number and aspect ratio effects on the leading-edge vortex for rotating insect wing planforms, J. Fluid Mech., Vol. 717, 2013, pp. 166-192.

[13] Jones, A.R., Pitt Ford, C.W., and Babinsky, H., Three-dimensional effects on sliding and waving wings, J. Aircraft, Vol. 48, No. 2, 2011, pp. 633-644.

[14] Hartloper, C., Kinzel, M., and Rival, D.E., On the competition between leading-edge and tip-vortex growth for a pitching plate, Exp. Fluids, Vol. 54, No. 1, 2013, p. 1447.

[15] Beem, H.R., Rival, D.E., and Triantafyllou, M.S., On the stabilization of leading-edge vortices with spanwise flow, Exp. Fluids, Vol. 52, No. 2, 2012, pp. 511-517.

[16] Wong, J.G., Kriegseis, J., and Rival, D.E., An investigation into vortex growth and stabilization for two-dimensional plunging and flapping plates with varying sweep, J. Fluid. Struct., Vol. 43, 2013, pp. 231-243.

[17] Wong, J., and Rival, D., Determining the relative stability of leading-edge vortices on nominally two-dimensional flapping profiles, J. Fluid Mech., Vol. 766, 2015, pp. 611-625.

[18] Jardin, T., and David, L., Spanwise gradients in flow speed help stabilize leading-edge vortices on revolving wings, Phys. Rev. E, Vol. 90, 2014, p. 013011.

[19] Klaassen van Oorschot, B., Mistick, E.A., and Tobalske, B.W., Aerodynamic consequences of wing morphing during emulated take-off and gliding in birds, J. Exp. Biol., Vol. 219, No. 19, 2016, pp. 3146-3154.

[20] Hayostek, S., Amitay, M., Zhang, K., Taira, K., He, W., and Theofilis, V., Wake dynamics of finite aspect ratio wings Part 1: An experimental study, AIAA Paper 2019-1384, 2019, pp. 1-13.

[21] Zhang, K., Taira, K., Hayostek, S., Amitay, M., He, W., and Theofilis, V., Wake dynamics of finite aspect ratio wings Part II: Computational study, AIAA Paper 2019-1385, 2019, pp. 1-10.

[22] Chowdhury, J., Cook, L., and Ringuette, M.J., The vortex formation of an unsteady translating plate with a rotating tip, AIAA Paper 2019-0348, 2019, pp. 1-19.

[23] Medina, A., Rockwood, M., Garmann, D.J., and Visbal, M.R., Integration of experiments and computations of swept-wing dynamic stall, AIAA Paper 2019-2324, 2019, pp. 1-18.

[24] Nikolic, V R., Optimal movable wing tip strake, J. Aircraft, Vol. 48, No. 1, 2011, pp. 335-341.

[25] Lee, T., and Pereira, J., Modification of static-wing tip vortex via a slender half-delta wing, J. Fluid. Struct., Vol. 43, 2013, pp. 1-14.

[26] Reynolds, K.V., Thomas, A.L.R., and Taylor, G.K., Wing tucks are a response to atmospheric turbulence in the soaring flight of the Steppe Eagle aquila nipalensis, J. R. Soc. Interface, Vol. 11, No. 20140645, 2014, pp. 1-11.

[27] Wang, S., Zhang, X., He, G., and Liu, T., Lift enhancement by bats? Dynamically changing wingspan, J. R. Soc. Interface, Vol. 12, No. 20150821, 2015, pp. 1-11.

[28] Harvey, C., Baliga, V.B., Lavoie, P., and Altshuler, D.L., Wing morphing allows gulls to modulate static pitch stability during gliding, J. R. Soc. Interface, Vol. 16, No. 20180641, 2019, pp. 1-8.

[29] Chin, D.D., Matloff, L.Y., Stowers, A.K., Tucci, E.R., and Lentink, D., Inspiration for wing design: how forelimb specialization enables active flight in modern vertebrates, J. R. Soc. Interface, Vol. 14, No. 20170240, 2017, pp. 1-18.

[30] Wibawa, M., Steele, S.C., Dahl, J.M., Rival, D.E., Weymouth, G.D., and Triantafyllou, M.S., Global vorticity shedding for a vanishing wing, J. Fluid Mech., Vol. 695, 2012, pp. 112-134.

[31] Steele, S.C., Dahl, J.M., Weymouth, G.D., and Triantafyllou, M.S., Shape of retracting foils that model morphing bodies controls shed energy and wake structure, J. Fluid Mech., Vol. 805, 2016, pp. 355-383.

[32] Scofield, T., Jia, K., Wei, M., and Bhattacharya, S., Vorticity-transfer in a leading-edge-vortex due to controlled spanwise-bending, AIAA Paper 2019-2161, 2019, pp. 1-12.

[33] Di Luca M,H.G.N.F., Mintchev S, and D.F., Bioinspired morphing wings for extended flight envelope and roll control of small drones, Interface Focus, Vol. 20160092, 2017.

[34] Granlund, K., Monnier, B., Ol, M., and Williams, D., Airfoil longitudinal gust response in separated vs. attached flows, Phys. Fluids, Vol. 26, 2014, p. 027103.

[35] Greenblatt, D., Müeller-Vahl, H., Strangfeld, C., Medina, A., Ol, M.V., and Granlund, K.O., High advance-ratio airfoil streamwise oscillations: Wind tunnel vs. water tunnel, AIAA Paper 2016-1356, 2016, pp. 1-19.

[36] Medina, A., Ol, M.V., Greenblatt, D., Müeller-Vahl, H., and Strangfeld, C., High-amplitude surge of a pitching airfoil: Complementary wind- and water-tunnel measurements, AIAA J., Vol. 56, No. 4, 2018, pp. 1703-1709.

[37] Mulleners, K., Mancini, P., and Jones, A.R., Flow development on a flat-plate wing subjected to a streamwise acceleration, AIAA J., Vol. 55, No. 6, 2017, pp. 2118-2122.

[38] Marzanek, M.F., and Rival, D.E., Separation mechanics of non-slender delta wings during streamwise gusts, J. Fluid. Struct., Vol. 90, 2019, pp. 286-296.

[39] Slaouti, A., and Gerrard, J.H., An experimental investigation of the end effects on the wake of a circular cylinder towed through water at low Reynolds numbers, J. Fluid Mech., Vol. 112, 1981, pp. 297-314.

[40] Mueller, T.J., and DeLaurier, J.D., Aerodynamics of small vehicles, Annu. Rev. Fluid Mech., Vol. 35, 2003, pp. 89-111.

[41] Lisoski, D.L.A., Nominally 2-Dimensional Flow about a Normal Flat Plate, Ph.D. thesis, California Institute of Technology, 1993.

[42] Ol, M., and Babinsky, H., Extensions of fundamental flow physics to practical MAV aerodynamics, Tech. Rep. TR-AVT-202, NATO STO, 2016.

[43] Dickson, W.B., and Dickinson, M.H., The effect of advance ratio on the aerodynamics of revolving wings, J. Exp. Biol., Vol. 207, No. 24, 2004, pp. 4269-4281.

[44] Harbig, R.R., Sheridan, J., and Thompson, M.C., The role of advance ratio and aspect ratio in determining leading-edge vortex stability for flapping flight, J. Fluid Mech., Vol. 751, 2014, p. 71-105.

[45] Johnson, W., Helicopter Theory, Dover Books on Aeronautical Engineering, Dover Publications, Newburyport, 2012.

[46] Jardin, T., Coriolis effect and the attachment of the leading edge vortex, J. Fluid Mech., Vol. 820, 2017, pp. 312-340.

Chapter 11 – UNSTEADY AERODYNAMIC LOADS ON AN AIRFOIL AT HIGH ANGLE OF ATTACK IN A RANDOMLY SURGING FLOW

David R. Williams
Illinois Institute of Technology
UNITED STATES

An unsteady surging flow with a von Karman turbulence spectrum is used to simulate atmospheric turbulence in a wind tunnel. The aerodynamic forces and moments produced by an NACA-0009 airfoil at $\alpha = 12^o$and $\alpha = 15^o$ in the unsteady freestream flow are documented and compared to the steady flow performance. Lift, drag, and pitching moment are recorded, as well as surface pressures on the suction surface of the airfoil. High-speed particle image velocimetry is used to measure the velocity field on the suction surface of the airfoil under steady and unsteady flow conditions. Correlations between the overall flow field and reference signals of freestream velocity and surface pressure are computed as functions of frequency using the cross power spectral density functions. Spatial maps of the correlations show the receptivity of the leading edge shear layer and the wake to specific frequencies in the freestream disturbances. The suction parameter is computed from the flow field velocity data and correlated with the leading edge flow separation. The critical suction parameter for separation is found to be larger than the suction parameter value that occurs when the flow is fully separated.

11.1 INTRODUCTION

The ability to predict the force and moment response of vehicles moving through turbulent and gusting flow environments is important for the design of aircraft [1], wind turbines [2], and road vehicles [3]. Aircraft landing on aircraft carriers experience large amplitude velocity disturbances during final approach through the `burble' region downstream of the flight deck [4]. When certifying new aircraft, the FAA requires the performance of the vehicle to be evaluated with both discrete gusts and broad band turbulence. Gusts are generally considered to be discrete finite energy events, usually with a $u(t) = A\left(1 - cos\left(\frac{2\pi Ut}{H}\right)\right)$ profile, where A is the amplitude and H is a characteristic length of the gust. 'Turbulence' is generally considered to be a continuous finite power process with broad spectrum of frequencies, whose individual amplitudes are smaller than the discrete gust. For atmospheric turbulence, the velocity frequency spectra are assumed to follow either the von Karman spectrum or the Dryden spectrum with -5/3 or -2 power law exponents, respectively.

Aircraft on final approach fly at low speeds and high angles of attack, which increases the probability of flow separation on their wings. We are interested in exploring how external flow disturbances induce flow separation or interact with an already separated flow on airfoils. The separated flow region on the suction surface of an airfoil begins with a thin separating shear layer, which is susceptible to external disturbances. Vertical velocity disturbances will create time-varying changes in the instantaneous angle of attack, and longitudinal disturbances will change the dynamic pressure. It is important to understand how the external disturbances interact with the separating shear layer and the overall separated flow region to be able to develop our predictive capabilities. In fact, many active flow control approaches, such as, synthetic jets, rely on the receptivity of the separated shear layer to flow disturbances in order to reattach the separating shear layer. Active flow control effectors can exploit the naturally occurring shear layer instability to delay flow separation or reattach a separated flow and achieve much larger lift coefficients relative to the uncontrolled case.

When the separated flow over a wing encounters external disturbances in the freestream flow, the separating shear layer is expected to amplify (or attenuate) some portion of the incoming flow disturbance spectrum. This phenomenon is referred to as the `receptivity' of the shear layer [5]. Intermittent and partial flow reattachment phenomena are expected to contribute to variations in the aerodynamic forces. At the same time, turbulence is a broad spectrum disturbance that will be filtered by the receptivity of the shear layer and overall separated flow region. We use the Cross Power Spectral Density (CPSD) calculation to identify connections between freestream disturbances and separating shear layer dynamics and wake dynamics. The CPSD is a time-averaged statistical method that computes correlations as a function of frequency.

In addition to the statistical approaches for analyzing the disturbance field interaction with the separated flow, a relative new method for identifying the initiation of leading-edge separation is examined. LESP is a new method for predicting the onset of flow separation on airfoils. The Leading-Edge Suction Parameter (LESP) was discovered by Ramesh and Gopalarathnam [6], [7] to reach a critical value at the onset of separation. The unsteady LESP can be estimated from the velocity field near the nose of the airfoil, and this will be correlated with the separated flow behavior. Ramesh and Gopalarathnam [7] used the critical LESP concept in a low dimensional model that predicted limit-cycle oscillations of a wing that was free to pitch and plunge. Eldredge [8] showed in general terms how the suction parameter derived from the partial circulation can be used as a boundary condition for unsteady flow separation in point vortex methods. It has been used as an upstream boundary condition in vortex element model simulations of gusting flows interacting with airfoils, Hou, et. al. [9]. Clearly, the critical LESP concept has important applications in modeling unsteady aerodynamic flows, and we examine how it is influenced by intermittent separation and reattachment.

In this chapter we conduct wind tunnel experiments on the response of the separated flow and near wake region of an NACA-0009 airfoil fixed at two angles of attack, $\alpha = 12^o$ and $\alpha = 15^o$ to longitudinal velocity component disturbances, u'.

The Fejer Unsteady Flow Wind tunnel is used to create broad spectrum velocity fluctuations that simulate the von Karman spectrum for the longitudinal velocity component. The mechanics of producing the `turbulence' can be found in Refs. [10], [11]. It is important to recognize that the broad band u' disturbances are not classical three-dimensional turbulence, but rather they are spanwise coherent fluctuations of the longitudinal component of velocity whose spectrum approximates the von Karman spectrum. We use the term 'turbulence' in this chapter for convenience.

The instantaneous freestream velocity is monitored with a hot wire anemometer, while the nominally two-dimensional flow field around the airfoil is recorded with a high-speed PIV system. Instantaneous surface pressures, and forces and moments acting on the airfoil are recorded as well. The receptivity of the separating shear layer to the turbulent freestream is explored by computing cross spectral density correlation maps between a reference point in the freestream and flow around the airfoil. The suction parameter measurements are computed from partial circulation contours at the leading edge.

Details of the experimental setup are provided in the following Section 11.2. Velocity, force, and moment measurements are presented in Section 11.3. Maps of the coherence functions with and without freestream turbulence are presented in Section 11.4. Conclusions of the investigation are presented in Section 11.5.

11.2 EXPERIMENTAL SETUP

The measurements are conducted in the Andrew Fejer Unsteady Wind Tunnel at Illinois Institute of Technology. The test section length is 2.1 m in longitudinal direction and the cross-section dimensions are 0.61 m x 0.61 m. The test airfoil is an NACA-0009 airfoil with a chord length of c = 245 mm, a wingspan of b = 600 mm, and aspect ratio $\frac{b}{c} = 2.45$. The chord-based Reynolds number is Re = 98,000. The airfoil model is positioned in the center of the test section as shown in Figure 11-1 on a 6-component force and moment transducer (ATI, Inc. model Nano-17). The wingspan is 10 mm shorter than the width of the test section to prevent contact with the wind tunnel sidewalls.

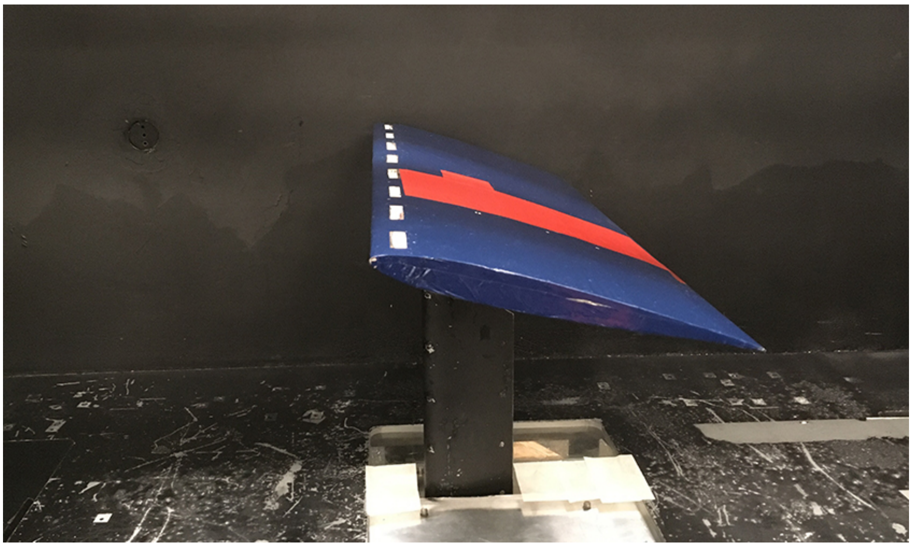

Figure 11-1: NACA-0009 Airfoil on the Pitch Mechanism in the Fejer Wind Tunnel.

The flow speed in the wind tunnel is measured with a pitot tube and a hot wire anemometer located 1 m upstream of the airfoil. The (x,y) coordinate system is defined with an origin at the location of the force transducer, which is at c/4 with the positive x-axis oriented in the downstream direction. The positive y-axis is perpendicular to the x-axis pointing upward in the direction of positive lift. The longitudinal velocity component is u and the vertical velocity is v. The average flow speed is U = 5.8 m/s. The freestream turbulence without louver motion is $u'_{rms} = 0.44\%$ of the freestream flow.

Four pressure sensors are placed on the upper surface in chord-wise direction to measure the instantaneous surface pressures. The sensors are located at x/c = 0.05, 0.31, 0.57 and 0.74. The sensor closest to the nose of the airfoil is designated as Sensor 1, and the farthest downstream sensor is Sensor 4.

Two-component velocity measurements are acquired with a LaVision high-speed Particle Image Velocimetry (PIV) system at 100 Hz with a spatial resolution of 320 x 200 velocity vectors per sample over a net area of 381 mm x 238 mm. The laser sheet illuminates the suction surface of the airfoil from the top of the test section. The PIV measurement domain covers the entire chord plus 1/4 chord length downstream from the trailing edge. The force, moment, pressure, and PIV measurements are synchronized during acquisition, so that the force and pressure measurements can be correlated with the flow field for each PIV frame.

Figure 11-2 provides a sample of a single snapshot of the PIV system measurement of the instantaneous velocity magnitude. The black circles are the locations of the points where the local velocity is extracted in later processing and analysis. Among these sample locations, the far left one is used as the freestream velocity reference point. Comparisons of the time plots and spectra of the freestream velocities that are measured by the hot wire anemometer and the PIV are shown in Figure 11-3(a). The correlation coefficient between the hot wire and PIV measurements is 0.91. The spectra also show good agreement between the hot wire and PIV measurements, especially in the low frequency range.

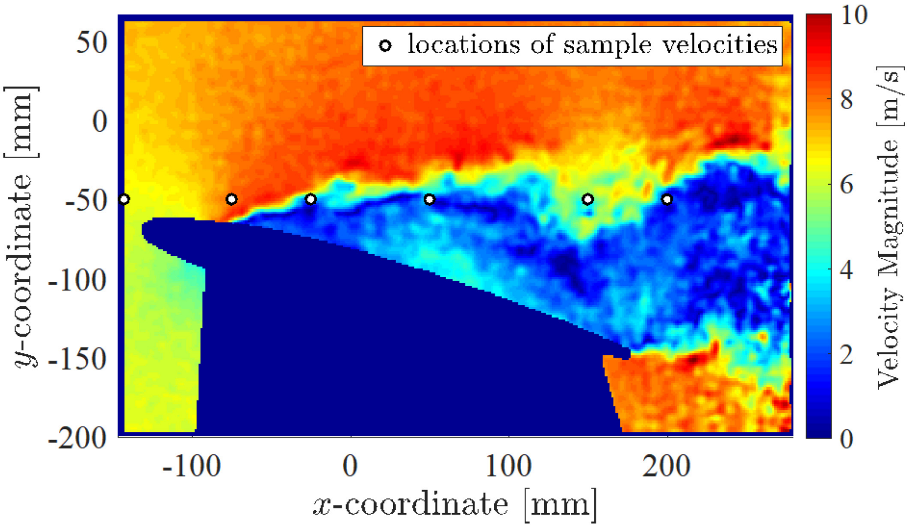

Figure 11-2: PIV Snapshot and Sample Velocity Locations.

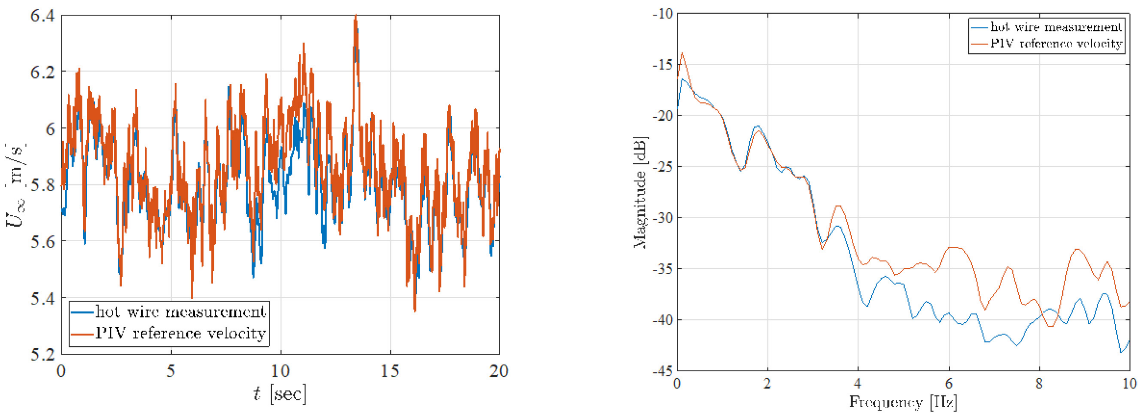

(a) Time Series Data.

(b) Spectra from Hot Wire and PIV.

Figure 11-3: Schematic of Three Types of Gust Encounters.

11.2.1 *u'* Disturbance Field

An array of louvers located at the downstream end of the test section is used to create the broad spectrum longitudinal velocity fluctuations by creating a time-varying resistance to the flow in the closed-return wind tunnel. Opening and closing the louvers produces a variable pressure drop that modulates the flow speed in the wind tunnel. Rennie, et al. [10], [12] developed a model for the wind tunnel dynamics that allowed different broad band spectra to be generated. In Rennie's procedure a spectrum that emulates atmospheric turbulence with a von Karman gust spectrum with a turbulent length scale $L_{vk} = 10\,m$ provides input to the inverted wind tunnel dynamics model to produce the required louver motion. An example of the velocity time series and spectra measured in the freestream of the wind tunnel is shown in Figure 11-3. The hot wire anemometer and high-speed PIV are in good agreement up to approximately 4 Hz disturbance frequency.

It is important to recognize that the randomness created by louver system is only in the streamwise component of velocity, *u*. The spatial gradients are insignificant, and the flow is spatially coherent. By contrast atmospheric turbulence consists of three-dimensional disturbances, and the spatial correlations decay as distance from a measurement reference point increase. The difference between the background wind tunnel turbulence and the louver driven *u*'-turbulence is illustrated by the correlations shown in Figure 11-4. The correlation coefficients between the hot wire velocity measurement and the PIV measured *u*-velocity component are shown for the 'steady' (louvers stationary) and the `turbulent' case with the louvers oscillating, Figure 11-4(a) and Figure 11-4(b), respectively. The correlations are not larger than 0.25 in the background turbulence case. With louver oscillations the maximum correlation exceeds 0.8 in the flow above the airfoil. The separated shear layer above the airfoil acts as a boundary between the regions of high and low correlation. Throughout this chapter we use the term 'turbulence' to refer to the louver driven oscillating flow with a broad band spectrum, but with the caveat that these disturbances are spatially correlated in the flow direction.

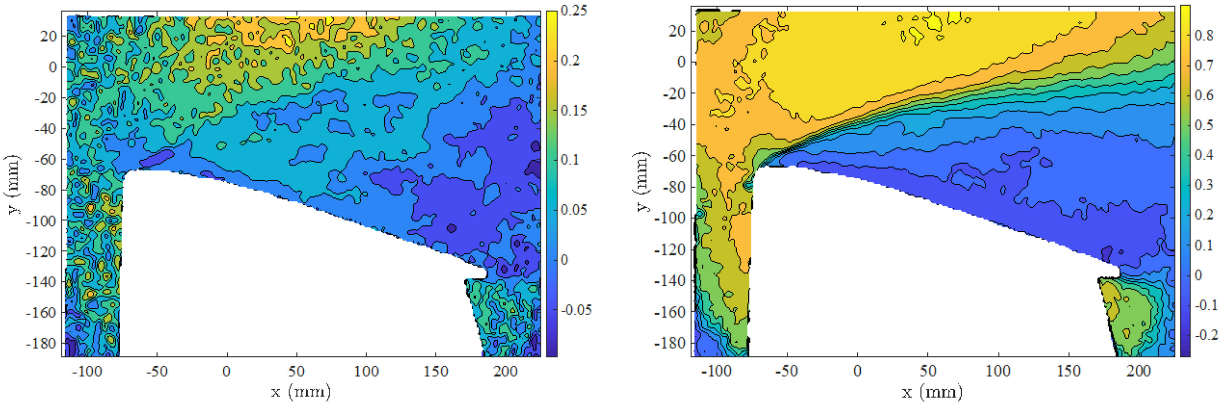

(a) Steady Case with Background Turbulence.

(b) Turbulent Flow with Unsteady Louver Motion.

Figure 11-4: Correlation Between Hot Wire Velocity and PIV Measured *u*-Velocity Component.

11.3 RESULTS

11.3.1 Force and Moment Measurements

The influence of the turbulent freestream flow on the steady state lift, drag, and pitching moment coefficients is shown in Figure 11-5. The lift-to-drag ratio is shown in Figure 11-5(d). To measure the steady state lift and drag coefficients the airfoil was pitched up and down at a slow rate of 0.3 deg/s for angles of attack between $-5^{\circ} < \alpha < 25^{\circ}$ as shown in Figure 11-5. The steady flow case without turbulence is shown by the blue lines. The red lines correspond to the case with turbulence.

In Figure 11-5(a) the maximum lift coefficient is observed near $\alpha = 13^{\circ}$ for both cases with and without turbulence. The turbulence has the effect of increasing the lift curve slope in the attached flow regime, $\alpha < 10^{\circ}$. Without turbulence $\frac{dC_L}{d\alpha} = 5.73$ rad^{-1}, whereas with turbulence $\frac{dC_L}{d\alpha} = 6.62$ rad^{-1}. At low angles of attack near $\alpha = 0^{\circ}$ the steady flow lift coefficient is positive. This is believed to be the result interference from the support mechanism for the wing model.

At $\alpha = 12^{o}$ the steady flow drag coefficient is slightly larger than the case with turbulent flow, which can be seen in Figure 11-5(b.) The difference in drag is attributed to the modification of the separated flow field over the suction surface of the wing by the turbulence. Details of the flow field modification will be presented in the following sections.

The pitching moment coefficient shown in Figure 11-5(c) is computed relative to the quarter-chord location, c/4. The center of gravity of the airfoil model was not located at the quarter-chord, so the moment created by the center of gravity was subtracted from the measured pitching moment to obtain the measured aerodynamic moment. At low angles of attack prior to stall, the pitching moment is slightly positive, which is the result of interference from the airfoil support mechanism. The onset of stall is evident in this figure by the rapid decrease in pitching moment that occurs above $\alpha = 12^o$.

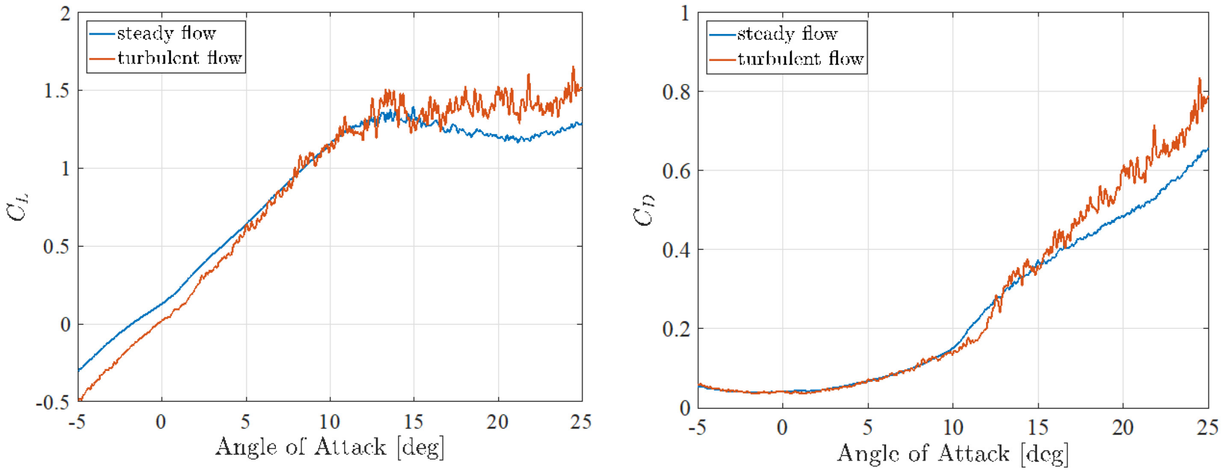

(a) Lift Coefficient.

(b) Drag Coefficient.

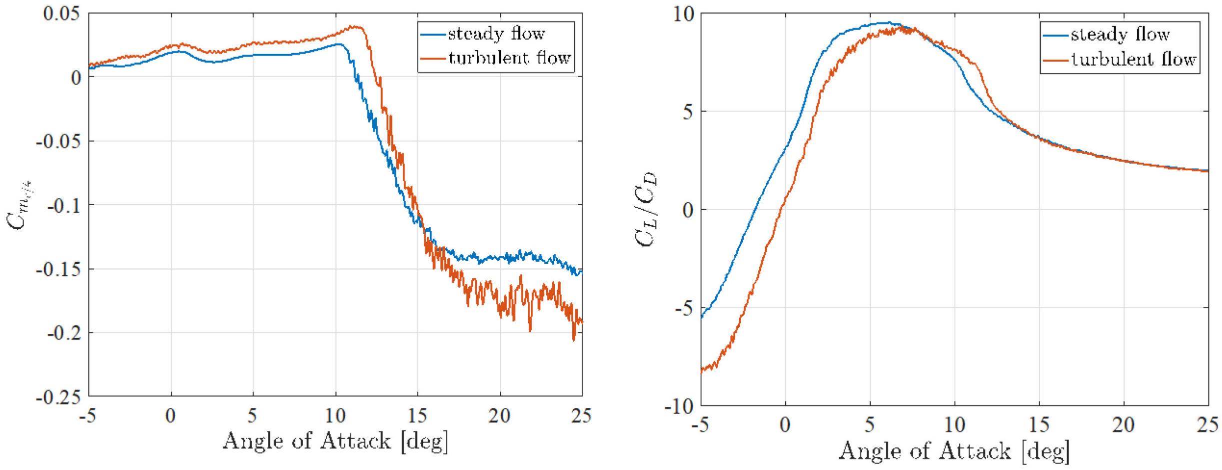

(c) Pitching Moment Coefficient.

(d) Lift/Drag Ratio.

Figure 11-5: Correlation Between Hot Wire Velocity and PIV Measured *u*-Velocity Component.

The influence of the turbulent flow is to reduce the lift/drag ratio when the angle of attack is less than $\alpha < 7^o$, as shown in Figure 11-5(d). At $\alpha = 12^o$ an increase in lift/drag is observed, and then the two curves overlap at higher angles of attack.

11.3.2 Mean and rms Velocity Fields

In the remainder of the chapter we focus on two angles of attack in the stalled flow regime, $\alpha = 12^o$ and $\alpha = 15^o$. The airfoil is partially stalled at $\alpha = 12^o$and, as previously discussed the aerodynamic properties, show a sensitivity to the turbulence. The $\alpha = 15^o$case is fully stalled. At this angle of attack, the aerodynamic properties shown in Figure 11-5 match each other. As a starting point we examine the influence of the turbulence on the details of the time-averaged mean and rms flow field structure.

The mean and rms velocity fields for the streamwise component of velocity with and without turbulence at $\alpha = 12^o$ are shown in Figure 11-6. Comparisons of the sub-figures show little noticeable effect of the turbulence on the flow field relative to the steady flow case.

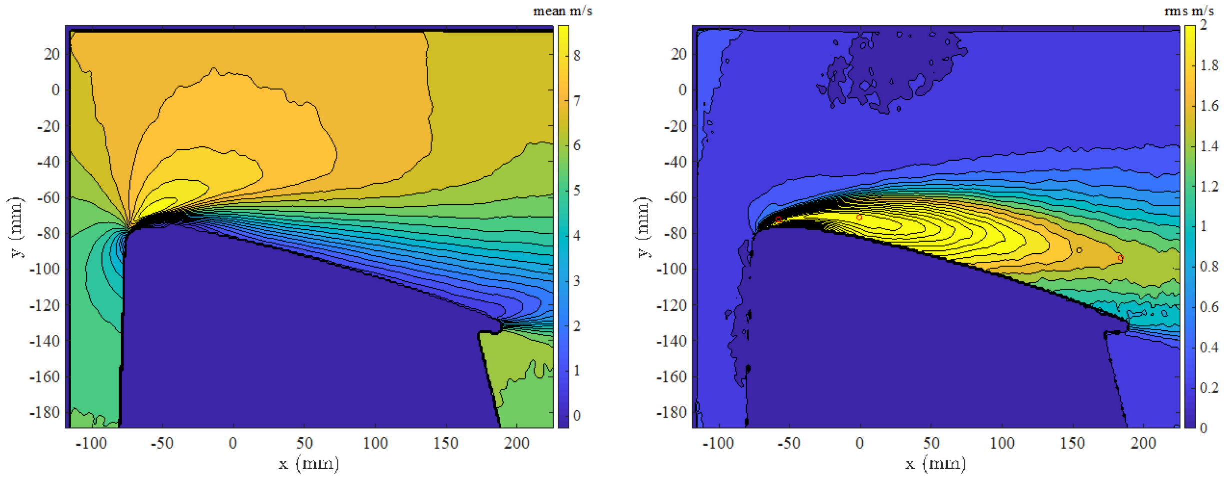

(a) Mean Velocity Steady Flow.

(b) rms Velocity Steady Flow.

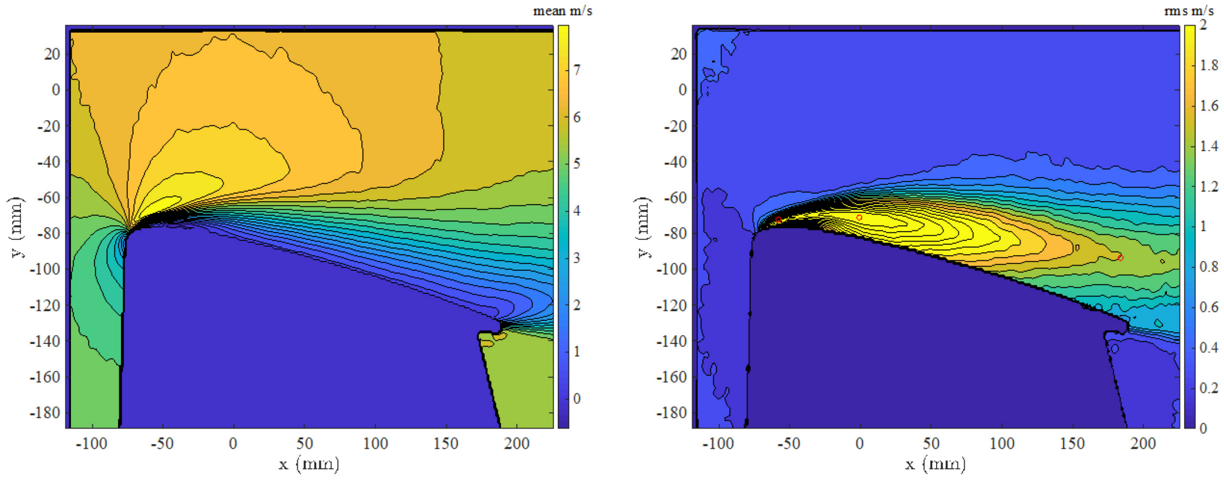

(c) Mean Velocity Turbulent Flow.

(d) rms Velocity Turbulent Flow.

Figure 11-6: u-Velocity Component Contours at $\alpha = 12^o$.

The mean and rms velocity fields at $\alpha = 15^o$are shown in Figure 11-7. By comparing Figure 11-7(a) with Figure 11-7(b) we find reverse flow regions next to the airfoil surface centered at approximately x = 100 mm. The size of the reverse flow region is enhanced by the turbulence.

The rms velocity distributions for the $\alpha = 12^o$ cases are shown in Figure 11-7(b) and Figure 11-7(d). The external turbulence has an observable effect on the rms velocity distributions. It is interesting and somewhat counter-intuitive that the rms velocity levels decrease in the presence of the turbulence. The maximum rms levels occur very close to the leading edge of the airfoil, where the shear layer is separating, indicate the presence of a leading-edge separation bubble. In the steady flow case Figure 11-7(b) the curvatures of the rms contours are created by the shear layer reattachment.

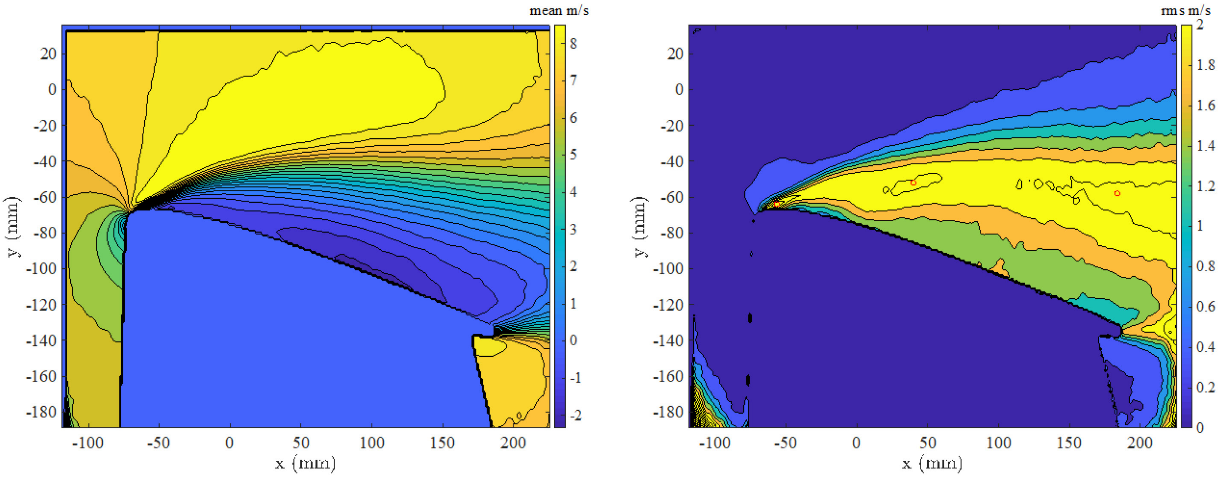

(a) Mean Velocity Steady Flow.

(b) rms Velocity Steady Flow.

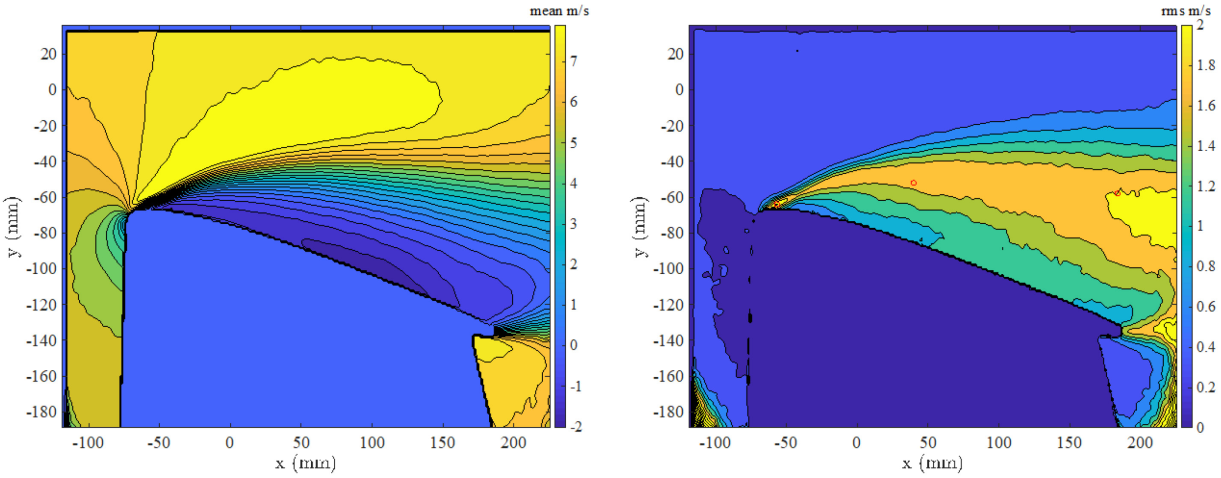

(c) Mean Velocity Turbulent Flow.

(d) rms Velocity Turbulent Flow.

Figure 11-7: u-Velocity Component Contours at $\alpha = 15^o$.

11.3.3 Surface Pressure Spectra

The spectra of the surface pressure fluctuations are shown in Figure 11-8 for $\alpha = 12^o$and $\alpha = 15^o$ with Cp1 to Cp4 corresponding to the four locations x/c = 0.05, 0.31, 0.57, and 0.74 in the steady flow case. The steady flow data are shown by the solid lines. Only the Cp1 and Cp4 spectra are shown (dashed lines) in the turbulent flow case. Peaks occur near f = 17.6 Hz in the $\alpha = 12^o$case, which corresponds to a Fage-Johansen [13] Strouhal number $St_{FJ} = \frac{f\, c \sin(\alpha)}{U} = 0.15$. The higher angle of attack case, $\alpha = 15^o$ has a peak at f = 15.6 Hz, which gives $St_{FJ} = 0.17$. Based on these values we conclude that the peaks are the result of the vortex shedding frequency in the wake of the airfoil.

Additional peaks in the pressure spectra can be seen in the 8 – 10 Hz range. These peaks appear in both the steady flow and turbulent flow cases. CPSD results presented later indicate that this peak is driven by the reverse flow region next to the surface.

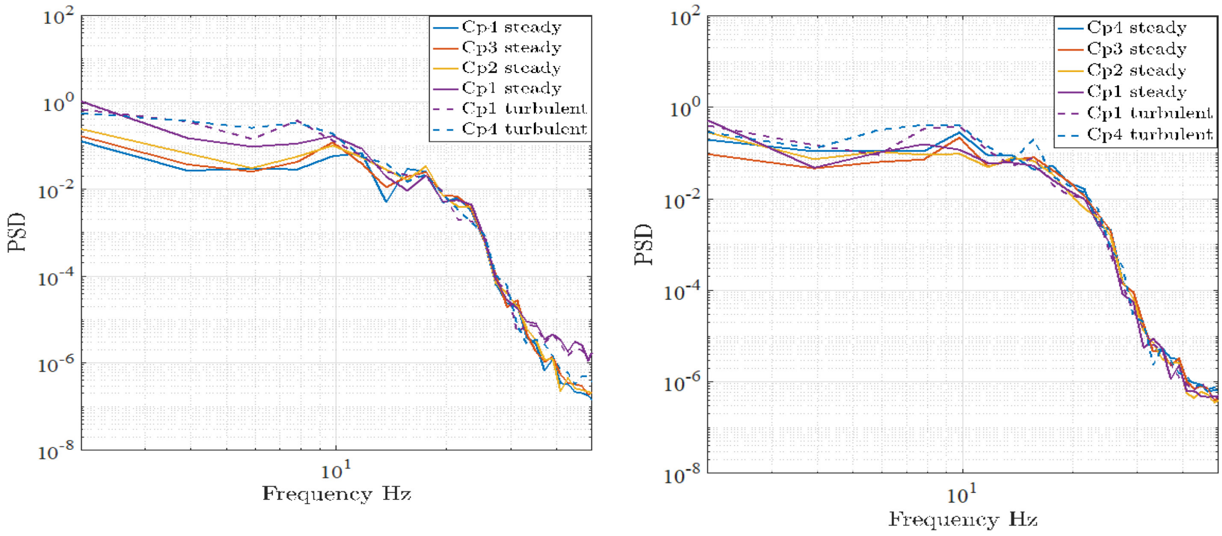

(a) α = 12°.

(b) α = 15°.

Figure 11-8: Surface Pressure Spectra with and Without Turbulence.

11.4 DISCUSSION OF RESULTS

One hypothesis in our investigation is that the separating shear layer near the nose of the airfoil is one region of receptivity for external disturbances to become amplified and influence the development of the separated flow region. Disturbances come from both the incoming freestream flow, as well as the wake downstream of the airfoil. If the shear layer is receptive to the freestream disturbances, then we expect to find a high correlation at certain frequencies between the hot wire anemometer signal and the velocity in the shear layer. Similarly, high correlation values can be expected between the shear layer velocity and the wake modes when the wake disturbances are significant.

11.4.1 Cross Spectral Density Analysis – Freestream Velocity to Separated Region

A conceptually simple approach to look for correlated regions is to choose a reference signal (velocity or pressure) at a point in the flow and compute the Cross Power Spectral Density (CPSD) function between the reference signal and every velocity point throughout the flow field. The correlation coefficient examined above is computed over the entire frequency spectrum. By contrast, the CPSD function measures the correlation between two signals as a function of frequency. The absolute value of the CPSD provides the correlation at specific frequencies.

The CPSD maps in Figure 11-9 indicate regions of correlation between the upstream hot wire velocity signal and the PIV measured velocity. The separating shear layer region has high correlations at low frequencies, and very specific frequencies. Figure 11-9(a) corresponds to f = 1.75 Hz (St = 0.074). The correlation is highest near the separation point and in the separated shear layer. The strong correlation at low frequency was unexpected, because the Kelvin-Helmholtz instability for the separating shear layer was estimated to be O (50 Hz).

At a slightly higher frequency f = 2.39 Hz (St = 0.10) the correlations are much stronger in the near wake region. Figure 11-9(b) shows that the near wake region is receptive to the external turbulence at that particular frequency. The hot wire reference signal is positioned 1 m upstream of the leading edge of the wing, which makes it unlikely that the near wake turbulence creates a signal that can be detected by the hot wire. We conclude that it is the turbulence that is driving the near wake at this frequency.

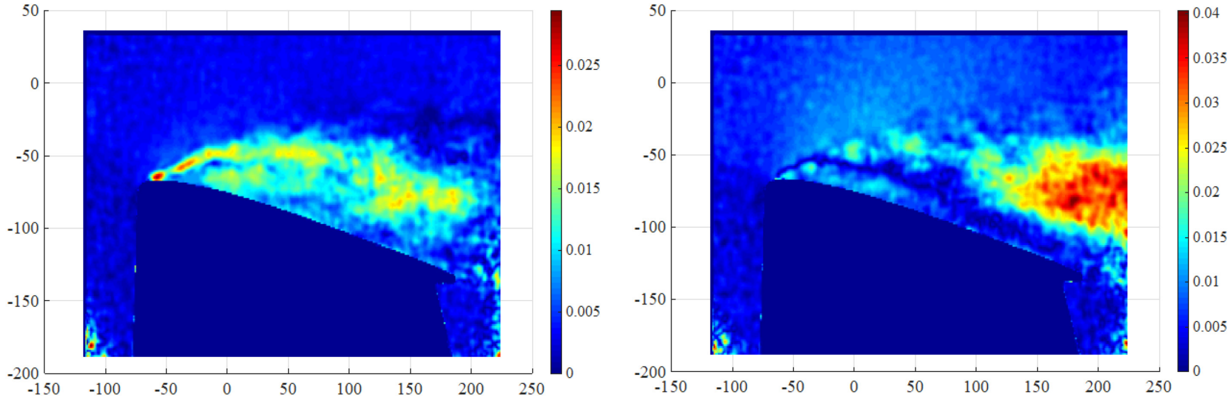

(a) Shear Layer Receptivity to Turbulence – CPSD at f = 1.75 Hz.

(b) Near Wake Receptivity to Turbulence – CPSD at f = 2.39 Hz °.

Figure 11-9: CPSD Between Hot Wire Velocity and the PIV Measured Velocity Field at $\alpha = 15^o$.

11.4.2 Cross Spectral Density Analysis – Surface Pressures to Separated Region

In this section the time-resolved PIV data is used to identify regions in the flow field that are driving the different flow interaction mechanisms responsible for surface pressure disturbances. From Raju, et al [14] we expect vortex formation in the separated shear layer, the wake instability, and the separation bubble to play both direct and indirect roles in determining the pressure fields that are established on the surface of the airfoil.

CPSD analysis between pressure Sensor 4 and the velocity field provides insight into the regions of the flow that are correlated at certain frequencies when $\alpha = 15^o$ and the flow is steady. Figure 11-10(a) shows that the near wake region above the airfoil is correlated with the surface pressure at f = 2.39 Hz (St = 0.10). Similarly, the higher frequency f = 5.47 Hz (St = 0.23) in Figure 11-10(b) shows the connection of this frequency with the separated shear layer. Shear layer vortex formation near the leading edge contributes to the pressure fluctuation field in the aft region of the airfoil.

The 10 Hz (St = 0.42) peak observed in the pressure spectra in Figure 11-8 is related to the reversed flow region near the surface of the wing. The largest CPSD correlations in Figure 11-10(c) are concentrated in the region next to the airfoil above pressure sensors 3 and 4. This is the only frequency that showed this type of correlation in the spectra below 16 Hz.

11.4.3 Critical Edge Suction Condition

Ramesh, et al. [7] recognized the strong connection between the suction peak at the leading edge of an airfoil and the initiation of flow separation and leading-edge vortex formation. The suction region around the leading edge of an airfoil is formed as the flow accelerates from the lower surface stagnation point to the upper surface. Using high-resolution skin friction data from CFD simulations of different airfoils, Ramesh showed that for a given airfoil shape and Reynolds number the initiation of the leading-edge vortex formation occurred at a specific (critical) suction parameter value, irrespective of the motion history. Ramesh then used the critical suction parameter concept to model intermittent leading-edge vortex formation on a wing undergoing pitch/plunge limit-cycle oscillations. In this section we search for connections between the instantaneous suction parameter and flow separation in the steady and unsteady turbulent flow.

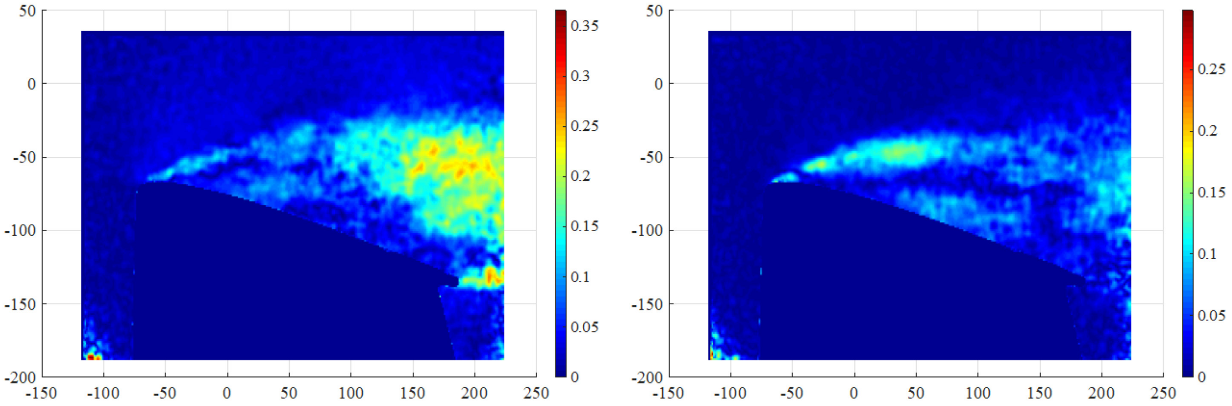

(a) Near Wake Region Correlated with Pressure Sensor 4 at f = 2.39 Hz, (St = 0.10).

(b) Shear Layer Region Correlated with Pressure Sensor 4 at f = 5.47 Hz (St = 0.23).

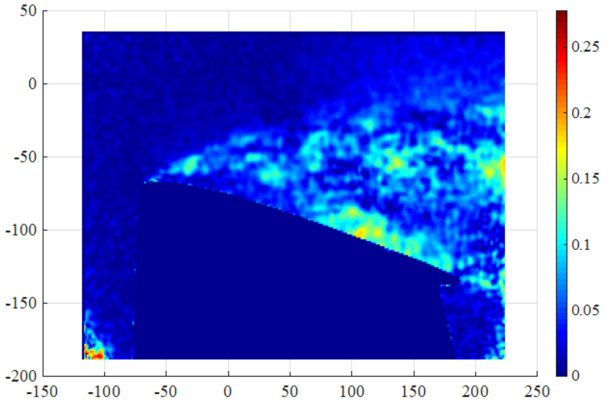

(c) Shear Layer Region Correlated with Pressure Sensor 4 at f = 10 Hz (St = 0.42).

Figure 11-10: CPSD Between Pressure Sensor 4 and the PIV Measured Velocity Field at $\alpha = 15^o$ and Steady Flow Conditions.

The suction parameter was defined using the potential flow and thin airfoil theory analysis by Garrick [15]. Ramesh, et al. showed that the suction parameter is equivalent to the first Fourier coefficient in the thin airfoil approximation. A more general approach can be found in Eldredge's [8] book on "Mathematical Modeling of Unsteady Inviscid Flows", where the partial circulation based on an open contour around the edge of a body is defined. It can be shown that the suction parameter σ can be related to the strength of the partial circulation at a corner.

$$\Gamma_{C_\varepsilon} = \pm 2\nu |S| L^{1-1/\nu} \epsilon^{1/\nu} \tag{11-1}$$

where ν determines the exterior angle of the corner flow, πν. For ν = 2 one has flow around a flat plate, and ν = 3/2 is a flow around a 90-degree wedge as shown in Figure 11-11. The strength of the flow is determined by $|S|$. The radius of the partial circulation contour is represented by ϵ.

The partial circulation vanishes in the limit as $\epsilon \to 0$. However, Eldredge introduced a normalized form of the partial circulation by defining the parameter σ that remains finite in the limit $\epsilon \to 0$, where:

$$\sigma = -\lim_{\epsilon \to 0} \frac{1}{2\nu L^{1-1/\nu} \epsilon^{1/\nu}} \int_{C_\epsilon} \bar{v} \cdot d\bar{l} \tag{11-2}$$

If the end points of the contour remain fixed and two contours with different radii ϵ are drawn, then the partial circulation will remain constant provided no vorticity is included between the contours. For the viscous flow around the airfoil, the vorticity is confined close to the surface of the airfoil in the boundary layer.

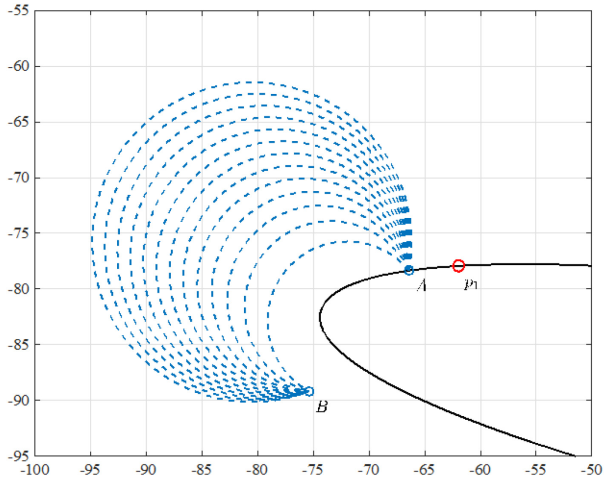

Figure 11-11: Contours Used to Calculate Partial Circulation.

It is not obvious that the Eldredge's inviscid flow analysis would apply to the viscous flow case, because in the viscous flow the vorticity is spatially distributed and not confined to a singular point. However, vorticity in the viscous flow is confined to a thin region near the leading edge before it separates. If contours are selected that contain the same amount of total vorticity, then it may be possible to identify a suction parameter for the airfoil. When analyzing experimental data, the suction parameter equation can be simplified to the form $\sigma = \frac{\Gamma}{aL'^p}$ where a is a constant with dimensions of length, L' is a normalized length of the partial circulation contour, and the exponent p is to be determined from curve fits to a sequence of contours as shown in Figure 11-11(b). If the suction parameter is a constant, then p is also constant. Thirteen contours were defined between points A and B in the velocity field around the leading edge of the airfoil. Point B is placed at the edge of the shadow region created by the airfoil blocking the laser sheet. The partial circulation is computed using the u and v velocity components measured around the contours and averaged over time. The results are shown in Figure 11-12(a) and Figure 11-12(b) for $\alpha = 12^o$ and $\alpha = 15^o$, respectively. The slopes are reasonably constant in each figure and show that $p = 0.1778$ for $\alpha = 12^o$, and $p = 0.1366$ for $\alpha = 15^o$.

The suction parameter σ should be independent of the contour integral. To check this, the partial circulation and suction parameter are plotted for the steady flow, $\alpha = 15^o$ case in Figure 11-13(a) and Figure 11-13(b), respectively. The partial circulation depends on the size of the contour, so the signals in Figure 11-13(a) do not collapse. However, the suction parameter signals do collapse as shown in Figure 11-13(b), indicating that the scaling is correct.

Movies of the velocity field around the airfoil showed intermittent flow reattachment occurring at random intervals. The intermittent flow reattachment and separation can also be seen by jumps in the suction parameter, which occur at t = 7.5, 9.0, 11.5, and 16 s in the time series shown in Figure 11-13(b). A large value of the suction parameter indicates that the flow is attached, at least locally in the vicinity of the leading edge. By studying movies of the u-velocity contour data we observed partial flow reattachment occurring near the leading edge at t = 7.5 s when σ jumps from σ = 0.2 to σ = 0.23. The flow suddenly detaches again at t = 9.0 s, when the jump back to σ = 0.2 occurs.

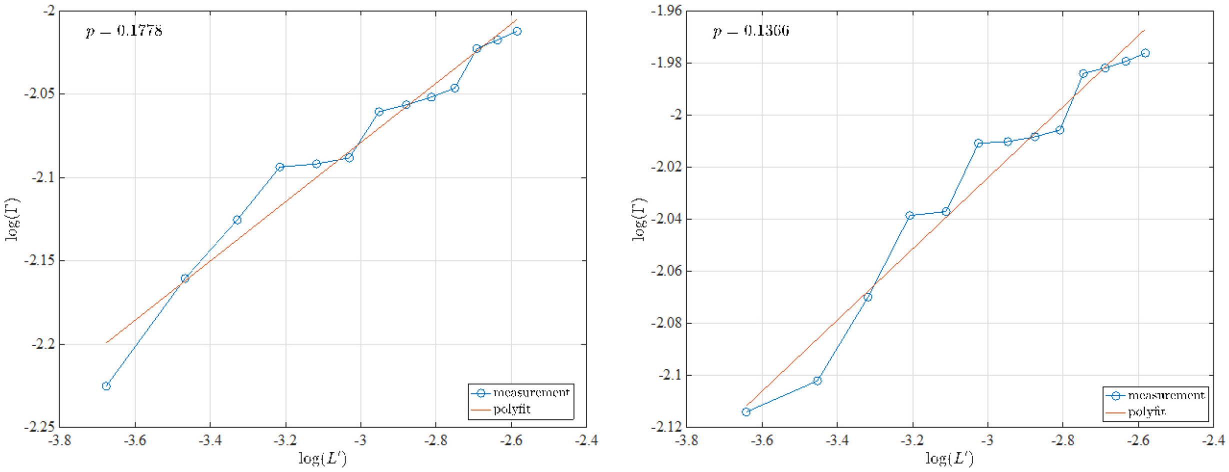

(a) $\alpha = 12^o$. **(b) $\alpha = 15^o$.**

Figure 11-12: Measurement of Partial Circulation for 13 Different Contours.

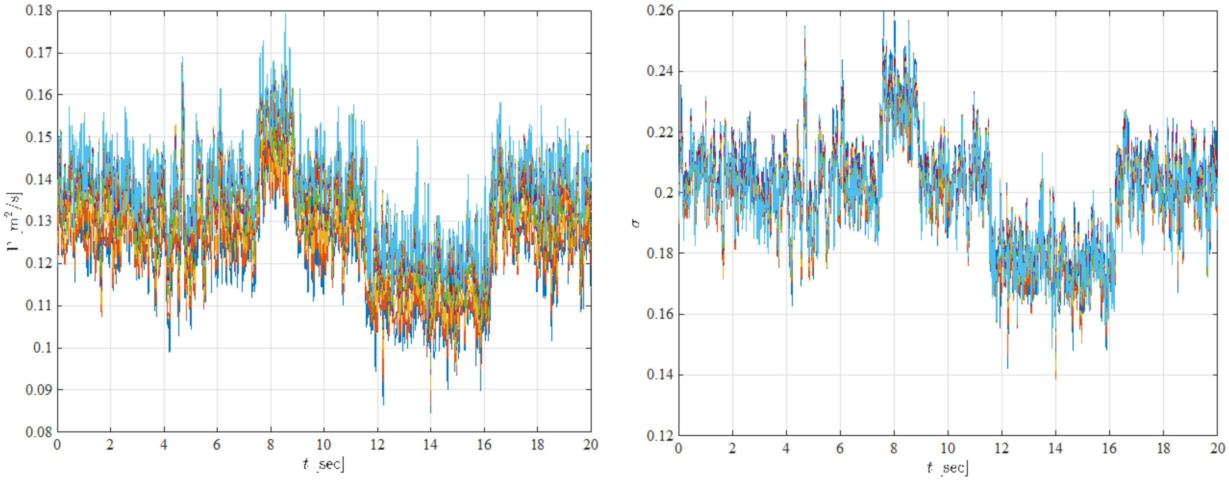

(a) Partial Circulation, Γ. **(b) Suction Parameter, σ.**

Figure 11-13: Measurement of Partial Circulation and the Suction Parameter Using 13 Different Contours for α = 15° Steady Flow.

To illustrate the change in the flow field, the u-velocity contours at two instants in time are plotted Figure 11-14. The results for t = 7.2 s corresponding to the separated flow state are shown in Figure 11-14(a) and the attached flow case at t = 7.95 s is shown in Figure 11-14(b). The upper left subfigure shows u-velocity contours. The top right shows color contours of the spanwise vorticity, ω_z, and the contour used to compute the partial circulation and σ. The two lower plots show the time series signals for C_D, U_{hw}, C_L, σ, and two pressure coefficients C_{p1} and C_{p2}. The location of the first pressure Sensor p1 is shown by the red dot in the top right subfigure.

The u-velocity contours in Figure 11-14(b) show the reattachment of the flow over the first half of the chord. The external flow near the nose of the airfoil is stronger than in the separated flow case, and the surface pressure coefficients follow the suction parameter. The vorticity in the shear layer near point A is strengthened when the flow reattaches, and the region of positive vorticity is reattached to the surface. The change in sign of surface vorticity is an indicator of the separated flow boundary. The surface vorticity ω_z in Figure 11-14(a) changes sign from positive to negative at x = -50 mm.

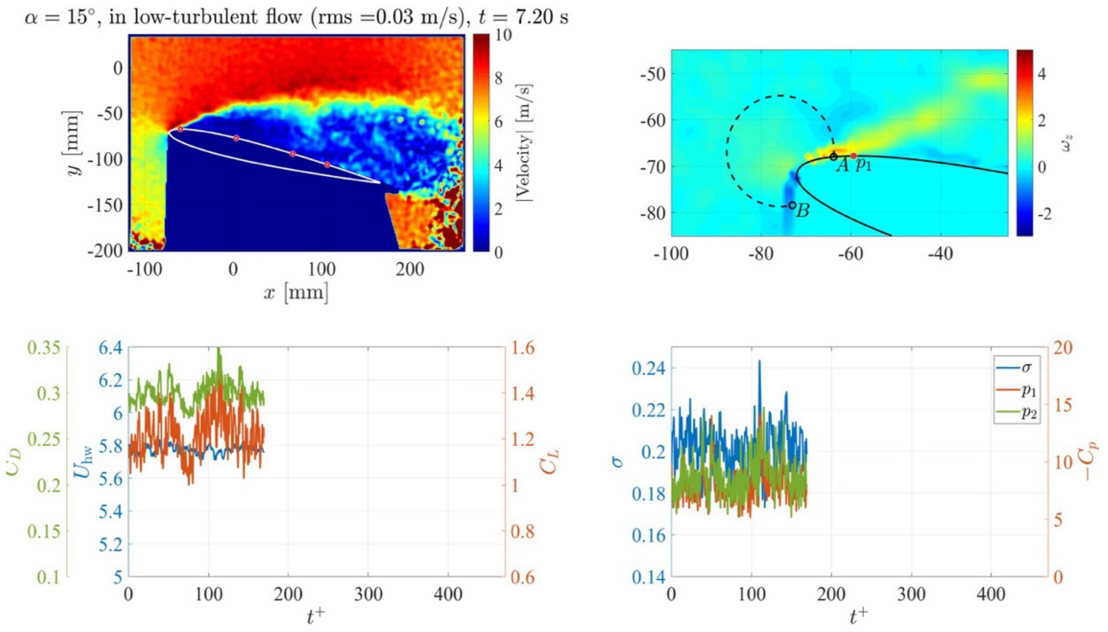

(a) Separated Flow, σ = 0.20.

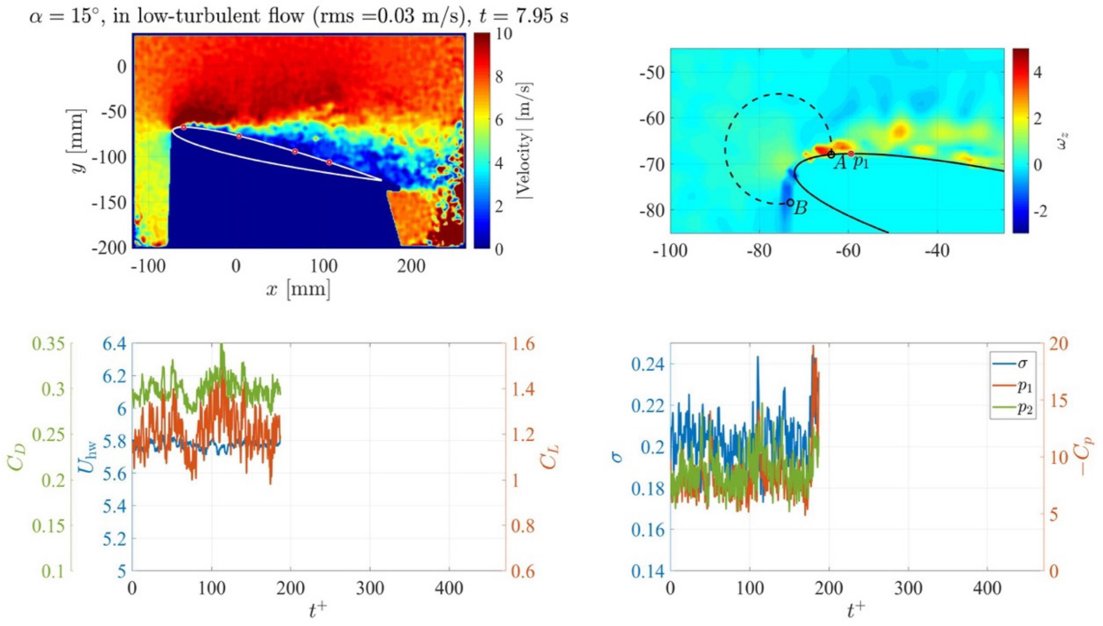

(b) Attached Flow, σ = 0.23.

Figure 11-14: Contours of u-Velocity and Vorticity, and Drag, Lift, Velocity, Suction Parameter, and Pressure Coefficient Time Series. $\alpha = 15^o$ with steady flow conditions.

A strong correlation between the suction parameter and the first pressure coefficient can be seen in the time series signals plotted in Figure 11-15. The suction parameter is shown by the blue line and the pressure coefficient by the red line. The two signals track each other when flow reattachment and separation occur. The correlation coefficient between the two signals is 0.55.

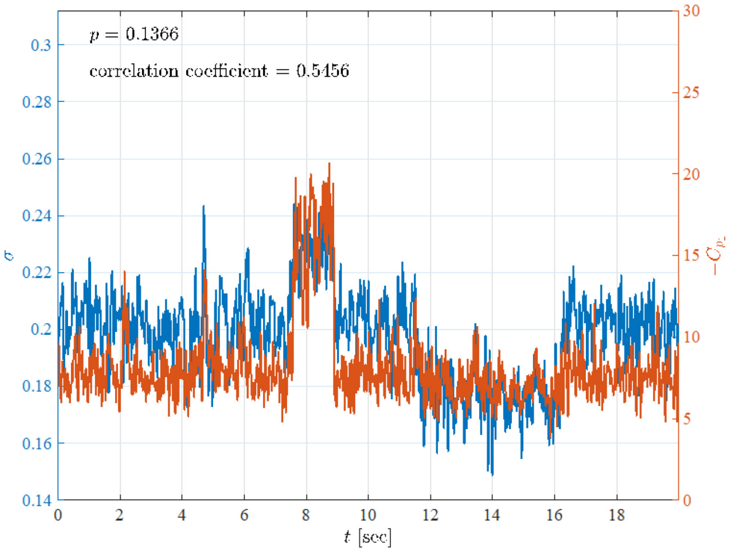

Figure 11-15: Suction Parameter and Cp1 Time Series for $\alpha = 15^o$, Steady Flow.

The changes in the suction parameter values from σ = 0.23 to σ = 0.2 when the flow separation occurs does not support the assumption by Ramesh, et al. [6] and Hou, et al. [9] that the LESP remains constant at its maximum value. As discussed by Eldredge [8], in vortex element simulations the flow is separated and once the critical suction value is reached. At that location new vortex elements are added to the flow to maintain the critical suction value. However, in the current experiment we find that the critical suction parameter for the onset of separation is approximately 15 percent larger than the separated flow suction parameter.

11.5 CONCLUSIONS

The separated flow field on a NACA-0009 airfoil is studied in steady and `turbulent' flow environments, where the term `turbulent' refers to broad spectrum u'-velocity fluctuations. The presence of turbulence the disturbances act to increase the lift curve slope in the mean lift coefficient and shift the peak in the $\frac{C_L}{C_D}$ curve to a higher angle of attack. When the airfoil is fully stalled at $\alpha = 15^o$ the freestream turbulence has an effect on the rms velocity levels and reduces the rms values. Surface pressure spectra indicate the presence of vortex shedding at frequencies consistent with the Fage-Johansen Strouhal number $St_{FJ} = 0.15 – 0.17$.

Time-resolved velocity field measurements with a high-speed PIV system are correlated with surface pressure measurements to identify regions in the flow that are responsible for specific frequencies in the pressure spectrum. The cross spectral density function was used to identify connections between the freestream turbulence and the shear layer and near wake velocity fluctuations. The correlations are high at only specific frequencies, indicating the receptivity of the separating shear layer and the near wake region to forcing by the turbulent field.

A broad peak in the pressure spectra is observed around f = 10 Hz (St = 0.42) that is connected with unsteadiness in the reverse flow field near the surface of the airfoil.

The concept of partial circulation is used to compute a leading-edge suction parameter from the experimental data. The suction parameter tracks the state of the flow, indicating whether it the flow is separated or not. When the flow is separated, the suction parameter is approximately 15 percent smaller than when the flow is attached.

11.6 ACKNOWLEDGEMENTS

This work was partially supported by the Air Force Office of Scientific Research DURIP Grant FA9550-18-1-0327 with program officer Dr. Gregg Abate, and ONR grant N00014-19-1-2280 with program officer Dr. Brian Holm-Hansen. Professor Jeff Eldredge's encouragement to investigate the suction parameter is gratefully acknowledged.

11.7 REFERENCES

[1] Hoblit, F., Gust Loads on Aircraft: Concepts and Applications, AIAA Education Series, 1988.

[2] Greenblatt, D., Ben-Harav, A., and Müller-Vahl, H., Dynamic stall control on a vertical-axis wind turbine using plasma actuators, AIAA Journal, Vol. 52, No. 2, 2014, pp. 456-462.

[3] Pfeiffer,J., Closed-loop active flow control for road vehicles under unsteady cross-wind conditions, Ph.D. thesis, T U Berlin, 2016.

[4] Cherry, B.E., and Constantino, M.M., The burble effect: Superstructure and flight deck effects on carrier air wake, U. S. Naval Academy Technical Report, Vol. DTIC ADA527798, 2010.

[5] Imai, T., and Asai, M., Receptivity of the shear layer separating from a rear edge of flat plate, Fluid Dynamics Research, Vol. 41, No. 3, 2009, p. 035506. doi:10.1088/0169-5983/41/3/035506.

[6] Ramesh, K., Gopalarathnam, A., Granlund, K., Ol, M., and Edwards, J., Discrete-vortex method with novel shedding criterion for unsteady airfoil flows with intermittent leading-edge vortex shedding, Journal Fluid Mechanics, Vol. 751, 2014, pp. 500-538.

[7] Ramesh, K., Murua, J., and Gopalarathnam, A., Limit-cycle oscillations in unsteady flows dominated by intermittent leading-edge vortex shedding, Journal of Fluids and Structures, Vol. 55, 2015, pp. 84-105.

[8] Eldredge, J.D., Mathematical modeling of unsteady inviscid flows, Interdisciplinary Applied Mathematics, Vol.50, Springer International Publishing, 2019.

[9] Hou, W., Darakananda, D., and Eldredge, J., Machine-learning based detection of aerodynamic disturbances using surface pressure measurements, AIAA Journal, 2019, pp. 1-15. DOI: 10.2514/1.J058486.

[10] Rennie, R., Catron, B., Feroz, M.Z., and Williams, D., Model predictive control of wind-tunnel wind speed for low-re unsteady aerodynamic testing, AIAA Paper 2018-0627, 2018.

[11] Williams, D.R., Stasse, Q., and Rennie, R.M., Lift, drag, and moment response of a UCAS model experiencing longitudinal von Karman gust spectra, AIAA Paper 2019-1149, 2019.

[12] Rennie, R.M., Catron, B., Feroz, M.Z., Williams, D., and He, X., Dynamic behavior and gust simulation in an unsteady flow wind tunnel, AIAA Journal, Vol. Jan 29, 2019. Accessed at https://doi.org/10.2514/1.J057186.

[13] Fage, A., and Johansen, F., On the flow of air behind an inclined flat plate of infinite span, Proceedings of the Royal Society of London. Series A, Containing Papers of a Mathematical and Physical Character, Vol. 116, No. 773, 1927, pp. 170-197.

[14] Raju, R., Mittal, R., and Cattafesta, L., Dynamics of airfoil separation control using zero-net-mass-flux forcing, AIAA Journal, Vol. 46, No. 12, 2008, pp. 3103-3115.

[15] Garrick, I., Propulsion of a flapping and oscillating aerofoil, NACA Report 567, 1937.

Chapter 12 – THE INTERACTION OF A SEARS-TYPE SINUSOIDAL GUST WITH A CAMBERED AEROFOIL IN THE PRESENCE OF NON-UNIFORM STREAMWISE FLOW

Anna M. Young
University of Bath
UNITED KINGDOM

Amanda S. M. Smyth
University of Cambridge
UNITED KINGDOM

The unsteady load response of an aerofoil encountering a gust is often modelled using analytical transfer functions, which assume idealised behaviour of both the flow and the aerofoil. One such transfer function is the Sears function, which models a pure transverse gust interacting with a flat plate aerofoil at zero mean incidence. The function was extended by Goldstein and Atassi to account for camber and incidence as well as the presence of a streamwise gust component. Atassi showed that the effects of camber and incidence (i.e., non-zero mean aerofoil loading) are not negligible when there is a streamwise gust component. In this work, new experimental data is shown for an aerofoil with non-zero loading encountering a gust with both streamwise and transverse components. The data gives validation of the Atassi model. Some of the flow physics behind the Atassi model is also investigated, including the superposition of the gust onto the aerofoil potential field and the propagation of the gust along the aerofoil surface.

12.1 INTRODUCTION

In many of the applications of fluid mechanics, it is necessary to know the unsteady load response of an aerofoil to a gust, but computing the response using a high-fidelity CFD code or undertaking detailed experimental analysis is often prohibitively expensive and time-consuming. For this reason, engineers tend to use analytical transfer functions, which assume idealised behaviour of both the flow and the aerofoil. One such transfer function is the Sears function [1], which assumes a pure transverse gust interacting with a flat plate aerofoil with zero mean incidence. The Sears-type gust is shown in Figure 12-1(a): a uniform streamwise flow of velocity $\boldsymbol{U_\infty}$ and a transverse sinusoidal gust of amplitude $\hat{\boldsymbol{v}}$ and reduced frequency $\boldsymbol{k_1}$ encounters a flat plate at zero mean incidence, giving rise to an unsteady incidence variation $\hat{\boldsymbol{\alpha}}_{\boldsymbol{G}}$.

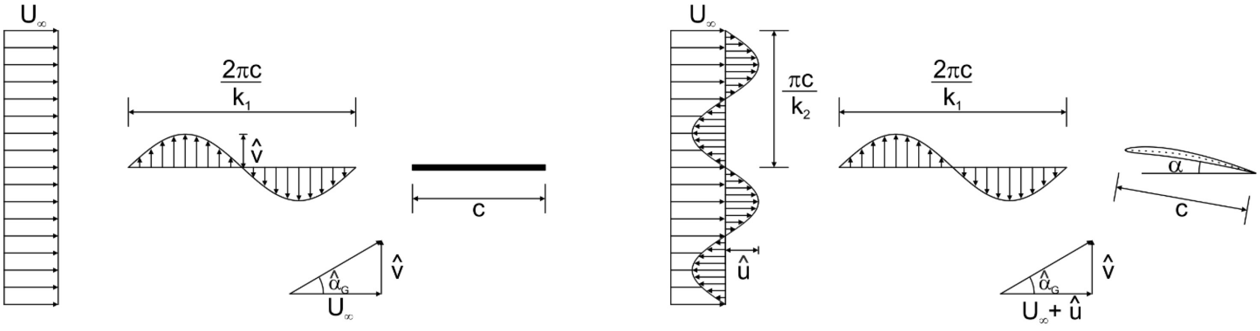

(a) Sears function.

(b) Atassi function.

Figure 12-1: Sketch of the Aerofoil Gust Encounters Modelled by the Sears and Atassi Functions, Including the Definitions of k_1, k_2 and $\hat{\alpha}_G$ Used in this Work.

An extension to the Sears function was derived by Goldstein and Atassi [2], [3]. The Atassi function models the flowfield shown in Figure 12-1(b), which has a transverse gust identical to the Sears gust, but an additional streamwise gust of magnitude $\hat{\boldsymbol{u}}$ and reduced frequency $\boldsymbol{k_2}$ is introduced. Further to this, the Atassi function models an aerofoil with both camber and incidence and thus takes into consideration the non-zero mean loading of the aerofoil and the arising potential field. Recent work by Wei et al. [4] studied an un-loaded aerofoil in a gust with both transverse and streamwise components. They showed that the Atassi function gives good agreement with wind tunnel data, and they show that in the absence of aerofoil loading (as is the case for their un-cambered aerofoil at zero angle of attack), the difference between the Sears and Atassi functions is simply a matter of normalisation. This is because the second order terms in the Atassi function are only present when the mean aerofoil load is non-zero, as will be discussed in Section 12.5.

Given the increased applicability of the Atassi function over the Sears function, it is perhaps surprising that little work has been undertaken on its validation and limitations. Furthermore, wind tunnel facilities that aim to generate a Sears-type gust will often use a series of flaps, or louvres. These flaps will either introduce a vertical variation in the flow due to the wakes from the flaps (if they are closely spaced) or allow deviation of the flow far from the flaps (if the flaps are spaced widely apart), and thus a smaller gust amplitude than expected. If a vertical variation is introduced to the flow, the gust will resemble the flow modelled by Atassi as opposed to that modelled by Sears. Wei et al. [4] showed the switch from Sears-type to Atassi-type flow by varying the flap spacing, while Jancauskas et al. [5] tested a gust generator with only two widely-spaced flaps and found generally good agreement with the Sears function.

One of the applications in which the Sears function is used is the estimation of tidal turbine blade fatigue life. In this chapter, therefore, an aerofoil representative of a tidal turbine blade is used for the experiments. This aerofoil is thicker (21% chord) than those typically used in aerodynamics experiments and has significant camber (2% chord). Some data of this type was presented by Cordes et al. [6] with a cambered Clark-Y section at different angles of attack, but it was later stated by Traphan et al. and Wei et al. that the gust in their facility has a substantial component in the spanwise direction (i.e., the gust is three-dimensional) [4], [7], and so the Atassi function would not be expected to apply.

The data shown in this chapter therefore gives new information on the response of an aerofoil with camber and at non-zero angle of attack to an Atassi-type gust; these are the conditions (when the aerofoil loading is non-zero) in which the Atassi function differs significantly from the Sears function and so these experiments provide new insights into the flow behaviour.

The chapter is structured as follows. After an overview of the Sears and Atassi functions, the experimental facility and method are described. The flowfield in the wind tunnel is examined under both steady and unsteady flow with and without the aerofoil with the aim of testing the assertion of Goldstein and Atassi that the incoming gust and the upstream aerofoil potential field will superpose linearly [2]. The unsteady lift measured in the experiments is then compared with the predictions of the Sears and Atassi functions, and the effects of both camber and incidence are examined. Some limits of agreement between the Atassi function and the experimental data are also found. Finally, a brief examination is undertaken of the propagation of the gust down each surface of the aerofoil, to see whether there is evidence of the gust being stretched on the suction surface due to the faster local flow.

12.2 UNSTEADY TRANSFER FUNCTIONS: THE SEARS AND ATASSI FUNCTIONS

The Sears function [1] can be used to find the unsteady lift caused on an aerofoil by a sinusoidal transverse gust, as shown in Figure 12-1(a). The function was derived assuming zero mean aerofoil loading (zero thickness, camber and mean angle of attack), but does not lose accuracy when applied to aerofoils with non-zero mean loading, if the gust is purely transverse (i.e., with no k_2 component). The Atassi function was developed by Goldstein [2] and Atassi [3], to account for the distorting effect of the mean aerofoil potential field on the gust, for gusts with both transverse and streamwise components of velocity fluctuations. It is shown schematically in Figure 12-1(b).

In order to obtain the unsteady lift amplitude, in each case a transfer function is multiplied by the quasi-steady lift, $\hat{L}_{qs}$. The Sears function gives the unsteady lift as:

$$\hat{L}_S = S(k_1)\hat{L}_{qs} \tag{12-1}$$

where $S(k_1)$ is the Sears transfer function. The Atassi function gives the lift as a combination of the Sears transfer function and two additional terms:

$$\hat{L}_A = \left[S(k_1)\frac{\mathrm{k}_1}{|k|} + \alpha\hat{L}_\alpha(k_1,k_2) + m\hat{L}_m(k_1,k_2) \right]\hat{L}_{qs} \tag{12-2}$$

The second and third terms in Equation 12-2 are both zero if k_2 is zero. The second term relates to the steady angle of attack, α, in radians, and the third to aerofoil camber, m, as a fraction of the aerofoil chord length. The expressions s $\hat{L}_\alpha(k_1,k_2)$ and $\hat{L}_m(k_1,k_2)$ are complicated functions of the gust frequencies, and can be found in the original work by Sears [2].

A recent study by Wei et al. [4] investigated the differences between Sears-style and Atassi-style gusts, and carried out experimental validation of both transfer functions for a thin symmetric aerofoil at zero mean angle of attack. This means that no aerofoil loading was included in the analysis, and any difference in load response between the Sears and Atassi gusts was due to the nature of the gust – whether or not it had a significant k_2 component. Wei et al. provide valuable insight into the Atassi function, showing that one of the primary differences from the Sears function is its definition of quasi-steady lift, $(\hat{L}_{qs})$. Both functions are normalised by the quasi-steady lift, and for the Sears function this is defined as:

$$(\hat{L}_{qs})_S = 2\pi\rho c U_\infty \hat{v} \approx \pi\rho c U_\infty^2 \hat{\alpha}_g \tag{12-3}$$

Where c is the aerofoil chord, and $\hat{\alpha}_g$ is the amplitude of the inflow angle fluctuation generated by the gust. For the Atassi function, the quasi-steady lift is instead given by:

$$(\hat{L}_{qs})_A = \pi\rho c U_\infty^2 \epsilon \tag{12-4}$$

This time, the gust amplitude is defined by the parameter ϵ, which is a combination of the amplitude of both the streamwise and transverse gust fluctuations, from the following relations:

$$\hat{u} = \frac{U_\infty \epsilon k_2}{|k|} \tag{12-5}$$

$$\hat{v} = \frac{U_\infty \epsilon k_1}{|k|} \tag{12-6}$$

Wei et al showed that, given that the gusts have small amplitudes ($\hat{u} \ll U_\infty$, $\hat{v} \ll U_\infty$), the parameters ϵ and $\hat{\alpha}_g$can be related as follows:

$$\hat{\alpha}_g = \tan^{-1}\left(\frac{\hat{v}}{U_\infty + \hat{u}}\right) \approx \tan^{-1}\left(\frac{\hat{v}}{U_\infty}\right) \approx \frac{\epsilon \mathrm{k}_1}{|k|} \tag{12-7}$$

where:

$$|k| = \sqrt{k_1^2 + k_2^2} \tag{12-8}$$

This relation means that the difference between the quasi-steady lift as defined in the Sears and Atassi functions lies in the factor $k_1/|k|$. Wei et al. [4] showed that for a symmetric aerofoil at zero mean angle of attack, the Atassi function was equivalent to the Sears function if multiplied by $k_1/|k|$., regardless of the value of k_2.

As explained by Atassi [3] and by Wei et al. [4], significant differences between the Sears and Atassi functions only emerge when there is both a k_2 component in the gust, and non-zero mean aerofoil loading due to camber or angle of attack.

An example of a case where the Atassi and Sears functions give significant differences in response is given in Figure 12-2(a). This figure shows the response functions obtained from the Sears and Atassi functions, for an aerofoil with 2% camber and 3° mean angle of attack, undergoing oblique gust forcing ($k_1 = k_2$). The response function is defined as follows for the Sears function:

$$R_S = \frac{\hat{L}_S}{(\hat{L}_{qs})_S} = S(k_1) \tag{12-9}$$

while for the Atassi function, it is given by:

$$R_A = \frac{\hat{L}_A}{(\hat{L}_{qs})_A} = S(k_1)\frac{\mathrm{k}_1}{|k|} + \alpha\hat{L}_\alpha(k_1,k_2) + m\hat{L}_m(k_1,k_2) \tag{12-8}$$

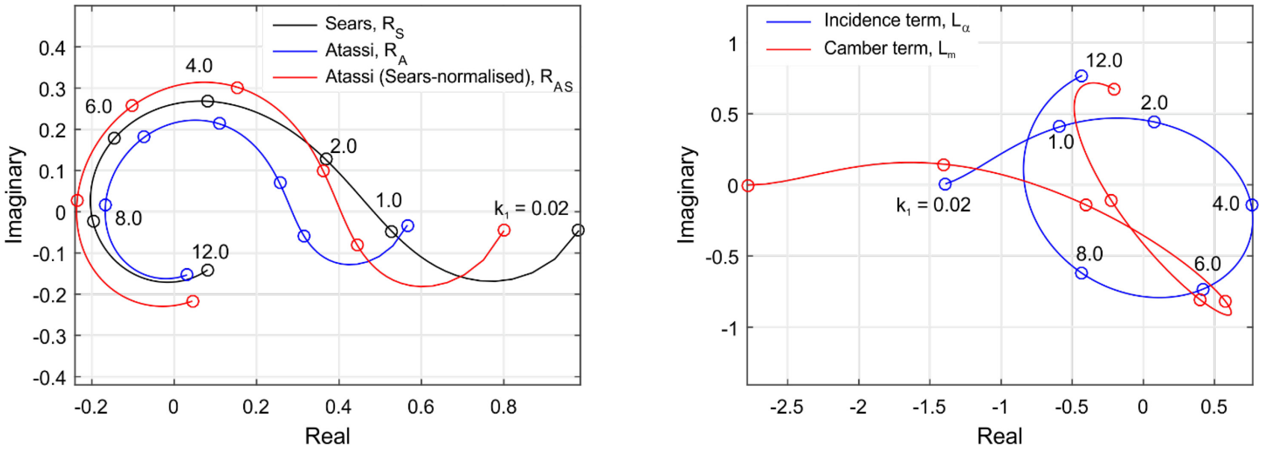

(a) Comparison of Sears and Atassi response functions.

(b) Camber and incidence terms for the Atassi function.

Figure 12-2: Example Sears and Atassi Response Functions for an Oblique Gust ($k_1 = k_2$) Interacting with an Aerofoil with 2% Camber at 3° Aerofoil Incidence.

In order to show a more direct comparison between the Sears and Atassi functions, a third response function is defined by multiplying the Atassi function by $|k|/k_1$, thus normalising it by the same quasi-steady lift as is used in the Sears function:

$$R_{AS} = \frac{\hat{L}_A}{(\hat{L}_{qs})_S} \tag{12-9}$$

In order to illustrate the differing contributions of the incidence and camber effects, the functions s $\hat{L}_\alpha(k_1,k_2)$ and $\hat{L}_m(k_1,k_2)$ are shown separately on Figure 12-2(b) for the same aerofoil and gust conditions.

Unlike the work of Wei et al. [4], the experiments undertaken in this work use an aerofoil with camber at different angles of incidence. This will test the assertion that it is only in the presence of *both* a vertical (k_2) gust component *and* non-zero mean aerofoil loading that the results differ significantly from the Sears result.

12.3 EXPERIMENTAL METHOD

A schematic of the wind tunnel is shown in Figure 12-3, and the key parameters of the tunnel are given in Table 12-1. The working section has solid side walls but is open at the top and bottom, to allow the flow to turn freely as it passes over the aerofoil. A 2D aerofoil is mounted at mid-height and two chords downstream of the tunnel inlet. The aerofoil profile was chosen to be representative of a tidal turbine aerofoil, and so has moderate camber (2% chord) and is relatively thick (21% chord). The aerofoil is mounted on a turntable in order to vary the angle of attack without moving the position of the leading edge in the tunnel. Circular fillets of radius 3% span were fitted at the junction between the aerofoil and the wind tunnel end walls. These fillets were found to suppress the end wall corner separation and prevent it from affecting the flow over the majority of the aerofoil span, thus giving the desired 2D flow at mid-span.

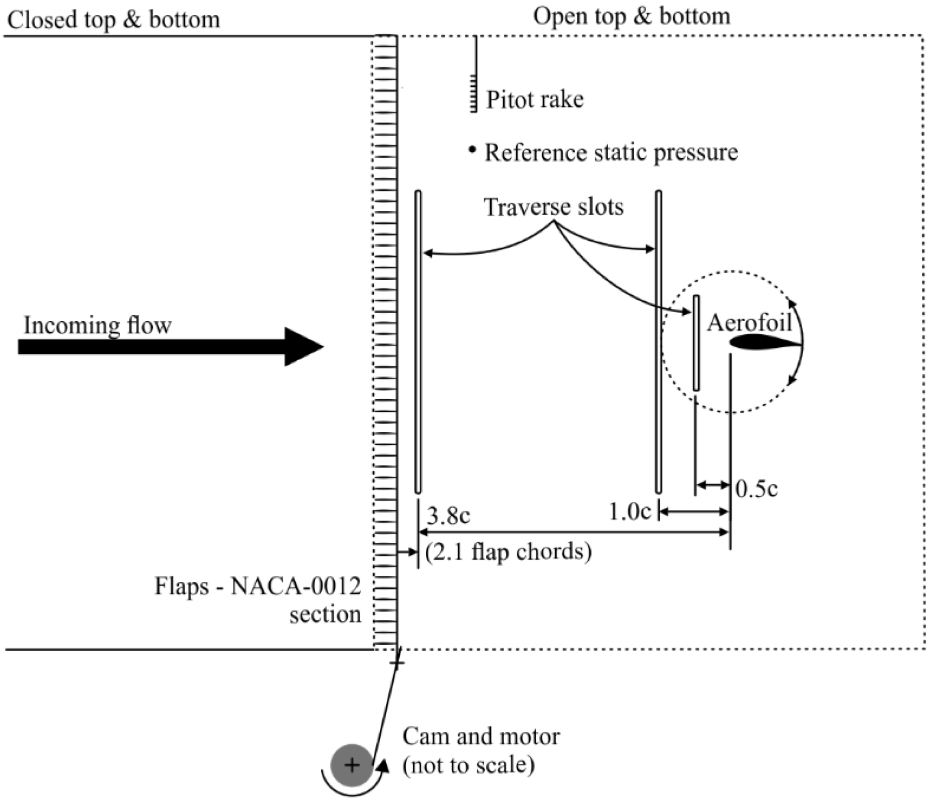

Figure 12-3: Schematic of the Wind Tunnel Test Facility Showing Traverse Plane Locations.

Upstream of the working section there are a vertical series of flaps. The flap cross-section is a NACA-0012. The flaps are extruded Aluminium, and on both surfaces of each flap there is a carbon-fibre stiffener of thickness 0.5 mm. The stiffeners prevent spanwise bending of the flap and were not found to have an adverse effect on the flow quality downstream of the flaps. The flap chord was chosen as a balance between the need for stiffness (which sets a minimum thickness) and the desire to minimise unsteady flow behaviour of the flaps (the reduced frequency of the flap motion will be related to the reduced frequency of the gust encountered by the main aerofoil by the ratio $c_{\text{flap}}/c_{\text{aerofoil}}$). The decision of how many flaps to install was made by considering the behaviour of an infinite number of flaps with infinitesimal loading. In this case, the flaps would generate a continuous vortex sheet as envisaged by Sears. The flaps were therefore packed as tightly as possible which gave a ratio of 0.5 between the flap chord and the vertical spacing of the flaps. Placing the flaps further apart would also risk introducing flow deviation away from the flap surfaces.

Table 12-1: Key Parameters of the Wind Tunnel.

Parameter	Value
Tunnel height (m)	1.00
Flow speed (m/s)	18.0 – 26.0
Aerofoil chord (m)	0.115
Aerofoil aspect ratio	2.96
Aerofoil Reynolds number	$1.41 – 2.08 \times 10^5$
Number of flaps	58
Flap chord (mm)	35
Flap frequency range (Hz)	0 – 8
Reduced frequency range	0 – 0.35

The flaps are mounted in bearings on an Aluminium frame and attached to a DC motor via a cam and a connecting rod. The mechanism can therefore generate a sinusoidal variation in flow incidence similar to the Sears' type gust. The amplitude of the gust can be varied by changing the cam size, and the frequency is adjusted by changing the speed of the motor. For steady-state tests, the flaps are held in either their fully up or fully down position.

The tunnel operating conditions are measured using a sidewall static pressure tapping and a rake of Pitot probes between the flaps and the aerofoil, as shown on Figure 12-3. The reference velocity from these probes is within 1% of the average inlet velocity integrated over the central portion of the wind tunnel. The incoming flow has a turbulence intensity of approximately 0.5%. The aerofoil pressure distribution is measured using 43 aerofoil surface pressure tappings at mid-span. The tappings are connected to fast-response pressure transducers via a set of semi-infinite lines. The use of semi-infinite lines enables high-frequency measurements to be taken in confined spaces by removing the requirement for the transducers to be mounted on the aerofoil surface [8]. The amplitude and phase of the response does, however, change with frequency and so the tappings with semi-infinite lines were calibrated against a surface-mounted fast-response transducer using a signal generator and a loudspeaker. The resonant frequency of the semi-infinite lines was found to be over 200 Hz, which is above the range of frequencies of interest in this work. For steady-state tests, the tappings are connected to the transducers without the semi-infinite lines.

An unsteady total pressure probe was traversed vertically through the flow at various axial locations upstream of the aerofoil (see Figure 12-3 for the positions). By measuring the flow three times with the probe oriented at three angles (-45°, 0°, +45°) the equivalent data from a fast-response three-hole probe could be reconstructed and thus the flow angle and speed could be calculated. This enabled the gust to be characterised in space and time both with and without the aerofoil installed.

Data were sampled at 20 kHz for 20 – 30 seconds depending on the frequency of the flap motion. All data were phase-locked to the motor frequency using a once-per-revolution sensor on the shaft. This enabled the harmonic response to be averaged over 50 – 150 cycles.

12.4 STEADY-STATE BEHAVIOUR OF THE AEROFOIL

The wind tunnel generates a finite jet with a height of approximately 8 times the aerofoil chord. This means that the aerofoil will behave slightly differently to an aerofoil in an ideal, infinite flow, as explained by Brooks et al. [9], [10], [11]. The most obvious consequence of the finite jet is that the lift is lower than expected and thus the lift curve does not follow the ideal 2π rule. This can be rectified by dividing the apparent angle of attack by a correction factor ζ. Correlations for ζ were developed for a zero-camber aerofoil by Brooks et al. [9], [10]. For the aerofoil used in this work, the correction factor was found to be 1.19, which agrees with their correlation. In tests with a larger aerofoil (which will be discussed briefly in Section 12.5), however, the correlation was found 5% higher than the value given by Brooks et al. [11]. This may be due to the fact that the aerofoil used in this work has non-negligible camber and thickness.

Steady-state tests were undertaken with the flaps in both the 'up' and 'down' positions, such that the true incidence was:

$$\alpha_{\mathrm{corr}} = \frac{(\alpha - \alpha_{\mathrm{flap}})}{\zeta} \tag{12-10}$$

A graph of lift coefficient against incidence corrected using Equation 12-12 with the flaps in two positions is shown in Figure 12-4(a). The data from the wind tunnel is compared with results from MSES (a coupled Euler-boundary layer solver [12]). It can be seen that both the flaps up (blue) and faps down (red) data follow the same line with gradient 2π as the MSES prediction (black line) at angles below the stall angle. The stalling behaviour of the aerofoil differs between MSES and the experiments; this is due to the large blockage generated when the aerofoil is at high angles of attack and the presence of aerofoil-end wall corner separations at high incidence. From this point onwards in the chapter, all incidence values given for experimental data have been corrected using Equation 12-12.

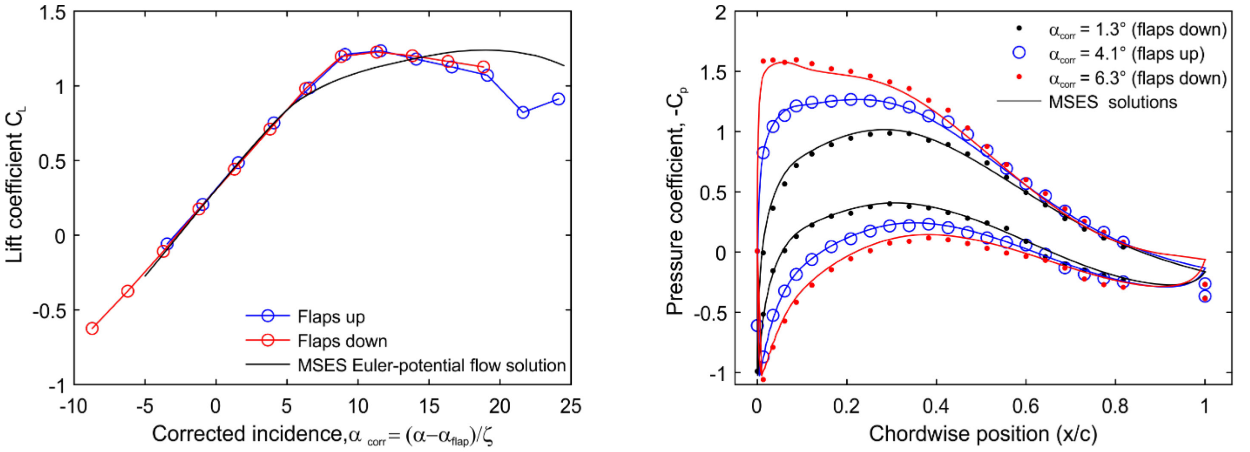

(a) Lift coefficient against corrected incidence. (b) Surface pressure distributions with the aerofoil at three different incidences.

Figure 12-4: Lift Curve and Surface Pressure Distributions from MSES and Experimental Data Showing Good Agreement When the Wind Tunnel Correction Factor is Applied to the Incidence.

The reason for the reduction in lift in a finite jet is explained by Brooks et al. [9] as being due to the restriction of the aerofoil potential field: there is a condition of zero velocity potential at the jet boundary and so the aerofoil can be considered to be in an infinite cascade. The correction found above will only match the total aerofoil lift – the surface pressure distribution will still be different in the finite jet case, and the potential field around the aerofoil will not match. It is possible to develop an aerofoil with an adjusted camber line which will produce the pressure distribution of the wind tunnel test when operating in an infinite jet. Brooks et al. give an analytical solution for this `free equivalent foil' which is valid for zero-camber, thin aerofoils [9].

For the aerofoil considered here, the error in pressure distribution is quite small. This is shown in Figure 12-4(b), where the measured surface pressure (dots) is compared with data from MSES (solid lines) at three different incidences. It can be seen that there is good agreement between the simulations and the experiments. This is may be due to fact that the jet height ratio of 8 used in this work is towards the upper end of those used in the literature (Brooks et al. [11] undertook tests with jet ratios from 0.5 to 11).

The aerofoil potential field will distort an incoming gust, and this may affect the resulting unsteady load. In the case of a Sears-type gust, the potential field and the gust will behave independently, but Atassi [3] argues that the presence of vertical non-uniformities in the gust will cause coupling between the gust and the potential field. Goldstein and Atassi [2] state that the incoming gust and potential field will superpose linearly, but that the gust convection speed will be different across the two surfaces of the aerofoil (in contrast to the frozen gust hypothesis, which is valid for an un-loaded aerofoil). This difference in convection speed is what causes the discrepancy between coupled and uncoupled gust response. These points will be discussed in the next three sections.

12.5 UNSTEADY GUSTS AND THEIR INTERACTION WITH THE AEROFOIL POTENTIAL FIELD

The flow angle variation due to the aerofoil potential field is shown in Figure 12-5(a), which is taken from an MSES simulation in infinite flow at zero angle of attack. As expected, the most substantial changes in flow angle are close to the aerofoil, but the aerofoil also exerts a non-negligible influence on the upstream flow. To see this more clearly, the change in flow angle relative to the mean incidence is shown in Figure 12-5(b); this distortion is defined as α_{d}. The data is taken from 0.5 chords upstream of the aerofoil and from simulations at incidences from -8° (black) to +4° (red). Distortions of up to 4° from the mean incidence are observed, with the flow being deflected up on the top surface of the aerofoil and down on the bottom surface. The distortion in the flowfield is not linear with average incidence or with vertical position, and the maximum distortion increases with aerofoil loading.

The flow angle measured in the wind tunnel with the aerofoil in place will be affected by this distortion. If the assertion of Goldstein and Atassi [2] is correct, then the measured distorted gust, α'_{GM}, will be the sum of the gust measured in the empty wind tunnel α_{G} and the distortion due to the quasi-steady aerofoil potential field, α_{d}. The quasi-steady distortion, α_{d}, can be found from the data shown in Figure 12-5(b), by interpolating for the measured empty tunnel incidence (this interpolation is done after the wind tunnel correction factor, ζ, has been applied to the empty tunnel data). We denote this predicted gust incidence as α'_{GP}:

$$\alpha'_{\mathrm{GP}} = \alpha_{\mathrm{G}} + \alpha_{\mathrm{d}} \tag{12-11}$$

In Figure 12-6, the incidence variation measured 0.5 chords upstream of the aerofoil with the aerofoil in place, α'_{GM}, (black) is compared with the empty wind tunnel measurements, α_G, (blue) and the predicted distorted gust, α'_{GP}, as defined in Equation 12-13 (red).

Figure 12-6(a) shows the flow angles with flaps stationary in two different positions. Considering first the empty wind tunnel data (blue), it can be seen that with the flaps in the `up' position, the flow angle is approximately -0.4°, while the angle reduces to -5.8° when the flaps are moved to the `down' position. In both cases, the wakes from the flaps are visible, causing a 1 – 2° variation in flow angle, but other than this the flow angle is approximately constant across the traverse range. When the aerofoil is in the wind tunnel, the measured angle, α'_{GM}, is indeed different from α_G. As expected from Figure 12-5, the effect of the aerofoil potential field is different at the two mean incidences shown in Figure 12-6(a): in the flap up case, the incidence is increased at positions above the aerofoil and reduced slightly below the aerofoil, while the flap down case shows a large reduction in incidence below the aerofoil, reducing to nothing at the top of the measurement plane.

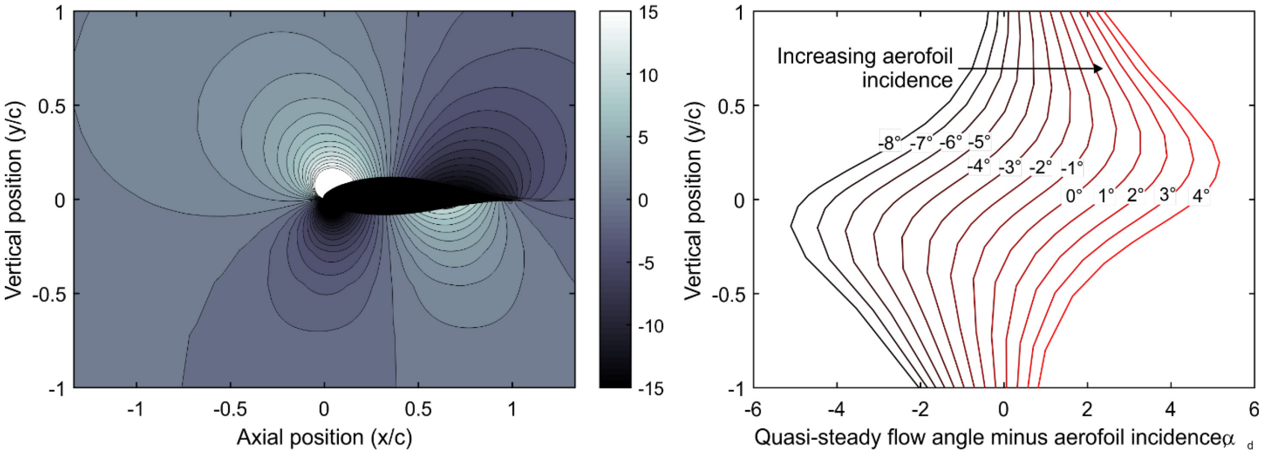

(a) Flow angles round the aerofoil at zero incidence.

(b) Distortion angle against vertical postion at x/c = -0.5.

Figure 12-5: Data from MSES Simulations Showing the Effect of the Aerofoil Potential Field on the Incoming Flow Angle.

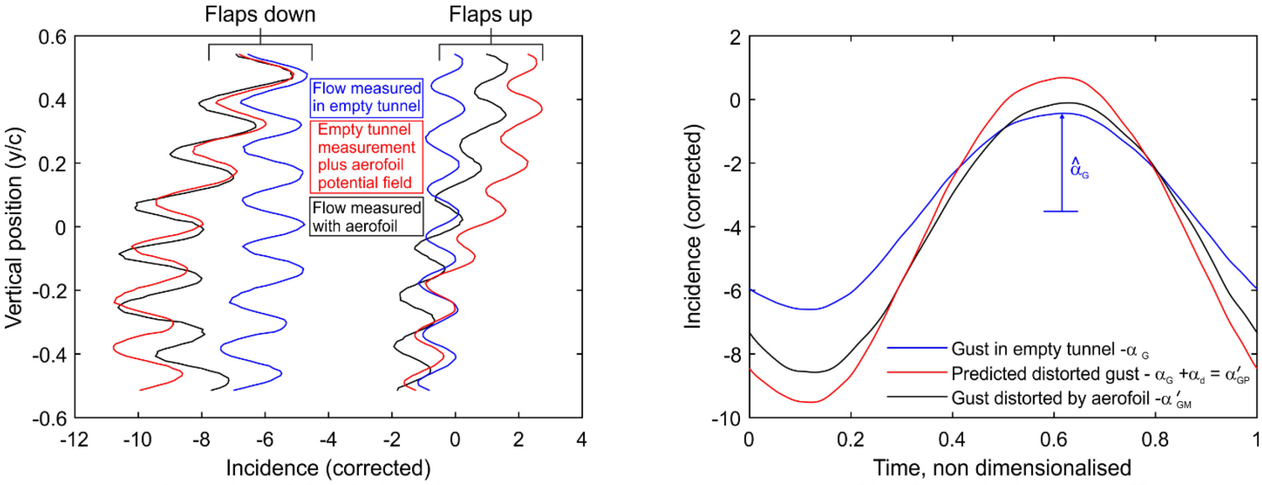

(a) incidence against vertical position for steady-state flow with the flaps in two positions.

(b) Incidence against time for a gust with reduced frequency k = 0.13.

Figure 12-6: Traverses at $x/c = -0.5$ with the Flaps in the Up and Down Position Showing the Effect of the Aerofoil on the Steady-State Flow Compared with the No-Aerofoil Case with the Predicted Potential Field from MSES.

The trend in the predicted flow angle, α'_{GP} (shown in red), is approximately correct, but the magnitude of the distortion is over-predicted. This is particularly apparent in the data from the top half of the traverse plane with the flaps up, where the distortion predicted by MSES, α_{d} (the difference between the blue and red lines), is approximately twice the size of the measured distortion (the difference between the blue and black lines). When averaged over the traverse plane, α'_{GP} for the flaps up case is 1.0° higher than the measured angle, α'_{GM}, while the difference in the flaps down cases is 0.2° (this smaller value is within the experimental error bounds). This discrepancy between the distortion predicted by MSES and the measured data suggests that the aerofoil potential field is, indeed, affected by the boundaries of the finite jet, despite the agreement of the surface pressure distributions with MSES (Figure 12-4(b)). The effect of finite jet height on the upstream potential field has not been studied in much detail, perhaps due to the historically greater difficulty in measuring the flowfield as opposed to the aerofoil forces and pressure distribution. A CFD study was conducted by Moreau et al. [13], in which they compared the potential field of an aerofoil in an infinite jet with those obtained with finite height to chord ratios of 1.0 and 3.8. Their results show qualitatively that the incoming flow behaves differently when the jet height changes but they do not suggest any means of correcting for this effect.

When the flaps are moving, a similar gust distortion is observed to that discussed above, i.e., the gust is larger when the aerofoil is installed than in the empty wind tunnel case. An example of this is shown in Figure 12-6(b), which shows the gusts generated by the flaps at a reduced frequency, k_1, of 0.13. The data is taken from the same traverse plane as Figure 12-6(a) and the incidence has been averaged over the whole vertical range at each time-step. It can be seen that the flaps generate a sinusoidal incidence variation in time when the wind tunnel is empty (blue line, α_G). This blue line gives the Sears gust amplitude $\hat{\alpha}_G$, as marked on the plot. With the aerofoil in place at a nominal incidence of 0° (black line)[1], the gust is distorted such that the minimum incidence is reduced by approximately 2 while the maximum incidence increases by under 0.5. The gust also deviates from a perfect sinusoid, with a slight skewing of the peak to a later time than that in the empty tunnel case. The predicted distorted gust, $\hat{\alpha}'_{GP}$ (Equation 12-13) is shown in red. Both the increase in gust magnitude and the skewing of the peak are predicted by this superposition. As in the steady case, however, the amplitude of the gust is over-predicted relative to the measured data.

Gusts of three different amplitudes were generated at a variety of reduced frequencies, k_1, from 0 (steady) to 0.35, and the gust was measured with and without the aerofoil in place at its nominal zero incidence as in Figure 12-6(b). The peak-to-peak amplitude of the predicted distorted gust ($2\hat{\alpha}'_{GP}$) is plotted against the actual gust amplitude measured with the aerofoil in place ($2\hat{\alpha}'_{GM}$) in Figure 12-7(a). The data points from this set of tests are shown in red, with different markers denoting each reduced frequency. The dotted black line denotes exact agreement between the measured and predicted gusts ($\hat{\alpha}'_{GP} = \hat{\alpha}'_{GM}$), while the solid black line shows a straight line through the red points which has equation $\hat{\alpha}'_{GP} = 1.18\hat{\alpha}'_{GM}$. The error between the predicted and measured gust size is shown in Figure 12-7(b), where it can be seen that the error is between 10 and 20 % for all but one case. This data therefore shows that the error between the gust distortion predicted by MSES and that measured in the wind tunnel is independent of gust size or frequency, and that adding the correct quasi-steady field to the unsteady gusts would give a distorted gust very close to the actual distorted gust. These results suggest that the superposition of the two flowfields is linear and is not affected by unsteady coupling over the frequency range tested.

The effect of reduced frequency on the amplitude of the gust both with and without the aerofoil is shown more clearly in Figure 12-8(a), which is a plot of incidence change against reduced frequency for the cases with the largest cam (which gives a peak-to-peak incidence variation of just under 6° in the empty wind tunnel case – Figure 12-6). Considering first the blue markers, which show the data from the empty wind tunnel, there appears to be a slight increase in gust amplitude with reduced frequency, but the change is within the range of the experimental error and there is significant scatter in the results. The actual gust amplitude (black markers) follows the same trend as the empty tunnel results: the steady-state and $k_1 = 0.35$ results are almost equal. When the empty gust data is superposed with the potential field from MSES, the data represented by the red markers are obtained. The slight upward trend in the no-tunnel data is exaggerated by the superposition process, but the error is approximately constant with reduced frequency.

The average error of 18% is very close to the wind tunnel incidence correction factor discussed in Section 12.4, which is 1.19. This adjustment has, however, already been taken into consideration in the calculations shown in Figure 12-7(a). Also shown on Figure 12-7(a) are three measurements taken with

---

[1] This corresponds to a corrected mean incidence of -3.2°, using Equation 12-12.

a larger aerofoil of 230 mm chord (blue)[2]. The wind tunnel correction factor for this aerofoil is 1.51, but the data lies on the same line as that from the smaller aerofoil, with an average error of 18%.

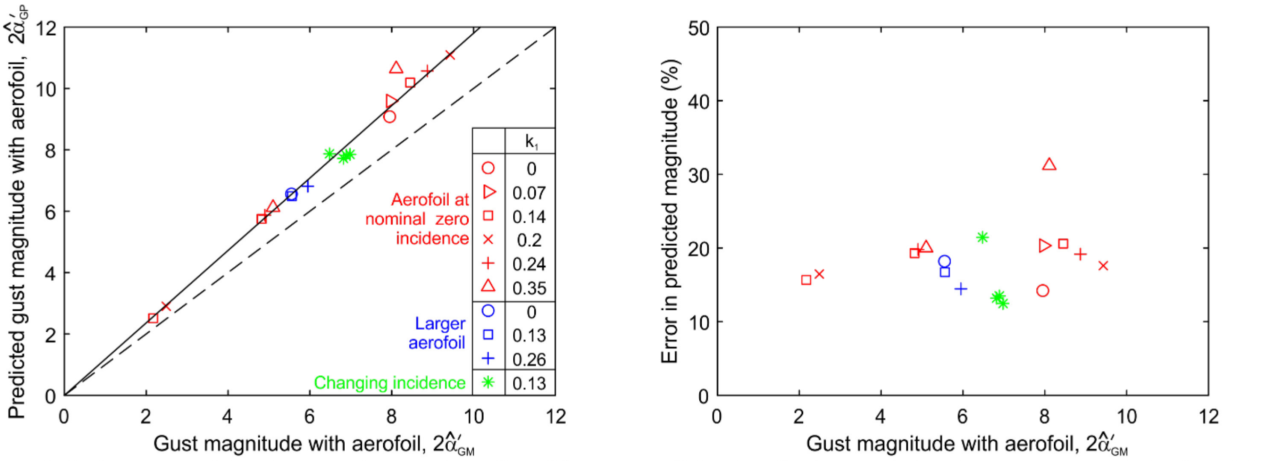

(a) Predicted gust magnitude against measured gust magnitude with aerofoil.

(b) Error in predicted gust magnitude against measured gust magnitude with aerofoil.

Figure 12-7: Measured Flow Angles at $x/c = -0.5$ with and Without the Aerofoil in Place, Compared with the Angles Obtained by Adding the No-Aerofoil Data to the Simulated Aerofoil Potential Field from Figure 12-5(b).

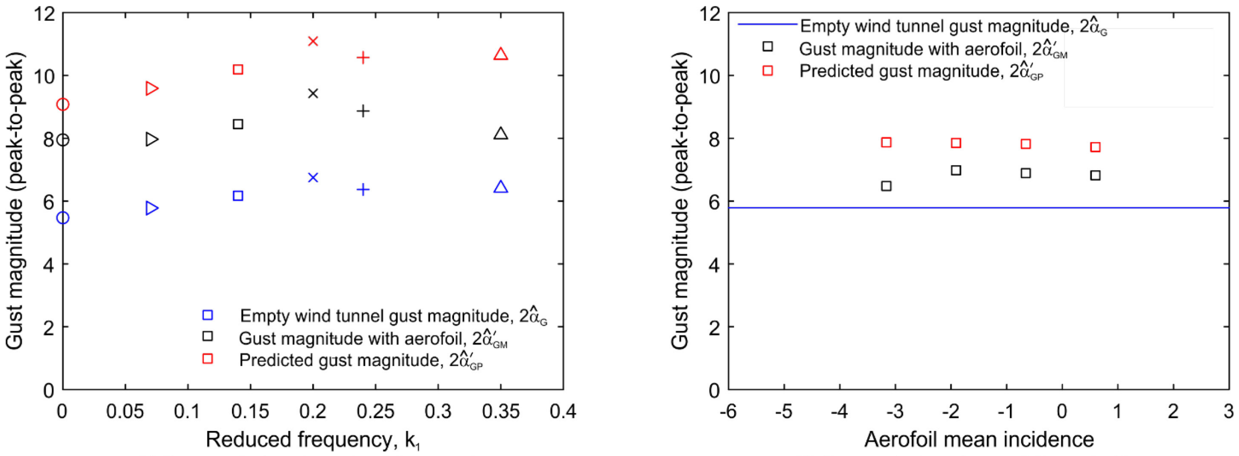

(a) Gust magnitude against reduced frequency, k_1.

(b) Gust magnitude against aerofoil mean incidence.

Figure 12-8: Effect of Reduced Frequency and Aerofoil Mean Incidence on the Magnitude of the Gust in the Empty Wind Tunnel and with the Aerofoil in Place (Both Predicted and Measured).

If the aerofoil incidence is changed, the quasi-steady potential field will change, as shown in Figure 12-5(b). The effect of this on the superposition of the gust with the potential field was investigated by measuring the gust with the aerofoil at four different angles. The results of this are shown in Figure 12-8(b), which is a plot of peak-to-peak amplitude change against aerofoil incidence for the gust with a reduced frequency, k_1 of 0.13 shown in Figure 12-6(b). Restrictions in the traverse slot arrangement meant that the flowfield had to be measured further upstream of the aerofoil (1.0 chords instead of 0.5 chords), and so the overall distortion is lower than in the other cases. Nevertheless, the same trend is observed – the blue line shows the magnitude of the gust in the empty wind tunnel, while the black squares show the gust with the aerofoil in place at each incidence. There is very little change in the distortion of the gust by the aerofoil across the incidence range

---

[2] This data is taken from 0.5 chords upstream of the larger aerofoil, i.e., twice as far away in absolute terms.

tested, despite the lift coefficient changing by approximately 0.4 over this range. As with all the previous data, the prediction from superposing the quasi-steady potential field with the empty tunnel gust (red squares) gives a larger amplitude than the actual data.

The data from the cases with varying aerofoil incidence is denoted by the green stars on Figure 12-7(a) and (b). It can be seen that the error is consistent with all the other cases, suggesting that aerofoil incidence does not affect the superposition of the gust with the potential field (at least for attached flow). Taken as a whole, this data shows that the gust and the aerofoil potential field superpose linearly regardless of gust reduced frequency, aerofoil chord and angle of attack. The reason for the consistent error between $\hat{\alpha}'_{GP}$ (the prediction obtained by addition of the simulated quasi-steady field to gust measured in the empty wind tunnel) and $\hat{\alpha}'_{GM}$, (the gust measured with the aerofoil in place) is unclear, but the fact that the error is unaffected by the magnitude of the aerofoil potential field or by the reduced frequency shows that there is no non-linear coupling of the two flowfields upstream of the aerofoil over the range of variables tested here.

The finding that the gust distortion is independent of reduced frequency is in line with the theory of Goldstein and Atassi [2], who state that the incoming gust will not have its amplitude changed by the steady-state flowfield. Goldstein and Atassi [2] do state, however, that the wavelength of the gust will change over the aerofoil chord, and this will be discussed briefly in Section 12.7. Now that the gusts generated have been quantified, the aerofoil lift response can be compared with that predicted by the models of Sears and Atassi. This will be done in the next section.

12.6 AEROFOIL LIFT RESPONSE

12.6.1 Measuring Unsteady Lift

The unsteady component of lift was found by direct integration of the Fourier coefficients, AN and BN, for each surface pressure measurement at the gust frequency, f_{gust}:

$$A_N = \frac{2}{M}\int_0^M P(t)\sin\left(2\pi f_{\text{gust}} t\right)\, dt \tag{12-12}$$

$$B_N = \frac{2}{M}\int_0^M P(t)\cos\left(2\pi f_{\text{gust}} t\right)\, dt \tag{12-13}$$

where $P(t)$ is the pressure signal and M is the length of the sample (which was set to be many gust cycles, see Section 12.3. The two Fourier coefficients combine to give the phase and amplitude of the response at each location (once a calibration has been applied to take into account the phase lag and attenuation due to the semi-infinite lines). The unsteady pressure difference is then integrated along the aerofoil chord to give the lift. This measured value of unsteady lift can then be compared with the load predicted by the Sears and Atassi functions.

12.6.2 Calculating k_2 and ϵ

The frequency, k_2, of the streamwise gust component has a significant impact on the result of evaluating the Atassi function. This means that it is vital to obtain an accurate estimate of k_2 when comparing experimental results with the Atassi function. An estimate of the spatial frequency in the vertical plane can be obtained from Figure 12-6(a) and the definition of k_2 given in Figure 12-1(b). By this process, k_2 was estimated to be approximately 20. Further investigation, however, suggests that this is not an appropriate way of measuring k_2. Instead, the approach of Wei et al. [4] should be taken and k_2 and ϵ must be calculated from the measured values of k_1 and $\hat{\alpha}_G$ via a two-parameter fit to Equation 12-7. The results of this two-parameter fit are shown in Figure 12-9.

Figure 12-9(a) shows the relationship between the gust amplitude parameter, ϵ and measured gust amplitude, $\hat{\alpha}_G$. It can be seen that ϵ increases linearly with $\hat{\alpha}_G$, as would be expected. Figure 12-9(b) shows the calculated k_2 values (blue stars), against measured gust amplitude, $\hat{\alpha}_G$. The measured ranges of k_1 are included in red for comparison. It can be seen that k_2 is relatively constant with increasing gust amplitude, and that it has a mean value of 0.035. The two-parameter fit method therefore gives a significantly lower value of k_2 than that which was calculated from the visual estimate of k_2 from Figure 12-6(a) (which gave k_2 = 20). In the following sections it will be shown that this lower value of k_2 gives far closer agreement between the Atassi function and experimental data.

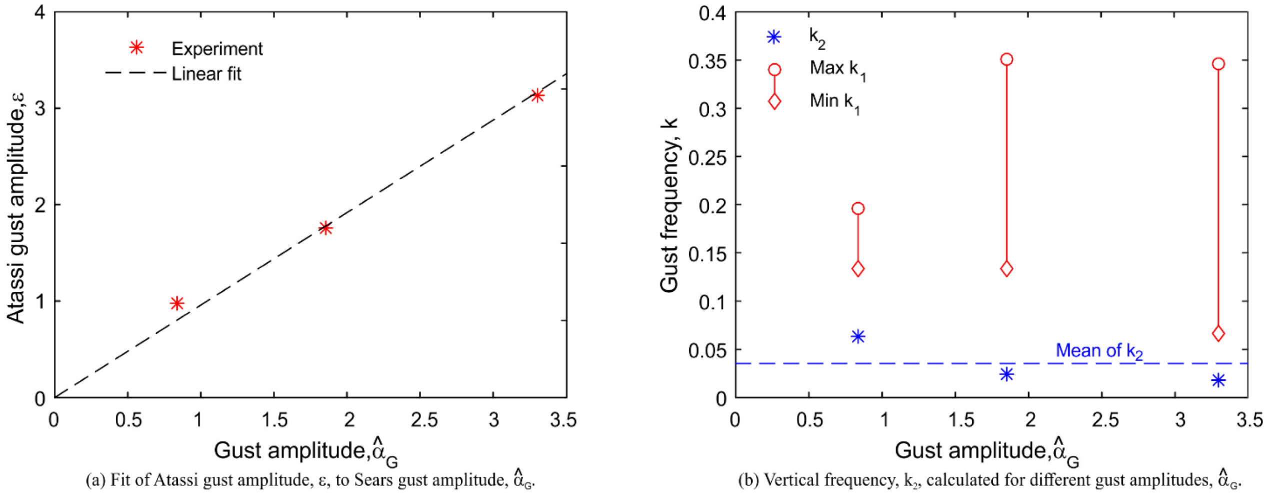

(a) Fit of Atassi gust amplitude, ε, to Sears gust amplitude, $\hat{\alpha}_G$.

(b) Vertical frequency, k_2, calculated for different gust amplitudes, $\hat{\alpha}_G$.

Figure 12-9: Results of the Two-Parameter Fit for ϵ and k_2 from Measured Values of $\hat{\alpha}_G$ and k_1.

12.6.3 Comparing Analytical Theory and Experiments

Figure 12-10 shows the amplitude of the unsteady lift against k_1, calculated from the unsteady transfer functions and measured in experiments. Figure 12-10(a) shows the load amplitude normalised by the quasi-steady lift as defined by Sears (Equation 12-3), while Figure 12-10(b) uses the quasi-steady lift defined for the Atassi function (Equation 12-4). The data is taken from tests at -0.7° mean angle of attack, which was the closest to zero of the available data range. The Atassi function is evaluated for the same aerofoil parameters, with k_2=0.035. Figure 12-10(a) shows that in these conditions the Sears and Atassi functions are nearly identical when normalised consistently, and only diverge at low reduced frequencies (k_1 <0.1).

The experimental results in Figure 12-10 have been categorised by gust amplitude, and the data from the intermediate gust amplitude (black dots, $\hat{\alpha}_G$= 2°) shows reasonable agreement with the transfer functions. The data from largest gust amplitude (red dots $\hat{\alpha}_G$= 3°) consistently shows lift amplitudes much lower than that predicted by Sears and Atassi, while the data from the smallest gust (blue dots $\hat{\alpha}_G$= 2°) is consistently higher than the model predictions. Looking at Figure 12-10(b), the shape of the data for all three gust amplitudes matches the trend in the Atassi function, even in cases where the magnitudes are incorrect.

The quasi-steady lift, by which the unsteady loading is non-dimensionalised, is dependent on the measured gust amplitude. The estimated error in the gust amplitude measurements is ±0.25°, which is a substantial proportion of the overall gust amplitude. This is especially the case for the smallest amplitude gust and changing the magnitude of the gust by 0.2° would bring the data for this gust into agreement with the analytical functions. The trends shown in the data in Figure 12-10 to Figure 12-12 will not be affected by this error, only the absolute values on the y-axis, as all the data for a given gust size is non-dimensionalised by the same quasi-steady value.

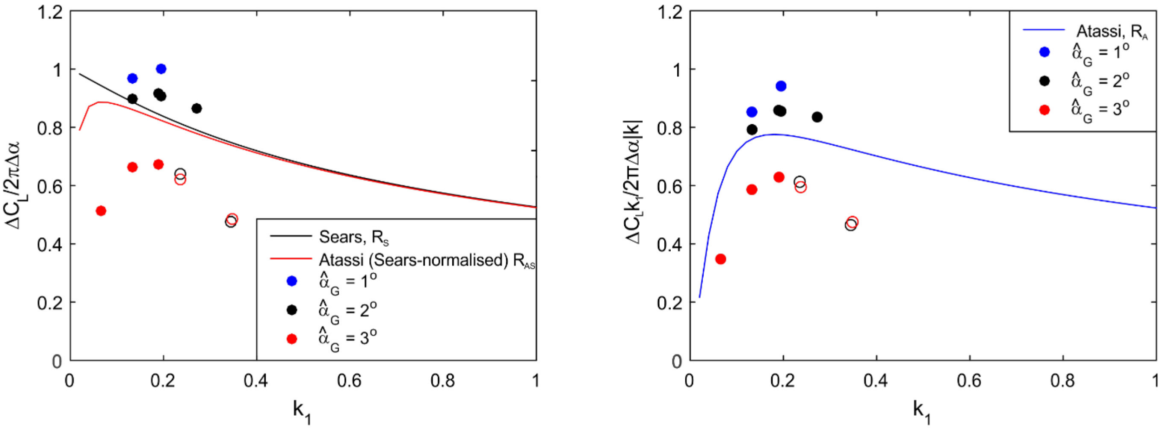

(a) Data compared with Sears and the Sears-normalised Atassi function. (b) Data compared with the Atassi function.

Figure 12-10: Comparison of Experimental Data with the Sears and Atassi Transfer Functions with the Aerofoil at a Mean Incidence of -0.7° Across a Range of Gust Amplitudes, $\hat{\alpha}_G$, and Reduced Frequencies, k_1.

Both transfer functions were developed for small amplitude perturbations, and as such are expected to lose accuracy in cases where the gust amplitude is large. It may be that the largest gust amplitude ($\hat{\alpha}_G$= 3°, i.e., a peak-to-peak amplitude of 6°), causes second order viscous effects that cannot be captured by the unsteady transfer functions.

An exception to the agreement between the transfer functions and the experimental data for the gust amplitude $\hat{\alpha}_G$ = 2° can be seen in Figure 12-10(a) and Figure 12-10(b), marked by hollow dots. These data points were all acquired during the same test run, and so it is likely that there was an error in the experimental method or post-processing during these tests. This set of data will, therefore, not be discussed further in this chapter.

The mean angle of attack (0.7°) for the results in Figure 12-10 was chosen such that the distorting effects of the aerofoil potential field were minimised, and the Sears and Atassi functions were similar in shape as possible, as in the work of Wei et al. [4]. Below, in Figure 12-11 and Figure 12-12, the lift amplitude is shown against the changing mean angle of attack, α, in order to illustrate the effect of changing the aerofoil potential field on the results. In these figures the lift amplitude has been normalised by $(\hat{L}_{qs})_S$.

Figure 12-11 shows the results for experimental gust amplitude $\hat{\alpha}_G$= 2°. Figure 12-11(a) shows the results from a single experimental run (blue circles) and compares the data with both the Sears (black line) and Atassi (red line) functions. It can be seen that there is a marked reduction in the unsteady load response as the angle of attack increases. The Sears function does not model the effect of angle of attack and therefore the solution is constant across the range of angles given here. This means that the Sears solution disagrees with the experimental data when the angle of attack is not negligible. The Sears and Atassi solutions cross near the angle at which the aerofoil produces zero lift, as this is the point at which the effect of the aerofoil potential field switches sign.

The blue vertical dash-dot line indicates the static stall angle of the aerofoil (see Figure 12-4a)). Below this angle, the agreement between the experiment and the Atassi function is good. After this the agreement deteriorates, as is expected when the viscous effects of a stalled aerofoil impact the results. As an illustration, the Atassi function is also shown evaluated with k_2=20 (red dashed line), which was the original visual estimate of k_2 from Figure 12-6(a). With the higher value of k_2, the Atassi function gives a much more dramatic variation in lift with changing α, indicating that the value of k_2 calculated from the two-parameter fit (Figure 12-9(b)) is the appropriate one to use, rather than the visual estimate.

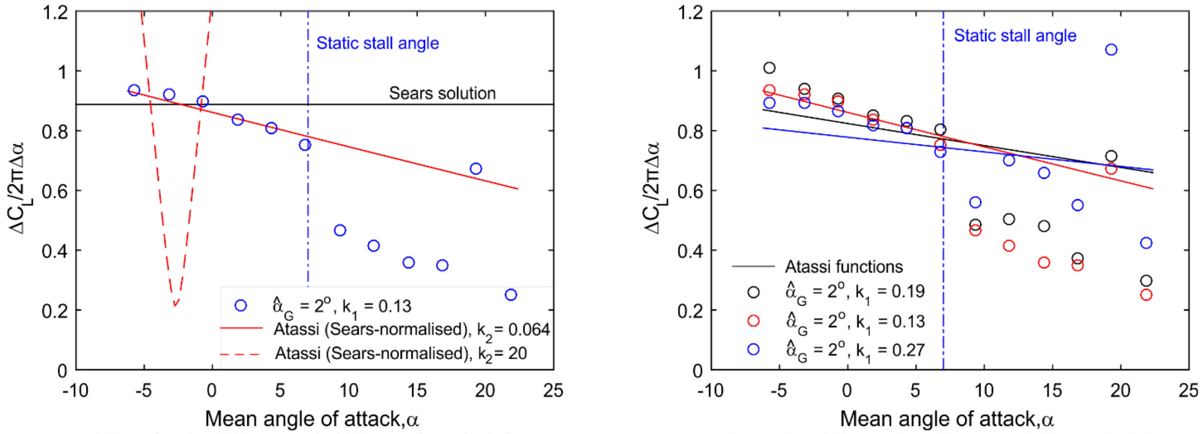

(a) Data from k_1 = 0.13 compared with Sears and Atassi solutions. (b) Data from different values of k_1 compared with Atassi solutions.

Figure 12-11: Amplitude of Unsteady Response Against Angle of Attack, Normalised by Quasi-Steady Response as Defined by Sears, Compared with the Sears and Atassi Functions ($\hat{\alpha}_G = 2°$).

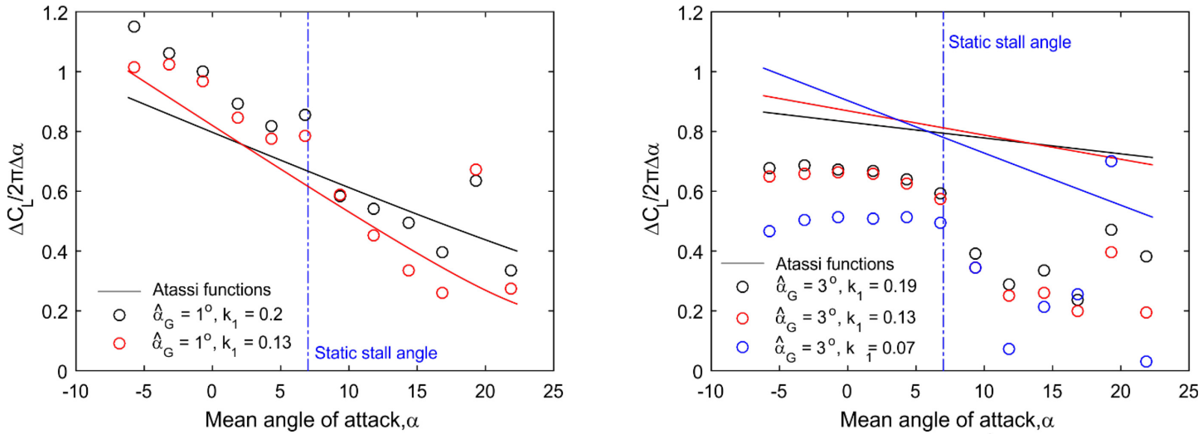

(a) Gust amplitude, $\hat{\alpha}_G$=2°. (b) Gust amplitude, $\hat{\alpha}_G$= 3°.

Figure 12-12: The Amplitude of the Unsteady Response for Increasing Mean Angle of Attack Compared with the Atassi Function with Two Different Gust Amplitudes.

Figure 12-11(b) shows the data from Figure 12-11(a) (red circles) along with measurements from tests at two higher values of k_1. The Atassi function evaluated at the respective values of k_1 is shown as a solid line. Again, the agreement is good up to the static stall angle of the aerofoil, though there is some disagreement in magnitude at the lowest angles of attack.

In Figure 12-10, it can be seen that the agreement between the data and the Atassi function is less good for the other gust amplitudes ($\hat{\alpha}_G$= 1° and 3°). This is shown in more detail in Figure 12-12, which shows plots of unsteady load amplitude against angle of attack with gust amplitudes, $\hat{\alpha}_G$, of 1° (Figure 12-12(a)) and 3° (Figure 12-12(b)). In Figure 12-12(a), the gradient of the unsteady lift response follows the Atassi function, although the magnitude of the response is slightly under-predicted by the Atassi function. Again, a small error in the gust amplitude would account for this difference in magnitude. Beyond the static stall angle the agreement with Atassi deteriorates, as in the cases shown in Figure 12-11.

Figure 12-12(b) shows the normalised lift against mean angle of attack for the largest gust amplitude ($\hat{\alpha}_G$ = 3°). As mentioned above, this relatively large gust amplitude is likely to cause deviation between the Atassi function and the experimental results. In all the cases in Figure 12-12(b), the experimental results give 50 – 70 % of the unsteady lift amplitude predicted by Atassi, and the gradients are not well-predicted. Beyond the static stall angle the unsteady effects are dramatic, and some very large lift amplitudes suggest the presence of dynamic stall (which is also seen in Figure 12-12(a), and in Figure 12-11).

12.7 SPEED OF GUST PROPAGATION ALONG THE AEROFOIL

As discussed in Section 12.5, the potential flow upstream of the aerofoil has been shown to superpose linearly onto the gust, in line with the work of Goldstein and Atassi [2]. Goldstein and Atassi, however, predict that aerofoil loading will cause a difference in the propagation of the gust along the two surfaces, i.e., it will propagate faster along the suction surface where the velocities are higher than the free-stream velocity, while it will move more slowly along the pressure surface. In this section we present some preliminary analysis suggesting that this is, indeed, the case.

From the Fourier analysis described in Section 12.6, the phase of the pressure fluctuations at each point on the aerofoil surface can be calculated:

$$\phi = \tan^{-1}\left(\frac{A_N}{B_N}\right) \tag{12-14}$$

The phases calculated in this way are plotted against axial position for four selected cases in Figure 12-13. It should be noted that the pressure moves in opposite directions on the two surfaces (i.e., an increase in incidence causes a reduction in the pressure on the suction surface and an increase on the pressure surface), so if the two surfaces were responding ‘in phase’ with one another there would be an offset of π radians in their calculated phase. In order to aid comparison, the pressure surface data has therefore been shifted by π radians. The data is all phase-locked to the cam once-per-revolution signal, and the offset at the leading edge is somewhat arbitrary, as it is made up of a combination of the convection time of the gust from the flaps to the aerofoil and the phase lag of the aerofoil response.

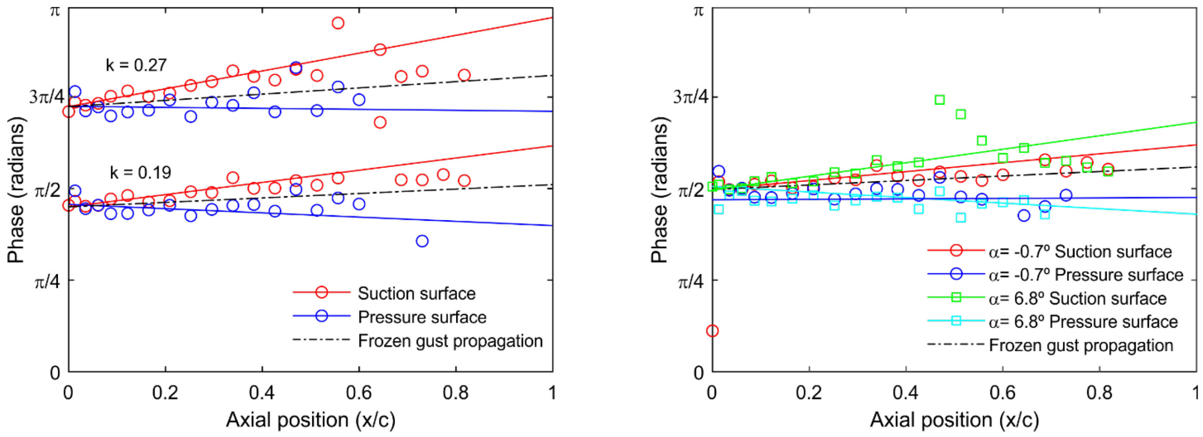

(a) Effect of reduced frequency with α= 1.8° and $\hat{\alpha}_G = 2°$.

(b) Effect of aerofoil incidence with $k_1 = 0.19$ and $\hat{\alpha}_G = 1°$.

Figure 12-13: Axial Variation in Phase of the Response Calculated from Aerofoil Surface Pressure Signals.

Figure 12-13(a) shows the phase lag of the response at two different reduced frequencies. In both cases, the gust amplitude, $\hat{\alpha}_G$, is 2° and the aerofoil incidence is 3°. The measurements from the pressure surface are shown as blue circles while those from the suction surface are shown in red. There is substantial scatter in the data over the rear portion of the aerofoil; this is because the response is very small towards the aerofoil trailing edge and so the measurement accuracy is low. For each case shown, a straight line fit has been applied to the data from between the leading edge and $x/c = 0.34$, and a dash-dot line shows the path of the gust if it were to convect at the free-stream velocity, which is given by:

$$\Delta\phi_{\text{frozen}} = 2\pi\frac{T_{\text{gust}}}{T_{\text{conv}}} = 2\pi\frac{c}{U_\infty}\frac{k_1 U_\infty}{2\pi c} = k_1 \tag{12-15}$$

where T_{gust}t is the gust time-period and T_{conv} is the time taken for the free-stream flow to pass over the aerofoil. It can be seen that in all cases there is a difference between the two aerofoil surfaces, with the suction surface points (red) showing increasing phase lag over the surface of the aerofoil, while those on the pressure surface show no change or a slight reduction in phase lag. When the reduced frequency is increased (top set of lines in Figure 12-13(a)) the difference in phase between the two surfaces increases. This is likely to be due to the increase in the phase lag of a frozen gust along the aerofoil (Equation 12-17).

Figure 12-13(b) shows the effect of aerofoil incidence on the phase change across the surfaces. The blue and red circles denote the phase on the pressure and suction surfaces, respectively, from a test with the aerofoil at -0.7° incidence, while the cyan and green squares are from a test with the aerofoil at 6.8° incidence. In these cases, the reduced frequency was fixed at 0.19 and $\hat{\alpha}_G$was 1°. Again, the frozen gust phase is denoted by the dash-dot line. As in the previous cases, the phase lag increases with axial distance along the suction surface, while it stays constant or reduces slightly on the pressure surface. A difference can also be observed between the two cases – the higher incidence case shows a larger increase in phase lag on the suction surface, and possibly a smaller one on the pressure surface. This change between the two incidences can be attributed to the increase in loading with increased mean incidence and the accompanying increase in speed changes across the aerofoil surfaces.

Intuitively, it seems that the suction surface should exhibit a phase lead over the pressure surface, i.e., the opposite of what has been shown here. More work is therefore required to understand this data fully, but the preliminary analysis suggests that there is a difference in the way in which the gust convects along each aerofoil surface. This finding is in line with the argument of Goldstein and Atassi [2] and suggests that their model therefore is capturing the major effect of the aerofoil potential field on the unsteady load response.

12.8 CONCLUSION

This chapter has presented an examination of the unsteady load generated by an Atassi-type gust on an aerofoil with non-zero mean load. The results presented above suggest that the Atassi function can predict the effect of changes in mean aerofoil loading on the unsteady lift experienced by aerofoils, for transverse gusts with a streamwise oscillating component. In cases with small-to-moderate gust amplitude, the trends in unsteady response are replicated accurately in terms of the effects of both reduced frequency and aerofoil angle of attack. The agreement is good when the mean angle of attack is smaller than the static stall angle of the aerofoil; at higher angle of attack the lift response is more erratic and the agreement deteriorates.

With very small gust amplitudes, the experimental error in measuring the gust generates substantial uncertainty in the quasi-steady response, and so the absolute magnitude of the data may not be reliable. With very large gust amplitudes, the trends in the data are also not replicated by the Atassi function, suggesting that the second order viscous effects have become significant.

One limitation of the Atassi function is that aerofoil thickness is not accounted for, although Goldstein and Atassi suggest that the effect of thickness may be of the same order of magnitude as that of camber and incidence angle [2]. The aerofoil used in the experiments above is chosen to represent the aerofoil section of a tidal turbine blade, which are generally thicker than those of for example wind turbines or aircraft. As such, discrepancies between the Atassi function and experiments could be caused by thickness effects.

Examination of the flowfield upstream of the aerofoil has shown that the gust and the aerofoil potential field can be considered to superpose linearly, i.e., there is no unsteady coupling of the incoming gust with the potential field. This was shown by comparing gust measurements with the aerofoil in place with the gust obtained by adding the quasi-steady potential field to the gust measured in the empty wind tunnel. This finding is in line with the analysis of Goldstein and Atassi [2].

A preliminary analysis was undertaken of the propagation of the gust along each surface of the aerofoil. Again, this data agrees with the statement of Goldstein and Atassi that the gust propagates at a different rate on the pressure and suction surfaces of the aerofoil due to the differing local flow velocities.

Overall, this chapter shows first-of-a-kind validation of the Atassi function for an aerofoil with non-zero mean load encountering a gust with both streamwise and transverse components. Furthermore, the results presented here suggest that gust generation through the use of many small vanes generates gusts with very low k_2 values, despite the visual image of the flowfield suggesting otherwise. Because of this, the lift amplitude is a relatively weak function of the mean angle of attack and camber, compared to what it would be at higher k_2. As future work, the flapping vanes will be fitted with serrated trailing edges, for the purpose of encouraging wake mixing and thus reducing k_2 even further and generating unsteady flow that is closer to a pure Sears-type gust.

12.9 ACKNOWLEDGEMENTS

The experiments described in this paper were funded by EPSRC grant EP/J010308/1. The authors wish to thank the technical staff of the Whittle Laboratory for their assistance in manufacturing the gust generator and test section – in particular, Mr David Barlow, Mr Ian Thornton and Mr Elliot Read. The authors would also like to thank Dr Ivor Day, Prof. Robert Miller, Dr Carl Sequeira and Mr Chris Freeman for the useful discussions during the course of this work.

12.10 REFERENCES

[1] von Kármán, T. and Sears, W., Airfoil theory for non-uniform motion, Journal of the Aeronautical Sciences, Vol. 5,1938, pp. 379-390.

[2] Goldstein, M. and Atassi, H., A complete second-order theory for the unsteady flow about an airfoil due to a periodic gust, Journal of Fluid Mechanics, Vol. 74, 1976, pp. 741-765.

[3] Atassi, H., The Sears problem for a lifting airfoil revisited-new results, Journal of Fluid Mechanics, Vol. 141, 1984, pp. 109-122.

[4] Wei, N., Kissing, J., Wester, T.T., Wegt, S., Schiffmann, K., Jakirlic, S., Hölling, M., Peinke, J. and Tropea, C., Insights into the periodic gust response of airfoils, Journal of Fluid Mechanics, Vol. 876, 2019, pp. 237-263.

[5] Jancauskas, E.D., and Melbourne, W.H., The aerodynamic admittance of two-dimensional rectangular section cylinders in smooth flow, Journal of Wind Engineering and Industrial Aerodynamics, Vol. 23, 1986, pp. 395-408. Special Issue 6th Colloquium on Industrial Aerodynamics Building Aerodynamics. ISSN: 0167-6105.

[6] Cordes, U., Kampers, G., Meißner, T., Tropea, C., Peinke, J. and Hölling, M., Note on the limitations of the Theodorsen and Sears functions, Journal of Fluid Mechanics, Vol. 811, 2017.

[7] Traphan, D., Wester, T.T., Peinke, J. and Guelker, G., On the aerodynamic behavior of an airfoil under tailored turbulent inflow conditions. 5th International Conference on Experimental Fluid Mechanics ICEFM 2018 Munich.

[8] Englund, D., and Richards, W., The infinite line pressure probe, NASA Technical Memorandum, Vol. 24, 1985.

[9] Brooks, T., Marcolini, M., and Pope, D., Airfoil trailing edge flow measurements and comparison with theory, incorporating open wind tunnel corrections. 9th Aeroacoustics Conference, 1984, p. 2266.

[10] Brooks, T, Marcolini, M., and Pope, D., Airfoil trailing-edge flow measurements, AIAA journal, Vol. 24, 1986, pp. 1245-1251.

[11] Brooks, T, Pope, D., and Marcolini, M., Airfoil self-noise and prediction. NASA Reference Publication 1218, 1989.

[12] Drela, M., A user’s guide to MSES 3.00. 2004.

[13] Moreau, S, Henner, M., Iaccarino, G., Wang, M. and Roger, M., Analysis of flow conditions in freejet experiments for studying airfoil self-noise, AIAA Journal, Vol. 41, 2003, pp. 1895-1905.

Chapter 13 – COMPARISON BETWEEN EXPERIMENTS AND SIMULATIONS OF FAST PLUNGE MANEUVERS

M. Moriche
Karlsruhe Institute of Technology
GERMANY

G. Sedky
University of Maryland
UNITED STATES

O. Flores
Universidad Carlos III de Madrid
SPAIN

A.R. Jones
University of Maryland
UNITED STATES

M. García-Villalba
Universidad Carlos III de Madrid
SPAIN

We present experiments and simulations of plunging maneuvers of large amplitude, for velocity ratios $G = 1$ and 2. We explore the effect of the airfoil shape by considering a NACA0012 wing and a flat plate. The experiments are performed with wings of aspect ratio 4 and 4.86, while the simulations are performed using a model of an infinite aspect-ratio wing. A good qualitative agreement is found between experiments and simulations, with small discrepancies in the maximum and minimum lift coefficients observed during the maneuvers and somewhat larger discrepancies during the post-maneuver phase. It is found that the airfoil shape seems to have a small effect on the lift coefficient but a somewhat larger effect on the drag coefficient.

13.1 INTRODUCTION

There is a growing interest in characterizing force production on wings in unsteady situations. One of the reasons behind is the proliferation of unmanned and micro air vehicles, which typically fly in unsteady environments such as urban areas. This poses a challenge to the controllability of the vehicle, in particular when the flow perturbations are of the same order of magnitude as the flight speed. If this is the case, classical solutions based on small perturbations and linear theory [1] are no longer applicable. The flow surrounding the wing is subject to non-linear phenomena involving flow separation and the formation of Leading-Edge Vortices (LEVs) and Trailing Edge Vortices (TEVs) that substantially influence the aerodynamic forces on the wings. As a consequence, in order to predict the aerodynamic forces in such unsteady situations it is necessary to resort to experiments and time-dependent numerical simulations.

The flow perturbations in unsteady environments are highly variable, so that researchers often consider canonical configurations to characterize the different contributions to the aerodynamic response of the wing. One recent example of the use of canonical configurations is the work of Leung et al. [2] who modelled transverse gusts using different airfoil motions: pitching, plunging and surging. Another example is the work of Mulleners et al. [3] who modelled a streamwise gust using surging motions of the wing. In this study we focus on plunge maneuvers, but the literature on canonical motions is broad, including also pitch maneuvers [4], [5], [6], surging maneuvers [7] or wing rotation [8], [9]. As already mentioned, plunge maneuvers have been used to model transverse gusts [2] but also they have been used for their relation to flapping flight. For example, Wang [10] used a plunge maneuver to characterize the formation and detachment of the leading-edge vortex and this led to the determination of the optimal frequency for the flapping motion.

More closely related to the modelling of gusts, Perrotta and Jones [11] performed unsteady force measurements on a plunging flat plate using a water-filled towing tank. The maneuvers were modelled after a sine-squared gust profile, to match the approximation of gust encounters and to facilitate comparison to gust encounter force measurements from a previous experimental campaign [12]. Forces were measured for a large variety of plunge maneuvers, varying the width and height traveled by the wing during the maneuver and also the geometric angle of attack of the wing. Moriche et al. [13] performed Direct Numerical Simulations (DNS) using some of the kinematics of Perrotta and Jones [11], but for a model of an infinite aspect-ratio NACA0012 wing. The lift coefficient predicted in the simulations was found to be in qualitative agreement with the measurements, however, some quantitative discrepancies were observed. The reason behind these discrepancies was unclear, however, there were some obvious differences between experimental and computational setups, e.g., in the experiment a flat plate was studied while in the simulation a NACA0012 airfoil was considered. In order to reduce these differences, new force measurements have been performed at the University of Maryland and additional direct numerical simulations have been performed. In this chapter, we report the direct comparison between the corresponding experiments and simulations.

13.2 FLOW CONFIGURATION

The maneuvers considered in this study were defined by Perrotta and Jones [11] modeled after a sine-squared gust profile. The motivation behind the selection of this profile was to match the canonical approximation of gust encounters [14] and to be able to compare to their previous transverse gust measurements [12]. The plunge maneuver is performed on a wing of chord c which is subject to a free stream of constant speed U_∞ and at time t = 0 is subject to a vertical motion with velocity:

$$V(t) = -V_{max}\sin^2\left(\frac{\pi t}{T}\right)\quad 0 \le t \le T \tag{13-1}$$

where V_{max} is the peak plunge velocity and T is the maneuver duration. Thus, the plunge maneuver consists of two phases, the acceleration phase until the maximum plunge velocity is reached and a subsequent deceleration phase until the vertical motion is stopped. The horizontal distance covered during the maneuver (or maneuver width) is given by $w = U_\infty T$ and the vertical distance (or maneuver height) is obtained by integration of (1), $h = V_{max}T/2$. The velocity ratio is defined by $G = V_{max}/U_\infty$.

Perrotta and Jones [11] performed an extensive parametric study by varying velocity ratio, G, duration of the maneuver, T, and angle of attack of the wing, α. In the present study, due to the high computational cost of the direct numerical simulations, we focus on a small set of parameters driven by the previous study of Moriche et al. [13]. We fix the duration of the maneuver $T = 2c/U_\infty$ so that the width is also fixed, w/c = 2, and the height depends on the velocity ratio, h/c = G. We consider two velocity ratios, G = 1 and G = 2. Concerning the angle of attack of the wing, the results of Perrotta and Jones [11] show that for large G, as the ones considered here, and for small angle of attack, the resulting lift coefficient is not significantly affected by the particular value of the angle of attack (see Ref. [11], Figure 8). In preliminary direct numerical simulations it was observed that it was easier to trigger the three-dimensionality of the flow at α = 5º than at α = 0º. Note also that for a symmetric airfoil there is no lift in steady conditions at α = 0º so that α = 5º might be a more relevant flight condition. As a consequence, we decided to perform the study fixing α = 5º. Finally, in order to evaluate the effect of the airfoil shape we consider two different shapes, a flat plate and a NACA0012 airfoil. Unfortunately, at the time of writing the simulation for the flat plate at G = 1 is underway, so that we cannot report it in this chapter.

13.3 EXPERIMENTAL SETUP

Experimental data collection was conducted in a free-surface water towing tank at the University of Maryland. The specifications of the facility can be found in Sedky et al. [15]. Plunging experiments were carried out at a Reynolds number Re = 20000 to maintain an adequate signal to noise ratio in the force measurements. Three finite aspect-ratio wings were studied; a NACA0012 wing with an aspect-ratio AR = 4.86 and a chord length c = 11.5 cm, a NACA0012 wing with AR = 4 and a chord length c = 7.62 cm, and, a flat plate with AR = 4 and a chord length c = 7.62 cm. Table 13-1 shows the cases carried out.

Table 13-1: Experimental Matrix.

Case	Airfoil	AR	G
1	NACA0012	4.86	1
2	NACA0012	4.86	2
3	NACA0012	4	3
4	NACA0012	4	4
5	Flat plate	4	5
6	Flat plate	4	6

The wing was towed with a trapezoidal speed profile with smoothed corners, which accelerated over 4.5 chord lengths before reaching a uniform tow speed. This towing velocity profile provided 60 chord lengths of travel at a constant speed before decelerating to rest. To ensure fully developed flow, the wing traveled for 2.5 m before plunging. All of the cases were repeated five times. Force data was sampled at 500 Hz, and the mean and standard deviation of each case across the five runs were found. To obtain the aerodynamic force contribution, the inertial force due to the acceleration of the wing and its mount during the plunging maneuver was subtracted from the total measured force. The coefficient of lift C_L data presented below were filtered using a zero-phase, digital Butterworth filter with a cut-off frequency of 5 Hz.

13.4 COMPUTATIONAL SETUP

The simulations have been performed with the in-house code TUCAN [16], [17], that solves the Navier-Stokes equations of the incompressible flow using a fractional step method on a non-uniform, Cartesian, staggered grid. The spatial discretization consists of second-order central differences for both convective and viscous terms. Time integration is performed with a low-storage, 3-stage, semi-implicit Runge-Kutta scheme. The wing is modelled using the immersed boundary method proposed by Uhlmann [18]. TUCAN has been extensively validated and employed for unsteady aerodynamics applications for infinite [19], [20], [21] and finite [22], [23], [24] aspect-ratio wings.

The simulations were performed by considering an infinite aspect-ratio wing, which is modelled by using periodic boundary directions on a computational domain of finite span. The Reynolds number is fixed to $Re = 5000$, limited by computational resources. It was not possible to reach the values considered in the experiments. A sketch of the computational domain is shown in Figure 13-1. The computational domain size is $12c \times 0.25c \times 9.5c$ in streamwise, x, spanwise, y, and vertical, z, directions, respectively. The inflow plane is located at $x/c = -3.5$. The top plane is located at $z/c = 3$. At $t = 0$, the leading edge of the wing is located at $x/c = 0$, $z/c = 0$ and at the end of the maneuver it is located at $z/c = -G$. The grid is uniform in the vicinity of the airfoil ($-0.5 < x/c < 2.5$, $-2.5 < z/c < 0.5$). The grid resolution in this region was defined after performing a grid refinement study in 2D simulations, as reported by Moriche et al. [13], resulting in a grid spacing in all three directions of $\Delta x = c/320$. Far from the airfoil along the x and z directions the grid is stretched using a 1% stretching, except upstream where a 3% stretching is used. This results in a total number of grid points of $1335 \times 80 \times 1459$ along the x, y and z directions, respectively.

As already mentioned, along the spanwise direction periodic boundary conditions are employed. At the inflow plane Dirichlet boundary conditions are imposed and at the outflow plane a convective boundary condition is imposed. At the top and bottom boundaries, free-slip boundary conditions are used. The initial condition for the maneuvers is determined by integrating the equations without moving the wing during a time interval in which the wake develops. A visualization of the flow field at the initial condition is shown in the Results section (see the top row of Figure 13-6). While for the NACA0012 wing the three-dimensionality of the flow is localized in a narrow region in the wake of the wing, for the flat plate three-dimensional structures can be seen already initially on top of the wing.

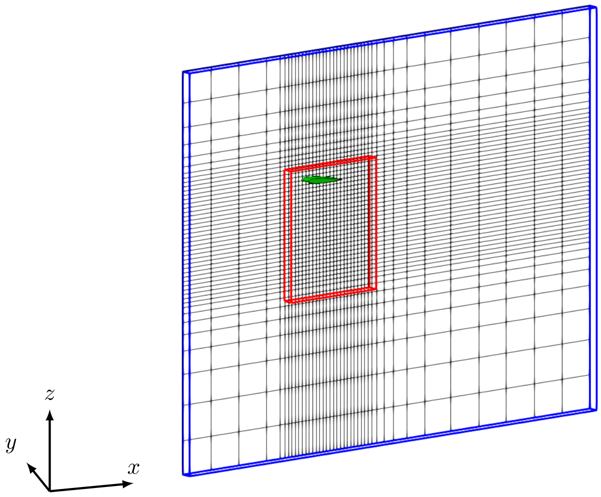

Figure 13-1: Sketch of the Computational Domain. The blue lines indicate the full domain and the red lines the refined area with constant grid spacing. The black lines represent actual grid locations in the x-z plane, but only one every 32 lines is shown.

13.5 RESULTS

We start analyzing the time evolution of the lift coefficient, C_L, defined as:

$$C_L(t) = \frac{2L(t)}{\rho U_\infty^2 S} \tag{13-2}$$

where L is the lift, ρ is the density and S is the wing surface. The curves of C_L for both experiments and simulations are shown in Figure 13-2. Moriche et al. [13] divide the time evolution into three intervals. The first interval is the acceleration phase, $0 \leq tU_\infty/c \leq 1$, where the C_L grows rapidly until a peak is reached at an instant before the end of the interval. The force peaks earlier because the lift response is influenced by both plunge velocity and plunge acceleration, as discussed by Perrotta and Jones [11], and at the end of this interval the plunge acceleration is zero. During the acceleration phase, a strong LEV is developed and subsequently detaches from the wing. The second interval is the deceleration phase, $1 \leq tU_\infty/c \leq 2$, until the end of the maneuver. In this phase, the lift decreases roughly until the middle of the interval where a local minimum is reached and then, while still decelerating at a reduced pace, the lift grows again. This trend coincides with the wing acceleration: at the mid of the interval the acceleration is minimum and then it grows until reaching a zero value at the end of the maneuver. Also note that during the final part of the interval the LEV that was left behind gets closer to the wing as the wing progressively stops its motion, and therefore, possibly having an influence on C_L. The third interval is the post-maneuver phase, where the lift coefficient slowly relaxes towards the corresponding static value.

Figure 13-2 shows the time evolution of C_L including both experimental data for the wings with AR = 4 and DNS data. The panel (a) of Figure 13-2 shows the results for the NACA0012 wing for both G = 1 and G = 2. Overall, the curves present qualitative agreement however there are some discrepancies that need to be highlighted. For both values of G, the growth of C_L during most part of the acceleration phase is in good agreement between experimental and DNS data. The difference is that in the experiment C_L^{max} is reached earlier, and as a consequence is lower than the C_L^{max} in the DNS. In the deceleration phase, the decrease in C_L occurs roughly at the same rate in experiment and DNS, i.e., the curves are quasi-parallel. Also, the difference between C_L^{max} and C_L^{min} is rather similar. However, since the C_L^{max} is lower in the experiment, then the C_L^{min} also reaches smaller values in the experiment compared to the DNS. The C_L recovery towards the end of the maneuver is qualitatively similar, however it seems more pronounced in the DNS, particularly for the case G = 2. The final phase of relaxation towards the static values seems to be somewhat different in experiment and DNS. In the experiment, the C_L still grows a bit once the maneuver is finished (at $tU_\infty/c = 2$) reaching a local maximum at $tU_\infty/c \approx 2.2$. In the DNS, the growth of C_L seems to stop at the end of the maneuver. This is followed by a short plateau and then the decay towards the static value sets in. Note that, since the value of C_L at the end of the maneuver is significantly higher in the DNS, the decay towards the static value needs to be more pronounced as well. This process does not seem to be monotonic, instead a few small oscillations are present. In the DNS the static value was not reached, because the computation was stopped to save computational resources. The panel (b) of Figure 13-2 shows the results for the flat plate. In this case, only the G = 2 case can be compared because the DNS for G = 1 was not ready at the time of writing. In general, for the flat plate the same observations as for the NACA0012 wing can be made. A small difference in the DNS for the flat plate is that at the end of the maneuver, the C_L does not seem to present a short plateau.

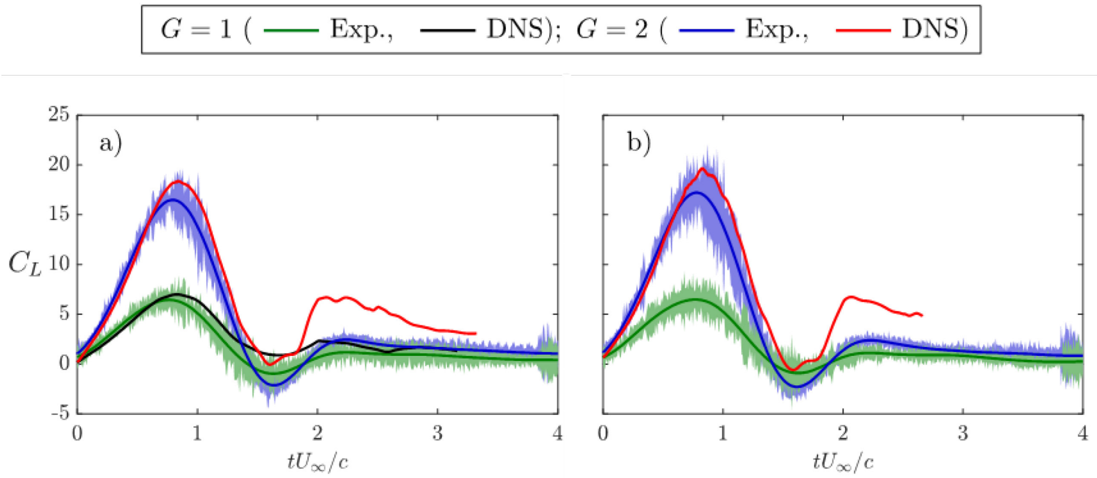

Figure 13-2: Time History of Lift Coefficient of (a) NACA0012 Wing and (b) Flat Plate. Both wings, AR= 4. The shaded regions correspond to the unfiltered ±$C_L^{std}(t)$

In order to assess the differences between experiments and DNS, it is worth to have a look at the variability of the experimental realizations using the unfiltered data. Figure 13-2 also includes shaded contours that correspond to plus/minus one standard deviation of the lift coefficient (±C_L^{std}) for each case, computed with respect to the ensemble-average of five realizations. The experiments present little uncertainty in the initial acceleration phase until about $tU_\infty/c = 0.5$, beyond that point C_L^{std} presents non-negligible values, with the biggest uncertainty occurring near C_L^{max} and C_L^{min}. Concerning the C_L^{max} for example, in the DNS a model for an infinite aspect-ratio wing is being considered while in the experiments the wing has an aspect ratio of 4. This modelling difference could already account for the discrepancy. However, the DNS data lies in the boundary of the shaded region of the experimental uncertainty. Therefore, it is unclear if the higher C_L^{max} obtained in the DNS is due to discrepancies in the flow configuration or if it is just within the measurement uncertainty. What is clear for the present results is that the discrepancy in the post-maneuver phase is not within the measurement uncertainties. There could be several reasons for the discrepancy during this phase. For example, in the experiment's finite-wing effects might play a role via the interaction of wing-tip vortices with the LEV, leading to a different overall flow structure around the wing. If this is the case, it is not possible to reproduce such interactions in the DNS with an infinite aspect-ratio wing. An alternative possible explanation is related to the limited size of the computational domain along the wingspan. This effect might have an influence on the development of flow structures in spanwise direction. It would be worth to perform simulations with wider computational domains to test this hypothesis. Even if it is unlikely, there exists the possibility that this discrepancy could be a Reynolds number effect, since the experiments were performed at Re = 20000 and the DNS at Re = 5000.

The effect of airfoil shape and aspect ratio is explored using the experimental data in Figure 13-3, that shows the time evolution of C_L including the measurement uncertainty for each G separately. Figure 13-3(a) shows the data for G = 1 and Figure 13-3(b) shows the data for G = 2. The uncertainty for case G = 1 appears to be larger but this is just a scale effect, note the difference between the scales in each plot. The experimental data suggests that the effect of airfoil shape is negligible. For G = 1 the C_L of both wings with AR = 4 is in excellent agreement while for G = 2 there are some small differences, but they are well below the measurement uncertainty. The main difference between NACA0012 wing and flat plate seems to be that the shaded region is somewhat larger in the case of the flat plate indicating a somewhat larger measurement uncertainty, in particular for the G = 2 case. Concerning the aspect ratio, the effect seems also to be negligible in the limited range covered in the study, AR = 4 and 4.86. One possible implication of this result is that it is less likely that the discrepancy between experiments and DNS on C_L^{max} to be due to an aspect-ratio effect.

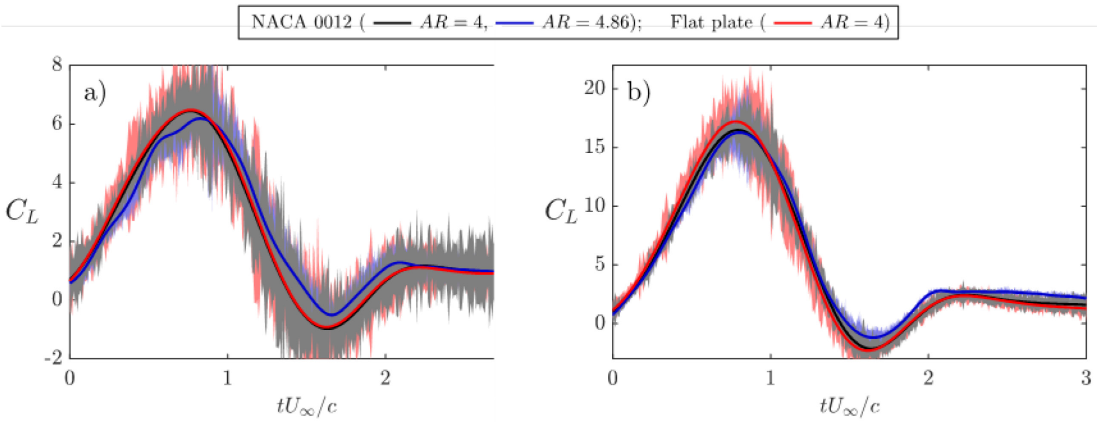

Figure 13-3: Experimental Data. Time history of lift coefficient. a) G = 1, b) G = 2. The shaded regions correspond to the unfiltered ±C_L^{std}(t).

The effect of the airfoil shape is now explored using the DNS data in Figure 13-4 that shows, for G = 2, the time evolution of C_L and drag coefficient, C_D, defined as:

$$C_D(t) = \frac{2D(t)}{\rho U_\infty^2 S} \tag{13-3}$$

where D is the drag force. The DNS seems to confirm the observation from the experiments that the airfoil shape does not significantly influence the C_L. As shown in Figure 13-4(a), the curves for NACA0012 and flat plate agree qualitatively well in the three phases, acceleration, deceleration and post-maneuver. Small differences are observed near C_L^{max} and C_L^{min}, with both higher C_L^{max} and lower C_L^{min} in the case of the flat plate. The time evolution of C_D (Figure 13-4(b)) tells a different story, with peak values during the maneuver four times larger for the flat plate than for the NACA0012 wing. The shape of the curve in the case of the flat plate resembles the shape of the corresponding C_L curve. In fact, analyzing the peak values, they are consistent with an aerodynamic force which is perpendicular to the plate. If the latter is defined by a normal force coefficient C_N, with a maximum value C_N^{max} = 20 then:

$$C_L^{max} = C_N^{max} \cos\alpha \approx C_N^{max} = 20 \tag{13-4}$$

$$C_D^{max} = C_N^{max} \sin\alpha \approx C_N^{max}\alpha = 1.745 \tag{13-5}$$

values which are consistent with the peak values obtained for the flat plate $C_L^{max} = 19.66$ and $C_D^{max} = 1.872$. The values for the NACA0012 wing are not consistent with this scenario, with $C_D^{max} = 0.656$, and a C_D time evolution which does not resemble that of the corresponding C_L.

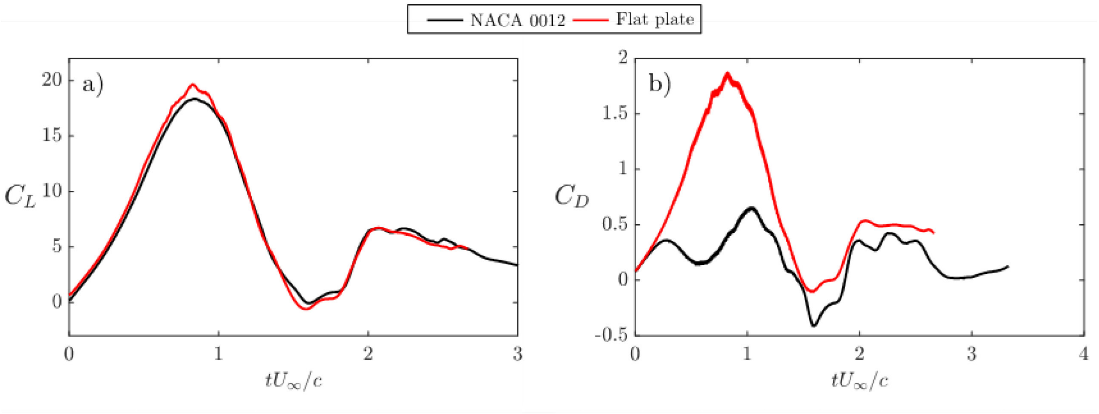

Figure 13-4: DNS Data for G = 2. Time history of a) Lift coefficient, b) Drag coefficient.

We turn now our attention to the flow surrounding the airfoil during the maneuver using the DNS data, using flow visualizations. Figure 13-5 shows contours of spanwise vorticity averaged along the spanwise direction, ω_y. The flow structure for both flat plate and NACA0012 wing is qualitatively similar. First, during the initial acceleration phase LEV and TEV develop. At the end of this phase, $tU_\infty/c = 1$, the LEV and TEV are both already detached. The TEV will be subsequently convected downstream so that it does not have a relevant influence on the lift coefficient. The contour of the LEV is more clearly defined in the case of the NACA0012, while for the flat plate the LEV seems more distorted. Below the LEV there is a dipole at the leading edge, from which the LEV in its rotation lifts vorticity up. During the deceleration phase the LEV grows in size and keeps on lifting vorticity from the leading edge. At the end of the maneuver, $tU_\infty/c = 2$, the LEV is again closer to the wing, but located at the rear part. At this instant, the vorticity that has been lifted from the leading edge keeps the form of a dipole for the NACA0012 wing while for the flat plate the shape of this vorticity is blurred. Once the maneuver is over, $tU_\infty/c = 2.5$, the LEV is leaving the trailing edge, lifting vorticity from the rear part of the wing, forming a rather vertical shear layer of negative vorticity. In addition a new LEV seems to be forming for both cases, note that this new LEV will need to be released from the wing in order to reach at the end the same flow structure corresponding to the static case ($tU_\infty/c = 0$). This explains the long relaxation interval required to reach that condition.

Figure 13-6 gives information on the three-dimensionality of the flow, by displaying shaded contours of the standard deviation of the spanwise velocity component, u_y^{std}, with respect to the spanwise-averaged mean. This is shown on top of two contour lines of ω_y, that serve as reference for the position of the main vortical structures. Initially, for the NACA0012 wing the three-dimensionality of the flow is localized in the wake of the wing while for the flat plate three-dimensional structures are already present on top of the wing. As a consequence, the flow is highly 3D during the whole maneuver for the flat plate. For the NACA0012 instead, during the acceleration phase, 3D effects are only visible at the trailing edge. The TEV is surrounded by 3D structures. The LEV remains essentially 2D during the whole maneuver. At some instant, 3D effects travel quickly upstream via the boundary layer on top of the wing, an effect which is barely visible in Figure 13-6 but that is clearly visible in corresponding animations. As a consequence, the LEV remains 2D, but the vorticity that the LEV lifts from the airfoil is clearly three-dimensional. This effect is incipient at tU∞/c = 1.5 and clearly visible at tU∞/c = 2 and 2.5.

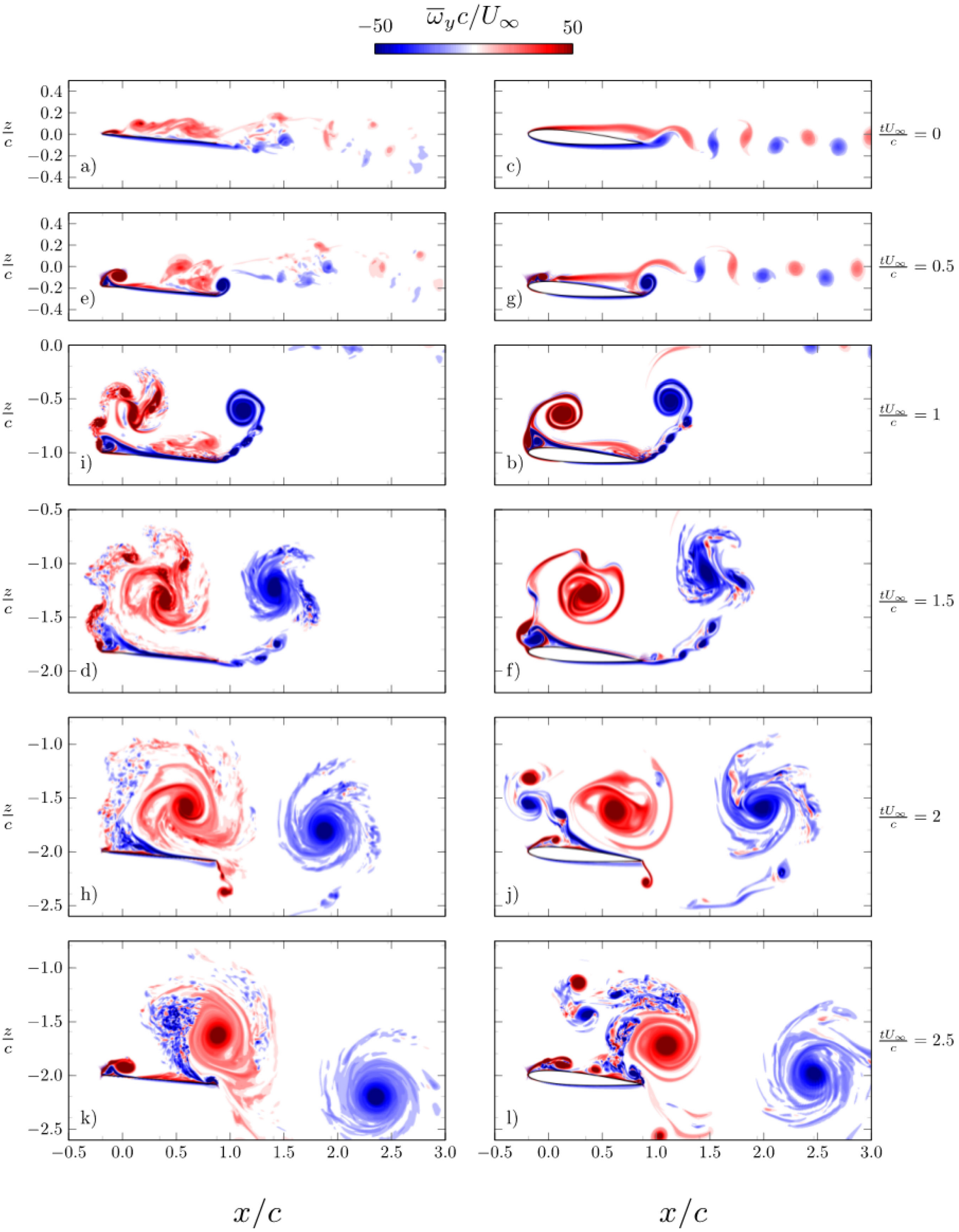

Figure 13-5: Flow Visualization of the DNS Results with G = 2. Contours of ω_y. Left column, flat plate. Right column, NACA0012 wing.

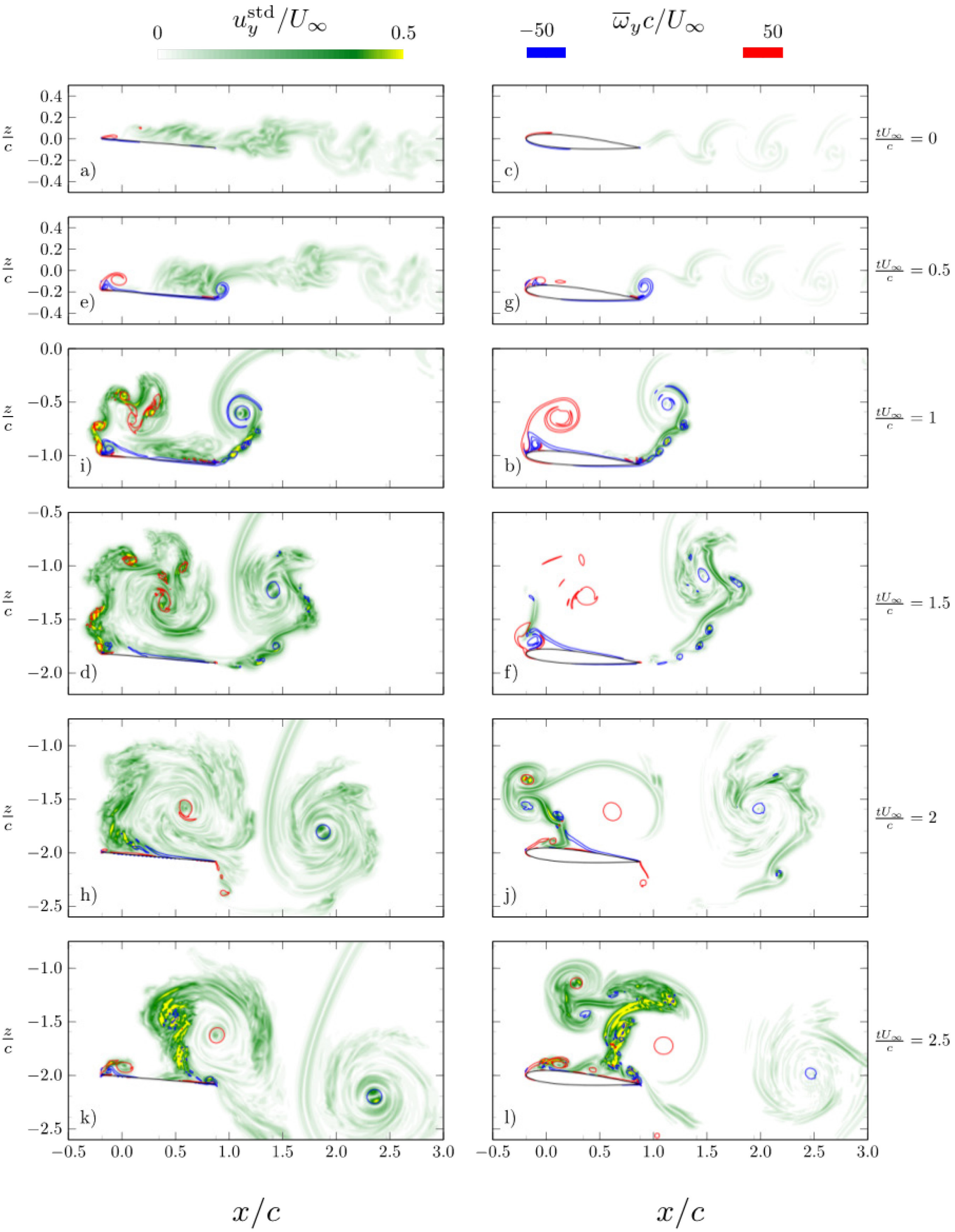

Figure 13-6: Flow Visualization of the DNS Results with G = 2. Contour lines, ω_y. Shaded contours, $u_y^{\rm std}$. Left column, flat plate. Right column, NACA0012 wing.

13.6 CONCLUSIONS

We have presented experiments and direct numerical simulations of plunging maneuvers with velocity ratios $G = 1$ and 2, and with two different wings, a flat plate and a NACA0012 wing. The experiments were conducted at Re = 20000 with wings of two aspect-ratios that were towed in a water-filled towing tank. The calculations were performed at Re = 5000 using a model of an infinite aspect-ratio wing by solving the Navier-Stokes equations using an immersed boundary method, prescribing the motion of the wing. We have analyzed the time evolution of the force coefficients during and after the maneuvers. We have also analyzed flow visualizations.

Concerning the lift coefficient, we have found qualitative agreement between experiments and simulations, with the DNS predicting a somewhat larger C_L^{max} during the acceleration and a somewhat smaller C_L^{min} during the deceleration phase. The largest discrepancies occur in the aerodynamic response during the post-maneuver phase, where the DNS predicts significantly larger values of C_L than the experiments. This difference might be ascribed to the differences between the experimental and computational setups: Reynolds number, finite aspect-ratio of the wing in the experiments, or to limitations in the DNS computations as a confinement effect due to the small width of the computational domain. This issue deserves further investigations. The experimental data suggests that the effect of airfoil shape is negligible in the aerodynamic response, a fact that is confirmed by the DNS data for the lift coefficient. For the drag coefficient, the DNS data suggests that there is indeed a different response for the flat plate, which is consistent with the aerodynamic force being perpendicular to the wing, while this is not the case for the NACA0012 wing. Flow visualizations show that for both wings the flow structure is qualitatively similar with a dominating leading-edge vortex and a less relevant trailing edge vortex.

13.7 ACKNOWLEDGEMENTS

This work was partially supported by grant DPI2016-76151-C2-2-R (AEI/FEDER, UE), and the Air Force Office of Scientific Research under grant FA9550-16-1-0508.

13.8 REFERENCES

[1] von Kármán, T. and Sears, W.R., Airfoil theory for non-uniform motion, J Aeronautical Sci., Vol. 5, No. 10, 1938.

[2] Leung, J., Wong, J., Weymouth, G., and Rival, D., Modeling transverse gusts using pitching, plunging and surging airfoil motions, AIAA J., Vol. 56, No. 8, 2018, pp. 3271-3278.

[3] Mulleners, K., Mancini, P., and Jones, A.R., Flow development on a flat-plate wing subjected to a streamwise acceleration, AIAA J., Vol. 55, No. 6, 2017, pp. 2118-2122.

[4] Eldredge, J., Wang, C., and Ol, M.V., A computational study of a canonical pitch-up, pitch-down wing maneuver, AIAA paper 2009-3687, 2009.

[5] Yilmaz, T.O. and Rockwell, D., Flow structure on finite-span wings due to pitch-up motion, J. Fluid Mech., Vol. 691, 2012, pp. 518-545.

[6] Jantzen, R.T., Taira, K., Granlund, K.O., and Ol, M.V., Vortex dynamics around pitching plates, Phys. Fluids, Vol. 26, No. 5, 2014, pp. 053606.

[7] Pitt Ford, C.W. and Babinsky, H., Lift and the leading-edge vortex, J. Fluid Mech., Vol. 720, 2013, pp. 280-313.

[8] Harbig, R.R., Sheridan, J., and Thompson, M.C., Reynolds number and aspect ratio effects on the leading-edge vortex for rotating insect wing planforms, J. Fluid Mech., Vol. 717, 2013, pp. 166-192.

[9] Garmann, D.J. and Visbal, M.R., Dynamics of revolving wings for various aspect ratios, J. Fluid Mech., Vol. 748, 2014, pp. 932-956.

[10] Wang, Z.J., Vortex shedding and frequency selection in flapping flight, J. Fluid Mech., Vol. 410, 2000, pp. 323-341.

[11] Perrotta, G. and Jones, A.R., Quasi-steady approximation of forces on flat plate due to large-amplitude plunging maneuvers, AIAA J., Vol. 56, No. 11, 2018, pp. 4232-4242.

[12] Perrotta, G. and Jones, A.R., Unsteady forcing on a flat-plate wing in large transverse gusts, Exp. Fluids, Vol. 58, No. 8, 2017, p. 101.

[13] Moriche, M., Gonzalo, A., Flores, O., and García-Villalba, M., Three-dimensional effects on plunging airfoils at low Reynolds numbers, submitted to AIAA J., AIAA paper 2019-0640, 2019.

[14] Hoblit, F.M., Gust loads on aircraft: concepts and applications, AIAA, 1988.

[15] Sedky, G., Jones, A.R., and Lagor, F., Lift modeling and regulation for a finite wing during transverse gust encounters, AIAA Scitech 2019 Forum, AIAA Paper 2019-1146, 2019.

[16] Moriche, M., A numerical study on the aerodynamic forces and the wake stability of flapping flight at low Reynolds number, Ph.D. thesis, Universidad Carlos III de Madrid, 2017.

[17] Gonzalo, A., Aerodynamic forces and vortex structures of flapping wings in forward flight, Ph.D. thesis, Universidad Carlos III de Madrid, 2018.

[18] Uhlmann, M., An immersed boundary method with direct forcing for the simulation of particulate flows, J. Comp. Phys., Vol. 209, No. 2, 2005, pp. 448-476.

[19] Moriche, M., Flores, O., and García-Villalba, M., Three-dimensional instabilities in the wake of a flapping wing at low Reynolds number, Int. J. Heat and Fluid Flow, Vol. 62, 2016, pp. 44-55.

[20] Moriche, M., Flores, O., and García-Villalba, M., On the aerodynamic forces on heaving and pitching airfoils at low Reynolds number, J. Fluid Mech., Vol. 828, 2017, pp. 395-423.

[21] Moriche, M., Raiola, M., Discetti, S., Ianiro, A., Flores, O., and García-Villalba, M., Assessing aerodynamic force estimation with experiments and simulations of flapping-airfoil flows on the verge of three-dimensionality, Proc. Inst. Mech. Eng. G J. Aerospace Eng., 2019.

[22] Gonzalo, A., Arranz, G., Moriche, M., García-Villalba, M., and Flores, O., From flapping to heaving: A numerical study of wings in forward flight, J. Fluids Struct., Vol. 83, 2018, pp. 293-309.

[23] Arranz, G., Moriche, M., Uhlmann, M., Flores, O., and García-Villalba, M., Kinematics and dynamics of the auto-rotation of a model winged seed, Bioinspir. Biomim., Vol. 13, 2018, p. 036011.

[24] Arranz, G., Gonzalo, A., Uhlmann, M., Flores, O., and García-Villalba, M., A numerical study of the flow around a model winged seed in auto-rotation, Flow Turbul. Combust., 101(2), 2018, pp. 477-497.

Chapter 14 – THE INFLUENCE OF AXIAL GUSTS ON THE DYNAMIC FLOW SEPARATION OF NON-SLENDER DELTA WINGS

David E. Rival and Matthew Marzanek
Queen's University
CANADA

In this chapter we examine the effects of axial gusts on a generic UCAV configuration. The experiments are conducted at a Reynolds number of 300,000 using a large, optical towing tank facility. Instantaneous force and moment measurements, pressure distributions and particle image velocimetry are used to extract critical features of the dynamic flow separation process for both gust events. For the axial-gust case, force augmentation both during and after the gust is shown to be dependent on the initial separation topology, with strong sensitivity at an angle of attack of 30°. It is shown that lift enhancement results from initially separated flow near the wing apex reattaching during the gust. Surface pressure measurements show that the reattachment is driven by a strong favorable pressure gradient that is maintained after the gust ends. The equations governing near-wall vortex dynamics state that vorticity flux from the wall increases with favorable pressure gradients, indirectly predicting an increase in circulation near the wing surface during a streamwise gust. However, circulation obtained through Particle Image Velocimetry (PIV) on the $z/c = 0.1$, 0.3, and 0.5 spanwise sections does not support this prediction, rather showing that the circulation in the wake (near the wing surface) remains nearly constant throughout the gust.

14.1 INTRODUCTION

Swept wings are prevalent on nearly all modern jet aircraft due to their improved efficiency at transonic speeds. In particular, non-slender sweep angles (<55°) and thick cross-sections are common traits in prototype blended bodies and Unmanned Combat Aerial Vehicles (UCAVs) (Liebeck, 2004 [1]; Cummings and Schuette, 2010 [2]). Despite the ubiquity of this geometry, little is understood about the aerodynamic response of swept wings to strong gust events. Classical theory of swept wings is often limited to slender configurations at steady state and moderate angles of attack. Such slender geometry, designated by their sweep angle greater than 55°, are thoroughly characterized (Polhamus, 1966 [3]; Earnshaw and Lawford, 1966 [4]; Brown and Michael Jr, 1955 [5]; Lee and Ho, 1990 [6]; Gursul, 2005 [7]). However, slender wings differ significantly in flow structure from their non-slender counterparts. These differences include Leading-Edge Vortex (LEV) structures forming closer to the wing surface for non-slender sweep angles (Ol and Gharib, 2003 [8]; Gursul et al., 2005 [9]). As a direct result, the formation of 'dual' primary vortex structures can be observed for non-slender geometry at low incidence angles (Taylor et al., 2003 [10]). Research on the Stability And Control CONfiguration (SACCON) model by Konrath et al. (2010) [11] and Cummings and Schuette (2012) [12] provide comprehensive references for unsteady behaviour of non-slender geometry, but further geometric simplification is required to make conclusions on the general dynamic-stall phenomenon for non-slender wings. More recently, Le Provost et al. (2018) [13] used a network of pressure sensors to predict roll moment on a USAS geometry (hybrid of a Lockheed Martin ICE-101 planform with SACCON cross-section), and He et al. (2018) [14] used pneumatic blowing to develop an active control model on similar geometry. The present work seeks to further generalize, and therefore a 45° delta wing with a NACA0012 cross-section is chosen to represent a baseline abstraction of non-slender swept wings. Experiments by Gad-el Hak and Blackwelder (1985) [15] were performed on the proposed geometry, using dye visualization to identify the leading-edge vortical structures. They found that the leading-edge vortices were formed from series of smaller vortices but were less coherent/identifiable at higher angles of attack. Moreover, Gad-el Hak and Ho (1985) [16] also studied the effects of pitching on a NACA0012 non-slender delta wing. They discovered a bifurcation in separation behaviour as the reduced frequency (k) of pitching was increased. Reduced frequencies greater than π resulted in the formation of a strong coherent shedding vortex that in turn kept the separation contained to a thin layer above the wing surface.

The goal of this study is to understand the sensitivity of a NACA0012 non-slender geometry to axial acceleration, analogous to an aircraft subjected to a "head-on" or streamwise gust. Equivalence of varying inflow conditions to acceleration of the model is supported by results from Granlund et al. (2014) [17], who compare an accelerating airfoil in a water tunnel, to a stationary airfoil in a wind tunnel with an accelerating freestream. When accounting for buoyancy forces in the wind tunnel, and inertial effects in the water tunnel, measured circulatory forces in each case were found to be in agreement, implying that a streamwise gust response can be studied through the acceleration of the test article. However, it should be noted that the study by Granlund et al. (2014) [17] was strictly for a two-dimensional case, at a lower range of reduced frequency than tested in this study. The equivalence of transient inflow conditions to that of accelerating bodies remains poorly understood for complex three-dimensional flows. Nonetheless, the effect of acceleration is still relevant in understanding unsteady flow phenomenon in relation to non-slender delta wings, especially in application to highly maneuverable aerial vehicles with minimal wing loading. From the unsteady Euler equations, Fernando et al. (2017) [18] demonstrated that spheres experience a favorable shift in azimuthal pressure gradient under acceleration, the premise of which is reproduced in Figure 14-1(a) and Figure 14-1(b). Particle Image Velocimetry (PIV) in this study showed that the separation line moves downstream with increasing acceleration, supporting the potential flow based prediction. Analogous to the sphere behaviour, it is predicted here that regions of detached flow over the delta wing will shrink under acceleration, resulting in augmented values of normalized lift and pitching moment.

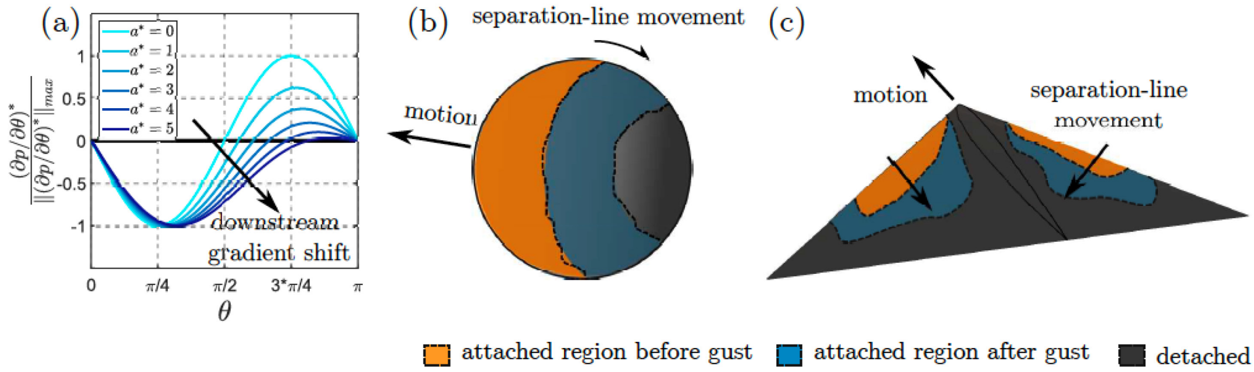

Figure 14-1: (a) Potential Flow Theory Shows a Reduction of Adverse Azimuthal Pressure Gradient on the Sphere in (b) with Increasing Axial Acceleration, a∗, Emulating a Streamwise Gust [18], (c) Outlines the Hypothesized Downstream Separation Line Movement Due to the Adverse Pressure Gradient Reduction on a Partially Attached Delta Wing Undergoing a Streamwise Gust [19].

14.2 EXPERIMENTAL METHODS

A combination of time-resolved force, pressure and PIV measurements are used to capture the dynamic-stall characteristics of the swept-wing model. Steady state measurements are initially taken to characterize the flow structure to be used as an initial condition for the gust. All experiments take place in the optical towing tank facility at Queen's University shown in Figure 14-2(a). The tank has a 1 m by 1 m cross-section and is 15 m long. To minimize free-surface effects, the tank has a roof section with a small slit that provides only enough space for a sting to pass. Axial accelerations approximate a ramp function from Re = 300,000 to Re = 450,000 over the range 1 < g*< 6, where g*is the normalized distance over which the gust takes place, normalized by the centre-span chord. Absolute distance travelled is also normalized by centre-span chord, denoted by s*= s/c. An s* value of zero is refers to the instant the acceleration begins. Figure 14-3(a) shows the range of gust magnitudes tested, where the models initial velocity is U = 1 m/s. Figure 14-3(b) shows that the traverse is capable of faithfully replicating a ramp motion up to g* = 0.75 (with 3 – 5 % steady state error).

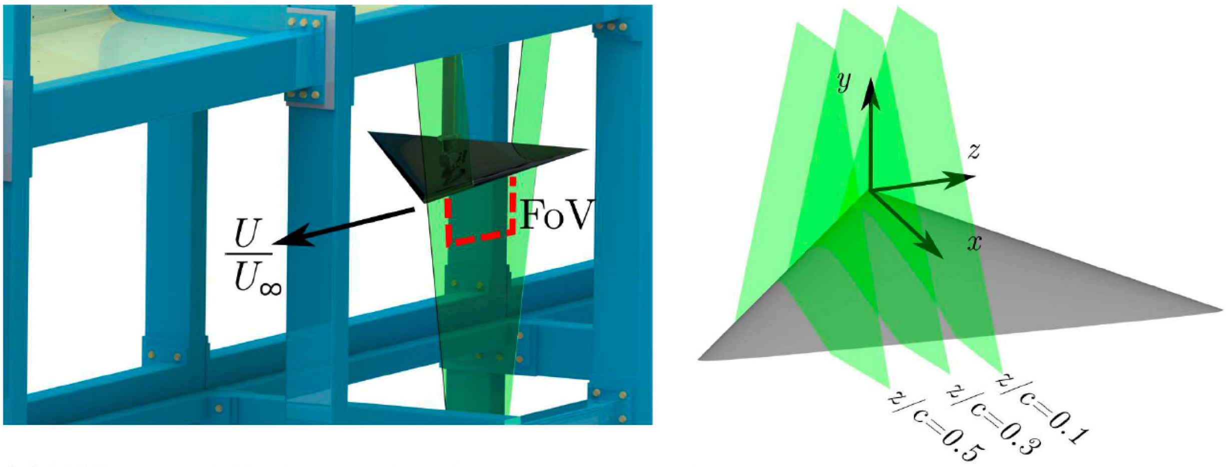

(a) FoV spans $1.33c$ in x, and $1c$ in y (b) planar PIV sections

Figure 14-2: Experimental Setup (a) Of Axial-Gust Experiments in the Optical Towing Tank Showing the Field of View (FOV), where (b) Multiple Time-Resolved PIV cuts are Performed Over the Wing Span. Direct force/moment and pressure measurements are carried out concurrently [19].

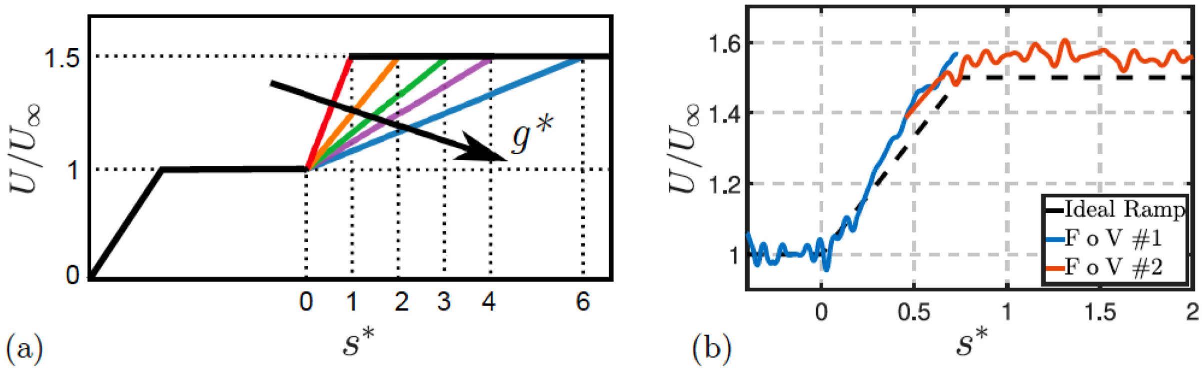

Figure 14-3: (a) A Ramp Motion Represents a Gust in Which a Steady State Model Rapidly Accelerates in the Streamwise Direction from Re = 300,000 to Re = 450,000, Gust Magnitude is Designated by g∗, Model Distance Travelled in Chords is Represented by s∗, and Velocity is Normalized by the Initial Freestream Velocity, (b) The Maximum Possible Gust Magnitude Achievable with the Model Rig in the Towing Tank at 20° Incidence is Approximately g∗= 0.75. 3 – 5 % Steady State Error is Observed at the Target Velocity [19].

14.2.1 Force, Moment, and Pressure

The model has a centre-span chord of 0.3 m, a sweep angle of 45°, and is Selective Laser Sintered (SLS) from nylon plastic material. The wing is treated 110 with cyanoacrylate to seal the porous surface, preventing water ingress into the inner volume. Sixteen 3.175 mm ID passages are printed directly into the model body, each with d = 1.588 mm tap diameter, and 3.175 mm depth. Tap diameter is sized yielding $d^+ = 300$. Pressure taps are spaced 0.2 chords in the streamwise direction, and 0.1 chords in the spanwise direction. The tap locations span $0.2c < x < 0.8c$, and $0.1c < z < 0.7c$, positioned as displayed in Figure 14-4(a). Pressure tubing is daisy-chained such that differential measurements are taken between taps, with absolute pressure only measured from the first tap near the leading edge. Four Omega PX409 bi-directional differential pressure transducers and one Omega PX419 absolute vacuum traducer 125 permitted measurement of five taps simultaneously. The transducers have a response time of < 0.001 s, and a claimed accuracy of 0.08% of Best Straight Line (BSL) linearity, hysteresis and repeatability combined. The pressure transducer daisy chain configuration is shown in Figure 14-4(b), with the fourth differential sensor omitted for clarity. The time-resolved surface pressure is plotted using a cubic interpolation over the spatial domain of the taps. A uniform grid representing a cubic surface, G = f (x, z), is fit to the point data at each pressure tap location. The interpolated surface always passes through the data points measured at each pressure tap. Pressure coefficient, Cp, is calculated using the instantaneous freestream velocity throughout the gust. An ATI Nano 25 six-axis force sensor is mounted at the centre-chord, on the symmetry plane of the NACA0012 profile as shown in Figure 14-4(a). The transducer has a static resolution of 0.125 N, with forces and moments sampled at a rate of 1000 Hz for all runs. Steady state forces are averaged over 5 runs, and 10 chords travelled. For each run, the model is accelerated from rest over 3 chords ($g^*= 3$), followed by additional 14 chords at a constant velocity before averaging. The steady measurements indicate a minimum of 10 chords of travel to reach steady state. Therefore, 14 chords of travel would be sufficient to guarantee a steady initial condition for the gust measurements. The additional 4 chords travelled are also used to verify that the steady portion of the gust measurements agreed with the initial steady measurements. Measurements of the gust cases are averaged over 25 runs. A 100-point span Savitzky-Golay filter is applied to the transient force and moment data, in order to smooth noise at high frequencies not relevant to the mean flow behaviour.

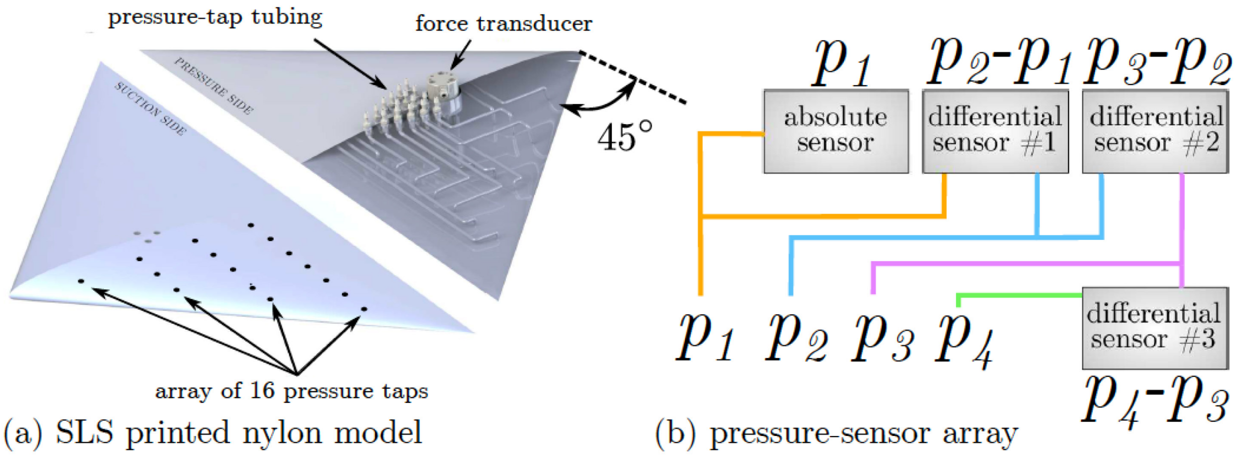

(a) SLS printed nylon model (b) pressure-sensor array

Figure 14-4: (a) Selective Laser Sintering (SLS) Printed Nylon Delta Wing Model with 45° Sweep, (b) Four Differential Pressure Sensors are Daisy-Changed, Referencing a Single Absolute Sensor, Allowing for Direct Measurement of the Pressure Gradient Across Taps (Fourth Differential Sensor Omitted for Space/Clarity) [19].

14.2.2 Particle Image Velocimetry

Time-resolved planar PIV measurements are conducted at three spanwise planar sections, z/c = 0.1, 0.3, and 0.5. The approximate Field of View (FoV) size is 40 cm Å~ 30 cm, or 1.33 chords in length, and 1 chord in height. Angles of attack are selected based on force and moment measurements, which show clear changes between 20◦ and 30◦. Particle images are captured at 1500 Hz using a Photron SA4 camera with

1024Å~1024-pixel resolution. A 40 mJ/pulse Photonics Industries laser is synchronized to the camera frame rate, with a sheet thickness of approximately 1.5 mm. PIV and pressure measurements are taken simultaneously, and ensemble averaged over 20 runs for each FoV. Velocity and vorticity fields are normalized by instantaneous freestream velocity throughout the gust.

14.3 RESULTS

A sweep of gusts ranging from g∗= 1 to g∗= 6 are conducted at α = 20° and α = 30° angles of attack. Force histories at α = 20° quickly converge to steady state following termination of the gust. Figure 14-5(a) shows that force and moment response vary linearly with gust magnitude. In contrast, at α = 30°, a bifurcation in force response occurs between g∗= 2 and g∗= 1. Proceeding the latter, is a sustained increase in lift, drag, and pitching moment for six chords of travel. Furthermore, Figure 14-5(b) shows that the lift and drag forces do not collapse for g∗= 1. Most interestingly however, is an inflection that occurs before peak values are reached. The remaining gusts from 2 < g∗< 4 exhibit less drastic behaviour, with peak forces collapsing along the same curve.

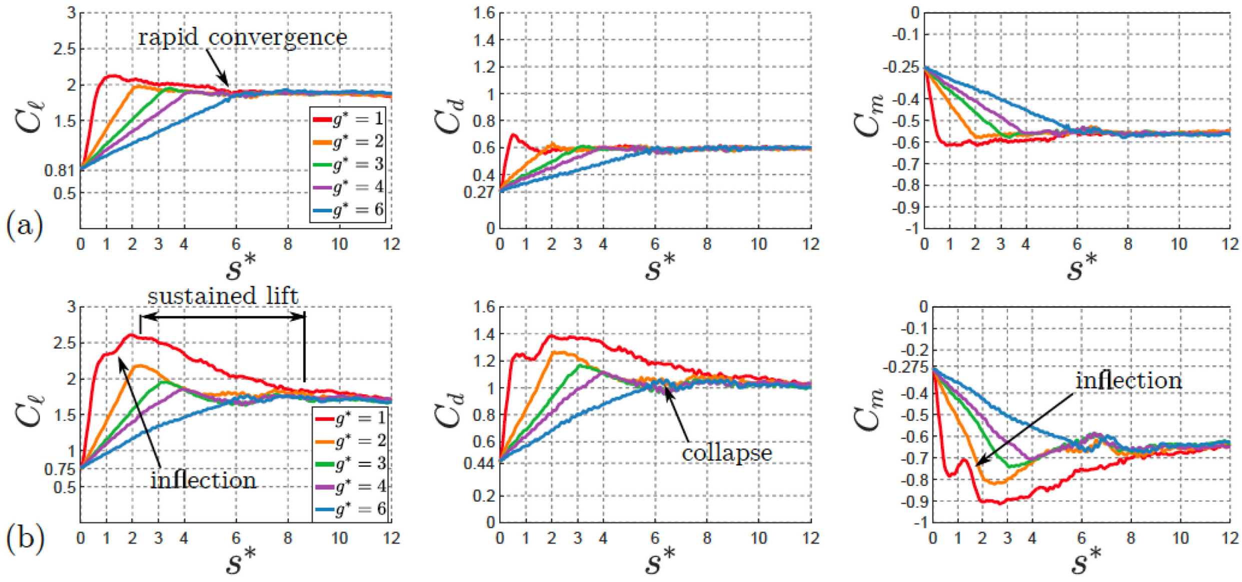

Figure 14-5: Lift, Drag, and Moment Response to a Range of Gusts (1 < g∗< 6) at (a) α = 20° and (b) α = 30° [19].

In consideration of the unsteady force results, evolution of the velocity-field for g∗ = 1 and g∗= 2 gusts are compared and shown in Figure 14-6. Prior to the gust, at α = 20°, the flow remains mostly attached, and only at the z/c = 0.5 plane does the shear layer totally separate from the wing surface. During the gust, in the sections where the flow is initially attached, there is an increase in instantaneous velocity, but no flow structure is shed. At α = 30°, the flow is characterized by fully separated shear layers at the gust onset. During the gust, reattachment of these separated shear layers is responsible for the bifurcation in force history. Moreover, this behaviour is not consistent across the span of the wing (see Figure 14-6). At the inboard sections (z/c = 0.1, 0.3), it appears that the effect of the gust is to increase vorticity flux at the leading edge, causing the shear layer to reattach approximately at the quarter-chord position (x/c = 0.4). Vorticity concentration at the leading edge appears to increase during the gust and Figure 14-7 shows the reattached shear layer halfway through the gust. At z/c = 0.5, the shear layer never reattaches regardless of gust magnitude. Instead, the shear layer rolls up into a vortex, that is in turn shed before the gust ends.

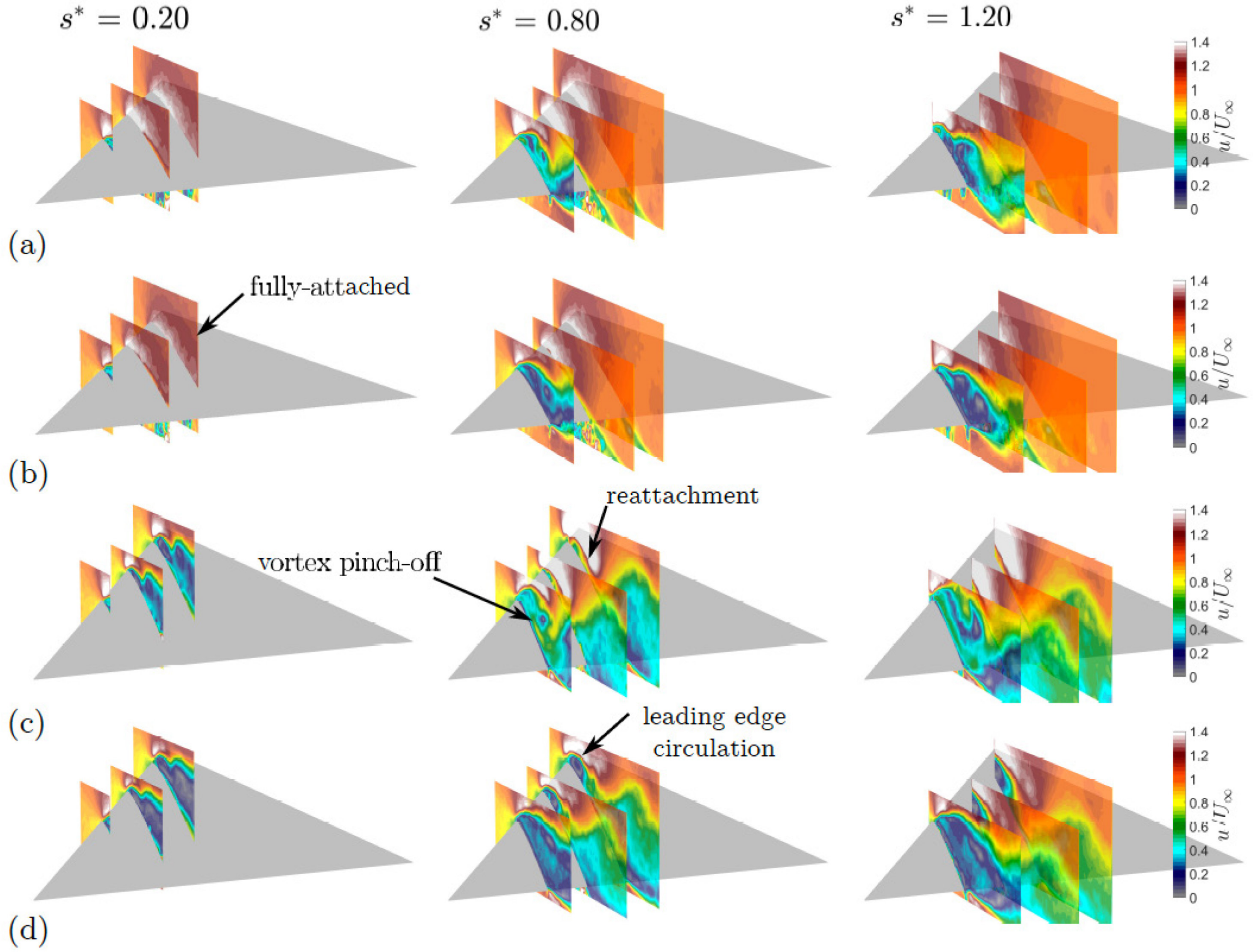

Figure 14-6: Evolution of Flow Over the Gust Duration for (a) α = 20°, g∗= 1, (b) α = 20°, g∗= 2, (c) α = 30°, g∗= 1, (d) α = 30°, g∗= 2 [19].

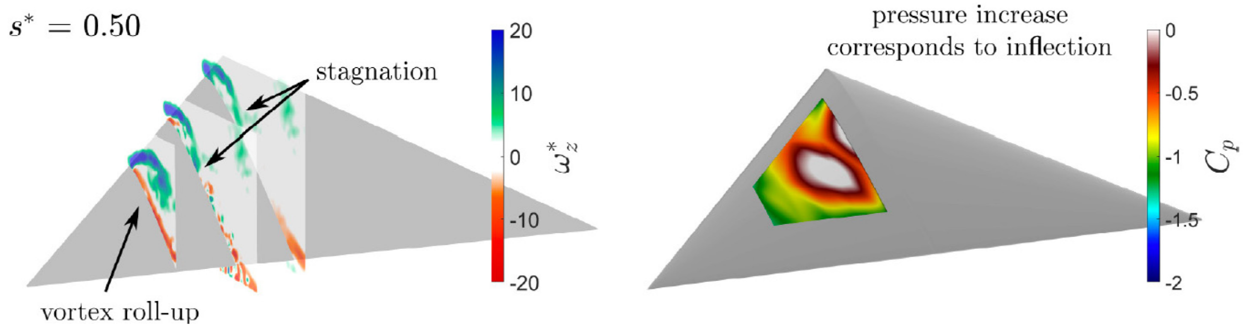

Figure 14-7: Vorticity Field and Surface Pressure at α = 30°, g∗= 1 Demonstrating Mechanism of Dynamic Flow Reattachment and Corresponding Pressure Increase [19].

The vorticity field in Figure 14-7 shows the shear layer feeding the leading-edge vortex on the z/c = 0.5 section. Midway through the gust (s∗ = 0.5), the shear layer on both the z/c = 0.1 and 0.3 sections stagnate on the wing surface at approximately x/c = 0.3, resulting in a temporary rise in pressure at this location. The rise in pressure corresponds to the inflection observed in the lift and drag history seen in Figure 14-5(b). Peculiarly, for α = 30° and g∗ = 1, lift continues to rise after the gust has ended, suggesting that the flow remains attached long after the gust has terminated. Further evidence supporting this sustained attachment is provided by the strong favorable pressure gradient that forms near the leading edge. This favorable pressure gradient drives the flow to remain attached where it is normally separated at steady state.

14.4 CONCLUSIONS

The dynamic-stall induced by streamwise gusts on non-slender delta wings is investigated experimentally. A NACA0012 cross-section, 45^{o} sweep model serves as the canonical geometry, and acceleration is used in place of varying inflow conditions. Forces, surface pressure, and planar PIV measurements are conducted simultaneously to capture the flow evolution. Force augmentation both during and after the gust is shown to be dependent on the structure of separated shear layers at the onset of the gust, with strong sensitivity to gust magnitude exhibited at a 30◦ angle of attack. During the gust, separated shear layers near the wing apex reattach, causing enhancement of lift, drag, and moments well beyond the end of the gust period. Drawing parallels to accelerating spheres (Fernando et al. (2017) [18]), the separation line on the delta wing moves downstream until complete reattachment is achieved on the $z/c = 0.3$ and 0.1 spanwise sections. However, in contrast to the sphere study, augmented forces are maintained after the gust ends. Immediately following the gust motion, a rapid drop in surface pressure near the leading edge further drives attachment, thereby sustaining force and moment values at this post-stall incidence angle. Disparity to the behaviour of accelerating spheres is attributed to the vertical nature of delta wing flows. Trends in leading-edge circulation are used to assist in explaining this disparity.

14.5 REFERENCES

[1] Liebeck R.H., Design of the blended wing body subsonic transport. Journal of Aircraft, Vol. 41, No. 1, 2004, pp. 10-25.

[2] Cummings, R., and Schuette A., An integrated computational/experimental approach to UCAV stability and control estimation: overview of NATO RTO AVT-161. 28th AIAA Applied Aerodynamics Conference, 2010.

[3] Polhamus, E., A concept of the vortex lift of sharp-edge delta wings based on a leading-edge-suction analogy. Technical Report; NASA Tech. Mem., 1966.

[4] Earnshaw, P., and Lawford, J., Low-speed wind-tunnel experiments on a series of sharp-edged delta wings. HM Stationery Office, 1966.

[5] Brown C.E., and Michael, Jr W.H., On slender delta wings with leading-edge separation. NACA Tech Mem., 1955.

[6] Lee, M, and Ho, C., Lift force of delta wings. Applied Mechanics Reviews, Vol. 43, No. 9, 1990, pp. 209-21.

[7] Gursul, I., Review of unsteady vortex flows over slender delta wings. Journal of Aircraft, Vol. 42, No. 2, 2005; pp. 299-319.

[8] Ol, M, and Gharib, M., Leading-edge vortex structure of nonslender delta wings at low Reynolds number. AIAA Journal, Vol. 41, No. 1, 2003, pp. 16-132.

[9] Gursul, I., Gordnier, R., and Visbal, M., Unsteady aerodynamics of nonslender delta wings. Progress in Aerospace Sciences, Vol. 41, No. 7, 2005; pp. 515-557.

[10] Taylor, G., Schnorbus, T., and Gursul I., An investigation of vortex flows over low sweep delta wings. AIAA Journal, 2003.

[11] Konrath, R., Roosenboom, E., Schroeder, A., Pallek, D., and Otter, D., Static and dynamic SACCON PIV tests, Part ii: Aft flow field. 28th AIAA Applied Aerodynamics Conference, 2010.

[12] Cummings, R., Schuette A. Integrated computational/experimental approach to unmanned combat air vehicle stability and control estimation. Journal of Aircraft, Vol. 49, No. 6, 2012, pp. 1542-1557.

[13] Le Provost, M., He, X., and Williams, D., Real-time roll and pitching moment identification with distributed surface pressure sensors on a UCAS wing. 2018 AIAA Aerospace Sciences Meeting, 2018.

[14] He, X., Le Provost, M., and Williams, D., Dynamic active flow control of the roll moment on a generic UCAS wing. 2018 AIAA Aerospace Sciences Meeting, 2018.

[15] Gad-el Hak, M., and Blackwelder, R., The discrete vortices from a delta wing. AIAA Journal, Vol. 23, No. 6, 1985, pp. 961-962.

[16] Gad-el Hak, M., and Ho, C., The pitching delta wing. AIAA Journal, Vol. 23, No. 11, 1985, pp. 1660-1665.

[17] Granlund, K., Monnier, B., Ol, M., and Williams, D., Airfoil longitudinal gust response in separated vs. attached flows. Physics of Fluids, Vol. 26, No. 2, 2014.

[18] Fernando, J., Marzanek, M., Bond, C., and Rival, D., On the separation mechanics of accelerating spheres. Physics of Fluids, Vol. 29, No. 3, 2017.

[19] Marzanek, M., and Rival, D., Separation mechanics of non-slender delta wings during streamwise gusts. Journal of Fluids and Structures, Vol. 90, 2019, pp. 286-296.

Chapter 15 – RESULTS AND CONTRIBUTIONS

Anya R. Jones
University of Maryland
UNITED STATES

Oksan Cetiner
Istanbul Technical University
TURKEY

To summarize and document the results and conclusions of the four years of collaborative planning and research undertaken by the AVT-282 group, members were asked to answer six research questions:

1) Describe the lift response (CL vs. t∗) of the wing-gust encounter you have studied. Is there a typical response? Can you explain it?
2) What are the sources of force on a body (e.g., wing) in a gust encounter? Which ones are most important? When?
3) How well do linear inviscid theories work to predict or model a wing's response to your gust encounter?
4) Does the idea of effective angle of attack help you to predict or model the lift response you observe? Regardless, how do you measure effective angle of attack?
5) Do you observe coupling of the gust flow with the flow around the wing? If yes, when does this effect become important? How/can you quantify it?
6) How do traditional computational codes model different gusts? Are modifications needed to accurately model a large amplitude gust encounter that incites large-scale flow separation? If so, when, why, and how?

The following sections briefly summarize the group's response to these questions. More details can be found in the conference papers (Refs. [1] to [14]) and many other publications (including Refs. [15] to [78]).

15.1 TYPICAL LIFT RESPONSES TO A GUST ENCOUNTER

A typical lift force response to a transverse gust encounter is given in Figure 15-1(a). The lift force on the wing grows as it enters the gust and experiences a peak while the wing is fully immersed in the transverse gust flow. Flow visualization and flowfield measurements, an example of which is given in Figure 15-1(b), have revealed the formation of a strong leading-edge vortex in the range of gust ratios studied here, $0.2 \leq GR \leq 2.6$, which is the primary cause of the lift peak observed. The maximum lift coefficient achieved increases with both gust ratio and the geometric incidence of the wing [20]. As the wing exits the gust, the lift force may (for high wing incidence and/or high gust ratio) experience a local minimum caused by formation of a trailing-edge vortex [58]. In these cases, a subsequent secondary lift peak may also form as the trailing-edge vortex induces a secondary leading-edge vortex. Eventually, lift relaxes back to its steady state as the wing recovers from the gust encounter. Full recovery is generally attained between 6 and ~20 convective times, with quicker recoveries occurring for lower wing incidences and gust ratios. At high wing incidence, for example, $\alpha = 45°$, recovery can take upwards of 20 convective times and closely resembles flow over a surging wing starting from rest [58]. In general, the magnitude of the lift response is approximately linearly sensitive to variations in gust ratio at large gust ratios, but nonlinearly sensitive to variations for small gust ratios [3]. For a plunging wing model of a transverse gust encounter, different airfoil profiles give slightly different lift responses despite massive flow separation [12].

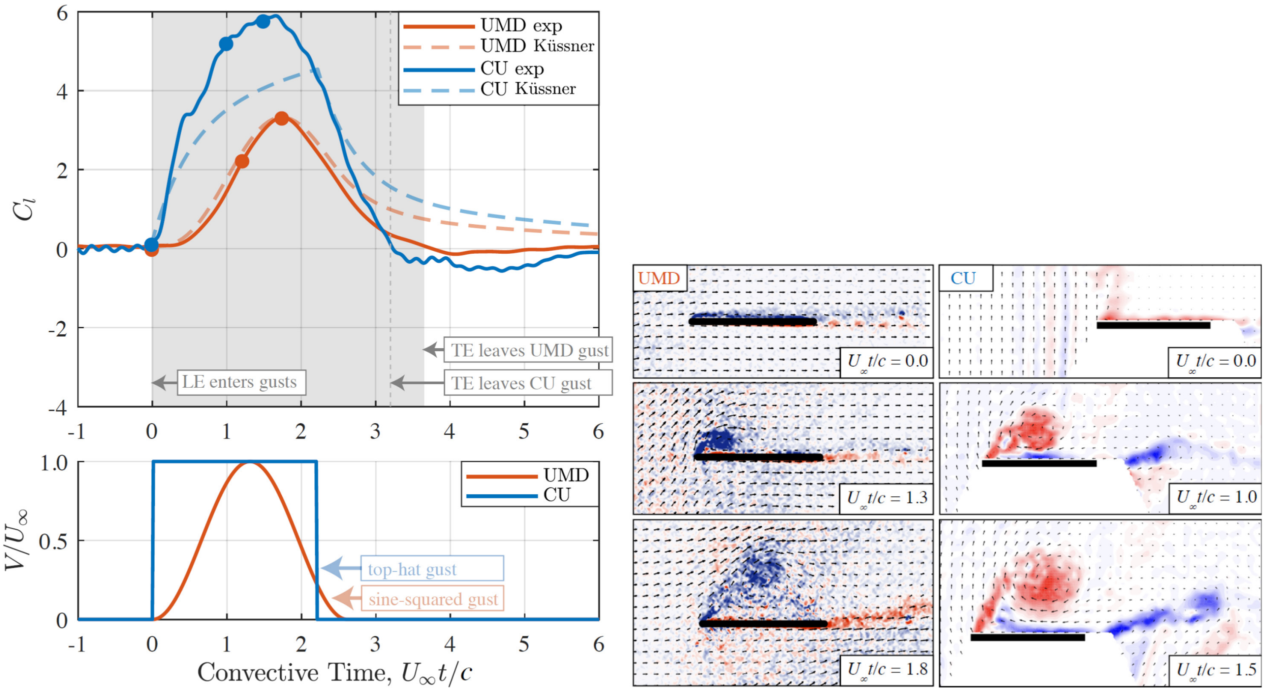

(a) Lift Histories from Experimental and Analytical Results from Küssner's Model Applied to an Arbitrary Gust Profile.

(b) Color Contours of Vorticity (Note Inverted Colors) Overlaid on Velocity Fields as Measured Using Time-Resolved Particle Image Velocimetry.

Figure 15-1: Results from a Top-Hat Transverse Gust Encounter in the University of Cambridge (CU) Towing Tank and a Sine-Squared Gust Encounter in the University of Maryland (UMD) Towing Tank. Both test models are a flat plate wing at zero incidence passing through a gust of *GR* = 1 [2], [44].

A typical lift force response to a transient **vortex gust** encounter is given in Figure 15-2. Here, the vortex gust passes under the wing, so the lift transient is negative. In Figure 15-3, the periodic gust shown, gust #4, passes over the wing and the lift transient is positive. As in the case of the transverse gust, the force response to a vortex gust depends on both the gust ratio and wing incidence. In this case, however, wing loading also depends on the vortex trajectory. Greater fluctuations in lift occur when the vortices pass nearer the wing [88]. For a series of small vortices spaced far apart, the force response is nominally the superposition of the response to a sinusoidal vortex street and the steady forcing on the wing [71]. For the passage of a single vortex, lift becomes increasingly stronger as the vortex approaches, and then changes sign abruptly as the vortex passes over the airfoil, jumping to a large value and decaying gradually [47]. This is an inviscid phenomenon captured well in Euler simulations [92], [93]. However, note that at high angles of attack, Euler simulations no longer accurately predict the early stage loading due to substantial contributions from leading-edge vortex formation [89], [90]. After the vortex gust passes, wing loading consists of lower amplitude but long-lasting perturbations attributed to the long relaxation time of the boundary layer recovery following the gust disturbance [92], [93].

Streamwise gusts were studied using both surging wings and unsteady flow wind tunnels. The lift response of a strong surging wing streamwise gust, shown in Figure 15-4, closely resembles that of a wing starting from rest [13], [59]. An airfoil in a sinusoidally varying freestream, however, produces oscillatory loading with the phase and amplitude of these loads varying with the gust amplitude and frequency [90]. Similarly, as shown in Figure 15-5, an airfoil in a randomly varying freestream experiences load fluctuations that reflect these variations [10]. Viscous effects due to boundary layer dynamics contribute to the phase lag between the wing loads and the streamwise velocity variation, even at low angles of attack [90]. At pre-stall angles of attack, where the flow is nominally attached, drag experiences an additional phase lag when compared to lift and moment. At post-stall angles of attack, lift, drag, and moment are all in phase with each other [90].

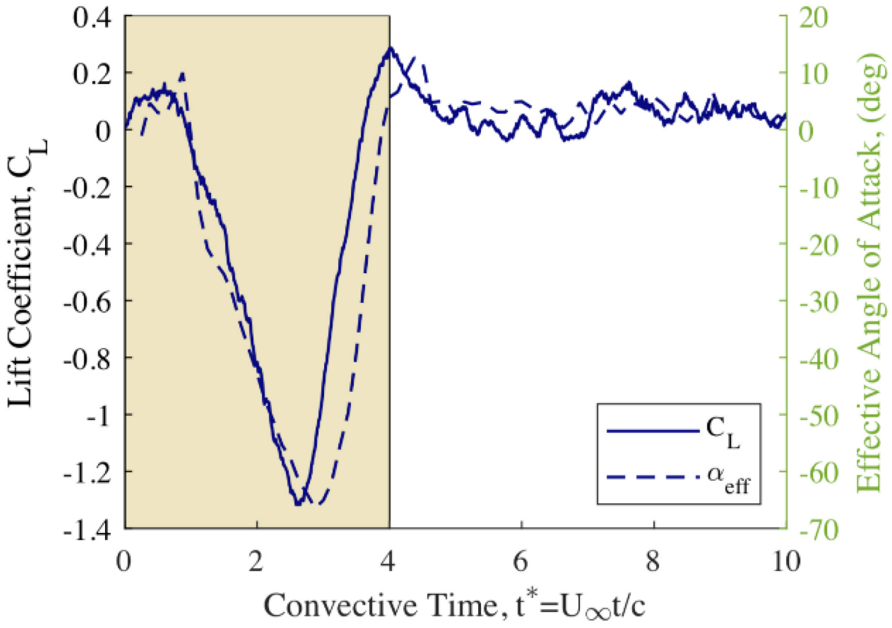

Figure 15-2: Lift Transient and Change in the Effective Angle of Attack for a Wing at Zero Incidence in a Vortex Gust [35].

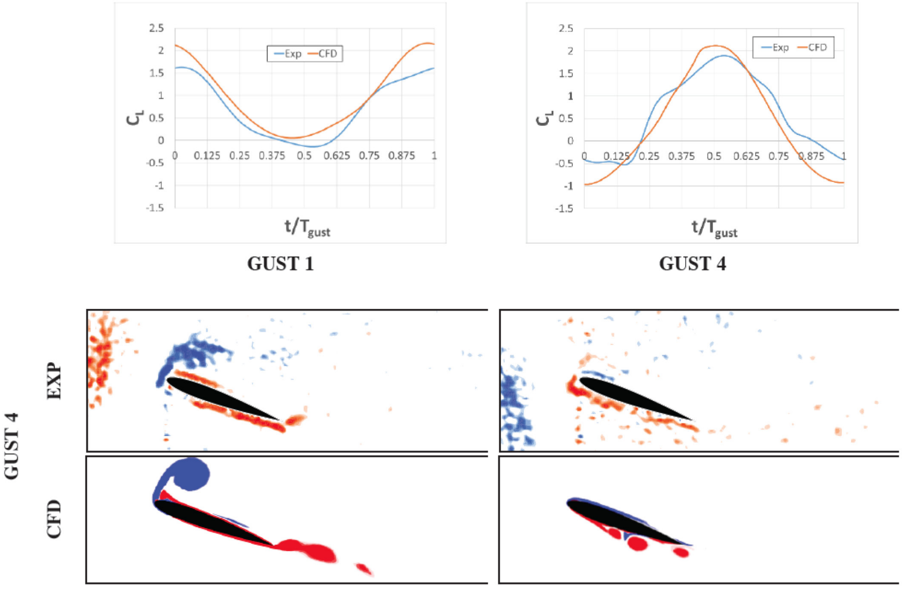

Figure 15-3: Numerical Results in Comparison with the Experimental Results for Two Strong Periodic Vortex Gust Cases. (Note that flowfields are only shown here for Gust 4. The full figure is given in Ref. [7].)

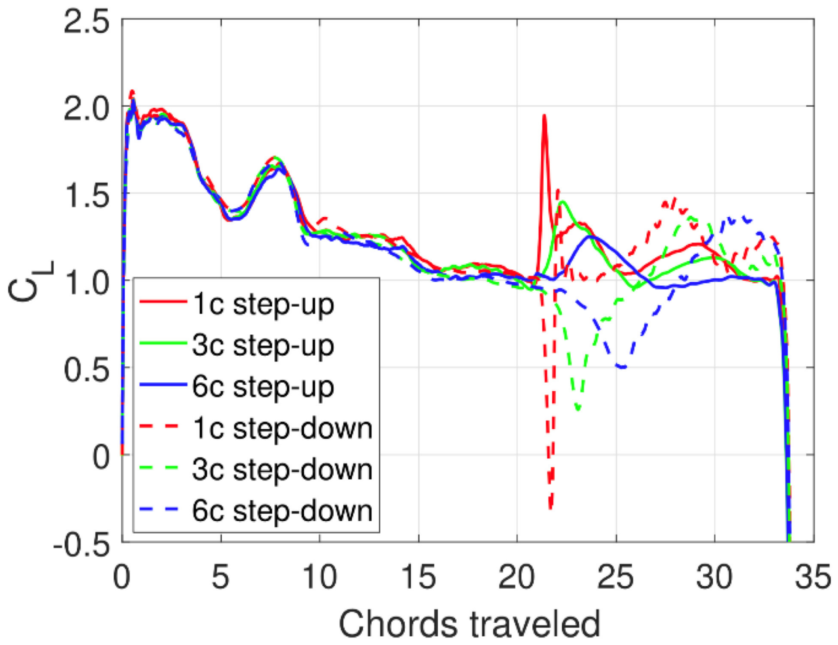

Figure 15-4: Force Measurements for Step-Up and Step-Down Streamwise Gusts on a Surging Wing. All gusts start at 21c of wing travel [13].

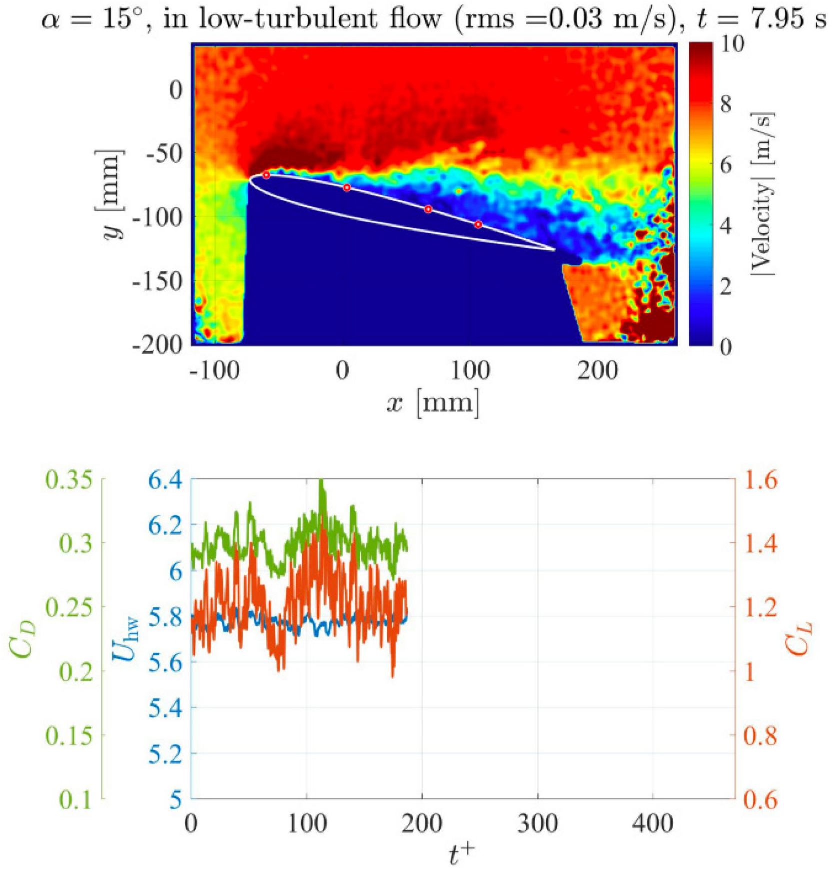

Figure 15-5: Contours of *u*-Velocity and Vorticity, and Time Series of Drag, Lift, and Velocity for a Wing in a Randomly Varying Freestream [10].

15.2 SOURCES OF FORCE IN A GUST ENCOUNTER

Large gust ratios in **transverse** or **vortex** gust encounters result in massive flow separation, and thus force production is dominated by inviscid effects: force that arises from the advection and growth of circulation shed from the wing, and non-circulatory force associated with the free vorticity in the gust itself. This non-circulatory force can be thought of as a result of the growth and re-distribution of the boundary layer vortex sheet induced by free vorticity in the flow [32], [44], [96]. For sharp-edged gusts with strong concentrations of vorticity in the gust shear layer, non-circulatory force dominates during the initial phase of the force response as the plate enters the gust (see Figure 15-6). Once the wing is fully in the gust, however, force production is dominated by circulatory contributions [96], [97].

In a **streamwise** gust, a high gust ratio does not necessarily result in flow separation. A wing at low incidence in a streamwise gust will experience variations in free-stream that significantly affect the boundary layer without causing separation. As such, forcing in a streamwise gust is both inviscid and viscous. Inviscid effects include circulatory forces, added mass (for a surging wing), and buoyancy forces (for an unsteady inflow). Viscous effects arise due to the dynamics of the boundary layer and exist for both in pre- and post-stall angles of attack [90].

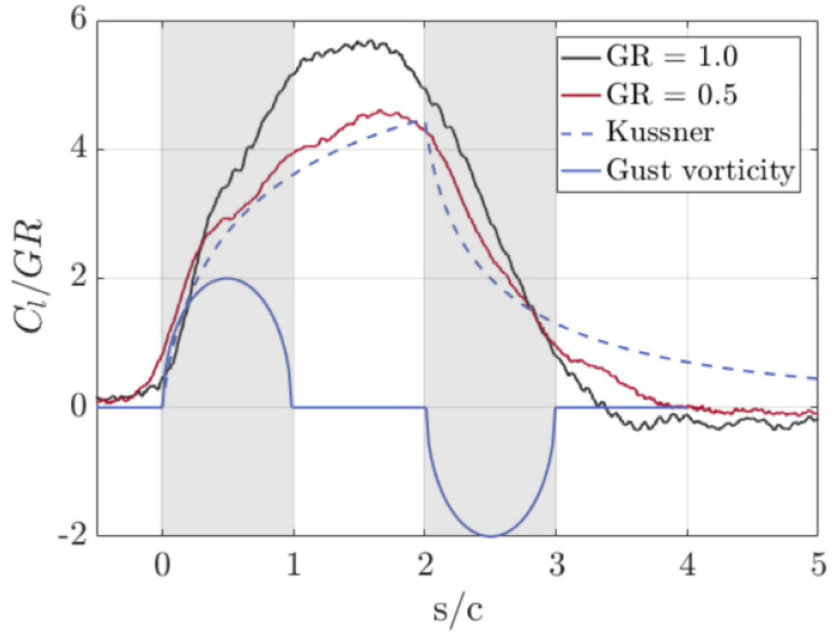

Figure 15-6: Typical Lift Response During a Top-Hat Shaped Gust Encounter Illustrating the Force Contribution from Gust Vorticity. The grey rectangles correspond to the regions of the motion where the wing is entering or exiting the gust [97].

15.3 APPLICATION OF LINEAR INVISCID THEORIES TO LARGE AMPLITUDE GUST ENCOUNTERS

Linear inviscid theories (e.g., Küssner, Greenberg, Sears) were found to provide reasonable predictions of the unsteady lift response for all three gust types considered, and to gust ratios much greater than those that strictly adhere to the assumptions inherent in these models. For **transverse gusts**, Küssner's model was found to work well for $GR \leq 0.5$ for sharp-edged gusts [2], [44], and to much higher gust ratios for smoother gusts [20]. Notably, as shown in Figure 15-1(a), application of Küssner's model to arbitrary gust profiles via application of Duhamel's integral has produced excellent results. In general, inviscid models match experimental results better on gust entry than on gust exit, where the separated flow physics are more complex. Two-dimensional linear inviscid theories of periodic transverse gusts (e.g., Sears, Atassi) do not work for three-dimensional finite-span geometries, especially at low aspect ratio, low reduced frequency, and near the wing tips. Three-dimensional linear inviscid models, however, are sufficient for first-order predictions if flow is largely attached [40].

For **vortex gusts**, inviscid models do well when the vortex is offset from the centerline of the airfoil by about 20% chord or more and/or the angle of attack is less than 20° (see Refs. [98] to [100]). For vortex gusts that pass very near the wing, offsets less than or equal to 0.1c, there is a strong viscous-inviscid interaction between the vortex and the airfoil boundary layer [100]. Sears's model was found to provide a good prediction of the response to the ITU vortex gust for wing incidence $\leq 20°$. On a pitching airfoil, modifications of the Leading-Edge Suction Parameter (LESP) were found to provide good predictions of separation on a pitching airfoil [16].

Linear inviscid theories also work well for **streamwise gusts** at high Reynolds numbers and low angles of attack where the boundary layer remains fully attached. They become inaccurate in the presence of even small separation effects such as those due to trailing-edge separation or laminar separation bubbles [90]. Differences between theory and experiments also exist due to the phase lag arising from boundary layer dynamics, though force amplitudes are reasonably well predicted by Greenberg [81], [90], [101]. Theodorsen's model has been found to work well for high aspect ratio wings, $AR > 3$, and high reduced frequency, $k \geq 1$ [40].

15.4 USING EFFECTIVE ANGLE OF ATTACK TO PREDICT LIFT IN A GUST ENCOUNTER

The effective angle of attack of a wing in a **streamwise gust** does not change because the flow disturbance is aligned with the freestream. However, for both **transverse and vortex gusts**, the time-varying effective angle of attack of the wing as it passes through the gust has been found to provide a good, if simple, model of the expected lift force [4], [35], [47]. Figure 15-2 gives one example of the change in lift coefficient and simultaneous change in effective angle of attack as measured using particle image velocimetry for a vortex gust encounter. The idea of using an effective angle of attack as found from flowfield measurements to predict unsteady lift works well for low angles of attack, $\alpha < 20°$, but not for high angles, $\alpha = \{30°, 45°\}$, where it is difficult to decouple the effects of inflow from those of the leading-edge vortex [4], [47]. For transverse gusts, models as simple as taking the instantaneous effective angle of attack at the leading edge of the wing given by the geometric incidence and theoretical gust velocity have given reasonable lift predictions [20]. It should be noted, however, that since a flowfield-measured effective angle of attack includes at the background gust velocity and does not account for non-circulatory forces that arise due to free vorticity in the gust flow, this method should be used with care in sharp gusts with concentrated vorticity [97].

15.5 THE EFFECT OF WING/GUST COUPLING

Transverse gust flows deform significantly as a wing passes through them. This is particularly clear in sharp-edged gusts as shown in Figure 15-7. Deformation of the gust shear layer, however, does not appear to be a dominant factor in the force production of the current wing-gust encounters [3], [44]. Coupling in **vortex gusts** is evident in that the presence of the wing deflects the vortex, altering both the velocity and trajectory of the vortex, as shown in Figure 15-8 (see Refs. [8], [47]). For harmonic gusts with some vertical velocity variation, there exists a coupling between the potential field of the wing and the gust itself. This causes an amplification of the gust as shown in Figure 1-2(d). Analytical work by Atassi [102] showed that it is the presence of the vertical non-uniformity in the flow that causes coupling between a **streamwise gust** and the wing.

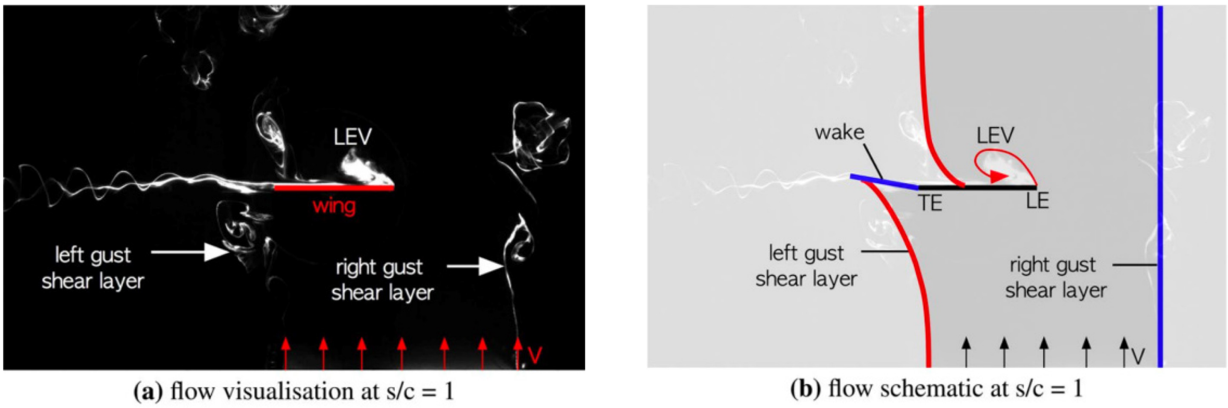

(a) flow visualisation at s/c = 1 **(b)** flow schematic at s/c = 1

Figure 15-7: Dye Flow Visualization in a Sharp-Edged Transverse Gust Encounter. Dye injection points are located at the leading and trailing wing edges and gust shear layers [44].

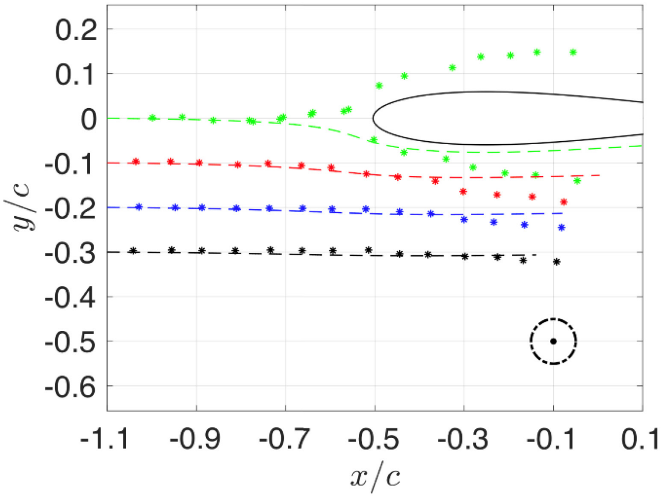

Figure 15-8: Comparisons of Analytical Simulation and Experimental Measurements on Vortex Trajectories with Different Initial Vertical Locations. Curves with asterisks are experimental results, dash lines are analytic results [8].

15.6 COMPUTING LARGE AMPLITUDE GUST ENCOUNTERS

Since the effect of coupling, i.e., the impact of the wing on the gust flow, in **transverse gust** encounters appears to have minimal effect on the resulting force production, current computational methods for the gust encounters of current interest have, for small gust ratios, neglected the coupling terms that arise from first-principles derivations. For larger gust ratios $GR > 0.5$, the non-linearities in the flow field become more important and these terms can no longer be neglected [3]. In this case, additional source terms are required to accurately model the physics [103], [104], [105]. If it is not possible or practical to modify the solver, the gust must be modeled via traditional boundary conditions and solvers. An overset mesh with dynamic motion is the traditional approach, where the wing mesh moves through the background mesh until it enters the gust, which is modeled via boundary conditions on the stationary background mesh [38]. A new approach that does not require overset meshes has recently been developed at Georgia Tech (GT) [3]. In this approach, the mesh moves with the wing while the boundary conditions for the gust flow remain stationary, creating the scenario where the wing flies through the gust, mimicking the experimental towing tank wing-gust interaction setup at CU [44] and UMD [20], [58].

15.7 COMPARISON OF FORCE RESPONSES IN TRANSVERSE AND VORTEX GUST ENCOUNTERS

After noticing similarities amongst the aerodynamic responses of the different gust types, a considerable amount of transverse and vortex gust data from different facilities and groups were collected for direct comparison. To ensure a similar initial condition, the data are collected here only for angles of attack less than or equal to 5°. Data were reported by each group as ΔC_L versus convective time. (Recall that $\Delta C_L(t^*) = C_L(t^*) - C_{L_{steady}}$ and $t^* = t\,U_\infty/c$.) To account for the wide variation in facilities and gust parameters tested, the results shown here are scaled in time by the gust encounter width, $W_e = w/c$, and in magnitude by the gust ratio, $GR = V/U_\infty$. For transverse gusts and periodic vortex gusts, the gust encounter width is the half of the disturbance wavelength and the time scaling is done by dividing the axis by the gust encounter width. However, for the transient gusts, the encounter width is the peak-to-peak distance of velocities in the vortex core and the time scaling is done by multiplying the axis by the gust encounter width. It is known from related studies [2], [3] that the timing of the peak force shifts slightly with gust ratio, but because of uncertainty in the timing of the gust encounter across data sets, the curves shown here are shifted to align the peaks in lift response for a clearer comparison. Note also that these data represent reasonably similar gust ratios and encounter widths; not all of the AVT-282 data is included here. In each of the figures below, the legends give the initials of the researcher and institution where the data were obtained. In Figure 15-12, the gust width, gust ratio, and the angle of attack of the model are also given.

Figure 15-9 shows results from all of the transverse gust cases available for α ≤ 5°. At first glance, all of the curves appear remarkably similar given the wide variation in the gust flows (e.g., magnitude, profile) and wings (e.g., incidence, aspect ratio) tested. Upon closer inspection, it becomes clear that the curves within each set of data (i.e., data acquired in the same facility) are considerably closer to each other than those outside of the set. This is thought to be due to the variation in gust velocity profiles between facilities [2].

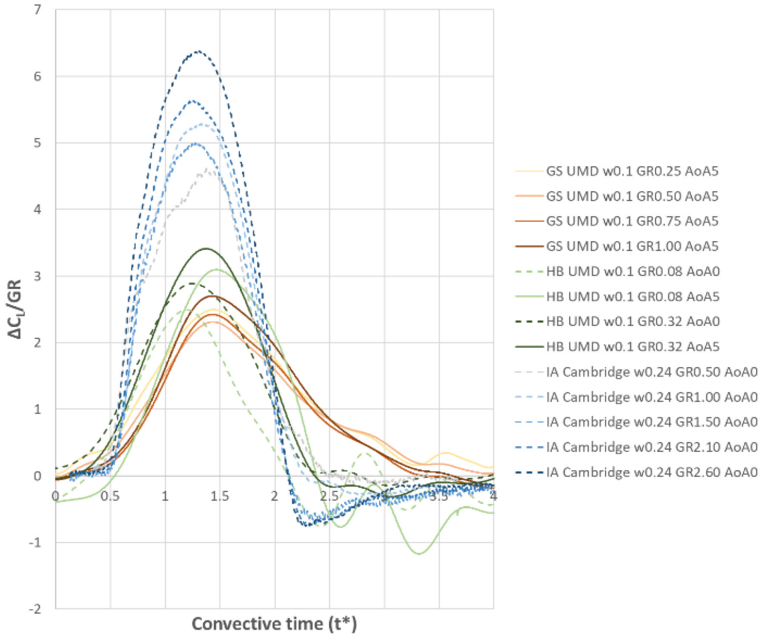

Figure 15-9: Comparison of Transverse Gust Encounters.

In a similar comparison for the vortex gust, Figure 15-10 shows the results from transient and periodic vortex gust encounters, and Figure 15-11 shows both the transient and periodic results on the same axes. It has been shown computationally that the change in the sense of rotation of the vortex causes the lift variation to flip about the *x*-axis [88]. Therefore, the experimental data obtained for a clockwise vortex interaction is flipped about the x-axis for better comparison with the rest of the reported data. The computational results (CB AFRL [88]) represent a single transient vortex encounter and thus a clean rise in lift as the vortex approaches the wing. However, since physical vortices are generated in pairs, the experimental results for a single transient vortex (ITU) cannot entirely avoid the influence of the opposite sign vortex.

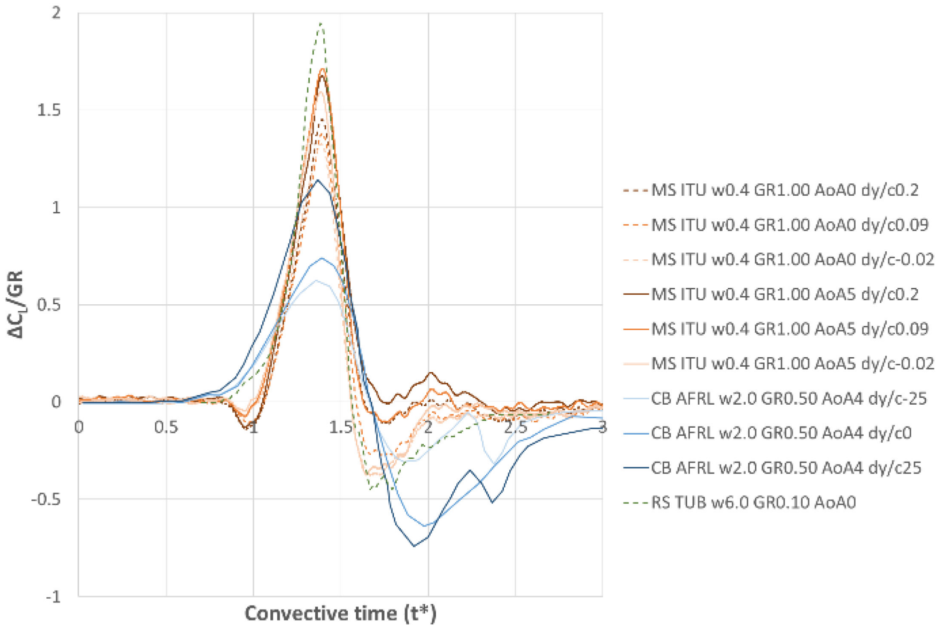

(a) Transient Vortex Gusts.

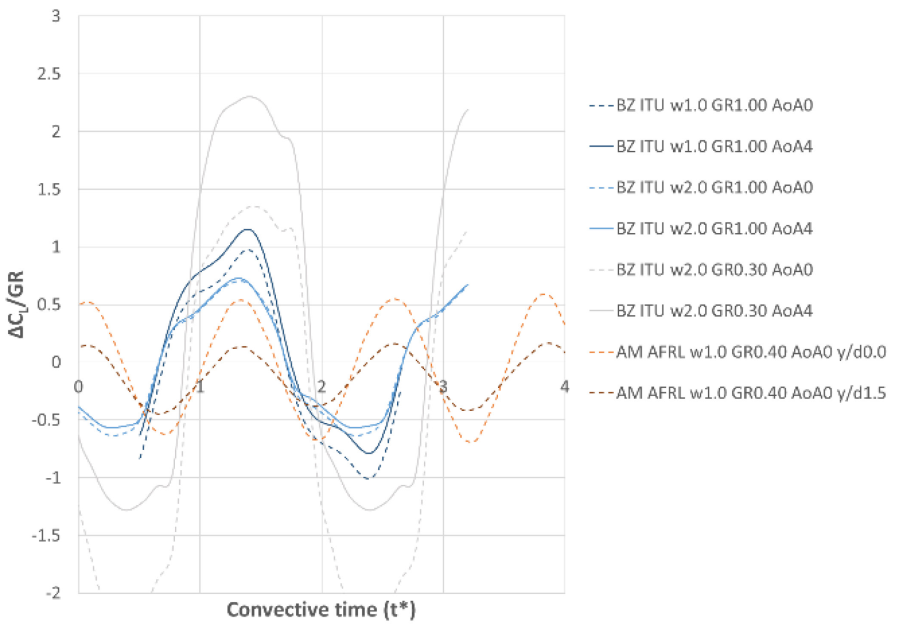

(b) Periodic Vortex Gusts.

Figure 15-10: Comparison of Vortex Gust Encounters.

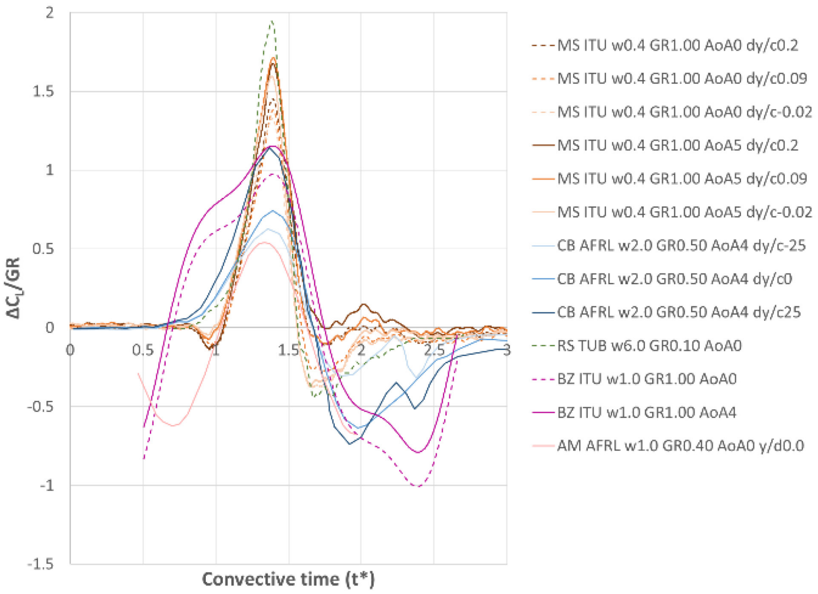

Figure 15-11: Comparison of Transient and Periodic Vortex Gust Encounters.

Although the flow was designed such that this opposite sign vortex moves away from the wing [47], its effect is still visible at $t^* = 1$ as a small region of negative lift in Figure 15-10(a). It should be noted that the methodologies in the two experimental facilities used to generate the transient vortex gust data (ITU and TUB) are quite different. The ITU data is acquired in water and the TUB data is acquired in air. Similarly, the methods used to generate the periodic gust that results in the data shown in Figure 15-10(b) are also different. Both the ITU and AM AFRL data were acquired in water, but the AFRL vortex gust is generated via vortex shedding in the wake of a circular cylinder, while the ITU vortex gust is produced by a feathering gust generator plate pitching and plunging at different frequencies and amplitudes upstream of the test model [70]. Despite many differences in facilities and methods, while the build-up of lift to its maximum may vary between data sets, all of the data for both transient and periodic vortex gusts yield similar decreases in lift past this point. (i.e., note the similarity in slope for $1.4 \leq t^* \leq 1.6$ in Figure 15-11). Furthermore, although the recovery time differs between cases, a local minima in lift is always observable past $t^* = 1.5$.

Finally, Figure 15-12 shows selected results from each set of data where, for clarity, only the curves representing an angle of attack as near 5° as possible are shown. Although scaling by the gust ratio does not perfectly collapse the entire data set, it does collapse the curves reported from each facility. That is, while gust ratio and effective angle of attack appear to be of primary importance to lift generation in a large-amplitude gust encounter, other factors (e.g., the velocity profile and/or vorticity distribution within the gust flow) also play a role.

Looking for a trend in ΔC_L for all of the data (both transverse and vortex gusts, transient and periodic), Figure 15-13 was created to highlight the effect of gust ratio on maximum ΔC_L. In both of the plots shown here, representing two regions of the parameter space, there appears to be a roughly linear relationship between maxΔC_L and gust ratio for the transverse gusts (CU and UMD, marked by squares). For the vortex gust cases, however, there are no obvious linear trends. Transverse gusts are relatively easily characterized by the gust ratio where the flow disturbance velocity, V, is measured at the location in the gust flow where the wing is expected to pass though the gust. Vortex gusts, however, have an extra degree of freedom: the distance at which the vortex passes the wing. For a given vortex strength, a vortex that passes closer to the wing will produce a larger force transient. As a result, the maximum lift force that occurs in a vortex gust encounter is not only a function of gust ratio, and thus these data do not collapse to a line. The vortex gust data instead spans the shaded region of Figure 15-13(b).

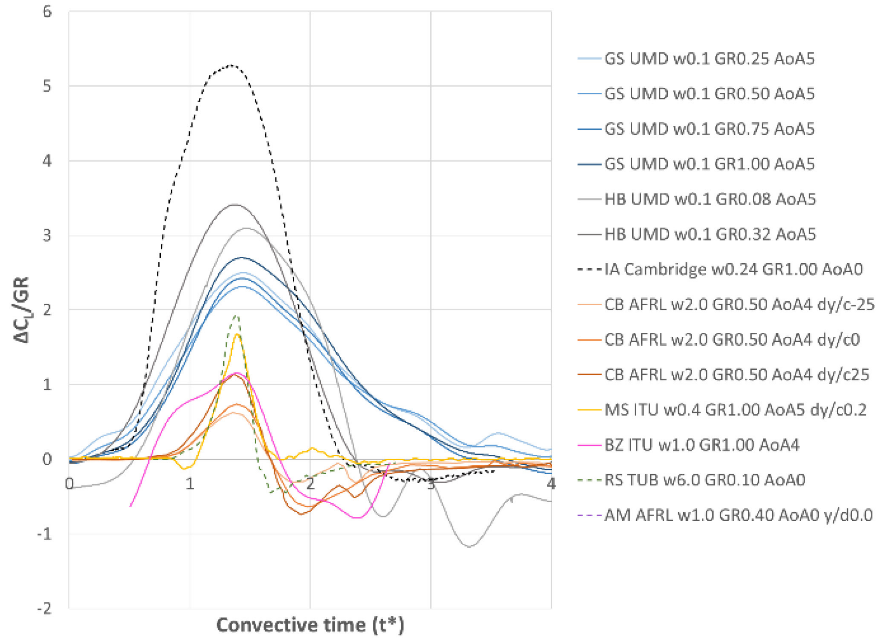

Figure 15-12: Comparison of Transverse and Vortex Gust Encounter Data for α ≤ 5°.

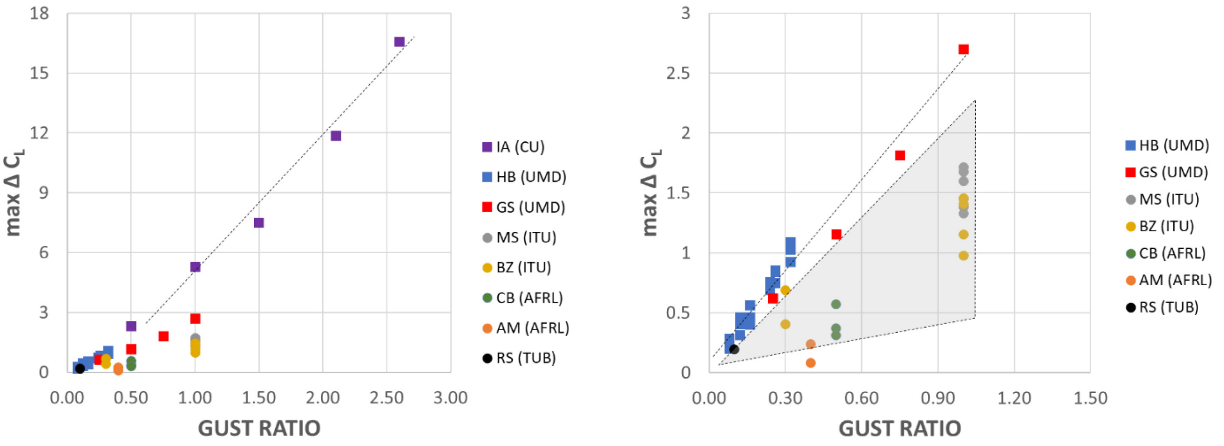

(a) Zoomed-Out View. **(b) Zoomed-In View.**

Figure 15-13: Maximum ΔC_L versus Gust Ratio. Transverse gusts are represented by squares; vortex gusts are represented by circles.

In Figure 15-14, more subtle characteristics of the force response are now shown: the response time (the time over which lift builds up during the gust encounter) versus the encounter width (the relative length of the gust encounter, We = w/c). Accounting for the encounter width brings most of the results together along the x-axis because this parameter was one of the design considerations in the experimental setups. As a result, most of the cases lie in a similar region of this plot, but response time does not appear to be obviously related to the encounter width.

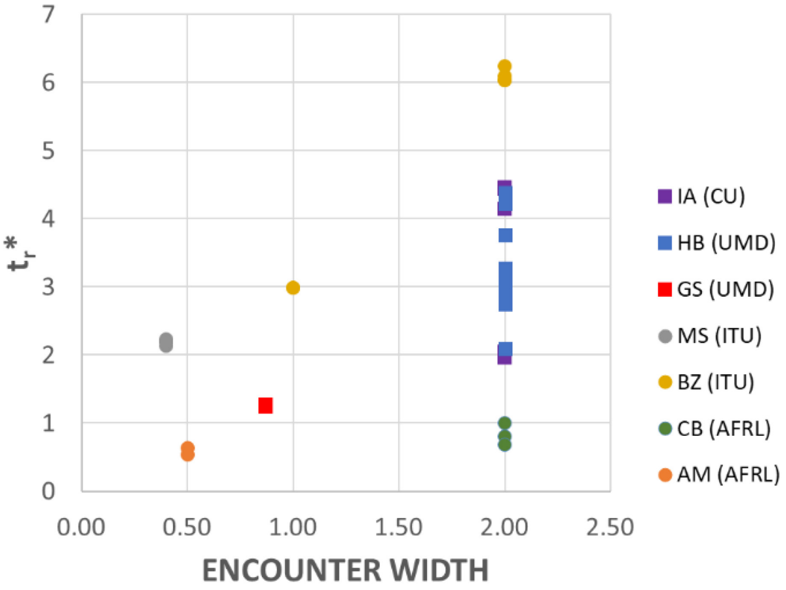

Figure 15-14: Time Response versus Encounter Width. Transverse gusts are represented by squares; vortex gusts are represented by circles.

Section III.B and Figure 1-6(b) introduced the idea of categorizing gust responses based on the magnitude of the force transient, maxΔC_L, and the time over which it occurs, t_r*. Unfortunately, as evident in Figure 15-15, the time response of the available data typically lies on a few vertical lines in the maxΔC_L versus 1/ t_r* parameter space. The experiments that produced the current dataset were designed for similar encounter widths (see Figure 15-14), and since the maximum force in these gust encounters is achieved when the wing is near the center of the gust, it should not be surprising that the data does not span a broad range of response times either. For a given facility, the gust width is generally fixed and wing size is limited by the capacity and sensitivity of the force sensor, so data tend to be acquired only at a few gust widths. Gust ratio, however, is more easily varied, and it is now well known that a larger gust ratio results in a larger maxΔC_L. For example, the three CU data points in Figure 15-15(a) where max$\Delta C_L > 6$ represent gust ratios larger than unity: $GR = \{1.5, 2.1, 2.6\}$. Gust ratios less than or equal to unity result in lower maxΔC_L and are represented by the remainder of the data points in Figure 15-15(a) and in Figure 15-15(b). Comparing the results of Figure 15-15 to the categorization of Figure 1-9(b), it appears that the current data does not span a broad enough parameter space to bin these gust encounters in separate categories. There is only one set of obvious outliers: the high gust ratio CU data. In this case, the magnitude of the response is large, but the response time is similar to the rest of the available data. To better categorize gust responses, the dataset must be broadened to include the rest of the results from AVT-282 and beyond.

Another way to interpret the gust response categorization of Figure 1-6(b) is based on the response slope, max$\Delta C_L/t_r$*, which quantifies how rapidly lift builds up in the gust encounter. Scaling the x-axis of Figure 15-15 in this way results in Figure 15-16. The data points that previously aligned in vertical lines of constant t_r* are now linear variations. For each data set, the peak response increases linearly with the response slope: maxΔCL = a max$\Delta C_L/t_r$*, where a varies with data set.

The *gust parameter* as defined in Section III.B, $G = GR/W_e$, combines the two characteristics of a gust that were hypothesized to dominate the force response on a wing in a large-amplitude gust encounter: the gust ratio and the encounter width. Consider for a moment this parameter to fully characterize the gust input to the system. The system output is then the lift response, which is characterized by the response slope. Figure 15-17 shows that there are, in general, linear variations between the input gust, G, and output lift response characteristics, max$\Delta C_L/t_r^*$. In Figure 15-17(b), note that the two sets of data from UMD lie on the same line. The same is true for the other facility with multiple datasets at similar gust ratios, ITU. This suggests that, in addition to the basic characteristics accounted for in the gust parameter, the shape of the gust profile affects force production and, in turn, the lift response. On the other hand, the same data sets from CU do not align as well, or align on two slopes depending on the gust ratio (see Figure 15-17(a)), i.e., the data points that have a gust ratio larger than unity lie on a different line than those at lower gust ratios. This could result from modifications to the facility that affected the gust profile, or there may be further things to consider at extremely high gust ratios. For example, at very gust ratios and low encounter widths, the wing experiences a very rapid change in effective angle of attack that may introduce complications. Data sets for the vortex gusts do not collapse as well. In this case, there may be different response slopes for the same gust parameter that depend on the vertical offset of the vortex trajectory.

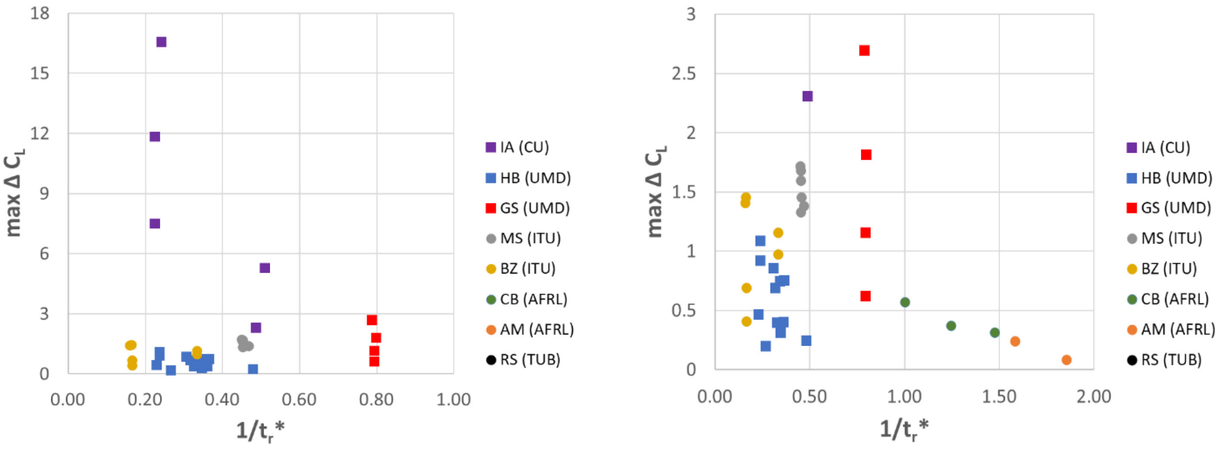

(a) Zoomed-Out View in y but Not x. **(b) Zoomed-In View in y but Out in x.**

Figure 15-15: Maximum ΔC_L versus Response Time. Transverse gusts are represented by squares; vortex gusts are represented by circles.

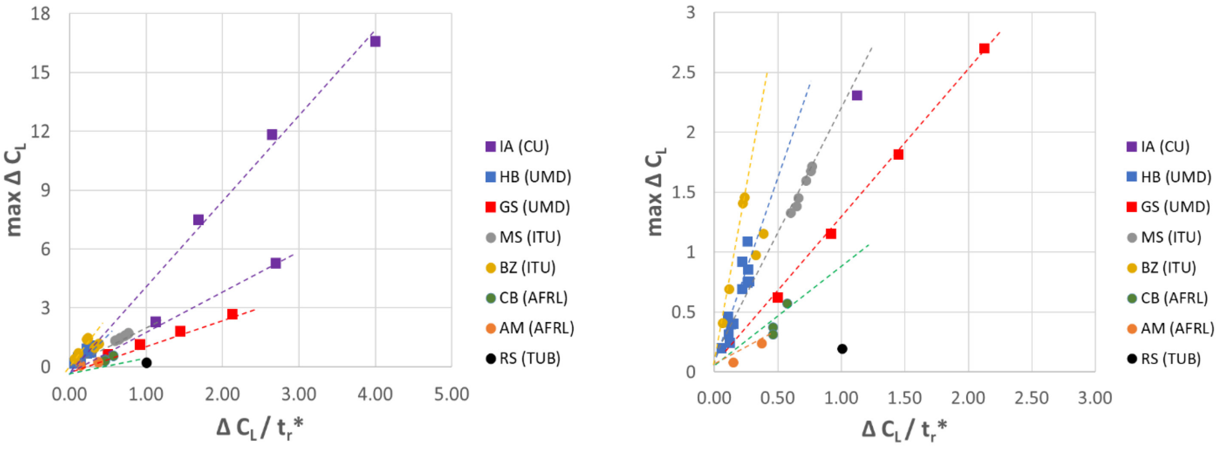

(a) Zoomed-Out View. **(b) Zoomed-In View.**

Figure 15-16: Maximum ΔC_L versus Response Slope. Transverse gusts are represented by squares; vortex gusts are represented by circles.

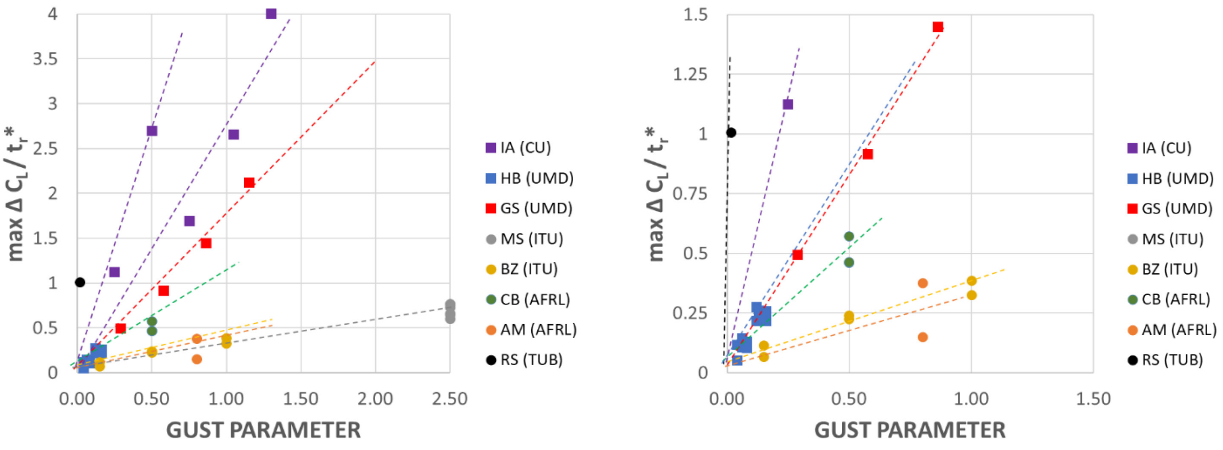

(a) Zoomed-Out View. **(b) Zoomed-In View.**

Figure 15-17: Response Slope versus Gust Parameter. Transverse gusts are represented by squares; vortex gusts are represented by circles.

All of that being said, the above analysis does oversimplify matters. One thing that has not yet been considered is the effect of the rate at which a wing passes through a gust. Intuitively, it would be possible to achieve different response slopes for a fixed gust parameter by passing through the gust faster or slower, thus changing the rate at which the wing interacts with the vorticity in the gust and the rate at which the effective angle of attack of the wing varies as it penetrates the gust flow. That is, a gust encounter not only affects the effective angle of attack of the wing, α_{eff}, but the effective pitch rate, $\dot{\alpha}_{eff}$. Ideally, a plot of response slope versus effective pitch rate would follow. This would allow us to:

1) Identify regions of the parameter space where the gust encounter can be simply modeled as an effective angle of attack variation, perhaps neglecting effective pitch rate after all; and

2) Quantify the effect of the steepness, i.e., vorticity concentration, of the gust flow itself. Unfortunately, in the current work, the effective angle of attack variation is obtained using time-resolved velocity field measurements which are not available for all data sets.

15.8 CONCLUSIONS

Over a four-year span from 2015 to 2019, the NATO STO AVT-282 research group has studied the unsteady aerodynamics of large-amplitude gust encounters. This collaborative research effort was undertaken by 31 group members representing 10 countries, as well as many more interested parties in ongoing communication with the group.

The group first set out to characterize the magnitude and length scales of real-world flow perturbations that would later define the gust encounter parameter space of interest. Using data from previous work in meteorology, flight in air wakes, rotorcraft, wind and tidal turbines, MAVs, UCAVs, vehicles in transition, and many other examples, a parameter space of interest was defined. In practice, the results obtained thus far have been limited by facility capabilities, many of which have been developed specifically for this work and some of which are not yet operational. To limit the scope of this report, most of the results reported here focus on gusts where the flow disturbance is of the same order of magnitude as the freestream and the gust length is of the same order of magnitude as the wing chord, but members of AVT-282 have explored gust encounters far beyond these constraints.

Three canonical gust types were defined: transverse gusts, vortex gusts, and streamwise gusts; and a considerable amount of data have been obtained, especially for transverse and vortex gusts. Fewer and mostly preliminary results are available for streamwise gusts as these facilities were generally in the design or construction phase at the start of the task group. A typical aerodynamic response has been obtained in terms of lift variation and numerical simulations, experiments, and theoretical models have successfully identified the physical mechanisms by which force transients are produced. Experimental results have been used to investigate the parameter space over which linear theories can be applied to large-amplitude gusts, and to validate CFD methods which have in turn provided insight into the underlying flow physics of a gust encounter, and have extended the bounds of the explored parameter space into that which is difficult or impossible to achieve in experiments. Notably, Grubb et al. [3] have performed a large parameter study on transverse gusts, the results which are too numerous to itemize here. More generally, while the current chapter is an attempt to summarize the overall results and conclusions from the group, it has inevitably and necessarily omitted many details and contributions. Readers are referred to the extensive reference list for further information.

The primary contribution of the current report is to present gust definitions, the parameter space of interest, and direct comparisons of a subset of the data generated by the group. The relationship between the aerodynamic gust response and basic gust parameters, namely gust ratio and encounter width, has been explored and these results suggest that future analysis should include the effects of the steepness of the gust profile, the distribution of vorticity in the gust, and the effective camber and pitch rate that is induced on the wing by the gust flow during the encounter.

Although preliminary closed-loop control based on the effective angle of attack has been promising [2], [14], control mechanisms to attenuate unsteady force responses in large amplitude gusts remain an important and unexplored area. As AVT-282 evolved, it became clear that the definition and characterization of large-amplitude gust encounters were a sufficiently complex problem that control for gust mitigation would not be achieved within the time limits of the group. As such, the mitigation problem will be tackled in the next four years in a new task group: AVT 347 on Large-Amplitude Gust Mitigation Strategies for Rigid Wings.

15.9 REFERENCES

[1] Jones, A.R., and Cetiner, O., Overview of NATO AVT-282: Unsteady aerodynamic response of rigid wings in gust encounters (Invited), AIAA SciTech, American Institute of Aeronautics and Astronautics, Orlando, FL, 2020.

[2] Andreu-Angulo, I., Babinsky, H., Biler, H., Sedky, G., and Jones, A., Wing-gust interactions: The effect of transverse velocity profile (Invited), AIAA SciTech, American Institute of Aeronautics and Astronautics, Orlando, FL, 2020.

[3] Grubb, A., Moushegian, A., Heathcote, D., and Smith, M., Physics and computational modeling of nonlinear transverse gust encounters (Invited), AIAA SciTech, American Institute of Aeronautics and Astronautics, Orlando, FL, 2020.

[4] Biler, H., and Jones, A.R., Force prediction during transverse and vortex gust encounters (Invited), AIAA SciTech, American Institute of Aeronautics and Astronautics, Orlando, FL, 2020.

[5] Gehlert, P., and Babinsky, H., Non-circulatory force on a finite thickness body encountering a gust (Invited), AIAA SciTech, American Institute of Aeronautics and Astronautics, Orlando, FL, 2020.

[6] Mulleners, K., Deparday, J., He, G., and Henne, S., Predicting unsteady flow separation in response to a flow disturbance (Invited), AIAA SciTech, American Institute of Aeronautics and Astronautics, Orlando, FL, 2020.

[7] Medina, A., Cetiner, O., Rockwood, M., Zaloglu, B., Saritas, M., and Gozukara, A., On the effects of discrete and continuous vortex-gust encounters (Invited), AIAA SciTech, American Institute of Aeronautics and Astronautics, Orlando, FL, 2020.

[8] Chen, H., and Jaworski, J., Aeroelastic encounters of spanwise vortex gusts and the self-rotation of trailing vortices (Invited), AIAA SciTech, American Institute of Aeronautics and Astronautics, Orlando, FL, 2020.

[9] Pohl, J., and Semaan, R., Quantification and modeling of dynamic lift on a DLR-F15 research airfoil with active trailing-edge flap (Invited), AIAA SciTech, American Institute of Aeronautics and Astronautics, Orlando, FL, 2020.

[10] He, X., and Williams, D.R., Unsteady aerodynamic loads on an airfoil at high angle of attack in a randomly surging flow (Invited), AIAA SciTech, American Institute of Aeronautics and Astronautics, Orlando, FL, 2020.

[11] Young, A., and Smyth, A., The interaction of a Sears-type sinusoidal gust with a cambered aerofoil in the presence of non-uniform streamwise flow (Invited), AIAA SciTech, American Institute of Aeronautics and Astronautics, Orlando, FL, 2020.

[12] Moriche, M., Flores, O., Sedky, G., Jones, A. R., and García-Villalba, M., Comparison between experiments and simulations of fast plunge maneuvers (Invited), AIAA SciTech, American Institute of Aeronautics and Astronautics, Orlando, FL, 2020.

[13] Chowdhury, J., Smith, C., and Ringuette, M., The lift force produced by an unsteady translating plate with a rotating tip, AIAA SciTech, American Institute of Aeronautics and Astronautics, Orlando, FL, 2020.

[14] Sedky, G., Lagor, F., and Jones, A.R., The unsteady aerodynamics of a transverse wing-gust encounter with closed-loop pitch control, AIAA SciTech, American Institute of Aeronautics and Astronautics, Orlando, FL, 2020.

[15] Jaworski, J. W., Sound from aeroelastic vortex-fibre interactions, Philosophical Transactions of the Royal Society A: Mathematical, Physical and Engineering Sciences, Vol. 377, No. 2159, 2019, p. 20190071.

[16] Deparday, J., and Mulleners, K., Modeling the interplay between the shear layer and leading edge suction during dynamic stall, Physics of Fluids, Vol. 31, No. 10, 2019, p. 107104.

[17] Marzanek, M.F., and Rival, D.E., Separation mechanics of non-slender delta wings during streamwise gusts, Journal of Fluids and Structures, Vol. 90, 2019, pp. 286-296.

[18] Gomez, D.F., Lagor, F.D., Kirk, P.B., Lind, A.H., Jones, A.R., and Paley, D.A., Data-driven estimation of the unsteady flowfield near an actuated airfoil, Journal of Guidance, Control, and Dynamics, Vol. 42, No. 10, 2019, pp. 2279-2287.

[19] Chen, H., and Jaworski, J.W., Acoustic emission of aeroelastic vortex-gust interactions, 23rd International Congress on Acoustics, Aachen, Germany, 2019.

[20] Biler, H., Badrya, C., and Jones, A.R., Experimental and computational investigation of transverse gust encounters, AIAA Journal, Vol. 13, No. 12, 2019, pp. 1-15.

[21] Corkery, S.J., Babinsky, H., and Graham, W.R., Quantification of added-mass effects using particle image velocimetry data for a translating and rotating flat plate, Journal of Fluid Mechanics, Vol. 870, 2019, pp. 492-518.

[22] Badrya, C., Baeder, J.D., and Jones, A.R., Application of prescribed velocity methods to a large-amplitude flat-plate gust encounter, AIAA Journal, Vol. 57, No. 8, 2019, pp. 3261-3273.

[23] Baddoo, P.J., Hajian, R., and Jaworski, J., A Jacobi spectral collocation method for the steady aerodynamics of porous aerofoils, AIAA Aviation 2019 Forum, American Institute of Aeronautics and Astronautics, Dallas, TX, 2019.

[24] Chen, H., Baddoo, P.J., and Jaworski, J., Modeling of Brown-Michael vortices in ground effect, AIAA Aviation 2019 Forum, American Institute of Aeronautics and Astronautics, Dallas, TX, 2019.

[25] Lefebvre, J.N., and Jones, A.R., Experimental investigation of airfoil performance in the wake of a circular cylinder, AIAA Journal, Vol. 57, No. 7, 2019, pp. 2808-2818.

[26] Rennie, R., Catron, B., Feroz, M., Williams, D., and He, X., Dynamic behavior and gust simulation in an unsteady flow wind tunnel, AIAA Journal, Vol. 57, No. 4, 2019, pp. 1423-1433.

[27] Manar, F.H., and Jones, A.R., Evaluation of potential flow models for unsteady separated flow with respect to experimental data, Physical Review Fluids, Vol. 4, No. 3, 2019, p. 034702.

[28] Gomez, D.F., Kirk, P.B., Lind, A., Lind, A.H., Jones, A.R., Paley, D., and Lagor, F., Unsteady DMD-based flow field estimation from embedded pressure sensors in an actuated airfoil, AIAA SciTech 2019 Forum, American Institute of Aeronautics and Astronautics, San Diego, CA, 2019.

[29] Gehlert, P., and Babinsky, H., Linking the unsteady force generation to vorticity for a translating and rotating cylinder, AIAA SciTech 2019 Forum, American Institute of Aeronautics and Astronautics, San Diego, CA, 2019.

[30] Badrya, C., and Baeder, J.D., Numerical study of a flat plate wing response to large transverse gusts at low Reynolds number, AIAA SciTech 2019 Forum, American Institute of Aeronautics and Astronautics, San Diego, CA, 2019.

[31] Medina, A., Suresh Babu, A.V., Rockwood, M.P., Gopalarathnam, A., Gopalarathnam, A., and Ahmed, A., Theoretical and experimental study of wake encounters on unsteady airfoils, AIAA SciTech 2019 Forum, American Institute of Aeronautics and Astronautics, San Diego, CA, 2019.

[32] Corkery, S.J., and Babinsky, H., An investigation into gust shear layer vorticity and the added mass force for a transverse wing-gust encounter, AIAA SciTech 2019 Forum, American Institute of Aeronautics and Astronautics, San Diego, CA, 2019.

[33] Pohl, J., Semaan, R., and Jones, A.R., Dynamic lift measurements on an airfoil with periodic flap motion at high Reynolds number, AIAA SciTech 2019 Forum, American Institute of Aeronautics and Astronautics, San Diego, CA, 2019.

[34] Smyth, A.S., Young, A.M., and Di Mare, L., The effect of 3D geometry on unsteady gust response, using a vortex lattice model, AIAA SciTech 2019 Forum, American Institute of Aeronautics and Astronautics, San Diego, CA, 2019.

[35] Biler, H., Jones, A.R., Saritas, M., Fenercioglu, I., Cetiner, O., and Bronz, M., Investigation of force transients during transverse and vortex gust encounters, AIAA SciTech 2019 Forum, American Institute of Aeronautics and Astronautics, San Diego, CA, 2019.

[36] Jarman, L., Lefebvre, J., Jones, A.R., and Smith, M.J., Dynamics of an airfoil moving through the wake of a circular cylinder, AIAA SciTech 2019 Forum, American Institute of Aeronautics and Astronautics, San Diego. CA, 2019.

[37] Williams, D.R., Stasse, Q., and Rennie, M.R., Lift, drag, and moment response of a UCAS model experiencing longitudinal von Karman gust spectra, AIAA SciTech 2019 Forum, American Institute of Aeronautics and Astronautics, San Diego, CA, 2019.

[38] Moushegian, A., and Smith, M.J., Analysis of a wing moving through a nonlinear gust, AIAA SciTech 2019 Forum, American Institute of Aeronautics and Astronautics, San Diego, CA, 2019.

[39] Chen, H., and Jaworski, J., Aeroelastic trajectory selection of vortex gusts impinging upon Joukowski airfoils, AIAA SciTech 2019 Forum, American Institute of Aeronautics and Astronautics, San Diego, CA, 2019.

[40] Smyth, A., and Young, A., Three-dimensional unsteady hydrodynamic modelling of tidal turbines, Proceedings of the European Wave and Tidal Energy Conference, 2019.

[41] Kirk, P.B., and Jones, A.R., Vortex formation on surging aerofoils with application to reverse flow modelling, Journal of Fluid Mechanics, Vol. 859, 2019, pp. 59-88.

[42] Sedky, G., Lagor, F.D., and Jones, A.R., Lift modeling and regulation for a finite wing during transverse gust encounters, AIAA SciTech, American Institute of Aeronautics and Astronautics, San Diego, CA, 2019.

[43] Perrotta, G., and Jones, A.R., Quasi-steady approximation of forces on flat plate due to large-amplitude plunging maneuvers, AIAA Journal, Vol. 56, No. 11, 2018, pp. 4232-4242.

[44] Corkery, S.J., Babinsky, H., and Harvey, J.K., On the development and early observations from a towing tank-based transverse wing-gust encounter test rig, Experiments in Fluids, Vol. 59, No. 9, 2018.

[45] Henne, S., Parikh, A., Deparday, J., and Mulleners, K., Dynamic stall vortex shedding and associated load fluctuations, 19th International Symposium on the Applications of Laser and Imaging Techniques to Fluid Mechanics, Lisbon, Portugal, 2018.

[46] Jaworski, J., Hydroelastic motions of flexible fibers, 2018 AIAA/CEAS Aeroacoustics Conference, American Institute of Aeronautics and Astronautics, Atlanta, GA, 2018.

[47] Engin, K., Aydin, E., Zaloglu, B., Fenercioglu, I., and Cetiner, O., Large scale spanwise periodic vortex gusts or single spanwise vortex impinging on a rectangular wing, 2018 Fluid Dynamics Conference, American Institute of Aeronautics and Astronautics, Atlanta, GA, 2018.

[48] Chen, H., and Jaworski, J., Vortex interactions with Joukowski airfoil on elastic supports, 2018 Fluid Dynamics Conference, American Institute of Aeronautics and Astronautics, Atlanta, GA, 2018.

[49] Leung, J.M., Wong, J.G., Weymouth, G.D., and Rival, D.E., Modeling transverse gusts using pitching, plunging, and surging airfoil motions, AIAA Journal, Vol. 13, No. 12, 2018, pp. 1-8.

[50] Kal, I., Son, O., Zaloglu, B., and Cetiner, O., Gust effect on a plunging flexible wing, 5th International Conference on Experimental Fluid Mechanics, Munich, Germany, 2018.

[51] Corkery, S.J., and Babinsky, H., Force production mechanisms for a flat plate wing at low Reynolds numbers, 2018 AIAA Aerospace Sciences Meeting, American Institute of Aeronautics and Astronautics, Kissimmee, FL, 2018.

[52] Corkery, S.J., Babinsky, H., and Harvey, J., Response of a flat plate wing to a transverse gust at low Reynolds numbers, 2018 AIAA Aerospace Sciences Meeting, American Institute of Aeronautics and Astronautics, Kissimmee, FL, 2018.

[53] Smith, Z.F., Jones, A.R., and Hrynuk, J.T., Micro air vehicle scale gust-wing interaction in a wind tunnel, 2018 AIAA Aerospace Sciences Meeting, American Institute of Aeronautics and Astronautics, Kissimmee, FL, 2018.

[54] Biler, H., Badrya, C., and Jones, A.R., Experimental and computational investigation of transverse gust encounters, 2018 AIAA Aerospace Sciences Meeting, American Institute of Aeronautics and Astronautics, Kissimmee, FL, 2018.

[55] Eroglu, B., Zaloglu, B., Cetiner, O., and Gozukara, A.C., A computational study for a wing at or pitching up to high angle of attack in presence of a spanwise gust, 9th Ankara International Aerospace Conference, Ankara, Turkey, 2017.

[56] Kal, I., Zaloglu, B., Fenercioglu, I., and Cetiner, O., An experimental investigation of a plunging wing under gust environment, 9th Ankara International Aerospace Conference, Ankara, Turkey, 2017.

[57] Manar, F.H., and Jones, A.R., Transient response of a single degree-of-freedom wing at high angle-of-attack, AIAA Journal, Vol. 55, No. 11, 2017, pp. 3681-3692.

[58] Perrotta, G., and Jones, A.R., Unsteady forcing on a flat-plate wing in large transverse gusts, Experiments in Fluids, Vol. 58, No. 8, 2017, p. 101.

[59] Mulleners, K., Mancini, P., and Jones, A.R., Flow development on a flat-plate wing subjected to a streamwise acceleration, AIAA Journal, Vol. 55, No. 6, 2017, pp. 2118-2122.

[60] Graham, W.R., Pitt Ford, C., and Babinsky, H., An impulse-based approach to estimating forces in unsteady flow, Journal of Fluid Mechanics, Vol. 815, 2017, pp. 60-76.

[61] Eldredge, J.D., and Jones, A.R., Leading-edge vortices: Mechanics and modeling, Annual Review of Fluid Mechanics, Vol. 51, No. 1, 2017, pp. annurev-fluid-010518-040334.

[62] Manar, F.H., and Jones, A.R., Vorticity production at the leading edge of flat plates at high incidence, 55th AIAA Aerospace Sciences Meeting, American Institute of Aeronautics and Astronautics, Grapevine, TX, 2017.

[63] Corkery, S.J., Stevens, R.J., and Babinsky, H., Low Reynolds number surge response of a flat plate wing at 90 degrees incidence, 55th AIAA Aerospace Sciences Meeting, American Institute of Aeronautics and Astronautics, Grapevine, TX, 2017.

[64] Son, O., Zaloglu, B., Percin, M., and Cetiner, O., Force measurement and load estimation studies at ITU for flexible flapping wings and maneuvering wings under gust, NIOPLEX International Workshop on Non-Intrusive Optical Flow Diagnostics, Delft, Netherlands, 2016.

[65] Mulleners, K., Mancini, P., and Jones, A.R., Experimental investigation of a large aspect ratio flat plate encountering a steam-wise gust, 46th AIAA Fluid Dynamics Conference, American Institute of Aeronautics and Astronautics, Washington, DC, 2016.

[66] Jaworski, J., Vortex sound generation from flexible fibers, 22nd AIAA/CEAS Aeroacoustics Conference, American Institute of Aeronautics and Astronautics, Lyon, France, 2016, p. 837.

[67] Perrotta, G.M., and Jones, A.R., Transient aerodynamics of large transverse gusts and geometrically similar maneuvers, 54th AIAA Aerospace Sciences Meeting, American Institute of Aeronautics and Astronautics, San Diego, CA, 2016.

[68] Mancini, P., Manar, F.H., Granlund, K., Ol, M.V., and Jones, A.R., Unsteady aerodynamic characteristics of a translating rigid wing at low Reynolds number, Physics of Fluids, Vol. 27, No. 12, 2015.

[69] Biler, H., Zaloglu, B., and Cetiner, O., Loading on a maneuvering NACA 0012 airfoil under spanwise gust and estimation of loads using DPIV, Workshop on Non-Intrusive Measurements for Unsteady Flows and Aerodynamics, Poitiers, France, 2015.

[70] Biler, H., Zaloglu, B., and Cetiner, O., Effect of a spanwise gust on a wing, 8th Ankara Interntional Aerospace Conference, Ankara, Turkey, 2015.

[71] Son, O., Zaloglu, B., and Cetiner, O., Experimental investigation of a wing performing a pitch-up motion under gust environment, 9th Ankara International Aerospace Conference, 2017.

[72] Klein, S., Hahn, D., Scholz, P., and Radespiel, R., Vortex interactions with a high-lift airfoil in a low speed wind tunnel, 43rd Fluid Dynamics Conference, San Diego, CA, 2013.

[73] Moriche, M., Gonzalo, A., Flores, O., and García-Villalba, M., Fast transverse maneuvers at low Reynolds numbers, AIAA SciTech 2019 Forum, American Institute of Aeronautics and Astronautics, San Diego, CA, 2019.

[74] Chowdhury, J., Cook, L., and Ringuette, M., The vortex formation of an unsteady translating plate with a rotating tip, AIAA SciTech, American Institute of Aeronautics and Astronautics, San Diego, CA, 2019.

[75] Rockwood, M., and Medina, A., Controlled generation of periodic vortical gusts by the rotational oscillation of a circular cylinder and attached plate, Experiments in Fluids, 2020, p. Ahead of Print.

[76] Dai, W., Pisetta, G., and Viola, I.M., Morphing blades for passive load control of tidal turbines, 13th European Wave and Tidal Energy Conference, 2019.

[77] Bird, H.J.A., Otomo, S., Ramesh, K., and Viola, I.M., A geometrically non-linear time-domain unsteady lifting-line theory, AIAA SciTech, San Diego, CA, 2019.

[78] Dai, W., Balaras, E., and Viola, I.M., Self-sustained limit-cycle oscillations in a flapping-foil energy harvester," European Conference on Computational Mechanics (Solids, Structures and Coupled Problems) (ECCM 6) and the European Conference on Computational Fluid Dynamics (ECFD 7), Glasgow, UK, 2018.

[79] NATO STO: Extension of fundamental flow physics to practical MAV aerodynamics, STO-TR-AVT-202, NATO STO, May 2016.

[80] NATO RTO: Investigation of airwake control for safer shipboard aircraft operations, RTO-TR-AVT-102, NATO RTO, June 2007.

[81] Granlund, K., Monnier, B., Ol, M., and Williams, D.R., Airfoil longitudinal gust response in separated vs. attached flows, Physics of Fluids, Vol. 26, No. 2, 2014.

[82] Greenblatt, D., Development and testing of an unsteady low-speed wind tunnel, 31st AIAA Aerodynamic Measurement Technology and Ground Testing Conference, American Institute of Aeronautics and Astronautics, Dallas, TX, 2015.

[83] Rennie, M., Catron, B., Feroz, M. Z., and Williams, D.R., Model predictive control of wind-tunnel wind speed for low-Re unsteady aerodynamic testing, AIAA SciTech, American Institute of Aeronautics and Astronautics, 2018.

[84] Choi, J., Colonius, T., and Williams, D.R., Surging and plunging oscillations of an airfoil at low Reynolds number, Journal of Fluid Mechanics, Vol. 763, 2015, pp. 237-253.

[85] Greenblatt, D., Unsteady low-speed wind tunnels, AIAA Journal, Vol. 54, No. 6, 2016, pp. 1817-1830.

[86] Greenberg, J.M., Airfoil in sinusoidal motion in a pulsating stream, Tech. Rep. 1326, NACA, Jun. 1947.

[87] Von Karman, T., and Sears, W.R., Airfoil theory for non-uniform motion, Journal of the Aeronautical Sciences, Vol. 5, 1938, pp. 379-390.

[88] Barnes, C.J., and Visbal, M.R., Effects of vertical position and orientation on a vortical-gust/airfoil interaction at a transitional Reynolds number, 47th AIAA Fluid Dynamics Conference, American Institute of Aeronautics and Astronautics, Denver, CO, 2017.

[89] Bansal, S., Azzam, A., and Lavoie, P., On the generation of unsteady flows using an active grid and the effect of freestream turbulence on longitudinal gust response of an airfoil, NATO STO AVT-282 meeting in Athens, Greece, Dec. 2018.

[90] Bansal, S., and Lavoie, P., UTIAS initial research findings for an airfoil in periodic streamwise gusts, Notes from AVT-282, 2019.

[91] Azzam, A., and Lavoie, P., Production of unsteady flows through the use of an active grid, APS Division of Fluid Dynamics, 2017.

[92] Barnes, C.J., and Visbal, M.R., Counterclockwise vortical-gust/airfoil interactions at a transitional Reynolds Number, AIAA Journal, Vol. 56, No. 7, 2018, pp. 2540-2552.

[93] Barnes, C.J., and Visbal, M.R., Clockwise vortical-gust/airfoil interactions at a transitional Reynolds number, AIAA Journal, Vol. 56, No. 10, 2018, pp. 3863-3874.

[94] Barnes, C.J., and Visbal, M.R., Further investigations of vortical gust/airfoil interactions at a transitional Reynolds number, 2018 AIAA Aerospace Sciences Meeting, American Institute of Aeronautics and Astronautics, Kissimmee, FL, 2018.

[95] Barnes, C., and Visbal, M., Angle of attack and core size effects on transitional counterclockwise vortical-gust/airfoil interactions, AIAA Journal, Under review.

[96] Corkery, S.J., Unsteady aerodynamics of wing gust encounters, Ph.D. thesis, Cambridge, UK, 2019.

[97] Gehlert, P., Andreu-Angulo, I., and Babinsky, H., AVT-282: Cambridge findings regarding a top-hat shaped gust, Notes from AVT-282, 2019.

[98] Peng, D., and Gregory, J.W., Asymmetric distributions in pressure/load fluctuation levels during blade-vortex interactions, Journal of Fluids and Structures, Vol. 68, 2017, pp. 58-71.

[99] Peng, D., and Gregory, J., Vortex dynamics during blade-vortex interactions, Physics of Fluids, Vol. 27, No. 5, 2015, p. 053104.

[100] Chen, H., and Jaworski, J., Aeroelastic interactions and trajectory selection of vortex gusts impinging upon Joukowski airfoils, Journal of Fluids and Structures, Sub judice.

[101] Granlund, K., Ol, M.V., and Jones, A.R., Streamwise oscillation of airfoils into reverse flow, AIAA Journal, Vol. 54, No. 5, 2016, pp. 1628-1636.

[102] Atassi, H.M., The Sears problem for a lifting airfoil revisited – New results, Journal of Fluid Mechanics, Vol. 141, No. 1, 1984, pp. 109-122.

[103] Wales, C., Jones, D., and Gaitonde, A., Prescribed velocity method for simulation of aerofoil gust responses, Journal of Aircraft, Vol. 52, No. 1, 2015, pp. 64-76. doi:10.2514/1.C032597.

[104] Golubev, V., Hollenshade, T., Nguyen, L., and Visbal, M., High-accuracy low-Re simulations of airfoil-gust and airfoil-vortex interactions, 40th Fluid Dynamics Conference and Exhibit, American Institute of Aeronautics and Astronautics, Chicago, IL, 2010.

[105] Smith, M.J., Jacobson, K., and Bern, A., Initial computational assessment for nonlinear gust analysis, Presentation at the NATO AVT 282 Panel Meeting, Avila, Spain, September 2016.

REPORT DOCUMENTATION PAGE

1. Recipient's Reference	2. Originator's References	3. Further Reference	4. Security Classification of Document
	STO-TR-AVT-282 AC/323(AVT-282)TP/974	ISBN 978-92-837-2295-3	PUBLIC RELEASE

5. Originator

Science and Technology Organization
North Atlantic Treaty Organization
BP 25, F-92201 Neuilly-sur-Seine Cedex, France

6. Title

Unsteady Aerodynamic Response of Rigid Wings in Gust Encounters

7. Presented at/Sponsored by

Transverse, streamwise, and vortex gust encounters strong enough to result in large-scale flow separation and large force transients are investigated.

8. Author(s)/Editor(s)	9. Date
Multiple	October 2020

10. Author's/Editor's Address	11. Pages
Multiple	282

12. Distribution Statement

There are no restrictions on the distribution of this document. Information about the availability of this and other STO unclassified publications is given on the back cover.

13. Keywords/Descriptors

Gust encounter; Lift; Unsteady aerodynamics; Vortex dynamics; Wakes

14. Abstract

Many modern air vehicle operations are currently limited by operational envelopes restricted to ensure vehicle safety and performance in highly unsteady aerodynamic environments. Surveillance, reconnaissance, pickups and deliveries, and search and rescue may all take place in complex terrain, airwakes, and severe weather, and are currently restricted to benign flow disturbances and conservative operational envelopes. AVT-282 aimed to extent the state of the art in unsteady lift modeling and prediction in support of the development of robust flight vehicle performance where wind gusts are of the same order of magnitude as the vehicle's flight speed, and where disturbance rejection may be achieved via closed-loop flow control. Several types of canonical large-amplitude gusts were studied, and similar lift responses were found for transverse, vortex, and streamwise gust encounters. Lift was found to be a direct result of flow separation and the subsequent formation of strong vortices, with an additional contribution from the free vorticity in the gust flow itself. Linear inviscid theories were found to provide reasonable predictions of lift response for gusts much larger than intended but failed in extreme cases. Stronger gusts resulted in stronger force transients and longer recovery times.

NORTH ATLANTIC TREATY ORGANIZATION

SCIENCE AND TECHNOLOGY ORGANIZATION

BP 25
F-92201 NEUILLY-SUR-SEINE CEDEX • FRANCE
Télécopie 0(1)55.61.22.99 • E-mail mailbox@cso.nato.int

DIFFUSION DES PUBLICATIONS
STO NON CLASSIFIEES

Les publications de l'AGARD, de la RTO et de la STO peuvent parfois être obtenues auprès des centres nationaux de distribution indiqués ci-dessous. Si vous souhaitez recevoir toutes les publications de la STO, ou simplement celles qui concernent certains Panels, vous pouvez demander d'être inclus soit à titre personnel, soit au nom de votre organisation, sur la liste d'envoi.

Les publications de la STO, de la RTO et de l'AGARD sont également en vente auprès des agences de vente indiquées ci-dessous.

Les demandes de documents STO, RTO ou AGARD doivent comporter la dénomination « STO », « RTO » ou « AGARD » selon le cas, suivi du numéro de série. Des informations analogues, telles que le titre est la date de publication sont souhaitables.

Si vous souhaitez recevoir une notification électronique de la disponibilité des rapports de la STO au fur et à mesure de leur publication, vous pouvez consulter notre site Web (http://www.sto.nato.int/) et vous abonner à ce service.

CENTRES DE DIFFUSION NATIONAUX

ALLEMAGNE
Streitkräfteamt / Abteilung III
Fachinformationszentrum der Bundeswehr (FIZBw)
Gorch-Fock-Straße 7, D-53229 Bonn

BELGIQUE
Royal High Institute for Defence – KHID/IRSD/RHID
Management of Scientific & Technological Research
for Defence, National STO Coordinator
Royal Military Academy – Campus Renaissance
Renaissancelaan 30, 1000 Bruxelles

BULGARIE
Ministry of Defence
Defence Institute "Prof. Tsvetan Lazarov"
"Tsvetan Lazarov" bul no.2
1592 Sofia

CANADA
DGSIST 2
Recherche et développement pour la défense Canada
60 Moodie Drive (7N-1-F20)
Ottawa, Ontario K1A 0K2

DANEMARK
Danish Acquisition and Logistics Organization
(DALO)
Lautrupbjerg 1-5
2750 Ballerup

ESPAGNE
Área de Cooperación Internacional en I+D
SDGPLATIN (DGAM)
C/ Arturo Soria 289
28033 Madrid

ESTONIE
Estonian National Defence College
Centre for Applied Research
Riia str 12
Tartu 51013

ETATS-UNIS
Defense Technical Information Center
8725 John J. Kingman Road
Fort Belvoir, VA 22060-6218

FRANCE
O.N.E.R.A. (ISP)
29, Avenue de la Division Leclerc
BP 72
92322 Châtillon Cedex

GRECE (Correspondant)
Defence Industry & Research General
Directorate, Research Directorate
Fakinos Base Camp, S.T.G. 1020
Holargos, Athens

HONGRIE
Hungarian Ministry of Defence
Development and Logistics Agency
P.O.B. 25
H-1885 Budapest

ITALIE
Ten Col Renato NARO
Capo servizio Gestione della Conoscenza
F. Baracca Military Airport "Comparto A"
Via di Centocelle, 301
00175, Rome

LUXEMBOURG
Voir Belgique

NORVEGE
Norwegian Defence Research
Establishment
Attn: Biblioteket
P.O. Box 25
NO-2007 Kjeller

PAYS-BAS
Royal Netherlands Military
Academy Library
P.O. Box 90.002
4800 PA Breda

POLOGNE
Centralna Biblioteka Wojskowa
ul. Ostrobramska 109
04-041 Warszawa

PORTUGAL
Estado Maior da Força Aérea
SDFA – Centro de Documentação
Alfragide
P-2720 Amadora

REPUBLIQUE TCHEQUE
Vojenský technický ústav s.p.
CZ Distribution Information Centre
Mladoboleslavská 944
PO Box 18
197 06 Praha 9

ROUMANIE
Romanian National Distribution
Centre
Armaments Department
9-11, Drumul Taberei Street
Sector 6
061353 Bucharest

ROYAUME-UNI
Dstl Records Centre
Rm G02, ISAT F, Building 5
Dstl Porton Down
Salisbury SP4 0JQ

SLOVAQUIE
Akadémia ozbrojených síl gen.
M.R. Štefánika, Distribučné a
informačné stredisko STO
Demänová 393
031 01 Liptovský Mikuláš 1

SLOVENIE
Ministry of Defence
Central Registry for EU & NATO
Vojkova 55
1000 Ljubljana

TURQUIE
Milli Savunma Bakanlığı (MSB)
ARGE ve Teknoloji Dairesi
Başkanlığı
06650 Bakanliklar – Ankara

AGENCES DE VENTE

The British Library Document
Supply Centre
Boston Spa, Wetherby
West Yorkshire LS23 7BQ
ROYAUME-UNI

Canada Institute for Scientific and
Technical Information (CISTI)
National Research Council Acquisitions
Montreal Road, Building M-55
Ottawa, Ontario K1A 0S2
CANADA

Les demandes de documents STO, RTO ou AGARD doivent comporter la dénomination « STO », « RTO » ou « AGARD » selon le cas, suivie du numéro de série (par exemple AGARD-AG-315). Des informations analogues, telles que le titre et la date de publication sont souhaitables. Des références bibliographiques complètes ainsi que des résumés des publications STO, RTO et AGARD figurent dans le « NTIS Publications Database » (http://www.ntis.gov).

NORTH ATLANTIC TREATY ORGANIZATION

BP 25
F-92201 NEUILLY-SUR-SEINE CEDEX • FRANCE
Télécopie 0(1)55.61.22.99 • E-mail mailbox@cso.nato.int

SCIENCE AND TECHNOLOGY ORGANIZATION

DISTRIBUTION OF UNCLASSIFIED STO PUBLICATIONS

AGARD, RTO & STO publications are sometimes available from the National Distribution Centres listed below. If you wish to receive all STO reports, or just those relating to one or more specific STO Panels, they may be willing to include you (or your Organisation) in their distribution.

STO, RTO and AGARD reports may also be purchased from the Sales Agencies listed below.

Requests for STO, RTO or AGARD documents should include the word 'STO', 'RTO' or 'AGARD', as appropriate, followed by the serial number. Collateral information such as title and publication date is desirable.

If you wish to receive electronic notification of STO reports as they are published, please visit our website (http://www.sto.nato.int/) from where you can register for this service.

NATIONAL DISTRIBUTION CENTRES

BELGIUM
Royal High Institute for Defence – KHID/IRSD/RHID
Management of Scientific & Technological Research for Defence, National STO Coordinator
Royal Military Academy – Campus Renaissance
Renaissancelaan 30
1000 Brussels

BULGARIA
Ministry of Defence
Defence Institute "Prof. Tsvetan Lazarov"
"Tsvetan Lazarov" bul no.2
1592 Sofia

CANADA
DSTKIM 2
Defence Research and Development Canada
60 Moodie Drive (7N-1-F20)
Ottawa, Ontario K1A 0K2

CZECH REPUBLIC
Vojenský technický ústav s.p.
CZ Distribution Information Centre
Mladoboleslavská 944
PO Box 18
197 06 Praha 9

DENMARK
Danish Acquisition and Logistics Organization (DALO)
Lautrupbjerg 1-5
2750 Ballerup

ESTONIA
Estonian National Defence College
Centre for Applied Research
Riia str 12
Tartu 51013

FRANCE
O.N.E.R.A. (ISP)
29, Avenue de la Division Leclerc – BP 72
92322 Châtillon Cedex

GERMANY
Streitkräfteamt / Abteilung III
Fachinformationszentrum der Bundeswehr (FIZBw)
Gorch-Fock-Straße 7
D-53229 Bonn

GREECE (Point of Contact)
Defence Industry & Research General Directorate, Research Directorate
Fakinos Base Camp, S.T.G. 1020
Holargos, Athens

HUNGARY
Hungarian Ministry of Defence
Development and Logistics Agency
P.O.B. 25
H-1885 Budapest

ITALY
Ten Col Renato NARO
Capo servizio Gestione della Conoscenza
F. Baracca Military Airport "Comparto A"
Via di Centocelle, 301
00175, Rome

LUXEMBOURG
See Belgium

NETHERLANDS
Royal Netherlands Military Academy Library
P.O. Box 90.002
4800 PA Breda

NORWAY
Norwegian Defence Research Establishment, Attn: Biblioteket
P.O. Box 25
NO-2007 Kjeller

POLAND
Centralna Biblioteka Wojskowa
ul. Ostrobramska 109
04-041 Warszawa

PORTUGAL
Estado Maior da Força Aérea
SDFA – Centro de Documentação
Alfragide
P-2720 Amadora

ROMANIA
Romanian National Distribution Centre
Armaments Department
9-11, Drumul Taberei Street
Sector 6
061353 Bucharest

SLOVAKIA
Akadémia ozbrojených síl gen M.R. Štefánika, Distribučné a informačné stredisko STO
Demänová 393
031 01 Liptovský Mikuláš 1

SLOVENIA
Ministry of Defence
Central Registry for EU & NATO
Vojkova 55
1000 Ljubljana

SPAIN
Área de Cooperación Internacional en I+D
SDGPLATIN (DGAM)
C/ Arturo Soria 289
28033 Madrid

TURKEY
Milli Savunma Bakanlığı (MSB)
ARGE ve Teknoloji Dairesi Başkanlığı
06650 Bakanliklar – Ankara

UNITED KINGDOM
Dstl Records Centre
Rm G02, ISAT F, Building 5
Dstl Porton Down, Salisbury SP4 0JQ

UNITED STATES
Defense Technical Information Center
8725 John J. Kingman Road
Fort Belvoir, VA 22060-6218

SALES AGENCIES

The British Library Document Supply Centre
Boston Spa, Wetherby
West Yorkshire LS23 7BQ
UNITED KINGDOM

Canada Institute for Scientific and Technical Information (CISTI)
National Research Council Acquisitions
Montreal Road, Building M-55
Ottawa, Ontario K1A 0S2
CANADA

Requests for STO, RTO or AGARD documents should include the word 'STO', 'RTO' or 'AGARD', as appropriate, followed by the serial number (for example AGARD-AG-315). Collateral information such as title and publication date is desirable. Full bibliographical references and abstracts of STO, RTO and AGARD publications are given in "NTIS Publications Database" (http://www.ntis.gov).

ISBN 978-92-837-2295-3